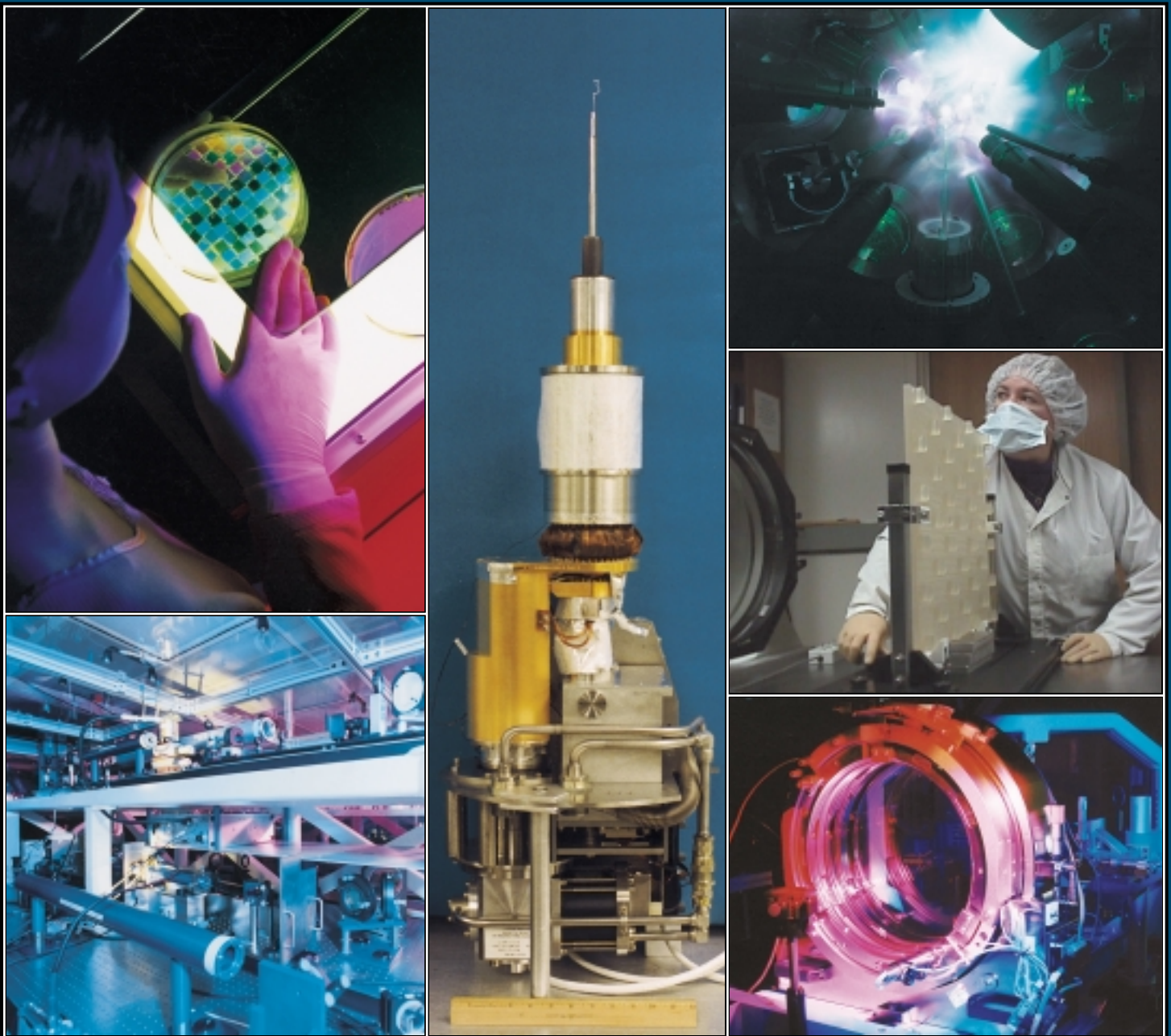# LLE 1999 Annual Report

October 1998 – September 1999

UR
LLE

Cover Photos

Upper Left: Over 300 liquid crystal (LC) optics are used in OMEGA for beam polarization control. Buffed polymer layers are critical for establishing macroscopic alignment over the large apertures required in the system. Here, Ph.D. student Tanya Kosc validates the long-term quality of alignment for a prototype LC distributed polarization rotator that was manufactured over 15 years ago.

Lower Left: A two-dimensional smoothing by spectral dispersion (2-D SSD) system recently installed on OMEGA is capable of producing phase-modulated spectra that can be frequency tripled to 1-THz bandwidth in the ultraviolet. This 2-D SSD system incorporates a high-frequency bulk-phase modulator operating at 10.4 GHz to produce 11 Å of bandwidth in the infrared. Efficient frequency tripling of this broadband signal requires dual-tripler frequency-conversion crystals that are currently installed on only 13 beams. The high-frequency bulk-phase modulator can also be operated at 3 Å with a higher dispersion grating to produce three SSD color cycles, which significantly improves beam smoothing at lower bandwidths on all 60 OMEGA beams.

Center: The moving cryostat maintains a target at a constant temperature to layer the DT ice and transports the target to the center of the target chamber. The cryostat base is shown. At the bottom is the cryo cooler. Above the cooler are the 4-axis positioner and two thermal shrouds that are maintained at 45 K and 16 K. The target assembly is at the top. The target is mounted on spiders silk in a C-shaped beryllium support.

Upper Right: The cryogenic target positioner (cryostat base) is used to place a 4-mm-diam pointing sphere at the center of the OMEGA chamber.

Center Right: Hope D'Alessandro, electronics technician, prepares a NIF deformable mirror substrate for surface figure testing on LLE's 18-in.-aperture interferometer. The mirror will allow wavefront correction of the NIF beam when the 39 posts on the back of the mirror are bonded to actuators on a reaction block. LLE will be coating the substrates with a low-stress, dielectric high reflector and assembling the deformable mirrors for Lawrence Livermore National Laboratory.

Lower Right: The experimental setup for off-line tuning of the dual-tripler, OMEGA frequency-tripling crystals. The frequency-tripling scheme for high-bandwidth conversion was proposed by D. Eimerl *et al.* [Opt. Lett. **22**, 1208 (1997)] and experimentally demonstrated by LLE [Opt. Lett. **23**, 927 (1998)]. In the off-line setup, a single laser pulse of 1053-nm wavelength, 100-ps duration, and approximately Gaussian spatial profile with 4-mm FWHM is generated using a Nd:YLF-based amplifier configuration. Broad bandwidth is simulated by varying the angle of incidence on the crystals. The off-line technique allows crystal phase-matching angles to be accurately determined and transferred into OMEGA. Conversion of 1-μm radiation to its third harmonic with an overall energy conversion efficiency approaching 70% and a UV bandwidth of ~1 THz was recently demonstrated on OMEGA.

University of Rochester
Laboratory for Laser Energetics

LLE 1999 Annual Report

October 1998 – September 1999

UR
LLE

Inertial Fusion Program and
National Laser Users' Facility Program

Contents

Executive Summary

The fiscal year ending September 1999 (FY99) concluded the second year of the cooperative agreement (DE-FC03-92SF19460) five-year renewal with the U. S. Department of Energy (DOE). This report summarizes research at the Laboratory for Laser Energetics (LLE), the operation of the National Laser Users' Facility (NLUF), and programs involving education of high school, undergraduate, and graduate students for FY99.

Progress in Laser Fusion

A principal mission of the University of Rochester's Laboratory for Laser Energetics is to study the direct-drive approach to inertial confinement fusion (ICF). During the past year we have made a number of advances in our understanding of direct-drive ICF through the use of the OMEGA facility and the use of our computational and theoretical capabilities. A major part of the LLE program is directed toward developing the potential for direct drive for an ignition demonstration on the National Ignition Facility (NIF) under construction at the Lawrence Livermore National Laboratory (LLNL).

Long-scale-length plasmas with parametric relevance to the NIF have been produced and characterized on the OMEGA system (pp. 1–11). On the basis of these experiments we have concluded that stimulated Raman scattering (SRS) and stimulated Brillouin scattering (SBS) are unlikely to cause unacceptable losses or produce unacceptable preheat through instabilities on NIF-scale targets.

We have modeled the stability of self-focused filaments in laser-produced plasmas. A wave-equation treatment of the laser light combined with self-consistent filament equilibrium simulations indicates that only very small filaments, where one waveguide mode is propagating, may be considered to be stable. When two or more waveguide modes can propagate, the filament tends to break up within tens of microns (pp. 191–196).

Direct drive requires high uniformity of irradiation. The article beginning on p. 12 describes our efforts using a number of beam-smoothing techniques to achieve increased uniformity on the OMEGA system and our projections for the uniformity that will be available on the NIF. We believe that on OMEGA the rms uniformity will be in excess of 99% (averaged over 300 ps) when beam-smoothing enhancements are completed for the facility. For the NIF, we project an even higher degree of uniformity using these same techniques.

Our study of hollow-shell implosions on the 60-beam OMEGA system (pp. 82–91) yielded information about target performance as a function of laser-irradiation uniformity and temporal laser pulse shape. We have found that pulse-shaped implosions place more stringent requirements on power balance and initial target-illumination uniformity. As improvements in laser drive are made, we expect higher neutron yields and higher areal densities than those obtained in these experiments.

In another set of experiments we investigated target performance enhancements when smoothing by spectral dispersion (SSD) was used to improve illumination uniformity. Time-integrated UV equivalent-target-plane imaging was used to compare two-dimensional SSD beam-smoothing rates to theoretical predictions for the 0.2-THz system on OMEGA (pp. 149–155). This work supports our confidence that larger-bandwidth SSD systems will produce enhanced smoothing.

Embedded titanium layers in spherical targets were used to determine the areal density of compressed shells. Target performance enhancement with the SSD beam smoothing is characterized using this method (pp. 139–148). A pinhole-array x-ray spectrometer captures core images below and above the K edge of titanium. The results are compared with two-dimensional *ORCHID* simulations.

The implementation of broadband smoothing on OMEGA with two-dimensional SSD is discussed beginning on p. 197. The article describes issues relevant to the architecture choices made during the design phase of the project, as well as measurements conducted to verify the laser bandwidth and ensure that FM to AM conversion is minimized.

The effect of temporal pulse shape on laser imprint and beam smoothing has been studied (pp. 203–208). Preimposed modulations on planar-foil targets were used to calibrate the mass equivalence of features imprinted by the laser, and the resulting growth rates are compared to numerical simulations.

A number of hydrodynamic instabilities arise in laser-driven implosions. While it is not possible to eliminate these instabilities, every effort must be made to limit the amount of implosion degradation they could cause. We have developed an analytic theory of the ablative Richtmyer–Meshkov instability. The principal result of this research (pp. 30–35) is that the instability exhibits a stabilizing mechanism due to the dynamic overpressure of the blowoff plasma with respect to target material.

While the effect of hydrodynamic instabilities on the performance of ICF targets is well known, techniques are required to characterize the sources of nonuniformities that can seed these instabilities. One such source is the surface roughness of the inside of the DT cryogenic fuel. Our numerical investigation of characterization of thick cryogenic-fuel layers using convergent beam interferometry (pp. 131–138) indicates that this optical technique can be used to isolate the surface under investigation and resolve the perturbations at the relevant level.

The nonlinear evolution of broad-bandwidth, laser-imprinted nonuniformities in planar targets accelerated by 351-nm laser light with beam-smoothing techniques was studied using throughfoil radiography. The saturation of three-dimensional perturbations produced by laser imprinting was observed and compared to those predicted by the Haan model (pp. 156–173). Modeling laser imprint in ICF targets is discussed in theoretical work (pp. 185–190) where the model describing the evolution of laser imprint shows that growth is determined by the velocity and acceleration perturbations generated by the laser-beam nonuniformities. Thermal smoothing inside a hot plasma corona suppresses only the acceleration perturbation, while the mass ablation suppresses both velocity and acceleration perturbations. The model predicts that directly driven NIF targets will remain intact during the implosion when the laser is smoothed with 1-THz SSD used on our current point designs.

In planning for direct-drive ignition on the NIF we have conducted a theoretical analysis of direct-drive NIF targets (pp. 121–130). We established that specifications required on the NIF ensure a successful direct-drive ignition demonstration using a baseline direct-drive target design. Independent

calculations conducted by the Lawrence Livermore National Laboratory have confirmed these calculations.

Diagnostics Development

The evolution of ever-increasing sophisticated diagnostics to measure ICF events has been remarkable to observe over the last 20 years. As experiments become more complex and quantitative, diagnostic instruments must meet significant challenges to measure many details required for a comprehensive understanding of the underlying physics in ICF. As the National program prepares for an ignition demonstration on the NIF, all of the participating institutions are developing the required diagnostics. Similarly, as our understanding of directly driven targets increases with our use of OMEGA, more and better diagnostics are constantly in demand.

A novel charged-particle diagnostic has been developed that performs simultaneous ρR measurements of the fuel, shell, and ablator regions of a compressed ICF target, consisting of an inner DT-fuel region, a plastic (CH) shell, and an ablator (CD), by measuring the knock-on deuteron spectrum (pp. 17–25).

LLE continues the productive collaboration with our colleagues at MIT and LLNL to develop charged-particle magnetic spectrometers. We have demonstrated on OMEGA the diagnostic capability of two of these spectrometers. As an initial application, the simultaneous measurements of the fuel areal density, shell areal density, and fuel temperature have been carried out using D^3He-filled imploding capsules (pp. 93–96). Our initial experiments demonstrated the ability to carry out these measurements at fuel ion temperatures of 3 to 6 keV, fuel areal densities in the range of 10 to 20 mg/cm^2, and shell areal densities in the range of 40 to 60 mg/cm^2. Measurements like these can be applied to the parameter region characteristic of cryogenic-fuel capsules on OMEGA. In future experiments, we will extend such measurements to higher fuel and shell areal densities and validate these techniques on cryogenic-fuel targets.

Laser and Optical Materials and Technology

We have designed and tested an efficient, bulk-phase modulator operating at approximately 10.5 GHz, which can produce substantial phase-modulated bandwidth with modest microwave drive power (pp. 53–61). This modulator is the cornerstone of the 1-THz UV bandwidth operation for OMEGA. The resonator design employs an adapted form of cutoff-waveguide coupling and velocity matching to yield a simple, high-Q microwave design with practical clear-aperture

dimensions suitable for applications in a 2-D SSD system. The design is scalable to other frequencies by simply changing the electro-optic crystal dimensions. The measured microwave performance of the modulator agrees well with performance predicted from fully anisotropic, three-dimensional numerical simulations.

Flexible modeling tools are required to simulate the generation and propagation of two-dimensional SSD pulsed laser beams. The Waasese code was developed to simulate the ideal and nonideal behavior of the many optical components that comprise the SSD driver line, including their relative positions (pp. 62–81). The code predicts measurable signatures that function as diagnostic tools since they are associated with particular optical components. Minimizing any amplitude modulation in the driver line will ensure the safety and lifetime of OMEGA optics by circumventing the effects of small-scale self-focusing. The code has proved to be an indispensable modeling tool for the OMEGA laser, and its inherent flexibility will provide a means to enhance its capabilities to model other laser propagation issues such as nonlinear propagation, on-target uniformity, amplifier gain, scattering losses, and pinhole clipping.

Laser-fusion experiments require precise control of the temporal profile of optical pulses applied to targets. While OMEGA has had a pulse-shaping capability for some time, the demands on the precision, flexibility, and repeatability of the optical pulse-shaping system have increased. To meet the new requirements, an aperture-coupled stripline electrical-waveform generator has been designed. The model we have developed (pp. 97–104) allows one to produce accurately shaped optical pulses suitable for injection into the OMEGA system. The model requires the solution of the telegraph equations using the method of characteristics.

A measurement technique has been developed that enables the complete characterization of electronic devices having any dynamic temporal and spectral frequency response, such as the photoconductive microwave switches on the OMEGA pulse-shaping system (pp. 105–113). The technique is a superset of a form of input–output relationships called the scattering or *S* parameter; this technique can also be applied to any microwave or millimeter-wave device whose properties vary rapidly, such as photoconductive attenuators, phase shifters, and directional couplers.

High-peak-power lasers for fusion applications, such as OMEGA, must constantly deal with optical damage in many

components. We have studied the damage to the fused-silica spatial-filter lenses on the OMEGA laser system (pp. 114–120). LLE has implemented a plan to maintain the quality of OMEGA optics that includes frequent inspection and *in-situ* cleaning of optics. With the establishment of safe operational damage criteria, laser operation has not been impeded. The implications, morphologies, possible causes, and ongoing long-term experiments of spatial-filter lens damage are discussed in the article.

Because of its excellent homogeneity and low-intrinsic absorption properties, fused silica remains the preferred material for high-power laser applications over a wide wavelength range. Deciding when to replace spot-damage-afflicted fused-silica optics or, in the case of inaccessible space-based lasers, predicting the useful service life of fused-silica optics before catastrophic, pulsed-laser-driven crack growth shatters a part has recently become simpler. We report results from stress-inhibited laser-crack propagation and stress-delayed damage-initiation experiments in fused silica at 351 nm (pp. 26–29). The damage-initiation threshold was observed to increase by 70% when a modest amount of mechanical stress was applied to the fused-silica optic. Research is underway presently to determine the ramifications of these findings for large-aperture systems, such as OMEGA. In related work (pp. 174–179), we have obtained experimental results on stress-inhibited, laser-driven crack growth and stress-delayed laser-damage-initiation thresholds in fused silica and borosilicate glass (BK-7). The use of different loading geometries providing uniaxial and biaxial stresses shows that the biaxial stress configuration offers superior efficiency in raising the laser-damage-initiation threshold by up to 78% and arresting crack growth down to 30% relative to stress-free conditions.

We have measured the output signal-to-noise ratio (SNR) of a Nd:YLF regenerative amplifier and have found that our measurements are in excellent agreement with the predictions of a simple theoretical model (pp. 209–212). The model includes amplified spontaneous emission and noise injected into the amplifier.

Magnetorheological finishing (MRF) is a novel and recently commercialized process for figuring and polishing plano, convex, and concave optics (both spherical and aspherical) from a wide variety of optical materials. We discuss the development of new magnetorheological fluids to extend the finishing technique to two soft, single-crystal, optical materials: CaF_2 and KDP (pp. 213–219). Material-removal functions are characterized through analysis of polishing

spots generated on a new research platform at the Center for Optics Manufacturing.

Advanced Technology

Rose bengal is a dye used in photodynamic therapy. Photodynamic therapy is a treatment in which the combination of a dye, light, and oxygen causes photochemically induced cell death. We present what we believe to be the first study of a triplet state of rose bengal that is produced by 1064-nm excitation of T_1 (pp. 36–47). The triplet-triplet absorption cross section was measured between 825 nm and 1100 nm. The state was further characterized using two-step laser-induced fluorescence to determine its thermalization rate, lifetime, and quantum yield of reverse intersystem crossing. Similar two-step laser-induced fluorescence measurements were made of the triplet excited by 632-nm light.

We have measured the picosecond response of optically driven YBaCuO (YBCO) microbridge and Josephson-junction integrated structures (pp. 48–52). Single-picosecond switching of a high-temperature-superconductor Josephson junction was observed, and the junction turn-on delay time was measured. These findings provide confirmation of the potential of YBCO for ultrafast optical and electrical transient detection and processing.

Charged particles interacting with an oscillating electromagnetic field will seek regions of low intensity. We have observed electron trapping in an intense single-beam ponderomotive optical trap (pp. 180–184). Thomson-scattered light from the electron trap was enhanced through the use of a novel trapping focus of the laser. The scatter distribution is compared with simulations for ordinary and trapping-focus beams.

Laser Facility Report

FY99 was a very productive year for the OMEGA system. We recorded 1207 shots on target for experiments for LLE, LLNL, LANL, and NLUF users. This is the second fiscal year where we have used an extended shot schedule (12 h/day, 3 days/week). Many of the shots took advantage of the 1-h cycle time for OMEGA. During FY99, a number of major system modifications were made; these modifications are discussed beginning on p. 222. Most notably, improved individual-beam uniformity resulting from an upgrade of the 2-D SSD system was achieved (see the article beginning on p. 197). We have also added second tripler frequency-conversion crystal assemblies to 13 of the 60 beams. These additional triplers

allow efficient frequency conversion for laser bandwidths up to 1 THz. This is the first stage of a project to modify all 60 beams to be able to use 1-THz SSD in future experiments.

In preparation for cryogenic-target experiments, the upper and lower pylons of the cryogenic target handling system were installed on OMEGA. The system will be fully activated in FY00.

National Laser Users' Facility (NLUF)

Beginning on p. 223, we report on FY99 NLUF experiments. During the year, significant progress was made on several NLUF projects. A total of 144 OMEGA target shots were dedicated to the NLUF program during FY99.

In addition to NLUF-supported programs, several direct- and indirect-drive experiments, also coordinated through the NLUF manager, were carried out on OMEGA by groups from LLNL and LANL. These experiments are conducted for both ICF research and research in support of the Stockpile Stewardship Program. This program was formally initiated by the FY94 Defense Authorization (PL 103-160) to "*establish a stewardship program to ensure the preservation of the core intellectual and technical competencies of the United States in nuclear weapons*." Since the Nova laser at LLNL was decommissioned in May 1999, the National laboratories are making increased use of the OMEGA facility.

Thirteen proposals were submitted to NLUF for FY00. A DOE technical evaluation panel reviewed the proposals and recommended approval of seven proposals for funding. The accepted proposals are summarized in Table 80.VIII on p. 225.

Education at LLE

As the only university major participant in the National ICF Program, education continues to be a most important mission for the Laboratory. Graduate students play a significant role in LLE's research activities and are participating in research using the world's most powerful ultraviolet laser for fusion research on OMEGA. Fourteen faculty from five departments collaborate with LLE's scientists and engineers. Presently 42 graduate students are pursuing Ph.D. degrees at the Laboratory. The research interests vary widely and include theoretical and experimental plasma physics, laser–matter interaction physics, high-energy-density physics, x-ray and atomic physics, nuclear fusion, ultrafast optoelectronics, high-power-laser development and applications, nonlinear optics, optical mate-

rials and optical fabrication technology, and target fabrication. Technological developments from ongoing Ph.D. research will continue to play an important role on OMEGA.

One hundred thirty-three University of Rochester students have earned Ph.D. degrees at LLE since its founding. An additional 63 graduate students and 20 postdoctoral positions from other universities were funded by NLUF grants. The most recent University of Rochester Ph.D. graduates and their thesis titles are

D. Jacobs-Perkins   *Design, Analysis, and Implementation of an Ultrafast Electro-Optic Electric-Field Imaging System*

V. Smalyuk   *Experimental Investigation of the Nonlinear Rayleigh–Taylor Instability in CH Foils Irradiated by UV Light*

R. Ejnisman   *Studies with Ultracold Atoms*

A. Chirokikh   *Stimulated Brillouin Scattering Experiments on OMEGA*

M. Currie   *Ultrafast Electro-Optic Testing of Superconducting Electronics*

R. Giacone   *Spatiotemporal Evolution and Nonlinear Kinetic Simulations of Stimulated Brillouin Scattering*

J. Bromage   *Creating Rydberg Electron Wave Packets Using Terahertz Pulses*

P. Rudy   *Manipulation of Laser Cooled Atoms Via Dynamical Optical Potentials*

E. Alfonso   *Chemistry and Processing of Polymer Shells*

B. Conger   *Polarized Photoluminescence from Nematic and Chiral-Nematic Films*

P. Rodney   *The Photophysics of Ionic Semiconductors at Low Temperatures: Silver Bromide, Silver Iodide, and Cuprous Oxide*

Approximately 50 University of Rochester undergraduate students participated in work or research projects at LLE this past year. Student projects include operational maintenance of the OMEGA laser system, work in the materials and optical-thin-film coating laboratories, programming, image processing, and diagnostic development. This is a unique opportunity for these students, many of whom will go on to pursue a higher degree in the area in which they have participated at the Laboratory.

LLE continues to run a Summer High School Student Research Program (pp. 220–221) where this year 12 high school juniors spent eight weeks performing individual research projects. Each student is individually supervised by a staff scientist or an engineer. At the conclusion of the program, the students make final oral and written presentations on their work. The written reports are published as an LLE report. One of this year's participants, Aman Narang of the Harley School, has been named a semifinalist in the 1999 Intel Science Talent Search for his summer project. His research topic was "Analysis of the 3ω SSD spectrum of an OMEGA laser beamline"; he was supervised by Dr. W. Donaldson.

In 1999, LLE presented its third William D. Ryan Inspirational Teacher Award to Mr. John Harvey of Honeoye Falls–Lima Senior High School. Alumni of our Summer High School Student Research Program were asked to nominate teachers who had a major role in exciting their interest in science, mathematics, and/or technology. The award, which includes a $1000 cash prize, was presented at the High School Student Summer Research Symposium. Mr. Harvey, a mathematics teacher, was nominated by Jeremy Yelle and David Rae, participants in the 1997 program. "I have never met another teacher that was so passionate for what he teaches, and communicates himself well enough to get even the most complicated of ideas into the simplest of minds," wrote Yelle in his nomination letter. Mr. Rae added, "Mr. Harvey must also be recognized for his dedication to students after the books have closed and the homework has been passed in."

Robert L. McCrory
Director

Laser–Plasma Interactions in Long-Scale-Length Plasmas Under Direct-Drive National Ignition Facility Conditions

The National Ignition Facility (NIF) (currently under construction), with a nominal laser energy of 1.8 MJ, is expected to achieve ignition in both direct-[1,2] and indirect-drive[3] configurations. The mission of the University of Rochester's Laboratory for Laser Energetics is to study the direct-drive approach to inertial confinement fusion (ICF), where the capsule is directly irradiated by a large number of symmetrically arranged laser beams. To validate the performance of high-gain, direct-drive target designs planned for the NIF,[2] an understanding of the laser–plasma interactions in the coronal plasmas of these targets is essential. These interactions include stimulated Raman scattering (SRS), stimulated Brillouin scattering (SBS), the two-plasmon decay instability (TPD), and filamentation.[4] Their significance for direct-drive capsule performance arises either from detrimental suprathermal-electron generation due to plasma wave–breaking or other nonlinear processes (SRS, TPD), or through a reduction in drive power or drive uniformity (SBS, filamentation).

When the incident laser beam intensity exceeds the threshold levels for the various parametric instabilities, power is transferred from the incident laser light to lower-frequency electromagnetic, electron-plasma, or ion-acoustic waves if the energy ($\omega_0 = \omega_1 + \omega_2$) and momentum conservation ($\underline{k}_0 = \underline{k}_1 + \underline{k}_2$) relationships are satisfied (phase matching). Here, ω_0 and $\underline{k}_0$ represent the pump-wave (laser) frequency and wave vector. The SRS decay products are an electron-plasma wave and a scattered electromagnetic wave, which are denoted by the subscripts 1 and 2. The TPD results when the incident laser light decays into two electron-plasma waves. Phase matching occurs for SRS and the TPD at electron densities n_e less than or equal to the quarter-critical density $n_c/4$. When the phase-matching conditions are satisfied for SBS, the incident laser light decays into an ion-acoustic wave and a scattered electromagnetic wave.

A 1.5-MJ, $\alpha = 3$ (α is defined as the ratio of the cold fuel pressure to the Fermi-degenerate pressure) laser pulse is planned for an all-DT direct-drive target design on the NIF.[2] This pulse has a peak on-target intensity I_{total} of 2×10^{15} W/cm^2 (summed over all beams) and a foot intensity of 4×10^{13} W/cm^2. The cluster intensities $I_{cluster}$ (summed over four individual beams) are approximately a factor of 10 lower than I_{total}. The coronal plasma predicted for this design has an electron temperature T_e of ~4 keV, a density scale length $L_n (= n_e / \nabla n_e)$ of ~0.75 mm, and a velocity-gradient scale length $L_v [(= c_s / \nabla v)$, where c_s is the ion-acoustic velocity and v is the velocity] of ~0.5 mm at the peak of the laser pulse and at densities of 0.1 n_c to 0.2 n_c. While parametric instabilities have been studied extensively under conditions relevant to indirect-drive ICF,[5,6] the results presented here represent their first study in NIF-scale direct-drive plasmas.

This article reports on experiments under plasma conditions representative of the peak of the NIF direct-drive laser pulse, since they are the most challenging to create. The experiments were performed on the 30-kJ, 351-nm, 60-beam OMEGA laser system,[7] with distributed phase plates (DPP's)[8] and $f/6$ focusing lenses on all beams. The targets, all made of CH, included exploding foils and solids. The exploding foils produced large, millimeter-scale plasmas with T_e ~4 keV and a peak on-axis n_e between 0.1 n_c and 0.2 n_c. These temperatures and densities were diagnosed using time-resolved x-ray and visible (SRS backscattering) spectroscopy, respectively, and the observations were found to be consistent with the predictions of the two-dimensional Eulerian hydrodynamics code *SAGE*.[9] The solid-target plasmas were predicted to reach similar temperatures and to have similar density profiles below ~0.1 n_c; however, while they lacked the large plateau region characteristic of exploding foils, they included a critical-density surface and were in this sense more representative of NIF conditions.

When both foil and solid-target plasmas were irradiated with an interaction beam at 1.5×10^{15} W/cm^2, the direct-backscattered SBS signal was found to be completely absent. Some direct-backscattered SRS was observed in the solid-target plasmas at a very low level, with a conservative upper limit of ~5%.

In the following sections simulations of the NIF direct-drive plasmas carried out with the one-dimensional hydrodynamics code *LILAC*[10] are presented; the production of long-scale-length plasmas on OMEGA is discussed together with *SAGE* simulations; the characterization of the plasma electron temperature and density and comparisons with *SAGE* predictions are analyzed; and the SRS and SBS measurements are presented. The main conclusion of this research is that SRS and SBS are not likely to have a significant impact on target performance at the peak of the NIF direct-drive laser pulse.

NIF Direct-Drive Plasmas

LILAC calculations of the 1.5-MJ, $\alpha = 3$ direct-drive target are shown in Fig. 77.1. This figure gives the predicted trajectories of the imploding target, the critical-density surface, and the $n_c/4$ and $n_c/10$ surfaces. It is seen that the density scale length and electron temperature increase with time as the laser pulse makes the transition from the foot to the peak intensity. The dashed line shows the laser power history.
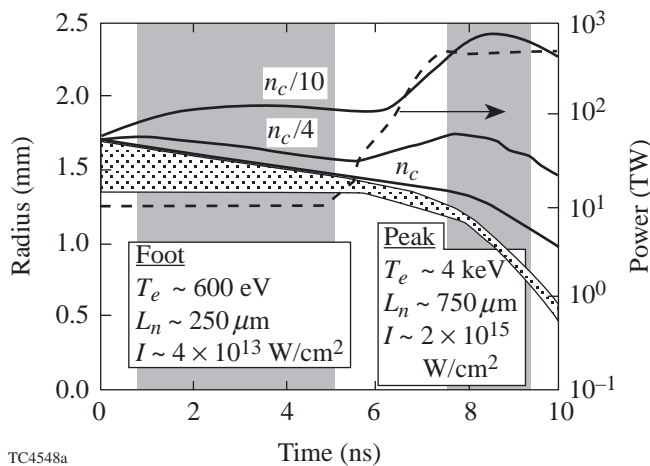

TC4548a

Figure 77.1
Radius versus time calculated by *LILAC* for a high-gain, direct-drive target planned for the NIF with 1.5 MJ and $\alpha = 3$. The dotted area represents the solid density region, and the solid lines give the trajectories of the critical, quarter-critical, and tenth-critical surfaces. The dashed line indicates the laser power as a function of time. The gray areas represent the "foot" and "peak" portions of the pulse, for which the calculated values of electron temperature T_e, density scale length $L_n (= n_e/\nabla n_e)$, and on-target intensity I (summed over all beams) are indicated.

A summary of parameters for the foot and peak of this pulse, including the predicted intensity thresholds $I_{\text{threshold}}$ for the SBS, SRS, and TPD instabilities, is given in Table 77.I. Approximations for these thresholds were taken from Kruer.[4] These thresholds may be compared with the cluster intensity I_{cluster}, i.e., the intensity summed over the four beams in a NIF

cluster, and the total overlapped intensity I_{total}. In the case of SRS it is anticipated that the phase-matching conditions will be satisfied only for the light within the *f*/8 NIF cluster, so that the appropriate comparison is with I_{cluster}. In the case of SBS, more than one cluster may drive the instability, but the relevant threshold intensity is likely to be significantly less than I_{total}. As shown in Table 77.I, I_{cluster} is less than $I_{\text{threshold}}$ for all the instabilities during the foot of the laser pulse. During the peak of the pulse I_{cluster} is about an order of magnitude lower than $I_{\text{threshold}}$ for SRS and SBS. These comparisons support the expectation that significant SRS and SBS will not occur in direct-drive NIF plasmas. However, the intensities quoted here represent averages over many speckles produced by the phase plates; inside the speckles the peak intensities may be several times higher. It should also be noted that I_{cluster} is 2.5 times greater than $I_{\text{threshold}}$ for the TPD instability during the peak of the pulse; thus, the TPD instability (not included in the present work because the geometrical configuration is not optimum for its study) should be investigated.

Production of Long-Scale-Length Plasmas on OMEGA

The long-scale-length plasmas created on OMEGA made use of a design similar to that used on the former 24-beam OMEGA laser system.[11] The 60 OMEGA beams were divided into various groups that irradiated the target from different angles and at different times (see Figs. 77.2 and 77.3). Both exploding foils and solid targets were irradiated first by primary beams (*P*), whose purpose is to form the plasma, and then by secondary beams (*S*), which heat the plasma and can be used to control its temperature. The CH foil targets were 1.2 mm in diameter, a little larger than the laser spot diameter, and 18 to 20 μm thick. The solid targets included 1.5-mm-diam planar slabs and partial spheres with thicknesses greater than 80 μm, predicted to result in similar plasma conditions. In both cases the plasmas were irradiated by an interaction beam of variable timing, incident along the initial target normal.

The timing sequence of the various groups of beams was similar for foils and solid targets. It is shown in Fig. 77.3, which gives the time history of the incident, absorbed, and transmitted laser powers. All beams were 1-ns square pulses with various delays. The primary beams were split into two groups: P_1, from 0 to 1 ns, with angle of incidence ~20°, and P_2, from 1 to 2 ns and incident at ~40°. For the foil targets, these beams served to explode the foils. By the end of the second group (P_2) the foils became underdense on axis because the phase-plate focal spot distribution is Gaussian-like with its maximum in the center. This resulted in some transmitted laser power starting at 1.5 ns, as seen in Fig. 77.3(a). The secondary beams

Table 77.I: Parameters for the foot and peak portions of the 1.5-MJ, $\alpha = 3$, direct-drive target planned for NIF, including coronal plasma conditions and intensity threshold approximations for parametric instabilities.

	Foot	Peak
T_e	0.6 keV	4 keV
L_n	0.25 mm	0.75 mm
L_v	0.5 mm	0.5–1.0 mm
I_{total}	4×10^{13} W/cm^2	2×10^{15} W/cm^2
$I_{cluster}$	4×10^{12} W/cm^2	2×10^{14} W/cm^2
$I_{threshold}$ (SBS)	4.6×10^{14} W/cm^2 at $n_c/10$	2×10^{15} W/cm^2 at $n_c/10$
$I_{threshold}$ (SRS)	5.0×10^{15} W/cm^2	1.7×10^{15} W/cm^2
$I_{threshold}$ (TPD)	3.4×10^{13} W/cm^2	8×10^{13} W/cm^2

E8705a
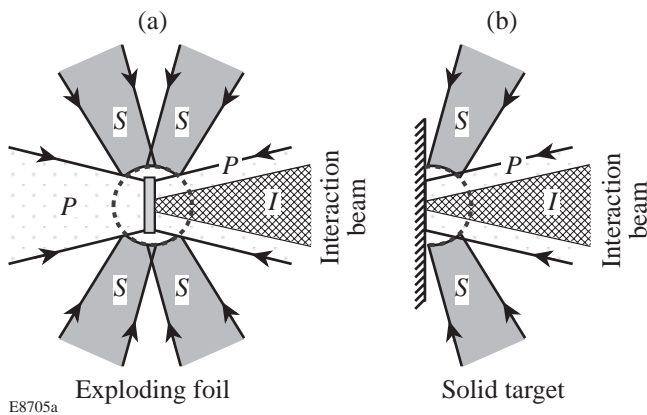
Figure 77.2

Geometry for the formation of long-scale-length plasmas on the OMEGA laser system. (a) A CH foil is irradiated and exploded with primary (*P*) and (delayed) secondary (*S*) laser beams. (b) A solid CH target is irradiated with primary and secondary laser beams from one side. In both cases the plasma (shown schematically by the dashed curves) is irradiated by an interaction beam (*I*) with variable timing.

The on-target laser energy was typically 500 J per beam. The exploding-foil plasmas were irradiated with a total of 19 kJ of laser energy from 38 beams. Depending on the number of secondary beams used, the solid targets were irradiated with either 19 or 29 beams from one side to deliver 8 to 12 kJ, producing plasmas with predicted electron temperatures of 3 and 4 keV, respectively.

The DPP's used on all beams except the interaction beam produced a focal-spot intensity distribution whose envelope was approximately Gaussian in shape with a full-width-at-half-maximum diameter of 480 μm and a diameter of 950 μm enclosing 95% of the energy. The interaction beam used a different DPP, designed to produce a similar focal-spot shape but scaled down a factor of 2.8 in diameter. The peak intensity in space and time for a nominal 500-J beam was 1.6×10^{15} W/cm^2 for the interaction beam and 2.1×10^{14} W/cm^2 for the other beams. On most shots 2-D SSD[12] was used (on all beams), with a bandwidth of 0.25 THz in the UV.

Contour plots of the predicted T_e and n_e at 2.6 ns are shown in Fig. 77.4 for the two types of plasma. Below eighth-critical density, the two plasmas have very similar density, temperature, and velocity profiles. These are similar to those anticipated for the NIF direct-drive target. For the exploding-foil plasma the density profile on axis has a full width at half-maximum of 1 mm. For the solid target, the scale length L_n ~0.5 mm.

arrived from 2 to 3 ns. Their absorption fraction is typically high, and they are effective at heating a plasma whose volume is ~1 mm^3. For the exploding foils, the transmitted power increases later in time as the plasma expands. The interaction beam typically provides little heating to the plasma and little perturbation to the hydrodynamics, the exception being the solid target after the end of the secondary beams when the interaction beam, if still present, is strongly absorbed and provides some localized heating.

One interesting feature seen in the density contour plot of Fig. 77.4(a) for the exploding foil is a high-density off-axis region, topologically a ring structure. This effect was also found in earlier experiments on the former 24-beam OMEGA

Run 2853 & 3029
TC4727b & TC4927

system.[11] It occurs because the centrally peaked primary beams cause a more rapid explosion of the on-axis portion of the foil. The edge of the foil is only weakly heated by the primary beams. The off-axis ring expands because of heating by the obliquely incident secondary beams, resulting in a flow of mass toward the axis. This compensates for what would otherwise be a rapid fall of density with respect to time in the center of the plasma.

The predicted temporal evolution of the temperature and density in the center of an exploding-foil plasma is plotted in Fig. 77.5. The temperature rises rapidly around 1 ns when the thermal front penetrates to the center, and it rises again at 2 ns when the secondary beams turn on. It falls rapidly at 3 ns when the secondary beams switch off. The density, which has fallen to $\sim n_c/5$ at the start of the secondary beams, stays between $n_c/5$ and $n_c/10$ for the next 2 ns as a result of the flow of mass from the off-axis ring seen in Fig. 77.4(a). NIF-relevant conditions are thus maintained throughout the time period of the secondary beams (2 to 3 ns).

Plasma Characterization

The electron temperature of the exploding-foil plasmas was diagnosed using time-resolved x-ray spectroscopy. High-Z microdots, composed of Ti and CaF (1000 Å thick and 200 μm in diameter), were embedded in the center of the foil targets. They served as tracer elements to diagnose the electron temperature predicted in Fig. 77.5(a), using the sensitivity of the
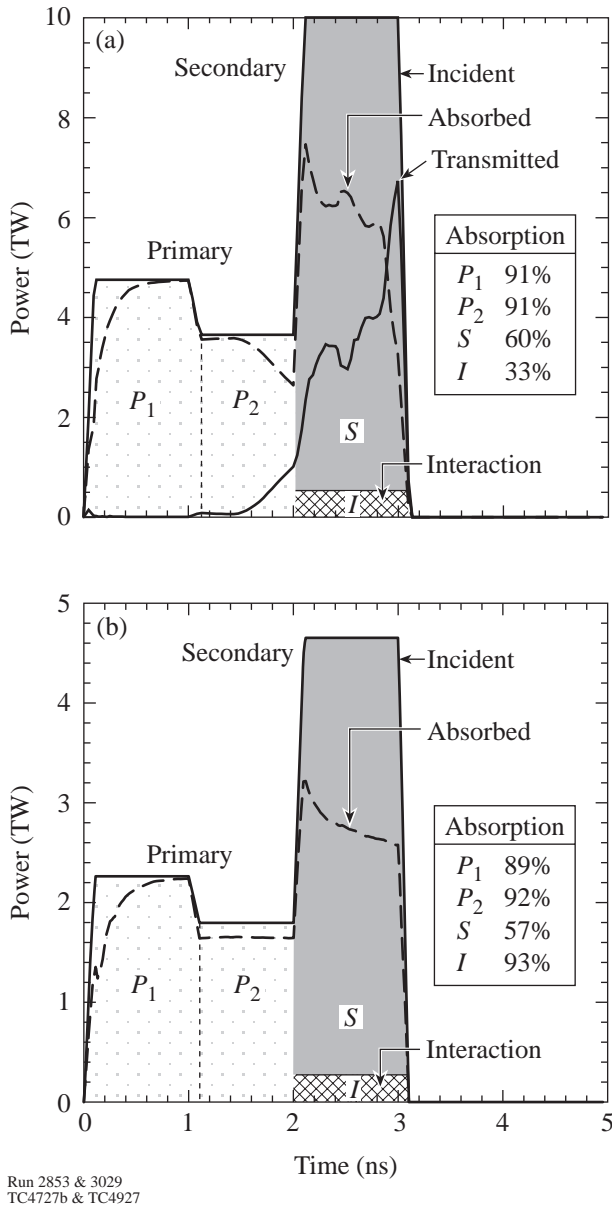
Figure 77.3

Timing sequence and total power delivered to the target for 1-ns flat-top laser pulses used to irradiate (a) exploding foils and (b) solid targets. The interaction beam is fired to probe the NIF-relevant plasma conditions, which usually occur between 2 and 3 ns, and can be timed to start anywhere from 2 to 3 ns. The figure also shows the calculated absorbed and transmitted powers as functions of time, summed over all beams, and the time-integrated absorption fractions of the primary (P_1, P_2), secondary (S), and interaction (I) beams.

Runs 3031, 3029
TC4895
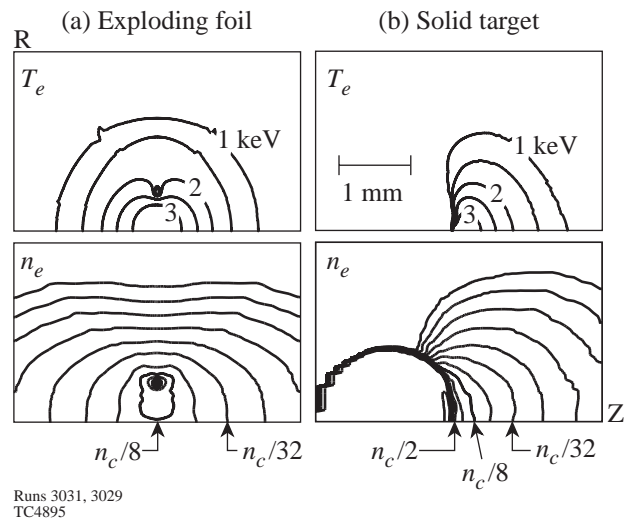
Figure 77.4

Contour plots of T_e and n_e at 2.6 ns simulated with *SAGE* for (a) an 18-μm-thick exploding foil and (b) a solid target (a 2-mm-diam CH sphere).

K-shell emission lines of Ti and Ca to variations in the electron temperature for temperatures up to the predicted maximum of ~4 keV. Exploding-foil plasmas were used for the temperature measurement because the tracer elements diagnosed the center of the plasma. In a solid target, a tracer element embedded at some depth in the target moves a significant distance through the corona during the interaction, encountering a wide range of electron temperatures and densities, and interpretation is more complex. Targets without microdots were investigated to verify that the microdot did not affect the parametric instabilities or plasma hydrodynamics in a significant manner.

Streaked and high-resolution, time-integrated x-ray spectra of Ti and Ca tracer elements in exploding-foil plasmas were recorded with flat crystal spectrographs. The time-resolved measurement shown in Fig. 77.6(a) was photometrically calibrated for spectral sensitivity with the time-integrated measurement shown in Fig. 77.6(b). The spectral range was selected to cover the *K*-shell emission of Ti and Ca. Both instruments had similar views of the plasma. The time-integrated instrument, which was calibrated using measured crystal reflectivities and published film sensitivities, utilized an ADP (ammonium dihydrogen phosphate) or a PET (pentaerythritol) crystal to

Figure 77.5

SAGE predictions for the time dependence of (a) T_e and (b) n_e at the center of an exploding-foil plasma. This temperature was diagnosed using a tracer layer containing Ti and Ca placed in the center of the target. The electron density inferred from the streaked Raman spectrum for a number of shots with different interaction beam timings is also plotted.

Figure 77.6

(a) Streaked x-ray spectra and (b) high-resolution, time-integrated x-ray spectra of Ti and Ca in a typical exploding-foil plasma.

disperse the spectrum onto Kodak DEF (direct exposure) film. The x-ray streak camera[13] utilized a RbAP (rubidium acid phthalate) crystal to disperse the spectrum onto a fluffy KBr photocathode with a 30-ps temporal resolution. The spectra were recorded on Kodak T-max 3200 film. The sweep speed of the streak camera was measured using a temporally modulated fiducial pulse. The film from both instruments was digitized using a PDS (Perkin-Elmer Photometric Data Systems) microdensitometer and corrected for film sensitivity.

The electron temperature was diagnosed using the measured line ratios of hydrogen- and helium-like charge states of Ca and Ti. In the exploding-foil plasmas the ionization time of the relevant Ca and Ti ions is longer than the interaction time (~1 ns); therefore, a non-steady-state calculation of the evolution of the line intensities was required. Using the time-dependent temperature and density predicted by *SAGE* for the target center (see Fig. 77.5), the evolution of the diagnostic lines (H_α and He_β of Ti and Ca) was calculated with the time-dependent *FLY* atomic physics code[14] (based on Ref. 15), which solves the ionic rate equations including ionization, excitation, and recombination (radiative, collisional, and dielectronic). The *SAGE/FLY* predictions of the Ti and Ca H_α:He_β emission line ratios (shaded region) are plotted in Fig. 77.7 with the measured line ratios (circle symbols). The shaded region is bounded by the *FLY* predictions for the *SAGE*-predicted T_e and 1.2 times the *SAGE*-predicted $T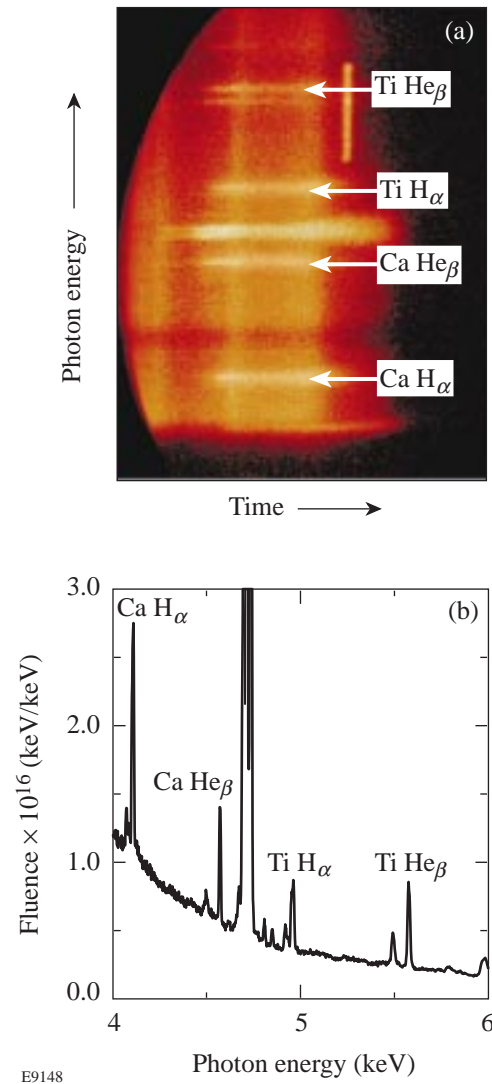_e$. The Ti measurement extends from just below the lower curve at 2 ns to just below the upper curve at 3 ns, and the Ca measurement is closer to the upper curve at all times. Based on this agreement with *SAGE/FLY* predictions for both line ratios, a peak T_e of ~4 keV is inferred. The opacity of these lines due to self-absorption was established experimentally to be insignificant: when the thickness of the microdot was doubled, the measured intensity doubled. The isoelectronic method[16] for measuring the electron temperature was not available due to uncertainty in the relative amounts of Ti and Ca.

The peak plasma electron density in the exploding-foil plasmas was diagnosed using the near-backscattered SRS spectrum.[4] In the center of an exploding foil, SRS is an absolute instability at the peak of the parabolic profile and consequently has an intensity threshold of 7×10^{13} W/cm². A narrow spectral emission was observed with a time-resolved spectrograph [see Fig. 77.8(a)]. The observed SRS wavelength determined from the 50% intensity point on the long-wavelength side of the narrow peak is compared with the wavelength predicted from a *SAGE* simulation in Fig. 77.8(b), using the

following relationship between the density and the scattered wavelength:

$$\frac{n}{n_c} = \left(1 - \frac{\lambda_0}{\lambda_s}\right)^2 + 3\frac{v_T^2}{c^2}\frac{\left(1 - 4\frac{\lambda_0}{\lambda_s} + \frac{\lambda_0^2}{\lambda_s^2}\right)}{1 - 12\frac{v_T^2}{c^2}}$$

$$-3\frac{v_T^2}{c^2}\frac{\sqrt{\left(1 - 4\frac{\lambda_0}{\lambda_s} + \frac{\lambda_0^2}{\lambda_s^2}\right)^2 - \left(1 - 12\frac{v_T^2}{c^2}\right)\left(1 - \frac{\lambda_0^2}{\lambda_s^2}\right)}}{1 - 12\frac{v_T^2}{c^2}},$$

E9493
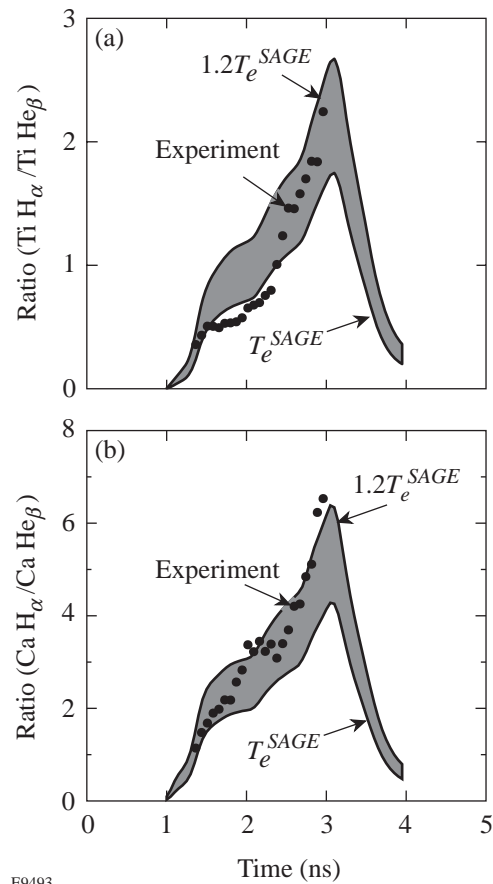
Figure 77.7
SAGE/FLY predictions of the Ti and Ca H_α:He_β emission line ratios (shaded region) together with the measured line ratios (circle symbols). The shaded region is bounded on the lower side by the *FLY* prediction using the *SAGE*-predicted T_e and on the upper side by the *FLY* prediction for 1.2 times the *SAGE* T_e. Agreement with *SAGE/FLY* predictions is found for the measured Ti and Ca line ratios, indicating a peak T_e of ~4 keV.

where v_T is the electron thermal velocity, c is the speed of light, λ_0 is the wavelength of the incident laser light, and λ_s is the scattered wavelength. This equation was obtained from the dispersion relations and phase-matching conditions for all the waves involved in the SRS.

The experimental wavelength data in Fig. 77.8(b) represent a series of shots with different interaction beam timings. The error bars on the experimental data represent the statistical variation in the measured wavelength over the compilation of shots. The experimental data of Fig. 77.8(b), translated into the inferred electron densities, are shown as an overlay in
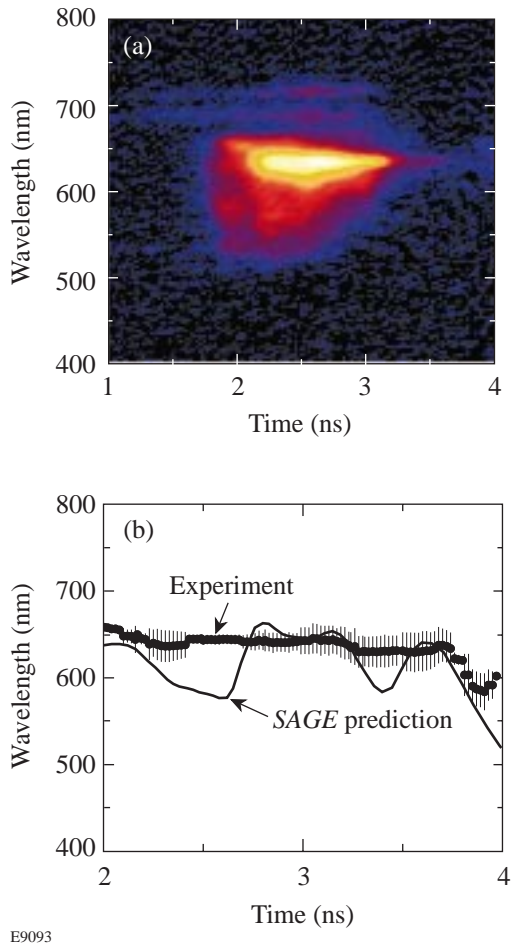
Figure 77.8
(a) Measured SRS spectrum of an exploding-foil plasma with the interaction beam timed to start at 2 ns, and (b) measured peak SRS wavelengths compiled from a series of shots with different interaction beam timings compared with *SAGE* predictions. The vertical lines associated with the experimental curve in (b) represent variations between different shots.

Fig. 77.5(b). From both figures the agreement between experiment and simulation is seen to be close, and the predicted onset of the drop in density around 3.7 ns is observed. The oscillations predicted by *SAGE* are associated with the off-axis mass converging onto the axis in a geometry with cylindrical symmetry. In the experiment the azimuthal asymmetries associated with the finite number of beams in each ring are expected to result in this behavior being averaged out. Both simulation and experiment are consistent with the production of a plasma with the peak n_e staying between 0.1 n_c and 0.2 n_c for approximately 2 ns.

Laser–Plasma Interaction Experiments

Signal levels of the direct backscatter of SRS and SBS from the interaction beam were recorded with the experimental setup shown in Fig. 77.9. The backscattered SRS and SBS signals were measured through the focusing lens with a full-aperture pickoff whose front surface was uncoated and whose back surface was AR (sol gel) coated for 351 nm. The back-surface reflectivity in the 400- to 800-nm range lies between 2% and 3% and is close to the reflectivity of the front surface. This unfortunately degrades the temporal resolution of the SRS measurements to ~250 ps and lengthens the SRS signals by the same amount.

A small fraction of the backscattered light was directed via optical fibers to two visible spectrographs, one near 351 nm to look for SBS and one covering the 400- to 700-nm range to look for SRS. Both spectrographs were outfitted with streak cameras. The remainder of the backscattered light was measured with an unfiltered calorimeter (which does not distinguish between SBS and SRS). This calorimeter resolved a small fraction of a joule of light backscattered from the target.

The SRS measurement used a 1/3-m Czerny-Turner spectrograph with 8-nm spectral resolution coupled to a streak camera. A 20-m, 50-μm gradient index fiber transmitted the SRS light from a pickoff at the backscatter station to the entrance slit of the spectrograph. The broad bandwidth of the SRS light necessitated a wavelength-dependent group-velocity dispersion correction, which amounted to ~5 ns between 351 nm and 700 nm. This correction was verified by measuring the time delay between the second-order 351-nm signal and a 700-nm SRS/TPD signal. Any error associated with this correction is estimated to be <50 ps over this spectral range and consequently negligible. It was found that there was no measurable contribution to the streaked SRS spectra from the secondary beams.
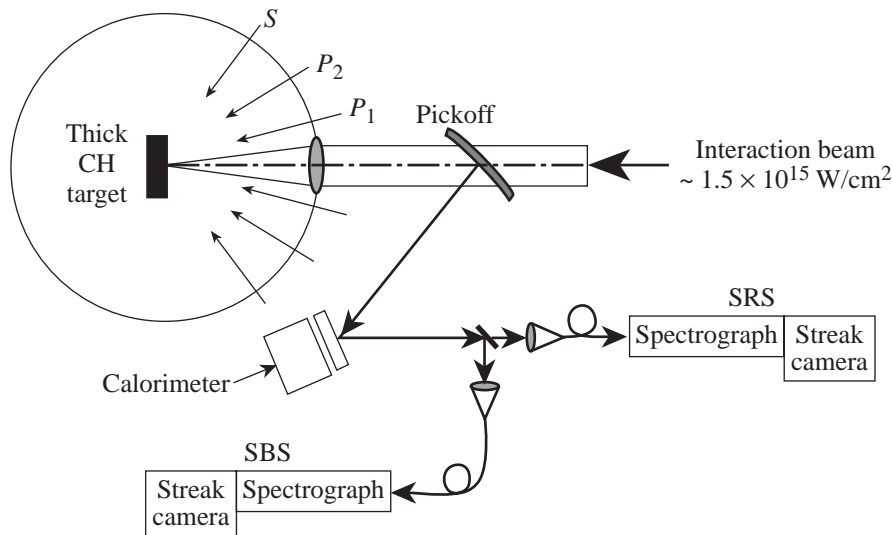
Figure 77.9
Experimental setup used to measure the SRS and SBS transmitted back through the focusing lens. The calorimeter measured the sum of the SRS and SBS energies reflected off the pickoff. Significant SRS reflections were made off each of the pickoff surfaces.

The SBS measurement used a 1-m Czerny-Turner spectrograph with ~0.05-nm spectral resolution, coupled to a streak camera with ~50-ps temporal resolution. The background light level entering this spectrograph was measured with shots without the interaction beam. For exploding-foil plasmas the time-resolved backscatter spectra were dominated by scattered light from the primary and secondary beams, and no SBS feature could be identified. Shots with and without the interaction beam at 1.5×10^{15} W/cm^2 were barely distinguishable. (This was in contrast to earlier experiments carried out without a DPP in the interaction beam, where the SBS reflectivity exceeded 10%.[17]) The energy response of the SBS spectrograph was estimated using shots taken without the interaction beam. In this case there was no scattered light in the SRS range, so the energy recorded in the calorimeter corresponded to the signal in the SBS spectrograph.

Measured backscatter SBS spectra are presented in Fig. 77.10 for the exploding-foil plasmas after the peak density has dropped to ~n_c/5. The time during which NIF temperatures and scale lengths are achieved extends from 2 to 3 ns. Figure 77.10(a) shows the temporal evolution of the spectrum near 351 nm when the interaction beam was not fired and was used to establish the level of background light. The interaction beam was fired at 2 ns in Fig. 77.10(b) and at 3 ns in Fig. 77.10(c). Since there are no significant differences between the three images, it is clear that no measurable contribution from the interaction beam to the signal near 351 nm was observed for either timing. The energy response of the spectrograph places an upper limit on the SBS reflectivity of 0.1% for these experiments.

A similar set of streaked spectra is shown in Fig. 77.11 for solid-target plasmas. The signal near $t = 0$ in all three cases is interpreted as light reflected from the critical surface with a Doppler blue shift from the expanding plasma. This is consistent with the *SAGE* prediction for the time-dependent absorbed power [Fig. 77.3(b)]. Less signal is seen during the second set of primary beams, as they were incident at greater angles from the collection lens. The feature around 351 nm in Fig. 77.11(b) between 2 and 3 ns corresponds to a 0.1% reflection of the interaction beam from near the critical-density surface. The total energy recorded by the spectrograph was 3.1 J, corresponding to 0.7% of the interaction beam energy, so most of the energy was in the scattered P_1 beams. The feature after 3 ns in Fig. 77.11(c) is from what would, in the absence of the interaction beam, be a rapidly cooling plasma. This plasma, which still has a critical-density surface, is strongly absorbing (close to 100% absorption is predicted) and is locally heated by the interaction beam. The observed backscatter is consistent with a backscattered SBS energy fraction of 0.2%. Thus, no significant SBS was observed in either the exploding-foil or solid-target interaction experiments under NIF direct-drive conditions.

Small amounts of SRS were observed in both types of plasma. For the exploding-foil plasmas SRS from the electron-density maximum was used as a density diagnostic (see preceding section). For solid-target plasmas, time-resolved SRS was measured through the focusing lens (direct backscatter) and at 20° from the backscatter direction (Fig. 77.12). Figures 77.12(a) and 77.12(b) show the temporal evolution of the SRS backscatter spectra through the lens, with the interaction

beam fired at 2 ns and 2.5 ns, respectively, with peak intensity 1.5×10^{15} W/cm^2. Both images exhibit broad spectral features coincident in time with the interaction beam and extending from 420 nm to 540 nm. The weak feature at 700 nm appears to be $\omega_0/2$ light from the two-plasmon decay instability driven by the primary and secondary beams.

An upper limit on the backscattered SRS energy can be estimated from the calorimetry and the SBS signal. As mentioned above, the spectral energy response of the SBS spectrograph was determined on shots where the interaction beam was not fired. By subtracting the SBS energy in the spectrograph from the total energy recorded in the calorimeter, the

energy in the SRS signal can in principle be estimated. Due to the shot-to-shot fluctuations in the signal levels, however, there is a large uncertainty associated with this subtraction. In addition, the final turning mirror has ~100% reflectivity at 351 nm but a flat ~12% reflectivity between 400 and 700 nm, further reducing the SRS contribution in the calorimeter. Taking all these factors into account, the residual SRS energy in the calorimeter is 0 J with an uncertainty of 25 J. The upper limit of 25 J corresponds to a maximum SRS backscattered energy fraction of 5%, but clearly a lower value is more likely. An accurate measurement of the SRS fraction will require further experiments.

Landau damping is very strong in this density–temperature regime ($k\lambda_D \approx 0.5$ at 570 nm during the high-temperature portion of the interaction), which suggests that the observed SRS originates in filaments where Landau damping is strongly reduced.[18]
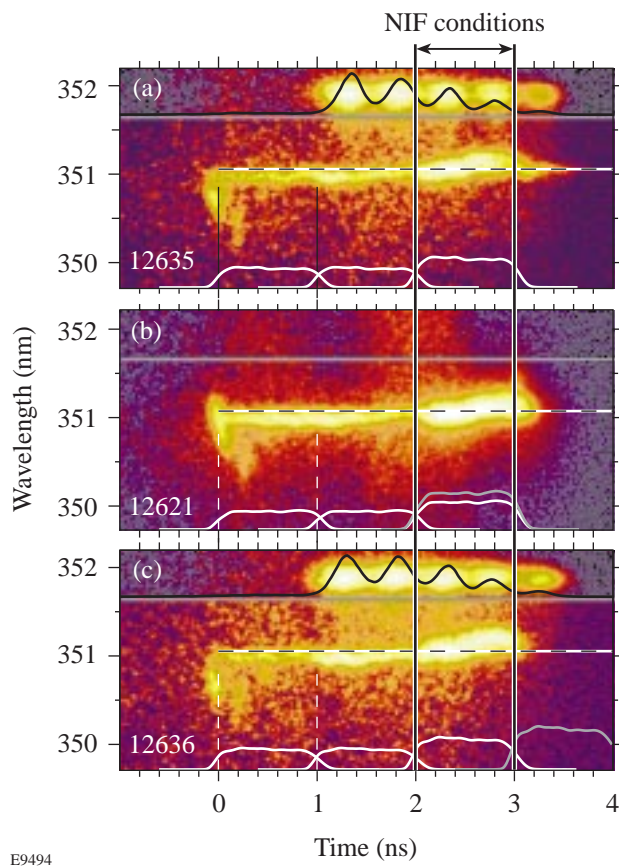
Figure 77.10

Streaked spectra around 351 nm of light backscattered from exploding-foil plasmas through the interaction-beam focus lens for (a) no interaction beam, (b) interaction beam at 2 ns, and (c) interaction beam at 3 ns. A multipulse timing fiducial [shown at the top of (a) and (c) with the solid line indicating its temporal shape] enabled an absolute time origin to be assigned to the backscattered light. The measured streak records of the four groups of laser beams are also shown. The horizontal dashed line indicates the unshifted laser wavelength.
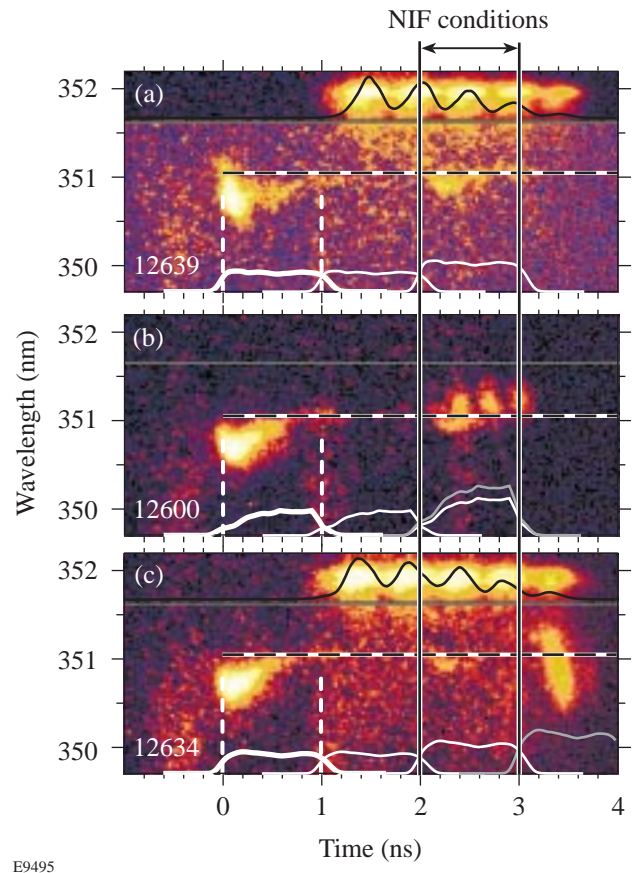
Figure 77.11

Same as Fig. 77.10 but for the solid targets (partial spheres of 2-mm diameter).
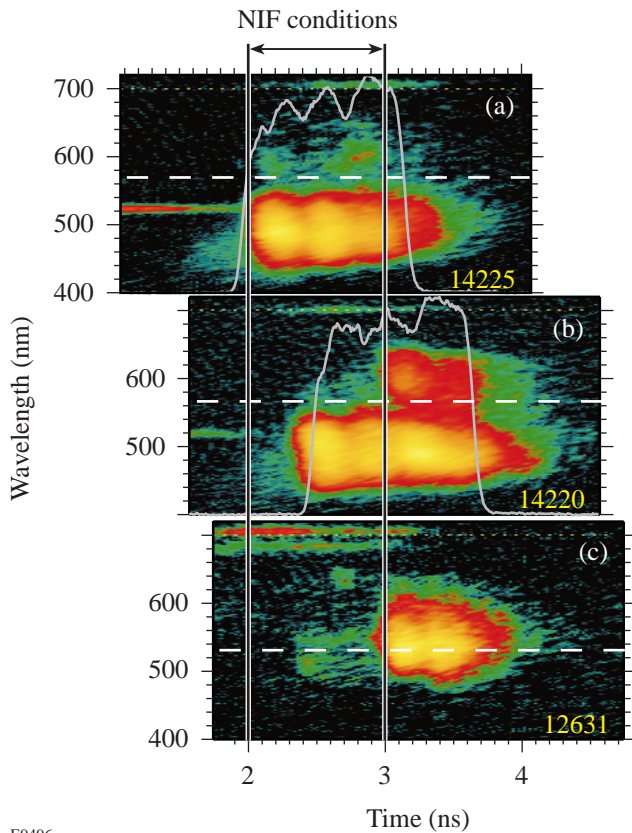
E9496

Figure 77.12
Streaked SRS spectra from solid-target plasmas: (a) and (b) directly back through the lens, with SSD on (0.25-THz UV bandwidth), and (c) at 20° to the lens with SSD off. The interaction beam was timed at 2 ns in (a) and at 2.5 ns in (b) and (c). The temporal shape of the interaction beam is shown as an overlay in (a) and (b). The targets were flat in (a) and (b) and a partial sphere of 2-mm diameter in (c).

A time-resolved sidescattered SRS spectrum from a solid target, at 20° from the interaction beam direction (the normal to the original target surface), is shown in Fig. 77.12(c) with the interaction beam fired at 2.5 ns. No SRS is observed in sidescattering during the hot NIF-like plasma phase between $t = 2$ and 3 ns, but sidescattering sets in abruptly when the secondary beams turn off at $t = 3$ ns. At this time the background plasma cools down, although this alone may not explain the abrupt onset of sidescattering. The sidescatter SRS appears at longer wavelengths (i.e., higher densities) than the filamentary SRS seen in backscattering between 2 and 3 ns. This is consistent with the onset of SRS at longer wavelengths in direct backscattering at 3 ns [Fig. 77.12(b)].

It is possible that some SRS was present just outside the f/6 cone of the interaction-beam focusing lens; however, this is unlikely to be significant, based on the lack of SRS at 20° from 2 to 3 ns.

Combining the backscatter and sidescatter SRS observations it is reasonable to conclude that the directionality of the filamentary (low-density) SRS signal is due to the "horn antenna" effect, which directs the incident 351-nm light into the filaments and then funnels the backscattered SRS signal through the same horn to the focusing lens. Within the filament the SRS signal is guided by the filament as well as by the SRS gain, while in the region of the horn geometrical optics is applicable and the backscattered SRS light is guided by the density structure making up the horn. It is impossible to determine the exact background density within which the filaments are created since the SRS wavelength merely reflects the density within the filaments. It is clear that the 2-D SSD bandwidth used in this experiment (0.25 THz in the UV) is insufficient to suppress the filamentation.

The density-gradient threshold for Raman scattering (e.g., that given by Kruer[4]) yields $I \sim 1.8 \times 10^{15}$ W/cm^2, and SRS would be expected to originate within the speckles produced by the phase plates. During the hot NIF-like plasma phase, however, Landau damping is strong enough to suppress this SRS completely, while in the cooling phase (past $t = 3$ ns) SRS can occur and is seen between 0.1 and 0.2 n_c. This type of Raman scattering (without filamentation) is still preferentially directed in the backward direction, but it is much less collimated, which thus allows its observation through the lens as well as at 20° away from the backscatter direction.

Conclusion

Long-scale-length plasmas, with parameters relevant to the peak of direct-drive NIF laser pulses, have been produced and characterized on the OMEGA laser system. Temperatures of ~4 keV and densities of ~0.2 n_c have been measured in agreement with hydrocode predictions and are consistent with density scale lengths of ~0.5 to 1.0 mm. Experiments have shown that these plasmas have an SBS reflectivity of less than 0.1% and an SRS reflectivity of less than ~5%, even when the interaction beam intensity is 1.5×10^{15} W/cm^2, eight times higher than the NIF cluster intensity. The measured backscattered SRS signals are believed to originate in filaments at $n_e < 0.1 \, n_c$, as otherwise they would be suppressed by the strong Landau damping that occurs at the measured temperatures. The threshold intensity for SRS was not determined since experiments were not performed with a lower-

intensity interaction beam. The calculated SRS and SBS intensity thresholds were comparable to the intensity of the interaction beam at 1.5×10^{15} W/cm^2; however, only SRS was observed in the experiment.

On the basis of these experiments it is concluded that SRS and SBS are not likely to present a problem for the coronal plasmas at the peak of the NIF direct-drive laser pulse. Future experiments on OMEGA will vary the intensity of the interaction beam and will address the parametric instabilities of the coronal plasmas in the foot and transition regions of the NIF direct-drive laser pulse.

REFERENCES

1. C. P. Verdon, Bull. Am. Phys. Soc. **38**, 2010 (1993).

2. S. E. Bodner, D. G. Colombant, J. H. Gardner, R. H. Lehmberg, S. P. Obenschain, L. Phillips, A. J. Schmitt, J. D. Sethian, R. L. McCrory, W. Seka, C. P. Verdon, J. P. Knauer, B. B. Afeyan, and H. T. Powell, Phys. Plasmas **5**, 1901 (1998).

3. J. D. Lindl, Phys. Plasmas **2**, 3933 (1995).

4. W. L. Kruer, *The Physics of Laser Plasma Interactions*, Frontiers in Physics, Vol. 73, edited by D. Pines (Addison-Wesley, Redwood City, CA, 1988).

5. J. C. Fernández *et al.*, Phys. Plasmas **4**, 1849 (1997).

6. B. J. MacGowan *et al.*, Phys. Plasmas **3**, 2029 (1996).

7. T. R. Boehly, D. L. Brown, R. S. Craxton, R. L. Keck, J. P. Knauer, J. H. Kelly, T. J. Kessler, S. A. Kumpan, S. J. Loucks, S. A. Letzring, F. J. Marshall, R. L. McCrory, S. F. B. Morse, W. Seka, J. M. Soures, and C. P. Verdon, Opt. Commun. **133**, 495 (1997).

8. Y. Lin, T. J. Kessler, and G. N. Lawrence, Opt. Lett. **21**, 1703 (1996).

9. R. S. Craxton and R. L. McCrory, J. Appl. Phys. **56**, 108 (1984).

10. M. C. Richardson, P. W. McKenty, F. J. Marshall, C. P. Verdon, J. M. Soures, R. L. McCrory, O. Barnouin, R. S. Craxton, J. Delettrez, R. L. Hutchison, P. A. Jaanimagi, R. Keck, T. Kessler, H. Kim, S. A. Letzring, D. M. Roback, W. Seka, S. Skupsky, B. Yaakobi, S. M. Lane, and S. Prussin, in *Laser Interaction and Related Plasma Phenomena*, edited by H. Hora and G. H. Miley (Plenum Publishing, New York, 1986), Vol. 7, pp. 421–448.

11. W. Seka, R. S. Craxton, R. E. Bahr, D. L. Brown, D. K. Bradley, P. A. Jaanimagi, B. Yaakobi, and R. Epstein, Phys. Fluids B **4**, 432 (1992).

12. S. Skupsky, R. W. Short, T. Kessler, R. S. Craxton, S. Letzring, and J. M. Soures, J. Appl. Phys. **66**, 3456 (1989).

13. D. H. Kalantar *et al.*, in *22nd International Congress on High-Speed Photography and Photonics*, edited by D. L. Paisley and A. M. Frank (SPIE, Bellingham, WA, 1997), Vol. 2869, pp. 680–685.

14. Available from Cascade Applied Sciences, Inc., P.O. Box 4477, Boulder, CO 80306.

15. R. W. Lee, B. L. Whitten, and R. E. Stout II, J. Quant. Spectrosc. Radiat. Transfer **32**, 91 (1984).

16. R. S. Marjoribanks, M. C. Richardson, P. A. Jaanimagi, and R. Epstein, Phys. Rev. A **46**, 1747 (1992).

17. A. V. Chirokikh, R. S. Craxton, D. D. Meyerhofer, A. Simon, W. Seka, and R. P. Drake, Bull. Am. Phys. Soc. **42**, 1882 (1997).

18. R. W. Short and A. Simon, Phys. Plasmas **5**, 4134 (1998).

Irradiation Uniformity for High-Compression Laser-Fusion Experiments

Various techniques are being used to achieve the high irradiation uniformity required for direct-drive, laser-fusion experiments on the OMEGA laser system. These techniques are directly applicable to the National Ignition Facility (NIF) being built at the Lawrence Livermore National Laboratory. The combination of two-dimensional smoothing by spectral dispersion (SSD),[1–3] distributed phase plates (DPP's),[4,5] polarization smoothing (DPR's),[6,7] and beam overlap should be sufficient to reach the rms level of 1% or less when the laser intensity has been averaged over a few hundred picoseconds. Of these, SSD is the dominant mechanism for reducing the nonuniformity.

The SSD beam-smoothing technique produces uniform laser beams in a time-averaged sense. The level of uniformity that can be achieved is determined by two factors: bandwidth and spectral dispersion. The amount of bandwidth determines the rate of smoothing, and the amount of spectral dispersion determines the level of uniformity that can be achieved (as well as the longest spatial wavelength of nonuniformity that can be smoothed). Frequency-tripled glass lasers (such as OMEGA and the NIF) place constraints on both bandwidth and spectral dispersion. Until recently, high-efficiency frequency tripling of laser light was limited to a bandwidth of 3 Å to 4 Å in the IR. Recent calculations and experiments[8,9] have shown that this bandwidth can be increased by a factor of 3 to 4 by using a second tripling crystal, resulting in ~1 THz in the UV, with a ~70% tripling efficiency. Second triplers will be installed on OMEGA during 1999.

The spectral dispersion of the bandwidth on OMEGA has been limited by the laser spatial-filter pinholes to an angular spread of ~50 μrad (relative to the output of the system). This will be increased on OMEGA during 1999 to accommodate asymmetric SSD dispersion, with 100 μrad in one direction and 50 μrad in the other. Polarization smoothing will provide an additional 50 μrad, resulting in a total angular spread of 100 μrad in each direction.[10] With these laser modifications,

it is expected that the levels of uniformity required for high-compression experiments on OMEGA will be achieved. The rms nonuniformity will drop below 1% after a smoothing time of ~250 ps. These same uniformity techniques are directly applicable to the NIF and will result in even higher levels of uniformity because of the larger number of beams (192 versus 60).

With the angular divergence of the beam that will be achieved on OMEGA during 1999, all spatial wavelengths of nonuniformity of concern for ICF will be smoothed. The longest wavelength of nonuniformity that can be smoothed by SSD and polarization smoothing can be estimated in the following way: Both SSD and DPR's smooth nonuniformities by shifting the speckle pattern produced by a phase plate. Two overlapped speckle patterns that have been shifted by a distance S will exactly smooth a nonuniformity of spatial wavelength $2S$. The maximum speckle shift is given by $S_{max} = F\Delta\theta$, where F is the focal length and $\Delta\theta$ is the beam angular divergence; thus, SSD can smooth spherical harmonic modes of nonuniformity down to $\ell_{cut} = 2\pi R/(2S_{max})$, where R is the target radius. Using OMEGA parameters $F = 180$ cm, $R = 500$ μm, and $\Delta\theta = 90$ μrad, we have $\ell_{cut} \sim 10$, which is well below the modes of concern for seeding hydrodynamic instabilities. For the NIF, the same angular divergence will produce essentially the same value of ℓ_{cut} since both the focal length and the target radius will be 3.5 to 4 times larger than for OMEGA.

The mathematical formalism describing 2-D SSD is presented in Ref. 2. We can use the approximate asymptotic expression for the SSD reduction factor [Eq. (20) in Ref. 2] to confirm the above estimates for the longest wavelength of nonuniformity that can be smoothed by SSD. First, this equation is modified to include the contribution of polarization smoothing as follows: Let the polarization dispersion be in the y direction, with Δ_p the spatial separation between e and o rays in the target plane. Then the superposition of the e and o intensities is $\frac{1}{2}\left[I\left(x, y + \Delta_p/2\right) + I\left(x, y - \Delta_p/2\right)\right]$. For the

asymptotically smoothed intensity, the SSD reduction factor R_{ij}^p is

$$R_{ij}^p = J_0\left(6\delta_1 \sin \tfrac{1}{2} k_i \Delta_1\right) \times J_0\left(6\delta_2 \sin \tfrac{1}{2} k_j \Delta_2\right)$$
$$\times \cos\left(\tfrac{1}{2} k_j \Delta_p\right) \tag{1}$$

for spatial modes $\left(k_i, k_j\right)$ in the (x, y) directions. The factor $6\delta_{1,2}$ is the number of spectral modes for each direction of SSD (after frequency tripling), and $\Delta_{1,2}$ is the separation of the modes. The first zero of the first Bessel function will determine the longest wavelength for which there is substantial smoothing in the x direction. Expanding the "sin" function for small k and using $S_1 = 6\delta_1\Delta_1$ as the maximum spectral shift, the argument of the Bessel function becomes $\tfrac{1}{2} \ell S_1/R$, where ℓ is the effective spherical harmonic mode number ($\ell = k \times R$). This gives $\ell_{\text{cut}} = 15$, where $J_0\left(\tfrac{1}{2} \ell_{\text{cut}} S_1/R\right) = 0$, which is a little higher than the rough estimate above.

In the perpendicular direction, there is smoothing from both the spectral dispersion and the polarization spread. For the strategy being implemented on OMEGA, the spectral angular spread in this direction is half the spread in the other direction $\left(S_2 = \tfrac{1}{2} S_1\right)$ in order to keep the laser pinholes as small as possible. The total speckle shift in this direction is then doubled by means of the polarization shift for $\Delta_p = S_2$. With these parameters, the "cos" term in Eq. (1) gives the lowest value

of ℓ for which R is zero in the y direction, namely $\ell \approx 20$. Of course there is still some smoothing below $\ell = 20$.

The smoothing of long-wavelength nonuniformities can be seen in the full time-dependent calculation shown in Fig. 77.13. Shown is the calculated rms nonuniformity for 60 overlapping beams on a spherical target (using the OMEGA irradiation geometry). The nonuniformity for each individual beam was calculated from the time-dependent SSD equations in Ref. 2, and the result was projected onto the sphere. The first image shows how the nonuniformity spectrum has decreased after 500 ps of smoothing for 500 modes, with 1 THz of bandwidth. [Plotted is the rms nonuniformity σ_ℓ of the spherical harmonic mode ℓ, defined such that the total rms nonuniformity is $\left(\Sigma\sigma_\ell^2\right)^{1/2}$]. The second image shows the spectrum for the first 50 modes, which is a region of particular concern for direct-drive laser fusion.

We first note that even without SSD, the nonuniformity in the very low-order modes ($\ell = 11$ to 30) is very small, 1%. After 500 ps of smoothing, this has been reduced to 0.15%. Smoothing is occurring for modes that are about a factor of 2 lower than indicated in the results of Rothenberg.[3] The reason is that this calculation has used twice the angular divergence of Rothenberg; he limited the angular spread of the beam to be 50 μrad. We have increased the spread to 100 μrad in one direction and doubled the 50-μrad spread in the second direc-
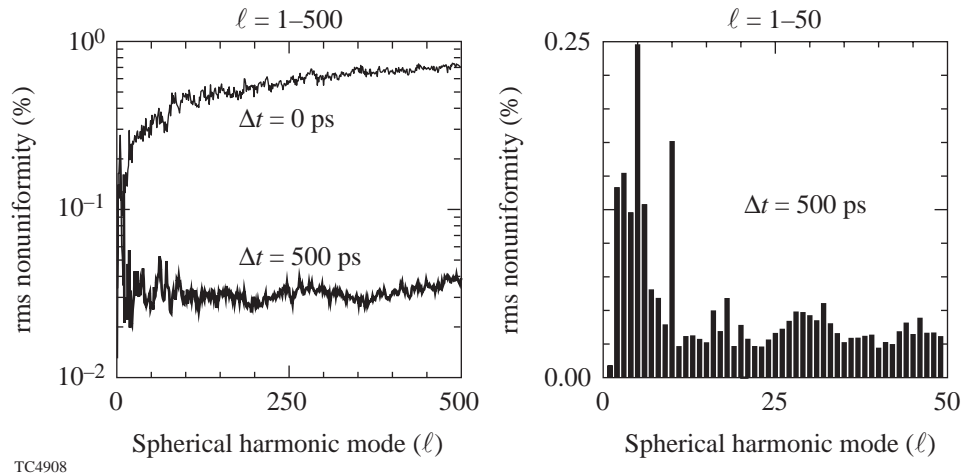

TC4908

Figure 77.13
The reduction in nonuniformity produced by SSD on OMEGA when the intensity is averaged over 500 ps, for a bandwidth of 1 THz and a total angular spread of 100 μrad. The IR bandwidths for the two modulators are 2.1 Å and 10.2 Å with modulation frequencies of 8.8 GHz and 10.4 GHz.

tion by means of the polarization wedge. This is consistent with the above analysis showing that when the total speckle shift is about 15% of the target diameter, modes below $\ell = 15$ are smoothed. These calculations have included the effect that the envelope, as well as the speckle, is shifted. The smoothing effect is more dramatic for higher-order modes; for $\ell = 31$ to 500 the nonuniformity is reduced from 13% to 0.6% rms.

The second image in Fig. 77.13 shows details of the long-wavelength nonuniformity structure after 500 ps of smoothing (note that the vertical scale has changed). It is now more clearly seen that modes down to $\ell = 11$ have been smoothed. The spike at $\ell = 10$ as well as the additional nonuniformity at lower ℓ is the result of how the 60 beams overlap on the spherical target; it is not the result of structure on an individual beam. This form of nonuniformity can be reduced by a careful choice of the radial beam profile that is generated by the phase plate. These calculations have used the sinc^2 profile that is generated by square phase-plate elements (and modified by SSD), with the target boundary near the 5% intensity contour.

The discussion after Eq. (1) shows that the asymptotic level of smoothing reached by SSD in the low-order modes depends only on the size of the speckle deflections: S_1, S_2, and Δ_p. (This is valid over the range of wavelengths for which the "sin" functions in that equation can be expanded to first order.) The amount of time required to reach this level can be decreased, however, by increasing the number of color cycles.[1–3] This occurs because the longer wavelengths of nonuniformity are produced by interference between phase-plate elements that are relatively close together. By increasing the number of color cycles, the relative phase between close phase-plate elements varies more rapidly, and faster smoothing occurs. This is at the expense, however, of reduced smoothing for very short wavelengths of nonuniformity (high ℓ) produced by interference between more-distant phase-plate elements.

One example of the effect of three color cycles compared to one cycle is shown in Fig. 77.14. This corresponds to an intermediate case that might be examined on OMEGA before the implementation of 1 THz of bandwidth. Both cases in Fig. 77.14 correspond to a bandwidth of 0.3 THz with one color cycle and a polarization wedge in one of the directions. In the second direction, one case has one color cycle and the other has three, produced by a threefold increase in modulation frequency. The results are given after 250 ps of smoothing. (The total nonuniformity is about 1.7% rms.) For three color cycles, the nonuniformity in modes 50 to 200 has been reduced by about 50%, at the expense of some increased nonuniformity
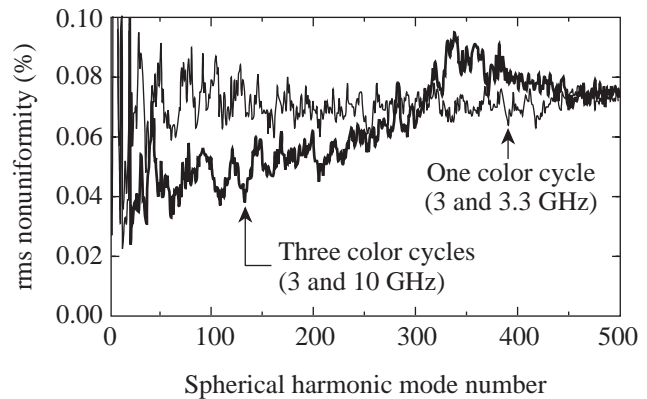
E9250

Figure 77.14
By increasing the number of color cycles, long wavelengths of nonuniformity can be reduced at a faster rate. The nonuniformity spectrum with 0.3 THz of bandwidth and 250 ps of smoothing time is compared for one and three color cycles. The bandwidths in both cases were 1.5×3 Å. For one color cycle the modulation frequencies were 3 and 3.3 GHz. For three color cycles (in one direction) the 3.3-GHz modulator was replaced by a 10-GHz modulator.

above $\ell = 300$. It is believed that this shift in the nonuniformity spectrum is beneficial, as modes below $\ell = 200$ are considered to be the most dangerous. After about 1 ns of smoothing time, however, both examples show about the same asymptotic level of nonuniformity for the long wavelengths.

Finally, in Fig. 77.15 we compare the effects of the different improvements in uniformity that are planned for OMEGA during 1999. The current SSD configuration consists of IR bandwidths of 1.25×1.75 Å with electro-optic (EO) modulators of 3 and 3.3 GHz. The spectral divergence is less than 50 μrad. A small number of polarization wedges are available for planar experiments. A full set of 60 wedges will be installed during 1999 for spherical experiments. At the same time, the bandwidth will be increased to 1.5×3.0 Å with the resulting spectral/polarization dispersion being ~100 μrad in each direction. During the latter half of the year, one of the EO modulators will be replaced by a 10-GHz modulator and the IR bandwidth increased to ~12 Å, resulting in a UV bandwidth of ~1 THz.

The improvements in irradiation nonuniformity planned for the OMEGA laser during 1999 will reduce the rms nonuniformity to less than 1% when the intensity is averaged over 300 ps. The total nonuniformity in the long-wavelength nonuniformities (spherical harmonic modes 11 to 30) can be smoothed to levels below 0.15%. This is being accomplished by the addition of three new features to the laser: (1) Second

TC4870

TC4896
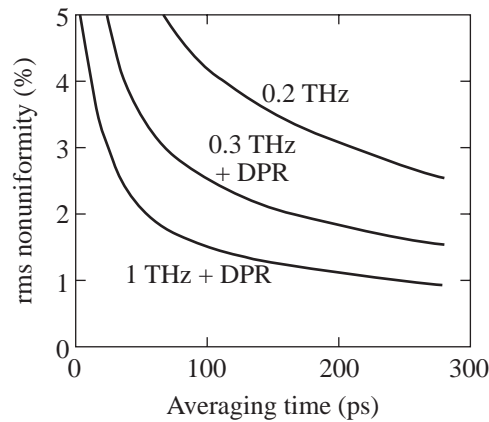
Figure 77.15

The rms nonuniformity as a function of time for the current SSD configuration on OMEGA and the upgrades planned for 1999, including the effect of multiple-beam overlap on a spherical target in the 60-beam geometry. Spherical harmonic modes up to $\ell = 500$ have been considered with no additional smoothing assumed in the plasma atmosphere around the target. The top curve shows the current level of irradiation uniformity. The middle curve corresponds to a higher bandwidth in one direction and the inclusion of polarization smoothing. The bottom curve is the result for 1 THz of UV bandwidth and polarization smoothing.

Figure 77.16

The rms nonuniformity as a function of time for the NIF and for OMEGA, assuming 1-THz bandwidth and polarization smoothing. All spherical harmonic modes between 5 and 500 are included.

triplers will allow the high-efficiency tripling of 3 to 4 times the current bandwidth. This will decrease the smoothing time by the same factor. (2) Polarization wedges added to all 60 beams will instantaneously reduce nonuniformity by $\sqrt{2}$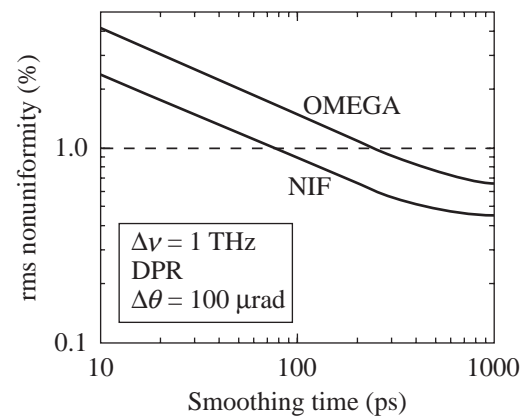 and double the maximum shift of speckle patterns on the target. (3) An increase in laser-pinhole size will double the allowed spectral spread in one direction from 50 μrad to 100 μrad. (The angular spread in the perpendicular direction will remain 50 μrad.) The combined effect of the polarization spread and the increased spectral spread will be a factor-of-2 reduction in the largest spherical harmonic mode of nonuniformity that can be smoothed, and a reduction in the asymptotic value of non-uniformity by almost the same factor.

These uniformity improvements are directly applicable to the NIF. As with OMEGA, the current pinhole specification for the NIF limits the angular spread of the beam to 50 μrad. The NIF optical design should be examined to determine if the pinhole can be opened further for direct-drive experiments as is being done on OMEGA. Using essentially the same SSD configuration as OMEGA, including polarization smoothing and dual-tripler frequency conversion, even higher uniformity will be achievable on the NIF due to the larger number of beams (192 versus 60). A comparison between NIF and

OMEGA uniformity is shown in Fig. 77.16. It is expected that this smoothing rate and the level of uniformity should be adequate for direct-drive ignition experiments.

REFERENCES

1. S. Skupsky, R. W. Short, T. Kessler, R. S. Craxton, S. Letzring, and J. M. Soures, J. Appl. Phys. **66**, 3456 (1989).

2. Laboratory for Laser Energetics LLE Review **69**, 1, NTIS document No. DOE/SF/19460-152 (1996). Copies may be obtained from the National Technical Information Service, Springfield, VA 22161; S. Skupsky and R. S. Craxton, "Irradiation Uniformity for High-Compression Laser Fusion Experiments," to be published in Physics of Plasmas.

3. J. E. Rothenberg, J. Opt. Soc. Am. B **14**, 1664 (1997).

4. T. J. Kessler, Y. Lin, J. J. Armstrong, and B. Velazquez, in *Laser Coherence Control: Technology and Applications*, edited by H. T. Powell and T. J. Kessler (SPIE, Bellingham, WA, 1993), Vol. 1870, p. 95.

5. Y. Lin, T. J. Kessler, and G. N. Lawrence, Opt. Lett. **21**, 1703 (1996).

6. Y. Kato, unpublished notes (1984); K. Tsubakimoto *et al.*, Opt. Commun. **91**, 9 (1992); K. Tsubakimoto *et al.*, Opt. Commun. **103**, 185 (1993).

7. Laboratory for Laser Energetics LLE Review **45**, 1, NTIS document No. DOE/DP40200-149 (1990). Copies may be obtained from the National Technical Information Service, Springfield, VA 22161; T. E. Gunderman, J.-C. Lee, T. J. Kessler, S. D. Jacobs, D. J. Smith, and S. Skupsky, in *Conference on Lasers and Electro-Optics*, Vol. 7, 1990 OSA Technical Digest Series (Optical Society of America, Washington, DC, 1990), p. 354.

8. D. Eimerl *et al.*, Opt. Lett. **22**, 1208 (1997).

9. A. Babushkin, R. S. Craxton, S. Oskoui, M. J. Guardalben, R. L. Keck, and W. Seka, Opt. Lett. **23**, 927 (1998).

10. R. S. Craxton and S. Skupsky, Bull. Am. Phys. Soc. **40**, 1826 (1995).

11. The description of the SSD formalism here is similar to the presentation in the internal report of Ref. 2.

12. Y. Kato *et al.*, Phys. Rev. Lett. **53**, 1057 (1984).

A Novel Charged-Particle Diagnostic for ρR in Compressed ICF Targets

Areal density—the product of density and thickness of specific ions (ρR) in ICF targets—is an important measure of compression that enables a comparison of ICF implosions with simulation. In particular, this quantity influences several crucial aspects of an igniting target: the degree of self-heating in the target, its fractional burn, and gain.[1]

Several methods involving nuclear reaction products have been employed to deduce this quantity in ICF implosions.[2–5] In this article, we will discuss the use of knock-on particles (deuterons and protons) that have been elastically scattered from the 14-MeV primary DT fusion neutrons. Both knock-on deuterons[2] and protons[5] have been discussed previously in the literature. The knock-on deuteron diagnostic has been used extensively to provide a measure of ρR.[2] The number of these knock-on particles can provide information on the areal densities of the layer in which they are produced, and the energy loss of these particles as they propagate out of the target will provide additional information about ρR along the propagation path. The deuteron diagnostic can provide information about the compressed target in a relatively model-independent way for values of target ρR up to ~100 mg/cm^2. For higher values of ρR, the knock-on spectrum is significantly distorted and becomes very dependent on temperature within the target.

Maximum information from the knock-on diagnostics is obtained using detailed information about the shape and magnitude of the knock-on spectrum. Until recently, the technique used to detect the knock-on deuterons has involved the counting of tracks satisfying selective criteria in stacked track detectors, consequently providing only gross information about the particle spectrum. This lack of spectral information has limited the use of knock-on ions as a diagnostic. With the deployment of the new charged-particle spectrometer[6] (CPS), detailed spectral information of charged reaction products from the imploding target can now be obtained, enabling a more detailed analysis of conditions in the target using the knock-on particles. Using a 7.5-kG magnet, the CPS can momentum-select incident charged particles, which are then impinged onto a detector plane consisting of track detectors.

The identity of each particle is then established by comparing the track diameters with known stopping powers of various particles at that momentum. In this manner, areal densities can now be measured not only through the knock-on deuteron diagnostic but also through diagnostics involving other charged particles such as the knock-on protons.

The knock-on proton diagnostic is somewhat similar to the knock-on deuteron diagnostic. The number of these particles is once again proportional to the areal density of the layer in which they are produced (such as the plastic shell). The spectrum of these particles, however, is significantly different from the deuterons, and a different analysis must be used to interpret the measurement. In earlier work, a somewhat model-dependent technique to interpret the proton signal was presented.[4] A more model-independent analysis of the proton spectrum can be devised that relies on the number of knock-on protons in a suitably defined energy range and is equally applicable to current experiments. Details of this analysis will be presented elsewhere.[7]

Here we present a novel knock-on deuteron–based diagnostic that will simultaneously diagnose three regions of a compressed target consisting of DT gas enclosed in a CH shell overcoated by CD. This diagnostic is primarily based on measuring the knock-on deuteron spectrum and relies on knock-on protons for an independent measurement of the areal density of the plastic layers. Self-consistency would then dictate a favorable comparison between the values of the areal density of the CH layer inferred using the deuterons and protons.

In a direct-drive ICF target implosion, degradation in target performance is believed to occur primarily through Rayleigh–Taylor instability,[8] which is seeded by either target imperfections or laser nonuniformity. This instability, occurring at the ablation surface, can then feed through to the rear surface of the shell (or the fuel–pusher interface) during the acceleration phase of the instability. During the deceleration phase, these distortions at the fuel–pusher interface can grow, resulting in a mixing of the fuel and the pusher. The knock-on particle spec-

trum carries information about conditions in the target during this latter phase of the implosion. This is when core temperatures and densities are high enough to initiate the fusion process and to produce the knock-on ions. The mixing of the fuel and the shell at these times in the implosion can significantly modify the neutron production rate relative to one-dimensional (1-D) simulations and consequently the production of the knock-on ions and their spectra. Current diagnostics on the mixing of various layers in the target use x-ray spectroscopic signatures from various dopants in the target.[9] Techniques based on nuclear particles would provide an independent assessment of hydrodynamic mix in the target and could probe conditions in the target that are not easily accessible by x-ray spectroscopy. In addition, the knock-on deuteron diagnostic when used in conjunction with other diagnostic tools such as the neutron temporal diagnostic (NTD)[10] (which can measure the thermonuclear burn history of a target in an experiment) may serve to probe conditions in the compressed target at the onset of significant mix due to hydrodynamic instabilities.

In the sections that follow, we discuss (1) the knock-on particles from a typical target consisting of only two regions: DT fuel and a plastic (CH) shell. Knock-on deuterons (and tritons) are produced in the fuel, and knock-on protons are produced in the CH shell. (2) We then discuss specifically the knock-on diagnostic in the context of the elastically scattered deuterons and protons. (3) A generalization of this technique infers ρR in three regions of the compressed target, using the detailed shape of the deuteron spectrum. The target involved has three layers: DT, CH and, CD. Knock-on deuterons are produced in both the DT and CD layers with two well-defined high-energy peaks in the spectrum, separated by an energy determined by the areal density of the intermediate plastic layer. Using the result from simulation as an example, we demonstrate the procedure for deducing the ρR of the three layers from this spectrum. (4) We discuss how hydrodynamic instabilities could modify the measured knock-on deuteron spectrum and examine the validity of our analysis for these modified spectra. Finally, we mention briefly how we might compare our inferred results from experimental measurements to simulation.

Knock-on Ions as a Diagnostic for ρR

The knock-on diagnostic relies on the elastic scattering of various ions (deuterons and protons) in the target from the 14.1-MeV primary DT neutrons (Fig. 77.17). The number of such elastically scattered particles, N_K, is then proportional to the number of primary neutrons, Y, the number density for the

particle of interest, n_K, the average distance that the neutron traverses in the target, $\langle R \rangle$, and is given by

$$N_K = n_K \langle R \rangle \, \sigma_K \, Y, \tag{1}$$

where the subscript K indicates the type of knock-on particle and σ_K is the corresponding cross section for elastic scattering (0.64b for deuterons and 0.69b for protons). Using the relation between the ion number density and the mass density, this can be rewritten for the number of knock-on deuterons produced in equimolar DT as

$$N_D = 7.7 \times 10^{-2} \, Y \, \langle \rho R \rangle \, \mathrm{cm}^2 / \mathrm{gm}, \tag{2}$$

where $\langle \rho R \rangle$, the areal density, is given by

$$\langle \rho R \rangle \equiv \int_0^R \rho \, dr. \tag{3}$$

The ratio of the number of knock-on deuterons to the number of 14.1-MeV DT primary neutrons provides a measure of the fuel's areal density. We note that knock-on tritons can also be produced in a similar elastic-scattering process with the energetic DT neutrons.
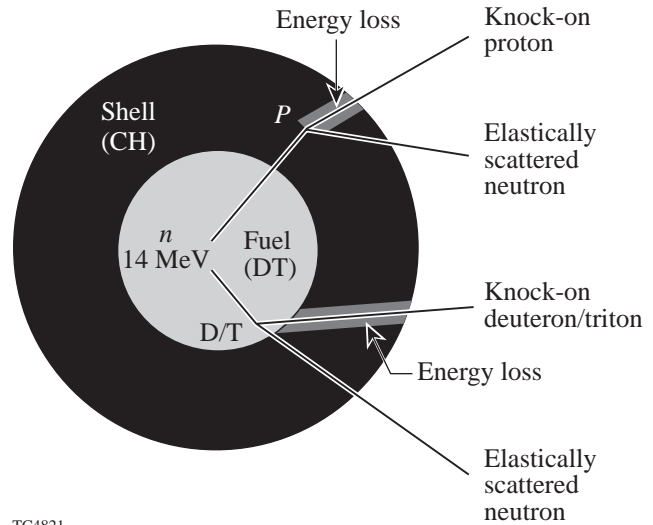
TC4821

Figure 77.17
Knock-on process.

Knock-on protons may be produced by the addition of hydrogen to the fuel or from the protons in the plastic, if the target is prepared with a plastic shell. For knock-on protons produced from the plastic (CH) layer, Eq. (1) for the number of elastically scattered protons can be rewritten as

$$N_P = 3.2 \times 10^{-2} \ Y \ \langle \rho R \rangle \ \text{cm}^2/\text{gm}. \qquad (4)$$

Again, the ratio of the number of elastically scattered protons to the number of DT neutrons is proportional to the areal density of the plastic layer.

In an experiment, however, it is not possible to detect all the knock-on particles produced. The CPS has a finite solid angle and therefore samples only a fraction of the knock-ons produced. Therefore, an assumption about isotropy in knock-on production is required to infer the total number of knock-on particles produced. (Deviations from isotropy can be checked because there are two CPS's that view the target from different directions).

The more challenging aspect of inferring the number of knock-ons produced relates to the spectrum of these particles. The knock-on spectrum is produced over a continuum of energies extending over several MeV (knock-on deuterons occur up to 12.5 MeV, while the proton spectrum extends up to 14.1 MeV) due to different neutron-impact parameters. The entire spectrum cannot be measured because the very low-energy knock-ons can be stopped in the target or in the filter in front of the CPS. Also, the very high density of background tracks at lower energies makes the measurement of the entire spectrum challenging. As a result, these diagnostics rely on the identification of specific features of the knock-on spectra to deduce the total number of ions produced and hence the areal density of the layer of interest.

1. Knock-on Deuterons

Even though the entire knock-on deuteron spectrum cannot be measured, the number of knock-ons produced can be reliably deduced using the high-energy region of the spectrum. The anisotropic differential cross section for elastic scattering results in a clearly identifiable peak in the spectrum (shown schematically in Fig. 77.18). The number of deuterons under this peak is about 16% of the total number of deuterons produced in the scattering process and is relatively independent of any distortion of the spectrum that may occur due to the slowing down of the deuterons in the target for a large range of areal densities. This useful feature allows a model-indepen-
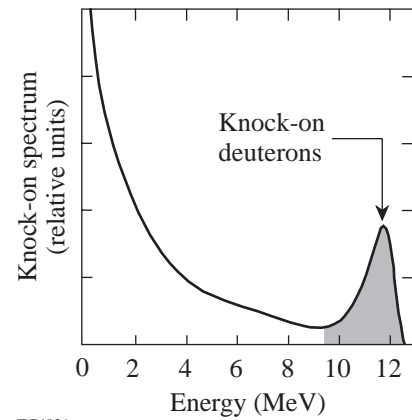
Figure 77.18
Schematic spectra of the knock-on particles.

dent inference of the total number of knock-on deuterons produced [and hence the ρR of the fuel, $(\rho R)_f$, through Eq. (2)].

In addition to the fuel areal density, the knock-on deuteron spectrum can also provide a measure of the shell's ρR. Knock-ons produced in the target slow down (primarily through energy loss in the shell), and as a result the spectrum is downshifted from its usual maximum of 12.5 MeV. Figure 77.19(a) shows the spectra due to different areal densities of the shell, $(\rho R)_{CH}$, calculated using a straight-line transport of the knock-on deuterons. The continuous energy loss of these charged ions is modeled using Ref. 11. The slowing down of the deuterons can be characterized by the end point of the spectrum (defined as the higher of the two energies of the half-maximum of the peak). As Fig. 77.19(b) indicates, this end point is proportional to the areal density of the shell, and this feature can be used to deduce this quantity in experiment.

An important feature of the knock-on deuteron diagnostic that enables a relatively model-independent measure of the shell's ρR is the temperature insensitivity of the high-energy peak of the deuteron spectrum. Figure 77.20 shows the deuteron spectra for two different shell ρR values at two different typical electron temperatures (the temperatures are typical of the shell in 1-D simulations of the implosions). Energy loss at these typical densities and temperatures in imploding ICF targets is dominated by losses to electrons (the electron density is related to the ion density and consequently the areal density of the material through its degree of ionization). Knock-on deuterons with energies greater than about 7 MeV typically have much higher velocities than electrons at the typical

Figure 77.20
The deuteron spectrum is relatively insensitive to temperatures in the cold portions of the target.

Figure 77.19
(a) The slowing down of the knock-on deuteron spectrum for different areal densities of the shell, $(\rho R)_{CH}$. (b) End-point energy of the spectrum as a function of the shell areal density.

temperatures in the cold plastic (~0.5 keV). In this limit, the energy loss is independent of the electron's temperature and is thus dependent only on the shell's ρR. As Fig. 77.19(a) indicates, for $\rho R \gtrsim 60$ mg/cm^2, the deuterons are slowed to less than 7 MeV. This value of ρR suggests a limit on the maximum value of the shell's areal density that can be deduced independent of temperature considerations in the shell. On the other hand, the knock-on tritons, being more massive, show a greater sensitivity to both the temperature and the ρR of the shell, limiting the range of temperatures and areal densities over which conditions in the target can be inferred reliably from their spectrum. However, the triton spectrum can be used as a self-consistency check on target conditions that have been measured by other diagnostics.

Detailed knock-on spectra have been recently measured experimentally using the CPS. These preliminary spectra show good agreement with those obtained from simulations of implosions. In the next section, we consider a generalization of the knock-on deuteron diagnostic that will enable more detailed information about the compressed target.

"Three-Layer" Targets

This extension of the deuteron diagnostic uses a target comprising three layers (shown in Fig. 77.21): an inner DT (or a DT+^{3}He) fuel region, a plastic (CH) shell, and an ablator (CD). This target is different from those considered previously, where only two layers (DT and CH) were present. Its characteristics and dimensions are commensurate with targets surrogate to future cryogenic targets designed for the OMEGA laser,[12] and the diagnostic design permits some flexibility in each layer's thickness while retaining its equivalence to currently used surrogate targets.

Several energetic nuclear particles, shown schematically in Fig. 77.21, can be used to diagnose areal densities. Knock-on protons are produced in the plastic, and the areal density of the plastic layer can be deduced from the ratio of the number of protons produced to the number of primary neutrons. The addition of ^{3}He to the DT fuel is optional. The presence of ^{3}He in the target, however, provides another independent measure of areal density; the energy loss of the energetic 14.7-MeV proton from the D-^{3}He reaction is proportional to the total areal density of the target.[4]
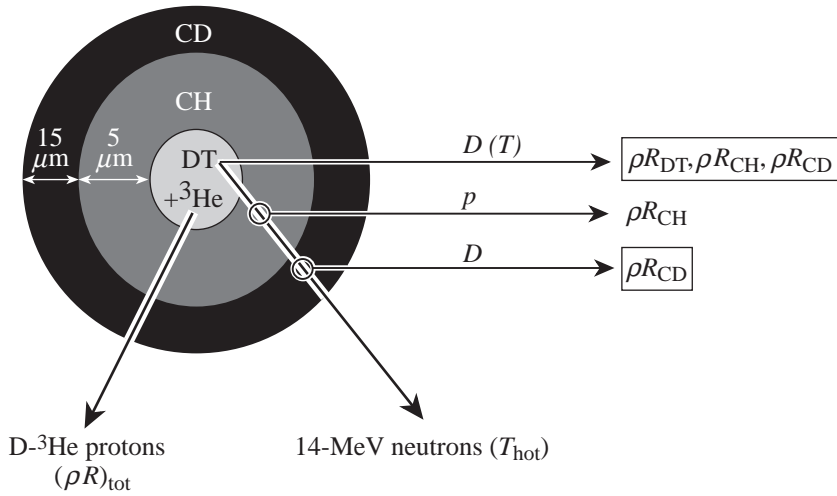
Figure 77.21
Sources of particles for the diagnosis of areal densities in three-layer targets.

TC4844

Knock-on deuterons are produced in both the fuel and the CD layer. The deuterons produced in the fuel lose energy as they traverse the target, causing the high-energy peak to shift downward. The spectrum of deuterons from the CD layer, on the other hand, has its maximum energy at the nascent value of 12.5 MeV. The complete simulated spectrum for a target with a combined ablator and shell thickness of 20 μm (5 μm CH and 15 μm CD) is shown in Fig. 77.22. The target is driven with a 1-ns square pulse, which has been chosen arbitrarily. The spectrum is produced from a 1-D simulation of the implosion using the hydrodynamic code *LILAC*[13] and a post-processor that transports the knock-ons in straight lines for every time

step using the simulated density and temperature profiles while accounting for their energy loss. The relevant features are the two high-energy peaks in the spectrum arising from the individual contributions of the fuel and CD layers (shown as dashed lines in Fig. 77.22). The area under the higher-energy peak is primarily a measure of the areal density of the CD layer, $(\rho R)_{CD}$, whereas the peak at the lower energy has contributions from both the fuel and the CD shell. The separation of the two peaks provides a measure of the areal density of the plastic layer, $(\rho R)_{CH}$. We note that for the typical electron temperatures in the cold shell and ablator, the energy range spanned by the peaks of such a deuteron spectrum is fairly temperature insensitive. This temperature independence will be exploited later to deduce the areal densities of the three regions of the target from the data.

The areal densities of the three layers can be deduced nearly model independently using the scheme outlined previously, if the peaks are well separated. We first consider the areal density of the plastic layer. For the spectrum shown in Fig. 77.23(a) (a solid line) the separation of the two high-energy peaks is about 3 MeV. The areal density of the plastic resulting in this separation should correspond to that value that results in a downshift of the end-point energy by the same amount. From Fig. 77.19(b), this separation corresponds to an areal density of about 40 mg/cm^2 to be compared with the value of 35 mg/cm^2 in the simulation. Next, to deduce the areal density of the CD layer, we calculate the total number of deuterons in the high-energy peak. This value is a known fraction of the total number of deuterons produced since this portion of the spectrum is unaffected by the presence of deuterons from the fuel. For the

TC4845

Figure 77.22
Simulated knock-on deuteron spectrum from a three-layer target with contributions from the individual layers.

Figure 77.23
(a) Comparison of test (simulated) spectrum (solid line) showing spectrum from best-fit model (dashed line). (b) Areal densities for the three layers that result in spectra whose difference squared is within 20% of the least-squares value. Each shaded region represents the set of areal densities of the fuel and CD layer satisfying the 20% criterion, for a fixed value of the areal density of the CH layer.

layer depends on the slowing down of the deuterons and the geometry of the paths through the target. An upper limit for $(\rho R)_f$ can be obtained by assuming that all the deuter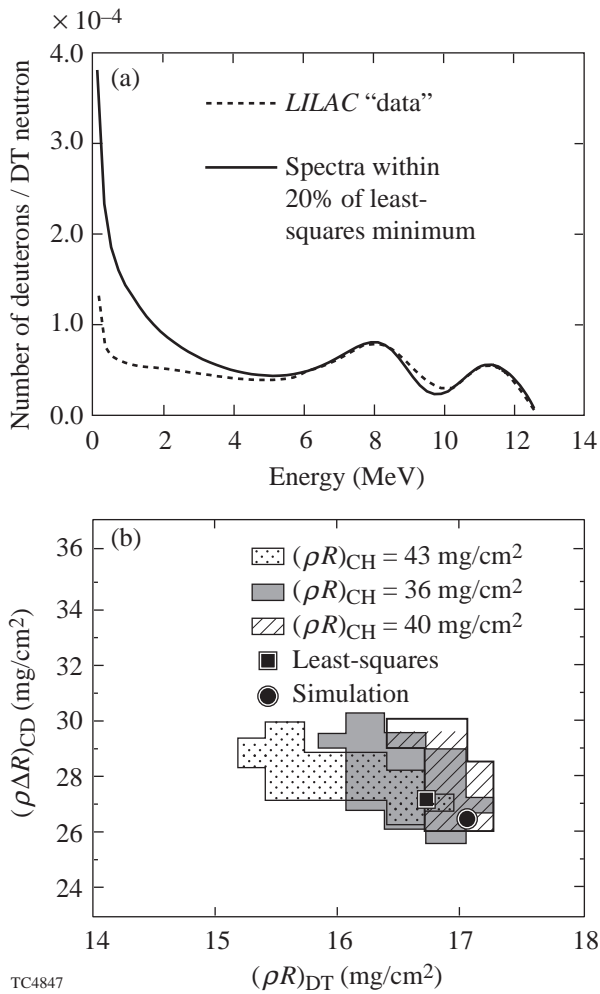ons under this peak are produced in the fuel. In this case, the inferred areal density of the fuel using Eq. (2) is 23.6 mg/cm^2 to be compared with the simulation value of 17.0 mg/cm^2.

This uncertainty in the value of the inferred fuel areal density can be mitigated through a different analysis of the knock-on deuteron spectrum. We consider deuteron spectra from a model where each layer is approximated by a constant density and temperature (an ice-block model). The density and the thickness of each layer are chosen by requiring a fixed mass for each layer (known from the specifications of the target being modeled) and a chosen ρR. We note once again that since the deuteron spectrum is insensitive for the ranges of areal densities expected in such implosions, temperatures in the colder plastic and CD can be ignored in this analysis. The choice of fuel temperature, however, cannot be made arbitrarily since the deuterons may lose some energy in the hot fuel. In this example, we choose the fuel temperature at peak neutron rate in the simulation as the relevant fuel temperature. In deducing areal densities from the experimentally measured spectrum, the temperature obtained experimentally from the width of the DT neutron spectrum[14] (measured through time-of-flight techniques) should be used in the model.

In this manner we construct a static representation of the target and fit the spectra from such a model by varying the areal densities of each layer. While the ice-block model is not expected to accurately describe the primary complexities of an imploding target such as the spatial and time-dependent variation of densities and temperatures, the spatial localization of neutron sources in the target, and the geometry of the knock-on trajectories through the target, it should provide a reasonable time and spatially averaged representation of the target relevant to the knock-on spectrum.

To test our scheme for deducing the areal densities, we consider again the simulated spectrum shown as a solid line in Fig. 77.23(a). Using the model described above, we vary the ρR of the three layers to minimize the least-squares difference between the spectrum from the model and the data. The energy range chosen for this minimization is the area determining the two peaks in the spectrum ($\gtrsim$5 MeV). The technique for minimization we choose is based on the Downhill Simplex Method of Nelder and Mead.[15] If we assume that the neutrons are created uniformly in the fuel, the resulting spectrum of

spectrum (solid line) in Fig. 77.23(a), this is the number of deuterons above 10.25 MeV, and again, from the spectra in Fig. 77.19(a) this corresponds to about 12% of the total knock-on deuterons produced. Using this fraction for the number of deuterons in the peak and a formula for CD [similar to Eq. (2)], we obtain a value of 26.5 mg/cm^2 for the CD layer that compares favorably with the value of 25.6 mg/cm^2 in the simulation. While the areal densities of the CH and CD layers can be determined model independently, some uncertainty is introduced in the value of the areal density of the fuel, $(\rho R)_f$, since not all the deuterons under the low-energy peak are produced in the fuel. The contribution to this peak from the CD

TC4847

such a minimization scheme is shown as the dashed line in Fig. 77.23(a). Our values for the areal densities for the DT, CH, and CD layers (16.5, 40, and 27.4 mg/cm^2, respectively) compare favorably with the results from the simulation (17, 35, and 25.6 mg/cm^2). These values agree very well with the model-independent extraction of the areal densities of the CH and CD layers, implying correctly well-separated peaks and, in addition, provide a tighter bound on $(\rho R)_f$.

To gauge the sensitivity of the spectrum to the least-squares values of ρR obtained in this manner, we consider Fig. 77.23(b), which shows sets of $(\rho R)_{CD}$ and $(\rho R)_f$ for different values of $(\rho R)_{CH}$. [Each shaded region represents a set of areal densities of CD and fuel, corresponding to a certain value of $(\rho R)_{CH}$.] For each value of $(\rho R)_{CH}$, this set corresponds to those values whose spectra are within 20% of the least-squares value. This range of areal densities of CD and the fuel has been obtained by fixing the areal density of the plastic in the model to the required value and varying the areal densities of the CD and fuel layers. In this manner, we find the range of acceptable values of the areal densities of each layer in the target. Also shown in the figure is the least-squares value (square) and the result from the 1-D simulation (circle). We see that by using this procedure we obtain values of ρR of the fuel and CD layer to within 10% of the true value. The larger range of acceptable values of $(\rho R)_{CH}$ (35.5 to 43 mg/cm^2 for the plastic layer compared to 15 to 17.2 mg/cm^2 for the fuel and 25.5 to 29.1 mg/cm^2 for the CD layer) indicates that the deuteron spectrum is less sensitive to the areal density of the plastic layer. This is probably due to the fact that $(\rho R)_{CH}$ does not determine an absolute number or energy; the relative separation of the two high-energy peaks is determined by this value. A comparison with the value deduced from the knock-on proton spectrum would, in addition, provide an independent check on the value of $(\rho R)_{CH}$. Finally, we note that the true set of areal density values obtained from the simulation is not excluded from our result at this 20% level, thus providing a measure of the sensitivity of the spectrum to the three areal densities.

If we assume that the neutrons are produced in the center of the fuel and repeat the above analysis, we obtain the following results: an areal density of 16.3, 40.4, and 30.5 mg/cm^2 for DT, CH, and CD, respectively. The least-squares difference between the model spectra and the test data for this case is higher than for the uniform source (4.3×10^4 and 2.1×10^4, respectively), implying correctly a uniform distribution of the DT neutrons in the simulation.

Modification of the Knock-on Deuteron Spectrum due to Mix

Our discussion has so far been based on a 1-D simulation of the implosion that does not include the effects of hydrodynamic instabilities and mix on the imploding target. In addition, any effects on the target due to long-wavelength asymmetries (possibly due to laser-beam imbalances in power and pointing errors) have also been ignored. The effects of such departures on nuclear and particle diagnostics are difficult to determine quantitatively from 1-D simulation.

During the deceleration phase, the Rayleigh–Taylor unstable fuel–pusher interface, seeded by its nonuniformity, can result in a mixing of the hot fuel and cold pusher. This mixing of materials at very different temperatures can result in a significant quenching of the neutron yield relative to 1-D simulations (that do not include this effect). Since the diagnostic should probe conditions in the compressed target corresponding to times of peak neutron and consequently knock-on production, this quenching can result in different conditions probed experimentally by the diagnostic relative to 1-D simulations. For the purposes of studying the feasibility of the diagnostic in the presence of such mixing, we assume that the effect of the deviations from 1-D is to exclusively change the neutron-production rate and hence the knock-on spectrum. In other words, the effect of such departures from 1-D behavior on the implosion dynamics is ignored.

To assess the effect of this mixing, we compare the spectra from purely 1-D simulations with two models of neutron rate truncation. These models should span the extremes of possible neutron rate truncations in the experiment. In the first model, we assume that a portion of the fuel implodes with a constant velocity acquired just before deceleration begins and is unaffected by the growing instabilities at the fuel–pusher interface. We then assume that the only neutron yield is from this portion of the fuel. The neutron rate from this model is shown in Fig. 77.24(a) as the free-fall rate and is significantly lower in magnitude relative to the 1-D simulation. Figure 77.24(b) shows the corresponding areal densities in the target from the simulation. As Figs. 77.24(a) and 77.24(b) indicate, the neutron rate in this model peaks earlier and thus probes earlier times in the implosion. This results in a deuteron spectrum (dotted line in Fig. 77.25) that is characteristic of smaller areal densities for all three layers. Our analysis provides values that agree reasonably with the results from simulation; the least-squares values are 9.8, 22.5, and 17.1 mg/cm^2, whereas the results of the simulation are 8.9, 26.7, and 15.8 mg/cm^2. We once again note that the independent measurement of $(\rho R)_{CH}$
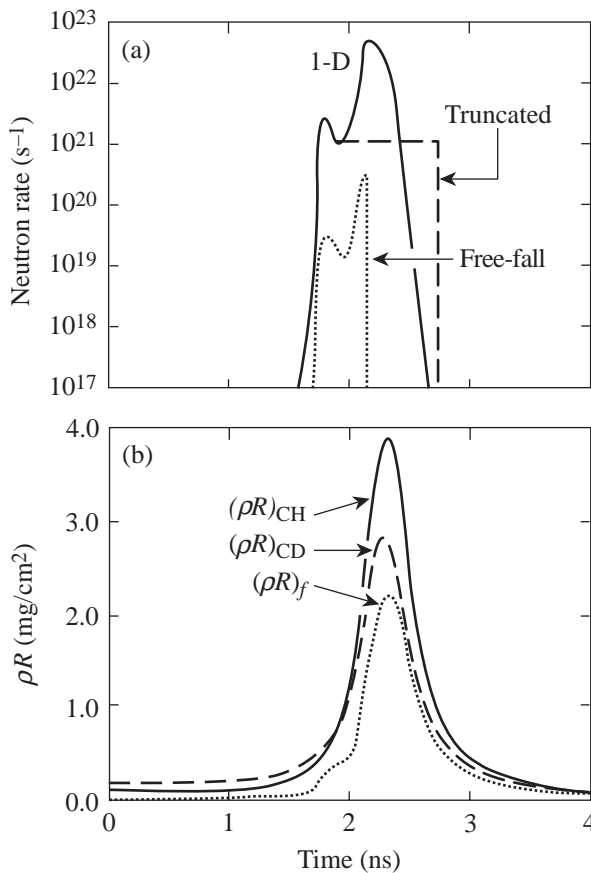
Figure 77.24

(a) Neutron rate curves for different models used for assessing the modification of the deuteron spectrum due to hydrodynamic mix: solid line—result of a 1-D simulation; dotted line—neutron rate obtained from a free-fall model (see text); and dashed line—neutron rate fixed to a constant value at a certain time. (b) ρR history of the target from 1-D simulations. In the simulations, the diagnostic is sensitive to areal densities near peak neutron rates and consequently peak compression.

using the knock-on proton spectrum can constrain the areal density of plastic inferred from the deuteron spectrum. The favorable comparison between the values of the areal densities inferred from the diagnostic and the true values suggests that the areal densities can still be deduced reasonably were such a modified spectrum the result of a measurement.

In a different model, we assume that the neutron rate proceeds as given by the 1-D simulation up to a certain time, and, thereafter, it proceeds at a constant rate given by the rate at the chosen time. This is shown in Fig. 77.24(a) as the constant burn rate model. A comparison with Fig. 77.24(b) indicates that the diagnostic then probes the times corresponding to the steep
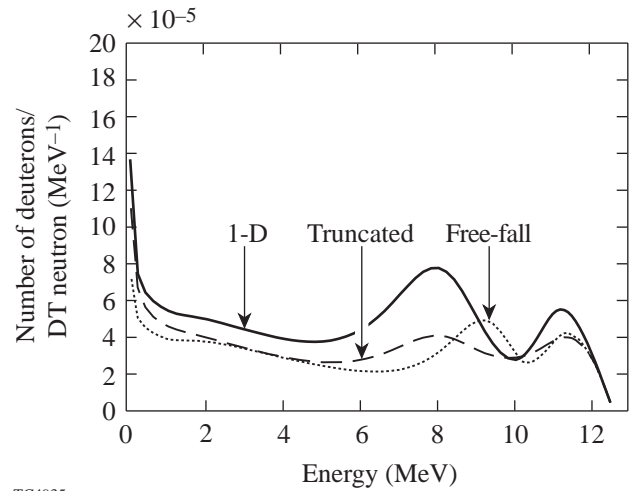
Figure 77.25
Knock-on deuteron spectra using the three models of neutron rate truncation shown in Fig. 77.24(a).

changes in the areal density. The significant neutron rate for a large fraction of time over which these changes in areal density occur in the target results in a considerably broadened emergent spectrum with less well defined peaks (dashed line in Fig. 77.25), which are to be compared with the results of the simulation (10.7, 32.3, and 16.0 mg/cm^2). Nevertheless, the least-squared values (8.9, 22.9, and 18.7 mg/cm^2) compare favorably with the results of the simulation (17.9, 36.0, and 23.0 mg/cm^2), suggesting that our analysis can be used to reliably infer the areal density of each of the layers, even when the peaks in the spectrum are less well defined.

Experimentally, the neutron rate history can be obtained through the neutron temporal diagnostic (NTD).[10] One method to compare the implosion with 1-D simulations could be as follows: The experimentally obtained neutron rate curve could be used to identify the times in the implosion probed by the diagnostic—the diagnostic probes times around the peak neutron burn rate. An identification of these times would allow us to calculate the areal densities of the three layers from the simulation. A comparison of these values with those obtained from the knock-on diagnostic would shed light on whether conditions in the experiment compare favorably with the 1-D simulation up to the time probed by the diagnostic. If the areal densities inferred from the diagnostic differ considerably from those in the simulation, this procedure will allow one to identify a time when mixing effects have already significantly influenced the fusion processes. Independent of any comparison with detailed hydrodynamics simulations, the areal densi-

ties deduced from the knock-on deuteron diagnostic should be nearly model independent and would provide information about the conditions in the target corresponding to times in the implosion identified using the NTD. Further, a comparison with detailed mixing models may enable the identification of conditions in the target that would result in the observed neutron rate curves and the inferred values of (ρR).

Summary and Conclusions

In this article, we have presented a new diagnostic based on knock-on deuterons, which will simultaneously diagnose the areal densities in three different regions of the compressed ICF target. These targets have three layers (DT, CH, and CD), and the areal density of each of these layers can be inferred from the deuteron diagnostic. In addition, knock-on protons from the CH layer can be used to independently deduce the areal density of the plastic.

When used in conjunction with a detector that measures the neutron rate history of an implosion (NTD), the time in the implosion probed by this diagnostic can be identified. This will permit a more detailed comparison between the simulation and experiment.

We have also examined the modification of the knock-on deuteron spectrum due to departures from 1-D behavior such as mixing. We conclude that while the spectrum may be influenced significantly by such departures from 1-D behavior, our method for analyzing the experimental spectrum should still reliably infer the areal densities in the three layers. Detailed mixing models would be required, however, to make any inferences about the mixing process in implosions. Experiments to measure these spectra from an imploding target are currently underway, and the results will be presented elsewhere.

REFERENCES

1. G. S. Fraley *et al.*, Phys. Fluids **17**, 474 (1974).

2. S. Skupsky and S. Kacenjar, J. Appl. Phys. **52**, 2608 (1981).

3. M. D. Cable and S. P. Hatchett, J. Appl. Phys. **62**, 2233 (1987).

4. Laboratory for Laser Energetics LLE Review **73**, 15, NTIS document No. DOE/SF/19460-212 (1997). Copies may be obtained from the National Technical Information Service, Springfield, VA 22161.

5. H. Nakaishi *et al.*, Appl. Phys. Lett. **54**, 1308 (1989).

6. D. G. Hicks, C. K. Li, R. D. Petrasso, F. H. Seguin, B. E. Burke, J. P. Knauer, S. Cremer, R. L. Kremens, M. D. Cable, and T. W. Phillips, Rev. Sci. Instrum. **68**, 589 (1997).

7. P. B. Radha and S. Skupsky, "A Novel Charged-Particle Diagnostic for ρR in Compressed ICF Targets," in preparation.

8. Lord Rayleigh, Proc. London Math Soc. **XIV**, 170 (1883); G. Taylor, Proc. R. Soc. London Ser. A **201**, 192 (1950).

9. D. K. Bradley, J. A. Delettrez, R. Epstein, R. P. J. Town, C. P. Verdon, B. Yaakobi, S. Regan, F. J. Marshall, T. R. Boehly, J. P. Knauer, D. D. Meyerhofer, V. A. Smalyuk, W. Seka, D. A. Haynes, Jr., M. Gunderson, G. Junkel, C. F. Hooper, Jr., P. M. Bell, T. J. Ognibene, and R. A. Lerche, Phys. Plasmas **5**, 1870 (1998).

10. R. A. Lerche, D. W. Phillion, and G. L. Tietbohl, Rev. Sci. Instrum. **66**, 933 (1995).

11. S. Skupsky, Phys. Rev. A **16**, 727 (1977); J. D. Jackson, *Classical Electrodynamics*, 2nd ed. (Wiley, New York, 1975).

12. F. J. Marshall, B. Yaakobi, D. D. Meyerhofer, R. P. J. Town, J. A. Delettrez, V. Glebov, D. K. Bradley, J. P. Knauer, M. D. Cable, and T. J. Ognibene, Bull. Am. Phys. Soc. **43**, 1784 (1998).

13. E. Goldman, Laboratory for Laser Energetics Report No. 16, University of Rochester (1973).

14. H. Brysk, Plasma Phys. **15**, 611 (1973).

15. W. H. Press *et al.*, *Numerical Recipes in FORTRAN: The Art of Scientific Computing*, 2nd ed. (Cambridge University Press, Cambridge, England, 1992).

Arresting UV-Laser Damage in Fused Silica

Deciding when to replace spot-damage-afflicted fused-silica optics or, in the case of inaccessible, space-based lasers, predicting the useful service life of fused-silica optics before catastrophic, pulsed-laser-driven crack growth shatters a part has recently become simpler. By empirically deriving a rule for laser-driven crack growth in fused silica as a function of the number of constant-fluence laser pulses, Dahmani *et al.*[1] provided laser systems designers and operators with guidance on the crack-growth kinetics as well as on the stress-related ramifications such a laser-driven crack entails. Specifically, a *hoop stress* in the immediate vicinity of a crack growing along the beam propagation direction was identified as strongly coupling to both the laser fluence and the crack.[2] It prompted the question of whether or not *breaking the hoop-stress symmetry* by some external perturbation will accelerate or stymie crack growth or, alternatively, will have no effect at all.

In this article, we report not only on the finding that, depending on the *magnitude* of a perturbing external stress, crack propagation in fused silica may *slow* relative to stress-free conditions, but also the more unexpected finding that the applied external stress *raises the damage-initiation fluence*. In gathering this evidence, a conventional experimental arrangement was used.

Pulses from a Nd:glass oscillator/single-pass amplifier system were frequency tripled in a dual-crystal KDP cell to yield temporally stable, 500-ps pulses at a repetition rate of one pulse every 10 s. Prior to frequency conversion, the IR pulse was sent through a nonmagnifying, vacuum spatial filter. UV pulses were focused by a 2-m-focal-length lens to an ~600-μm spot size at the sample entrance surface. For each pulse, a record of the fluence distribution in this spot was acquired by a charge-injection-device camera located in a sample-equivalent plane and digitized to 8-bit accuracy. Spatially integrated UV energy per pulse was also monitored on each exposure. The UV beam-incidence direction was chosen to be a few degrees (<10) off-normal to the sample entrance face to prevent (1) any back-reflection of residual, unconverted IR from seeding the amplifier in the backward direction, and (2) setting

up a 351-nm interference pattern between sample entrance and exit surfaces that would invalidate the calculated fluence distribution. Damage initiation anywhere between the two sample surfaces, i.e., along the pulse-propagation direction, was recorded by 110×-magnification dark-field microscopy. After damage initiation, the crack length was measured microscopically by viewing the sample *orthogonally* to the laser-pulse propagation direction.

Fused-silica samples (Corning 7940, UV Grade A), with length $L = 64$ mm, width $w = 13.6$ mm, and thickness $t = 4.6$ mm, were conventionally pitch polished to *laser quality* on the entrance and exit surfaces and to *cosmetic quality* around the edges.

Samples were mechanically stressed by first centering each between apertured aluminum plates separately attached to a load cell (Eaton, Model 3397-25, maximum load capacity: 25 lbs). A predetermined, constant, uniaxial, compressive load was applied in such a manner that the compressive-force direction nearly coincided with the laser-pulse propagation direction (Fig. 77.26). The laser pulse entered and exited the samples through the apertures in the aluminum plates. The need for having beam-passage apertures *ipso facto* brings about stress conditions that vary from point to point within the aperture, both in magnitude and in principal directions (compressive or tensile). At first, this may appear as complicating data interpretation; for the following reason, however, it does not.

Laser-damage thresholds (for pulse lengths greater than picoseconds) are always reported as *average values* derived from a statistical number of sample sites *per tested specimen*. In all *nondeterministic*, i.e., extrinsic-impurity-driven, laser-damage processes the occurrence of damage hinges on the statistical presence or absence of one or more absorbing impurities within a given irradiated area. This statistical distribution in defect volume density is now convoluted by a site-to-site–varying stress distribution. In an ideal experiment, a large enough number of tests on samples and sites with precisely
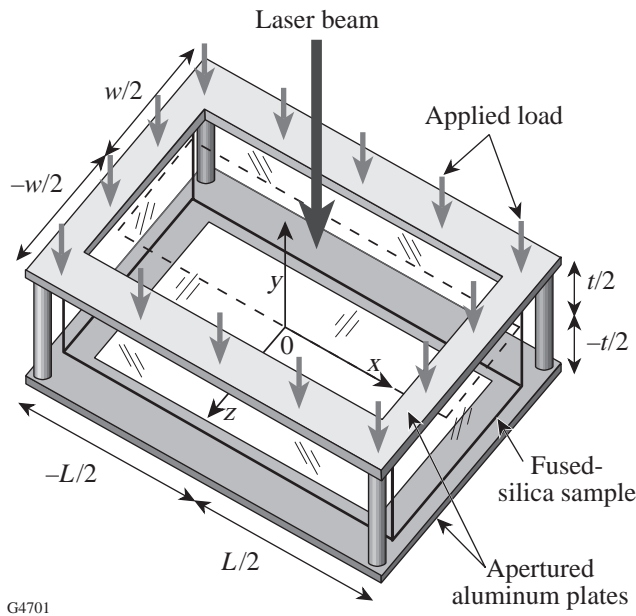
Figure 77.26
Experimental arrangement for applying compressive loads to fused-silica surfaces by clamping the conventionally polished sample between aluminum plates. The static pressure applied is measured by the load cell. Sample dimensions are length $L = 64$ mm, width $w = 13.6$ mm, and thickness $t = 4.6$ mm oriented relative to the Cartesian coordinate system as indicated.

known local stress will deconvolve the two distributions; in practice, however, this is unrealistic. Rather, simulation of local stress conditions by finite-element methods,[3] or when possible by analytic approaches, permits one to find with acceptable accuracy, for various aperture boundary conditions, the compressive and tensile stresses within the aperture, based on which one may choose many irradiation sites on a single sample. To guarantee good statistics, however, the current measurements still rely on more than one sample. All stress values quoted here are numerically derived from experimentally measured sample-loading conditions. The total applied force on the sample is 10 kgf (1 kgf = 9.8 N) in this case.

The onset of damage is defined as follows: for the given microscopic magnification and lighting conditions, any observable, permanent, irradiation-induced, surface or bulk modification. Throughout this article, initiation thresholds are reported for *1-on-1 mode*, i.e., each sample site is irradiated only once. For well-known reasons,[4] conventionally polished material of good bulk purity damages first at the exit surface. In these experiments, this is not only confirmed but *damage propagation* effects under multiple irradiation conditions are, for now, deliberately restricted to those events in which throughout

damage-crack initiation and growth no entrance-surface damage is encountered, i.e., the laser fluence at the damage site remains unobscured by upstream obstacles.

We first report the effect of stress on *damage initiation*. In Fig. 77.27, the 351-nm, damage-onset fluence threshold is plotted for exit-surface damage (× symbols) against applied stress magnitude (sign convention: + tensile, − compressive). Here the load is applied nearly collinear with the pulse-propagation direction. As is immediately evident, regardless of whether the stress character is tensile or compressive, *threshold enhancements* of up to 70% are attainable from modest stresses, and the largest, relative threshold-improvement increments can be garnered from the smallest stresses. Note how the symmetry around zero stress tends to imply that the underlying damage-initiation process is independent of whether the stress is compressive or tensile. Over how large a tensile-stress range this holds true is yet to be ascertained.
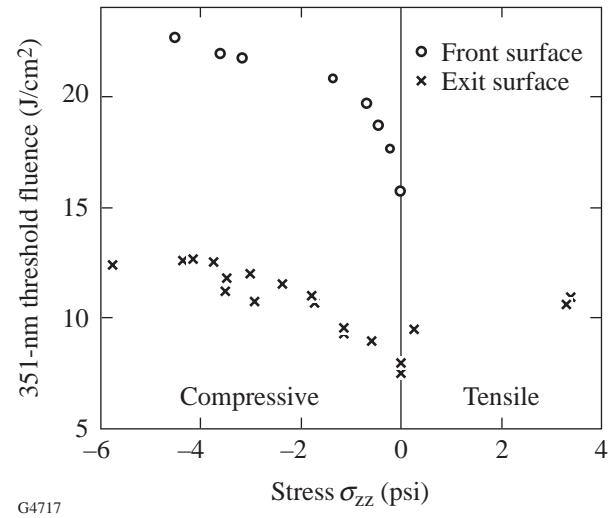
Figure 77.27
Entrance (*x*)- and exit (*o*)-surface, 351-nm damage-*initiation* threshold as a function of applied stress follows similar trends.

For the laser systems designer it is important to know if the beneficial stress effect is an *exit-surface phenomenon only* or if an equivalent advantage can be gained for the entrance surface as well. Collecting the data for which *front-surface damage* was incurred, i.e., data excluded so far, Fig. 77.27 also plots a similar trend for the entrance-surface damage-initiation threshold (open circles) as for the exit surface.

We next concentrate on *laser-driven crack growth*. Once the exit-surface damage-initiation threshold $F_{\text{exit/thr}}$ is determined as described above, a *flaw* is deliberately created at a

new site, which upon further irradiation becomes the source for both crack formation and crack propagation. Cracks observed in these experiments are not empty voids but are filled with granular glass debris that scatters light efficiently. The growth dynamics of such cracks as a function of incident fluence and number of exposures has already been reported elsewhere.[2] To underscore the influence of stress on the crack-growth kinetics, we compare here results obtained under extreme conditions, i.e., for irradiation of a flaw by 270 consecutive laser pulses of constant fluence $F_L = 2.1 \times F_{\text{exit/thr}}$, a far-from-normal condition for most lasers. By choosing extreme irradiation conditions, *crack-growth arrest* is most convincingly demonstrated. Figure 77.28 displays side-by-side micrographs of cracks formed in (a) the unstressed sample ($\sigma_{zz} = 0$) and (b) the stressed sample ($\sigma_{zz} = -6$ psi). Note that in Fig. 77.28(a) the crack growth has pushed the crack tip beyond the field of view. A less-striking, though quantitative, account of crack arrest as a function of applied stress is displayed in Fig. 77.29, where the length of cracks from multiple sites, all irradiated at the above-fluence condition, is plotted against the stress prevailing at any particular site. The functional dependence on applied stress displayed in Fig. 77.29 offers promise: much can be achieved in altering, by modest stress, the crack-propagation outcome, while the empirical crack-length-reduction *limit* for larger stresses renders these unnecessary in practice. The concomitant penalty in stress-induced birefringence that such crack-growth preven-

tion entails is also kept within bounds: the maximum stress of 6 psi plotted in Figs. 77.27 and 77.29 causes 0.5-nm retardance. A second, intriguing ramification of the slope in Fig. 77.29 pertains to damage testing in general: there exists evidence[5] that the polishing process leaves a thin, densified layer of silica at/near the air interface, the stress within which may locally vary or may vary from sample to sample. Depending on the extent of such variation, the statistical error on measured surface-damage initiation thresholds should correspondingly be large since the slope in Fig. 77.27 is steepest near zero stress. An unfortunate paucity of reported 351-nm, fused-silica, surface-damage thresholds makes it, at this time, difficult to corroborate this correlation from literature data. In the same vein, there should be a damage-initiation stress effect for interfacial damage on *coated* or *cladded* silica surfaces whenever the thermal-expansion mismatch between the substrate and the film stack or cladding material introduces interfacial stress. This would be most readily observable in antireflective coatings as these permit significant laser intensity to reach the substrate interface. Finally, there remains an urgent question to be resolved as to whether this phenomenon is unique to fused silica or may be present also in other glasses.

We presented here results from stress-inhibited laser-driven crack propagation and stress-delayed damage-initiation experiments in fused silica at 351 nm. Within the stress interval of $-6 \leq \sigma_{zz} \leq 4$ psi, the damage initiation threshold is raised by

G4713
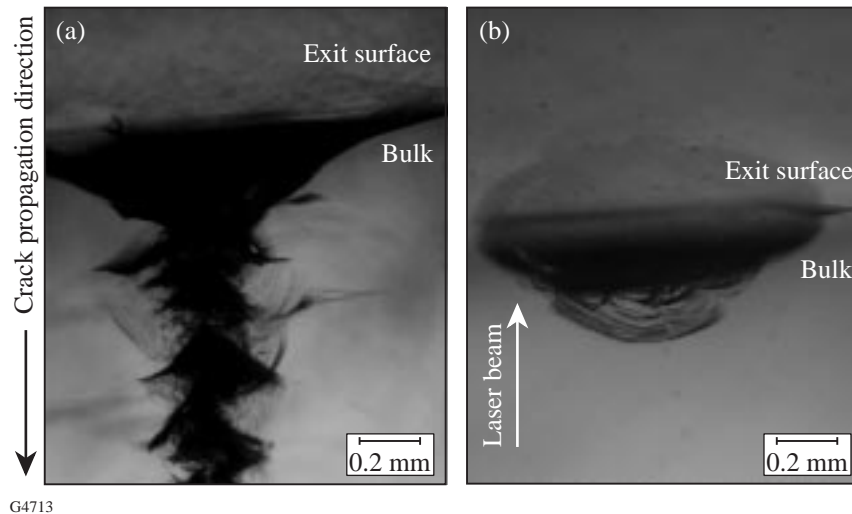
Figure 77.28
Cross-sectional micrographs of laser-induced cracks after 270 exposures to constant fluences $F_L = 2.1 \times F_{\text{exit/thr}}$ in (a) a sample free of external stress and (b) a sample with $\sigma_{zz} = -6$ psi. The crack tip in micrograph (a) is, for the given magnification, located already outside the field of view.

70%. For such modest stresses, both compressive or tensile stresses appear to raise this threshold while keeping the induced-birefringence penalty ≤0.5-nm retardation. The ramifications of these findings for large-aperture systems, such as OMEGA, are yet to fully emerge: aperture scaling must commence and the stress-magnitude regime must be extended to higher stresses in order to evaluate whether or not the apparent saturation (near-zero slope) at 6 psi remains. These tasks are in progress at this time.
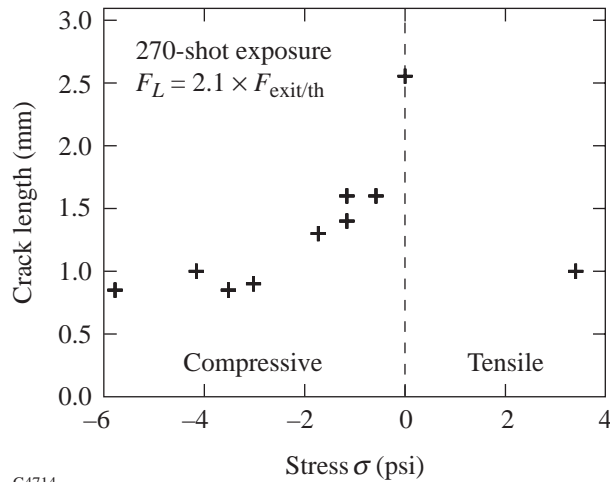
G4714

Figure 77.29
Crack length as a function of applied external stress for identical irradiation conditions as in Fig. 77.28.

REFERENCES

   1. F. Dahmani, J. C. Lambropoulos, A. W. Schmid, S. Papernov, and S. J. Burns, "Fracture of Fused Silica with 351-nm-Laser-Generated Surface Cracks," to be published in Journal of Materials Research.

   2. F. Dahmani, A. W. Schmid, J. C. Lambropoulos, and S. J. Burns, Appl. Opt. **37**, 7772 (1998).

   3. ANSYS 5.4® is a finite-element code developed by Ansys Inc.

   4. N. L. Boling, M. D. Crisp, and G. Dubé, Appl. Opt. **12**, 650 (1973).

   5. H. Yokota *et al.*, Surf. Sci. **16**, 265 (1969).

Theory of the Ablative Richtmyer–Meshkov Instability

In inertial confinement fusion (ICF) implosions, a laser irradiation induces a shock wave propagating through the target. During the shock transit time, the ablation front travels at a constant velocity, and any surface perturbations could grow due to the Richtmyer-Meshkov (RM)–like instability.[1–5] Later, when a rarefaction wave reaches the ablation surface, the acceleration of the interface becomes finite, and ablation-front perturbations (multiplied by the RM growth) grow due to the Rayleigh–Taylor (RT) instability. It is important to study the perturbation evolution during the shock transit time mainly for two reasons: (1) to determine the initial conditions for the RT phase of instability and (2) to analyze the level of laser imprint on directly driven ICF targets.

The RM instability occurs when a plane shock interacts with a corrugated interface between two fluids (see Fig. 77.30). As a result of such an interaction, interface perturbation starts to grow because the transmitted shock is converging at the peak (point A) and diverging at the valley (point B). Converging shock increases pressure and accelerates perturbation peak into fluid 2. Similar instability occurs at the distorted interface of an ablatively driven target, where ablation pressure generates a rippled shock that induces pressure perturbation at the ablation front and causes distortion growth. The classical treatment of the RM problem leads to a linear-in-time asymptotic perturbation growth[1] $\eta(kc_s t \gg 1) \simeq \eta_0 kc_s t$, where η is the interface perturbation, k is the mode wave number, c_s is the sound speed of the compressed material, and η_0 is a constant depending on the initial conditions. Recent studies showed that the ablation of material from the target surface turns such a growth into damped oscillations.[4,5] During the last two years, several researchers have made attempts to develop an analytic theory of the ablative Richtmyer–Meshkov instability. In Refs. 4 and 5, the authors, on the basis of a gas dynamic model, found saturation of perturbations. At the ablation front, however, they used an heuristic boundary condition that, as will be shown later, contradicts the result of the self-consistent theory.[6–8] In Ref. 3 the boundary conditions at the ablation front were derived by using the Chapman–Jouget deflagration model. As criticized in Ref. 5, however, this
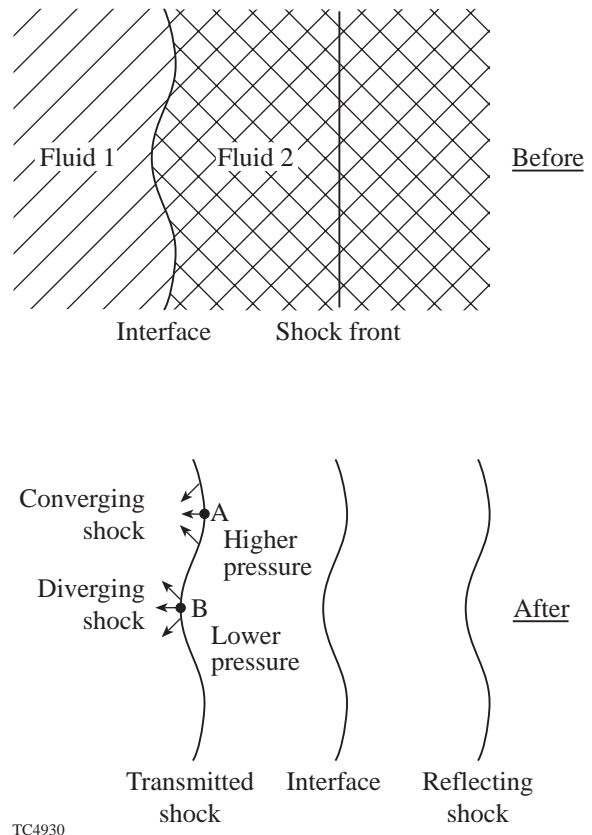
Figure 77.30
Richtmyer–Meshkov instability occurs when a plane shock interacts with a corrugated interface between two fluids.

model does not give an adequate description of the ablative process. In this article, we develop a sharp-boundary model to study the imposed mass-perturbation growth during the shock-transit time. The boundary conditions at the shock front are derived using the Hugoniot relations. At the ablation front the result of the self-consistent analysis[6–8] is applied, and it is shown that the asymptotic behavior of the ablation-front perturbations is quite different from the earlier theoretical predictions.[3–5] In particular, the dynamic overpressure causes

perturbation oscillations in time (in agreement with the numerical results)[2,5] with the frequency $\omega = k\sqrt{V_a V_{bl}}$ and the amplitude $\eta_0 c_s/\sqrt{V_a V_{bl}}$, where V_a and V_{bl} are the ablation and blow-off velocity, respectively. In addition, the mass ablation damps the oscillation amplitude on a time scale $1/(kV_a) \gg 1/\omega$.

To study the linear perturbation growth during the shock-transit time, we consider a sharp-boundary model and identify the following three constant-density regions (see Fig. 77.31): (1) uncompressed material (undriven portion of the target) $y < y_s$ ($\rho = \rho_1$), (2) material compressed by the shock $y_s < y < y_a$ ($\rho = \rho_2$), and (3) ablated plasma $y > y_a$ with the density $\rho = \rho_3$. In the ablation-front frame of reference, the compressed material and blowoff plasma are moving in a positive y direction with velocities V_a and $V_{bl} = V_a\rho_2/\rho_3$, respectively. In the shock-front frame of reference, the undriven- and compressed-fluid velocities are $U_1 = \sqrt{\rho_2/\rho_1(P_2 - P_1)/(\rho_2 - \rho_1)}$ and $U_2 = \rho_1 U_1/\rho_2$, where $P_{1(2)}$ is the pressure in the region 1(2).
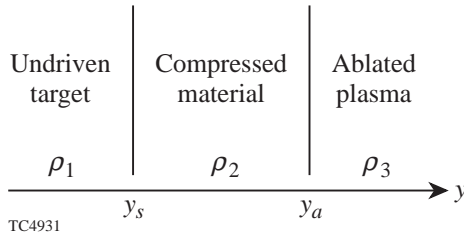
Figure 77.31
The equilibrium configuration is represented by the three regions (1) undriven target, (2) compressed material, and (3) ablated plasma.

The stability analysis of the described equilibrium is performed in the standard fashion. First, all perturbated quantities are decomposed in the Fourier space $Q_1 = \tilde{Q}(y,t)e^{ikx}$. Then, in the frame of reference moving with the compressed-region velocity, the linearized conservation equations are combined into a single partial differential equation for the pressure perturbation $\tilde{p}$:[1,3,9]

$$\partial_t^2 \tilde{p} - c_s^2 \partial_y^2 \tilde{p} + k^2 c_s^2 \tilde{p} = 0, \tag{1}$$

where c_s is the sound speed of the compressed material. The boundary conditions at the ablation front can be derived by integrating the perturbed conservation equations across the interface $y = y_a$. The result is

$$\frac{\tilde{v}_x - \tilde{v}_x^l}{c_s} = i\zeta_a\Omega(1-\delta), \quad (1-\delta)\,d_\tau\zeta_a = \tilde{v}_y - \delta\,\tilde{v}_y^l,$$

$$\tilde{w} - \tilde{w}^l = 2\frac{V_a}{c_s}\Omega(1-\delta)\zeta_a, \tag{2}$$

where superscript l denotes the blowoff region variable, $\Omega = V_{bl}/c_s$, $\delta = \rho_3/\rho_2$, $\tau = kc_s t$, $\tilde{w} = \tilde{p}/(\rho_2 c_s^2)$, and $\zeta_a = k\eta_a$ is the normalized ablation-surface perturbation. It is well known[10,11] that the sharp-boundary model cannot be solved in closed form in the presence of ablation without a supplementary boundary condition at the surface of discontinuity. The closure equation can be derived only by using the self-consistent stability analysis of ablation fronts. In Refs. 6–8 such an analysis was carried out by keeping finite thermal conductivity in the energy-conservation equation. Taking the limit of zero ablation-front thickness in the analytical solution, one can derive the jump conditions for the hydrodynamic quantities at the ablation front.[8,10] In addition to the conditions (2), the following jump in the perturbed transverse velocity is found:

$$\tilde{v}_y - \tilde{v}_y^l = -\zeta_a V_{bl}(1-\delta). \tag{3}$$

Observe that by combining Eqs. (2) and (3) one can derive an equation for the perturbation evolution $d_t\eta_a + kV_a\eta_a = \tilde{v}_y$ that contradicts the boundary condition chosen heuristically in Eq. (10) of Ref. 5. At the shock front the boundary conditions are obtained by using the perturbed Hugoniot relations. The details of calculation can be found in Ref. 9. Next, to simplify the matching procedure we introduce new variables $r = \sqrt{\tau^2 - k^2 y^2}$ and $\theta = \tanh^{-1}(ky/\tau)$; then Eq. (1) and the boundary conditions at the shock and ablation fronts take the following form:

$$\partial_r^2 \tilde{w} + \frac{1}{r}\partial_r \tilde{w} + \tilde{w} - \frac{1}{r^2}\partial_\theta^2 \tilde{w} = 0, \tag{4}$$

$$\tilde{w}_s = \frac{L_1}{\cosh\theta_s}d_r\zeta_s, \tag{5}$$

$$\partial_\theta \tilde{w}_s = -rL_3\frac{\sinh^2\theta_s}{\cosh\theta_s}\zeta_s - \frac{rL_2}{\cosh\theta_s}d_r^2\zeta_s, \tag{6}$$

$$(1-\delta)d_r^2\zeta_a - \delta\Omega^2\zeta_a + \frac{\partial_\theta\tilde{w}_a}{r} + \tilde{w}_a = O(\delta^2), \qquad (7)$$

$$d_r\left(\delta\Omega d_r\zeta_a + \delta\Omega^2\zeta_a - \tilde{w}_a\right)$$
$$= \delta\Omega\tilde{w}_a + \delta^2\Omega^2 F(r) + O(\delta^3), \qquad (8)$$

where $\tanh\theta_a = -V_a/c_s$, $\tanh\theta_s = -U_2/c_s$, $\tilde{w}_s = \tilde{w}(r,\theta_s)$, $\tilde{w}_a = \tilde{w}(r,\theta_a)$, and

$$L_1 = \frac{4}{\gamma+1}\tanh\theta_s, \quad L_2 = 2\frac{M_1^2+1}{M_1^2(\gamma+1)},$$

$$L_3 = 2\frac{M_1^2-1}{2+(\gamma-1)M_1^2},$$

$$F(r) = \frac{1}{L_1}\left(\frac{4}{\gamma+1}-L_2-L_3\right)\tilde{w}\left(\frac{-\delta\Omega r}{\sinh\theta_s},\theta_s\right).$$

Here $M_1 = U_1/c_1$ is the shock Mach number, and c_1 is the sound speed of the undriven material. A general solution of Eq. (4) can be written as an infinite sum of Bessel functions $J_\mu(r)$:[3,9]

$$\tilde{w} = \sum_\mu\left(M_\mu\cosh\mu\theta + N_\mu\sinh\mu\theta\right)J_\mu(r), \qquad (9)$$

where constants M_μ and N_μ are determined from the boundary conditions (5)–(8). The temporal evolution of the front-surface perturbations is described by Eqs. (7) and (8) that can be solved by using the multiple-scale analysis. Next, we introduce a long-scale variable $T = \sqrt{\delta}r$ and make the following ordering: $\Omega \sim 1$, $(V_a/c_s) \sim \delta \ll 1$. Also we assume that

$$\tilde{w}_a \sim \delta, \ \partial_r\tilde{w}_a \sim \delta, \ \partial_\theta\tilde{w}_a \sim 1. \qquad (10)$$

The last assumptions will be verified *a posteriori*. The system (7)–(8) then reduces to

$$\partial_r^2\zeta_a + 2\sqrt{\delta}\partial_{rT}^2\zeta_a + \delta\partial_T^2\zeta_a + \delta\ \Omega\partial_r\zeta_a$$
$$+ \delta^{3/2}\Omega\partial_T\zeta_a + \frac{\partial_\theta\tilde{w}_a}{r} = f(T), \qquad (11)$$

$$\partial_r^2\zeta_a + 2\sqrt{\delta}\partial_{rT}^2\zeta_a + \Omega\partial_r\zeta_a + \sqrt{\delta}\Omega\partial_T\zeta_a$$
$$+ \Omega^2\zeta_a - \frac{\tilde{w}_a}{\delta} = f(T), \qquad (12)$$

where $f(T)$ satisfies the first-order differential equation

$$d_T f(T) = \Omega\tilde{w}_a/\sqrt{\delta} + \sqrt{\delta}\ \Omega^2 F(T).$$

In Eqs. (11) and (12) the ablation-front perturbation ζ_a and constants N_μ and M_μ are expanded in powers of δ: $Q = Q^0 + \delta Q^1 + \dots$. To the first order in $\sqrt{\delta}$, the solution of Eq. (11) is

$$\zeta^0 = A(T) + Br - \int_0^r dt\int_0^t d\xi\left(\frac{\partial_\theta\tilde{w}_a(\xi)}{\xi}\right)^0. \qquad (13)$$

The constant B and function $A(T)$ are determined from the matching conditions. The functions $M_\mu(T)$ can be found by solving Eqs. (11)–(13) and keeping only terms up to the order of $\sqrt{\delta}$. The result is $M_i^0 = 0$, $M_0^1 = \Delta_2 - N_1^0/2$, and

$$M_{2i}^1 = 2\Delta_2 - \frac{1}{2}\left[4\Omega^2\sum_{k=1}^i(2k-1)N_{2(i-k)+1}^0\right.$$
$$\left.+N_{2i-1}^0 + N_{2i+1}^0\right], \ i = 1,2\dots, \qquad (14)$$

$$M_{2i+1}^1 = 2(2i+1)B\Omega^2$$
$$-2\Omega\left[\sum_{k=0}^i N_{2k+1}^0 - (i+1)N_{2i+1}^0\right], \ i = 0,1\dots, \qquad (15)$$

where $\Delta_2 = \Omega\sqrt{\delta}A'(T) + \Omega^2 A(T) + \Omega B - f(T)$. Observe that Eqs. (14) and (15) confirm our initial assumption (10). Next, we derive an equation for the δ correction to the front perturbation. Keeping δ- and $\delta^{3/2}$-order terms in Eq. (11) yields

$$\partial_r^2\zeta^1 = -A''(T)$$
$$-\Omega\sqrt{\delta}A'(T) - \Omega\partial_r\zeta^0 - \left(\frac{\partial_\theta\tilde{w}}{r}\right)^1 + f(T). \qquad (16)$$

Following the standard procedure of the multiple-scale analysis, we eliminate the secular terms in the last equation. This condition gives the following differential equation for $A(T)$:

$$A''(T) + \sqrt{\delta}\Omega A'(T) + \Omega(B + C_t) + \left(\frac{\partial_\theta \tilde{w}}{r}\right)^1\Bigg|_{r\to\infty} = f(T), \quad (17)$$

where

$$\left(\frac{\partial_\theta \tilde{w}}{r}\right)^1 = \frac{1}{2}\Bigg[N_1^1 J_0(r) + N_2^1 J_1(r)$$

$$+ \sum_{\mu=2}^{\infty} J_\mu(r)\left(N_{\mu-1}^1 + N_{\mu+1}^1\right) \Bigg], \quad (18)$$

and $C_t = -\sum_{i=0}^{\infty} N_{2i+1}^0$. The functions $N_\mu(T)$ can be found by solving Eqs. (5) and (6). After some straightforward algebra, in the limit of $\mu \gg 1$, we obtain $N_\mu^1 \simeq M_\mu^1$, and Eq. (18) becomes

$$\left(\frac{\partial_\theta \tilde{w}}{r}\right)^1\Bigg|_{r\to\infty} = \Delta_2 - C_1\Omega^2 + \Omega C_t + (B + C_t)\Omega^2 r, \quad (19)$$

where $C_1 = -\sum_{i=0}^{\infty}(2i+1)N_{2i+1}^0$. Eliminating the secular terms in Eq. (16) with the help of Eq. (19) gives $B = -C_t$, and

$$A'' + 2\sqrt{\delta}\Omega A' + \Omega^2 A = 2f(T) + \Omega^2 C_1. \quad (20)$$

Substituting Eq. (20) into Eq. (13) and using the fact that the coefficients $N_{i>3}^0$ are numerically small for an arbitrary Mach number M_1 yields

$$\frac{\eta_a(kc_s t \gg 1)}{\eta_0} = \Sigma_3 e^{kV_a t} \int_\infty^{-kV_a t/\sinh\theta_s} e^{\eta\sinh\theta_s} J_1(\eta)d\eta$$

$$+ \left[\frac{c_s\Sigma_2}{\sqrt{V_a V_{bl}}}\sin\omega t + (1 - \Sigma_1 + \Sigma_4)\cos\omega t\right]e^{-2kV_a t}, \quad (21)$$

where $\omega = k\sqrt{V_a V_{bl}}$ and

$$\Sigma_0 = \frac{16(M_1^2 - 1)M_1^2}{(2\gamma M_1^2 - \gamma + 1)(3M_1^2 + 1)},$$

$$\Sigma_1 = 2\Sigma_0 \frac{M_1^4(5\gamma - 1) + 2M_1^2(\gamma + 3) - 3\gamma - 1}{M_1^4(17\gamma - 7) + 2M_1^2(\gamma + 9) - 3\gamma + 5},$$

$$\Sigma_2 = \frac{1}{3}(\Sigma_0 + \Sigma_1),$$

$$\Sigma_3 = \frac{\Sigma_0}{L_1}\left(\frac{4}{\gamma + 1} - L_2 - L_3\right)\frac{\sinh^2\theta_s}{\Omega},$$

$$\Sigma_4 = \Sigma_3(1 - \tanh\theta_s).$$

Equation (21) shows that the ablation-front perturbations oscillate in time with the frequency ω proportional to the ablation velocity V_a. In addition, the amplitude of oscillations is damped by the mass ablation [term $e^{-2kV_a t}$ in Eq. (21)]. The period of oscillations is much smaller, however, than the damping rate $kV_a/\omega = \sqrt{V_a/V_{bl}} = \sqrt{\delta} \ll 1$. In the limit of zero ablation velocity, $\sin\omega t \simeq k\sqrt{V_a V_{bl}}t$, and Eq. (21) leads to a classical asymptotic linear growth $\eta(kc_s t \gg 1) \simeq \eta_0(1 - \Sigma_1 + kc_s\Sigma_2 t)$.

The oscillatory behavior of the perturbations can be explained on the basis of the following simple model. Let us consider a slab of a uniform-density fluid with the perturbed right interface. If the applied pressure at the left and right sides of the slab is P_L and P_R, then the effective acceleration experienced by the slab is $g_{eff} = -(P_R - P_L)/M$, where $M = \rho L$ is the mass of the slab and L is its length. In the case where the effective acceleration is pointing in the direction from a perturbed interface toward the slab, such a configuration is hydrodynamically stable, and any surface perturbations oscillate in time (gravity wave). For a target driven by a laser irradiation, the dynamic pressure in the blowoff region $P_R = \rho_3 V_{bl}^2 = \rho_2 V_a V_{bl}$ is greater than the dynamic pressure in the shock-compressed region $P_L = \rho_2 V_a^2 = P_R\delta < P_R$, and the effective acceleration is pointing in the direction of the density gradient (from the perturbed ablation surface toward the shock compressed region). From the equation describing the temporal evolution of a gravity wave $\ddot{\eta} = kg_{eff}\eta$, it follows

that the frequency of oscillations is $\omega = \sqrt{-kg_{\text{eff}}} \simeq \sqrt{kV_a V_{\text{bl}}/L}$, and we recover the result of Eq. (21) with $L = 1/k$. The simple model described above shows that the dynamic overpressure is the main stabilizing mechanism of the ablation-surface perturbations during the shock-transit time. The estimate of the oscillation frequency can be also obtained by using the result of the self-consistent theory of the ablative RT instability.[6–8] For the large Froude number case (small acceleration), the perturbation growth rate is $\gamma \simeq \sqrt{kg - k^2 V_a V_{\text{bl}} - 2kV_a}$. Taking the limit of $g \to 0$ in the last expression gives the oscillation frequency $\omega = i\gamma = k\sqrt{V_a V_{\text{bl}}}$, in agreement with Eq. (21).

For a quantitative comparison of the model [Eq. (21)] with the result of numerical simulations, one needs to estimate the value of blowoff velocity V_{bl}. Simulations and the self-consistent analysis of ablation fronts[6–8] show that the velocity of ablated plasma is not uniform, and it increases in the direction toward the blowoff plasma. As shown in Refs. 7, 8, and 10, however, the appropriate value of the blowoff velocity to be substituted into the sharp-boundary model is $V_{\text{bl}} \equiv V_a/\delta = V_a/\left[\mu(v)(kL_0)^{1/v}\right]$, where v is the power index for the thermal conduction, L_0 is the characteristic thickness of ablation front (proportional to the minimum density-gradient scale length),[7] $\mu = (2/v)^{1/v}/\Gamma(1 + 1/v) + 0.12/v^2$, and $\Gamma(x)$ is the gamma function. The effective power index v and the thickness of the ablation front L_0 can be determined by fitting the hydrodynamic profiles obtained using the 1-D hydrodynamic code with the solution of the isobaric model.[12] For plastic (CH) targets directly driven by a flat-top laser pulse with an intensity of 50 to 200 TW/cm^2, $L_0 \simeq 0.1\,\mu$m, $v \simeq 1$, and the oscillation period is

$$T_{\text{CH}} \simeq 2.8 \left/ \left[V_a(\mu\text{m/ns})\sqrt{k(\mu\text{m}^{-1})}\right]\right. \text{ns}.$$

Cryogenic DT targets have a much smaller density-gradient scale length $L_0 \simeq 0.01\,\mu$m, $v \simeq 2$, and

$$T_{\text{DT}} \simeq 2 \left/ \left[V_a(\mu\text{m/ns})k^{3/4}(\mu\text{m}^{-1})\right]\right. \text{ns}.$$

For the cryogenic NIF target designs, $V_a \simeq 2\,\mu$m/ns during the shock-transit time, and $T_{\text{DT}} = 2.5$ ns for 20-μm perturbation wavelength. In this case the ablation-front perturbations will experience several oscillations (the breakout time for such targets is around 5 ns). Figure 77.32 shows the front-perturbation evolution of the 200-μm-thick DT foil driven by a square
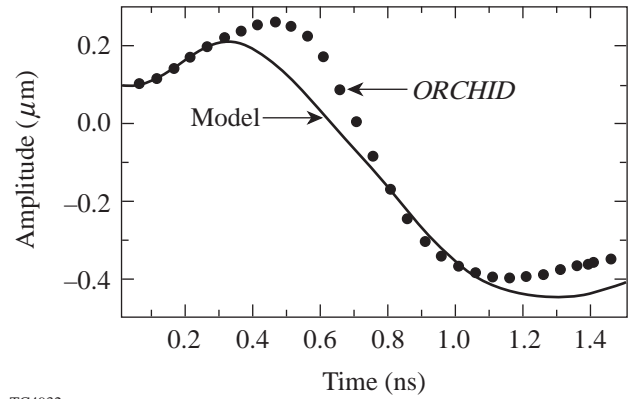
TC4932

Figure 77.32
Time evolution of the ablation-front perturbation calculated using analytic formula (22) (solid line) compared with the numerical results (dots) of the 2-D hydrocode ORCHID.

pulse with an intensity of 100 TW/cm^2. The initial amplitude of perturbation is 0.1 μm, and its wavelength is 20 μm. The dots represent the result of 2-D hydrocode ORCHID,[13] and the solid line shows the prediction of the sharp-boundary model. Observe that the analytic formula (21) reproduces not only the period of oscillation but also its amplitude.

In summary, the analytic theory of the ablative Richtmyer–Meshkov instability was developed. It was shown that the main stabilizing mechanism of the ablation-front perturbations is the dynamic overpressure of the blowoff plasma with respect to a target material.

REFERENCES

1. R. D. Richtmyer, Commun. Pure. Appl. Math. **XIII**, 297 (1960).

2. S. E. Bodner, D. G. Colombant, J. H. Gardner, R. H. Lehmberg, S. P. Obenschain, L. Phillips, A. J. Schmitt, J. D. Sethian, R. L. McCrory, W. Seka, C. P. Verdon, J. P. Knauer, B. B. Afeyan, and H. T. Powell, Phys. Plasmas **5**, 1901 (1998).

3. R. Ishizaki and K. Nishihara, Phys. Rev. Lett. **78**, 1920 (1997).

4. R. J. Taylor *et al.*, Phys. Rev. Lett. **79**, 1861 (1997).

5. A. L. Velikovich *et al.*, Phys. Plasmas **5**, 1491 (1998).

6. J. Sanz, Phys. Rev. Lett. **73**, 2700 (1994).

7. V. N. Goncharov, R. Betti, R. L. McCrory, P. Sorotokin, and C. P. Verdon, Phys. Plasmas **3**, 1402 (1996).

8. V. N. Goncharov, "Self-Consistent Stability Analysis of Ablation Fronts in Inertial Confinement Fusion," Ph.D thesis, University of Rochester, 1998.

9. P. M. Zaidel, J. Appl. Math. Mech. **24**, 316 (1960).

10. A. R. Piriz, J. Sanz, and L. F. Ibanez, Phys. Plasmas **4**, 1117 (1997).

11. S. E. Bodner, Phys. Rev. Lett. **33**, 761 (1974).

12. R. Betti, V. N. Goncharov, R. L. McCrory, and C. P. Verdon, Phys. Plasmas **5**, 1446 (1998).

13. R. L. McCrory and C. P. Verdon, in *Computer Applications in Plasma Science and Engineering*, edited by A. T. Drobot (Springer-Verlag, New York, 1991).

Reverse Intersystem Crossing from a Triplet State of Rose Bengal Populated by Sequential 532-nm plus 1064-nm Laser Excitation

Photodynamic therapy is a treatment in which the combination of a dye, light, and oxygen causes photochemically induced cell death. Observations of this effect occurred at least as early as the end of the last century. In 1900, Raab reported that the dye acridine rapidly killed paramecia when exposed to light, but had no effect in the dark.[1] This observation quickly inspired attempts to use this effect to treat disease. Light and the dye eosin were combined to treat skin cancer in 1903;[2] however, significant progress in applying photodynamic therapy to the treatment of cancer did not occur until the 1940s and 1950s, when it was discovered that porphyrin-based photosensitive dyes preferentially accumulated in malignant tissues.[3,4] A sustained series of studies into the mechanisms and applications of photodynamic therapy for the treatment of a broad range of cancers was initiated by Dougherty in the 1970s.[5] This work led the U.S. Food and Drug Administration in December 1995 to approve the treatment of advanced esophageal cancer using photodynamic therapy with Photofrin®, a porphyrin-based photosensitizer. In 1998 this approval was extended to cover the treatment of early-stage lung cancer. Other countries have also approved photodynamic therapy for the treatment of bladder, gastric, and cervical cancers. Several review articles have been published that provide an overview of the clinical results as well as the open questions about this therapy that require further research.[6,7]

The photodynamic effect is a result of three primary processes. First, the ground state of the dye (S_0) is optically excited to produce the excited singlet state (S_1). Population from this excited state is transferred by intersystem crossing (a radiationless transition) to the dye's lowest triplet state (T_1). Finally, collisional energy transfer from the triplet dye to ground-state molecular oxygen ($^3O_2$) produces highly reactive singlet oxygen ($^1O_2$) and returns the dye to its ground state:

$$S_0 + h\nu \rightarrow S_1$$
$$S_1 \rightarrow T_1$$
$$T_1 + {}^3O_2 \rightarrow S_0 + {}^1O_2 .$$
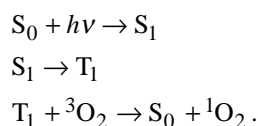
The singlet oxygen produced as a result of this three-step process reacts readily with many biological targets and, in sufficient quantity, can destroy a wide variety of cells.

Since the cell damage produced by conventional photodynamic therapy is due to singlet oxygen, an abundant supply of oxygen is critical for an effective treatment. One factor leading to oxygen depletion is the consumption of oxygen by the photodynamic process at a rate faster than it can be resupplied by the circulatory system. In addition, some tumors are inherently poorly oxygenated. A possible solution to this limitation has been suggested by observations that several dyes produce oxygen-independent damage following population of their higher-lying states. It is believed that these states contain sufficient energy to allow for the cleavage of one of the molecular bonds, producing radicals that are even more reactive than singlet oxygen. The production of these radicals does not require the presence of oxygen. Understanding this process requires greater knowledge of the properties of these higher-lying states. In this article we report on our studies of rose bengal, a dye that has been found to produce oxygen-independent damage following excitation of one of its higher-lying triplet states.[8] In particular, we have studied a decay mechanism based on reverse intersystem crossing from high-lying triplet states that may compete with the bond-cleavage process.

Although intersystem crossing has been identified primarily with transitions from the lowest excited singlet state of a molecule to an even lower-lying triplet state, triplet to singlet intersystem crossing also may occur. Well-known examples of reverse (triplet to singlet) intersystem crossing include E- and P-type delayed fluorescence.[9] E-type delayed fluorescence, also known as delayed thermal fluorescence, is observed when thermal activation causes population transfer from T_1 back to the more-energetic S_1 state. The strength of E-type delayed fluorescence is temperature dependent, and its lifetime reflects that of T_1. P-type delayed fluorescence results when the activation energy is provided by triplet-triplet annihilation ($T_1 + T_1 \rightarrow S_1 + S_0$). The strength of the P-type delayed fluorescence increases quadratically with the triplet concentration.

Reverse intersystem crossing may also occur from higher-lying triplet states where intersystem crossing to the singlet manifold competes with direct internal conversion to the lowest triplet state. This process of reverse intersystem crossing from higher-lying triplets is responsible for two-step laser-induced fluorescence (TSLIF) observed in several dyes.[10–13] The quantum yield of reverse intersystem crossing, Φ_{risc}, can be quite small ($<10^{-5}$),[10] but there are reports of exceptionally high yields ($\Phi_{risc} > 0.1$) in 9,10-dibromoanthracene,[11] several merocyanine derivatives,[12] tetraphenylporphyrin,[13] erythrosin B,[13] and rose bengal.[13]

Several reports of reverse intersystem crossing in rose bengal (RB) have been published.[13–15] Durán and Cilento[14] describe observations of fluorescence following generation of RB triplets by energy transfer from excited triplet acetone. It was believed that higher-lying triplets were populated through triplet-triplet excitation transfer and subsequently relaxed to S_1 through reverse intersystem crossing. The magnitude of the emission was compared for a series of xanthene dyes (fluorescein, eosin, and rose bengal), which revealed that heavy-atom substitution enhanced the effect. This process was not associated with a particular triplet state, and no attempt was made to quantify its yield. Ketsle *et al.*[15] investigated transient absorption changes following two-pulse excitation (532 nm + 694 nm) of various fluorescein derivatives, including rose bengal, incorporated in polymer hosts. Photobleaching of the T_1 absorption due to the second pulse was observed to have a component that was irreversible on the microsecond time scale. It was observed that the decrease in concentration of T_1 equaled the increase in concentration of S_0, providing evidence for a photophysical rather than photochemical process. Fluorescence emission was also observed coincident with the second pulse. A reverse intersystem crossing quantum yield of 0.72 was reported for T_3, the triplet state excited by red light. Most recently, the work of Reindl and Penzkofer[13] reported an 80% quantum yield of reverse intersystem crossing for T_4, the state excited through absorption of green light by T_1. Using a model of the population dynamics, the yield was extracted from measurements of the pulse-to-pulse variation in fluorescence for a train of picosecond pulses.

The present work is the first study to identify and investigate the properties of T_2, a triplet state in rose bengal populated by near-infrared light ($\lambda = 1064$ nm). We have used laser flash photolysis and two-step laser-induced fluorescence measurements to determine the triplet-triplet absorption cross-section spectrum in the near infrared and the quantum yield of reverse intersystem crossing and lifetime of T_2. In addition,

upper limits on the reverse intersystem crossing yield for T_3 are established.

Experimental

The foundation of the laser system is a mode-locked Nd:YAG laser that generates a train of pulses at 76 MHz. Every 400 ms a single pulse is selected using an electro-optic switch and amplified using a regenerative amplifier followed by a flashlamp-pumped two-pass amplifier (both Nd:YAG). The amplified pulses have a wavelength of 1064 nm, a pulse length of ~190 ps, and energies exceeding 2 mJ. The second harmonic is generated from this pulse using a KDP crystal, resulting in a pulse with a wavelength of 532 nm, a pulse length of ~134 ps, and an energy greater than 250 μJ.

The experimental setup for the laser flash photolysis measurements is shown in Fig. 77.33 using the symbols defined in Table 77.II. In this configuration the second-harmonic pulse ($\lambda = 532$ nm) is separated from the fundamental by a dichroic mirror (DM) with any residual light at the fundamental wavelength ($\lambda = 1064$ nm) further attenuated by a filter (F). The majority of this frequency-doubled pump pulse is focused by a cylindrical lens (CL) onto the masked sample cuvette, exciting a 2-mm by 1-cm cross-sectional area. A small fraction of the pump pulse is reflected by a glass plate (BS) prior to the cylindrical lens, attenuated by neutral density filters, and then detected by silicon photodiode PD1. This signal is captured by gated integrator GI1 and transferred to a computer. By removing the sample cuvette and placing an energy meter behind the beam mask, the pump pulse monitor signal measured by PD1 can be calibrated with respect to the energy reaching the
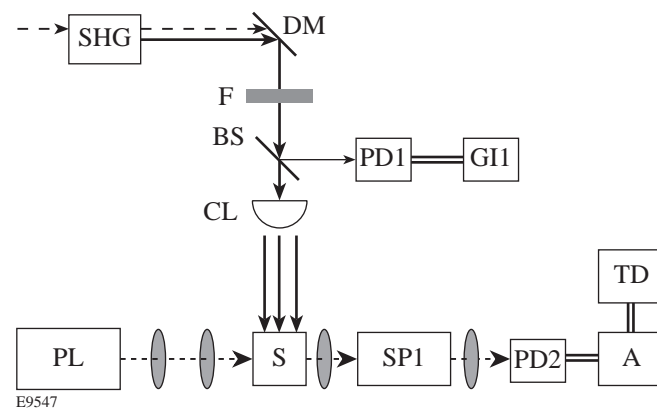
Figure 77.33
Experimental setup for laser flash photolysis measurements. See Table 77.II for symbol definitions.

Table 77.II: Equipment used in the laser flash photolysis and two-step laser-induced fluorescence experiments.

	Description	Manufacturer, Model
A	Fast ampifier	EG&G, 574
BS	Glass plate (microscope slide)	
CL	Cylindrical lens	
DM	Dichroic mirror, R@532 nm, T@1064 nm	
F	Short-pass filter	Schott, KG3
GI1–4	Gated integrator	Stanford Research Systems, 250
L1–3	Lenses	
P	Prism	
PD1–2	Silicon photodiodes	EG&G, FND-100
PL	Mercury lamp Fast shutter Long-pass filter	Vincent Associates, Uniblitz VS25 Schott, RG695
PMT	Photomultiplier tube	Burle, 6199
PS	Polarizing beam splitter	
S	Sample cuvette and beam mask	
SHG	Second-harmonic generator (KDP crystal)	
SP1	Monochromator, bandwidth ~13 nm	Instruments SA, H20
SP2	Monochromator, bandwidth ~4 nm	Photon Technology Intl., 102
TD	Digitizing oscilloscope	Hewlett-Packard, HP54201A
WP	Half-wave plate ($\lambda = 1064$ nm)	

sample. Transient absorption changes are probed by a broadband light beam traveling along the length of the irradiated zone (perpendicular to the pump pulse). The probe pulse has a 20-ms duration and is produced by a mercury lamp followed by a long-pass filter and a fast mechanical shutter. This collection of elements is represented by PL in Fig. 77.33. The probe pulse passes through monochromator SP1 before being detected by silicon photodiode PD2. The photodiode signal is increased by multistage amplifier A and then recorded by digital oscilloscope TD. The average signal from 64 shots at 9-bit resolution is then transferred to a computer for analysis.

The two-step laser-induced fluorescence measurements probing T_2 are made with the optical layout shown in Fig. 77.34. To achieve a high degree of spectral separation between the fundamental and second-harmonic pulses, prism P is used to spatially disperse the two beams. The first pump pulse (P1) has a wavelength of 532 nm, and the second pump pulse (P2) has a wavelength of 1064 nm. P2 is delayed by 34 ns relative to P1 by traversal of a greater optical path length.

The delay path includes a half-wave plate followed by a polarizing beam splitter, allowing for continuous variation of the second pump pulse energy. The pump pulses, P1 and P2, are recombined spatially at dichroic mirror DM. The pulses pass through two pinholes, ensuring collimation, before irradiating a 2-mm-diam spot at the sample cuvette. As in the laser flash photolysis layout, a small fraction of the excitation light is reflected by a glass plate to a silicon photodiode. This signal is split before sampling by two gated integrators, GI1 and GI2, which distinguish between the P1 and P2 signals. The pump-pulse signals are calibrated individually using an energy meter. Emission from the excited sample is collected, spectrally resolved using monochromator SP2, and detected by a photomultiplier tube. The signal from the PMT is split and sampled by the gated integrators GI3 and GI4. The temporal gate of GI3 is centered on the fluorescence excited by P1. The center of the GI4 temporal gate is set to be 34 ns later than the center of the GI3 gate, corresponding to the time delay between the pump pulses. Both gates are 20 ns wide. The values of all four gated integrators are recorded by a computer for each shot.
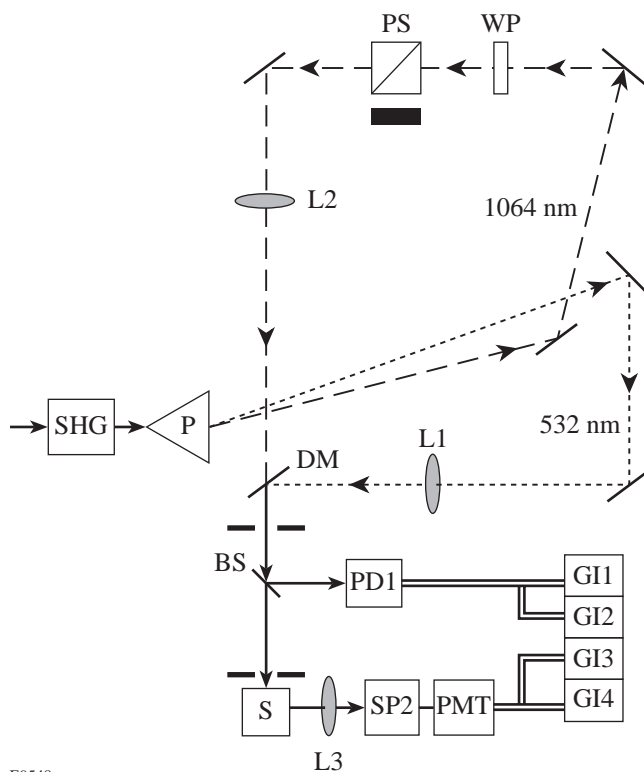
E9548

Figure 77.34
Experimental setup for two-step laser-induced fluorescence measurements.
See Table 77.II for symbol definitions.

Two-step laser-induced fluorescence measurements probing T_3 are made using a similar setup. In this case P2, the 1064-nm pump pulse, is replaced by a 632-nm-wavelength pump pulse, while the first pump pulse remains at 532 nm. The 632-nm pulse is generated by stimulated Raman scattering of the Nd:YAG second harmonic in an 18-cm ethanol cell, resulting in 60 μJ/pulse with a pulse length of approximately 80 ps. The 632-nm light is separated from the 532-nm light by a pair of prisms before P2 enters the delay line. The pulses are spatially recombined at the dichroic mirror DM, and from this point the system is identical to the previously described two-step, laser-induced fluorescence apparatus.

Rose bengal was purchased from Sigma (St. Louis) and used without further purification. All experiments were carried out in phosphate-buffered saline with a pH of 7. Effects of photobleaching were minimized by continuously stirring all samples with a micro-stirbar during irradiation. Photobleaching was monitored by measuring the decrease in fluorescence as a function of the number of excitation pulses. There was a less-than-5% decrease in fluorescence after more than 3700 two-

step excitations. Samples had a concentration of approximately 20 μM and were stored in the dark prior to use.

Analysis

Several photophysical parameters associated with an upper triplet state can be determined from two-step laser-induced fluorescence (TSLIF) measurements collected over a range of second pump-pulse (P2) fluences. These measurements are sensitive to the lifetime of the upper triplet state excited by P2, the quantum yield of intersystem crossing from this state back to the singlet manifold, and its thermalization rate. The upper triplet photophysical parameters are determined by fitting a model of the two-step laser-induced fluorescence process to the fluence-dependent TSLIF data.

The kinetic model used to analyze the TSLIF experiments is shown in Fig. 77.35(a). The rate equations describing this model are

$$\frac{dp_{S_0}}{dt} = -\sigma_{S_0 S_1}\left(p_{S_0} - p_{S_{1'}}\right) I_1(t)$$
$$+ \left(1 - \Phi_{\text{isc}}\right)\tau_{S_1}^{-1} p_{S_1} + \tau_{T_1}^{-1} p_{T_1},$$

$$\frac{dp_{T_1}}{dt} = \Phi_{\text{isc}}\tau_{S_1}^{-1} p_{S_1} - \tau_{T_1}^{-1} p_{T_1} - \sigma_{T_1 T_4}\left(p_{T_1} - p_{T_4}\right) I_1(t)$$
$$- \sigma_{T_1 T_n}\left(p_{T_1} - p_{T_n'}\right) I_2(t)$$
$$+ \left(1 - \Phi_{\text{risc},T_4}\right)\tau_{T_4}^{-1} p_{T_4} + \left(1 - \Phi_{\text{risc},T_n}\right)\tau_{T_n}^{-1} p_{T_n},$$

$$\frac{dp_{S_1}}{dt} = k_r p_{S_{1'}} - \tau_{S_1}^{-1} p_{S_1},$$

$$\frac{dp_{S_{1'}}}{dt} = \sigma_{S_0 S_1}\left(p_{S_0} - p_{S_{1'}}\right) I_1(t) - k_r p_{S_{1'}}$$
$$+ \Phi_{\text{risc},T_4}\tau_{T_4}^{-1} p_{T_4} + \Phi_{\text{risc},T_n}\tau_{T_n}^{-1} p_{T_n}, \qquad (1)$$

$$\frac{dp_{T_n}}{dt} = k_{r,T_n} p_{T_n'} - \tau_{T_n}^{-1} p_{T_n},$$

$$\frac{dp_{T_n'}}{dt} = \sigma_{T_1 T_n}\left(p_{T_1} - p_{T_n'}\right) I_2(t) - k_{r,T_n} p_{T_n'},$$

$$\frac{dp_{T_4}}{dt} = \sigma_{T_1 T_4}\left(p_{T_1} - p_{T_4}\right) I_1(t) - \tau_{T_4}^{-1} p_{T_4},$$

where the p_i's are the populations of $S_0, T_1, S_1, S_1', T_n, T_n'$, and T_4 (arranged in order of increasing energy), where $n = 2$ or 3. Table 77.III lists the definitions and values of the photophysical parameters. The unknown parameters are Φ_{risc, T_n}, τ_{T_n}, and k_{r, T_n}. The pump pulses P1 and P2 have a Gaussian temporal profile such that

$$I_1(t) = \frac{F_1}{\sqrt{2\pi\delta_1^2}} \exp\left[-(t + \Delta/2)^2 \big/ (2\delta_1^2)\right] \qquad (2)$$

and

$$I_2(t) = \frac{F_2}{\sqrt{2\pi\delta_2^2}} \exp\left[-(t - \Delta/2)^2 \big/ (2\delta_2^2)\right], \qquad (3)$$

where F_1 and F_2 are the fluences, δ_1 and δ_2 are related to the full-width-at-half-maximum pulse lengths by FWHM $= \sqrt{8 \ln 2}\ \delta$, and Δ is the time delay between the peaks of P1 and P2.

Excited-state absorption from states other than T_1 has been neglected. Previous experiments have found no evidence for absorption of 532-nm light by S_1.[16] The state T_4 may absorb 532-nm light and thus populate an even higher-lying state, but we assume with Reindl and Penzkofer[13] that any such extremely high-lying state will relax back to T_4 immediately. This process would affect transmission measurements, but since the present studies are concerned only with emission, it appears reasonable to omit it in this case. Finally, absorption by T_n is also not included in this model. The validity of this assumption will be discussed in the **Results** section.

As a result of the large time delay between the pump pulses ($\Delta = 34$ ns), it is possible to separate the system of rate equations [(Eq. (1)] into two subsets. The set of equations describing the effects of the first pump pulse is

(a)　　　　　　　　　　(b)　　　　　　　　　　(c)

E9549,50,51
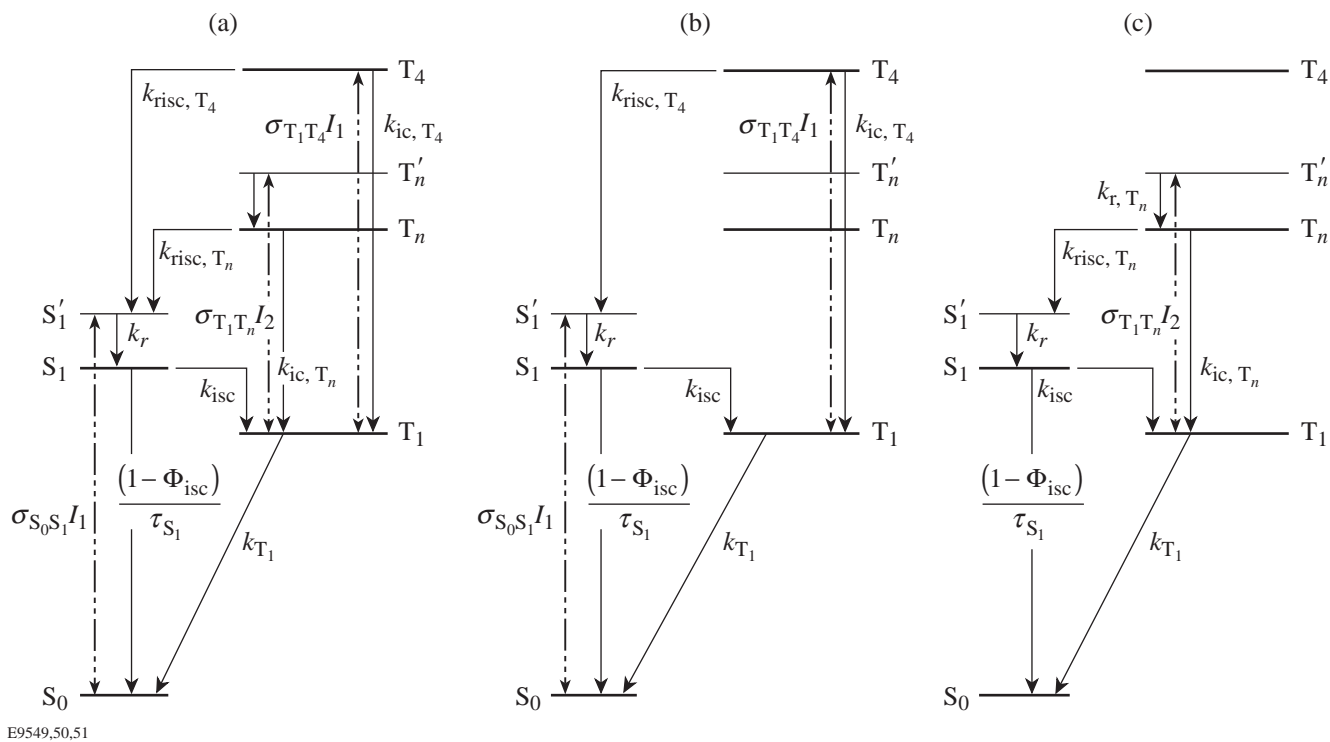
Figure 77.35
Energy-level scheme for description of two-color excitation dynamics. (a) Complete two-step model, (b) P1 subset of model, (c) P2 subset of model. See Table 77.III for parameter descriptions and values.

Table 77.III: Parameters used in the two-step laser-induced fluorescence model for rose bengal.

Parameter	Description	Value	Reference
$\sigma_{S_0 S_1}$	Ground-state absorption cross section at 532 nm $\left(S_0 + \hbar\omega \rightarrow S_1'\right)$	$1.8 \times 10^{-16} \, cm^2$	16
$\sigma_{T_1 T_2}$	Triplet absorption cross section $\left(T_1 + \hbar\omega \rightarrow T_2'\right)$	$(1.1 \pm 0.1) \times 10^{-16} \, cm^2$	This work
$\sigma_{T_1 T_4}$	Triplet absorption cross section at 532 nm $\left(T_1 + \hbar\omega \rightarrow T_4\right)$	$7.4 \times 10^{-17} \, cm^2$	16
τ_{S_1}	S_1 lifetime	89 ps	16–18
τ_{T_1}	Lifetime of T_1 (includes both phosphorescence and oxygen quenching)	3 μs	19
τ_{T_4}	Lifetime of T_4	50 fs	16
τ_{T_n}	Lifetime of T_n	fitting parameter	
Φ_{isc}	Intersystem crossing yield ($S_1 \rightarrow T_1$)	0.98	18,19
Φ_{risc,T_4}	Reverse intersystem crossing yield $\left(T_4 \rightarrow S_1'\right)$	0.8	13
Φ_{risc,T_n}	Reverse intersystem crossing yield $\left(T_n \rightarrow S_1'\right)$	fitting parameter	
F_1	First pump-pulse fluence ($\lambda = 532$ nm)	$(8.8 \pm 0.5) \times 10^{15}$ photons/cm^2	
F_2	Second pump-pulse fluence ($\lambda = 1064$ nm)	varied	
k_{ic,T_4}	Internal conversion rate ($T_4 \rightarrow T_1$)	$\left(1 - \Phi_{risc,T_4}\right)/\tau_{T_4}$	
k_{ic,T_n}	Internal conversion rate ($T_n \rightarrow T_1$)	$\left(1 - \Phi_{risc,T_n}\right)/\tau_{T_n}$	
k_{isc}	Intersystem crossing rate	Φ_{isc}/τ_{S_1}	
k_{r,T_n}	Thermalization rate $\left(T_n' \rightarrow T_n\right)$	fitting parameter	
k_r	Thermalization rate $\left(S_1' \rightarrow S_1\right)$	$10^{12} \, s^{-1}$	16
k_{risc,T_4}	Reverse intersystem crossing rate $\left(T_4 \rightarrow S_1'\right)$	$\Phi_{risc,T_4}/\tau_{T_4}$	
k_{risc,T_n}	Reverse intersystem crossing rate $\left(T_n \rightarrow S_1'\right)$	$\Phi_{risc,T_n}/\tau_{T_n}$	
k_{T_1}	T_1 relaxation rate	$1/\tau_{T_1}$	

$$\frac{dp_{S_0}}{dt} = -\sigma_{S_0 S_1}\left(p_{S_0} - p_{S_1'}\right)I_1(t) + \left(1 - \Phi_{isc}\right)\tau_{S_1}^{-1}p_{S_1}$$
$$+ \tau_{T_1}^{-1}p_{T_1},$$

$$\frac{dp_{T_1}}{dt} = \Phi_{isc}\tau_{S_1}^{-1}p_{S_1} - \tau_{T_1}^{-1}p_{T_1} - \sigma_{T_1 T_4}\left(p_{T_1} - p_{T_4}\right)I_1(t)$$
$$+ \left(1 - \Phi_{risc,T_4}\right)\tau_{T_4}^{-1}p_{T_4},$$

$$\frac{dp_{S_1}}{dt} = k_r p_{S_1'} - \tau_{S_1}^{-1}p_{S_1}, \tag{4}$$

$$\frac{dp_{S_1'}}{dt} = \sigma_{S_0 S_1}\left(p_{S_0} - p_{S_1'}\right)I_1(t) - k_r p_{S_1'}$$
$$+ \Phi_{risc,T_4}\tau_{T_4}^{-1}p_{T_4},$$

$$\frac{dp_{T_4}}{dt} = \sigma_{T_1 T_4}\left(p_{T_1} - p_{T_4}\right)I_1(t) - \tau_{T_4}^{-1}p_{T_4},$$

which are used for $t = -\infty$ to $t = 0$. The time $t = 0$ is midway between the peaks of P1 and P2, which are separated by a delay much greater than their pulse lengths and the lifetimes of all excited states except T_1. The processes included in this first segment, where only the effects of P1 are relevant, are shown in Fig. 77.35(b). This set of equations describing the effects of P1 neglects all terms containing I_2. Since T_n and T_n' are only populated by P2, corresponding terms can be eliminated from Eq. (1) since $p_{T_n} = p_{T_n'} = 0$. The process of reverse intersystem crossing is included in this model of the interaction of P1 with the sample. The first pump pulse may be absorbed by both S_0 and by any T_1 population created by preceding parts of the same pulse. Absorption of P1 light by the T_1 state populates the T_4 state, which has been shown to have a high yield of reverse intersystem crossing.[13] It is necessary to include this process for pulses longer than the $S_1 \rightarrow T_1$ intersystem crossing time since it can lead to an apparent enhancement of the fluorescence yield, particularly at fluences resulting in depletion of the ground state. At the P1 fluence used experimentally, the solution of Eq. (4), which includes the reverse intersystem crossing process, led to a 29%-greater integrated fluorescence compared to an otherwise identical set of equations that neglected this process. It is important to emphasize that the reverse intersystem crossing described above occurs from the triplet state populated by secondary absorption of the first pump pulse and is easily distinguished temporally from the process this experiment is designed to measure: reverse inter-system crossing from the triplet state populated by the second pump pulse.

The effects of P1 and P2 can be separated cleanly since the system has relaxed such that only S_0 and T_1 are populated at $t = 0$. The effects of only the second pump pulse are considered from this time to $t = +\infty$. The model of this second excitation step is shown in Fig. 77.35(c). The equations describing this segment are

$$\frac{dp_{S_0}}{dt} = \left(1 - \Phi_{isc}\right)\tau_{S_1}^{-1}p_{S_1} + \tau_{T_1}^{-1}p_{T_1},$$

$$\frac{dp_{T_1}}{dt} = \Phi_{isc}\tau_{S_1}^{-1}p_{S_1} - \tau_{T_1}^{-1}p_{T_1} - \sigma_{T_1 T_n}\left(p_{T_1} - p_{T_n'}\right)I_2(t)$$
$$+ \left(1 - \Phi_{risc,T_n}\right)\tau_{T_n}^{-1}p_{T_n},$$

$$\frac{dp_{S_1}}{dt} = k_r p_{S_1'} - \tau_{S_1}^{-1}p_{S_1}, \tag{5}$$

$$\frac{dp_{S_1'}}{dt} = -k_r p_{S_1'} + \Phi_{risc,T_n}\tau_{T_n}^{-1}p_{T_n},$$

$$\frac{dp_{T_n}}{dt} = k_{r,T_n} p_{T_n'} - \tau_{T_n}^{-1}p_{T_n},$$

$$\frac{dp_{T_n'}}{dt} = \sigma_{T_1 T_n}\left(p_{T_1} - p_{T_n'}\right)I_2(t) - k_{r,T_n} p_{T_n'}.$$

In this segment all terms containing I_1 and p_{T_4}, the population of T_4, are dropped from Eq. (1).

The fluorescence due to the two pulses is proportional to the population of S_1 such that

$$f_1 = \frac{\Phi_f}{\tau_{S_1}} \int_{-\infty}^{0} p_{S_1}(t)\, dt \tag{6}$$

and

$$f_2 = \frac{\Phi_f}{\tau_{S_1}} \int_{0}^{+\infty} p_{S_1}(t)\, dt, \tag{7}$$

where Φ_f is the fluorescence yield. The two-step, laser-induced fluorescence ratio f_R is defined by

$$f_R \equiv \frac{f_2}{f_1}. \qquad (8)$$

This is a convenient quantity to compare with experimental results since fluorescence yield, collection, and detection efficiency factors are eliminated.

The T_n photophysical parameters are determined by fitting this model of the two-step, laser-induced fluorescence process to the fluence-dependent f_R obtained experimentally. As will be discussed later, extraction of the parameters requires f_R measurements over a range of P2 fluences, which, at the upper limit, are sufficient to partially deplete the lowest triplet state. In addition, the length of the second pump pulse must exceed the lifetime of T_n. A numerical approach is required since under these conditions analytical solutions cannot be obtained easily. The numerical analysis consists of three major components: (a) a calculation of the fluence-dependent f_R for a given set of T_n photophysical parameters, (b) an algorithm that optimizes these parameters to provide the best fit to the experimental data, and (c) an estimate of the precision to which the extracted parameters are known based on a randomization and re-optimization technique.

Calculation of the fluence-dependent, two-step laser-induced fluorescence ratio was based on the sequential solution of the rate equations given in Eqs. (4) and (5). These rate equations were solved using Runge–Kutta numerical integration. The agreement between the f_R obtained from this model and the experimental data can be quantified by the χ^2 statistic, which is summed over the set F_1, F_2 for which experimental measurements of the TSLIF ratio, $f_{R,expt}$, were made. The standard deviations of those measurements are given by $\sigma_{R,expt}$. The next step is to search parameter space in order to find the values of k_{r,T_n}, τ_{T_n}, and Φ_{risc,T_n} that minimize χ^2. The optimization algorithm used is the downhill simplex method.[20]

The downhill simplex method will find the set of parameters that minimizes χ^2, but it does not report the precision with which these parameters are known given the uncertainties in the experimental measurements. This precision was estimated by running the optimization routine on sets of TSLIF ratio measurements, $f_{R,mix}$, calculated from

$$f_{R,mix}(F_1, F_2) = f_{R,expt}(F_1, F_2) + r\sigma_{R,expt}(F_1, F_2), \quad (9)$$

where r is a uniformly distributed random number between -1 and 1. The standard deviations of the parameters found in minimizing ten such data sets provide the estimated precision to which the parameters are known.

An analytical model of two-step laser-induced fluorescence that is limited to low-intensity and low-fluence conditions can be developed. In this regime the fluorescence signals are given by

$$f_1 = a\sigma_{S_0 S_1} F_1 \qquad (10)$$

and

$$f_2 = a\Phi_{isc}\Phi_{risc,T_n} \sigma_{S_0 S_1} F_1 \sigma_{T_1 T_n} F_2, \qquad (11)$$

where a includes fluorescence yield, collection, and detection factors. Calculating the two-step laser-induced fluorescence ratio from Eqs. (10) and (11) gives

$$f_R = \Phi_{isc}\Phi_{risc,T_n}\sigma_{T_1 T_n} F_2. \qquad (12)$$

Although this expression cannot be used to determine τ_{T_n} and k_{r,T_n}, it is useful for estimating upper limits on Φ_{risc,T_n} when there is an undetectable two-step laser-induced fluorescence signal.

Results

The triplet-triplet absorption spectrum of rose bengal in the near infrared (Fig. 77.36) is derived from a series of transient absorption measurements acquired by laser flash photolysis. There is no measurable ground-state absorption in this region. Detector insensitivity prevented the extension of this spectrum beyond 1100 nm. Using the intensity variation method[21] it was found that the absorption has a peak between 1050 and 1075 nm with a cross section $\sigma_{T_1 T_2} = (1.1 \pm 0.1) \times 10^{-16}$ cm^2.

Figure 77.37 shows two-step laser-induced fluorescence results for T_2. The ratio of two-step to one-step fluorescence $f_{R,expt}$ versus the fluence of the second pump pulse ($\lambda_2 = 1064$ nm) is plotted. The first pump-pulse fluence ($\lambda_1 = 532$ nm) was held approximately constant at 3.3 ± 0.2 mJ/cm^2, and the resulting one-step fluorescence varied by less than 2%. No emission following P2 was detected when P1 was blocked. Each point in this plot represents the average of from 26 to 370 double-pulse excitations. The error bars indicate the corresponding standard deviations. In addition, the spectrum of the 532-nm + 1064-nm excited emission was measured and found to be the same as the $S_1 \rightarrow S_0$ fluorescence spectrum,
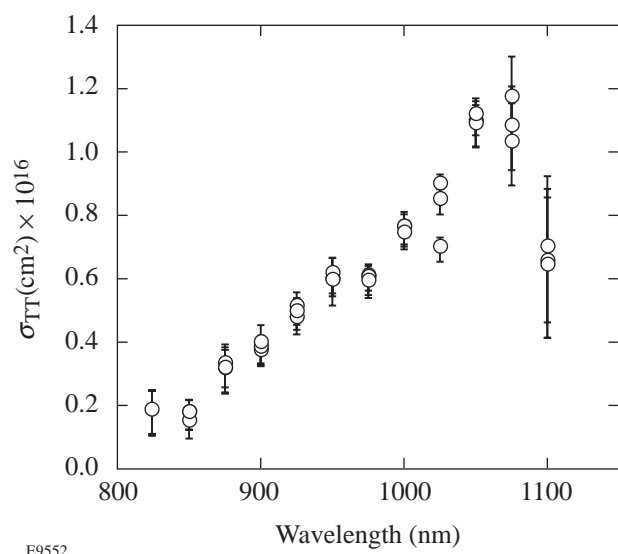
E9552

Figure 77.36
Triplet-triplet absorption spectrum of rose bengal in the near infrared.

E9553

Figure 77.37
Fluence dependence of two-step laser-induced fluorescence ratio f_R. Delay between excitation pulses: 34 ns. Circles are averages of from 26 to 370 double-pulse excitations with error bars indicating the standard deviations. The curve represents the best fit ($\chi^2 = 0.011$) calculated from solutions of Eqs. (4) and (5) using the parameter values given in Table 77.III. The photophysical parameters determined from the fitting procedure are $\Phi_{\text{risc},T_2} = 0.0142\pm0.0003$, $\tau_{T_2} = 5.8\pm1.6$ ps, and $k_{r,T_2} = 1.30\pm0.18$ ps^{-1}.

confirming that the TSLIF results from repopulation of S_1. The parameters Φ_{risc,T_2}, τ_{T_2}, and k_{r,T_2} can be determined by analyzing the nonlinear dependence of f_R on F_2 using the multistate kinetic model described in the **Analysis** section. This analysis of the data shown in Fig. 77.37 gives $\Phi_{\text{risc},T_2} = 0.0142\pm0.0003$, $\tau_{T_2} = 5.8\pm1.6$ ps, and $k_{r,T_2} = 1.30\pm0.18$ ps^{-1} with $\chi^2 = 0.011$.

Similar measurements probing T_3 ($\lambda_1 = 532$ nm, $\lambda_2 = 632$ nm) failed to detect any two-step laser-induced fluorescence. Based on the fluorescence detection limits, the quantum yield of reverse intersystem crossing from T_3 can be constrained to $\Phi_{\text{risc},T_3} < 0.06$ using Eq. (12) with $\sigma_{T_1T_3}$ determined from Ref. 22 and f_R set equal to the uncertainty in the TSLIF measurement.

Discussion

Although no analytical expression can be given for $f_R(F_1,F_2)$ that is applicable for the high fluences used in these experiments, it is possible to explain qualitatively the shape of the f_R versus F_2 curve shown in Fig. 77.37. This explanation also provides some justification for why the kinetic model analysis is sensitive to the lifetime and thermalization rate of the upper triplet state. Under low-fluence and low-intensity conditions, Eq. (12) predicts that f_R will increase linearly with F_2. Deviations from the predicted linear response are expected to occur for P2 with sufficiently high intensity or fluence. Under conditions where the pulse length is shorter than the lifetime of T_2, the saturation fluence $F_{\text{sat}} = \left(\sigma_{T_1T_2}\right)^{-1}$ for

$T_1 \rightarrow T_2$ excitation is 9×10^{15} photons/cm^2 (1.7 mJ/cm^2). Multiple excitations are possible, however, for pulses that are longer than the lifetime of T_2. This allows the two-step laser-induced fluorescence ratio to continue to grow beyond the short-pulse saturation fluence limit. Limits on the growth of the two-step laser-induced fluorescence are not solely fluence dependent. The maximum rate at which population can be excited to the upper triplet state is limited by the thermalization rate k_{r,T_2}. In addition, the maximum number of excitation cycles that can be achieved during a pulse is limited by the upper triplet lifetime τ_{T_2} and the length of the second pump pulse δ_2. Since the nonlinear portion of the f_R curve is dependent on the upper triplet lifetime and its thermalization rate, it is possible to extract these parameters from a fit of the kinetic model to data obtained under high-intensity and high-fluence conditions where the deviation from linearity becomes significant.

The multistate kinetic model described in Eq. (1) and Fig. 77.35 is not the only possible explanation for fluorescence following 532-nm + 1064-nm excitation. An alternative

model that deserves consideration includes absorption of 1064-nm light by T_2 to populate T_4, a state already known to have a high reverse intersystem crossing yield.[13] On the basis of energetic considerations, the $T_2 \rightarrow T_4$ absorption process appears to be plausible, although restrictions such as those based on parity may disallow this transition. If reverse intersystem crossing were to occur predominantly from T_4, then the expression for f_R given in Eq. (12) should be modified to give

$$f_R = \Phi_{\text{isc}} \Phi_{\text{risc},T_4} \sigma_{T_1 T_2} \sigma_{T_2 T_4} F_2^2 . \tag{13}$$

According to this model, f_R increases quadratically rather than linearly in F_2 since population of T_4 from T_1 requires the sequential absorption of two 1064-nm photons. In addition, f_R is expected to saturate at a value greater than $\Phi_{\text{isc}} \Phi_{\text{risc},T_4} = 0.78$. The experimental data shown in Fig. 77.37 do not exhibit this behavior, which justifies our elimination of this alternative model.

No two-step laser-induced fluorescence was detected in the 532-nm + 632-nm experiment. This experiment was performed under conditions much less favorable than for the 532-nm + 1064-nm experiment. Both the maximum P2 fluence and the triplet-triplet absorption cross section were significantly less at 632 nm compared to 1064 nm. Even with these limitations, however, the value of Φ_{risc,T_3} can be determined to be less than 0.06. This result disagrees with a yield of 0.72 for this state reported previously.[15]

Ketsle *et al.* attempted to measure the yield of reverse intersystem crossing through measurements of the change in T_1 absorption (and therefore, concentration) in a two-step excitation experiment.[15] Immediately following P2, a decrease in the concentration ΔC_{ab} of T_1 was observed, which was followed by a partial recovery ΔC_{ac}, as shown in Fig. 77.38, which is a sketch showing the key features in the transient signal plotted in Fig. I of Ref. 15. The points a, b, and c in Fig. 77.38 represent the times immediately prior to P2, immediately following P2, and after the fast recovery of the transient bleaching, respectively. The lack of complete recovery is due to reverse intersystem crossing from the higher-lying triplet populated by P2. From these concentration changes Ketsle *et al.* calculated the reverse intersystem crossing yield using the formula

$$\frac{\Delta C_{ac}}{\Delta C_{ab}} = \Phi_{\text{risc},T_3}. \tag{14}$$
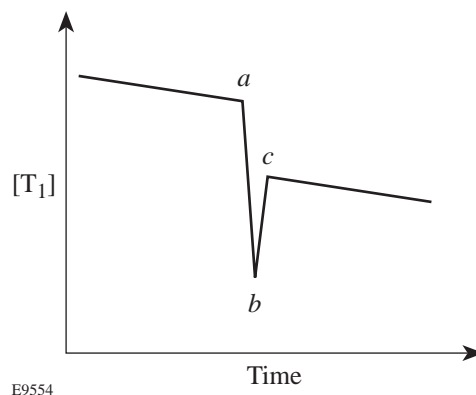
Figure 77.38

Schematic of transient changes in T_1 concentration (based on Fig. I in Ref. 15). The points a, b, and c in the figure represent the times immediately prior to P2, immediately following P2, and after the fast recovery of the transient bleaching, respectively.

Equation (14) attributes the bleaching to the entire fraction undergoing reverse intersystem crossing. It is more appropriate, however, to interpret bleaching as due to the fraction that undergoes reverse intersystem crossing and in addition does not repopulate the triplet manifold through $S_1 \rightarrow T_1$ transfer, implying

$$\frac{\Delta C_{ac}}{\Delta C_{ab}} = \Phi_{\text{risc},T_3} \left(1 - \Phi_{\text{isc}} \right). \tag{15}$$

Indeed, this latter interpretation of the bleaching fraction agrees with that used by Redmond *et al.*[12] Recalculating a yield based on Eq. (15) using the Ketsle *et al.* bleaching fraction data found in Table I of Ref. 15 gives $\Phi_{\text{risc},T_3} \gg 1$. Since this quantum yield cannot exceed unity, it appears that their experimental data was obtained under conditions in which the assumptions used to derive these equations do not apply. In particular, these equations are valid only under conditions in which ΔC_{ab} is proportional to the number of photons absorbed by T_1. This can occur only when the length of the exciting pulse is shorter than the lifetime of the upper triplet state $\left(\delta_2 \ll \tau_{T_3} \right)$ and when the transient absorption detection system is capable of responding on this same time scale. Ketsle *et al.* do not report the length of their second pump pulse but state only that it is from a ruby laser. It appears likely that their excitation pulse is longer than several nanoseconds, which is much greater than the expected upper triplet lifetime of picoseconds or less. In addition, the time response of their transient absorption detection system is not reported. The use of long pulses or slow detection systems with this transient

absorption technique will lead to an underestimate of the number of absorbed photons, thus leading to values of Φ_{risc,T_3} that exceed unity. The equipment requirements are not as demanding for fluorescence methods of measuring reverse intersystem crossing.

Reverse intersystem crossing yields have been calculated for a growing number of molecules. An aspect of this study that makes it of particular interest is that these yields have now been measured for several triplet states of rose bengal. Previous workers in this field have suggested that population excited to T_n relaxes rapidly to the next-lowest triplet state, and that the triplet-singlet transfer is predominantly due to reverse intersystem crossing from this less-energetic state.[13,23] According to this model, the reverse intersystem crossing yield should be independent of the high-lying triplet state initially excited; experimental measurements clearly contradict this prediction with high yields of $\Phi_{risc,T_4} = 0.80$ if T_4 is initially excited,[13] to much lower yields of $\Phi_{risc,T_2} = 0.0142$ for the case of direct population of T_2 (measured in this work).

To understand these results it is instructive to consider the energies of the relevant triplet and singlet states. The energies of the singlet states can be estimated from the peaks of the ground-state absorption spectrum. Similarly, the energies of the triplet states relative to T_1 can be estimated from triplet-triplet absorption spectra (the present work and Refs. 8 and 24). The energy of T_1 in methanol is 1.75 eV.[25] These results have been compiled in Table 77.IV. The energy gaps between the excited triplet states and the nearest less-energetic singlet state are ΔE (T_2–S_2) = 0.51 eV, ΔE (T_3–S_3) = 0.35 eV, and ΔE (T_4–S_4) = 0.08 eV. Thus we find that the transition with the smallest energy gap exhibits the greatest reverse intersystem crossing yield (Φ_{risc,T_2} = 0.0142, Φ_{risc,T_3} < 0.06, Φ_{risc,T_4} = 0.80). Although this ordering is consistent with a simple interpretation of the energy gap law for nonradiative transitions, which states that reverse intersystem crossing is likely to be most favorable when there is a small energy gap between the triplet state and a nearby singlet, such an interpretation must be considered critically. As developed by Englman and Jortner,[26] the energy gap law applies to a particular triplet-singlet pair, whereas here we are considering three such pairs. The strength of the spin-orbit coupling between different states may vary by several orders of magnitude. Since we do not know the values of the coupling parameters for the three transitions under consideration, it is impossible to definitively attribute the entire variation in reverse intersystem crossing yield to differences in the energy gap.

Table 77.IV: Energies of rose bengal excited states. Singlet-state energies are estimated from the ground-state absorption spectrum. Triplet-state energies are estimated from the T_1 absorption spectrum.

State	Energy (eV)	Ref.
S_1	2.10	This work
S_2	2.41	This work
S_3	3.51	This work
S_4	3.95	This work
T_1	1.75	25
T_2	2.92	This work
T_3	3.86	8
T_4	4.03	24

Conclusion

We have presented what we believe to be the first study of a triplet state of rose bengal that is produced by 1064-nm excitation of T_1. The triplet-triplet absorption cross section was measured between 825 nm and 1100 nm. This state was further characterized using two-step laser-induced fluorescence to determine its thermalization rate, lifetime, and quantum yield of reverse intersystem crossing. Similar two-step laser-induced fluorescence measurements were made of the triplet excited by 632-nm light.

In earlier work, the reverse intersystem crossing yield was predicted to be independent of which higher-lying triplet state was initially excited. The present work finds that the yields for triplets excited by red and near-infrared light, T_3 and T_2, are much less than those reported earlier for the more-energetic state T_4, which is populated by green light.[13] An analysis of the triplet-triplet absorption spectrum and the ground-state absorption spectrum shows that T_4 is energetically close to a state in the singlet manifold, whereas the corresponding gaps are significantly greater for T_2 and T_3.

REFERENCES

1. O. Raab, Infusoria Z. Biol. **39**, 524 (1900).

2. V. H. Tappeiner and A. Jesionek, Muench. Med. Wochneshr. **47**, 2042 (1903).

3. F. H. J. Figge, G. S. Weiland, and L. O. J. Manganiello, Proc. Soc. Exp. Biol. Med. **68**, 640 (1948).

4. R. L. Lipson, E. J. Baldes, and A. M. Olsen, J. Natl. Cancer Inst. **26**, 1 (1961).

5. T. J. Dougherty, J. Natl. Cancer Inst. **52**, 1333 (1974).

6. H. I. Pass, J. Natl. Cancer Inst. **85**, 443 (1993).

7. T. J. Dougherty *et al.*, J. Natl. Cancer Inst. **90**, 889 (1998).

8. G. Smith *et al.*, Photochem. Photobiol. **59**, 135 (1994).

9. S. P. McGlynn, T. Azumi, and M. Kinoshita, *Molecular Spectroscopy of the Triplet State* (Prentice-Hall, Englewood Cliffs, NJ, 1969).

10. S. Kobayashi, K. Kikuchi, and H. Kokubun, Chem. Phys. Lett. **42**, 494 (1976); S. Kobayashi, K. Kikuchi, and H. Kokubun, Chem. Phys. **27**, 399 (1978).

11. W. G. McGimpsey and J. C. Scaiano, J. Am. Chem. Soc. **111**, 335 (1989).

12. R. W. Redmond *et al.*, J. Phys. Chem. A **101**, 2773 (1997).

13. S. Reindl and A. Penzkofer, Chem. Phys. **211**, 431 (1996).

14. N. Durán and G. Cilento, Photochem. Photobiol. **32**, 113 (1980).

15. G. A. Ketsle, L. V. Levshin, and S. N. Letuta, Opt. Spectrosc. (USSR) **68**, 202 (1990).

16. H. Stiel *et al.*, J. Photochem. Photobiol. B: Biol. **33**, 245 (1996).

17. G. R. Fleming *et al.*, J. Am. Chem. Soc. **99**, 4306 (1977).

18. M. A. J. Rodgers, Chem. Phys. Lett. **78**, 509 (1981).

19. P. C. C. Lee and M. A. J. Rodgers, Photochem. Photobiol. **45**, 79 (1987).

20. W. H. Press *et al.*, *Numerical Recipes in FORTRAN: The Art of Scientific Computing,* 2nd ed. (Cambridge University Press, Cambridge, England, 1992).

21. I. Carmichael and G. L. Hug, J. Phys. Chem. Ref. Data **15**, 1 (1986).

22. P. Murasecco-Suardi *et al.*, Helv. Chim. Acta. **70**, 1760 (1987).

23. H. Fukumura *et al.*, J. Photochem. Photobiol. A: Chem. **42**, 283 (1988).

24. C. R. Lambert *et al.*, Photochem. Photobiol. **63**, 154 (1996).

25. T. Shen *et al.*, J. Photochem. Photobiol. A: Chem. **47**, 203 (1989).

26. R. Englman and J. Jortner, Mol. Phys. **18**, 145 (1970).

# Picosecond Response of Optically Driven Y-Ba-Cu-O Microbridge and Josephson-Junction Integrated Structures

Photoexcitation studies of superconductors have been a subject of intense investigation for the last 20 years. Early experiments were performed on metallic superconductors using nanosecond and picosecond pulses and were concentrated on the dynamics of the photon-induced, superconducting-to-normal transition.[1,2] The discovery of high-temperature superconductors (HTS) prompted a new series of transient photoexcitation experiments. Experiments with optical-pulse-driven current-biased samples and direct measurements of the resulting voltage transient provide the most direct information on nonequilibrium processes in HTS. These experiments are also most relevant when evaluating the potential of HTS materials for fast photodetector applications. Recently, we have observed the single-picosecond electrical response of a current-biased $YBa_2Cu_3O_{7-x}$ (YBCO) microbridge exposed to femtosecond optical pulses.[3–6] The experiments were conducted in the temperature range from 4.2 K to 80 K, using our subpicosecond electro-optic (EO) sampling system.[4] The two mechanisms responsible for the picosecond response of the YBCO microbridge have been identified: nonequilibrium kinetic inductance and hot-electron heating.[7] The corresponding electrical transient was either a 2-ps-wide oscillation for the kinetic inductance response, or a single-picosecond spike for electron heating in the resistive state.[6]

Picosecond-impulse excitation of Josephson junctions has been extensively studied theoretically.[8–10] The simulations showed that a junction response is delayed with respect to the excitation impulse by a turn-on delay time τ_D, which depends on both the junction bias and the critical current I_c overdrive (I_c is defined as the maximum superconducting current that can flow through a Josephson junction). The rise time τ_R of the junction switching transient was also calculated and found to depend on the amount of the I_c overdrive, as well as on the product of the junction's normal resistance × the junction's capacitance ($R_N C_J$). In the case of the single-flux-quantum (SFQ) pulse generation by resistively shunted junctions (RSJ), the generated pulse has been predicted to have an amplitude equal to $2I_c R_N$ and a width corresponding to $\Phi_0/2I_c R_N$,[11] where $\Phi_0 = 2.07$ mV•ps.

In this article, we report our studies on the picosecond photoresponse of a current-biased YBCO microbridge coupled to a bicrystal YBCO Josephson junction. Femtosecond optical pulses were used to excite the microbridge in the resistive state[5] and to generate a series of picosecond-duration electrical transient pulses. These transients were in turn applied to switch the grain-boundary Josephson junction. The junction response was superimposed on the large feedthrough signal, but the junction signal could be identified due to its dependence on the bias current.

Sample Fabrication and Experimental Setup

The test structures, consisting of coplanar strip (CPS) transmission lines, were fabricated on (100) MgO bicrystal substrates, using a standard laser ablation technique and ion-beam etching.[12] YBCO films 50 to 100 nm thick were deposited at the substrate temperature 800°C and at the ambient oxygen pressure of 0.35 mbar. The deposition was followed by an annealing cycle in pure oxygen. Next, a 50-nm-thick gold layer was sputtered *in situ* on top of YBCO thin film at room temperature at an argon pressure of 0.05 mbar. The test structures were prepared in a two-step process. First, they were photolithographically defined and then etched with a low-current-density (1 mA/cm^2) ion argon beam. In the second step, the Au layer was removed from the top of the junction and bridge areas, using the same low-intensity ion etching. As a result, eight 8-mm-long CPS lines, containing 10-μm × 5-μm bridges and 5-μm-wide bicrystal Josephson junctions, were fabricated on each substrate. The 8-mm length of CPS was chosen to restrict the end-of-line reflections, assuring a 50-ps-long reflection-free measurement time-window. The schematic of our CPS line and the measurement configuration are shown in Fig. 77.39. We note that the test structure is not a Josephson-junction transmission line,[11] but rather a high characteristic impedance (80 Ω) CPS line with the junction electrodes representing high inductance. This type of experimental configuration was chosen for practical fabrication considerations and will be improved in future designs.
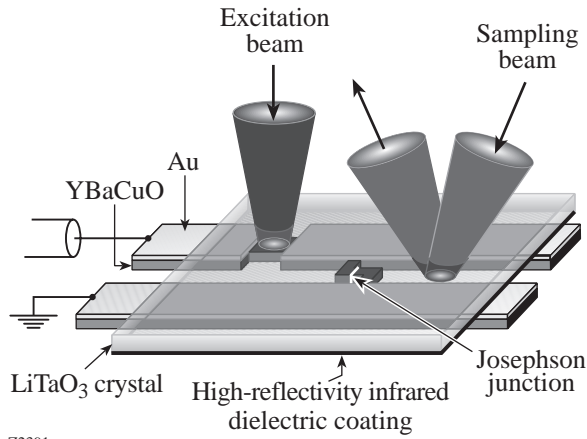
Figure 77.39
Experimental setup of CPS line and measurement configuration.

Z2391

Our optical system for the femtosecond pulse excitation and EO sampling detection is described in detail in Ref. 4. Briefly, a mode-locked Ti:sapphire laser, operating at a repetition rate of 76 MHz, was used to generate 100-fs pulses at a wavelength of 800 nm. To perform EO characterization, the laser beam was split into two paths: a frequency-doubled ($\lambda = 400$ nm) excitation beam used for inducing the photoresponse signal in the bridge, and an 800-nm sampling beam for monitoring the electric field penetrating an EO (LiTaO$_3$) crystal during the electrical pulse propagation (see Fig. 77.39). The sampling beam was time delayed with respect to the excitation beam by a computer-controlled translation stage, directed between the coplanar lines through the LiTaO$_3$ crystal less than 100 μm away from the bridge, and reflected to the analyzer by a high-reflectivity dielectric coating at the bottom of the LiTaO$_3$ crystal. The sampling beam sensed the instantaneous birefringence introduced in LiTaO$_3$ by the photogenerated transient that propagated in the CPS underneath the crystal. By varying the relative delay between the moment of photoresponse generation (excitation beam) and the signal probing (sampling beam), the whole time-domain waveform could be resolved. From the operational point of view, our EO system can be regarded as a sampling oscilloscope[4] featuring <200-fs time resolution and <150-μV voltage sensitivity, which are well below the characteristics of transients reported here.

The samples were mounted in a continuous-flow helium optical cryostat. All the experiments were carried out in a temperature range from 20 K to 80 K with the temperature control of ±0.2 K. Our test structures were connected to dc current and voltage sources, for biasing and characterizing the in-situ current voltage (*I–V*) of the junction and the microbridge, as well as to a 14-GHz-bandwidth oscilloscope for aligning the experiment and monitoring the bolometric response.

Experimental Results

The studied YBCO thin films, junctions, and microbridges exhibited standard, high-quality characteristics. The superconducting transition temperature T_c of as-prepared, 100-nm-thick films was in the 85 K to 87 K range. The *I–V* characteristics of a bicrystal Josephson junction on a MgO substrate showed an RSJ-like behavior with $I_c = 700$ μA and $I_c R_N = 2.5$ mV, and $I_c = 40$ μA and $I_c R_N = 0.1$ mV, at 4.2 K and 77 K, respectively (Fig. 77.40). The microbridge *I–V* curves exhibited a flux-flow transition into a resistive state at $J_c \approx 10^6$ A/cm^2 at 77 K. At higher bias currents, hot-spot formation occurred and the microbridge was driven into a switched (resistive) state. The microbridges were biased with a voltage source to prevent their destruction.[4]
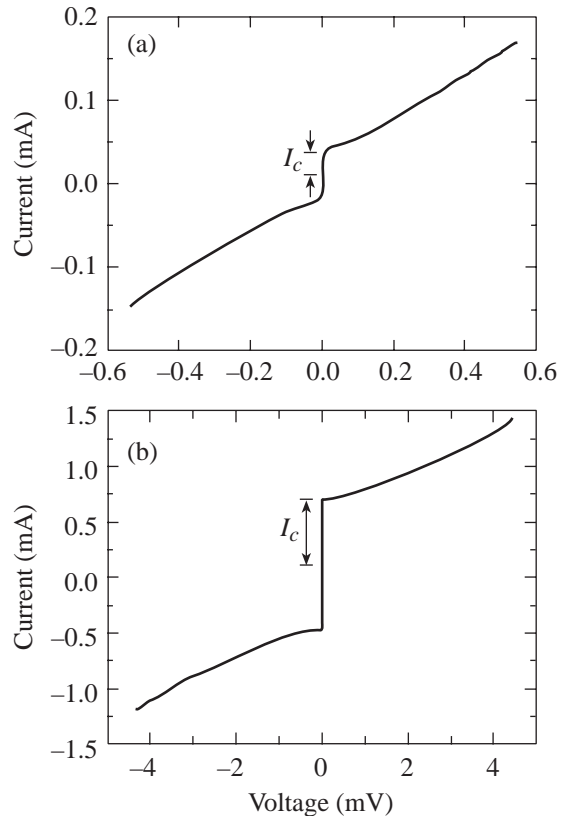

Z2418

Figure 77.40
Current-voltage characteristics of a bicrystal Josephson junction with $I_c = 40$ μA and $I_c = 700$ μA at 77 K and 4.2 K, respectively.

Figure 77.41 shows the EO sampling measurement of a 2.1-ps-wide electrical transient, typical for the microbridge biased in the resistive state.[5] Pulses of this type were used in all experiments presented in this article. Typically, the pulse amplitude was about 25 mV, which, for the approximately 80-Ω CPS line, corresponded to an ~300-μA current pulse.
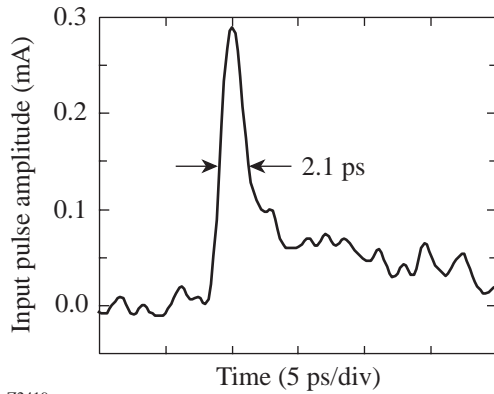
Z2419

Figure 77.41
Photogenerated electrical transient of the YBCO microbridge.

The pulse from Fig. 77.41 was applied to the junction, and the resulting signal was electro-optically detected approximately 50 μm after the junction (see Fig 77.39). Experiments were performed at 20 K, and the junction I_c was 650 μA ($I_c R_N \approx 2$ mV). To elicit a junction response from the measured output, we used the following procedure: We biased our junction in five different points on the I–V curve, namely at 0 I_c, $\pm 0.7 \, I_c$, and $\pm 1.5 \, I_c$, and recorded the response. The "+" bias corresponded to the positive amplitude of the input pulse, while in the "–" polarity, the junction was biased in the opposite direction to the excitation pulse. Figure 77.42(a) shows the normalized transient responses from the junction at 0 I_c, +0.7 I_c, and +1.5 I_c. We note that the initial, positive part of each response overlaps, while some differences are visible in the remainder of the pulse. After the initial oscillatory transient, we observe additional oscillations, which are very noisy and, therefore, difficult to analyze. A similar set of responses was collected for the −0.7 I_c, −1.5 I_c, and 0 I_c bias points and is shown in Fig. 77.42(b). All signals presented in Fig. 77.42 look very similar since they are dominated by the inductive response of the junction leads combined with the CPS resistance. Thus, the oscillatory transient with no bias applied to the junction (thin lines in Fig. 77.42) will be referred to as the *feedthrough* in further discussion.

Discussion

We believe that despite the fact that due to the design constraints all the waveforms presented in Fig. 77.42 look very similar and are dominated by the feedthrough signal, they contain information about switching dynamics of the YBCO Josephson junction; thus, we have subtracted the 0 I_c feedthrough signal from each measured waveform (results are shown in Fig. 77.43). For clarity, we separately showed the responses for the $\pm 1.5 \, I_c$ biased junction [Fig. 77.43(a)] and for $\pm 0.7 \, I_c$ [Fig. 77.43(b)]. In both cases, we overlaid the traces with the 0 I_c signal, which can be regarded as the zero-time reference for the junction response. From Fig. 77.43(a) we observe that when the junction is in the voltage state, the junction response for both bias polarities is positive and consists of an ~1-ps-wide transient with a turn-on delay of 0.7 ps. The response is consistent with our simulations (not shown)
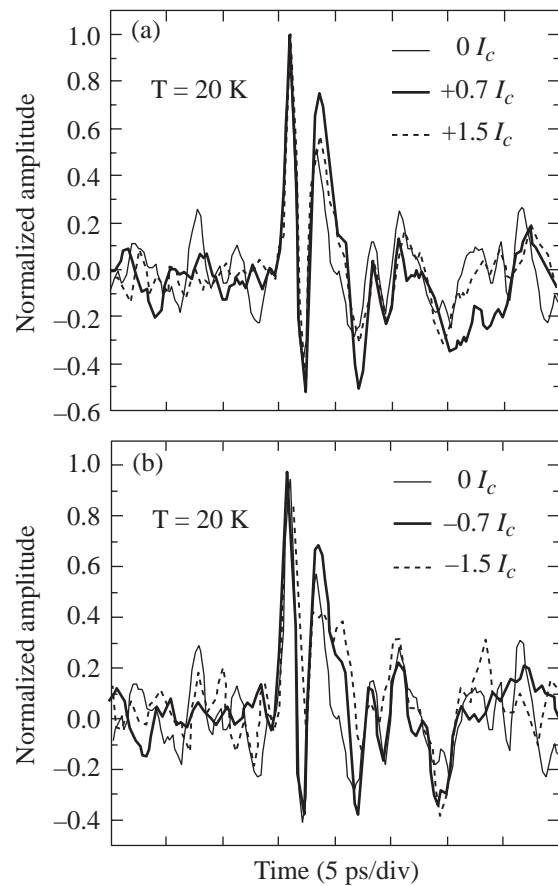
Z2420

Figure 77.42
The test structure response to the ultrafast input pulse measured for different junction biases on the CPS line 50 μm after the Josephson junction. All signals are normalized to the zero-bias feedthrough signal.
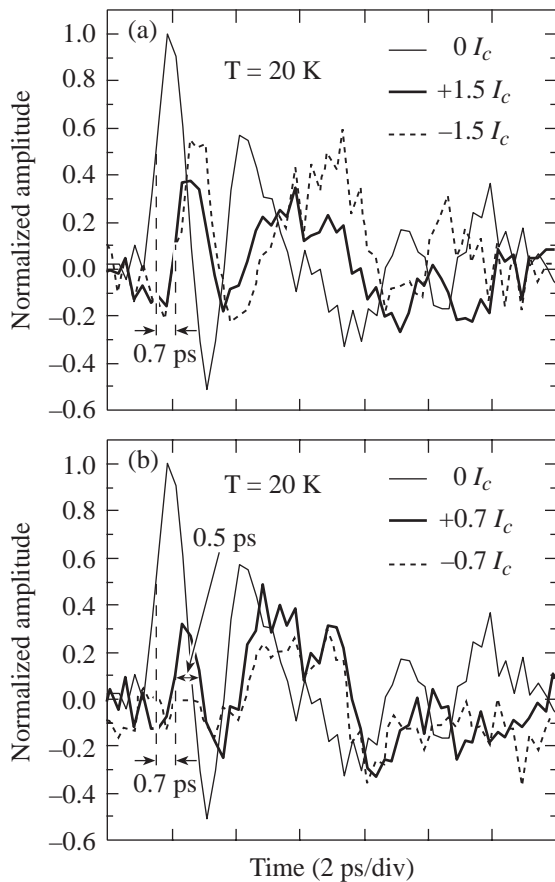
Figure 77.43

Response of the Josephson junction to the 2.1-ps electrical input pulse measured for different junction biases.

that in the voltage state, when junction current is oscillating with the frequency corresponding to the bias voltage, a small (compared to the bias) current-pulse perturbation generates a signal always in the direction of the excitation pulse polarization. In addition, the signal response is delayed with respect to the excitation.

The transients obtained for the junction biased in the superconducting state ($\pm 0.7\,I_c$) are shown in Fig. 77.43(b). When the dc bias polarity is in the same direction ($+0.7\,I_c$) as the $0.46\,I_c$ input-pulse amplitude, the excitation "knocks" the junction out of the zero-voltage state and we observe an SFQ-like, 0.5-ps-wide transient. We note that, at 20 K, $I_cR_N \approx 2$ mV; thus, the SFQ amplitude is expected to be ~ 4 mV, which leads to ~ 0.5-ps SFQ width, in good agreement with our observation. In the case of the negative bias ($-0.7\,I_c$), however, the incoming pulse is unable to switch the junction and no response is

detected. The measured τ_D of the $+0.7\,I_c$ biased junction is 0.7 ps, the same as for the $\pm 1.5\,I_c$ case. We must finally note that signals observed in Figs. 77.43(a) and 77.43(b) after the initial pulse responses discussed above are associated with the secondary input-pulse reflections and resulting secondary switching of our junction. Their detailed analysis and comparison with numerical circuit simulations will be presented in a later publication.

Conclusion

Picosecond electrical pulses, optically generated in current-biased YBCO microbridges, were used to excite the response of a bicrystal Josephson junction placed in the YBCO superconducting coplanar transmission line. The transients recorded just past the junction contained large feedthrough signals, but the junction response could be separated by subtracting the feedthrough from the signals obtained under different bias conditions. As a result, we were able to observe single-picosecond switching of HTS Josephson junctions, as well as to measure the junction turn-on delay time. Our findings provide confirmation of the potential of YBCO for ultrafast optical and electrical transient detection and processing. In the future, however, a new feedthrough-free test structure representing YBCO Josephson-junction coplanar transmission line is needed. The development of such a circuit is currently underway.

REFERENCES

1. V. F. Elesin and Yu. V. Kopaev, Sov. Phys. Usp. **24**, 116 (1981), and references therein.

2. R. Sobolewski, D. P. Butler, T. Y. Hsiang, C. V. Stancampiano, and G. A. Mourou, Phys. Rev. B **33**, 4604 (1986), and references therein.

3. F. A. Hegmann, D. Jacobs-Perkins, C.-C. Wang, S. H. Moffat, R. A. Hughes, J. S. Preston, M. Currie, P. M. Fauchet, T. Y. Hsiang, and R. Sobolewski, Appl. Phys. Lett. **67**, 285 (1995).

4. M. Lindgren, M. Currie, C. A. Williams, T. Y. Hsiang, P. M. Fauchet, R. Sobolewski, S. H. Moffat, R. A. Hughes, J. S. Preston, and F. A. Hegmann, IEEE J. Sel. Top. Quantum Electron. **2**, 668 (1996).

5. M. Lindgren, M. Currie, C. Williams, T. Y. Hsiang, P. M. Fauchet, R. Sobolewski, S. H. Moffat, R. A. Hughes, J. S. Preston, and F. A. Hegmann, IEEE Trans. Appl. Supercond. **7**, 3422 (1997).

6. M. Lindgren, M. Currie, C. A. Williams, T. Y. Hsiang, P. M. Fauchet, R. Sobolewski, S. H. Moffat, R. A. Hughes, J. S. Preston, and F. A. Hegmann, "Intrinsic Picosecond Response Times of Y-Ba-Cu-O Superconducting Photodetectors," to be published in Applied Physics Letters.

7. R. Sobolewski, in *Superconducting and Related Oxides: Physics and Nanoengineering III*, edited by I. Bozovic and D. Pavuna (SPIE, Bellingham, WA, 1998), Vol. 3481, pp. 480–491.

8. S. H. Dhong and T. Van Duzer, IEEE Trans. Electron Devices **ED-27**, 1965 (1980).

9. M. Darula and M. Kedro, J. Low Temp. Phys. **78**, 287 (1990).

10. D. G. McDonald *et al.*, IEEE Trans. Electron Devices **ED-27**, 1945 (1980).

11. K. K. Likharev and V. K. Semenov, IEEE Trans. Appl. Supercond. **1**, 3 (1991).

12. R. A. Hegmann, R. A. Hughes, and J. S. Preston, Appl. Phys. Lett. **64**, 3172 (1994).

High-Frequency Bulk Phase Modulator for Broadband Smoothing by Spectral Dispersion on OMEGA

High laser-irradiation uniformity is an important requirement for successful direct-drive inertial confinement fusion (ICF). Direct-drive laser-irradiation uniformity is achieved on OMEGA for different ranges of spatial frequencies using smoothing by spectral dispersion (SSD), polarization smoothing with distributed polarization rotators (DPR's), and multiple-beam overlap.[1] SSD significantly improves irradiation uniformity by rapidly shifting the laser speckle pattern generated by distributed phase plates (DPP's). A high-frequency electro-optic phase modulator produces a wavelength modulation that is subsequently converted by a diffraction grating into the angular deflection required to shift the speckle pattern. The low spatial frequency cutoff of the smoothing produced by SSD is determined by the maximum deflection of the beam. Extremely smooth, time-averaged intensity profiles are achieved on a time scale corresponding to the inverse bandwidth impressed by the phase modulator; thus, larger SSD bandwidths are desirable. Two-dimensional SSD (2-D SSD) extends the smoothing benefits of SSD by using two separate stages of bulk electro-optic phase modulators and gratings to deflect the laser speckle pattern in orthogonal directions.

For OMEGA, implementing a high-frequency modulator in the second direction of the 2-D SSD system is advantageous since the bandwidth from the second modulator is not dispersed until after the most-limiting spatial-filter pinhole, which is located in the large-aperture ring amplifier (LARA)[2] in the driver line. This constraint requires that high-frequency phase modulation be generated in a bulk electro-optic modulator to accommodate the dispersed bandwidth from the first modulator.

Design methods used to develop the current generation of 3.0- and 3.3-GHz bulk phase modulators[3] are directly relevant to higher-frequency designs, but several factors merit special attention in higher-frequency modulators designed to generate large SSD bandwidths. First, resonant designs are attractive since higher electric fields can be developed in the electro-optic material without expensive, high-power microwave sources. Velocity-matching the optical and microwave fields is also important to achieve efficient optical phase modulation. Lastly, controlling FM-to-AM conversion at higher-modulation frequencies is a more difficult system problem.

A number of bulk electro-optic phase modulator designs are found in the literature.[4–10] An approximately 9-GHz modulator[4] implemented on the original 24-beam OMEGA laser system incorporated a lithium niobate ($LiNbO_3$) crystal inside an evacuated, high-Q microwave resonator, but it suffered difficulties coupling microwave power from the resonator mode into the crystal. Velocity-matched waveguide resonator designs[5–7] operate at microwave frequencies near the waveguide cutoff to match the optical and microwave phase velocities. This matching allows arbitrarily long interaction lengths to be used to achieve increased modulation efficiency. A quasi-velocity-matched concept[8] uses periodically poled lithium tantalate ($LiTaO_3$) to approximately realize this same advantage with the added advantage of a TEM modulation field, but it suffers from the inherently lower Q factor of a micro strip resonator. An ~20-GHz dielectric resonator design[9] achieves a high Q factor, but the electric field distribution of the TM_{101} resonant mode is poorly suited for 2-D SSD applications. Convenient coupling of microwave power into a resonator structure is also a critical design issue. Electric-probe[6,9] and magnetic-loop[7] coupling require that the resonator structure be partially air filled, but this reduces the maximum clear aperture. Cutoff-waveguide coupling eliminates this disadvantage and, in addition, offers the possibility of tuning the resonance frequency.[10]

Incorporating a higher-frequency phase modulator in the 2-D SSD system offers two approaches to improving irradiation uniformity on OMEGA. First, larger SSD bandwidths can be generated for a given number of FM sidebands and propagated through the laser system since less grating dispersion is required to achieve a single color cycle. Increased SSD bandwidths smooth laser irradiation faster. An asymmetric 2-D SSD configuration on OMEGA using phase modulators operating at 3.0 and ~10 GHz could achieve infrared bandwidths of 1.5 × 12 Å, respectively, to generate 1 × 1 color cycles nominally.

This infrared bandwidth corresponds to a UV bandwidth of approximately 1 THz. To efficiently convert this infrared bandwidth to the ultraviolet, dual-tripler frequency-conversion crystals[11] (FCC's) must be implemented on all 60 OMEGA beams. This upgrade will be completed before the end of 1999.

Alternately, multiple SSD color cycles can be produced with a higher modulation frequency for a given grating design, and the same SSD bandwidth can be propagated without exceeding the beam divergence limit imposed by the laser system pinholes. Increasing the number of color cycles redistributes the beam nonuniformity to higher spatial frequencies and accelerates the smoothing at the mid-range spatial frequencies ($\ell = 50$–200) that pose the greatest threat of seeding hydrodynamic instabilities in direct-drive implosions.[1] The current OMEGA FCC configuration can efficiently convert infrared bandwidths of 1.5×3.0 Å from modulators operating at 3.0 and ~10 GHz to generate 1×3 color cycles, respectively. Experiments utilizing both 1-THz UV bandwidth and multiple color cycle improvements are planned for OMEGA this year.

High-Frequency Modulator Design

A velocity-matched, waveguide-coupled, $LiNbO_3$ dielectric resonator modulator design was selected for the 2-D SSD, high-frequency modulator application. A simple sketch of a generic cutoff-waveguide-coupled resonator[10] is presented in Fig. 78.1(a). A TE_{10} mode of the input waveguide delivers microwave radiation to a high-Q, TE_{10n} standing-wave resonator formed by locating an electro-optic material in an air waveguide that would otherwise be below cutoff at the resonance frequency.

Velocity mismatches between the microwave and optical phase velocities in an electro-optic material reduce phase-modulation efficiency,[12] particularly at high modulation frequencies. In the resonant microwave cavities used for SSD bulk phase modulators, standing waves are impressed across the electro-optic crystal, which can be decomposed into fields co-propagating and counter-propagating with the laser beam. For this case, the velocity-mismatch reduction factor β is given by[12]

$$\beta = \frac{1}{2}\left| \frac{\sin(u_+)}{u_+} + \frac{\sin(u_-)}{u_-} \right|, \tag{1a}$$

$$u_\pm = \left(\frac{\pi f_m L}{c} \right)\left(\sqrt{\varepsilon_3} \mp n_3 \right), \tag{1b}$$

where ε_3 is the relative dielectric constant of the electro-optic crystal for polarizing the applied microwave field at the modulation frequency f_m, n_3 is the index of refraction of the crystal, and c is the speed of light in vacuum. The first term of Eq. (1a) accounts for the contribution of the optical beam interacting with the co-propagating microwave, while the second term is associated with the counter-propagating microwave field. The maximum effective interaction length βL for a 10.5-GHz $LiNbO_3$ modulator with no velocity matching is limited to approximately 2 mm, as shown in Fig. 78.2.

Velocity matching is achieved in the configuration shown in Fig. 78.1(a) by setting the width of the crystal, a, to adjust the microwave phase velocity in the waveguide geometry,

$$v_{\text{phase}} = \frac{c}{\sqrt{\varepsilon_3}\sqrt{1-\left(f_c/f_0\right)^2}},$$

$$f_c = \frac{c}{2a\sqrt{\varepsilon_3}}, \tag{2}$$

to match the optical phase velocity in the electro-optic material, c/n_3, where f_c is the cutoff frequency of the waveguide section loaded with the crystal and f_0 is the resonance frequency of the modulator. Figure 78.2 plots the effective interaction length as a function of crystal length for waveguide resonators with different degrees of velocity matching. For a perfectly velocity-matched design, the effective interaction length grows linearly with some modulation caused by the interaction with the counter-propagating microwave field. An almost negligible penalty is observed for a 10% velocity mismatch with a 26.3-mm crystal length shown in Fig. 78.1(c).

The height b of the crystal is arbitrary for a TE_{10n} mode; however, minimizing b increases the electric field magnitude for a given microwave drive power and can eliminate spurious TE_{01m} modes in the crystal that would divert microwave energy if mode-coupling mechanisms exist. The length of the electro-optic material determines the modulator resonance frequency based on the microwave phase velocity in the waveguide. A resonance exists for crystals that are an integer number of half-wavelengths, plus any phase shifts associated with the reflections at the cutoff-waveguide sections. For materials with a high dielectric constant, these phase shifts are generally small and only change the effective length of the resonator by about 1%.[10]

(a) Top view   (b) End view

Cutoff-waveguide sections

Air-filled input
waveguide
(TE$_{10}$ mode)

a' a

Optical axis

Electro-optic crystal (ε_3, n_3)

d_{coupling} L d_{cutoff}

x

y z

E_{micro}

E_{opt}

$\hat{c}$

b

x

z y

(c)

WR-90 waveguide-
coaxial adapter

Waveguide
elbow section

Temperature
controller

Crystal holder

Tapered input
waveguide section

Image relay
lens cell

Image relay
lens cell

$3.05 \times 2.0 \times 26.3$-mm
LiNbO$_3$ crystal

Beam
port

E9672

Figure 78.1

(a) Generic cutoff-waveguide-coupled resonator. The electro-optic crystal of length L is positioned in an air-filled, rectangular waveguide of width a and height b. The waveguide width sets the cutoff frequency above the modulator operating frequency in the air-filled sections, but below cutoff in the crystal. The cutoff-waveguide sections act as high reflectors for the standing waves inside the electro-optic crystal resonator. The input waveguide width a' supports traveling waves at the operating frequency that evanescently couple through the coupling distance d_{coupling}. (b) The microwave and optical electric fields, E_{micro} and E_{opt}, are oriented along the crystalline c axis to take advantage of the large electro-optic tensor element r_{33} in LiNbO$_3$. The beam size is small enough so that the variation of the microwave field in the x direction is only 15%. (c) A tapered input waveguide provides a transition from standard waveguide dimensions to dimensions required for critical coupling into the modulator crystal. A small beam port in the input waveguide bend provides optical access to the crystal but does not disturb the microwave input since it is significantly smaller than the microwave wavelength.

All SSD modulators designed and built at LLE have used $LiNbO_3$, which is a well-developed electro-optic crystalline material. Other electro-optic materials are commercially available and were considered for the new high-frequency modulator design, including $LiTaO_3$, potassium titanyl phosphate (KTP) and its crystal isomorphs, rubidium titanyl arsenate (RTA), and cesium titanyl arsenate (CTA). Relevant optical and microwave properties of these materials are reported in Table 78.I. A large electro-optic coefficient is obviously desirable, but the index of refraction and relative dielectric constant also play a significant role in maximizing the phase-modulation performance, as indicated by the electro-optic figure of merit. The loss tangent is inversely related to the fundamental limit on the Q factor that can be achieved in a resonant design[13] since it represents the dielectric losses in each material. Lastly, the laser-damage threshold is an important performance parameter. Both bulk and surface laser-damage thresholds were measured for undoped $LiNbO_3$ and are presented in Table 78.I. The surface finish of the samples limited the surface-damage threshold, while a lower bound on the bulk damage threshold was established that was limited by catastrophic surface damage. Doped samples of $Zn:LiNbO_3$ and $MgO:LiNbO_3$ showed poorer damage thresholds. RTA is a potentially attractive alternative possessing a high electro-optic figure of merit, a loss tangent almost four times lower than $LiNbO_3$, plus a lower dielectric constant that would facilitate approximately 20% larger crystal clear apertures. The optical quality of RTA, however, is not currently adequate for SSD applications since strong birefringence gradients are reported and the laser-damage threshold is significantly lower than commercially available $LiNbO_3$.

Setting the beam size in a TE_{10n}-mode waveguide modulator requires a compromise between maximizing the uniformity of the phase-modulation depth across the beam and minimizing FM-to-AM conversion. The electric field of the standing wave varies across the transverse dimension, as shown in Fig. 78.1(b). This field distribution produces an index-of-refraction variation equivalent to a time-varying cylindrical gradient-index lens. Minimizing the SSD beam size to the central portion of the aperture minimizes this effect but increases the difficulty of SSD system imaging. The phase-modulated bandwidth dispersed by the SSD gratings must be carefully imaged to prevent FM-to-AM conversion resulting from propagation out of a grating image plane; otherwise,

E9673

Figure 78.2
Effective interaction length with velocity matching in $LiNbO_3$ modulators. Bulk modulator with no velocity matching (heavy solid line); perfect velocity matching essentially linear with respect to interaction length, with modulation due to interaction with counter-propagating microwave fields (light solid line); variations of velocity mismatch in 10% graduations (dashed lines).

Table 78.I: Electro-optic material properties.

	$LiNbO_3$ (Refs. 14,15)	$LiTaO_3$ (Refs. 16,17)	KTP (Ref. 18)	RTA (Ref. 16)	CTA (Ref. 16)
Crystalline type	uniaxial	uniaxial	biaxial	biaxial	biaxial
Electro-optic coefficient (pm/V)	$r_{33} = 28.8–30.8$	33	35.0	40.5	38.0
Index of refraction	$n_3 = 2.1561$ (extraordinary)	2.143	$n_z = 1.840$	$n_z = 1.890$	$n_z = 1.930$
Relative dielectric constant	$\varepsilon_{33} = 23.7–27.9$	41.4–43	15.4	19	29
Loss tangent (at 10 GHz)	0.0015	0.001	0.70	0.0004	0.002
Electro-optic figure of merit $n_3^6 r_{33}^2 / \varepsilon_r \left(pm^2/V^2 \right)$	3304	2548	2705	3935	2573
Laser-damage threshold (GW/cm^2)	>22 (bulk) >2.0 (surface)		>1	0.4	0.4

intensity modulation develops even from a perfectly FM-modulated beam according to

$$\frac{\Delta I}{I} \propto \delta_{\text{mod}} \cdot \left(\omega_{\text{mod}} \, d\theta/d\lambda\right)^2 z \propto \delta_{\text{mod}} \cdot \left(\frac{N_{\text{cc}}}{D_{\text{beam}}}\right)^2 z, \quad (3)$$

where δ_{mod} is the phase-modulation depth, ω_{mod} is the phase-modulation angular frequency, $d\theta/d\lambda$ is the effective grating dispersion, z is the distance from the nearest image plane, N_{cc} is the number of color cycles impressed on the SSD beam, and D_{beam} is the beam diameter. Demagnifying the SSD beam to fit through the modulator increases the sensitivity to imaging errors and color separation of the dispersed FM beam on system optics that can lead to amplitude modulation. This is especially true for systems employing multiple color cycles.

The 10.5-GHz, waveguide-coupled LiNbO$_3$ modulator design [shown in Fig. 78.1(c)] includes four parts: a LiNbO$_3$ crystal, a crystal holder, a tapered input waveguide section, and a temperature controller. For a LiNbO$_3$ modulator operating at 10.5 GHz, the ideal crystal width to achieve velocity matching according to Eq. (2) sets $a = 3.064$ mm. All four sides of the crystal are gold coated to form a standing-wave waveguide resonator that is approximately $2 \cdot \lambda_{\text{microwave}}$ long, while the ends are antireflection coated for the SSD beam. The height is the smallest possible consistent with a 1.1-mm beam size chosen to limit the time-varying cylindrical phase error to a reasonable level.

The crystal holder and tapered input waveguide sections are machined from copper to maximize electrical and thermal conductivity and are gold plated to prevent oxidation of the copper. The high electrical conductivity of copper minimizes conduction losses in both the input waveguide and the waveguide resonator since the gold coatings on the crystal are only a fraction of a skin depth at 10.5 GHz. Good thermal conduction is also beneficial in maintaining a uniform temperature across the crystal.

The crystal holder is machined from three pieces of copper that confine the LiNbO$_3$ crystal on three sides while a copper foil holds it in place. This configuration ensures high-conductivity walls next to the crystal with no air gaps in the direction of the microwave electric field and minimal stress on the crystal. Active temperature control of the modulator crystal is planned to stabilize the resonance frequency and provide a limited range of tuning. The simulated results discussed below are based on the modulator operating at 50°C to provide a

±20°C range of temperature to accommodate uncertainties in the dielectric constant and crystal fabrication tolerances. A significant advantage of the modulator design is that the crystal holder can accept various crystal sizes designed to operate at different resonance frequencies.

The tapered input waveguide section transfers microwave power from a standard coaxial-to-WR-90 waveguide adapter to a 4-mm-high waveguide section suitable for coupling the microwave energy into the modulator crystal. The taper length is $\lambda_{\text{microwave}}/2$ to minimize reflections associated with the waveguide discontinuities. A $\lambda_{\text{microwave}}/2$-long waveguide elbow is also included with a small beam port for optical beam access to the microwave input side of the crystal.

Maximizing microwave power transfer into a cutoff-waveguide-coupled resonator at resonance is accomplished by adjusting d_{coupling} to vary the coupling coefficient,[10]

$$\beta_{\text{coupling}} = \frac{16}{\pi^3} \frac{Q_0}{L_{\text{eff}}} \frac{\dfrac{a'}{a} \cos^2\left(\dfrac{\pi}{2} \dfrac{a'}{a}\right)}{\left[1 - \left(\dfrac{a'}{a}\right)^2\right]^2} \frac{\varepsilon_r - \left(\dfrac{\lambda_0}{2a'}\right)^2}{\varepsilon_r(\varepsilon_r - 1)}$$

$$\times \; \lambda_0 \sqrt{1 - \left(\frac{\lambda_0}{2a}\right)^2} \; \exp\left[-\frac{2\pi d_{\text{coupling}}}{a'} \sqrt{1 - \left(\frac{2a}{\lambda_0}\right)}\right], \quad (4)$$

to achieve critical coupling ($\beta_{\text{coupling}} = 1$), where Q_0 is the resonator Q factor, L_{eff} is the effective length of the LiNbO$_3$ crystal, and λ_0 is the free-space microwave wavelength; the remaining dimensions are defined in Fig. 78.1(a). Critical coupling maximizes the power transferred into the resonator.[19] Equation (4) was derived assuming no reaction of the cavity field on the waveguide field and is valid only for positive coupling distances. Using this analytic expression, the coupling coefficient calculated for the modulator presented in Fig. 78.1(c) is plotted in Fig. 78.3, where it is seen that critical coupling is not achieved, even for $d_{\text{coupling}} = 0$. This results from the poor overlap between the input waveguide and crystal resonator modes, which is limited by the large mismatch between the input waveguide width and the small crystal width imposed by the velocity-matching constraint. Although Eq. (4) cannot be extrapolated to negative coupling distances, it strongly suggests that allowing the modulator crystal to extend into the input waveguide would achieve critical coupling.
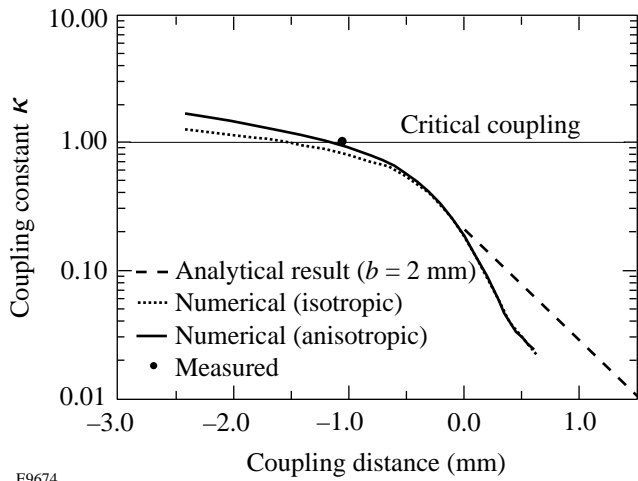
E9674

Figure 78.3
Coupling coefficient plotted versus coupling distance for waveguide-coupled LiNbO$_3$ modulator. The analytic values calculated from Eq. (4) are plotted in the dashed line only for positive coupling distances assuming the input waveguide and crystal heights are equal. Values from Micro-Stripes simulations modeling LiNbO$_3$ as an isotropic dielectric, as well as using the tensor values for the dielectric constant are plotted as dotted and solid lines, respectively. Critical coupling was experimentally observed for $d_{coupling}$ = 1.07 mm and plotted.

Accurately analyzing configurations where the crystal protrudes into the input waveguide was accomplished numerically using Micro-Stripes, a commercial three-dimensional electromagnetic analysis package.[20] Micro-Stripes yields both time- and frequency-domain electromagnetic solutions for arbitrary geometries, including tensor material properties such as the dielectric constant for materials like LiNbO$_3$, which are difficult to treat analytically. A particular strength of this simulation package is that wideband frequency-domain results with fine resolution are obtained from a single time-domain simulation.

A typical Micro-Stripes model and the results from a simulation are shown in Fig. 78.4. All the geometric details and material properties of the modulator shown in Fig. 78.4(a) are represented in the model. In a simulation, an electromagnetic impulse is launched in the input waveguide, and the fields throughout the model are calculated as a function of time. Field values are saved at probe points for post-simulation analysis, including digital filtering, resolving incident and reflected waves, and transforming into the frequency domain. The complex reflection coefficient can be calculated as a function of frequency from the simulated forward and reflected microwave field components. The complex reflection coefficient can then be analyzed using a personal computer program QZERO[19] to yield the three important resonator parameters: the resonance frequency, the resonator Q factor, and the coupling coefficient.

(a)

E9675

(b)
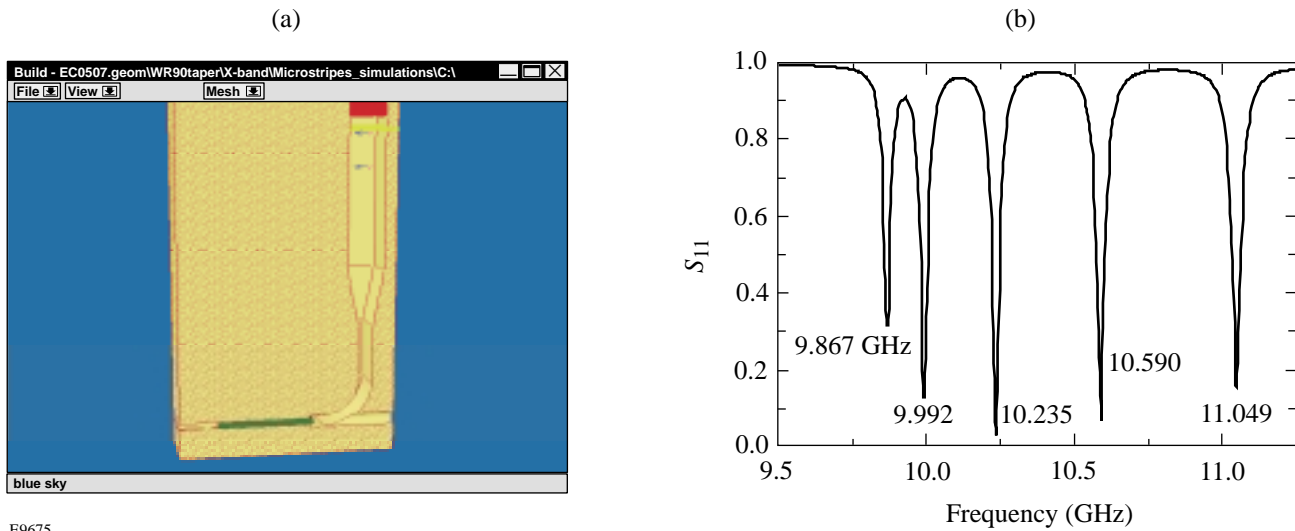
Figure 78.4
Micro-Stripes numerical simulations. (a) The complete three-dimensional, anisotropic geometry of the LiNbO$_3$ modulator shown in Fig. 78.1(c) is modeled with spatial resolution required to yield accurate results; (b) the magnitude of the complex reflectivity plotted versus excitation frequency reflects the harmonic spectrum of the waveguide resonator formed by the LiNbO$_3$ crystal.

Micro-Stripes simulations were performed using an isotropic dielectric constant equal to the value along the designed microwave electric field direction (ε_{33}), as well as the tensor values available from the literature.[15] Simulations for a range of crystal positions were calculated and the coupling coefficient plotted in Fig. 78.3. For both cases, the coupling increases as the LiNbO$_3$ crystal protrudes farther into the input waveguide. Critical coupling is achieved for $d \approx 1.2$ mm for the anisotropic calculation. The magnitude of the complex reflection coefficient plotted versus frequency for this crystal position is shown in Fig. 78.4(b). Nearly critical coupling into a high-Q resonance is evident from the narrow, low-reflection feature representing the $4 \cdot \lambda_{microwave}/2$ mode of the crystal resonator. Another feature evident from Fig. 78.4(b) is that the modulator can be optimally coupled for any of the other resonances to access even higher modulation frequencies; however, given the fixed resonator geometry defined by the crystal, a velocity-mismatch penalty would be incurred.

Figure 78.5 shows the predicted variation of the resonance frequency f_0 and the resonator Q factor over the same range of crystal positions for the $4 \cdot \lambda/2$ resonance as covered in Fig. 78.3. The resonance frequency shows a relatively small variation, and the Q factor is essentially unchanged over the range of crystal positions producing significant microwave coupling into the crystal. Interestingly, the resonance frequency plotted in Fig. 78.5(a) initially decreases as the length of the crystal protruding into the input waveguide increases, after which it increases monotonically. The initial drop in resonance frequency, as well as the initially widening differences between the isotropic and anisotropic simulations of the resonance frequency, indicate that the effective length of the resonator increases as the resonator fields extend into the input waveguide and the fields distort near the crystal input. This field distortion introduces electric field components that interact with the higher dielectric constant (ε_{11}) in the x and z directions. After reaching minima, values for the resonance frequency for both cases increase at the same rate since the crystal length inside the crystal holder decreases. For positive values of the coupling distance $d_{coupling}$, the predicted resonance frequency approaches the value characteristic of the crystal loaded in an infinitely long, cutoff waveguide. The predicted Q factor in Fig. 78.5(b) also increases since the coupling losses into the input waveguide rapidly decrease, as seen in Fig. 78.3.

Modulator Performance

Microwave measurements of the X-band modulator and adjustments to optimize coupling were performed using a microwave vector network analyzer (HP Model 8720B). As designed, the length of the crystal protruding into the input waveguide was set to maximize microwave coupling into the $4 \cdot \lambda/2$ resonance. Excellent coupling was achieved for a coupling distance of -1.07 mm. Within experimental uncertainties the measured return loss of -35 dB represents critical coupling and is plotted in Fig. 78.3. Excellent agreement with predicted values of the coupling coefficient is observed.
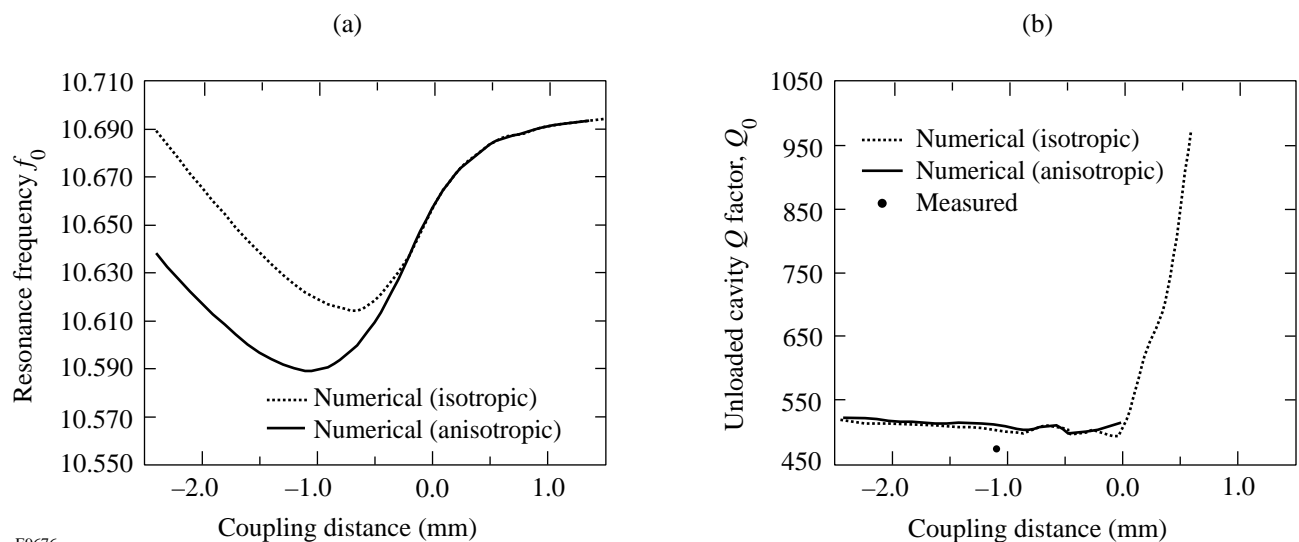
(a)

(b)

E9676

Figure 78.5
(a) Resonance frequency and (b) Q factor for cutoff-coupled, LiNbO$_3$ waveguide modulator.

The measured complex reflectivity of the modulator was also analyzed to evaluate the resonance frequency and Q factor. The measured resonance frequency at critical coupling is 10.412 GHz, which is 1.7% lower than predicted from the Micro-Stripes simulations. This discrepancy is attributed to three factors: First, the cutoff-waveguide cross section at the end of the crystal opposite the input waveguide was enlarged slightly to simplify alignment of the modulator in the SSD system, which would increase the effective length of the resonator and reduce the resonance frequency. Second, crystal fabricating tolerances resulted in slightly larger width and length dimensions that also increase the effective resonator length. Lastly, the actual dielectric tensor values for the LiNbO$_3$ crystal may differ from the literature values[15] used in the simulations. The measured Q factor plotted in Fig. 78.5(b) agrees well with the predicted values.

Experimentally, double-pass operation yields 1.95-Å SSD bandwidths with approximately 14.4 W of microwave power delivered to the modulator. This measurement of phase-modulation performance shows reasonable agreement with a simple estimate based on microwave measurements. The microwave energy stored in the resonator, E_{stored}, can be calculated from the definition of the unloaded Q factor,

$$Q_0 \equiv \omega_0\, E_{stored}/P_{in}\,,$$

where P_{in} is the power delivered to the modulator and ω_0 is the angular microwave frequency $\omega_0 = 2\pi f_0$. The stored energy E_{stored} can be related easily to the electric field strength inside the crystal, E_0, by approximating the field distribution with the mode of a TE$_{10n}$ resonator and spatially integrating to derive

$$E_{stored} = \varepsilon_{33}/8\,(abL)\,E_0^2\,,$$

where ε_{33} is the dielectric constant, and a, b, and L are the crystal width, height, and length, respectively. These expressions can be combined with the expression for phase-modulation depth,[3]

$$\delta_{mod} = \frac{\pi\cdot\beta\,L\cdot n_3^3\,r_{33}}{\lambda_{opt}}\,E_0\,,$$

where βL is the effective crystal length including velocity mismatch, n_3 is the index of refraction, r_{33} is the electro-optic coefficient, and λ_{opt} is the optical wavelength. Using the measured values for Q_0, a, b, and L, literature values for ε_{33}, n_3, and r_{33}, a calculated value of $\beta L = 0.95$ to account for some velocity mismatch tolerance, a phase-modulation depth of 1.59 is calculated. For a single pass, this corresponds to an SSD bandwidth $\Delta\lambda_{single} = 1.22$ Å, or a double-pass bandwidth $\Delta\lambda_{double} = 2.44$ Å.

Additional SSD bandwidth can be achieved by increasing the number of passes through the modulator or increasing input power. Based on the measured performance, a double-pass configuration would require approximately 520 W of microwave drive power to generate 12 Å of phase-modulated bandwidth, while an active multipass scheme with four passes would require less than 130 W at the expense of greater system complexity.

Conclusion

The design of an efficient, bulk phase modulator operating at approximately 10.5 GHz, which can produce substantial phase-modulated bandwidth with modest microwave drive power, has been presented. The waveguide resonator design employs an adapted form of cutoff-waveguide coupling and velocity matching to yield a simple, high-Q microwave design with practical clear-aperture dimensions suitable for application in a 2-D SSD system. The design is easily scalable to other frequencies by simply changing the electro-optic crystal dimensions. The measured microwave performance of the modulator agrees well with performance predicted from fully anisotropic, three-dimensional numerical simulations.

REFERENCES:

1. S. Skupsky and R. S. Craxton, Phys. Plasmas **6**, 2157 (1999).

2. Laboratory for Laser Energetics LLE Review **58**, 90, NTIS document No. DOE/SF/19460-17 (1994). Copies may be obtained from the National Technical Information Service, Springfield, VA 22161.

3. Laboratory for Laser Energetics LLE Review **68**, 192, NTIS document No. DOE/SF/19460-139 (1996). Copies may be obtained from the National Technical Information Service, Springfield, VA 22161.

4. Laboratory for Laser Energetics LLE Review **48**, 169, NTIS document No. DOE/DP40200-175 (1991). Copies may be obtained from the National Technical Information Service, Springfield, VA 22161.

5. G. Carter, Appl. Phys. Lett. **32**, 810 (1978).

6. T. F. Gallagher, N. H. Tran, and J. P. Watjen, Appl. Opt. **25**, 510 (1986); N. H. Tran *et al.*, Appl. Opt. **24**, 4282 (1985); T. F. Gallagher and J. P. Watjen, U.S. Patent No. 4,733,397 (22 March 1988).

7. A. A. Godil, U.S. Patent No. 5,414,552 (9 May 1995).

8. F.-Z. Guo *et al.*, IEEE J. Quantum Electron. **33**, 879 (1997).

9. A. A. Godil *et al.*, Opt. Lett. **16**, 1765 (1991).

10. E. Bonek *et al.*, AEU **32**, 209 (1978).

11. A. Babushkin, R. S. Craxton, S. Oskoui, M. J. Guardalben, R. L. Keck, and W. Seka, Opt. Lett. **23**, 927 (1998).

12. I. P. Kaminow and J. Liu, Proc. IEEE **51**, 132 (1963).

13. D. M. Pozar, *Microwave Engineering*, 2nd ed. (Wiley, New York, 1998).

14. Y. Ohmachi, K. Sawamoto, and H. Toyoda, Jpn. J. Appl. Phys. **6**, 1467 (1967).

15. R. S. Weis and T. K. Gaylord, Appl. Phys. A **37**, 191 (1985).

16. Crystal Technology data sheet, Palo Alto, CA 94303 (May 1993).

17. J. R. Teague, R. R. Rice, and R. Gerson, J. Appl. Phys. **46**, 2864 (1975).

18. Crystal Associates data sheet, Waldwick, NJ 07463 (May 1996).

19. D. Kajfez, *Q Factor* (Vector Fields, Oxford, MS, 1994).

20. Micro-Stripes[TM], available from Sonnet Software, Inc., Liverpool, NY 13090.

Angular Spectrum Representation of Pulsed Laser Beams with Two-Dimensional Smoothing by Spectral Dispersion

Pulsed laser beams with two-dimensional smoothing by spectral dispersion (2-D SSD), used in inertial confinement fusion (ICF), improve the on-target uniformity on the OMEGA laser system;[1–4] however, 2-D SSD is highly susceptible to significant amplitude modulation (AM) during its generation and propagation.[5–8] In addition to on-target uniformity, the smoothness of the pulsed beam as it propagates through the long laser amplifier chain is important because of the perennial concern regarding laser damage. Small-scale, nonlinear self-focusing can occur as the pulsed beam propagates through various optical components because of the large fluences inherent in ICF applications. Any AM, in space or time, present on the pulsed beam may induce self-focusing and lead to damage. OMEGA utilizes many spatial filters to help alleviate the buildup of high spatial frequencies that tend to self-focus. In an effort to reduce the overall AM, it is imperative that the AM produced by the SSD driver line is at an absolute minimum.

A complete analysis of the SSD driver line requires a model that accounts for diffraction and spatiotemporal spectral effects of the many optical components that comprise the driver during both the generation and propagation of 2-D SSD beams. AM sources and other nonideal behavior can occur at any point in the SSD driver line, and the impact of a particular optical component depends on its relative location and the parameters that describe the SSD operation. Laser beam propagation codes that include SSD as part of an entire ICF laser system modeling exist at other laboratories, for example, Prop92 at LLNL and Miró at CEA; however, they do not emphasize the underlying optical components in the SSD driver line. A comprehensive understanding of the AM issue and other nonideal behavior entails a rigorous examination of the specific optics involved in the SSD driver line, including the effects of multiple-layered dielectric media, crystal birefringence, multiple co-propagating beams, nonlinear grating behavior, and far-field distortion. A model must be able to simulate the nonideal effects, predict the relative impact, and characterize the behavior so that experimental measurements can be used to diagnose and excise the problem.

The code (Waasese) developed to address the AM issue in the SSD driver line simulates many optical components, predicts the degree of AM, and characterizes the AM mechanisms in terms of measurable signatures. Different AM sources are measured on near-field streak camera images and exhibit distinct spatiotemporal patterns, trends in the temporal spectrum, and/or AM that varies as a function of an SSD parameter. Waasese simulations associate these distinct characteristics or signatures to particular optic components. These signature/component relationships are then exploited to diagnose, locate, and eliminate the AM sources when used in conjunction with experimental measurements. Waasese has been successfully used to locate some AM sources and identify solutions in the new double-pass 2-D SSD driver line scheduled for installation on OMEGA. Waasese is based on the angular spectrum representation, which accurately models diffraction and spatiotemporal spectral effects. Waasese is not limited to AM issues and has been used to model observed far-field distortion. Waasese's inherent flexibility facilitates future enhancements as other laser propagation issues arise.

Waasese models the individual optical components of the SSD driver line using a transfer-function approach as opposed to applying the ideal spatiotemporal dependent phase term. An angular spectrum representation and/or a thin optic phase transformation describes the transfer functions of the optical components. This approach models SSD generation in a stepwise fashion so that nonideal components, such as wave plates, may be included at any point in the process such as in between the preshear and dispersion gratings. This is an important issue because the degree to which optical components contribute to AM depends on their relative location in the SSD driver line. For example, surface roughness of a far-field retro mirror of the second SSD dimension will produce AM on the first but not the second dimension because the second dimension has not been dispersed at this point. Also, the AM induced by the crystal birefringence of the second SSD dimension can be compensated, provided that re-imaging takes place prior to the final grating. Additional examples of the modeling capabilities of

Waaese include nonlinear behavior of gratings, multiple surface reflections from a crystal in combination with an end mirror that produce co-propagating beams with offset spatiotemporal spectra, angular-dependent phase modulation depth that produces distorted far-field spectra, multiple-layered dielectric coatings that model high-reflection (HR) or antireflection (AR) coatings, etalon effects that modulate the temporal spectrum, spatial phase modulation of irregular surfaces, and image rotation between grating pairs. Waaese is capable of modeling arbitrary initial spatial and temporal profiles such as Gaussian, hyperbolic tangent, square, round, and elliptical. A postprocessor for Waaese incorporates various instructional data-visualization techniques of the spatiotemporal intensity and phase history of 2-D SSD pulsed beams: a spatiotemporal cross section, a spatial cross section, a false-color instantaneous wavelength overlay, a time-averaged far-field view, and a time evolution of the far-field pattern. These data-visualization techniques provide valuable insight into various problems that arise and their subsequent solutions.

The angular spectrum representation provides a straightforward analytical and numerical method to accurately analyze the generation and propagation of 2-D SSD pulsed laser beams. The angular spectrum representation decomposes a pulsed beam into a continuous linear sum of harmonic plane waves that individually propagate with a unique direction and temporal frequency through the laser system. Each harmonic plane wave is completely described by three parameters: k_x, k_y, and ω. When the resultant harmonic plane waves are summed, a representation of a 2-D SSD pulsed laser beam is obtained that accurately models diffraction and spatiotemporal spectral effects. Certain optical components require a thin optic phase transformation operation, in real space, whenever the optical surfaces are not planar, e.g., lenses, irregular surfaces on mirror coatings, and surface roughness of optical finishing.

In this article we first describe the angular spectrum representation of the two main elements of the SSD operation used in Waaese: gratings and electro-optic (EO) phase modulators. We then apply these transfer functions to the ideal generation of 2-D SSD, which provides a foundation of comparison for the nonideal cases. Ideal 2-D SSD utilizes a linearized grating equation and a pure phase-modulation operation. Analytical expressions and Waaese demonstrate that the application of the ideal transfer functions reduces the problem to the well-known spatiotemporal-dependent phase term that describes 2-D SSD.[1,2] We also introduce the frequency domain and real-space data visualization capabilities of the Waaese post-

processor. Finally in a section covering nonideal 2-D SSD generation we discuss various errors and/or nonideal effects that include nonideal gratings, nonideal phase modulators, crystal birefringence, Littrow mount error, image rotation, temporal spectrum modulation, spatial spectrum modulation, and image-plane errors.

Angular Spectrum Representation

Consider the electromagnetic field of the pulsed laser beam that propagates along the beam axis $\hat{\mathbf{z}}$ within a nonmagnetic, nonconducting, source-free, linear, causal, spatially and temporally homogeneous, isotropic, and spatially and temporally locally linear dielectric medium described by a constant refractive index $n \equiv \sqrt{\mu\varepsilon/\mu_0\varepsilon_0}$. Let the electric field $\mathbf{E}'(\mathbf{r},t)$ of the pulsed laser beam be defined on an image plane at $z = z_0$:

$$\mathbf{E}_0{}'(\mathbf{r}_T,t) \equiv \mathbf{E}'(\mathbf{r},t)\Big|_{z=z_0}, \qquad (1)$$

where the position vector and transverse position vector are defined, respectively, by

$$\mathbf{r} \equiv x\hat{\mathbf{x}} + y\hat{\mathbf{y}} + z\hat{\mathbf{z}} \qquad (2)$$

and

$$\mathbf{r}_T \equiv x\hat{\mathbf{x}} + y\hat{\mathbf{y}} \qquad (3)$$

in the right-handed rectangular coordinate system (x, y, z) with the corresponding unit vectors $(\hat{\mathbf{x}}, \hat{\mathbf{y}}, \hat{\mathbf{z}})$. In addition, let the pulsed laser beam possess the form of a modulated carrier of angular frequency ω_c:

$$\mathbf{E}_0{}'(\mathbf{r}_T,t) \equiv \mathbf{E}_0(\mathbf{r}_T,t)e^{i\omega_c t}, \qquad (4)$$

where $\mathbf{E}_0(\mathbf{r}_T,t)$ is the spatiotemporal envelope of the pulsed beam. The angular spectrum of the electric field at the image plane is given by the forward, three-dimensional, spatial spatiotemporal Fourier-Laplace transform (compare Ref. 9, §5.1 and Ref. 10, Chap. 4):

$$\tilde{\mathbf{E}}_0(\mathbf{k}_T,\omega) \equiv \tilde{\mathbf{E}}(\mathbf{k}_T,z_0,\omega)$$

$$= \iiint_{-\infty}^{\infty} \mathbf{E}_0(\mathbf{r}_T,t)e^{i\omega t}e^{-i\mathbf{k}_T\cdot\mathbf{r}_T}\,dt\,dx\,dy. \qquad (5)$$

The wave vector and transverse wave vector are defined, respectively, as

$$\mathbf{k} \equiv k_x \hat{\mathbf{x}} + k_y \hat{\mathbf{y}} + k_z \hat{\mathbf{z}} \tag{6}$$

and

$$\mathbf{k}_T \equiv k_x \hat{\mathbf{x}} + k_y \hat{\mathbf{y}} , \tag{7}$$

where the transverse wave numbers or spatial frequencies k_x and k_y are real-valued and the longitudinal wave number k_z is given by the principle root of the expression

$$k_z \equiv \sqrt{k_0^2 n^2 - k_T^2} , \tag{8}$$

and $k_T^2 \equiv k_x^2 + k_y^2$. The quantity $k_0 \equiv 2\pi/\lambda = \omega'/c$ is the vacuum wave number, ω' is the angular frequency of the electromagnetic disturbance that is centered about the carrier ω_c,

$$\omega' \equiv \omega_c + \omega, \tag{9}$$

and $c \equiv 1/\sqrt{\mu_0 \varepsilon_0}$ is the vacuum speed of light.

Free-space propagation of the electric field of the pulsed laser beam along the beam axis in any source-free and homogenous region of dielectric is given exactly by the angular spectrum representation (compare Ref. 9, §5.1)

$$\mathbf{E}(\mathbf{r}_T, z, t)$$
$$= \frac{1}{(2\pi)^3} \int\int\int_{-\infty}^{\infty} \tilde{\mathbf{E}}_0(\mathbf{k}_T, \omega) e^{i\Delta z k_z} e^{-i\omega t} e^{i\mathbf{k}_T \cdot \mathbf{r}_T} d\omega dk_x dk_y , \tag{10}$$

where $\Delta z \equiv z - z_0$. The expression given in Eq. (10) is an exact solution to Maxwell's equations in an isotropic, source-free dielectric medium. Any inaccuracies associated with this method amount to assumptions made about the field behavior $\mathbf{E}_0(\mathbf{r}_T, t)$ on the initial plane $z = z_0$ (such as assuming scalar fields or Fresnel-Kirchoff boundary conditions) or when approximating the integrals as summations when performing numerical simulations. When $k_T^2 \leq k_0^2 n^2$, the longitudinal wave number k_z is real-valued and the integrand of Eq. (10) represents homogenous plane waves with spectral amplitudes or angular spectra $\tilde{\mathbf{E}}_0(\mathbf{k}_T, \omega)$ whose phase fronts propagate in the direction given by the wave vector $\mathbf{k} \equiv k_x \hat{\mathbf{x}} + k_y \hat{\mathbf{y}} + k_z \hat{\mathbf{z}}$. Thus, the angular spectrum representation decomposes an arbitrary pulsed laser beam into a continuous sum of homogeneous plane waves that propagate in a unique direction and

with an angular frequency ω'. The expression in Eq. (10) represents the general case of vectors and is certainly valid for each individual vector component; therefore it is applicable to the scalar diffraction problems presented in this article.

A useful measure that marks the boundary between the near field and far field for diffraction problems is the Rayleigh range given by (Ref. 11, p. 714)

$$z_R \equiv \frac{A}{\lambda_c} , \tag{11}$$

where A is the area of the beam (see Table 78.II for typical numbers on OMEGA). Another useful parameter is the Fresnel number given by

$$N \equiv \frac{a^2}{\lambda_c \Delta z} , \tag{12}$$

which measures the number of Fresnel zones contained within an aperture of width or diameter $2a$. For full-aperture illumination, the Fresnel number will determine the number of strong ripples apparent in the near-field diffraction pattern. However, a beam with a supergaussian profile or other rounded square shapes such as a hyperbolic-tangent will not exhibit these strong ripples (Ref. 11, p. 739). For this reason, the simulations presented here utilize these shapes to reduce the edge diffraction ripples in order to emphasize other diffraction effects. Waasese is based on the angular spectrum representation and is therefore inherently capable of modeling any beam shape or temporal profile.

Elements of the SSD Operation

The two basic elements of the SSD operation in terms of the angular spectrum representation—gratings and EO phase modulators—are presented as transfer functions in both real and frequency space to describe the complex 2-D SSD system as a set of interchangeable operations. This method also develops a sense of the resultant frequency-domain effects of each operation and its relation to the real space.

1. The Grating Equation

The grating equation relates an incident harmonic plane wave to a transmitted (or reflected) harmonic plane wave that is given by[12]

$$\sin(\theta_i) + \sin(\theta_t) = -m\frac{\lambda}{d} , \tag{13}$$

Table 78.II: The Rayleigh range Δz_R, the color-separation distance Δz_{crit}, and their ratio $\Delta z_{crit}/\Delta z_R$ for various beam diameters and two values of applied bandwidth for a dispersion of $d\theta_t/d\lambda = 197~\mu rad/\text{Å}$ and grating beam diameter $D_{grating} = 44$ mm.

	Diameter (cm)								
	0.11	0.22	0.55	1.938	4.4	8.488	14.63	19.52	27.33
Δz_R (m)	0.902	3.608	22.55	280	1443	5371	15956	28405	55683
Δz_{crit} (m), 1.5 Å	0.186	0.745	4.653	57.77	297.8	1108.2	3292.4	5861.1	11489
$\Delta z_{crit}/\Delta z_R$	0.206	0.206	0.206	0.206	0.206	0.206	0.206	0.206	0.206
Δz_{crit} (m), 3.0 Å	0.093	0.372	2.327	28.89	148.9	554.12	1646.2	2930.6	5744.7
$\Delta z_{crit}/\Delta z_R$	0.103	0.103	0.103	0.103	0.103	0.103	0.103	0.103	0.103

where θ_i and θ_t are the incident and transmitted angles relative to the grating normal, m is the order of the grating, d is the groove spacing, $\lambda \equiv 2\pi c/\omega'$ is the wavelength, and $\omega' \equiv \omega_c + \omega$ is the angular frequency that is centered about the carrier ω_c. The gratings in the SSD driver lines at LLE are used in transmission mode with an order $m = -1$ (see Fig. 78.6). Solving Eq. (13) for θ_t with an order $m = -1$ yields

Grating

θ_t

y_t

$\mathbf{k}_t$

z

θ_i

Transmitted coordinate system

$\mathbf{k}_i$

z

Incident coordinate system

y_i

TC4941

Figure 78.6
The coordinate systems for the incident and transmitted pulsed beams that traverse a grating in transmission mode of order $m = -1$. Notice that the beam axis (z) remains unaltered as a result of the grating operation; indicating the rotation from the incident to the transmitted coordinate system as the beam axis follows the course of the real beam.

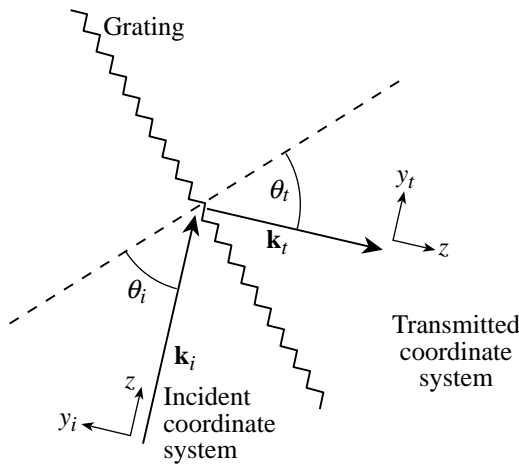$$\theta_t = \sin^{-1}\left[\frac{\lambda}{d} - \sin(\theta_i)\right]. \qquad (14)$$

Taking the derivative of Eq. (14) with respect to λ yields the grating dispersion

$$\frac{d\theta_t}{d\lambda} = \frac{1}{d\sqrt{1 - \left[\frac{\lambda}{d} - \sin(\theta_i)\right]^2}}. \qquad (15)$$

For the SSD laser systems at LLE, the gratings are typically in a Littrow mount, which is defined to be when the angles of the incident and transmitted plane waves are equal for a particular design wavelength, i.e., $\theta_{Litt} \equiv \theta_i = \theta_t$. Under this condition, an incident pulsed beam will retain its incident beam diameter and is described by

$$\sin(\theta_{Litt}) = \frac{\lambda_c}{2d}, \qquad (16)$$

where $\lambda_c = 2\pi c/\omega_c$ is the central or design wavelength. Typically, the design parameters for a grating are the central wavelength λ_c and a desired amount of dispersion $d\theta_t/d\lambda$ while assuming a Littrow mount, which then determines the grating groove spacing d by substituting Eq. (16) into Eq. (15). Once a grating design is realized, an operating point has been determined on the $d\theta_t/d\lambda$ curve, which can be seen in the example illustrated in Fig. 78.7. When the bandwidth $\Delta\lambda$ that is induced by the SSD system is small enough, then the slope

Figure 78.7
The design points on (a) the grating equation θ_t and (b) the grating dispersion equation $d\theta_t/d\lambda$ for $\lambda_c = 1053$ nm, $\theta_{\text{Litt}} = 46°$, and $d = 0.732$ μm/groove.

$d\theta_t/d\lambda$ is nearly constant over that bandwidth; however, since Eq. (15) is inherently nonlinear, beam distortion becomes more significant as the bandwidth increases.

Consider an incident modulated pulsed laser beam with an angular carrier frequency of ω_c, pulse duration τ, and diameter D impinging upon a grating that disperses along the $\hat{\mathbf{y}}$ direction. Define the incident beam axis (z) to make an angle Θ_i with regard to the grating normal in the y-z plane. Then define a transmitted-beam axis that makes an angle Θ_t with regard to the grating normal. (This situation is illustrated in Fig. 78.6.) By decomposing the incident pulsed laser beam into its angular spectrum, the grating equation (14) may be used to accurately describe the action of the grating in the spatiotemporal frequency space. The grating acts as an angular transformation operation that redirects or maps each incident plane wave (completely described by the parameters k_x, k_y, and ω) onto the transmitted-beam axis. Notice that the image plane will be rotated onto the transmitted-beam axis as indicated in

Fig. 78.6. Only the wave number in the $\hat{\mathbf{y}}$ direction is altered during this transformation, and, in general, the new transverse wave number is a function of both the transverse wave number and the angular frequency, i.e., $k_{y_g}(k_y, \omega)$. The transformation operation $k_{y_g}(k_y, \omega)$ is referred to as the grating angular dispersion, which acts along the $\hat{\mathbf{y}}$ direction as denoted by the subscript y. The grating angular dispersion may be expressed as [compare Eq. (14)]

$$k_{y_g}(k_y, \omega)$$
$$= k_0 n \sin\left\{\Theta_t - \sin^{-1}\left[\frac{\lambda}{d} - \sin\left(\Theta_i + \sin^{-1}\left\{\frac{k_y}{k_0 n}\right\}\right)\right]\right\}, \quad (17)$$

where $k_0 \equiv \omega'/c$, $\lambda \equiv 2\pi c/\omega'$, and $\omega' \equiv \omega_c + \omega$. The electric field of the transmitted pulsed laser beam is expressed, in general, by

$$E_g(\mathbf{r}_T, t) = \frac{1}{(2\pi)^3} \iiint\limits_{-\infty}^{\infty} \tilde{E}_g(\mathbf{k}_T, \omega) e^{-i\omega t} e^{i\mathbf{k}_T \cdot \mathbf{r}_T} d\omega dk_x dk_y \quad (18)$$

with the associated distorted angular spectrum given by

$$\tilde{E}_g(k_T, \omega) = \tilde{E}_0\left(k_x, k_{y_g}, \omega\right). \quad (19)$$

The action of the grating may be interpreted as a nonlinear mapping of the angular spectrum onto a new spectral grid, which is nonuniform in general. Consequently, in general, Eq. (18) is not suitable for fast Fourier transform (FFT) algorithms, and a proper treatment requires a slow Fourier transform operation to regrid the data. Under certain approximations, however, Eq. (18) is suitable for FFT algorithms, which are then used to regrid the angular spectrum back onto the original grid: first, assuming that the angular dispersion is a linear function of the transverse wave number k_y and, second, assuming an additional linear dependence of the temporal frequency ω. Waasese can be configured to run in any of these three modes to calculate the grating effects where a tradeoff of speed versus accuracy must be made.

The first assumption may be expressed as a first-order Taylor series expansion about the transverse wave number k_y:

$$k_{y_g}(k_y, \omega) = k_{y_g}(k_y, \omega)\big|_{k_y=0} + k_y \frac{\partial}{\partial k_y} k_{y_g}(k_y, \omega)\big|_{k_y=0}. \quad (20)$$

TC5015

The partial derivative in Eq. (20) is given by

$$
\frac{\partial}{\partial k_y} k_{y_g}\left(k_y, \omega\right)
$$

$$
= \frac{\cos\left\{\Theta_t - \sin^{-1}\left[\dfrac{\lambda}{d} - \sin\left(\Theta_i + \sin^{-1}\left\{\dfrac{k_y}{k_0 n}\right\}\right)\right]\right\}}{\sqrt{1 - \left[\dfrac{\lambda}{d} - \sin\left(\Theta_i + \sin^{-1}\left\{\dfrac{k_y}{k_0 n}\right\}\right)\right]^2}}
$$

$$
\times \frac{\cos\left(\Theta_i + \sin^{-1}\left\{\dfrac{k_y}{k_0 n}\right\}\right)}{\sqrt{1 - \left[\dfrac{k_y}{k_0 n}\right]^2}} \ . \tag{21}
$$

If the grating is in the Littrow mount and is tuned to the center frequency ω_c, then evaluating the partial derivative at $k_y = 0$ yields

$$
k_{y_g}\left(k_y, \omega\right)\Big|_{k_y=0} = k_0 n \sin\left\{\Theta_t - \sin^{-1}\left[\frac{\lambda}{d} - \sin(\Theta_i)\right]\right\} , \tag{22}
$$

and while assuming that $\omega' \cong \omega_c$,

$$
\frac{\partial}{\partial k_y} k_{y_g}\left(k_y, \omega\right)\Big|_{k_y=0} \cong 1. \tag{23}
$$

Substituting Eqs. (22) and (23) into Eq. (20) gives

$$
k_{y_g}\left(k_y, \omega\right) = \hat{k}_{y_g} + k_y \ , \tag{24}
$$

where $\hat{k}_{y_g}(\omega) \equiv k_{y_g}(0, \omega)$. A change of variables defined by Eq. (24) yields [compare Eq. (18)]

$$
E_g(\mathbf{r}_T, t) = \frac{1}{(2\pi)^3} \iiint_{-\infty}^{\infty} \left\{ \tilde{E}_0\left(k_x, k_{y_g}, \omega\right) \right.
$$

$$
\left. \times e^{-i\omega t} e^{i\left[k_x x + k_{y_g} y - \hat{k}_{y_g}(\omega) y\right]} \right\} d\omega \, dk_x \, dk_{y_g}. \tag{25}
$$

Since $\hat{k}_{y_g}$ is only a function of the temporal angular frequency ω, the inverse 2-D spatial Fourier transform operation yields

$$
E_g(\mathbf{r}_T, t) = \frac{1}{2\pi} \int_{-\infty}^{\infty} \tilde{E}_0(\mathbf{r}_T, \omega) e^{-i\omega t} e^{-i\hat{k}_{y_g}(\omega) y} d\omega , \tag{26}
$$

where

$$
\tilde{E}_0(\mathbf{r}_T, \omega) = \frac{1}{(2\pi)^2} \iint_{-\infty}^{\infty} \tilde{E}_0(\mathbf{k}_t, \omega) e^{i\mathbf{k}_T \cdot \mathbf{r}_T} dk_x dk_y . \tag{27}
$$

The distorted angular spectrum is then given by

$$
\tilde{E}_g(\mathbf{k}_T, \omega) = \iint_{-\infty}^{\infty} \tilde{E}_0(\mathbf{r}_T, \omega) e^{i\hat{k}_{y_g}(\omega) y} e^{-i\mathbf{k}_T \cdot \mathbf{r}_T} dx \, dy
$$

$$
= \int_{-\infty}^{\infty} \tilde{E}_0(k_x, y, \omega) e^{-i\hat{k}_{y_g}(\omega) y - i k_y y} dy. \tag{28}
$$

The utility of Eq. (28) lies in the ability to regrid the angular spectrum using conventional FFT algorithms. Waasese applies three operations to the initial angular spectrum $\tilde{E}_0(\mathbf{k}_T, \omega)$ to regrid the distorted angular spectrum $\tilde{E}_g(\mathbf{k}_T, \omega)$ onto the original numerical grid: inverse spatially transform the k_y dimension, apply the distortion term

$$
e^{-i\hat{k}_{y_g}(\omega) y},
$$

and, finally, forward spatially transform the y dimension.

The second assumption may be expressed as a bivariate, first-order Taylor series expansion:

$$
k_{y_g}\left(k_y, \omega\right) = k_{y_g}\left(k_y, \omega\right)\Big|_{k_y=0, \omega=0}
$$

$$
+ k_y \frac{\partial}{\partial k_y} k_{y_g}\left(k_y, \omega\right)\Big|_{k_y=0, \omega=0}
$$

$$
+ \omega \frac{\partial}{\partial \omega} k_{y_g}\left(k_y, \omega\right)\Big|_{k_y=0, \omega=0}, \tag{29}
$$

where $\omega' \equiv \omega_c + \omega$. The partial derivative with regard to ω in Eq. (29) is given by

$$
\frac{\partial}{\partial \omega} k_{y_g}(k_y, \omega)
$$

$$
= \frac{1}{c} \sin\left\{\Theta_t - \sin^{-1}\left[\frac{\lambda}{d} - \sin\left(\Theta_i + \sin^{-1}\left\{\frac{k_y}{k_0 n}\right\}\right)\right]\right\}
$$

$$
+ k_0 n \frac{\cos\left\{\Theta_t - \sin^{-1}\left[\frac{\lambda}{d} - \sin\left(\Theta_i + \sin^{-1}\left\{\frac{k_y}{k_0 n}\right\}\right)\right]\right\}}{\sqrt{1 - \left[\frac{\lambda}{d} - \sin\left(\Theta_i + \sin^{-1}\left\{\frac{k_y}{k_0 n}\right\}\right)\right]^2}}
$$

$$
\times \left[\frac{\lambda}{\omega' d} - \frac{\cos\left(\Theta_i + \sin^{-1}\left\{\frac{k_y}{k_0 n}\right\}\right)}{\sqrt{1 - \left[\frac{k_y}{k_0 n}\right]^2}} - \frac{k_y}{k_0 \omega'}\right]. \quad (30)
$$

If the grating is in a Littrow mount tuned to the center frequency ω_c, then

$$
k_{y_g}(k_y, \omega)\Big|_{k_y = 0, \omega = 0} = 0, \quad (31)
$$

$$
\frac{\partial}{\partial k_y} k_{y_g}(k_y, \omega)\Big|_{k_y = 0, \omega = 0} = 1, \quad (32)
$$

and

$$
\frac{\partial}{\partial \omega} k_{y_g}(k_y, \omega)\Big|_{k_y = 0, \omega = 0} = \frac{1}{d\sqrt{1 - \left[\frac{\lambda_c}{d} - \sin(\Theta_i)\right]^2}} \frac{\lambda_c}{c}. \quad (33)
$$

Equation (29) can then be written as

$$
k_{y_g}(k_y, \omega) = k_y + \xi_g \omega \quad (34)
$$

and is known as the linearized grating angular dispersion, where Eq. (15) has been used in the definition

$$
\xi_g \equiv \frac{\lambda_c}{c} \frac{d\theta_t}{d\lambda}\Big|_{\omega = 0, \theta_i = \Theta_i}.
$$

The transmitted pulsed laser beam then becomes a temporally skewed or sheared version of the incident pulsed beam:

$$
E_g(\mathbf{r}_T, t) = \frac{1}{2\pi} \int_{-\infty}^{\infty} \tilde{E}_0(\mathbf{r}_T, \omega) e^{-i\omega(t - \xi_g y)} d\omega
$$

$$
= E_0(\mathbf{r}_T, t - \xi_g y), \quad (35)
$$

where a temporal delay is imposed across the beam by an amount defined by

$$
\tau_D = \xi_g D. \quad (36)
$$

The angular spectrum is also sheared and is given by

$$
\tilde{E}_g(\mathbf{k}_T, \omega) = \tilde{E}_0(k_x, k_y + \xi_g \omega, \omega). \quad (37)
$$

During numerical simulations, Waasese regrids the initial angular spectrum $\tilde{E}_0(\mathbf{k}_T, \omega)$ using the technique described in association with Eq. (28).

2. The EO Phase Modulator

A strong microwave or radio frequency (RF) field inside a cavity resonator can modulate the optical refractive index of a nonlinear crystal such as lithium niobate (LiNbO$_3$).[13] The ideal EO phase modulator operates only in the time domain by applying the sinusoidal time-varying phase function $e^{i\delta_M \sin(\omega_M t)}$ to the optical electric field as

$$
E_M(\mathbf{r}_T, t) = E_0(\mathbf{r}_T, t) e^{i\delta_M \sin(\omega_M t)}, \quad (38)
$$

where δ_M is the modulation depth and $\upsilon_M \equiv \omega_M / 2\pi$ is the RF modulation frequency. This modulation scheme is referred to as pure-tone phase modulation that is a specific type of a general class known as exponential or angle modulation and is inherently a nonlinear process. In general, the bandwidth applied by phase modulation has infinite extent, and discarding any portion will result in distortion and a degradation of signal fidelity, e.g., AM. Practically, the significant bandwidth applied by phase modulation is concentrated in a finite spectral region, which is a function of the modulation depth δ_M. The question then becomes How much bandwidth is required to retain adequate signal integrity? (See Carlson Ref. 14, pp. 239–245 for an in-depth discussion.)

The applied bandwidth is estimated by Carson's rule:

$$\Delta \upsilon = \frac{\Delta \omega}{2\pi} \approx 2(\delta_M + 1)\upsilon_M \;, \tag{39}$$

which appropriately goes to the limiting cases.

$$\Delta \upsilon = \begin{cases} 2\delta_M \upsilon_M & \delta_M \gg 1 \\ 2\upsilon_M & \delta_M \ll 1 \end{cases}; \tag{40}$$

however, Carson's rule underestimates the bandwidth for the range $2 < \delta_M < 10$. The bandwidth is more accurately estimated by

$$\Delta \upsilon \approx 2(\delta_M + 2)\upsilon_M \tag{41}$$

for modulation depths $\delta_M > 2$. The applied bandwidth may also be expressed in terms of the wavelength as

$$\Delta \lambda = 2\left(\lambda_c - \frac{c}{\dfrac{c}{\lambda_c} - \dfrac{\Delta \upsilon}{2}} \right) \cong \frac{\Delta \upsilon \lambda_c^2}{c} \;, \tag{42}$$

where any estimate for $\Delta \upsilon$ can be applied. Typically, the estimate for the bandwidth given by $2\delta_M \upsilon_M$ is quoted in the literature on SSD applications (even for modulation depths $\delta_M < 10$). This convention will be followed in this article for consistency not accuracy.

Equation (38) can be written as an equivalent series expansion given by (compare Ref. 14, p. 228)

$$E_M(\mathbf{r}_T, t) = E_0(\mathbf{r}_T, t) \sum_{l=-\infty}^{\infty} J_l(\delta_M) e^{il\omega_M t}. \tag{43}$$

The spatiotemporal Fourier-Laplace transform of Eq. (43) yields the replicated angular spectrum

$$\tilde{E}_M(k_T, \omega) = \tilde{E}_0(k_T, \omega) * \sum_{l=-\infty}^{\infty} J_l(\delta_M)\delta(\omega - l\omega_M) \;. \tag{44}$$

The original angular spectrum $\tilde{E}(k_T, \omega)$ is replicated with a spacing of ω_M and amplitudes determined by the Bessel functions of the first kind $J_l(\delta_M)$ by virtue of the convolution process denoted in Eq. (44) by the symbol $*$. If the original bandwidth is not small compared to the modulation frequency, some overlap will exist from one band to the next. As long as

the overlap is small, which is generally the case for well-defined systems, the spectral peaks will be well defined. Even if overlap does occur, it does not affect the validity of the linear superposition implied by Eq. (44). Figure 78.8(a) illustrates a spectrum obtained for a 1-ns pulse using the parameters $\delta_M = 6.15$ and $\upsilon_M = 3.3$ GHz.

Like any form of exponential modulation, pure-tone phase modulation possesses the unique property of constant amplitude. Maintaining a constant amplitude with a sinusoidal phase variation is best understood using a phasor interpretation where phasors for the carrier plus every sideband are vector-summed in phasor space as illustrated in Fig. 78.9. The resultant phasor sinusoidally sweeps back and forth (by an amount determined by the modulation depth δ_M) in phasor space while maintaining constant amplitude. All of the odd-order sideband pairs are in phase quadrature (due to the fact that the components of an odd-order pair have equal magnitude with opposite sign, i.e., $J_{-1}(\delta_M) = (-1)^l J_l(\delta_M)$ [see Ref. 15, p. 258, Eq. (9.1.5)], and all of the even-order sideband pairs
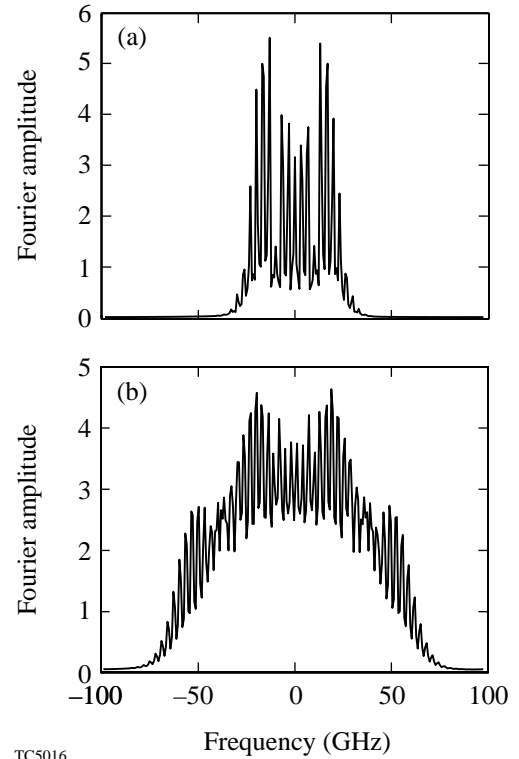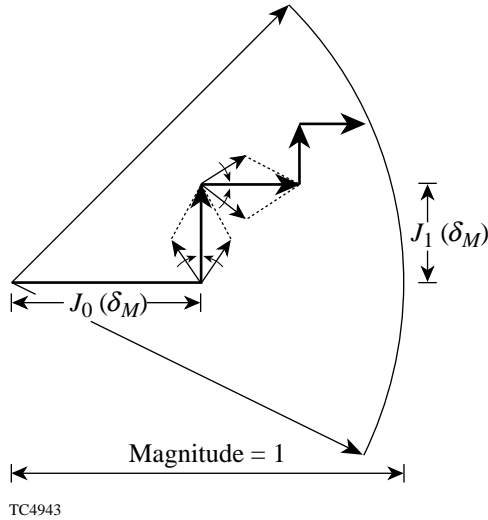

Figure 78.8
The temporal spectrum for (a) a pure-tone and (b) a two-tone phase-modulated optical pulse. The pulse duration is $\tau = 1$ ns and the parameters are $\delta_{M1} = 6.15$, $\upsilon_{M1} = 3.3$ GHz, $\Delta \lambda_{M1} = 1.5$ Å, $\delta_{M2} = 13.5$, $\upsilon_{M2} = 3.0$ GHz, and $\Delta \lambda_{M2} = 3.0$ Å.

are collinear with regard to the carrier. The odd-order pairs contribute to the desired sinusoidal phase modulation plus unwanted amplitude modulation. The even-order pairs compensate for the unwanted amplitude modulation imposed by the odd-order pairs (see pp. 230–233 of Ref. 14 for a complete

TC4943

Figure 78.9

Phasor diagram of pure-tone phase modulation that depicts the phasor pairs for a small modulation depth. The diagram depicts how the even-order pairs compensate for the unwanted amplitude modulation imparted by the odd-order pairs. (Adapted from Ref. 14, p. 232, Fig. 6.7.)

discussion). The constant amplitude inherent in phase modulation relies on the delicate balance of the amplitudes and phases of its spectral components. Any deviation in this balance results in distortion that can exhibit itself as AM.

Ideal 2-D SSD Generation

Here we describe the step-by-step process that Waasese uses to generate 2-D SSD. Ideal 2-D SSD is produced when the transfer functions given by Eqs. (37) and (44) are used. Analytical expressions are also developed and are shown to be equivalent to a generalization of Ref. 3, which includes beam shape. Ideal 2-D SSD is generated by a series of two ideal 1-D SSD operations performed on the two orthogonal transverse spatial directions of a seed-pulsed laser beam. Each 1-D SSD operation consists of an EO phase modulator sandwiched between a grating pair, such that an image plane exists at each grating plane. The angular spectrum representation of the grating and EO modulator, developed in the previous section, is drawn upon to illustrate the frequency-domain effects and how they relate to real space.

1. 1-D SSD Operation

Since each of the gratings is assumed to be at an image plane, this implies that some kind of image-relaying system must be in place. For practical SSD systems, these are afocal image relay telescopes with slow lenses that do not contribute significant aberrations. Figure 78.10 depicts the 1-D SSD
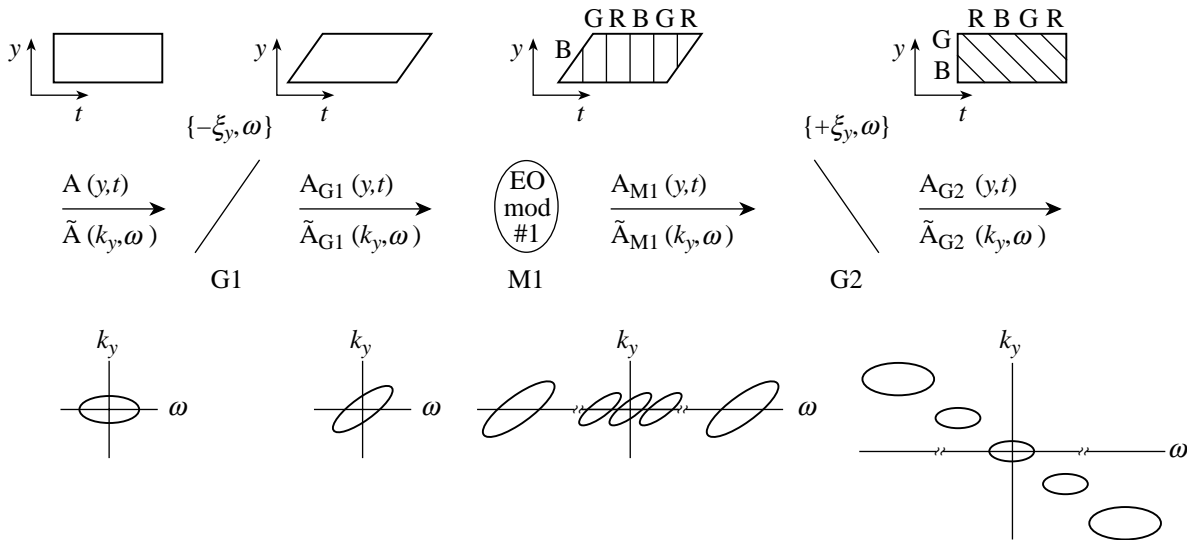
TC4944

Figure 78.10

A schematic representation of the 1-D SSD operation showing the two important functions: gratings and EO phase modulator. In addition, the image planes are indicated along with the function names and a rough sketch of the field shape, in both real and frequency space, after each operation.

operation with the three major components, including the field names at certain locations. If the bandwidth $\Delta\lambda$ (typically 1 Å $< \Delta\lambda < 12$ Å) introduced by the SSD system is small relative to the operating wavelength λ_c (for OMEGA the IR wavelength is 1053 nm), then the linearized grating angular dispersion Eq. (34) is an adequate representation of the grating and serves this section by demonstrating the ideal or desired response of an SSD system.

Consider a seed-modulated pulsed laser beam with an angular carrier frequency of ω_c, pulse duration τ, and diameters D_y and D_x. The electric field is defined on an image plane as $E_0(\mathbf{r}_T, t)$ with the associated angular spectrum $\tilde{E}_0(\mathbf{k}_T, \omega)$ and is image relayed onto the input of grating G1. Let the first grating G1 preshear the pulsed beam with a linearized angular dispersion of $-\xi_y$ along the $\hat{\mathbf{y}}$ direction. Consequently, the sheared field after the grating G1 is given by [compare Eq. (35)]

$$E_{G1}(\mathbf{r}_T, t) = E_0(\mathbf{r}_T, t + \xi_y y),\qquad (45)$$

where a temporal delay is imposed across the field by an amount given by $\tau_{D_y} = \xi_y D_y$. The angular spectrum is also sheared and is given by [compare Eq. (37)]

$$\tilde{E}_{G1}(\mathbf{k}_T, \omega) = \tilde{E}_0(k_x, k_y - \xi_y\omega, \omega),\qquad (46)$$

where the angular spectrum has been distorted only in the direction parallel to the k_y axis by the quantity $\xi_y\omega$. A representation of the sheared field and angular spectrum is illustrated in Fig. 78.10. Let the EO phase modulator have a modulation depth of δ_{M1} and a RF modulation frequency of $\upsilon_{M1} = \omega_{M1}/2\pi$. By combining the results from Eqs. (43) and (45), the electric field becomes

$$E_{M1}(\mathbf{r}_T, t) = E_{G1}(\mathbf{r}_T, t) e^{i\delta_{M1}\sin(\omega_{M1}t)}$$

$$= E_{G1}(\mathbf{r}_T, t)\sum_{l=-\infty}^{\infty} J_l(\delta_{M1}) e^{il\omega_{M1}t}\qquad (47)$$

and the replicated-sheared angular spectrum is given by

$$\tilde{E}_{M1}(\mathbf{k}_T, \omega) = \tilde{E}_{G1}(\mathbf{k}_T, \omega) * \sum_{l=-\infty}^{\infty} J_l(\delta_{M1})\delta(\omega - l\omega_{M1}).\qquad (48)$$

A representation of the phase-modulated sheared field and angular spectrum is illustrated in Fig. 78.10. The second grating G2 now acts to disperse the increased bandwidth and remove the preshear from the first grating G1. Let the linearized angular dispersion be of equal magnitude and in the same direction as the first grating but with opposite sign, i.e., $+\xi_y$ (this is realized through the image flip of an odd number of image relays), so that the electric field becomes

$$E_{G2}(\mathbf{r}_T, t) = E_{M1}(\mathbf{r}_T, t - \xi_y y),\qquad (49)$$

and the unsheared angular spectrum is given by

$$\tilde{E}_{G2}(\mathbf{k}_T, \omega) = \tilde{E}_{M1}(k_x, k_y + \xi_y\omega, \omega).\qquad (50)$$

After substituting the results of Eqs. (45)–(47)

$$E_{G2}(\mathbf{r}_T, t) = E_{G1}(\mathbf{r}_T, t - \xi_y y) e^{i\delta_{M1}\sin[\omega_{M1}(t + \xi_y y)]}$$

$$= E_0(\mathbf{r}_T, t) e^{i\delta_{M1}\sin[\omega_{M1}(t + \xi_y y)]}$$

$$= E_0(\mathbf{r}_T, t)\sum_{l=-\infty}^{\infty} J_l(\delta_{M1}) e^{il\omega_{M1}(t + \xi_y y)}.\qquad (51)$$

The angular spectrum of the 1-D SSD operation is then given by the spatiotemporal Fourier-Laplace transform of Eq. (51):

$$\tilde{E}_{G2}(\mathbf{k}_T, \omega) = \tilde{E}_0(\mathbf{k}_T, \omega)$$

$$* \sum_{l=-\infty}^{\infty} J_l(\delta_{M1})\delta(k_x, k_y - l\xi_y\omega_{M1}, \omega + l\omega_{M1}),\qquad (52)$$

where it is important to notice that exact replicas of the original spectrum, modified only by the amplitude of the Bessel functions of the first kind $J_l(\delta_{M1})$, are centered on a regularly spaced line or comb of delta functions described by the summation operation. The comb of delta functions lies along the line $k_y = \xi_y\omega$ on the $k_y - \omega$ plane of the 3-D spatiotemporal spectrum and are spaced by $\xi_y\omega_{M1}$ on the k_y axis and ω_{M1} on the ω axis. A representation of the final field and angular spectrum is illustrated in Fig. 78.10. Each replica of the original angular spectrum in Eq. (52) can be interpreted as an individual colored-pulsed beam with an associated wavelength or color $\lambda \equiv 2\pi c/\omega'$, where $\omega' = \omega_c + l\omega_{M1}$, whose phase front advances in the direction $\mathbf{k} \equiv k_x\hat{\mathbf{x}} + (k_y - l\xi_y\omega_{M1})\hat{\mathbf{y}} + k_z\hat{\mathbf{z}}$.

It is important to notice that, for propagation distances Δz $\ll z_R$ (such that minimal edge diffraction takes place for rounded square beams), the individual colored-pulsed beams retain their shape and continue to propagate along the beam axis and only the phase fronts break across the beam in a different direction. The individual colored beams will eventually separate since the energy flows along the direction **k**. The distance that colored-pulsed beam shifts in the transverse direction is given approximately by

$$\Delta y_l = \Delta z \tan\left(\Delta\theta_l\right), \tag{53}$$

where

$$\Delta\theta_l = \xi_g \frac{c}{\lambda_c} \Delta\lambda_l \frac{D_{\text{grating}}}{D}, \tag{54}$$

$\Delta\lambda_l \cong \left(\lambda_c^2/c\right) l\nu_{\text{M1}}$ is the spectral offset of a particular color, and D_{grating} is the beam diameter at the grating. The critical propagation distance for color separation is defined as when the outermost colored-pulsed beam has shifted by one beam diameter, i.e., $\Delta y = D_y$, and is approximated by

$$\Delta z_{\text{crit}} = \frac{D_y}{\tan(\Delta\theta)} \cong \frac{D_y}{\Delta\theta} = \frac{2}{\xi_g} \frac{\lambda_c}{c\Delta\lambda} \frac{D_y^2}{D_{\text{grating}}}, \tag{55}$$

where $\Delta\lambda$ is the applied bandwidth given by Eq. (42). The data in Table 78.II represents Δz_R, Δz_{crit}, and $\Delta z_{\text{crit}}/\Delta z_R$ for various OMEGA beam diameters for the system parameters: $d\theta_t/d\lambda|_{\omega=0} = 197\ \mu\text{rad/Å}$, $\Delta\lambda_{\text{M1}} = 1.5$ Å, 3.0 Å, and D_{grating} = 44 mm.

The electric field of a pulsed beam is a complex three-dimensional object whose intensity distribution, in space, is suitably described as a *brick of light* that moves along the propagation axis at the group velocity of the pulse. At one position of the propagation axis, the intensity of the brick of light is distributed about the transverse spatial dimensions as described by the beam profile and in time as described by the pulse shape. Taking different kinds of cross sections or slices of the brick of light is a way to visualize the multidimensioned data. A spatiotemporal cross section illustrates the intensity history of the pulsed beam. As an example, a spatiotemporal slice of a 1-D SSD pulsed laser beam is shown in Fig. 78.11 for two orthogonal directions with the system parameters $\delta_{\text{M1}} = 6.15$, $\nu_{\text{M1}} = 3.3$ GHz, $\Delta\lambda_{\text{M1}} = 1.5$ Å, $\tau = 1$ ns, $D_y = D_x = 44$ mm, and where stepped hyperbolic-tangent profiles were used in the spatial and temporal dimensions. In addition a false-color representation of the instantaneous wavelength is defined by
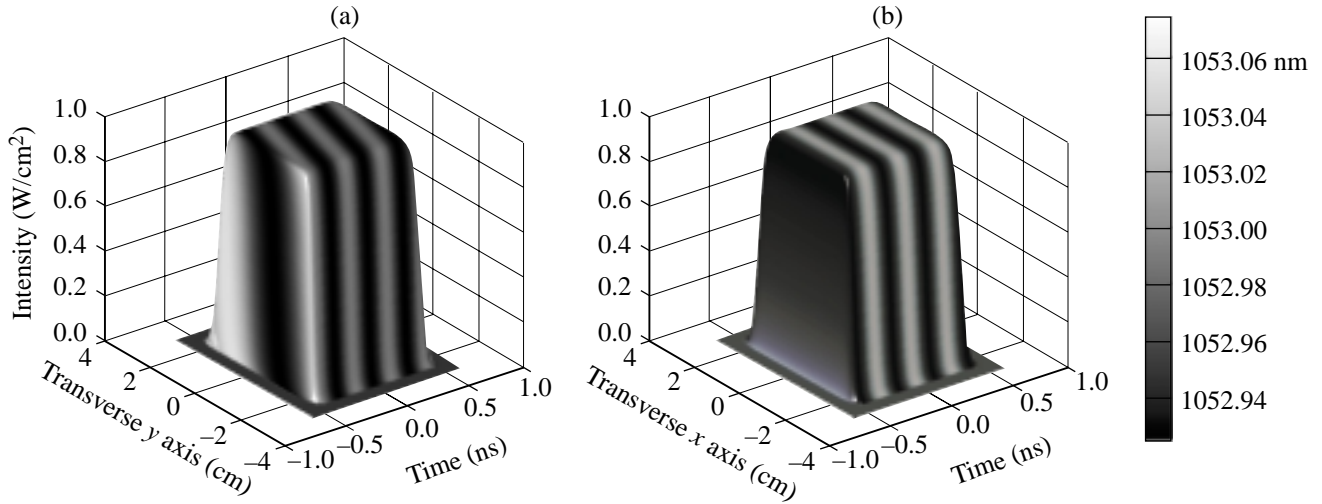
TC5017

Figure 78.11

Spatiotemporal slices along (a) the *y-t* plane and (b) the *x-t* plane of a 1-D SSD pulsed beam with an overlay of the instantaneous wavelength $\hat{\lambda}(\mathbf{r}_T, t)$ superimposed onto the intensity profile for the system parameters $\delta_{\text{M1}} = 6.15$, $\nu_{\text{M1}} = 3.3$ GHz, $\Delta\lambda_{\text{M1}} = 1.5$ Å, $\tau = 1$ ns, $N_{c_y} \cong 1$, $\tau = 1$ ns, $D_y = D_x = 44$ mm, and where hyperbolic-tangent profiles were used in the spatial and temporal dimensions.

$$\hat{\lambda}\left(\mathbf{r}_T, t\right) \equiv \frac{c}{\dfrac{c}{\lambda_c} - \hat{v}} \;, \qquad (56)$$

where the instantaneous frequency is given by

$$\hat{v} \equiv \frac{1}{2\pi} \frac{\partial \varphi}{\partial t} \qquad (57)$$

and φ is the instantaneous phase of the field of the form $e^{i\varphi(y,t)} e^{i\omega_c t}$. The instantaneous wavelength is shown mapped onto the 3-D intensity surface, in effect, displaying the phase information of the electric field as a fourth dimension of data. The resultant dispersed spectrum of the 1-D SSD operation is displayed across the beam as one cycle of instantaneous wavelength or color, i.e., every color is displayed twice as the RF phase modulation cycles through 2π radians. In general, the fraction of RF phase-modulation cycles completed during the temporal shear $\tau_{D_y} = \xi_y D_y$, imposed by the first grating G1, and displayed across the beam as a result of the second grating G2, is determined by the number of color cycles (compare to Ref. 1):

$$N_{c_y} \equiv \tau_{D_y} v_{\text{M1}} \;. \qquad (58)$$

The instantaneous wavelength (or color) is not to be confused with the discrete colored-pulsed beams mentioned in the previous paragraph; the instantaneous wavelength is a continuous function defined in the temporal domain, whereas the other forms a discrete set defined in the temporal frequency domain. The bandwidth of the instantaneous frequency is given by

$$\Delta \hat{v} \equiv 2\delta_{\text{M1}} v_{\text{M1}} \;. \qquad (59)$$

Notice that no approximation is made here as compared to the frequency-domain bandwidth described by Eqs. (39) and (41), and that it equals the bandwidth in the limit of large modulation depths given by Eq. (40). This fact illustrates the important

difference between the instantaneous frequency and that of the frequency domain. When used with care, however, the instantaneous frequency is useful in describing some optical effects (such as etalons) since the modulation rate is slow compared to the underlying optical carrier. Another very important difference is that $\hat{\lambda}\left(\mathbf{r}_T, t\right)$ is a smooth, continuous function, and the frequency-space spectrum is comprised of a discrete set of frequencies (broadened only by the finite duration of the pulse width) as described by Eq. (44).

2. Series of Two 1-D SSD Operations

Consider, in a manner analogous to the previous subsection, a seed-modulated pulsed laser beam with an angular carrier frequency ω_c, pulse duration τ, and diameters D_y and D_x. The electric field is defined on an image plane as $E_0\left(\mathbf{r}_T, t\right)$ with the associated angular spectrum $\tilde{E}_0\left(\mathbf{k}_T, \omega\right)$ and is image relayed onto the input of grating G1. A diagram of the 2-D SSD system is shown in Fig. 78.12. Let the first SSD operation be given by Eqs. (51) and (52). Let the first grating of the second-dimension G3 operation preshear the pulsed beam with a linearized angular dispersion of $-\xi_x$ along the direction $\hat{\mathbf{x}}$. Consequently, the sheared field after the grating G3, in terms of the results from the first dimension Eq. (35), is given by

$$E_{\text{G3}}\left(\mathbf{r}_T, t\right) = E_{\text{G2}}\left(\mathbf{r}_T, t + \xi_x x\right) \;, \qquad (60)$$

where a temporal delay imposed across the field is an amount given by $\tau_{D_y} = \xi_x D_x$. The sheared angular spectrum is given by [compare Eq. (37)]

$$\tilde{E}_{\text{G3}}\left(\mathbf{k}_T, \omega\right) = \tilde{E}_{\text{G2}}\left(k_x - \xi_x \omega, k_y, \omega\right), \qquad (61)$$

where the angular spectrum has been distorted only in the direction parallel to the k_x axis by the quantity δ_{M2}. Let the second EO phase modulator have a modulation depth of δ_{M2} and a RF modulation frequency of $v_{\text{M2}} = \omega_{\text{M2}}/2\pi$. The electric field becomes
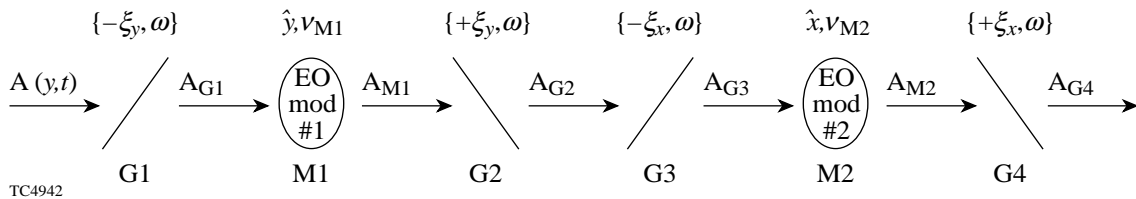

Figure 78.12
A schematic representation of the 2-D SSD operation, which exhibits a series of two 1-D SSD operations that act on two orthogonal directions $\hat{\mathbf{x}}$ and $\hat{\mathbf{y}}$.

$$E_{M2}(\mathbf{r}_T, t) = E_{G3}(\mathbf{r}_T, t) e^{i\delta_{M2}\sin(\omega_{M2}t)}$$

$$= E_{G3}(\mathbf{r}_T, t) \sum_{m=-\infty}^{\infty} J_m(\delta_{M2}) e^{im\omega_{M2}t}, \quad (62)$$

and the replicated-sheared angular spectrum is given by

$$\tilde{E}_{M2}(\mathbf{k}_T, \omega) = \tilde{E}_{G3}(\mathbf{k}_T, \omega)$$

$$* \sum_{m=-\infty}^{\infty} J_m(\delta_{M2}) \delta(\omega - m\omega_{M2}) . \quad (63)$$

The second grating of the second dimension G4 now acts to disperse the increased bandwidth and removes the preshear from the grating G3. Let the linearized angular dispersion be of equal magnitude to the grating G3 but with opposite sign, i.e., $+\xi_x$, so that the electric field becomes

$$E_{G4}(\mathbf{r}_T, t) = E_{M2}(\mathbf{r}_T, t - \xi_x x) \quad (64)$$

and the unsheared angular spectrum is given by

$$\tilde{E}_{G4}(\mathbf{k}_T, \omega) = \tilde{E}_{M2}(k_x + \xi_x \omega, k_y, \omega) . \quad (65)$$

After substituting the results of Eqs. (52), (55), (57), and (60),

$$E_{G4}(\mathbf{r}_T, t) = E_{G3}(\mathbf{r}, t + \xi_x x) e^{i\delta_{M2}\sin[\omega_{M2}(t + \xi_x x)]}$$

$$= E_{G2}(\mathbf{r}_T, t) e^{i\delta_{M2}\sin[\omega_{M2}(t + \xi_x x)]}$$

$$= E_0(\mathbf{r}_T, t) e^{i\delta_{M1}\sin[\omega_{M1}(t + \xi_y y)]} e^{i\delta_{M2}\sin[\omega_{M2}(t + \xi_x x)]}$$

$$= E_0(\mathbf{r}_T, t) \sum_{l=-\infty}^{\infty} J_l(\delta_{M1}) e^{il\omega_{M1}(t + \xi_y y)}$$

$$\times \sum_{m=-\infty}^{\infty} J_m(\delta_{M2}) e^{im\omega_{M2}(t + \xi_x x)} . \quad (66)$$

Equation (66) represents a generalization of Ref. 3, which includes beam shape. The angular spectrum of the 2-D SSD

operation is then given by the spatiotemporal Fourier-Laplace transform of Eq. (66):

$$\tilde{E}_{G4}(\mathbf{k}_T, \omega) = \tilde{E}_0(\mathbf{k}_T, \omega)$$

$$* \sum_{l=-\infty}^{\infty} J_l(\delta_{M1}) \delta(k_x, k_y - l\xi_y \omega_{M1}, \omega + l\omega_{M1})$$

$$* \sum_{m=-\infty}^{\infty} J_m(\delta_{M2}) \delta(k_x - m\xi_x \omega_{M2}, k_y, \omega + m\omega_{M2})$$

$$= \tilde{E}_0(\mathbf{k}_T, \omega) * \sum_{l=-\infty}^{\infty} \sum_{m=-\infty}^{\infty} [J_l(\delta_{M1}) J_m(\delta_{M2})$$

$$\times \delta(k_x - m\xi_x \omega_{M2}, k_y - l\xi_y \omega_{M1}, \omega + l\omega_{M1} + m\omega_{M2})], \quad (67)$$

where it is important to notice that exact replicas of the original spectrum, modified only by the amplitudes of the Bessel functions of the first kind $J_l(\delta_{M1})$ and $J_m(\delta_{M2})$, are centered on a regularly spaced grid or field of delta functions formed by the innermost convolution operation. The field of delta functions lies on the plane $k_x/\xi_x + k_y/\xi_y = \omega$ in the 3-D spatiotemporal spectrum and are spaced by $\xi_y \omega_{M1}$ in the direction of the k_y axis, by $\xi_x \omega_{M2}$ in the direction of the k_x axis, and by linear combinations of both ω_{M1} and ω_{M2} in the direction of the ω axis. Notice that there exist sum and difference frequencies, which is characteristic of two-tone phase modulation (see Ref. 14, pp. 233–234). An example of a two-tone phase-modulated temporal spectrum is illustrated in Fig. 78.8(b) for the parameters $\delta_{M1} = 6.15$, $\nu_{M1} = 3.3$ GHz, $\delta_{M2} = 13.5$, and $\nu_{M2} = 3.0$ GHz.

Spatiotemporal cross sections of a 2-D SSD pulsed laser beam with the instantaneous wavelength overlay is shown in Fig. 78.13 for two orthogonal directions for the system parameters $\delta_{M1} = 6.15$, $\nu_{M1} = 3.3$ GHz, $\Delta\lambda_{M1} = 1.5$ Å, $\delta_{M2} = 13.5$, and $\nu_{M2} = 3.0$ GHz, $\Delta\lambda_{M2} = 3.0$ Å, $\tau = 1$ ns, $D_y = D_x = 44$ mm, and where hyperbolic-tangent profiles were used in the spatial and temporal dimensions. At any particular moment in time, the resultant dispersed spectrum from the first dimension of the 2-D SSD operation is seen displayed across the beam as a smaller window of color (relative to the overall bandwidth). As time progresses, the window of color is swept across the total bandwidth. The number of color cycles of the second SSD dimension is given by

$$N_{c_x} \equiv \tau_{D_x} \nu_{M2} , \quad (68)$$

where $\tau_{D_x} = \xi_x D_x$. The brick of light can also be sliced in another direction, i.e., a spatial cross section at a particular instant of time that illustrates how the instantaneous colors move across the beam profile as time changes. Two examples of the 3-D intensity profile of the beam, as viewed from above, are illustrated in Fig. 78.14 with an instantaneous wavelength overlay. The color center is seen to move across the beam. The number of color cycles in each direction is readily observed.
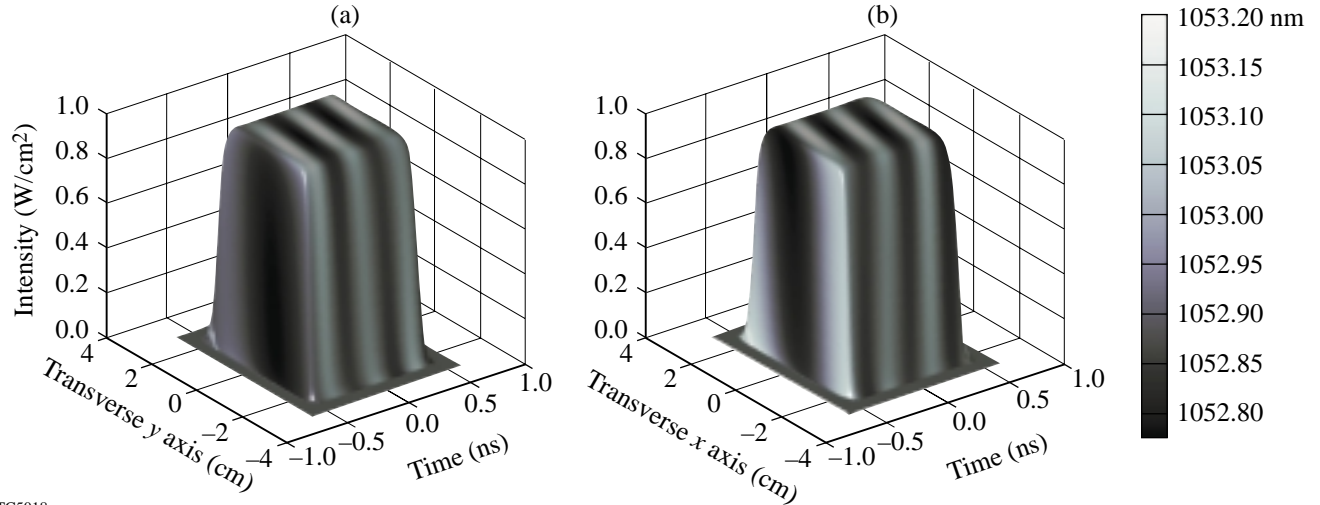
TC5018

Figure 78.13

Spatiotemporal slices along (a) the y-t plane and (b) the x-t plane of a 2-D SSD pulsed beam. with an overlay of the instantaneous wavelength $\hat{\lambda}(\mathbf{r}_T, t)$ superimposed onto the intensity profile for the system parameters: $\delta_{M1} = 6.15$, $\nu_{M1} = 3.3$ GHz, $\Delta\lambda_{M1} = 1.5$ Å, $N_{c_y} \cong 1$, $\delta_{M2} = 13.5$, and $\nu_{M2} = 3.0$ GHz, $\Delta\lambda_{M2} = 3.0$ Å, $N_{c_x} \cong 0.9$, $\tau = 1$ ns, $D_y = D_x = 44$ mm, and where hyperbolic-tangent profiles were used in the spatial and temporal dimensions.
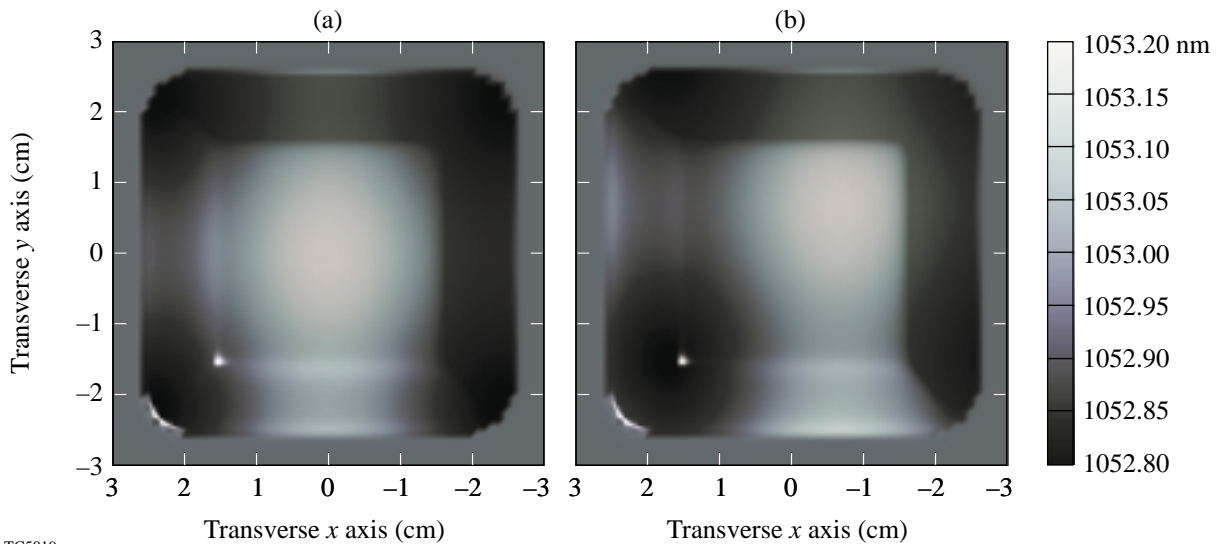
TC5019

Figure 78.14

Spatial cross sections of a 2-D SSD pulsed beam with an overlay of the instantaneous wavelength $\hat{\lambda}(\mathbf{r}_T, t)$ for the system parameters: $\delta_{M1} = 6.15$, $\nu_{M1} = 3.3$ GHz, $\Delta\lambda_{M1} = 1.5$ Å, $N_{c_y} \cong 1$, $\delta_{M2} = 13.5$, and $\nu_{M2} = 3.0$ GHz, $\Delta\lambda_{M2} = 3.0$ Å, $N_{c_x} \cong 0.9$, $\tau = 1$ ns, $D_y = D_x = 44$ mm, and where hyperbolic-tangent profiles were used in the spatial and temporal dimensions. The images are for two instants of time: (a) $t_1 = 0$ ps and (b) $t_2 = 46$ ps.

A useful diagnostic for 2-D SSD systems is the time-averaged, far-field intensity structure of the pulsed beam. A far-field camera operates by propagating the 2-D SSD pulsed beam through a lens onto its focal plane, where a CCD or film captures the image in a time-integrated sense. This process takes advantage of the Fourier-transforming properties of lenses. The object is assumed to be one focal length in front of the lens (otherwise a phase curvature is imposed across the far field), and the image is in the focal plane of the lens (see Ref. 16, pp. 86–87). Waaese simulates this data by taking the time average of the expression

$$\tilde{I}_{\text{far field}}(\mathbf{k}_T, t) \equiv \frac{1}{2} n \varepsilon_0 c \left| \int\int_{-\infty}^{\infty} E_0(\mathbf{r}_T, t) e^{-i\mathbf{k}_T \cdot \mathbf{r}_T} \, dx \, dy \right|^2 . \qquad (69)$$

The expression given by Eq. (64) is equivalent to the far field in real space, at the focal plane of the lens, by making the transformations $k_x \equiv 2\pi x_{\text{ff}}/\lambda_c f$ and $k_y \equiv 2\pi y_{\text{ff}}/\lambda_c f$, where x_{ff} and y_{ff} are the real-space, far-field coordinates and f is the focal length of the lens. A time-averaged plot of Eq. (69) is illustrated in Fig. 78.15 for the same system parameters of this section. If the expression Eq. (64) is plotted directly as a function of time, a movie of the far field can be generated. The underlying far-field pattern remains constant while the spec-
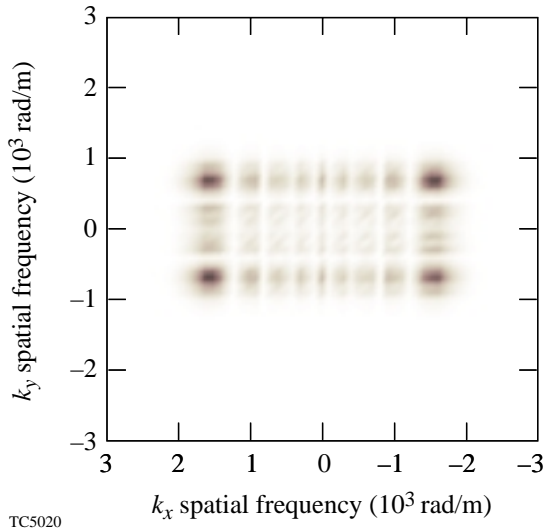
tral peaks change amplitude and can give the appearance of movement when the number of color cycles is less than 1 (provided there are no other smoothing mechanisms).

Nonideal Effects

In realistic SSD driver lines, a variety of mechanisms complicate the ideal situation described in the previous section. Some mechanisms simply distort the pulsed beam and others lead to AM. For example, if the preshear and dispersion grating are misaligned, the dispersion grating will not completely remove the distortion placed on the beam by the preshear grating. The result is a slight increase to the rise time of the pulse as well as a distorted far-field pattern in the rough shape of a rhombus. If the EO phase modulator has an angular-dependent modulation depth, the bandwidth imposed by the modulator will depend on the incident angle of the incident harmonic plane waves. This effect in combination with a grating misalignment explains the observed distorted far-field images (see Fig. 78.16); however, these two effects do not induce AM.

1. PM-to-AM Conversion Mechanisms

A variety of mechanisms destroy the ideal situation described in the previous section by producing AM. In general, they are referred to as PM-to-AM conversion mechanisms since any disruption to the spectral components of perfect phase modulation results in amplitude modulation. These mechanisms fall basically into two main categories that refer to the manner in which the spectral components can be altered: phase and amplitude effects. If the relative phases or the amplitudes of the spectral components are altered (with the exception to a linear phase variation), the phasor components will not add properly, resulting in AM. Waaese is well suited to analyze all of these effects in the spatiotemporal domain since it is based on the angular spectrum representation.

PM-to-AM conversion mechanisms further divide into temporal or spatial domain effects. Temporal domain effects directly control the phase or amplitudes by spectral filtering through devices such as etalons and amplifiers with nonconstant bandwidth. The transmissivity of etalons varies as a function of wavelength, which modulates the spectral amplitudes of a PM pulse. A similar and stronger effect is produced when a first-order ghost image co-propagates at a slight angle to the main beam, which has made one round-trip in a cavity. A streak camera measurement of this effect along with a simulation is shown in Fig. 78.17. Spatial domain effects indirectly control the spectral phase or amplitudes since, as a result of the gratings, the temporal spectrum has been coupled with the

Figure 78.15
Simulation of the time-averaged far field of a 2-D SSD pulsed beam for the system parameters: $\delta_{\text{M1}} = 6.15$, $\nu_{\text{M1}} = 3.3$ GHz, $\Delta\lambda_{\text{M1}} = 1.5$ Å, $N_{c_y} \cong 1$, $\delta_{\text{M2}} = 13.5$, and $\nu_{\text{M2}} = 3.0$ GHz, $\Delta\lambda_{\text{M2}} = 3.0$ Å, $N_{c_x} \cong 0.9$, $\tau = 1$ ns, $D_y = D_x = 44$ mm, and where hyperbolic-tangent profiles were used in the spatial and temporal dimensions.
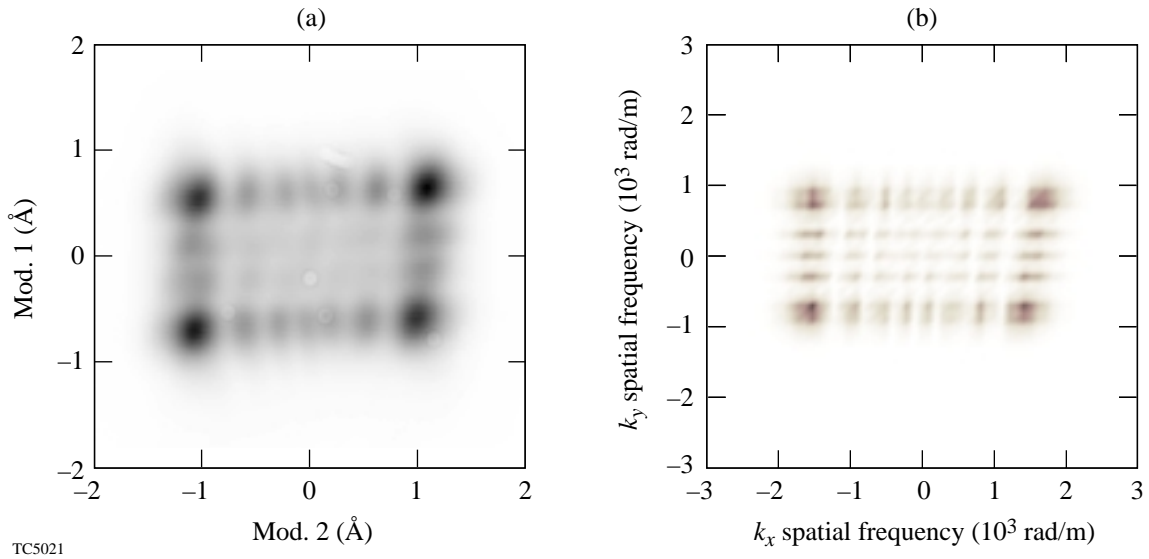
TC5020

TC5021

Figure 78.16
(a) A measured distorted far-field image of the double-pass 2-D SSD system and (b) a simulation of the time-averaged far field with an angular-dependent modulation depth and a G3 and G4 misalignment for the system parameters: $\delta_{M1} = 6.15$, $\nu_{M1} = 3.3$ GHz, $\Delta\lambda_{M1} = 1.5$ Å, $N_{c_y} \cong 1$, $\delta_{M2} = 13.5$, and $\nu_{M2} = 3.0$ GHz, $\Delta\lambda_{M2} = 3.0$ Å, $N_{c_x} \cong 0.9$, $\tau = 1$ ns, $D_y = D_x = 44$ mm, and where hyperbolic-tangent profiles were used in the spatial and temporal dimensions.
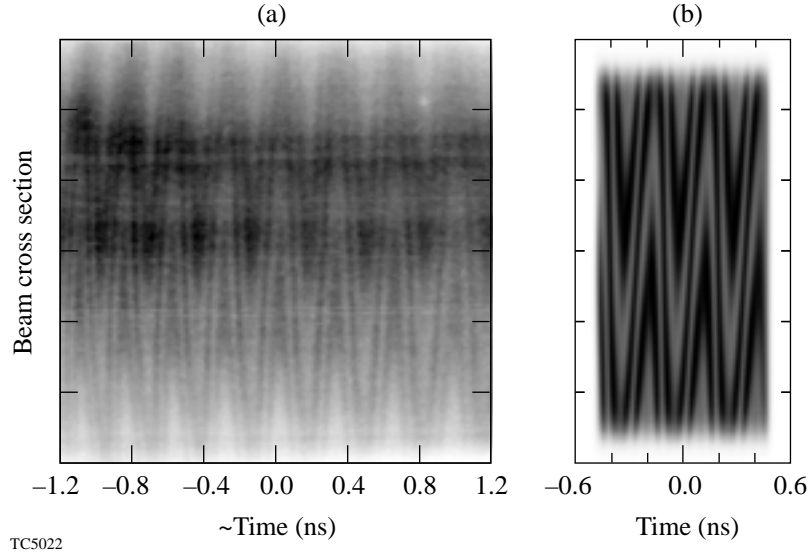

TC5022

Figure 78.17
(a) A measured streak camera image (showing 2.4 ns of time) resulting from a noncollinear co-propagating reflection and (b) a simulation (showing 1 ns of time) of the interference from a first-order ghost delayed by 50 ps co-propagating at an angle of 40 μrad to the main beam. The simulation is limited to 1 ns due to practical memory constraints; however, 1 ns is sufficient to illustrate the pattern that repeats at a rate of $1/\nu_M$.

spatial spectrum, i.e., the dispersed bandwidth. Therefore, spatial domain effects play a role only after the dispersion gratings G2 of the first dimension and G4 of the second dimension and include propagation and pinhole clipping. Propagation leads to AM since each color's phase front propagates in a different direction, which imparts a different amount of phase to each color. The AM grows unbounded in a nonlinear manner as the propagation distance increases, but image relaying has the ability to restore PM at an image plane. Table 78.III contains some simulation results of propagation out of the image plane for various locations on OMEGA and for different 2-D SSD configurations. Pinhole clipping leads to AM since, in the far field, the dispersed bandwidth is splayed across the focal plane and, if the outermost colors are blocked by the pinhole, AM results.

Spatial phase variations in the near field of an SSD pulsed beam do not directly convert to AM, but the far field may be significantly broadened. If this image is passed through an image relay with a pinhole filter, spectral clipping can occur, which leads to AM. On the other hand, nonlinear spatial phase variations in the far field convert directly to AM in the near field since the spectral components are distributed in the far field as shown in Fig. 78.15. For example, surface roughness of a mirror that is placed in the far field of an image relay cavity alters the phase front of the reflected beam. Waasese simulates the surface roughness by spectrally filtering a random-number generator to match observed surface roughness statistics; an example is shown in Fig. 78.18. The effect on a 1-D SSD pulsed beam is shown in the example in Fig. 78.19. As another example, a curved retro mirror was unknowingly placed in the far-field retro stage of the second dimension and was sheared

to produce planar phase fronts. When planar mirrors were substituted for the curved mirror, extremely large AM was observed. The signature of propagation out of an image plane was used to identify the AM source as a curved far-field mirror since propagation also induces a curved phase on the angular spectrum (see Fig. 78.20). Combinations of devices can also lead to AM. For example, a Faraday rotator with a wavelength-sensitive rotation in combination with a cavity ejection wave plate and a polarizer will result in an effective spectral filter.

Nonideal phase-modulator effects can be included in addition to applying the ideal PM described in Eq. (43). If the angular spectrum of the input beam is significantly broad in the direction of the optic axis, i.e., a 1-D SSD beam entering the second-dimension modulator, the crystal birefringence must
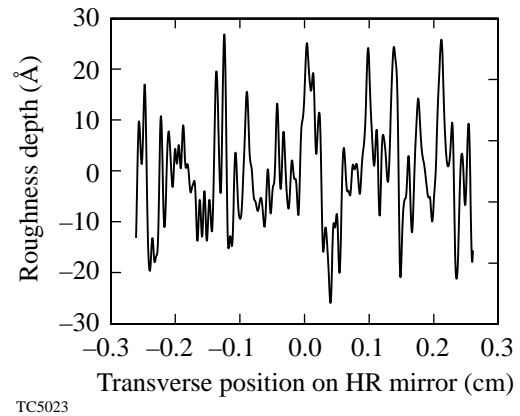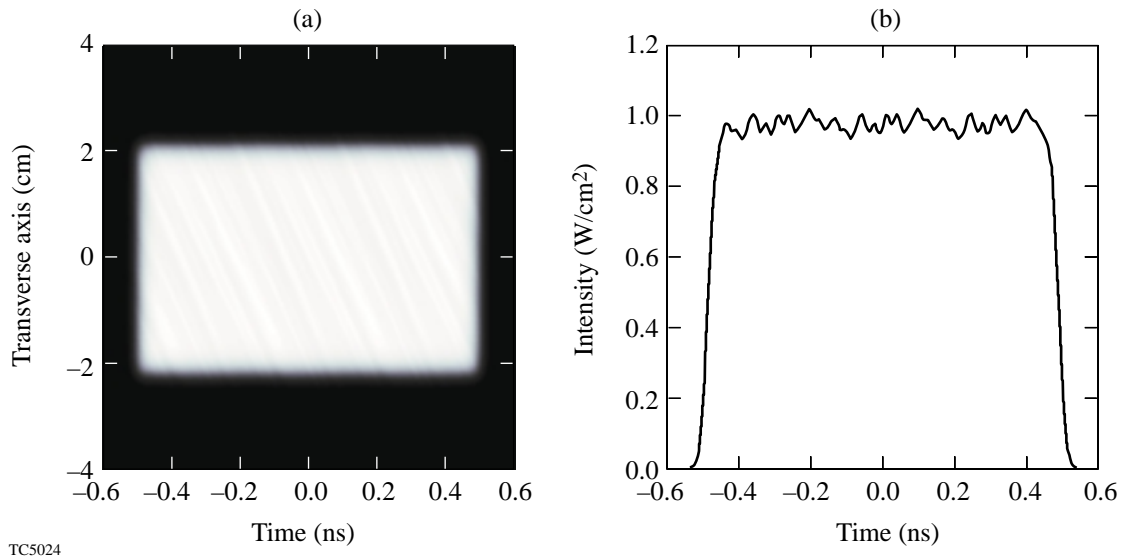

TC5023

Figure 78.18
Modeled surface roughness on a far-field, high-reflecting dielectric mirror.

Table 78.III: The AM, given as a percentage of peak-to-initial value, that results from propagation out of an image plane for different locations on OMEGA and for different 2-D SSD configurations.

Component Location	Beam Diameter (cm)	1 THz $N_c = 2,1$ 2.1, 10.4 Å 8.8, 10.2 GHz	$N_c = 1,3.6$ 1.5, 3.0 Å 3.3, 12 GHz	$N_c = 1, 1$ LLNL 5.0 Å 17 GHz	$N_c = 2, 1$ LLNL 5.0 Å 17 GHz	Current $N_c = 1, 1$ 1.25, 1.75 Å 3.3, 3.0 GHz
Focus lens (3ω)	27.3	13.6	31.3	2.08	8.90	5.83
FCC	27.3	0.731	1.45	0.120	0.482	0.328
F spatial filter	19.5	3.06	6.23	0.496	2.01	1.36
E spatial filter	14.6	3.88	7.98	0.626	2.55	1.72
C relay	8.49	18.9	46.1	2.81	12.3	7.91

TC5024

Figure 78.19
(a) Spatiotemporal cross section and (b) lineout of a 1-D SSD pulsed beam incident on a far-field mirror with surface roughness as modeled in Fig. 78.18 that yielded a peak-to-mean AM of 4.8%.
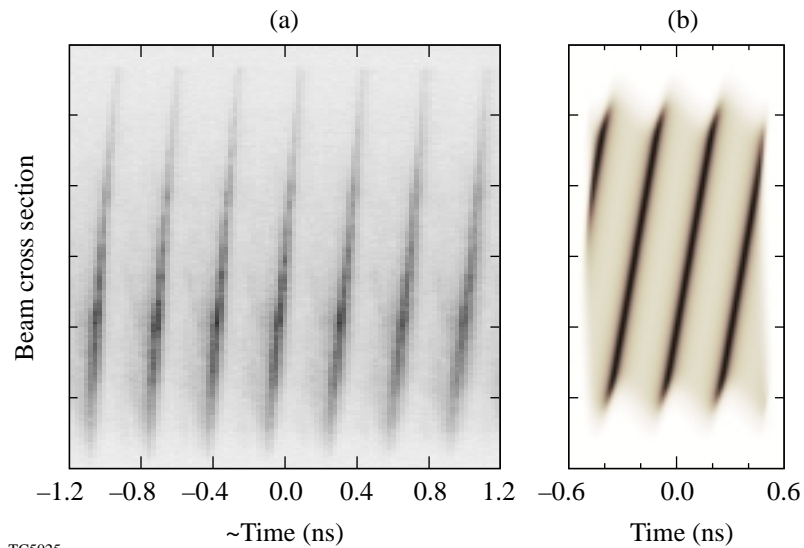
TC5025

Figure 78.20
(a) A measured streak camera image (showing 3 ns of time) resulting from a phase curvature caused by an improperly placed retro mirror at the second SSD dimension double-pass cavity and (b) a simulation of the same effect, resulting in 110% peak-to-mean AM. The simulation is limited to 1 ns due to practical memory constraints; however, 1 ns is sufficient to illustrate the pattern that repeats at a rate of $1/\nu_M$.

be taken into account. This effect is exhibited by a quadratic phase distortion in the spatial frequency domain (in the direction corresponding to the optic axis) that results from the index ellipsoid of uniaxial crystals (see Ref. 17, pp. 86–90). Each harmonic plane wave produced by the first SSD dimension will experience a different phase delay as it propagates through the second modulator, which results in AM in the first dimension. Before the second dimension has been dispersed by G4, an adjustment of the image plane will correct for this AM source because propagation induces a compensating phase curvature on the angular spectrum (see Fig. 78.21). This is permissible because the spread of the angular spectrum in the second dimension is not significant before it has passed through the dispersion grating.

One other source of PM to AM is the nonlinear mapping of the grating. In the ideal case, Eq. (34) is used to describe this mapping. If the more complete nonlinear mapping is used [Eq. (17)], large enough bandwidths and color cycles will lead to a distorted mapping onto the spatial spectrum and subsequently will introduce AM. Waasese simulates this effect and shows that the distortion is greatest near the edge of the beam as seen in Fig. 78.22.
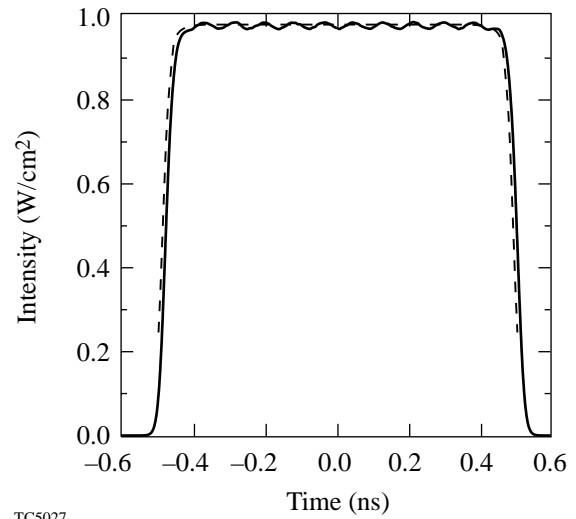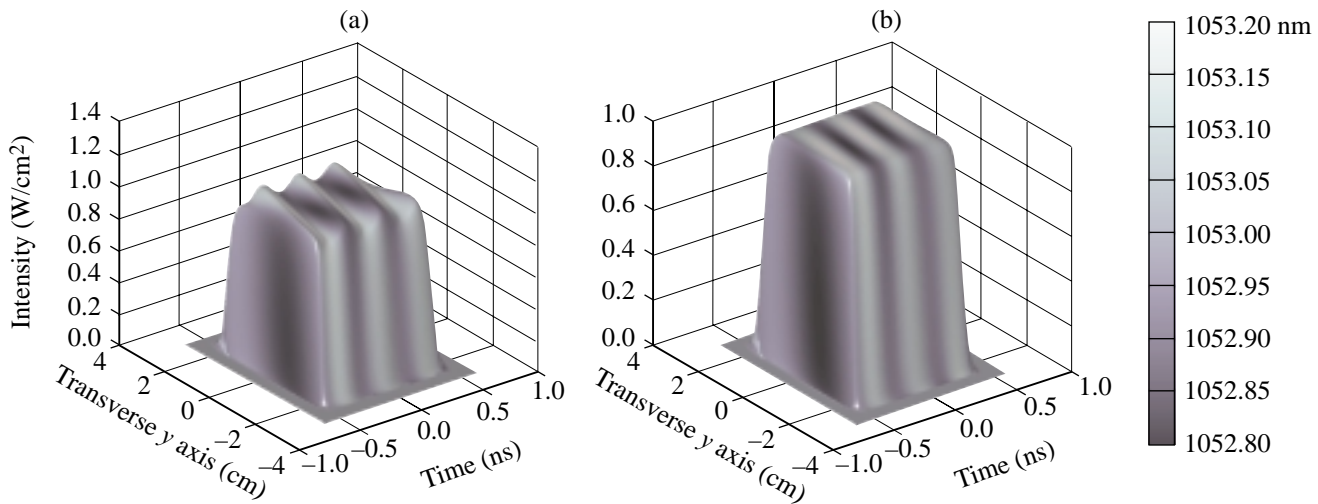

TC5027

Figure 78.22
Simulation of the nonlinear grating equation effect on a 2-D SSD pulsed beam using a double-grating set. The distortion is greatest near the edge of the beam and results in a peak-to-mean AM of about 1%. The lineout is taken at $x = 1.5$ cm and $y = 0$ cm. The system parameters: $\delta_{M1} = 6.15$, $\nu_{M1} = 3.36$ GHz, $\Delta\lambda_{M1} = 1.5$ Å, $N_{c_y} \cong 1$, $\delta_{M2} = 3.38$, $\nu_{M2} = 12.06$ GHz, $\Delta\lambda_{M2} = 3.0$ Å, and $N_{c_x} \cong 3.65$.

TC5026

Figure 78.21
(a) Simulation of the propagation of a 1.1-mm beam through the second SSD dimension modulator while including crystal birefringence results in a peak-to-mean AM of 4%; (b) simulation of the compensating effect of a 0.56-mm adjustment to the image plane prior to the final grating at the 1.1-mm beam diameter. The system parameters: $\delta_{M1} = 6.15$, $\nu_{M1} = 3.3$ GHz, $\Delta\lambda_{M1} = 1.5$ Å, $N_{c_y} \cong 1$, $\delta_{M2} = 13.5$, and $\nu_{M2} = 3.0$ GHz, $\Delta\lambda_{M2} = 3.0$ Å, $N_{c_x} \cong 0.9$, $\tau = 1$ ns, $D_y = D_x = 44$ mm, where hyperbolic-tangent profiles were used in the spatial and temporal dimensions, and an effective LiNbO$_3$ crystal length of 36 mm.

Conclusion

Waasese provides a flexible modeling tool for simulating the generation and propagation of 2-D SSD pulsed laser beams. Waasese simulates ideal and nonideal behavior of the many optical components that comprise the SSD driver line including their relative positions. Waasese predicts measurable signatures that function as diagnostic tools since they are associated with particular optical components. The signature/component relationships act together with experimental measurements to help locate and eliminate a troublesome component. Minimizing any AM in the driver line will ensure the safety level and lifetime of OMEGA optics by circumventing the effects of small-scale self-focusing. Waasese proves to be an indispensable modeling tool for the OMEGA laser, and its inherent flexibility will provide a means to enhance its capabilities to model other laser propagation issues such as nonlinear propagation, on-target uniformity, amplifier gain, scattering losses, and pinhole clipping.

REFERENCES

1. S. Skupsky, R. W. Short, T. Kessler, R. S. Craxton, S. Letzring, and J. M. Soures, J. Appl. Phys. **66**, 3456 (1989).

2. S. Skupsky and R. S. Craxton, "Irradiation Uniformity for High-Compression Laser Fusion Experiments," to be published in Physics of Plasmas.

3. Laboratory for Laser Energetics LLE Review **69**, 1, NTIS document No. DOE/SF/19460-152 (1996). Copies may be obtained from the National Technical Information Service, Springfield, VA 22161.

4. J. E. Rothenberg, J. Opt. Soc. Am. B **14**, 1664 (1997).

5. P. W. McKenty, S. Skupsky, J. H. Kelly, and C. T. Cotton, J. Appl. Phys. **76**, 2027 (1994).

6. Y. H. Chuang, L. Zheng, and D. D. Meyerhofer, "Amplification of Broad-Band Phase-Modulated Laser Pulses for Beam Smoothing by Spectral Dispersion," LLE, memorandum (August 1991).

7. R. Short, LLE, private communication (1989).

8. J. E. Rothenberg, D. F. Browning, and R. B. Wilcox, "The Issue of FM to AM Conversion on the National Ignition Facility," to be published in SPIE's Proceedings on Solid State Lasers for Application (SSLA) to Inertial Confinement Fusion, 3rd Annual International Conference, Monterey, CA, 7–12 June 1998.

9. J. A. Marozas, "Angular Spectrum Representation of Ultrawideband Electromagnetic Pulse Propagation in Lossy, Dispersive Dielectric Slab Waveguides," Ph.D. Thesis, University of Vermont, 1998.

10. K. E. Oughstun and G. C. Sherman, *Electromagnetic Pulse Propagation in Causal Dielectrics*, Springer Series on Wave Phenomena, Vol. 16 (Springer-Verlag, Berlin, 1994).

11. A. E. Siegman, *Lasers* (University Science Books, Mill Valley, CA, 1986).

12. E. G. Loewen and E. Popov, *Diffraction Gratings and Applications*, Optical Engineering, Vol. 58 (Marcel Dekker, New York, 1997).

13. Laboratory for Laser Energetics LLE Review **68**, 192, NTIS document No. DOE/SF/19460-139 (1996). Copies may be obtained from the National Technical Information Service, Springfield, VA 22161.

14. A. B. Carlson, *Communication Systems: An Introduction to Signals and Noise in Electrical Communication*, McGraw-Hill Electrical and Electronic Engineering Series (McGraw-Hill, New York, 1968).

15. M. Abramowitz and I. A. Stegun, eds. *Handbook of Mathematical Functions with Formulas, Graphs, and Mathematical Tables*, Applied Mathematics Series 55 (U.S. Government Printing Office, Washington, DC, 1964).

16. J. W. Goodman, *Introduction to Fourier Optics* (McGraw-Hill, New York, 1968).

17. A. Yariv, in *Quantum Electronics,* 2nd ed. (Wiley, New York, 1975).

Hollow-Shell Implosion Studies on the 60-Beam, UV OMEGA Laser System

Direct-drive inertial confinement laser fusion is accomplished by uniformly illuminating spherical fuel-bearing targets with high-power laser beams, ablatively driving implosions that result in large increases in density and temperature. Current large laser systems such as the University of Rochester's OMEGA laser, which is capable of both direct- and indirect-drive implosion experiments,[1,2] and the Lawrence Livermore National Laboratory's Nova laser,[3,4] which is designed primarily for indirect-drive implosions, are smaller in size and total output energy than what is believed necessary to obtain ignition and gain. Attaining conditions for ignition to occur (densities of ~200 g/cm^3 and temperatures of ~3 to 4 keV) awaits the completion of the National Ignition Facility[5] (NIF) and other megajoule-class drivers currently being planned. In addition to the high temperatures and densities, ignition requires fuel areal densities (density–radius product) $\gtrsim 0.3$ g/cm^2 to stop the 3.5-MeV alpha particles in order to obtain thermonuclear burn propagation.[6,7] To reach these conditions in direct-drive implosions requires controlling the growth of the Rayleigh–Taylor (RT) instability, which is seeded by nonuniformities in the laser illumination. The RT instability can lead to shell breakup and mixing of shell material into the gas-fill or central voided region in the case of evacuated targets. We are currently studying the attainment of near-ignition-scale areal densities on OMEGA and the effects of beam smoothing and pulse shaping thereon, by using surrogate cryogenic targets where the shell acts as the fuel layer. These will be followed by actual cryogenic (DD or DT) targets, when the cryogenic target–handling facility is completed.

Previously reported direct-drive OMEGA experiments have demonstrated the ability to achieve high relative temperatures[8] (kT_e ~3 to 4 keV, kT_i ~14 keV) attaining DT neutron yields of $>10^{14}$. Additionally, the acceleration- and deceleration-phase target stability has been studied in spherical implosions using thin polymer layers containing various high-Z elements, such as Ti, Cl, and Si, with D_2 fills containing a small Ar component.[9]

In the present experiments, we have studied the stagnation phase (maximum density and temperature conditions) of the implosions designed to attain high areal densities ($\gtrsim 0.1$ g/cm^3) using both x-ray and neutron spectroscopic techniques. The targets consist of both deuterated and undeuterated polymer shells with either zero-pressure (evacuated) or low-pressure (3-atm) D_2 or D^3He fills. The zero-pressure- or low-pressure-fill targets are "surrogates" for cryogenic targets since in actual cryogenic targets the gas pressure will be at or below the triple-point vapor pressure of D_2 or DT gas (0.2 atm at 20 K).[10] An equivalent particle density is obtained for a pressure of 3 atm at room temperature (300 K). The hydrodynamics of the central gas-filled region of a 3-atm-filled target will therefore be the same as an actual cryogenic target at the triple point. Conversely, the shell of the surrogate cryogenic target is not expected to evolve the same but will have a different in-flight aspect ratio (mean radius/thickness) and convergence ratio (initial radius/final radius). Also, the RT growth in a CH shell will be larger than for a DT shell because the reduced ablation velocity leads to a lesser ablative stabilization. Nevertheless, high areal densities ($\gtrsim 0.1$ g/cm^2), high convergence ratios (>20), and moderately high central temperatures ($\gtrsim 2$ keV) can be studied with a surrogate cryogenic target. The measurements described in this work have revealed significant information about the implosion of surrogate cryogenic targets and the effects of beam smoothing and pulse shaping thereon.

Experiments

The targets used for these experiments were manufactured by General Atomics.[11] Hollow spherical shells were produced by coating layers of deuterated plastic (CD) and then undeuterated plastic (CH) over a depolymerizable spherical mandrel. The coatings were accomplished by the method of glow discharge plasma (GDP) polymerization. The CD-layer thicknesses ranged from 5 to 10 μm, while the CH-layer thicknesses ranged from 10 to 30 μm. Layer thicknesses were measured to an accuracy of 0.5 μm, and the target diameter was measured to an accuracy of 1 μm. In each case the targets were

held in place in the target chamber using low-mass stalks consisting of a short length of spider silk (~100 μm) that had been previously overcoated with parylene to add mechanical stability. The spider silks were glued to boron fibers ~20 μm in diameter, and the parylene-overcoated stalk end was attached to the target with UV-curable epoxy. The UV epoxy glue spots were the largest single mass perturbation introduced by the stalks; these spots ranged from 10 to 30 μm in diameter. Targets were either prepared and kept evacuated ($<10^{-3}$ Torr) or filled with 3 atm of D_2, H_2, or an equal molar mixture of D^3He gases.

Three laser-irradiation conditions were used for these experiments: (1) Coherent beam illumination (no beam smoothing) was used with the beams focused so as to nearly tangentially illuminate the target at the beam edge. (2) Each beam was modified using a distributed phase plate (DPP)[12] at best focus (diffraction minimum spot ~0.95 mm). (3) Beams with DPP's were smoothed using SSD[13] along two axes (2-D SSD)[12] with frequencies of 3.5 and 3.0 GHz and bandwidths of 1.7 and 1.2 Å (0.25-THz bandwidth). The estimated illumination uniformity for 60 overlapping OMEGA beams (σ_{rms} for ℓ-modes 1 to 500) was ~15% for the coherent beam illumination, ~20% for DPP-only illumination, and ~2.5% for the DPP+SSD illumination. All values quoted are calculated from the idealized effect on the beam distribution and averaged over the length of the pulse. While the distributed phase plates produce a smooth envelope to the beam, they also introduce small-scale laser speckle, hence the larger value of σ_{rms} for the DPP-only illumination. Although the value of σ_{rms} for the DPP+SSD illumination is lower than the other cases, two additional effects not accounted for by this time-averaged quantity must be considered: (1) Beam balance at current levels (~7% rms

beam-to-beam energy variation) would produce an on-target illumination nonuniformity of ~2.5% rms even with perfectly smooth beams, with most of that contribution in modes 1 through 5. (2) The smoothing time of the present level of SSD may not be fast enough to avoid imprinting laser-beam speckle onto the target.

The three pulse shapes used in these experiments (Fig. 78.23) were the 1-ns square pulse shape, the 1:6 ratio foot-to-main-pulse shape (also known as PS26), and the 1:40 ratio pulse shape known as $\alpha = 3$. Examples of the actual pulse shapes are shown along with the design shape. Good pulse-shape repeatability was obtained. The purpose of varying the pulse shape in these experiments is to investigate target performance versus pulse shape. Ideally a gradually rising intensity, if properly designed, will produce a final target compression greater than a sharply rising pulse. Figures 78.24(a) and 78.24(b) show the calculated primary neutron yield (D-D) and the fuel and shell areal densities as a function of time for the three different pulse shapes. All simulations (accomplished with the hydrodynamics code *LILAC* as described in the next section) are for an assumed total energy on target of 25 kJ, and in each case the target was a 0.95-mm-diam, 20-μm-thick CH shell filled with 3 atm of D^3He. For these conditions it is clear that the highest yield and compression are obtained for the highest-contrast pulse shape. This trend also holds for the evacuated targets.

The two instruments used to obtain x-ray spectra of the implosion cores were a Kirkpatrick-Baez–type (KB) microscope outfitted with a diffraction grating[14] and a crystal spectrometer outfitted with an imaging slit.[15] The KB microscope has Ir-coated mirrors and a sensitive energy band from ~2 to
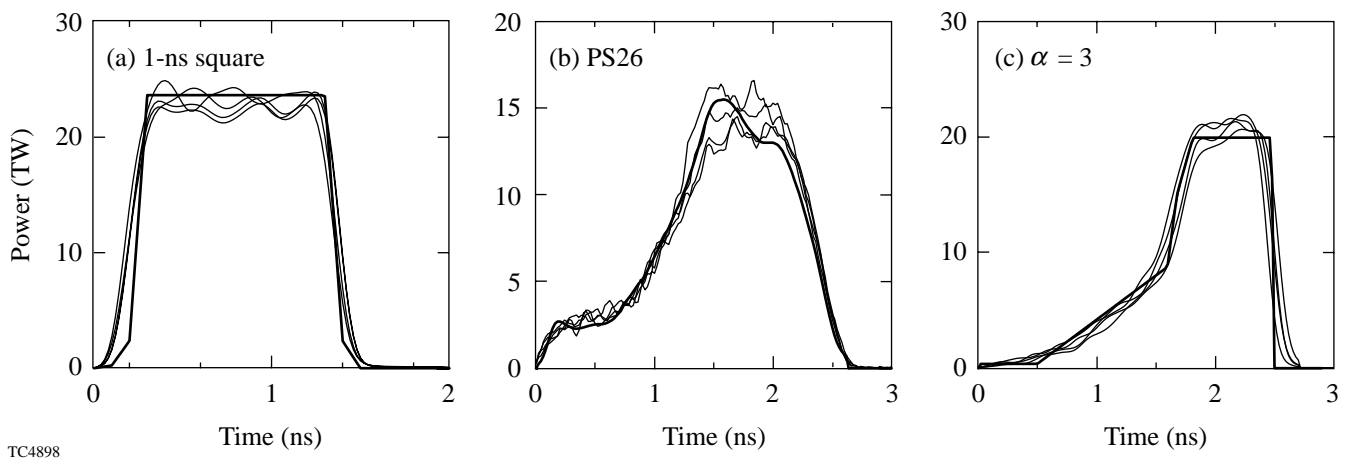

TC4898

Figure 78.23
The three pulse shapes used in these experiments: (a) the 1-ns square pulse, (b) PS26, a 1:6 ratio foot-to-main pulse shape, and (c) $\alpha = 3$, a 1:40 ratio pulse shape.

8 keV. The absolute response of the microscope was determined both in the laboratory and *in situ*. Figure 78.25(a) shows a typical grating-dispersed image of an imploded hollow-shell target. The bright central peak is the overexposed image of the core (zeroth-order image), while the indicated lines are diffracted images of the core (±first-order images). The spectrum of the core emission, after correction for instrument response, is shown in Fig. 78.25(b) along with a model fit to the spectrum (thermal bremsstrahlung with absorption). (The details of this analysis will be described in the next section.) The crystal spectrometer consisted of an imaging slit in front of a diffraction crystal viewing the target. Diffracted x rays were recorded with DEF film as were the spectrally dispersed images from the

KB microscope. The emission from the implosion core was separated from the total flux by the narrow size of the imaging slit (~100 μm). The spectrometer was set to view a region of the spectrum from ~4 to 6 keV containing continuum emission from the targets. This was compared to the KB microscope–derived spectra on certain shots. A limited number of shots were taken with targets containing a Ti-doped layer, and in such cases the observed jump in the spectrum at the Ti K edge was used to infer the shell areal density.[15]

Primary neutron yield (D-D neutrons) was measured with an array of cross-calibrated scintillator detectors. Secondary neutron yield was measured with an 824 detector array of
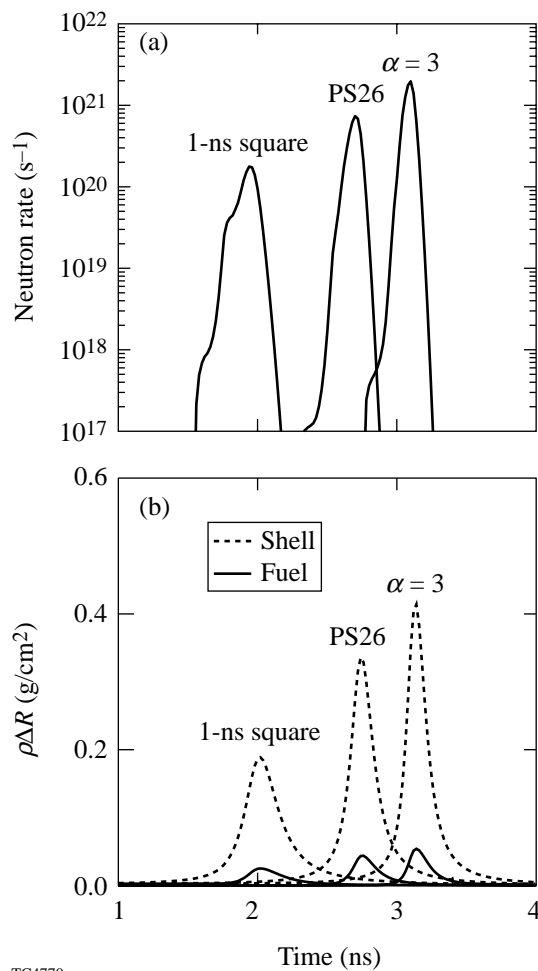
TC4770

Figure 78.24
Simulations of the (a) D-D neutron-generation rate and (b) the fuel and shell areal densities as functions of time for the three pulse shapes. The targets were all assumed to be 20-μm-thick CH shells, filled with 3 atm of D^{3}He, imploded by a total energy of 25 kJ.
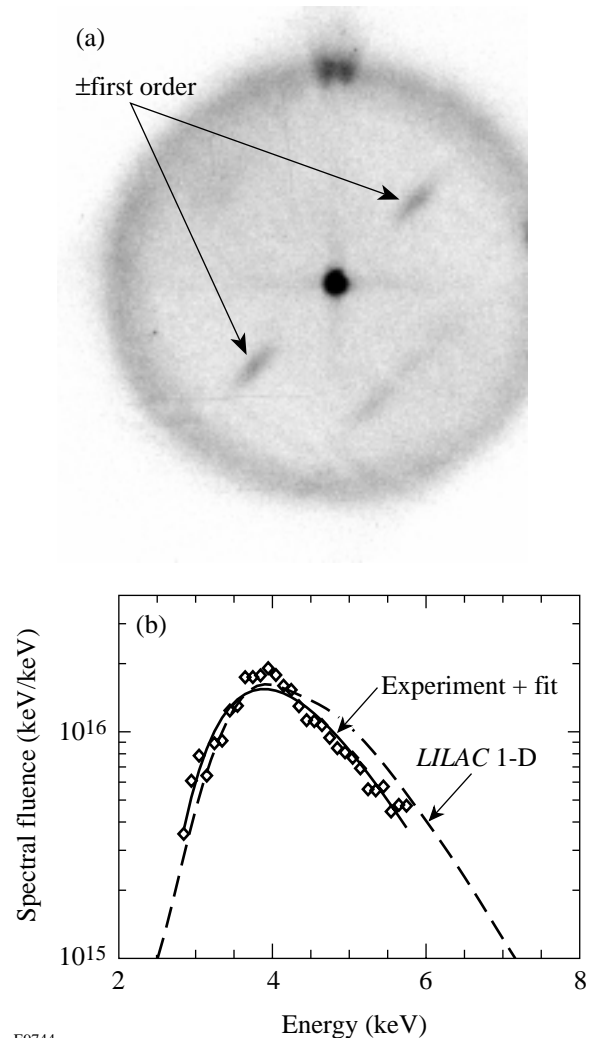
E9744

Figure 78.25
Grating-dispersed KB microscope image of OMEGA shot 9130 (see Table 78.IV): (a) the zeroth-order image with ±first-order diffracted images of the core (indicated), and (b) the core spectrum after correction for instrument response, along with 1-D (*LILAC*) simulations of the same.

scintillators, each of which records the neutron arrival time to an accuracy of ~0.5 ns, which translates into an accuracy in energy of ~0.5 MeV. This instrument, called MEDUSA (Multi-Element Detector Using a Scintillator Array),[16] allows for the determination of the much smaller secondary neutron yield (D-T neutrons) due to their earlier arrival time at the detector. Figure 78.26 shows an example spectrum from MEDUSA on a 20-μm-thick CD/CH shell imploded with a 1-ns square pulse and coherent beam illumination. The secondary neutron yield is clearly seen, appearing as the broad peak between 12 and 17 MeV. The integral of this peak is proportional to the secondary yield.
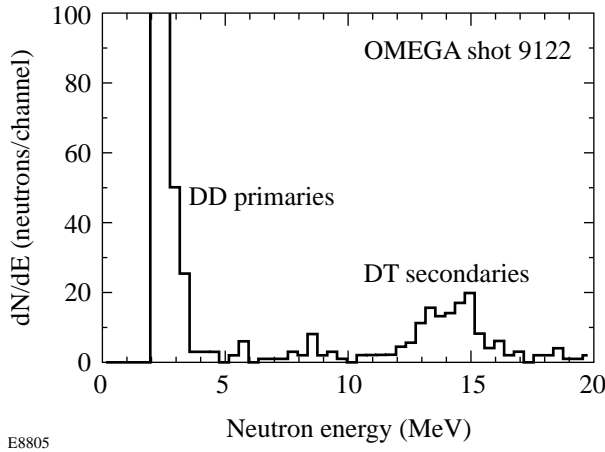

Figure 78.26
Example of the neutron spectrum emitted by a CD target as determined by MEDUSA. The neutrons with energies from 12 to 17 MeV are from DT fusion reactions generated by primary-fusion-product (secondary) tritons fusing with primary deuterons.

Results

Several combinations of shell thicknesses (CD/CH and CH only), fill gases, and pulse shapes were investigated. We present here a representative set from which x-ray and neutron spectral information was obtained. Table 78.IV is a sample of the target shot conditions and experimentally measured values. The conditions for each shot, illumination type, energy, D-D yield, D-T yield (where measured), kT_e, and ρR, along with *LILAC* predictions of these quantities, are grouped by type of pulse shape. The implosions were simulated with the one-dimensional hydrocode *LILAC*, which uses tabulated equation of state (SESAME),[17] flux-limited electron transport, and multi-group radiation transport using local thermodynamic equilibrium (LTE) opacities,[18] and inverse-bremsstrahlung-absorption energy deposition through a ray-tracing algorithm in the underdense plasma. A flux limiter of $f = 0.06$ with a

sharp cutoff was used. The primary fusion reaction products were transported using a multi-angle straight-line method, which also includes the production of neutrons from the secondary D-T reactions. The detailed space-resolved x-ray spectra generated for comparison with the observations were calculated with a postprocessor.

As shown in previous works,[14,19] the x-ray spectrum emitted by an undoped polymer shell can, to a good approximation, be represented by

$$I_x = I_{\text{hot}} \, e^{-E/kT_{\text{hot}}} \, e^{-\langle \mu(E)\rho R \rangle_{\text{shell}}} , \qquad (1)$$

where I_{hot} is the intensity of the thermal bremsstrahlung emission from the core region, which has a characteristic temperature kT_{hot}. Absorption will occur in the shell as x rays exit the core through the surrounding colder shell whose optical depth $\tau = \langle \mu(E)\rho R \rangle$, where $\mu(E)$ is the energy-dependent mass absorption coefficient and ρR is the areal density (the brackets indicate an average over the shell). To a good approximation μ is given by

$$\mu = 1.9 \times 10^3 \, \frac{1}{E^3} \, g(\rho, kT) \quad (\text{cm}^2/\text{g}), \qquad (2)$$

where E is in keV and $g \leq 1$. Using this approximation, a lower limit on ρR_{shell} can be determined by fitting the observed spectrum to I_X with the optical depth given by

$$\tau = 1.9 \times 10^3 \, \frac{\rho R_{\text{cold}}}{E^3}, \qquad (3)$$

where ρR_{cold} is the areal density of the cold shell material and, therefore, a lower limit on the total ρR_{shell}. Both ρR_{cold} and the average electron temperature kT_e are determined by fitting Eq. (1) to the observed spectrum.

The combined measurements of the primary neutron yield from the D-D reaction and the secondary neutron yield from the D-T reaction allow us to estimate the areal density of the deuterium-bearing shell material ρR_{CD} using the following:

$$\rho R_{\text{CD}} \geq \left[\frac{Y_{\text{DT}}}{Y_{\text{DD}}} \middle/ 4.3 \times 10^{-2} \right] \quad (\text{g/cm}^2), \qquad (4)$$

where we have used the results of Azechi, Cable, and Stapf[20] scaled to CD (which has a 6:1 ratio of carbon to deuterium

mass) and we have taken the maximum calculated ratio as a function of temperature as the limit given above. Since the range of the primary 1-MeV tritons may be smaller than the total areal density of the CD layer ρR_{CD} and since ρR_{CD} is less than the total ρR_{shell}, this value again places a lower limit on ρR_{shell}.

Figure 78.27 shows the measurements of kT_e and *LILAC* predictions of these values for the voided targets imploded by 1-ns square pulses. (The values obtained from simulations are averaged over the stagnation, as is the case for all comparisons to measurements that follow. The simulated x-ray measurements are weighted by emitted x-ray intensity, whereas the simulated neutron measurements are values averaged over the time of neutron emission.) The measured values of kT_e show little discernible difference for the three illumination conditions. (Note that slightly less energy was used to implode the targets with DPP+SSD illumination.) The thinnest-shell

targets have measured kT_e values that are slightly lower than the predicted values.

Figure 78.28 shows the measured values of ρR_{cold} from the x-ray spectra for 1-ns-square-pulse illumination. Here we have included both the voided CD/CH shells and the 3-atm-filled CH shells. The higher measured values of ρR_{cold} for the thicker-shell targets are evident, following the trend of the simulations, which is expected since the implosion cores of thicker targets reach a lower temperature. (Therefore the shell material is less stripped and can more heavily absorb the continuum emission from the core.) The significantly lower values of ρR_{cold} for the DPP-only cases are also noticeable. This difference is largest for the 3-atm-filled CH targets pointing to the gas–shell interface as a source of disruption to the symmetry of the implosion. The differences between DPP+SSD and DPP-only illumination for gas-filled targets are further apparent when one compares their spectra

Table 78.IV: Measured and simulated values for a representative sample of voided CD/CH target experiments. The numbered columns contain the following: (1) pulse type, (2) beam-smoothing condition, (3) shell thickness, (4) energy on target, (5) the measured D-D neutron yield [Y_n (D-D)], (6) error of measurement of Y_n (D-D), (7) the measured D-T neutron yield [Y_n (D-T)], (8) error of measured Y_n (D-T), (9) the CD layer areal density ρR_{CD} determined from Eq. (4), (10) error of ρR_{CD} value, (11) *LILAC*-predicted value of Y_n (D-D), (12) YOC (D-D), the ratio of the measured-to-predicted values of Y_n (D-D), (13) *LILAC*-predicted value of Y_n (D-T), (14) *LILAC*-predicted value of ρR_{CD}, (15) *LILAC*-predicted

| Shot	1 Pulse Type	2 Illumination Condition	3 CD+CH (μm)	4 Energy (kJ)	5 Y_n(D-D)	6 Y_n(D-D) error	7 Y_n(D-T)	8 Y_n(D-T) error	9 ρR_{MED} (mg/cm^2)	10 ρR_{MED} error (mg/cm^2)	11 Y_n(D-D) 1-D	12 YOC (D-D)
7817	1-ns sq	Coherent	31.8	26.2	2.3(8)	6.7(6)					4.9(8)	0.47
9130	1-ns sq	Coherent	39.4	28.4	7.4(7)	2.5(6)					1.1(8)	0.66
9266	1-ns sq	Coherent	25.6	29.2	5.4(8)	7.0(6)					6.1 (9)	0.09
9267	1-ns sq	Coherent	34.4	30.2	1.6(8)	3.7(6)					5.2(8)	0.31
14010	1-ns sq	DPP's only	21.2	28.0	1.4(9)	3.2(7)	4.1(6)	2.6(5)	69.0	4.8	1.7(10)	0.08
14012	1-ns sq	DPP's only	31.0	27.2	2.5(8)	1.4(7)	5.0(5)	8.6(4)	45.4	8.3	5.9(8)	0.43
11561	1-ns sq	DPP's + SSD	19.9	27.3	2.6(9)	2.0(8)	7.3(6)	3.7(5)	64.9	6.1	1.8(10)	0.15
11562	1-ns sq	DPP's + SSD	30.9	28.3	2.5(8)	6.4(7)	4.6(5)	8.3(4)	42.2	13.2	5.7(8)	0.44
11576	1-ns sq	DPP's + SSD	38.9	27.7	1.4(8)	1.6(6)	1.8(5)	5.1(4)	30.1	8.7	6.7(7)	2.03
12538	1-ns sq	DPP's + SSD	21.1	24.0	1.4(9)	5.5(7)	6.0(6)	3.3(5)	102.3	7.0	5.9(9)	0.23
12548	$\alpha = 3$	DPP's + SSD	21.1	20.6	1.7(8)	2.6(6)	7.2(4)	3.2(4)	9.7	4.4	8.6(9)	0.02
12549	$\alpha = 3$	DPP's + SSD	26.9	21.2	1.1(8)	2.0(6)	5.7(4)	2.9(4)	12.5	6.3	1.3(9)	0.08
12551	$\alpha = 3$	DPP's + SSD	30.8	21.0	4.4(7)	1.3(6)	2.8(4)	2.0(4)	15.0	10.6	3.8(8)	0.12
12562	PS26	DPP's + SSD	21.3	19.6	7.8(7)	1.3(7)	1.1(5)	4.1(4)	34.4	13.5	1.0(10)	0.01
12563	PS26	DPP's + SSD	26.9	19.8	6.5(7)	1.2(7)	1.4(5)	4.5(4)	50.9	18.6	3.0(9)	0.02
12567	PS26	DPP's + SSD	30.7	20.0	7.8(7)	1.3(7)	2.9(5)	6.4(4)	85.6	24.0	1.7(9)	0.05

OMEGA voided CD/CH targets
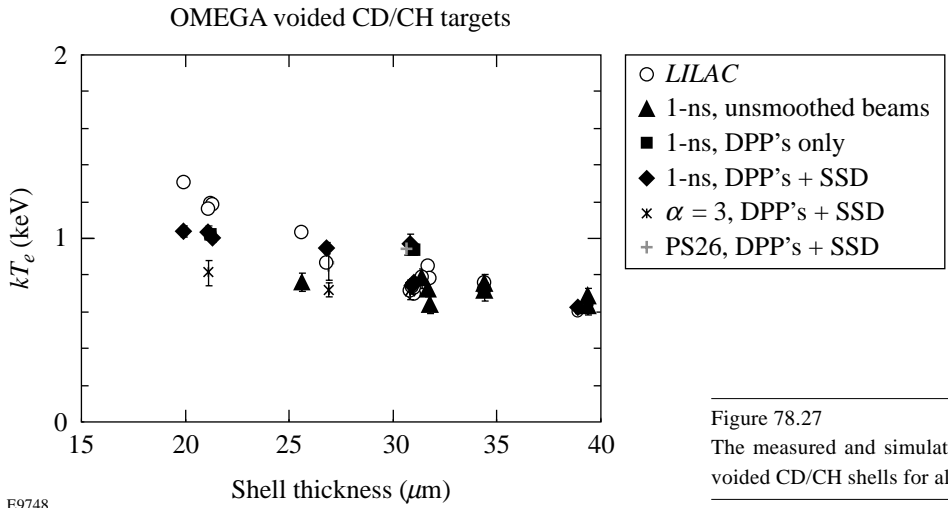
Figure 78.27
The measured and simulated values of kT_e versus shell thickness for the voided CD/CH shells for all pulse shapes.

E9748

value of ρR_{shell} averaged over the time of neutron production, (16) *LILAC*-predicted value of the ion temperature (kT_i) averaged over the time of neutron production, (17) the x-ray-spectrum determined electron temperature (kT_e), (18) error of (kT_e), (19) the *LILAC*-predicted value of the kT_e, as would be determined from the x-ray spectrum, (20) the x-ray spectrum determined cold shell density (ρR_{cold}), (21) error of ρR_{cold}, (22) the *LILAC*-predicted value of ρR_{cold}, (23) the inferred shell areal density (ρR_{shell}), and (24) error of experimentally determined value of ρR_{shell}. [*Numbers in ( ) indicate the power of 10; i.e., 2.3(8) = 2.3×10^8].

13	14	15	16	17	18	19	20	21	22	23	24
Y_n(DT) 1-D	ρR_{MED} 1-D (mg/cm²)	$<\rho R>_n$ 1-D (mg/cm²)	$<kT_i>_n$ 1-D (keV)	kT_e (KB) (keV)	kT_e error (keV)	kT_e 1-D (keV)	ρR_{cold} (KB) (mg/cm²)	ρR_{cold} error (mg/cm²)	ρR_{cold} 1-D (mg/cm²)	ρR_{shell} (KB) (mg/cm²)	ρR_{shell} error (mg/cm²)
1.3(6)		199	0.67	0.64	0.05	0.78	31	6	67	93	18
2.3(5)		170	0.58	0.68	0.05	0.65	61	7	74	140	16
2.6(7)		268	1.03	0.76	0.05	1.03	26	5	76	92	18
1.3(7)		196	0.68	0.71	0.05	0.72	38	6	74	100	16
9.0(7)	127.3	320	1.19	1.02	0.03	1.19	8	1	89	29	4
1.5(6)	58.6	196	0.68	0.94	0.03	0.73	22	1	69	63	3
9.7(7)	128.6	312	1.22	1.04	0.03	1.30	13	1	58	71	5
1.4(6)	59.1	201	0.68	0.74	0.04	0.73	27	3	70	78	9
1.3(5)	43.5	165	0.54	0.62	0.03	0.60	52	7	76	113	15
2.4(7)	96.2	329	1.02	1.03	0.05	1.16	16	3	38	139	22
4.3(7)	117.4	323	1.11	0.81	0.07	1.19	0	3	111	0	
4.0(6)	72.9	254	0.75	0.72	0.04	0.85	16	2	91	45	6
9.3(5)	56.9	224	0.61	0.72	0.05	0.66	22	3	92	54	7
5.4(7)	123.1	346	1.25			1.30			150		
1.2(7)	95.1	338	0.88	0.86	0.09	0.89	29	4	179	54	7
6.6(6)	88.2	368	0.80	0.94	0.03	0.85	42	2	209	74	4

[shown for two different shell thicknesses, 20 and 25 μm, in Figs. 78.29(a) and 78.29(b)]. The low-energy portions of the spectra exhibit a marked difference indicative of lower compression for the DPP-only cases, despite the fact that the high-energy portions of the spectra are nearly identical. This indicates that conditions in the highest-temperature regions of the implosion (i.e., the gas-filled cores and inner edge of the shell) were unaffected by the different conditions obtained in the shell. Additionally, differences between the three pulse shapes are seen in the measured values of ρR_{cold} (Fig. 78.30). The shaped-pulse implosions have lower measured shell areal densities than with a square pulse (see Fig. 78.28), with the highest-contrast-pulse-shape implosions ($\alpha = 3$) having the lowest values. All DPP-only cases are lower than the comparison DPP+SSD cases.

The measured primary (D-D) neutron yields of the voided CD/CH targets for all pulse shapes are shown in Fig. 78.31(a). The ratios of the measured primary yield to the *LILAC*-calculated yield (normalized yield) are shown in Fig. 78.31(b). The primary yields obtained from implosions with 1-ns-square-pulse illumination follow a fairly well-defined trend with the highest yields obtained for the thinnest shells (highest calculated central temperatures and areal densities). Little difference is seen for the three uniformity conditions, indicative of the insensitivity of the shell/void interface to the illumination conditions employed. Lower absolute yields were obtained for the shaped-pulse implosions [Fig. 78.31(a)]; although, due to current OMEGA laser operation conditions, the maximum on-target energy is less for the shaped pulses (~21 kJ). Nevertheless, lower normalized yields were obtained for the
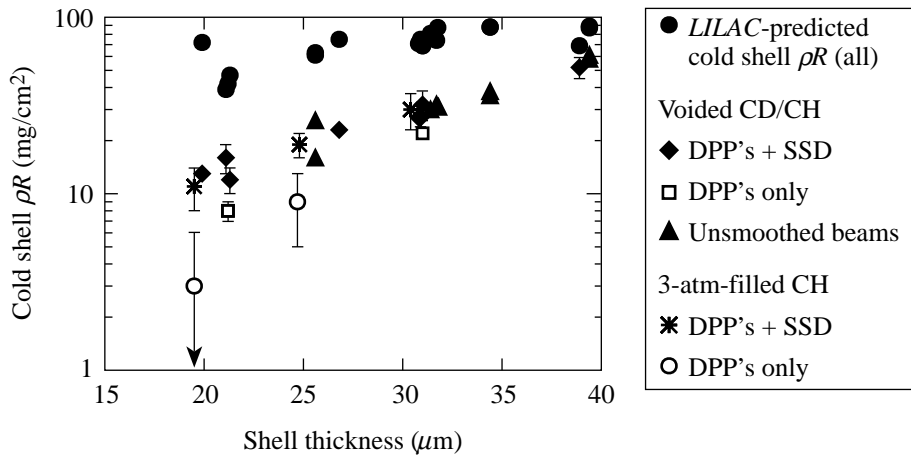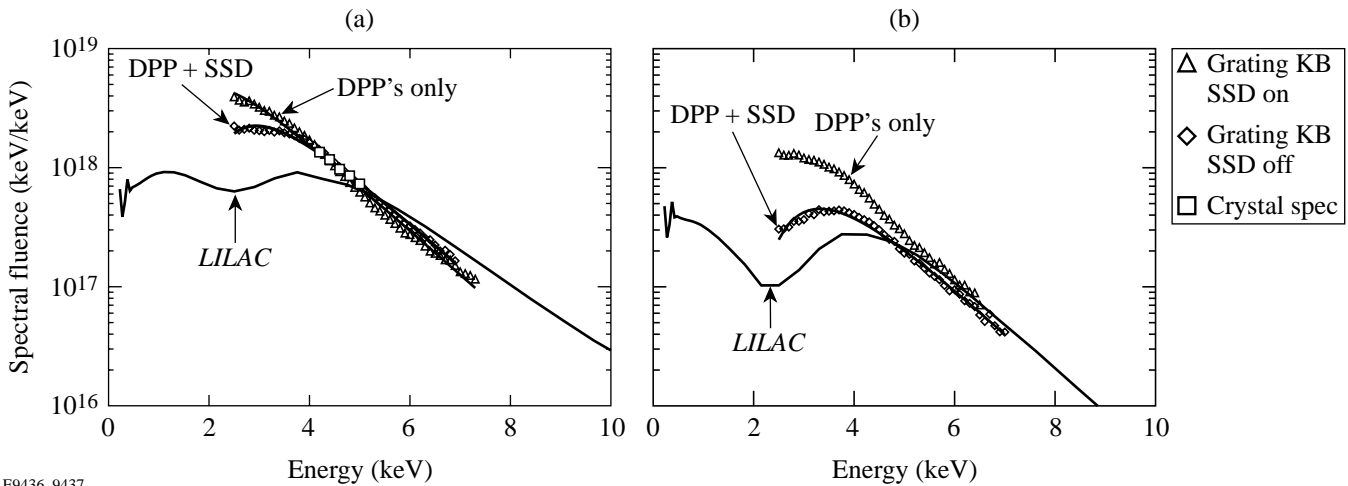

Figure 78.28
The measured values of ρR_{cold} for the voided CD/CH and 3-atm-filled CH targets from shots with 1-ns-square-pulse illumination. Cases of all three laser-beam conditions are shown: unsmoothed beams, DPP only, and DPP+SSD smoothed beams. The values of ρR_{cold} expected from *LILAC* simulations are also shown.

E9440
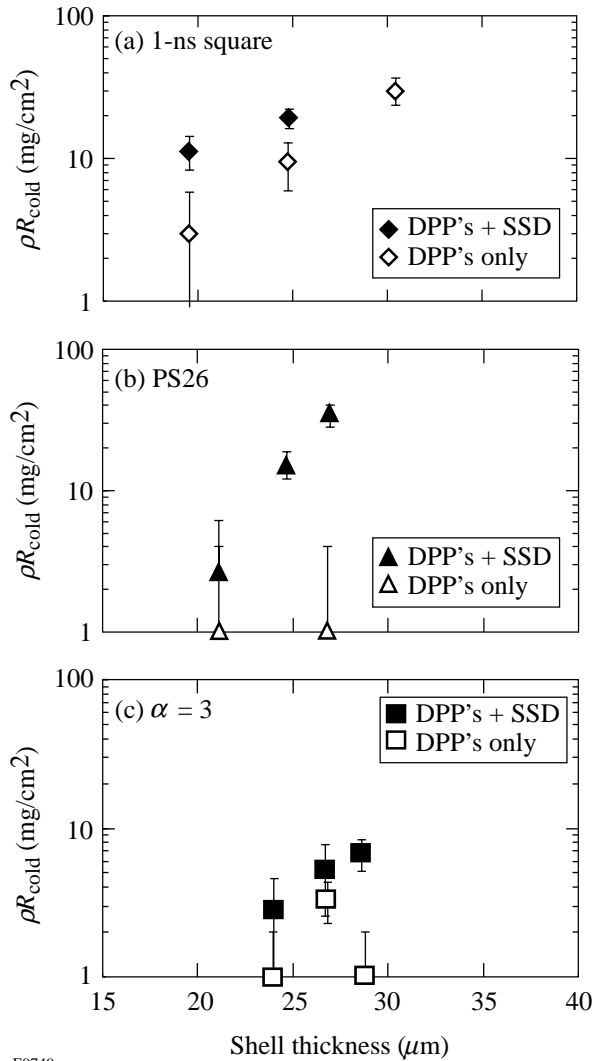

Figure 78.29
The measured and predicted core x-ray spectra from two DPP-only/DPP+SSD pairs of CH targets filled with 3 atm of D³He and imploded with 1-ns square pulses: (a) a 20-μm-thick pair and (b) a 25-μm-thick pair. Note the agreement between KB-microscope- and crystal-spectrometer-determined spectra in (a).

shaped pulses [Fig. 78.31(b)] with the lowest yield for the PS26 pulse shape.

Figures 78.32(a) and 78.32(b) show the measured primary and secondary neutron yields along with the *LILAC*-simulated yields for the voided CD/CH shells imploded with the 1-ns-pulse shape. Again the trend is to lower yields for thicker shells, with the measured yields for thicker shells closer to the simulated yields, indicating less disruption during implosion for the thicker shells. As discussed previously, a lower limit on ρR_{shell} is determined from the simultaneous measurements of primary (D-D) and secondary (D-T) neutron yield. Fig-

ure 78.33 shows the values so obtained for the voided CD/CH shells along with *LILAC* predictions of the measurements. The thinner targets have both higher measured and predicted ρR_{shell} values, opposite to the trend seen in the x-ray measurements, because of the larger range of tritons in the higher-temperature conditions, expected and obtained, for the thinner shells. Quite striking is the trend to lower ρR_{shell} for the thinner shells imploded with shaped pulses, which is lowest for the highest-contrast pulse shape ($\alpha = 3$). This again is indicative of shell disruption for the shaped-pulse implosions (resulting in lower apparent compression at the time of this measurement). The trend is similar to that seen for ρR_{shell} measurements obtained from the x-ray spectra (Fig. 78.29). The observed compression is less for the shaped-pulse implosions from both sets of measurements.

The combined measurements of ρR_{shell} from both the x-ray spectra and the primary-to-secondary-yield ratio for the voided targets are shown in Fig. 78.34. The dotted line and arrows indicate the lower limit on ρR_{shell} obtained from the
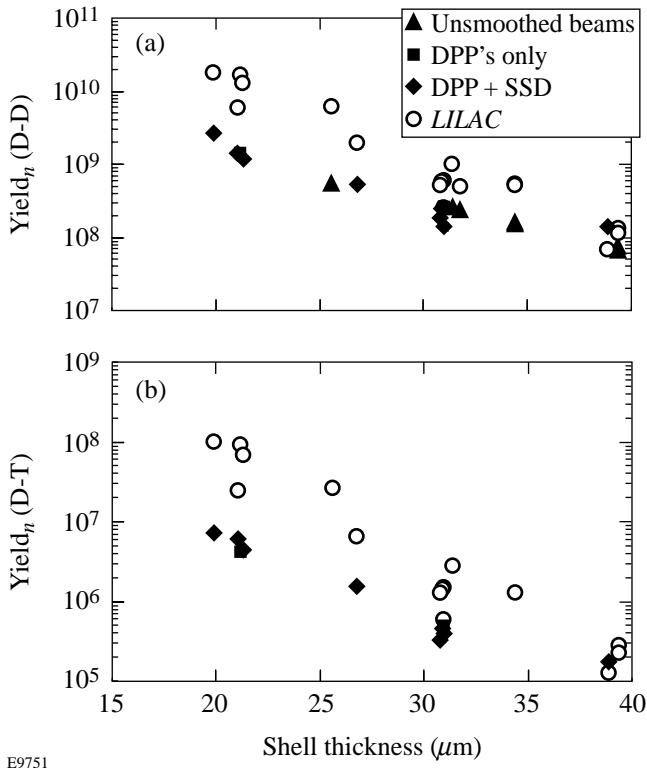

Figure 78.30
The measured values of ρR_{cold} for 3-atm-filled CH targets from shots with (a) 1-ns square, (b) PS26, and (c) $\alpha = 3$ pulse illumination.
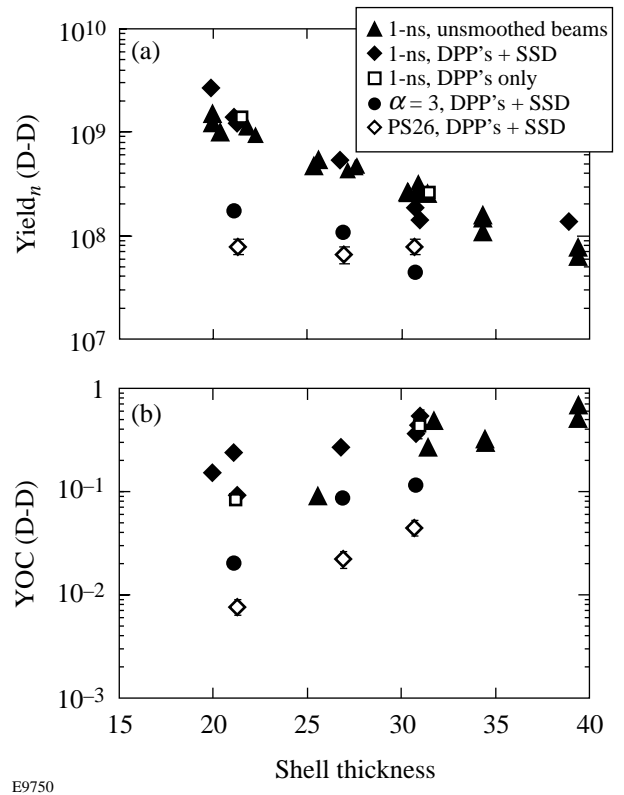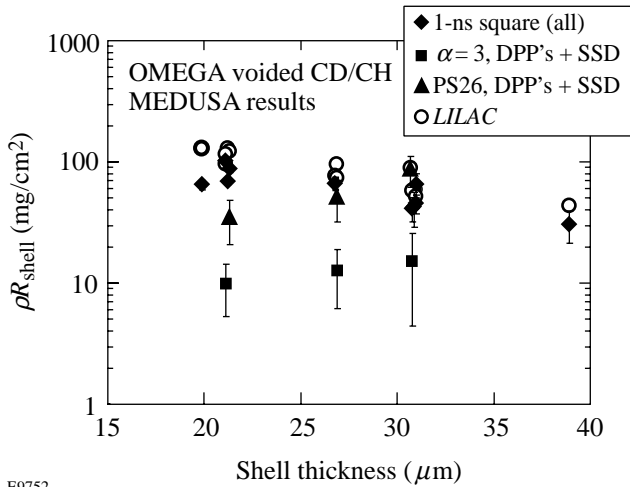

Figure 78.31
Measurements of the primary (D-D) neutron yield from voided CD/CH shells for all three pulse shapes versus shell thickness: (a) the absolute measured yield and (b) the normalized yield (measured/calculated).

E9751

Figure 78.32

Measurements of (a) primary (D-D) and (b) secondary (D-T) neutron yield from voided CD/CH shells imploded with 1-ns square pulses from the three beam-uniformity cases versus shell thickness. *LILAC* predictions of the measurements are also shown.
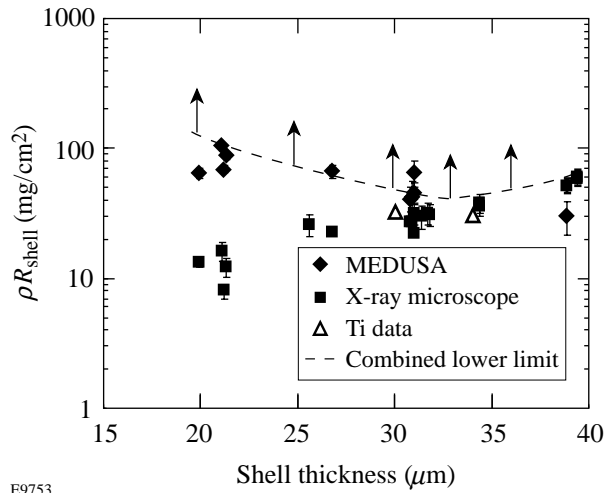
combined measurements. The estimates of ρR_{shell} obtained from Ti-doped shells as reported by Yaakobi and Marshall[15] are also shown (these values are lower limits as well). Both sets taken together indicate that ρR_{shell} in excess of ~60 mg/cm^2 has been obtained in every case. Assuming that the ionization state of the target is properly predicted by the hydrocode simulations, an estimate of the full ρR_{shell} can be determined by correcting the x-ray measurements of ρR_{cold} by the predicted ionization fraction. Values so determined are shown in Fig. 78.35. The estimated x-ray–averaged ρR_{shell} ranges from ~60 to 130 mg/cm^2.

Conclusions

In conclusion, we have performed experiments on hollow-shell (CD/CH and CH only), evacuated or low-pressure-filled (3-atm) targets with the OMEGA laser system demonstrating compression of the shell material (surrogate-cryogenic fuel) to areal densities of ~60 to 130 mg/cm^2. The survey of various implosion conditions (unsmoothed to smoothed beams; high-intensity, short-pulse shapes to ramped-intensity, longer-pulse shapes) has yielded information about the target performance as a function of illumination (laser drive) relevant to cryogenic-target experiments to follow. Specifically for a 1-ns square pulse and evacuated targets, the primary neutron yield from the core is not greatly affected by the differences in illumination uniformity at current levels; however, both the illumination uniformity and the initial shell thickness affect the final shell areal density. The thicker-shell targets compress to

E9752

Figure 78.33

The measured lower limits on ρR_{shell} of the voided CD/CH shells from MEDUSA measurements versus shell thickness for the various cases of pulse shape and beam uniformity. The values expected from *LILAC* simulations are shown for comparison.

E9753

Figure 78.34

Combined upper-limit values on ρR_{shell} of the voided CD/CH shells imploded by 1-ns square pulses determined from both the x-ray and neutron spectra. Additional measurements determined from Ti-doped targets are shown to give consistent lower limits.
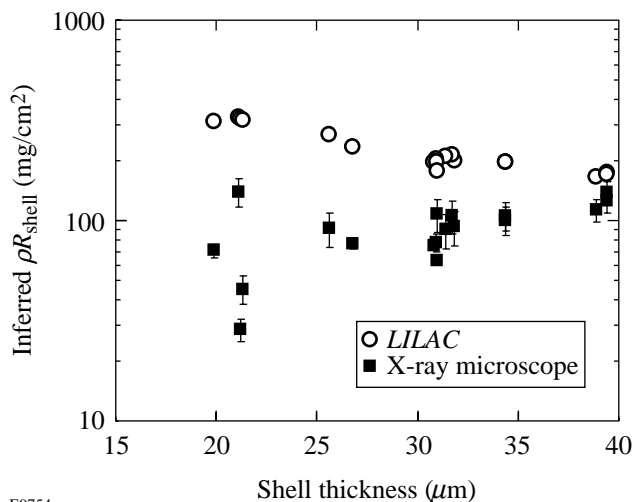
E9754

Figure 78.35
Estimates of ρR_{shell} for the voided CD/CH shells imploded by 1-ns square pulses determined from the lower limits (ρR_{cold}) given in Fig. 78.28. The values are determined assuming the ionization fraction predicted by *LILAC*.

areal densities as high as the thinner shells (at least as inferred by currently available techniques) despite the lower specific energy applied to the target, which implies that they are less affected by instabilities. All targets perform more poorly (lower yield, less compression) when imploded by the longer, shaped pulses because they have higher levels of laser imprint and lower ablative stabilization, which leads to large growth rates; thus, shaped-pulse implosions place more stringent requirements on power balance and initial target and illumination uniformity. For all pulse shapes, the gas-filled targets have the most significant increase in measured shell areal density when SSD is turned on (compared to DPP's only). This demonstrates the benefit of SSD in reducing the added instabilities that occur at the gas–shell interface. It is expected that as more-uniform illumination conditions are obtained, the thinner targets will outperform the thicker targets. This would be evidenced in higher neutron yields and higher areal densities as measured by x-ray and neutron spectral diagnostics.

ACKNOWLEDGMENT

REFERENCES

1. T. R. Boehly, D. L. Brown, R. S. Craxton, R. L. Keck, J. P. Knauer, J. H. Kelly, T. J. Kessler, S. A. Kumpan, S. J. Loucks, S. A. Letzring, F. J. Marshall, R. L. McCrory, S. F. B. Morse, W. Seka, J. M. Soures, and C. P. Verdon, Opt. Commun. **133**, 495 (1997).

2. T. J. Murphy, J. M. Wallace, N. D. Delamater, C. W. Barnes, P. Gobby, A. A. Hauer, E. Lindman, G. Magelssen, J. B. Moore, J. A. Oertel, R. Watt, O. L. Landen, P. Amendt, M. Cable, C. Decker, B. A. Hammel, J. A. Koch, L. J. Suter, R. E. Turner, R. J. Wallace, F. J. Marshall, D. Bradley, R. S. Craxton, R. Keck, J. P. Knauer, R. Kremens, and J. D. Schnittman, Phys. Rev. Lett. **81**, 108 (1998).

3. J. D. Kilkenny, in *Current Trends in International Fusion Research*, edited by E. Panarella (Plenum Press, New York, 1997), pp. 295–296.

4. M. D. Rosen, Phys. Plasmas **3**, 1803 (1996).

5. J. T. Hunt *et al.*, Lawrence Livermore National Laboratory, Livermore, CA, UCRL-JC-117399 (1994).

6. J. Nuckolls *et al.*, Nature **239**, 139 (1972).

7. R. E. Kidder, Nucl. Fusion **19**, 223 (1979).

8. J. M. Soures, R. L. McCrory, C. P. Verdon, A. Babushkin, R. E. Bahr, T. R. Boehly, R. Boni, D. K. Bradley, D. L. Brown, R. S. Craxton, J. A. Delettrez, W. R. Donaldson, R. Epstein, P. A. Jaanimagi, S. D. Jacobs, K. Kearney, R. L. Keck, J. H. Kelly, T. J. Kessler, R. L. Kremens, J. P. Knauer, S. A. Kumpan, S. A. Letzring, D. J. Lonobile, S. J. Loucks, L. D. Lund, F. J. Marshall, P. W. McKenty, D. D. Meyerhofer, S. F. B. Morse, A. Okishev, S. Papernov, G. Pien, W. Seka, R. Short, M. J. Shoup III, M. Skeldon, S. Skupsky, A. W. Schmid, D. J. Smith, S. Swales, M. Wittman, and B. Yaakobi, Phys. Plasmas **3**, 2108 (1996).

9. D. K. Bradley, J. A. Delettrez, R. Epstein, R. P. J. Town, C. P. Verdon, B. Yaakobi, S. Regan, F. J. Marshall, T. R. Boehly, J. P. Knauer, D. D. Meyerhofer, V. A. Smalyuk, W. Seka, D. A. Haynes, Jr., M. Gunderson, G. Junkel, C. F. Hooper, Jr., P. M. Bell, T. J. Ognibene, and R. A. Lerche, Phys. Plasmas **5**, 1870 (1998).

10. P. C. Souers, *Hydrogen Properties for Fusion Energy* (University of California Press, Berkeley, 1986).

11. The Department of Energy's designated target supplier for the U.S. ICF Program is General Atomics, Inc., San Diego, CA 92121-1194.

12. T. J. Kessler, Y. Lin, L. S. Iwan, W. P. Castle, C. Kellogg, J. Barone, E. Kowaluk, A. W. Schmid, K. L. Marshall, D. J. Smith, A. L. Rigatti, J. Warner, and A. R. Staley, in *Solid State Lasers for Application to Inertial Confinement Fusion*, edited by M. L. André (SPIE, Bellingham, WA, 1997), Vol. 3047, pp. 272–281.

13. S. Skupsky, R. W. Short, T. Kessler, R. S. Craxton, S. Letzring, and J. M. Soures, J. Appl. Phys. **66**, 3456 (1989).

14. F. J. Marshall, J. A. Delettrez, R. Epstein, and B. Yaakobi, Phys. Rev. E **49**, 4381 (1994).

15. B. Yaakobi, R. Epstein, and F. J. Marshall, Phys. Rev. A **44**, 8429 (1991).

16. J. P. Knauer, R. L. Kremens, M. A. Russotto, and S. Tudman, Rev. Sci. Instrum. **66**, 926 (1995).

17. B. I. Bennett *et al*., Los Alamos National Laboratory Report LA-7130 (1978).

18. W. F. Huebner *et al.*, Los Alamos National Laboratory Report LA-6760-M (1977).

19. B. Yaakobi and F. J. Marshall, J. Quant. Spectrosc. Radiat. Transfer **61**, 465 (1999).

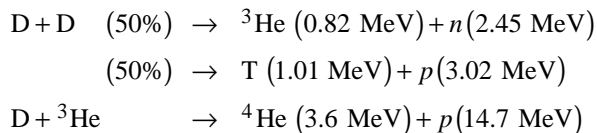20. H. Azechi, M. D. Cable, and R. O. Stapf, Laser Part. Beams **9**, 119 (1991).

Simultaneous Measurements of Fuel Areal Density, Shell Areal Density, and Fuel Temperature in D³He-Filled Imploding Capsules
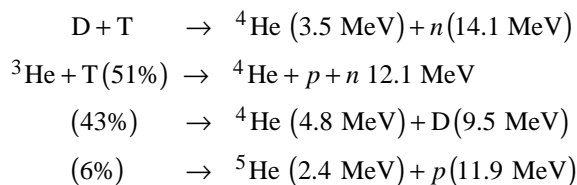
Measurements of the charged-particle products of the fusion reactions from an imploding inertial fusion capsule can provide a direct means of characterizing key aspects of the implosion dynamics. Parameters such as the fusion yield, fuel ion temperature, capsule convergence, fuel and shell areal densities, and implosion asymmetry can be inferred by these measurements and can complement and augment similar measurements made using fusion neutrons or x-ray techniques. In addition, such measurements provide unique information on charging up the target and on charged-particle acceleration. In collaboration with MIT and LLNL, LLE has developed two charged-particle magnetic spectrometers that have been implemented on OMEGA.

An initial application of these spectrometers to characterize the compressed capsule parameters involved the compression of capsules containing a mixture of deuterium (D_2) and helium-three (^{3}He). The fusion reactions arising from such a fuel include three primary and four secondary reactions:

Primary:

$$D + D \quad (50\%) \quad \rightarrow \quad ^3\text{He}\,(0.82 \text{ MeV}) + n\,(2.45 \text{ MeV})$$
$$(50\%) \quad \rightarrow \quad T\,(1.01 \text{ MeV}) + p\,(3.02 \text{ MeV})$$
$$D + {}^3\text{He} \quad\quad \rightarrow \quad ^4\text{He}\,(3.6 \text{ MeV}) + p\,(14.7 \text{ MeV})$$

Secondary:

$$D + T \quad\quad \rightarrow \quad ^4\text{He}\,(3.5 \text{ MeV}) + n\,(14.1 \text{ MeV})$$
$$^3\text{He} + T\,(51\%) \quad \rightarrow \quad ^4\text{He} + p + n \;\; 12.1 \text{ MeV}$$
$$(43\%) \quad \rightarrow \quad ^4\text{He}\,(4.8 \text{ MeV}) + D\,(9.5 \text{ MeV})$$
$$(6\%) \quad \rightarrow \quad ^5\text{He}\,(2.4 \text{ MeV}) + p\,(11.9 \text{ MeV})$$

The richness of particles and energies produced by the fusion of D^3He provides the opportunity for simultaneous measurement of several key capsule parameters. First, by measuring the ratio of D-D protons (or neutrons) to D^3He protons, the temperature of the fuel ions at burn time can be inferred. Figure 78.36(a) plots the ratio of the D-D to D-^{3}He reaction rate as a function of ion temperature. Second, the spectrum of the emergent fusion-produced protons will be affected by energy loss upon escape from the capsule. The 3-MeV D-D protons, for example, have a range of approximately 40 mg/cm^2, whereas the 14.7-MeV D-^{3}He protons have a range greater than 300 mg/cm^2 [see Fig. 78.36(b)]. Measurements of the slowing down of the charged particles therefore indicate the capsule's total areal density at burn time. In addition, the yield of neutron secondaries from the D-D reaction provides an independent measure of the fuel areal density. Thus, it is possible, in principle, to obtain simultaneous characterization of yield, fuel temperature, shell areal density, and fuel areal density by measuring the spectrum of fusion particles emerging from the implosion and burn of a D^3He–filled capsule. A series of such measurements carried out on OMEGA with the newly implemented charged-particle spectrometers (CPS) in conjunction with the single-hit neutron detector array (MEDUSA) provided information on the secondary reaction product yield for these experiments.

Spectrometer Description

The charged-particle spectrometer[1] consists of a 7.6-kG permanent magnet with CR-39 track-etch detectors.[2] A schematic of the magnet and sample particle trajectories is shown in Fig. 78.37. Constructed of a neodymium–iron–boron alloy with a steel yoke, this dipole magnet weighs 160 lb and has a long dimension of 28 cm and a 2-cm gap between pole faces. CR-39 pieces are positioned throughout the dispersed beam, normal to the particle directions, using the mounting structure shown in Figs. 78.38(a) and 78.38(b), which allows greater than 80% coverage between the proton-equivalent energies of 0.1 to 57 MeV. Accurate, and calibrated, particle trajectory calculations determine the energy of particles arriving at each position on the detectors. The presence of multiple particle species is conveniently managed since, at any given detector position, the track diameters from each species are clustered into discrete diameter groups—the heavier particles (such as alphas) having larger diameters than the lighter particles (such as protons)—and thus may be easily distinguished. Identifica-
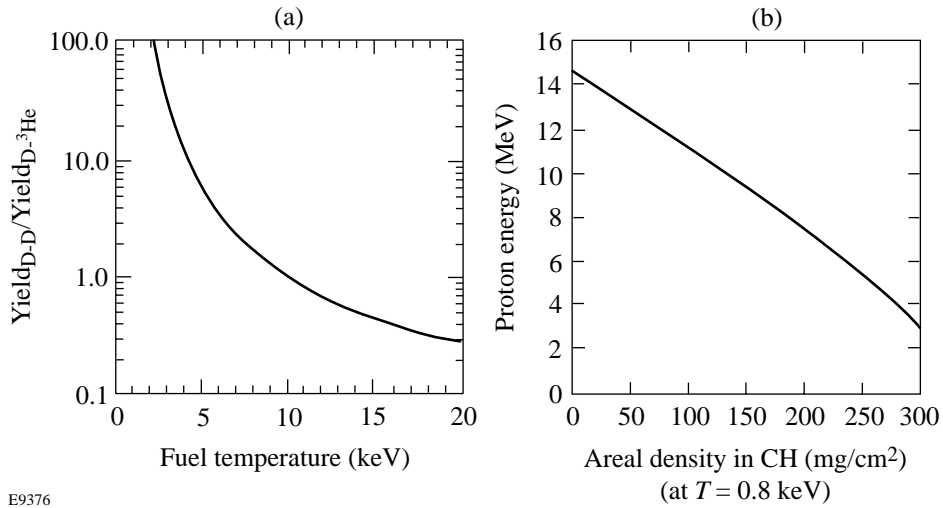
E9376

Figure 78.36

(a) Plot of the temperature dependence of the ratio of D-D fusion reactions to D-^{3}He reactions; (b) plot of the energy reduction as a function of areal density of 14.7-MeV protons traversing CH at a temperature of 800 keV.
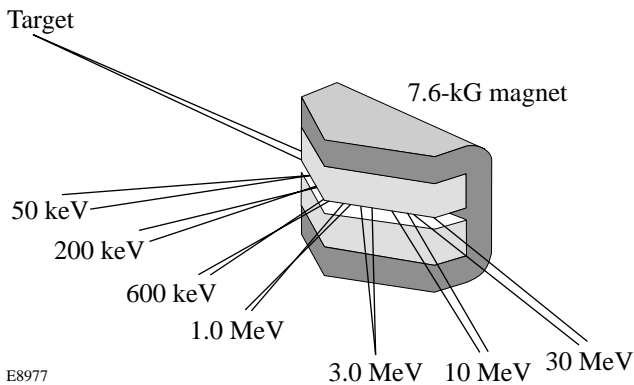

E8977

Figure 78.37

Schematic of the spectrometer and sample particle trajectories. A 7.6-kG pentagonal dipole magnet, 28 cm at its longest dimension, disperses protons in the range of 0.1 to 57 MeV. A linear array of CR-39 nuclear track detectors is placed normal to the dispersed beam. The large dynamic range of these detectors allows measurement of particle yields from 10^8 to 10^{17}.

E9738
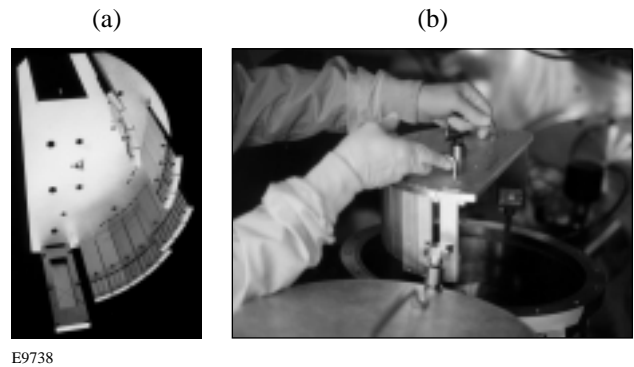
Figure 78.38

The mounting plate assembly that accurately positions pieces of CR-39 in the dispersion arc of the magnet. (a) The mounting plate assembly viewed from the perspective of the magnet. Pieces of CR-39 are positioned in each of the finger structures; these fingers are arranged in arcs that cover the dispersion region of the magnet. The finger at the bottom of the photo is positioned to view the target directly. X-ray film is placed at this position to ascertain the alignment of the spectrometer. The collimator slit is shown at the top of the photo. (b) The loaded mounting plate assembly being lowered onto the magnet (which is obscured) inside the vacuum chamber of CPS-1. After every shot, the mounting plate must be removed, and the CR-39 must be unloaded. A new, freshly loaded plate must then replace it in preparation for the next shot.

tion of each particle species is aided by using a track growth prediction model, calibrated to known particles and energies.

To assess the symmetry of all measurements, two virtually identical spectrometers are operating, one positioned inside the OMEGA chamber, at 100 cm from the target, and the other positioned outside, at 235 cm. The spectrometer inside the chamber is surrounded by a polyethylene-lead shielding structure designed to minimize the neutron noise levels on the CR-39. Incoming particles are collimated by a slit that can be varied from 1 to 10 mm wide, depending on the expected flux levels, giving solid angles between 10^{-6} and 10^{-5}. The measurement range of the instruments covers yields of 10^8 to more than 10^{17}, while the energy resolution is better than 4% over all energies. After every shot, the CR-39 detectors are removed from the spectrometer and replaced by a new set. The exposed detectors are then etched in sodium hydroxide and examined under a microscope. A rapid, automated scanning system has been developed that allows up to 10^6 tracks to be counted per shot.

Demonstration Experiments

Polymer ablator capsules, as illustrated in Fig. 78.39, were used to test the concept of simultaneous density and temperature measurements with D^{3}He–filled capsules. The principal diagnostics used for these experiments were the two charged-particle spectrometers, MEDUSA (to measure the fuel areal density via secondary reaction products[3]), and In activation (to measure the DD neutron yield).

In one series of shots, capsules of CH filled with a mixture of deuterium and ^{3}He were irradiated with up to 28.5 kJ in 1-ns near-square-top pulses with 2-D SSD beam smoothing. The capsule wall thickness ranged from 14.5 to 18.5 μm. Computer simulations of these implosions were performed using the one-dimensional hydrodynamic code *LILAC*,[4] and the spectra were calculated using the particle-tracking code *IRIS*.[5] The assumption of ideal performance (i.e., no mix, one-dimensional performance) in these simulations indicated that fuel ion temperatures in the range of 3.5 to 5.0 keV and capsule convergence ratios (ratio of initial target radius to compressed target radius) up to 28 could be achieved.

Figure 78.40 shows the measured proton spectrum obtained on one of these experiments. Table 78.V is a summary of the predicted and measured target parameters for this shot. The measured spectrum generally shows a greater slowing down for the thicker CH shells compared to thinner CH shells. This increased slowing down is apparent in the simulation results. The simulations, however, predict much larger areal densities, corresponding to an increased slowing down in the target, than are observed experimentally (Table 78.V), indicating departures from one-dimensional, unmixed implosions.
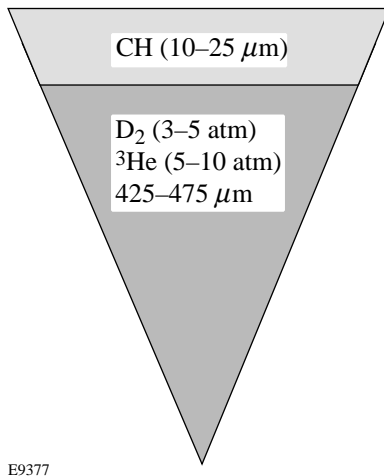

E9377

Figure 78.39
Polymer shell capsules filled with D^{3}He were used to test the CPS.
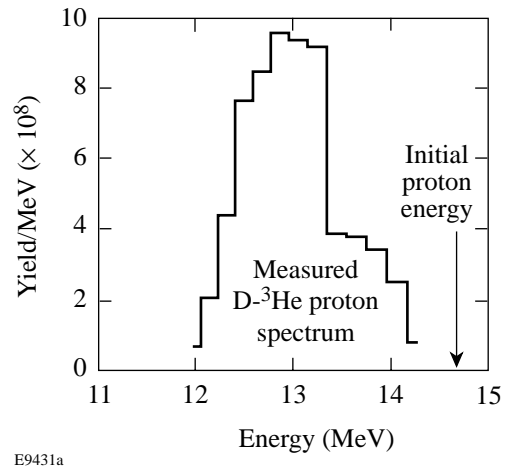

E9431a

Figure 78.40
D-^{3}He proton spectrum measured on shot 13799. For this shot the laser energy was 28.3 kJ (1-ns square pulse), and the CH ablator was 18.4 μm thick. The capsule was filled with 2.8 atm of D$_2$ and 4.9 atm of ^{3}He.

Table 78.V: Predicted and Measured Parameters—Shot 13799.

Parameter	Predicted	Measured/Inferred
D-D neutron yield	5.4×10^{10}	2.1×10^{10}
D-^{3}He proton yield	3.1×10^9	1.3×10^9
Fuel temperature	3.6 KeV	3.9 keV
Proton downshift	4.2 MeV	1.9 MeV
Shell areal density	120 mg/cm^2	60 mg/cm^2
Fuel areal density	32 mg/cm^2	13 to 17 mg/cm^2
Convergence ratio	28	16 to 18

The simulated fuel temperature in Table 78.V is well reproduced by the experiment. This is probably due to the fact that higher temperatures occur earlier in the implosion history of the target when capsule conditions are closer to one-dimensional predictions. The difference between the measured and calculated areal densities is probably due to the fact that the areal density is predicted to increase later in the implosion. In this later phase, the mixing of the fuel and the shell due to hydrodynamic instabilities can cause significant departures from one-dimensional behavior and can reduce the fusion burn significantly. This may be the principal cause of the observed discrepancy between simulation and experiment. More detailed modeling using either mix models or multidimensional hydrodynamic simulations is necessary to correlate the measured spectra with conditions in the target. This analysis is presently being carried on.

In conclusion, simultaneous measurements of the fuel areal density, shell areal density, and fuel temperature have been carried out on OMEGA using D^{3}He–filled imploding capsules and the recently installed charged-particle spectrometers. The initial experiments demonstrated the ability to carry out these measurements at fuel ion temperatures of 3 to 6 keV, fuel areal densities in the range of 10 to 20 mg/cm^2, and shell areal densities in the range of 40 to 60 mg/cm^2. Measurements such as these can be applied to the parameter region characteristic of cryogenic-fuel capsules on OMEGA: total areal density of several hundred mg/cm^2 and fuel temperature of several keV. In future experiments, we will extend such measurements to higher fuel and shell areal densities and attempt to validate these techniques on cryogenic-fuel targets.

REFERENCES

1. D. G. Hicks, C. K. Li, R. D. Petrasso, F. H. Seguin, B. E. Burke, J. P. Knauer, S. Cremer, R. L. Kremens, M. D. Cable, and T. W. Phillips, Rev. Sci. Instrum. **68**, 589 (1997).

2. T. W. Phillips *et al.*, Rev. Sci. Instrum. **68**, 596 (1997).

3. M. D. Cable and S. P. Hatchett, J. Appl. Phys. **62**, 2233 (1987), and references therein.

4. E. Goldman, Laboratory for Laser Energetics Report No. 16, University of Rochester (1973).

5. S. Cremer, *IRIS* – a particle-tracking Monte Carlo code, 1992 (unpublished).

The Design of Optical Pulse Shapes with an Aperture-Coupled-Stripline Pulse-Shaping System

Laser-fusion experiments require precise control of the temporal profile of optical pulses applied to targets. An optical pulse–shaping system has been in operation on OMEGA for several years.[1] During this time the demands on the precision, flexibility, and repeatability of the optical pulse–shaping system have steadily increased. To meet these new demands, a new pulse-shaping system based on an aperture-coupled stripline (ACSL) electrical-waveform generator has been developed and discussed previously.[2] This new system will be implemented on OMEGA in the next few months. In addition to its simplicity, the new system will include significant improvements to the modeling, performance, and diagnostics of the pulse-shaping system to meet the challenging demands required of the system. The shaped optical pulses produced by this system become the seed pulses that are injected into the OMEGA laser system. Details of the on-target pulse shape from the OMEGA laser are critically related to the details of the seed-pulse shape. This article describes the modeling of an ACSL pulse-shaping system that is used to produce an optical seed pulse with a specified temporal shape.

An ACSL generates temporally shaped electrical waveforms that are applied to electro-optic modulators to produce shaped optical pulses. The electro-optic modulators exhibit a finite response time to an applied voltage. This response time has been measured and is included in the calculation of the voltage waveform required from the ACSL to produce a specific optical pulse shape. An ACSL is modeled as two coupled and interacting striplines. Striplines are modeled as transmission lines that obey a set of equations known as the telegraph equations.[3] A new approach to solving the telegraph equations using the method of characteristics is presented here along with a straightforward extension of this approach to ACSL's. The modeling presented here leads to a prescription for determining the necessary ACSL geometry to produce a desired on-target pulse shape on OMEGA.

The Optical Modulator Voltage Waveforms

Given the temporal profile of the optical pulse required on target from the OMEGA laser, the temporal profile of the optical seed pulse that must be produced by the pulse-shaping system is determined from the extensive modeling of the laser system that has evolved over the years. As shown in Fig. 78.41, this low-energy optical seed pulse is shaped by applying shaped voltage waveforms to a dual-channel electro-optic amplitude modulator synchronous with the transit through the modulator of an optical pulse from a single-longitudinal-mode (SLM) laser.[4] If we neglect the finite response time of the modulator, the intensity profile of an optical pulse exiting a modulator is given by

$$I_{\text{out}}(t) = I_{\text{in}}(t)\sin^2\left\{\pi/2\left[V_1(t)/V_\pi + \phi_1\right]\right\}$$

$$\times \sin^2\left\{\pi/2\left[V_2(t)/V_\pi + \phi_2\right]\right\}, \qquad (1)$$

where $I_{\text{in}}(t)$ is the intensity profile of the optical pulse sent into the modulator from the SLM laser; the two sine-squared factors represent the transmission functions of the two modulator channels with $V_1(t)$ the voltage waveform applied to channel 1 of the modulator, $V_2(t)$ the voltage waveform applied to channel 2 of the modulator, V_π the half-wave voltage of the modulator (typically less than 10 V), and ϕ_1 and ϕ_2 the offsets
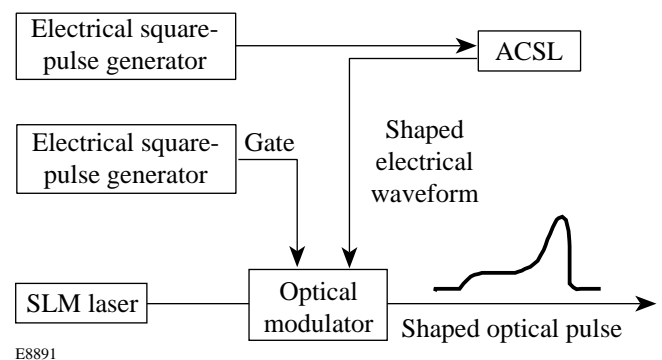
Figure 78.41
The aperture-coupled-stripline (ACSL) optical pulse–shaping system. The output from an electrical square-pulse generator is temporally shaped by an ACSL and used to drive an optical modulator. A separate electrical square-pulse generator is used to gate the second channel of the modulator.

set to zero by the application of a dc bias to each of the modulator channels. The input intensity profile to the modulator is assumed to be unity for our application since the short-duration (<5 ns) voltage waveforms $V_1(t)$ and $V_2(t)$ are applied to the modulators during the peak of the 200-ns Gaussian optical pulse from the SLM laser.

On one channel of the modulator, a shaped electrical waveform from an ACSL is applied. The exact shape of the voltage waveform required from the ACSL is determined by the shape of the optical pulse required from the modulator and by the response of the modulator to an applied voltage. This channel is referred to as the shaping channel of the modulator. On the other channel of the modulator, a square electrical waveform is applied. This channel is intended to produce a square optical waveform that acts as a gate to block unwanted pre- and post-pulses from the modulator and enhances the contrast of the output shaped optical pulse from the modulator. This channel of the modulator is referred to as the gate channel. The optical pulse produced by the gate channel should ideally have a fast rise and fall time with constant amplitude over its duration. The application of a square electrical pulse (with 45-ps rise time) to this channel from a pulse generator (Model 10,050A from Picosecond Pulsed Laboratories, Boulder, CO) produces the optical pulse shape shown in Fig. 78.42. This figure reveals the bandwidth limitations of the modulator for this "ideal" (high-bandwidth) square input electrical pulse. In particular, the optical pulse from this channel does not reach its full amplitude during the first 200 to 300 ps of the pulse, which, if not properly

compensated for, can cause pulse distortion on the beginning of a shaped optical pulse and severe pulse distortion for short-pulse generation. This distortion caused by the modulator bandwidth limitation is minimized by including this effect when calculating the voltage waveform applied to the modulator's shaping channel as discussed below.

Numerical Solution of the Telegraph Equations

Transmission line problems can be classified into two categories. The first category deals with determining the transmission line properties required to produce a specific electrical waveform reflected from the line, given the input electrical waveform to the line. The second category is the reciprocal of the first and deals with determining the electrical waveform reflected from a transmission line, given the input electrical waveform to the line and the properties of the transmission line.

In the present OMEGA pulse-shaping system, shaped electrical waveforms are generated by the reflection from a variable-impedance micro stripline and sent to the shaping channel of the modulator.[2] The micro striplines are designed using a layer-peeling technique that treats the micro stripline as a simple transmission line.[5] This technique allows one to calculate the reflection coefficient along the line (and from that the electrode width) needed to synthesize a given electrical waveform in reflection. The reciprocal of this calculation is to determine the electrical waveform reflected from a transmission line given the reflection coefficient along the line. This latter calculation is discussed here and, in the next section, will be extended to include modeling ACSL's to generate shaped electrical waveforms.

In this section we develop the equations that describe the electrical waveforms propagating along a transmission line starting from the well-known telegraph equations for the line.[3] First we model a stripline or micro stripline as a transmission line that obeys the telegraph equations:

$$\frac{\partial v(x,t)}{\partial x} = -L(x)\frac{\partial i(x,t)}{\partial t}, \qquad (2a)$$

$$\frac{\partial i(x,t)}{\partial x} = -C(x)\frac{\partial v(x,t)}{\partial t}, \qquad (2b)$$

where v is the voltage along the line, i is the current flowing along the line, L is the inductance per unit length along the line, and C is the capacitance per unit length along the line. In these
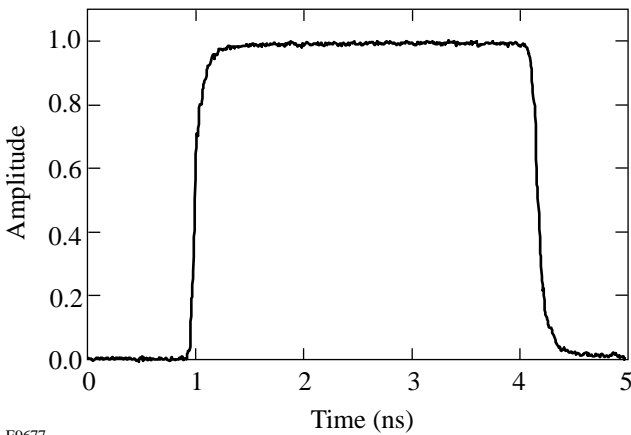
E9677

Figure 78.42
The measured optical pulse shape from a single channel of an electro-optic modulator with a square electrical waveform applied to the RF port. The square electrical waveform has a rise time of 45 ps.

equations we introduce the characteristic impedance of the line $Z(x) = \sqrt{L(x)/C(x)}$ and the wave propagation velocity $dx/dt = c = 1/\sqrt{LC}$ along the line. We assume that the propagation velocity c (not to be confused with the speed of light) along the line is constant. With these substitutions Eqs. (2) become

$$\frac{\partial V(x,t)}{\partial x} = -k(x)\,V(x,t) - c\,\frac{\partial I(x,t)}{\partial t}, \qquad (3a)$$

$$\frac{\partial I(x,t)}{\partial x} = k(x)\,I(x,t) - c\,\frac{\partial V(x,t)}{\partial t}, \qquad (3b)$$

where the variables are defined as

$$V(x,t) = v(x,t)\,Z^{-1/2}(x) \qquad (4a)$$

and

$$I(x,t) = i(x,t)\,Z^{1/2}(x) \qquad (4b)$$

and where

$$k(x) = \frac{1}{2Z(x)}\,\frac{dZ(x)}{dx} \qquad (5)$$

is the reflection coefficient per unit length along the line.

If we add and subtract Eqs. (3), we get a set of reduced wave equations

$$\frac{\partial WR(x,t)}{\partial x} + \frac{1}{c}\,\frac{\partial WR(x,t)}{\partial t} = -k(x)\,WL(x,t) \qquad (6a)$$

and

$$\frac{\partial WL(x,t)}{\partial x} + \frac{1}{c}\,\frac{\partial WL(x,t)}{\partial t} = -k(x)\,WR(x,t), \qquad (6b)$$

where

$$WR(x,t) = \big[V(x,t) + I(x,t)\big]/2$$

$$= \big[v(x,t)Z^{-1/2}(x) + i(x,t)Z^{1/2}(x)\big]/2 \qquad (7a)$$

is a wave traveling to the right along the line with velocity c and

$$WL(x,t) = \big[V(x,t) - I(x,t)\big]/2$$

$$= \big[v(x,t)Z^{-1/2}(x) - i(x,t)Z^{1/2}(x)\big]/2 \qquad (7b)$$

is a wave traveling to the left along the line with velocity c. In the appendix we show that the form of Eqs. (6) is identical to the form of the equation obtained if one substitutes a plane wave with slowly varying amplitude into the wave equation. Therefore, Eqs. (6) are referred to as the reduced wave equations and are the main results of this section. In the next section we show how to extend these equations to model an ACSL and give a numerical prescription for solving the resulting equations using the method of characteristics.

Extension to an ACSL

The geometry of an ACSL is shown in Fig. 78.43. In principle, an ACSL is a directional coupler consisting of two striplines that are coupled through an aperture in their common ground plane. In operation, a square electrical waveform is launched into port 1 and propagates along electrode 1 to the terminated port 2 of the ACSL. As the square electrical waveform propagates along electrode 1 in the coupling region, a signal is coupled through an aperture to electrode 2 in the backward direction and exits at port 4. The electrical waveform exiting port 4 is sent to the shaping channel of the modulator and must have the proper temporal profile to produce the desired optical pulse shape out of the modulator. By varying the width of the coupling aperture (shown in Fig. 78.43) along the length of the ACSL, a temporally shaped electrical waveform can be generated at port 4. The details of how to calculate the width of this aperture along the line to produce a specific electrical waveform from the ACSL are the main topic of this article.

The ACSL is modeled as two coupled transmission lines. We can extend the formalism in the previous section to an ACSL by writing four reduced wave equations. Two equations describe the waves $WR1(x,t)$ and $WR2(x,t)$ traveling to the right along lines 1 and 2, respectively, and two equations describe the waves $WL1(x,t)$ and $WL2(x,t)$ traveling to the left along lines 1 and 2, respectively. In each reduced wave equation we include the reflection coefficient $k(x)$ along the line as above, and we introduce a coupling term $C(x)$ that allows for coupling waves from one line to the other through the aperture.

The resulting equations are given by

$$\frac{\partial\,\mathrm{WR1}(x,t)}{\partial x} + \frac{1}{c}\frac{\partial\,\mathrm{WR1}(x,t)}{\partial t}$$

$$= -k(x)\,\mathrm{WL1}(x,t) - C(x)\,\mathrm{WL2}(x,t), \qquad (8a)$$

$$\frac{\partial\,\mathrm{WL1}(x,t)}{\partial x} - \frac{1}{c}\frac{\partial\,\mathrm{WL1}(x,t)}{\partial t}$$

$$= -k(x)\,\mathrm{WR1}(x,t) - C(x)\,\mathrm{WR2}(x,t), \qquad (8b)$$

$$\frac{\partial\,\mathrm{WR2}(x,t)}{\partial x} + \frac{1}{c}\frac{\partial\,\mathrm{WR2}(x,t)}{\partial t}$$

$$= -k(x)\,\mathrm{WL2}(x,t) - C(x)\,\mathrm{WL1}(x,t), \qquad (8c)$$

$$\frac{\partial\,\mathrm{WL2}(x,t)}{\partial x} - \frac{1}{c}\frac{\partial\,\mathrm{WL2}(x,t)}{\partial t}$$

$$= -k(x)\,\mathrm{WR2}(x,t) - C(x)\,\mathrm{WR1}(x,t). \qquad (8d)$$

The coupling coefficient $C(x)$ is the coupling from one line to the other in the backward direction. In general, another coupling term should be added to the above equations to model coupling from one line to the other in the forward direction. This forward coupling term can be trivially added to this model; however, for directional couplers of this sort, coupling in the forward direction is negligible.

The reduced wave equations (8) for an ACSL [as well as Eqs. (6) for striplines] can be solved by transforming them along the characteristic curves

$$\xi = ct - x \quad \text{and} \quad \eta = ct + x. \qquad (9)$$
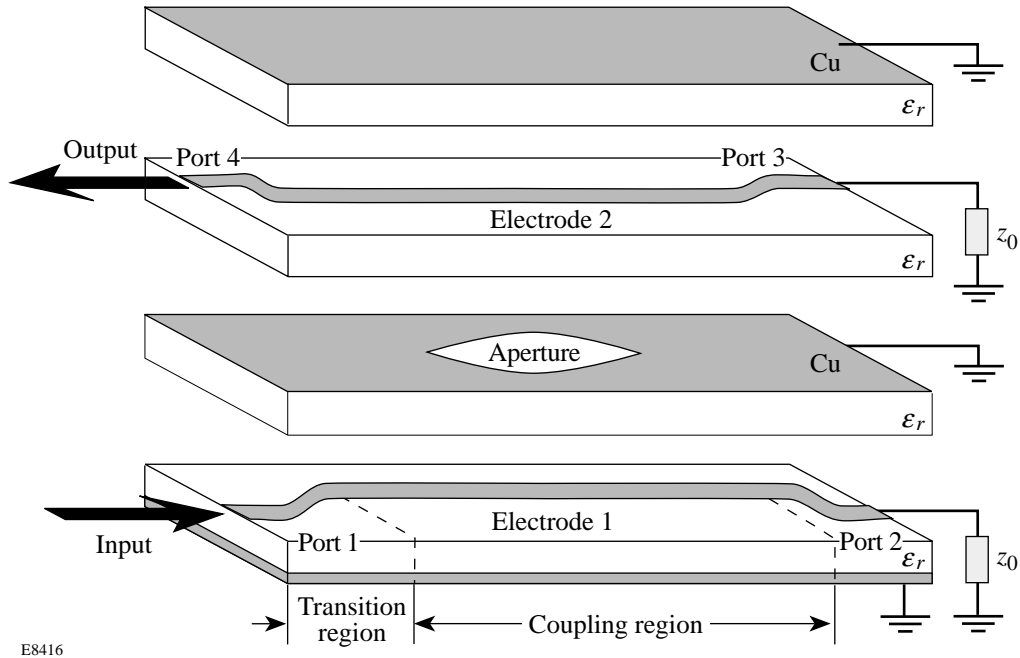
E8416

Figure 78.43
Exploded view of a practical four-layer, four-port ACSL. A square electrical waveform is launched into port 1 and propagates along electrode 1 to the terminated port 2. An electrical signal is coupled through an aperture to electrode 2 in the backward direction, and a shaped electrical waveform exits at port 4.

For this transformation we use the chain rules

$$\frac{\partial}{\partial x} = \frac{\partial}{\partial \xi}\frac{\partial \xi}{\partial x} + \frac{\partial}{\partial \eta}\frac{\partial \eta}{\partial x} = \left(-\frac{\partial}{\partial \xi} + \frac{\partial}{\partial \eta}\right) \quad (10a)$$

and

$$\frac{\partial}{\partial t} = \frac{\partial}{\partial \xi}\frac{\partial \xi}{\partial t} + \frac{\partial}{\partial \eta}\frac{\partial \eta}{\partial t} = c\left(\frac{\partial}{\partial \xi} + \frac{\partial}{\partial \eta}\right) \quad (10b)$$

to obtain

$$\frac{d\mathrm{WR1}(\eta)}{d\eta} = -\left[k(x)\mathrm{WL1}(\xi) + C(x)\mathrm{WL2}(\xi)\right]/2, \quad (11a)$$

$$\frac{d\mathrm{WL1}(\xi)}{d\xi} = \left[k(x)\mathrm{WR1}(\eta) + C(x)\mathrm{WR2}(\eta)\right]/2, \quad (11b)$$

$$\frac{d\mathrm{WR2}(\eta)}{d\eta} = -\left[k(x)\mathrm{WL2}(\xi) + C(x)\mathrm{WL1}(\xi)\right]/2, \quad (11c)$$

$$\frac{d\mathrm{WL2}(\xi)}{d\xi} = \left[k(x)\mathrm{WR2}(\eta) + C(x)\mathrm{WR1}(\eta)\right]/2, \quad (11d)$$

where we have used the fact that WR1,2 are waves propagating in the positive x direction and WL1,2 are waves propagating in the negative x direction and obey wave equations with solutions of the form

$$\mathrm{WR1,2}(x,t) = \mathrm{WR1,2}(ct+x) = \mathrm{WR1,2}(\eta) \quad (12a)$$

and

$$\mathrm{WL1,2}(x,t) = \mathrm{WL1,2}(ct-x) = \mathrm{WL1,2}(\xi). \quad (12b)$$

With this transformation the derivatives in Eqs. (11) become total derivatives.

The coordinate transformation expressed by Eqs. (9) lends itself to a simple geometric interpretation that leads to a numerical solution algorithm for the reduced-wave Eqs. (11). The transformation Eqs. (9) with $dx = cdt$ can be seen to be a rotation of the x,ct coordinate system by 45° into the ξ,η coordinate system as shown in Fig. 78.44. In the new ξ,η coordinate system, Eqs. (11) describe how the right-going waves WR1,2 evolve in the η direction and how the left-going waves WL1,2 evolve in the ξ direction. The differential ele-

ment in this new system is seen to be

$$d\eta = \frac{\partial \eta}{\partial x}dx + \frac{\partial \eta}{\partial t}dt = dx + cdt = 2dx, \quad (13)$$

where we have used $dx = cdt$. To solve Eqs. (11) numerically, we define a matrix as shown in Fig. 78.44 for each of the four waves and write the finite difference equations

$$\mathrm{WR1}(i,j) = \mathrm{WR1}(i-1,j-1)$$

$$-\left[k(i)\mathrm{WL1}(i+1,j-1) + C(i)\mathrm{WL2}(i+1,j-1)\right]dx, \quad (14a)$$

$$\mathrm{WL1}(i,j) = \mathrm{WL1}(i+1,j-1)$$

$$-\left[k(i)\mathrm{WR1}(i-1,j-1) + C(i)\mathrm{WR2}(i+1,j-1)\right]dx, \quad (14b)$$

$$\mathrm{WR2}(i,j) = \mathrm{WR2}(i-1,j-1)$$

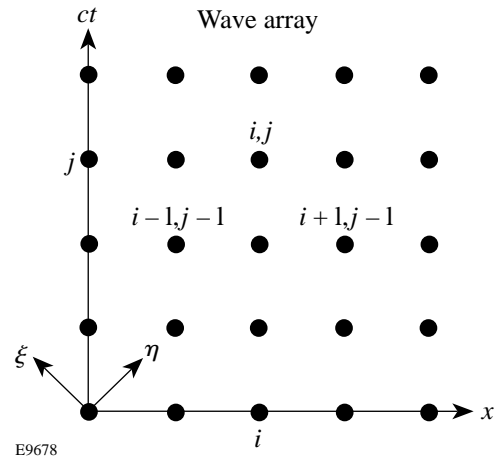$$-\left[k(i)\mathrm{WL2}(i+1,j-1) + C(i)\mathrm{WL1}(i+1,j-1)\right]dx, \quad (14c)$$

Figure 78.44
An array used by the numerical solution technique to represent a wave propagating along a transmission line. The value at each location in the array gives the amplitude of the wave at some fixed position along the line at some time. Four such arrays are used in the calculation to represent the four waves propagating in an ACSL.

$$WL2(i,j) = WL2(i+1, j-1)$$

$$-\left[k(i)WR2(i-1, j-1) + C(i)WR1(i+1, j-1)\right]dx, \quad (14d)$$

where the index i represents the position x along the line and the index j represents the time t. In these equations, for example, the value of the matrix element at the location i,j in the WR1 array is the amplitude of the wave WR1 at position x along the line at time t. Equations (14) give the values of the four waves at some time, given values of the waves at an earlier time and the reflection and coupling coefficients (k and C) along the line. Therefore, given the coupling coefficients and the initial values of the waves along the line (at $j = 0$ for all i) and the values of the waves at the boundaries for all time (at the first and last i value for all j), Eqs. (14) can be used to find all other values in the arrays. Knowing all values in the four arrays determines the amplitudes of the four waves at all locations along the line for all time. In particular, we specify the right-going wave on line 1 (the pulse from the pulse generator applied to port 1), and we calculate the left-going wave on line 2 (the pulse at port 4 that is applied to the modulator shaping channel). In the next section we show how to apply this technique to the design of optical pulse shapes from the ACSL pulse-shaping system.

Optical Pulse Shape Design/Performance

It is important to use actual measured waveforms or accurately modeled waveforms as input to the pulse-shaping model whenever possible to compensate for imperfections introduced by these waveforms that cannot be corrected by other means. The temporally shaped voltage waveform [V_2 in Eq. (1)] that must be produced by the ACSL and applied to the pulse-shaping channel of the modulator is calculated from Eq. (1). In Eq. (1), I_{out} is the desired temporally shaped optical pulse from the modulator, and the gate channel transmission function is modeled after data similar to that shown in Fig. 78.42. With these substitutions in Eq. (1), the required voltage waveform V_2 is determined, and an ACSL can be designed and fabricated to produce this voltage waveform.

The numerical solution described in the previous section allows one to calculate the electrical waveforms from all four ports of an ACSL given the reflection coefficient $k(x)$ and coupling coefficient $C(x)$ along the line. Experiments show that for any aperture width along the line, these coefficients are equal at each point along the line. To obtain a first approximation to these coefficients a modified version of the layer-peeling technique[5] is used. In the modified layer-peeling

technique, the effective reflection coefficient at each point along the line is calculated given the desired output electrical waveform from port 4 and given an ideal input square electrical pulse (i.e., square pulse with an infinite bandwidth) applied to port 1 of the ACSL. (The layer-peeling technique, unfortunately, has difficulties when using an actual measured electrical waveform as input to the line.) Using this first approximation for the reflection and coupling coefficients and using the measured electrical square pulse from the square-pulse generator (Model 4500E from Picosecond Pulsed Laboratories) as input to port 1 of the ACSL, the shaped voltage waveform exiting port 4 of the ACSL is calculated as described in the previous section. This calculated electrical waveform from port 4 of the ACSL is then compared to the required electrical waveform V_2 from this port; this comparison is then used to derive a second approximation to the coupling coefficients. This iteration process can be continued until the calculated output waveform from port 4 of the ACSL is identical to the required output waveform to any degree of accuracy (in practice, one iteration gives sufficient accuracy). Once the coupling coefficient C is determined in this way, the aperture width along the line is obtained from the relationship of the aperture width to the coupling coefficient shown in Fig. 78.45.[2]

E8893
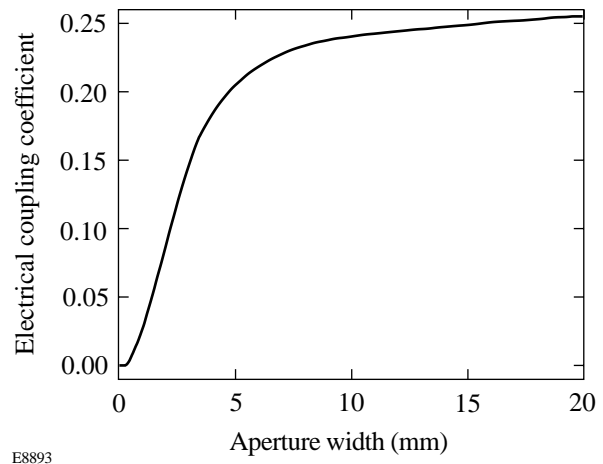
Figure 78.45
The electrical coupling coefficient, defined as the ratio of the output voltage at port 4 to the input voltage applied to port 1 shown in Fig. 78.43, plotted as a function of aperture width for an ACSL with the geometry discussed in the text.

Figure 78.46 shows the design of a specific pulse shape for the OMEGA laser. In Fig. 78.46(a), the design voltage waveform V_2 is compared to the measured voltage waveform from port 4 of the fabricated ACSL. In Fig. 78.46(b), the design optical waveform required from the modulator is compared

to the measured optical waveform from the modulator. Figure 78.46(c) shows the predicted on-target OMEGA UV pulse shape calculated from the measured optical pulse shape from the modulator [Fig. 78.46(b)] and compared to the desired on-target OMEGA UV pulse shape.

Summary

In conclusion, an ACSL pulse-shaping system will be implemented on OMEGA. A model has been developed that allows one to produce accurately shaped optical pulses suitable for injection into the OMEGA laser system. The ACSL electrical-waveform generator is modeled with a numerical solution of the telegraph equations using the method of characteristics. The model uses as input the measured electrical square pulse from the pulse generator used in the pulse-shaping system. The model also compensates for the pulse-shape distortion due to bandwidth limitations of the modulator introduced primarily by the gate pulse. The ACSL pulse-shaping system is a significant improvement over the existing pulse-shaping system currently on OMEGA because of its simplicity, enhanced performance and diagnostics, and improved modeling capabilities.

ACKNOWLEDGMENT

Appendix A: Derivation of the Reduced Wave Equation

In this appendix we derive the reduced wave equation that results by substituting a plane wave with slowly varying amplitude into the wave equation. For simplicity, we assume that the

Figure 78.46

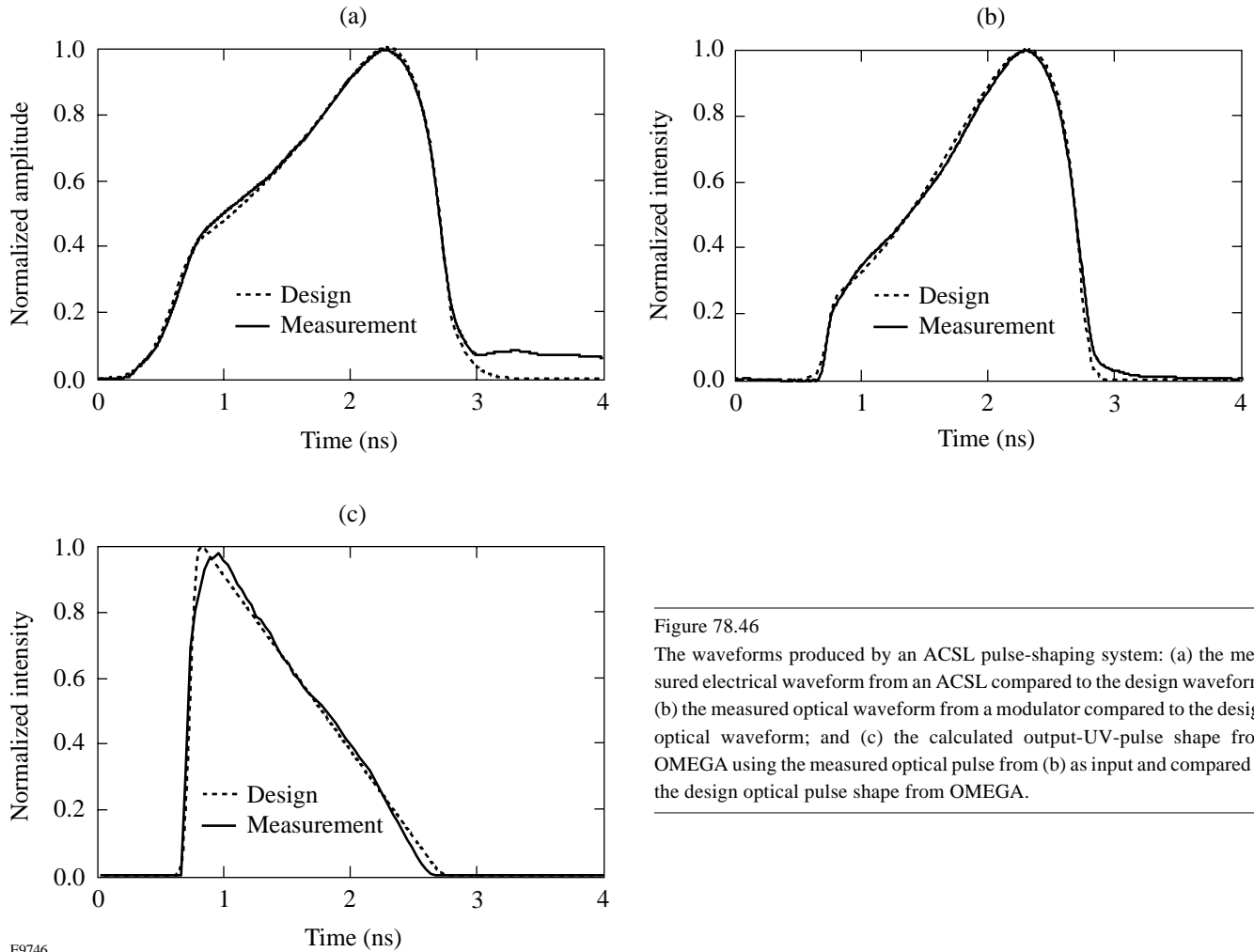The waveforms produced by an ACSL pulse-shaping system: (a) the measured electrical waveform from an ACSL compared to the design waveform; (b) the measured optical waveform from a modulator compared to the design optical waveform; and (c) the calculated output-UV-pulse shape from OMEGA using the measured optical pulse from (b) as input and compared to the design optical pulse shape from OMEGA.

E9746

wave is linearly polarized and propagating in the x direction in a nondispersive medium. The plane wave can be represented by

$$E_\pm(x,t) = A_\pm(x,t)\exp\left[i(\omega t \mp kx)\right] + \text{cc},\qquad \text{(A1)}$$

where $A_\pm$ is the complex amplitude of the wave, the upper sign representing a wave propagating to the right and the lower sign representing a wave propagating to the left; $\omega = 2\pi\nu$ is the angular frequency of the wave with frequency ν; $k = 2\pi/\lambda$ is the propagation constant of the wave with wavelength λ; and cc implies complex conjugate. The purpose of representing the waves in this form is to factor out the slow variations (the temporal profile of the electrical waveform) from the rapid oscillations (referenced to some microwave carrier frequency $\omega/2\pi$). The one-dimensional wave equation is given by

$$\frac{\partial^2 E_\pm(x,t)}{\partial x^2} - \frac{1}{c^2}\frac{\partial^2 E_\pm(x,t)}{\partial t^2} = 0,\qquad \text{(A2)}$$

where $c = \omega/k$ is the velocity of the wave. If we substitute A1 into A2, after some manipulation we get

$$\frac{\partial^2 A_\pm}{\partial x^2} \mp 2ik\frac{\partial A_\pm}{\partial x} - \frac{1}{c^2}\frac{\partial^2 A_\pm}{\partial t^2} + 2i\frac{\omega}{c^2}\frac{\partial A_\pm}{\partial t} = 0,\qquad \text{(A3)}$$

where we have used $c = \omega/k$ to eliminate terms. We now use the fact that the amplitude is slowly varying, that is

$$\frac{\partial A_\pm}{\partial x} \ll \left|kA_\pm\right|\qquad \text{(A4a)}$$

and

$$\frac{\partial A_\pm}{\partial t} \ll \left|\omega A_\pm\right|.\qquad \text{(A4b)}$$

Equation (A4a) implies that the amplitude of the wave does not change significantly over a distance of one wavelength λ, and Eq. (A4b) implies that the amplitude of the wave does not change significantly over a time duration of $1/\nu$. With these slowly varying amplitude approximations, Eq. (A3) reduces to

$$\frac{\partial A_\pm(x,t)}{\partial x} \mp \frac{1}{c}\frac{\partial A_\pm(x,t)}{\partial t} = 0.\qquad \text{(A5)}$$

This equation is the reduced wave equation referred to in the text.

REFERENCES

1. A. V. Okishev, W. Seka, J. H. Kelly, S. F. B. Morse, J. M. Soures, M. D. Skeldon, A. Babushkin, R. L. Keck, and R. G. Roides, in *Conference on Lasers and Electro-Optics, Vol. 11*, 1997 OSA Technical Digest Series (Optical Society of America, Washington, DC, 1997), p. 389.

2. Laboratory for Laser Energetics LLE Review **73**, 1, NTIS document No. DOE/SF/19460-212 (1997). Copies may be obtained from the National Technical Information Service, Springfield, VA 22161.

3. W. C. Johnson, *Transmission Lines and Networks*, 1st ed., McGraw-Hill Electrical and Electronic Engineering Series (McGraw-Hill, New York, 1950).

4. A. V. Okishev and W. Seka, IEEE J. Sel. Top. Quantum Electron. **3**, 59 (1997).

5. S. C. Burkhart and R. B. Wilcox, IEEE Trans. Microw. Theory Tech. **38**, 1514 (1990).

Measurement Technique for Characterization of Rapidly Time- and Frequency-Varying Electronic Devices

The conventional method for measuring the transfer function of an electronic device uses Fourier transform theory and convolutions and is, therefore, limited to either time-invariant or frequency-invariant devices. The measurement technique presented here enables the complete characterization of electronic devices having any dynamic temporal and spectral frequency response. A technique presented earlier[1] applied the windowing of signals in the time and frequency domains (called time-frequency distributions) to characterize photoconductive switches that vary in time *and* frequency; however, windowing requires a slowly varying envelope approximation, which limits the allowed rate of temporal and spectral variations. The more general technique allows us to measure the frequency response of the optoelectronic (photoconductive) microwave switches on OMEGA's pulse-shaping system. Unlike microwave diode switches, photoconductive switches do not have a constant conductive on-state, but rather decay monotonically to the off-state after the illumination ceases. A complete linear model for such a device must incorporate both filtering and modulation into a general time-varying filter (or equivalently, band-limited modulator). Any microwave or millimeter-wave device whose properties vary rapidly requires the application of this technique for complete characterization, including elements that depend on charge-carrier dynamics such as photoconductive attenuators, phase shifters, and directional couplers.

The general concept of a linear, time-varying filter is well established in the signal-processing,[2,3] communication,[4] and automatic control[5] fields. In the microwave-device field, however, the linear variations of filter properties are typically due to slowly varying mechanisms (e.g., mechanical) or are generated by rapid transitions between steady-state regimes (e.g., microwave diode switches); therefore, a form of windowing is usually adequate for characterization. The analysis presented here introduces a characterization technique analogous to (and a superset of) a form of input–output relationships called the scattering or *S* parameters, which can be applied to devices that can be considered linear filters with rapid modulation of amplitude and/or phase (e.g., photoconductive switches). In the next section we briefly discuss the complementary relationship between linear filters and linear modulators. From this conceptual viewpoint, we derive an extension of the filter and modulator characterization functions $S(\omega)$ and $k(t)$ to a general linear device characterization or system function $\tilde{S}(\omega, t)$. Based on the limitations of conventional *S*-parameter analysis in the **Mathematical Formulation** section, we present some important properties of the $\tilde{S}$ parameter and explain conditions under which this form of analysis can be implemented. In the **Analytical Example** section we apply our $\tilde{S}$-parameter concept to device analysis by considering a simplified lumped-element example, deriving the $\tilde{S}$ parameters from the theory and directly from the differential equations, and demonstrate the limitations of windowing. Photoconductive switches used on OMEGA pulse shaping have been optimized through the application of the $\tilde{S}$-parameter technique; these results will be presented in a separate article.

Background

Conventional microwave device characterization depends on shift-invariant device models for characterization, taking advantage of the property that a convolution in one domain Fourier transforms to multiplication in the other. In Table 78.VI the canonical input–output relationships of the two ideal shift-invariant microwave devices are presented to emphasize their complementary nature. All dependent variables are complex, $a(\omega)$ and $b(\omega)$ are the Fourier transforms of the respective input and output temporal power waves $A(t)$ and $B(t)$, $S(\omega)$ and $h(t)$ are the scattering parameter and its Fourier transform (the impulse response), k and K are the modulation parameter and its Fourier transform, and the subscripts refer to the microwave input–output ports of the device. The linear-frequency-invariant (LFI) model of a modulator is valid when narrow-band input signals (relative to the modulator bandwidth) are applied, and the linear-time-invariant (LTI) filter model is valid when the device's temporal variations are longer than the signal duration. Note that here and throughout this article, for the convenience of using notation familiar in measurement practice, we use ω for $j\omega$ and draw no distinction between real and analytic time-series signals.

Table 78.VI: A comparison of the transfer functions of shift-invariant devices: an ideal, linear-time-invariant (LTI) filter and frequency-invariant (LFI) modulator.

	Time Domain	Frequency Domain
Time-invariant filter	$B_i(t) = \int\limits_{-\infty}^{\infty} h_{ij}(t-\tau) A_j(\tau) d\tau$	$b_i(\omega) = S_{ij}(\omega) \cdot a_j(\omega)$
Frequency-invariant modulator	$B_i(t) = k_{ij}(t) \cdot A_j(t)$	$b_i(\omega) = \int\limits_{-\infty}^{\infty} K_{ij}(\omega-\xi) \cdot a_j(\xi) d\xi$

The analysis based on the equations in Table 78.VI cannot be applied to a device that is neither time invariant nor frequency invariant. As Fig. 78.47 indicates, a time-varying filter will have different impulse responses at different times [(b) and (c)], or equivalently a modulator with finite frequency response will modulate different frequencies differently [(d) and (e)]; so neither model in Table 78.VI is adequate for complete characterization. If the device can be held constant in one domain independently of the other, or if the variations are slow relative to the signal applied, conventional analysis can be applied by using some form of windowing; inaccuracies will depend on how strongly the LTI or LFI assumptions are violated. If the filtering and modulating aspects of this general linear device cannot be controlled independently (i.e., cannot be made separable) and the variations in time and frequency are rapid, characterization of the device under test (DUT) using either $k(t)$ modulator functions or $S(\omega)$ filter parameters cannot account for complete device behavior. Since conventional methods of linear microwave circuit characterization (e.g., spectrum and network analyzers) are based on the application of Fourier transforms and the convolution integral, their use can lead to incorrect or even misleading characterization results.

Motivated by these limitations, we combine the separate (but complementary) one-dimensional (1-D) LTI and LFI transfer functions to a single two-dimensional (2-D) transfer (or system) function, calling it $\tilde{S}(\omega,t)$ to emphasize its similarity to conventional $S(\omega)$ parameters. For illustration, a conceptual example of the amplitude of an exponentially decaying, low-pass filter is shown in Fig. 78.47(f). This 2-D parameter can be more difficult to measure than a conventional device's $S(\omega)$ parameters; however, the measurement process can be simplified by taking advantage of the 2-D nature of $\tilde{S}$ and using methods that are not applicable 1-D functions. For example, the theory of generalized projections as used in 2-D phase retrieval allows us to reconstruct the full, vector (complex) 2-D transfer function $\tilde{S}$ by measuring only the magnitude $|\tilde{S}|$. Although generalized projections are restricted to

functions that are zero outside some finite temporal and spectral window (i.e., that have known, compact support along both axes[6]), in practice the transfer functions of microwave devices satisfy this criteria.

$\tilde{S}(\omega,t)$ can be applied to device characterization in the *frequency domain* or the *time domain*. Conceptually, in the frequency-domain approach a single-frequency wave can be applied to the DUT for the time duration of interest, and then the temporal evolution of the resulting output signal's amplitude and phase can be recorded. Next, to separate the device's effect on signal amplitude and phase, the same input wave is applied, phase shifted by $\pi/4$, over the same time duration relative to the trigger, and again the temporal evolution of amplitude and phase is recorded (i.e., this is equivalent to measuring the analytic signal). Finally, by reapplying signals at different frequencies, a map of $\tilde{S}(\omega,t)$ can be generated for the DUT by constructing successive time slices at each frequency. Alternatively, in the time-domain approach a series of impulse functions can be applied at appropriate time intervals over the period of interest, and the impulse response corresponding to each input can be recorded. Although these descriptions are intuitively appealing, it may not be readily apparent how to extract an input–output relationship such as $\tilde{S}(\omega,t)$ from the measured signals, apply it to the calculation of output signals given an arbitrary input signal properly, and avoid the effects of windowing. The following analysis will clarify the technique and the method of calculation.

Mathematical Formulation

To derive a combined system function $\tilde{S}(\omega,t)$ that is capable of characterizing the input–output relationships of devices that are neither exclusively modulators nor filters and is easily determined by measuring the incident and emerging signals, we must revisit some of the assumptions used in microwave circuit/network analysis and synthesis. To emphasize the utility of our more generalized transfer function, we will frame our discussion in terms of filters and S-parameter characterization; however, the system function $\tilde{S}(\omega,t)$ sub-

sumes both LFI and LTI devices as special cases, so it is equally applicable to modulators. The route taken is motivated by the observation that, in the equations for filters and modulators presented in the previous section, the roles of time and frequency are complementary, i.e., the 1-D characterization functions are along orthogonal axes in the complex plane. From this comes the realization that a more general, 2-D characterization is possible by considering and measuring the device's response on the entire plane.

A convenient place to begin the derivation is with the time-domain differential equation describing a linear lumped-element device with time-variable coefficients:

$$\alpha_0(t)\frac{d^n}{dt^n}B(t) + \alpha_1(t)\frac{d^{n-1}}{dt^{n-1}}B(t) + \cdots + \alpha_n(t)B(t)$$

$$= \mathcal{L}(p,t)B(t) = A(t), \tag{1}$$

where the coefficients α are determined by the (time-varying) dependencies between the ports (e.g., the lumped-element models of resistance, capacitance, and inductance). The signals $A(t)$ and $B(t)$ are defined as in Table 78.VI, and we've used the operator notation

$$\mathcal{L}(p) = \alpha_0(t)p^n + \alpha_1(t)p^{n-1} + \cdots + \alpha_n(t),$$

where p is the differential operator d/dt.[7] Note that although the following derivation is for a device with a finite number of (time-varying) poles and zeros, $\tilde{S}(\omega,t)$, like $S(\omega)$, is equally applicable to distributed-element devices.

For the ideal filter model there is no time variation in the coefficients and Eq. (1) simplifies to

$$\mathcal{L}_{ij}(p)B_1(t) = A_j(t). \tag{2}$$

Assuming complex exponentials for the basis functions (so that the differential operator becomes ω) and converting to S-parameter notation $S_{ij}^{-1}(\omega) = \mathcal{L}_{ji}(p)$, we derive the frequency-domain filter transfer function of Table 78.VI, and the process is analogous for the ideal modulator model. The use of complex exponential basis functions as solutions in the transform integral leads to the formalism of Fourier transforms. Fourier transforms are useful for microwave-device characterization because they transform between a system of differential equations and a system of algebraic equations; that is to say they are *compatible* integral transform operators.[8] Non-compatible transforms do not result in simple convolution or multiplicative relationships between input and output ports.
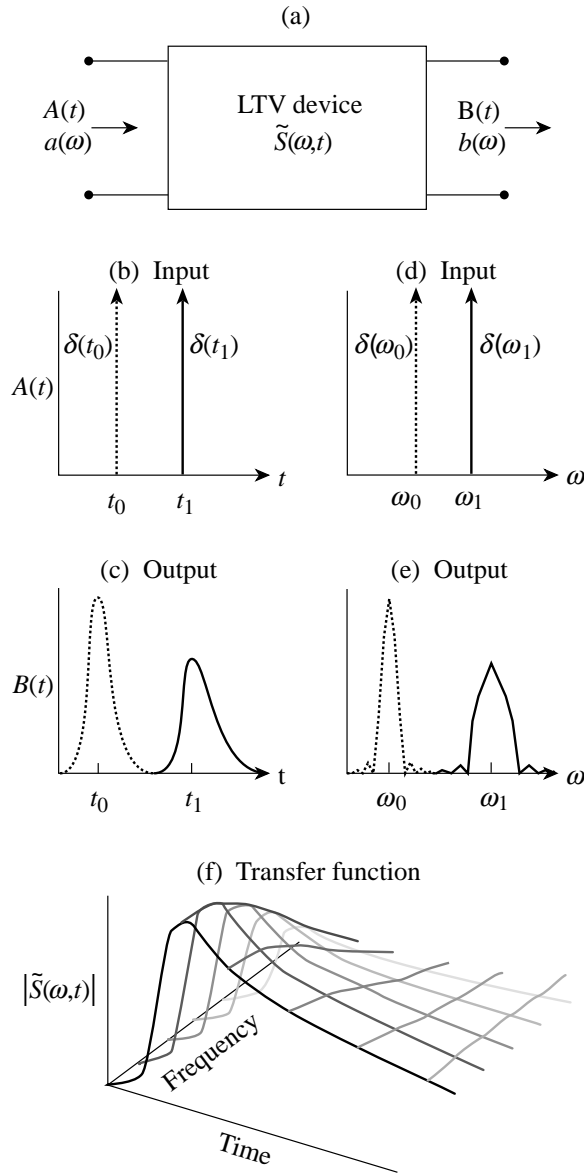
Figure 78.47

(a) Signal flow for a general linear-time- and frequency-varying device. Time variation is shown schematically by (b) identical impulses applied at different times, which result in (c) different impulse responses. Frequency variation is shown by (d) two different input sine waves and (e) differences in their modulated output spectral functions. (f) A representative sketch of the magnitude of the resulting transfer function $\tilde{S}(\omega,t)$ shows exponential time decay and low-pass filtering, such as might occur with OMEGA's photoconductive switches.

In contrast to ideal modulators and filters, for a general device a compatible integral transform operator depends on the functional form of the variable coefficients in Eq. (1). This means that the basis functions are not, in general, $e^{\pm j\omega t}$ but rather are dependent on the particular form of modulation and frequency response. To keep the analysis independent of the details of the modulation and frequency response, we will choose a noncompatible transform such that we are able to continue to use $e^{\pm j\omega t}$ basis functions; this is the key point of this characterization technique. Some important implications of this choice will be mentioned as we derive properties of the system function resulting from this choice of integral transform.

A definition of the general linear device system function is

$$\tilde{S}_{ij}(\omega,t) = \frac{B_i(t)}{A_j(t)}\bigg|_{A_j(t)=e^{j\omega t}}, \qquad (3)$$

which differs from the traditional S-parameter definition in that it is now a function of time as well as frequency. In addition $\tilde{S}_{ij}^{-1}(\omega,t) = \mathcal{L}_{ji}(p,t)$, where the differential operator p transforms to ω by differentiation of $e^{j\omega t}$; therefore, $B_i(t) = \tilde{S}_{ij}(\omega,t)e^{j\omega t}$ is the output of the device for an input $A_j(t) = e^{j\omega t}$, given that the device is in a known state at every time $t \geq t_0$ (i.e., the variable coefficients evolve deterministically from time $t = t_0$). Due to the linearity of the device, by superposition the output $B_i(t)$ is defined in terms of $A_j(\tau)$ according to

$$B_i(t) = \int_0^t \tilde{h}_{ij}(\tau,t) A_j(\tau)\,d\tau. \qquad (4)$$

Equation (4), where the impulse response function $\tilde{h}_{ij}(\tau,t)$ is now the more general Green's function, is a generalization of the time-invariant convolution in Table 78.VI in that the impulse response no longer depends only on the *age* from impulse time τ to observation t. Substituting Eq. (4) into Eq. (3) results in a transform relationship between the system function $\tilde{S}(\omega,t)$ and the new generalized impulse response $\tilde{h}_{ij}(\tau,t)$:

$$\tilde{S}_{ij}(\omega,t) = \int_{-\infty}^{\infty} \tilde{h}_{ij}(\tau,t)\,e^{-j\omega(t-\tau)}d\tau. \qquad (5)$$

Notice that (a) $\tilde{S}(\omega,t)$ and $\tilde{h}_{ij}(\tau,t)$ are related by a Fourier transform of the first axis and (b) two other system function definitions result from transforming each of these in the second

variable. We can visualize the fundamental difference between (a) these 2-D system functions that are characterizations of time- and frequency-varying devices and (b) system functions that are determined from windowed signals: the feature size of a 2-D system function (the mountains and valleys of the surface plot) along one axis is independent of the other axis, whereas (due to the uncertainty principle) the features of a system function along each axis generated by windowing are related to each other by the Fourier transform. In other words, a narrow windowing of a signal in time (necessary to prevent averaging of the system's time fluctuations) implies a widening of the spectral window (which forces averaging over spectral fluctuations), and vice versa. In the next section we show this difference in more detail by applying ambiguity functions and time-frequency distributions.[9–12]

From Eq. (4) we get a relationship between input and output by replacing $A_j(t)$ with its transform $\int a_j(\omega)e^{j\omega t}\,d\omega$, inverting the order of integration, and substituting from Eq. (5):

$$B_i(t) = \mathcal{F}^{-1}\left\{\tilde{S}_{ij}(\omega,t)\,a_j(\omega)\right\}, \qquad (6)$$

where the differential transform operator $\mathcal{F}^{-1}\{\ \}$ is essentially the inverse Fourier transform but with the variable t held as a constant parameter. Equation (6) is similar to the frequency-domain filter relation in Table 78.VI in that the signal $B(t)$ is the transform of the product of the S (or in this case $\tilde{S}$) parameter and the input spectral function. Unlike conventional Fourier transforms, however, Eq. (4) is not a convolution, and the argument inside the brackets of Eq. (6) is not the product of two 1-D functions; therefore, it is not possible to relate the output signal algebraically to the input signal:

$$b_i(\omega) \neq \tilde{S}_{ij}(\omega,t)\,a_j(\omega). \qquad (7)$$

Importantly, the complete function $\tilde{S}(\omega,t)$ cannot be found by taking a quotient $b(\omega)/a(\omega)$ as it can be when finding $S(\omega)$ for LTI devices. For network synthesis, where a model (or equivalently a differential equation) must be synthesized from a given (measured) $\tilde{S}(\omega,t)$ or $G(\tau,t)$, this consequence of non-compatible transforms has no major implications and in fact choosing the noncompatible Fourier transform allows one to use standard transform tables, making the synthesis easier. For network analysis, however, where the output $B(t)$ is found in terms of $A(\tau)$, the significance of Eq. (7) is that only simple linear time- and frequency-varying device models (having first- or second-order differential equations) can be used since

signal flow graphs and the combination of series and parallel devices are no longer algebraic or even analytic, as explained in the next paragraph.

For network analysis using $\tilde{S}(\omega,t)$ of microwave systems with time- and frequency-varying elements, the network must be broken down into block diagrams where the linear time- and frequency-varying element is isolated from the rest of the (conventionally analyzed) LFI or LTI components. The block diagram approach then requires operational methods that combine the general linear element with other components, both in cascade and parallel, to determine the overall system function. For two linear devices in parallel this is trivial; they can be combined by adding their impulse response functions, or equivalently adding their transfer functions.[13] For two devices in series, however, the combination depends on shift invariance: the overall transfer function of two LTI devices in series is accomplished by multiplying the individual transfer functions together, or equivalently convolving their impulse responses. For two LFI devices in series the transfer (modulation) functions are multiplied, while the spectral transform of the modulation is convolved.

To derive the transfer function of two general linear devices in series, we begin with the repeated operation of the transfer function (in operational form):

$$\tilde{S}(p,t)[a(\omega)] = \tilde{S}_b(p,t)\left\{\tilde{S}_a(p,t)[a(\omega)]\right\}, \qquad (8)$$

where $\tilde{S}_a(p,t)$ and $\tilde{S}_b(p,t)$ are the transfer functions for the first and second device, respectively, and $a(\omega) = e^{j\omega t}$ is assumed. Since $\tilde{S}_b(p,t)$ will operate on both $\tilde{S}_a(p,t)$ [now $\tilde{S}_a(\omega,t)$ due to the form of its operand] and $A(t)$, we get

$$\tilde{S}e^{j\omega t} = \tilde{S}_b\left(e^{j\omega t}\frac{\partial}{\partial t}\tilde{S}_a + \tilde{S}_a\frac{\partial}{\partial t}e^{j\omega t}\right)$$
$$\qquad\qquad (9)$$
$$= \tilde{S}_b\frac{\partial}{\partial t}\tilde{S}_a e^{j\omega t} + \tilde{S}_b\omega\tilde{S}_a e^{j\omega t}$$

and therefore

$$\tilde{S}(p,t)a(\omega) = \tilde{S}_b(p+\omega,t)\left[\tilde{S}_a(p,t)a(\omega)\right]. \qquad (10)$$

Analytical Example

To demonstrate the application of $\tilde{S}$ to microwave-device characterization, a representative lumped-element device will be solved analytically. The device shown in Fig. 78.48 is a single-pole, low-pass RC filter with a sinusoidally varying capacitive element $C(t) = C_0 + C_m\sin(\omega_m t)$, where suitable values of the variables are chosen for convenience: $C_0 = 1$ pF is the steady-state capacitance, $C_m/C_0 = 0.2$ is the modulation depth, and $\omega_m = 2.3$ Grad/s is the modulation rate.
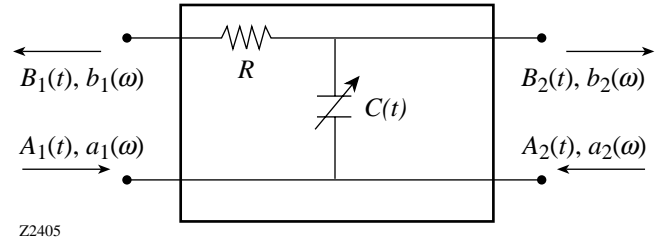

Z2405

Figure 78.48
An example linear device with a time-varying capacitance and therefore time-varying pole location (bandwidth). This device is linear but cannot be modeled as only a filter or a modulator.

The differential equation for this device, written in the form of Eq. (1), is

$$\left[\frac{1}{2}C(t)(R+Z_0)\right]\frac{d}{dt}B(t)$$
$$+\left[1+\frac{1}{2}R\Big/Z_0+\frac{1}{2}(R+Z_0)\frac{d}{dt}C(t)\right]B(t) = A(t). \qquad (11)$$

From S-parameter analysis the S_{21} for a conventional LTI filter like Fig. 78.48 is

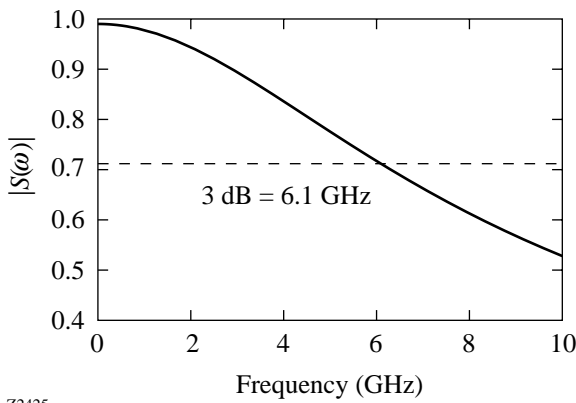$$S_{21}(\omega) = \frac{2Z_0}{2Z_0 + R + j\omega C Z_0(R+Z_0)}. \qquad (12)$$

Applying Eq. (10) to the cascade elements of the resistor and shunt capacitor, we get

$$\tilde{S}_{21}(\omega,t) = \frac{2Z_0}{2Z_0 + R + (p+j\omega)CZ_0\cdot(R+Z_0)}, \qquad (13)$$

which could also be found by directly solving the differential equation in Eq. (11). The $|S_{21}(\omega)|$ plot for the LTI version of this device (where the time invariant $C = C_0$) is shown in Fig. 78.49, and $|\tilde{S}_{21}(\omega,t)|$ is shown in the elevation plot of

Fig. 78.50 for one cycle of modulation. Observe in both figures the low-pass attenuation along the frequency axis and for Fig. 78.50 the sinusoidal modulation of the frequency response along the temporal axis.
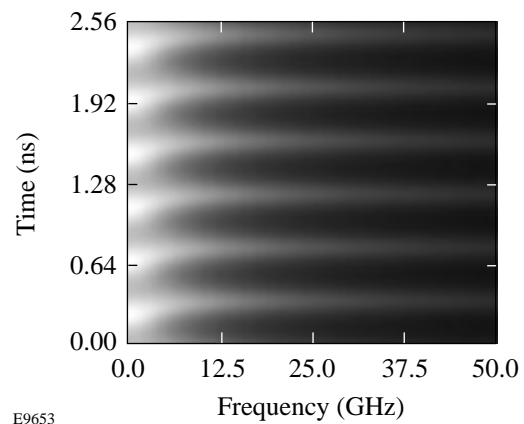
To further illustrate the properties of the time-varying system function we show a surface-density plot of $\left|\tilde{S}(\omega,t)\right|$ (Fig. 78.51) over several cycles of modulation and from dc to 50 GHz. Figure 78.51 will also be used in conjunction with the windowed signal to show the limitations of windowing. An aspect of this $\tilde{S}$ shown clearly here is the skew in the peak of the temporal modulation near the 3-dB point of 6.1 GHz, due to the phase shift in the transmission function that occurs at this frequency.

Figure 78.52 is a cross section of the transfer function along the time axis, showing the modulating aspect of the device, which is seen to be frequency dependent. The cross sections of $\left|\tilde{S}\right|$ along the frequency axis (Fig. 78.53) show the low-pass filter effect of the device and indicate that the shape of the frequency response depends on time. Although stability considerations are outside the scope of this article, both Figs. 78.52 and 78.53 indicate that the instantaneous magnitude can rise momentarily above unity, resulting in a gain in the system over a short time span and finite spectral band. Modulating the capacitance causes a transfer of energy in and out of the system, and with proper terminations it is possible to create an oscillator.


Z2425

Figure 78.49
Magnitude of the transfer function $\left|S_{21}(\omega)\right|$ of a low-pass, single-pole filter that is equivalent to the circuit in Fig. 78.48 but with no time-variation in the capacitance.

E9653

Figure 78.51
Surface-density plot of $\left|\tilde{S}(\omega,t)\right|$ for six cycles of modulation along the time axis and demonstrating low-pass filtering along the frequency axis.
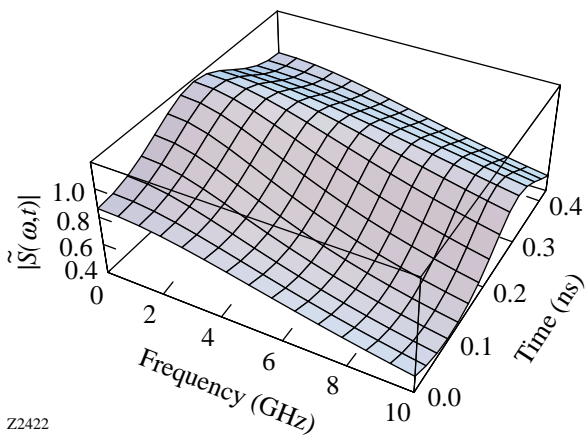
Z2422

Figure 78.50
Magnitude of the transfer function $\left|\tilde{S}_{21}(\omega,t)\right|$ of a low-pass, single-pole filter with sinusoidally varying capacitance, plotted over one cycle of modulation in time and over 150% of the bandwidth in frequency.
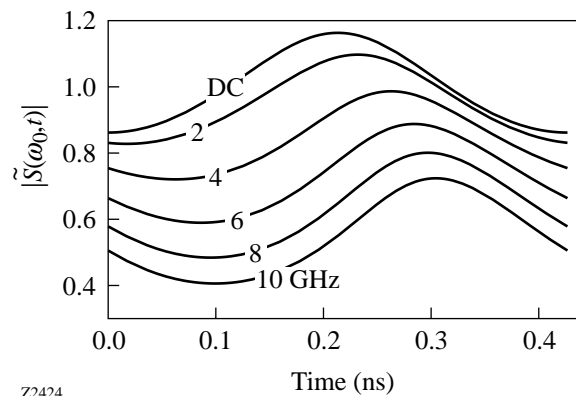
Z2424

Figure 78.52
A series of cross sections through $\left|\tilde{S}(\omega,t)\right|$ along the time axis, showing the change in the magnitude and phase of the modulation for different frequencies.

Using Eqs. (6) and (13) we simulated the propagation of the sum of 5.9- and 19.5-GHz sine waves through the device. The attenuation and dispersion of each spectral component are demonstrated in Fig. 78.54, where the low-pass features are readily apparent in the output signal (solid line) as compared with the input signal (dashed line). The influence of the modulation can best be compared in Fig. 78.55, where the sinusoidal modulation puts discrete sidebands on each spectral component; however, since only magnitude is plotted, the phase shift of the modulation between different frequencies cannot be observed. Since this device not only modulates each frequency differently but also filters the signals, application of network or spectrum analysis would not adequately characterize the device.
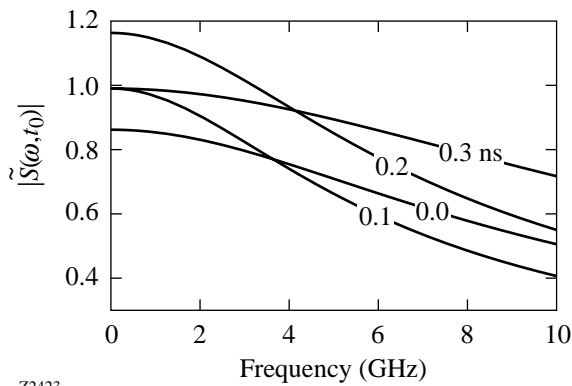
In the remainder of this section we use windowed signals in an attempt to adequately characterize our time-varying filter with conventional *S*-parameter analysis, and we compare the results to our previous approach. For the windowing we use time–frequency distributions because of their appealing representation, and because they more intuitively demonstrate the fundamental constraint; due to the uncertainty principle, a narrow windowing in time necessarily leads to a broad frequency window. This is seen on a time–frequency representation by the phenomenon of *minimum area*: a surface-density plot of the time–frequency distribution of a signal consists of areas (or regions) where the signal exists at a localized time and frequency, which cannot be smaller than a constant determined by the uncertainty principle. The uncertainty is inherent to windowing in general and not time–frequency distributions in specific, so therefore the choice of specific time–frequency distributions to demonstrate the uncertainty limitations of windowing doesn't detract from the generality of the result.

To demonstrate the limitations of windowing, the particular choice of algorithm to generate a time–frequency representation is a matter of convenience: for this example we will use

$$A(\omega;t) = \int_{-\infty}^{\infty} A(t)\,\omega\,e^{-j\omega^2(t-\tau)^2}\,dt, \qquad (14)$$

where $A(\omega;t)$ is the time–frequency distribution of $A(t)$ and a semicolon is used between the joint time–frequency variables to stress the dependence of the axes. This definition has the virtues of showing all the essential features of time–frequency

Z2423

Figure 78.53

A series of cross sections through $\left|\tilde{S}(\omega,t)\right|$ along the frequency axis, showing the change in instantaneous bandwidth at different times.
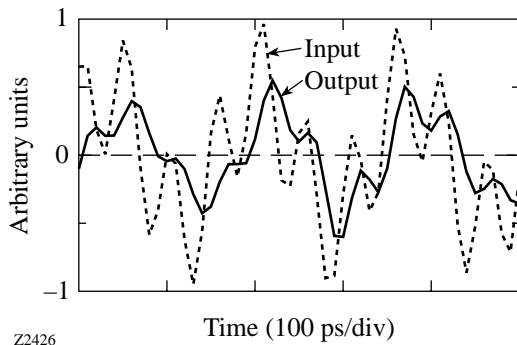

Z2426

Figure 78.54

Plot of input and output signals showing the DUT's low-pass filtering effect. Dashed line is the input signal; solid line is the output signal.
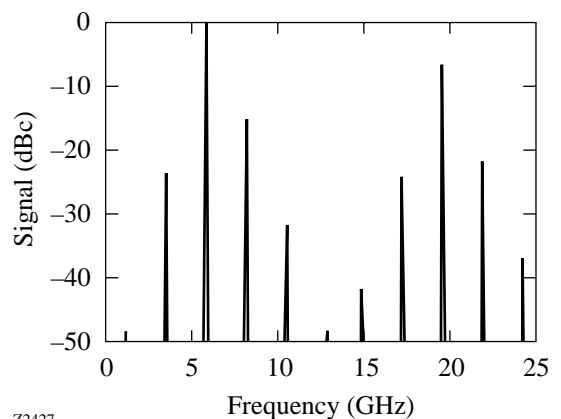

Z2427

Figure 78.55

Spectral plot of output signal, showing the change in modulation characteristics for different frequencies.

distributions and (due to the use of a Gaussian window) being easily transformable back into the Fourier transform of the signal $a(\omega)$ by integration:

$$a(\omega) = \int_{-\infty}^{\infty} A(\omega;t)\,\mathrm{d}t. \qquad (15)$$

Figure 78.56 shows an example windowed signal to be propagated through our system: a 2-GHz sine wave that abruptly transitions after 1.28 ns (with broadband noise) to a 20-GHz sine wave. The smearing of the signal in time (for the low-frequency signal) and frequency (for the high-frequency signals) due to windowing trade-offs (which are ultimately due to the uncertainty relationship) can be easily seen. The use of the FFT to generate the time–frequency distribution (which assumes a continuous, periodic signal) caused leakage to occur across the time boundary (top and bottom) of each spectral component of the signal; for the low-frequency signal, the leakage is significant enough to bridge the span over which it is ostensibly "off."
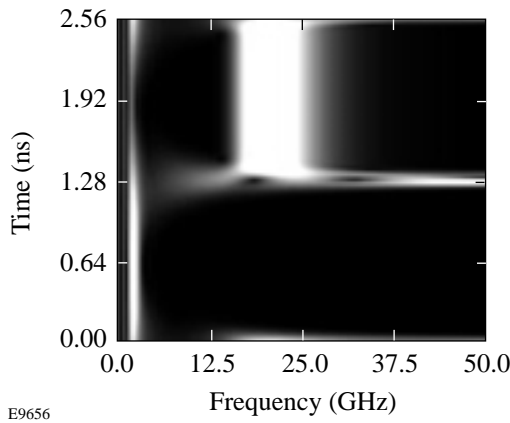

E9656

Figure 78.56
Time–frequency representation (ambiguity function) of a 2-GHz sine wave that transitions abruptly to a 20-GHz sine wave with broadband noise at the transition.

By multiplying the input signal $A_1(\omega;t)$ of Fig. 78.56 with the system function $\tilde{S}_{21}(\omega,t)$ of Fig. 78.51 we get the time–frequency distribution of the output signal $B_2(\omega;t)$ (shown in Fig. 78.57). Important features of the resulting output signal, as evidenced in the time–frequency distribution, are the significantly different modulation of each spectral component and the low-pass filtering, which attenuates the high-frequency component. Converting back to the time domain using Eq. (15) and then inverse Fourier transforming, we can com-

pare the resulting output signal with our technique. The windowing technique gives the solid line in Fig. 78.58, while our result is the dashed line. It is evident that although windowing produced acceptable results for the second half of the signal when the modulation was much slower than the signal (i.e., the slowly varying envelope approximation), for the first half of the signal, the modulation was comparable to the signal frequency so the window effectively smeared the modulation

E9654
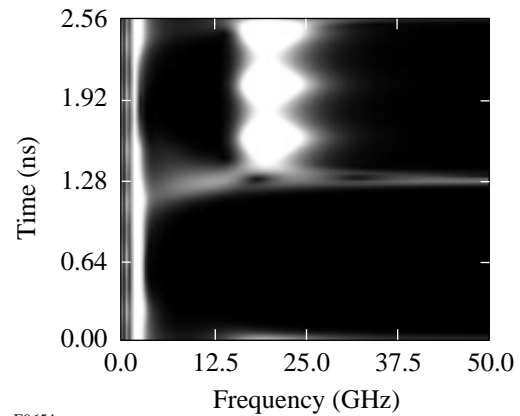
Figure 78.57
Time–frequency representation of the output signal, after multiplication of the input time–frequency distribution with the system function $\tilde{S}(\omega,t)$. The effect of the system function is shown by the attenuation of the broadband noise and the ripple in the two spectral components of the signal.

E9655

Figure 78.58
Time-domain comparison of output signals using the technique described in this article (dashed) and the windowing method (solid). The windowing appears acceptable for high-frequency signal component where the modulation is gradual, but it washes out the temporal modulation for the low-frequency component.

in time. Choosing a narrower window would not solve the fundamental problem since doing so would necessarily broaden the spectral window, causing increased smearing of the spectral response.
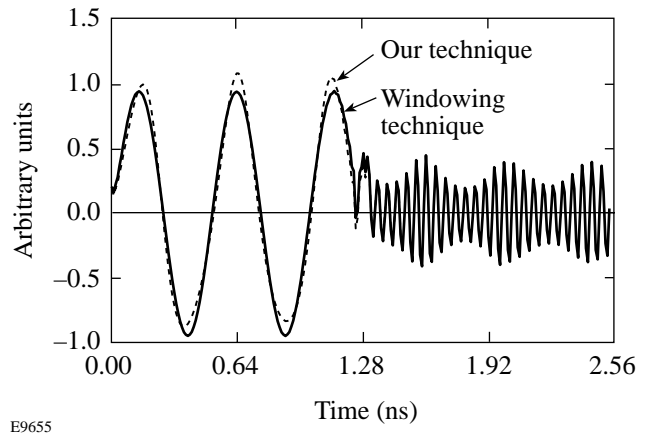
Conclusions

The goal of this work is to completely characterize photo-conductive microwave switches regardless of the temporal and spectral variations in their frequency response (transfer function). The unique photoconductive properties of these devices that enable their use in OMEGA's pulse-shaping system also require a characterization technique that accounts for the switch's frequency and time variations simultaneously. The analysis presented in this article provides such a characterization technique and is currently being applied to the switches to optimize their pulse-shaping performance. To characterize such devices, we take advantage of the complementary aspects of LTI and LFI 1-D transfer functions and combine them into a single linear device system function $\tilde{S}(\omega, t)$. This 2-D transfer function allows us to synthesize network models based on measurements of device responses that vary rapidly in frequency as well as time. We discussed several important properties of this new $\tilde{S}$ parameter, showing similarities to conventional S-parameter analysis that preserve most features of the familiar Fourier transform tables. The transfer function of an analytical linear time-varying device was calculated and compared to that of an LTI filter, and the utility of the $\tilde{S}(\omega, t)$ function concept was demonstrated while also showing the limitations of windowing.

REFERENCES

1. Laboratory for Laser Energetics LLE Review **76**, 225, NTIS document No. DOE/SF/19460-264 (1998). Copies may be obtained from the National Technical Information Service, Springfield, VA 22161.

2. G. W. Wornell, Proc. IEEE **84**, 586 (1996).

3. C. Bor-Sen, C. Yue-Chiech, and H. Der-Feng, IEEE Trans. Signal Process. **46**, 3220 (1998).

4. L. Heung-No and G. J. Pottie, IEEE Trans. Commun. **46**, 1146 (1998).

5. L. M. Silverman, IEEE Trans. Autom. Control **AC-16**, 554 (1971).

6. H. Stark, ed. *Image Recovery: Theory and Application* (Academic Press, Orlando, 1987).

7. G. H. Owyang, *Foundations for Microwave Circuits* (Springer-Verlag, New York, 1989), Chap. 10, pp. 541–606.

8. H. D'Angelo, *Linear Time-Varying Systems: Analysis and Synthesis*, The Allyn and Bacon Series in Electrical Engineering (Allyn and Bacon, Boston, 1970).

9. B. Boashash, Proc. IEEE **80**, 520 (1992).

10. H. N. Kritikos and J. G. Teti, Jr., IEEE Trans. Microw. Theory Tech. **46**, 257 (1998).

11. S. R. Kunasani and C. Nguyenj, IEEE Microw. Guid. Wave Lett. **6**, 1 (1996).

12. H. Ling *et al*., IEEE Trans. Antennas Propag. **41**, 1147 (1993).

13. W. Kaplan, Operational Methods for Linear Systems, Addison-Wesley Series in Mathematics (Addison-Wesley, Reading, MA, 1962), Chap. 2, pp. 64–103.

Damage to Fused-Silica, Spatial-Filter Lenses
on the OMEGA Laser System

Vacuum surface damage to fused-silica, spatial-filter lenses is the most prevalent laser-damage problem occurring on the OMEGA laser system. Approximately one-half of the stage-C-input and output, D-input, E-input, and F-input spatial-filter lenses are currently damaged with millimeter-scale fracture sites. With the establishment of safe operational damage criteria, laser operation has not been impeded. These sol-gel-coated lenses see an average fluence of 2 to 4 J/cm^2 (peak fluence of 4 to 7 J/cm^2) at 1053 nm/1 ns. Sol-gel coatings on fused-silica glass have small-spot damage thresholds at least a factor of 2 higher than this peak operational fluence. It is now known that the vacuum surfaces of OMEGA's spatial-filter lenses are contaminated with vacuum pump oils and machine oils used in the manufacture of the spatial-filter tubes; however, development-phase damage tests were conducted on uncontaminated witness samples. Possible explanations for the damage include absorbing defects originating from ablated pinhole material, contamination nucleated at surface defects on the coating, or subsurface defects from the polishing process. The damage does not correlate with hot spots in the beam, and the possibil-ity of damage from ghost reflections has been eliminated. Experiments have been initiated to investigate the long-term benefits of ion etching to remove subsurface damage and to replace sol-gel layers by dielectric oxide coatings, which do not degrade with oil contamination.

In this article, we discuss the implications of spatial-filter lens damage on OMEGA, damage morphologies, possible causes, and ongoing long-term experiments. The staging diagram depicted in Fig. 78.59 plots the peak design fluence (average fluence times 1.8 intensity modulation factor) at each stage of a single beamline on OMEGA; the bold lines indicate regions where spatial-filter lens damage is occurring.[1] These lenses are all fused-silica optics with a sol-gel-dipped, antireflection coating at 1053 nm. Several issues have been identified regarding these lenses. The first concern is the mechanical fracture of the lenses. As the damage continues to grow, a flaw-size criteria must be determined to prevent catastrophic lens failure (fracture into two pieces) and ensure safe laser operation. The damage morphology is important to understanding
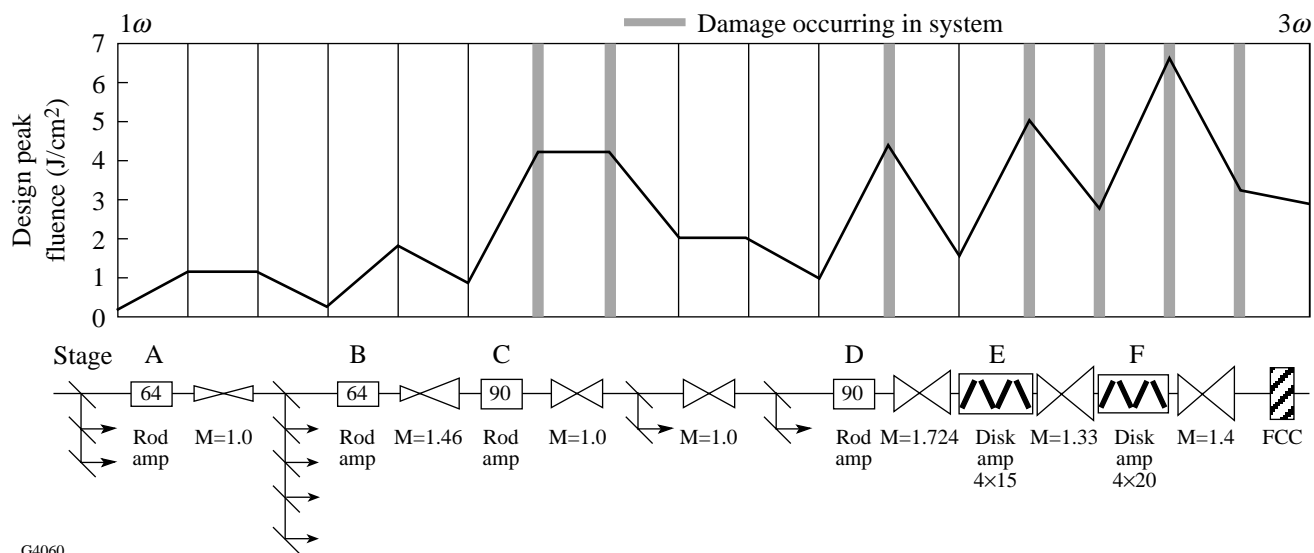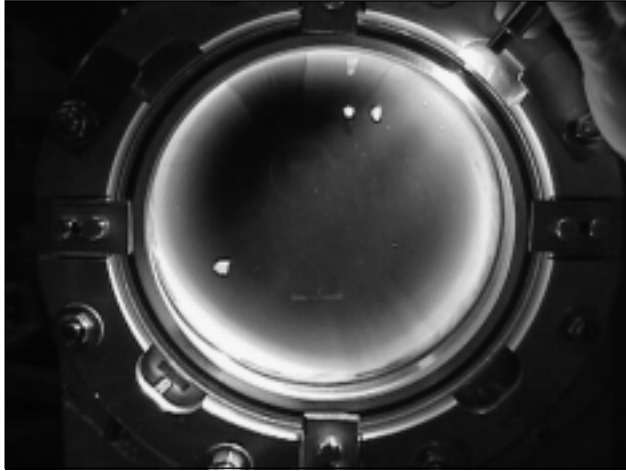

Figure 78.59
Peak design fluence plotted at each stage of the OMEGA laser. Operational laser damage is occurring at the high-fluence positions.

the initiator for large-scale fracture sites observed in Fig. 78.60 and discussed later in this article. A secondary and possibly related problem is the change in the sol-gel coating's reflectivity after exposure to the spatial-filter tube's vacuum environment. A few early experiments to investigate the damage cause are reviewed later.

G4745

Figure 78.60
An OMEGA stage-E-input, spatial-filter lens with multiple fracture sites. The largest site is approximately 10 mm.

Mechanical Fracture

The vacuum surface of an OMEGA spatial-filter lens is under tensile stress, and any damage to this vacuum surface can lead to catastrophic crack growth if a flaw reaches a size above the critical value a_c. The critical flaw depth a_c depends on the shape of the flaw with respect to the applied stresses and can be calculated with the following equation:[2]

$$a_c = \frac{(K_c)^2}{p(Ys)^2},$$

where K_c = fracture toughness of the glass, Y = geometrical factor of the flaw, and s = bending stress induced by atmospheric pressure p.

Actual defects on OMEGA spatial-filter lenses are shallow and elliptical in cross section, and these defects can be simulated with a half-penny–shaped defect ($Y = 1$), which has a surface diameter of twice the defect depth. This model assumes the defect to be located at the vacuum-side center of the lens where the tensile stresses are greatest; therefore, the critical-flaw-size calculations are a worst-case scenario. For an OMEGA

stage-F-input lens, 25 mm thick, 283 mm in diameter, and subjected to a tensile stress of 615 psi, calculation for a half-penny defect on the vacuum side of a lens yields a critical flaw depth of 10 mm. A defect of this size will be easily detected before catastrophic failure occurs.

Lens fracture on Nova and Beamlet was modeled at Lawrence Livermore National Laboratory (LLNL), arriving at a "fail-safe" lens-design criterion with two key parameters: (1) a peak tensile stress of less than 500 psi and (2) the ratio of thickness to critical flaw size of less than six.[3] The definition of a fail-safe lens requires catastrophic fracture to proceed without implosion. An implosion refers to the action of a spatial-filter lens fracturing into many pieces and then being accelerated into the evacuated volume inside the spatial-filter housing due to atmospheric pressure.[4] Given these conditions, a properly mounted window under full vacuum load will break into two pieces only, provided the air leak through the fracture is rapid enough to reduce the load on the window before secondary crack growth ensues. The list of LLE spatial-filter lens specifications in Table 78.VII indicates that all OMEGA spatial-filter lenses meet the criteria for a fail-safe optic. Data for LLNL optics are provided in Table 78.VIII. Based on radial-fracture observations in these optics, one may expect no more than a single radial fracture in an OMEGA spatial-filter lens.

If the model is correct, fully vacuum-loaded OMEGA lenses should not implode into multiple fragments when defects reach their critical flaw size but should crack into two pieces and lock together as long as the mount restrains the radial motion of the fragments. While there have been several hundred observations of damage on the vacuum side of OMEGA spatial-filter lenses, there have been no incidents of an OMEGA spatial-filter lens fracturing into two or more pieces. For safety reasons, OMEGA optics are removed when defects reach one-half their critical flaw size.

Damage Morphology

Operational damage to 1ω, fused-silica, spatial-filter lenses occurs exclusively on the vacuum side of the lens, regardless of the beam propagation direction, and is dominated by two damage morphologies originating at or near the surface. The first morphology is that of a massive fracture greater than 100 μm on the surface, while the second is a surface crack linked to a planar, clam-shell flaw in the bulk. The photograph in Fig. 78.61 shows an example of the former. After initiation of this type, fractures grow in lateral size on subsequent laser shots until the defect reaches one-half the critical flaw size. At this time, the lens is replaced. Current OMEGA lenses have

defects ranging in size from less than 0.5-mm to 10-mm diameter, and multiple damage sites on a len's vacuum surface are common. The damage depth tends to be less than one-third its surface diameter, and defects occur at apparently random radial locations. A clam-shell defect is depicted in a side view in Fig. 78.62 and in a head-on view in Fig. 78.63. The flaw's discoloration may signal that it is being filled by an absorbing material. On repeated irradiation, the clam-shell morphology is eventually obliterated and a crater develops, as in Fig. 78.61.

While this clam-shell morphology is one initiator of millimeter-sized fractures, it remains inconclusive whether it is the only one. To further evaluate clam-shell damage, a sample was cleaved, as depicted in Fig. 78.64, and the exposed clam-shell cross section was analyzed by scanning electron microscopy (SEM). SEM/EDAX (energy dispersive x-ray analysis) element identification revealed the presence of carbon within the fracture while reporting its absence outside the fractured area. It is surmised that once a crack appears on the vacuum-side

Table 78.VII: Summary of peak tensile stresses and critical flaw size for OMEGA vacuum spatial-filter lenses.

Lens	Diameter (mm)	Peak stress (psi)	Peak stress (MPa)	Center thickness t (mm)	Flaw size a_c (mm)	t/a_c
C-in	149.4	656	4.52	12.5	8.8	1.4
D-in	149.4	683	4.71	12.5	8.1	1.5
E-in	213.5	538	3.71	20.0	13.0	1.5
F-in	283.4	615	4.24	25.0	10.0	2.5

Table 78.VIII: Summary of peak tensile stresses and critical flaw size for various vacuum optics in a LLNL study.[3]

Lens/Window	Peak stress (psi)	Peak stress (MPa)	Thickness t (mm)	Flaw size a_c (mm)	t/a_c	Number of radial fractures
Beamlet L3	1490	10.10	35.0	2.1	16.7	9–11
Nova SF-7	810	5.51	37.0	5.5	6.7	2–3
Nova 3ω focus	515	3.50	83.0	15.0	5.5	<1
15-cm SiO_2 plate	830	5.65	9.5	5.4	1.8	≤1
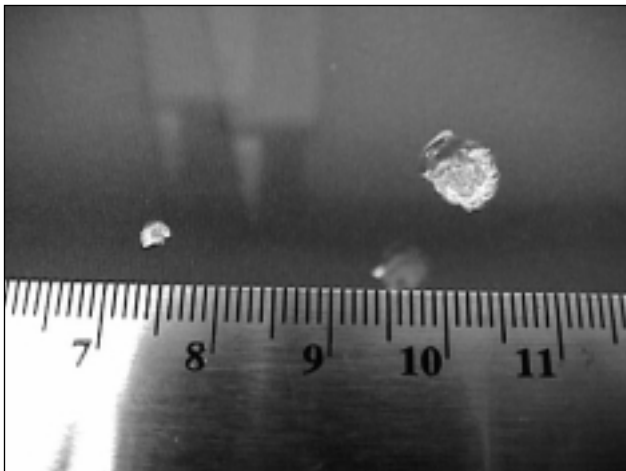
G4746

Figure 78.61
Fractures on the vacuum side of an OMEGA lens. Scale units in centimeter.

E4747

Figure 78.62
Clam-shell defect originating at the vacuum side (bulk view).

surface, oils from the machined surfaces of the spatial-filter tubes or oils from the mechanical pumping system seep into the crack over time. The combination of absorption by the trapped fluid and physical–chemical assistance in crack-front propagation during subsequent exposure is surmised to form the ring structure observed within the clam shell.

The cause of damage initiation to 1ω, fused-silica, spatial-filter lenses remains undetermined. Possible causes include (1) absorbing defects ablated from the tube wall or pinhole material, (2) oils or contamination nucleated at specific defects on the lens or coating, (3) oils absorbed into subsurface fractures expanded by tensile surface forces, and (4) isolated contamination remaining from coating application. Related
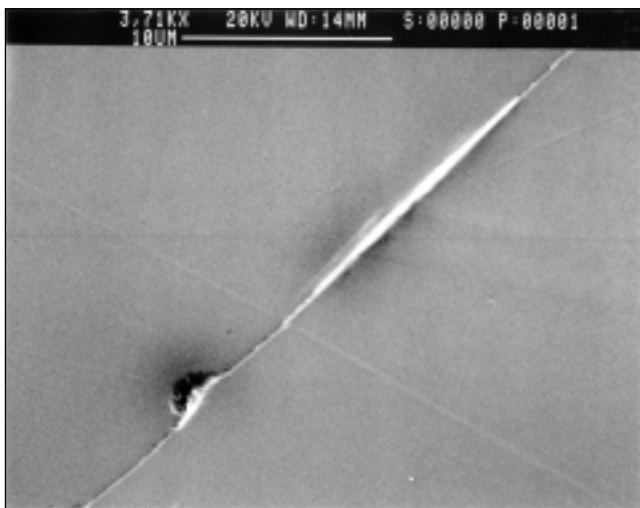
G4748

Figure 78.63
SEM vacuum surface view of a clam-shell defect on an OMEGA lens (top view).
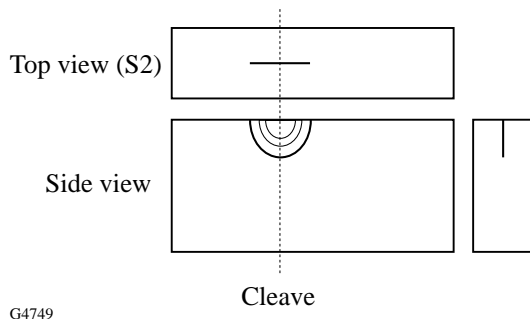
G4749

Figure 78.64
Illustration of cleave sample orientation.

work for the National Ignition Facility (NIF[5]) laser found (1) that the cause of 3ω damage was polishing-process defects within 500 μm of the surface and (2) that removal of these defects by etching improved the surface damage thresholds.[6] LLE-based ion-etching experiments to improve surface damage threshold are discussed later.

Sol-Gel Coating Degradation

OMEGA sol-gel coatings show a significant change in reflectivity when exposed to a vacuum contaminated with oil from mechanical pumps. A fiber-optic spectrometer is used to measure the lens reflectivity *in situ*. While the instrument provides only relative photometric measurements, the spectral-curve shapes provide essential information on coating performance. Spectra in Fig. 78.65 show an example for how spectral response among the two sol-gel-coated surfaces of a single lens is affected by exposure to oil. While the S1, nonvacuum-side reflectivity curve is expected for a 1ω anti-reflection coating, the spectral characteristics of the S2, vacuum-side data show an increase in reflectivity at 1ω from 0.1% to 3.4%, owing to refractive-index changes resulting from adsorbed organic material. Evaluation of the S2 sol-gel coating by gas chromatography/mass spectrometry detected the presence of vacuum-pump oil and other organic contamination. The effect of oil contamination on the film index on a fixed-thickness sol-gel coating is modeled in Fig. 78.66. As the film index varies from 1.23 to 1.44 (film thickness is constant), reflectivity minima disappear into a flat line similar to the experimental observation in Fig. 78.65. This coating problem is seen on all OMEGA sol-gel-coated spatial-filter lenses that are collectively pumped by a single mechanically pumped vacuum system. Coatings are found to fail at different rates, however, as a result of differing cleanliness conditions or
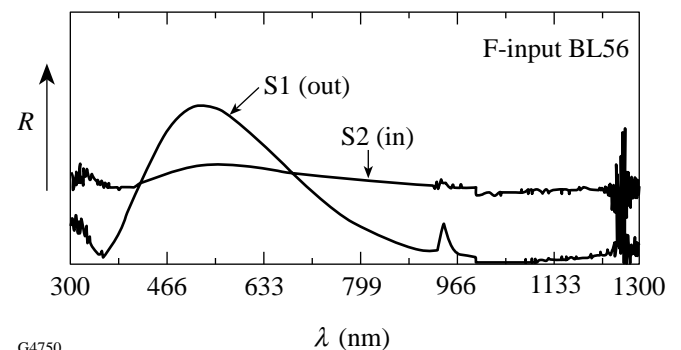
G4750

Figure 78.65
Reflectance data measured on a sol-gel-coated spatial-filter lens. The S2 (in) surface is the vacuum interface; the S1 (out) surface resides in air.

vacuum pressure levels within the spatial-filter tubes. Loss of reflectivity on a mechanically pumped tube is suffered in about six weeks or more. Hard-oxide dielectric coatings pumped under similar vacuum conditions show no change in reflectivity after exposure for similar periods.

The prototype beamline laser (PBL) assembled years earlier was disassembled about the same time as this study. The sol-gel-coated lenses in those tubes showed no coating degradation due to contamination. The tubes were first pumped mechanically and were then switched to a titanium sublimation pump, which maintained a pressure of 1×10^{-5} mbar. No record exists to indicate what method was used to clean the tubes in this PBL. To gauge the effect of different pumping methods on OMEGA, a freshly sol-gel-coated lens was placed in a spatial-filter tube that was isolated from the OMEGA mechanical pumping system. The tube was then connected to a cleaner turbo-pumping system although the tube itself could not be decontaminated *in situ*. A properly run turbo pump will exhibit very little back streaming of high-molecular-weight oils such as those used by a mechanical pump. Surprisingly, the coating was contaminated after less than four days' exposure to this environment. It was surmised that the greater mean free path in the lower pressure allowed faster transport of the oil from the contaminated walls to the sol-gel coating. This rules out the relatively simple solution of redesigning the pumping system. Improvement of the oil-contaminated system could be effected only by removing the tubes, then cleaning and baking them, possibly in a vacuum along with all the associated

plumbing. This would produce an unacceptable lapse in the OMEGA firing schedule.

A causal link between sol-gel contamination and lens damage is suspected but has yet to be fully proven. Experiments to investigate this link and solve this damage problem are ongoing, and some results are reported in the next section. In addition, several solutions to this sol-gel-coating degradation problem are being examined to recover the light loss imposed by each "bad" surface: (1) replace sol-gel coatings with hard-oxide dielectric coatings (damage threshold is a key factor); (2) improve the spatial-filter pumping system and clean the spatial-filter tubes; and (3) add a "getter" material to adsorb the contamination before it reaches the coating.

Experiments

Several experiments were started to investigate the cause of damage to the vacuum surfaces of OMEGA spatial-filter lenses. One experiment resulted from a LLNL report that the damage threshold of fused silica at 3ω can be improved with etching. Etching appeared to remove polishing-process defects within a few hundred microns of the surface. Another experiment was proposed to examine the cleanliness conditions of the spatial-filter tubes and explore the probability that ablated pinhole debris produce damage-initiation sites.

1. Ion-Etching Tests

Since LLE developed an ion-etch capability for manufacturing distributed phase plates, it was logical to set up a process to ion etch the vacuum surface of spatial-filter lenses.[7] An experiment was designed to remove $3\,\mu$m of material from side 2 (vacuum side) of OMEGA stage-F-input, fused-silica, spatial-filter lenses, and then coat and install the optics on OMEGA to observe damage and coating failure. The following matrix was established with five lenses to be processed for each type:

(a) ion etch and sol-gel coat,
(b) ion etch and hard-oxide coat,
(c) ion etch and no coating, and
(d) no etch and no coating.

The hard-oxide coating is a hafnia/silica, e-beam-evaporated, antireflection coating.[8]

Once the optics are installed on OMEGA, observation over a long period of time (possibly one year) is required as damage onset times remain uncertain. The statistics of damage occurrence on these lenses in comparison to the damage statistics on OMEGA over the last three years will be reviewed. The experi-
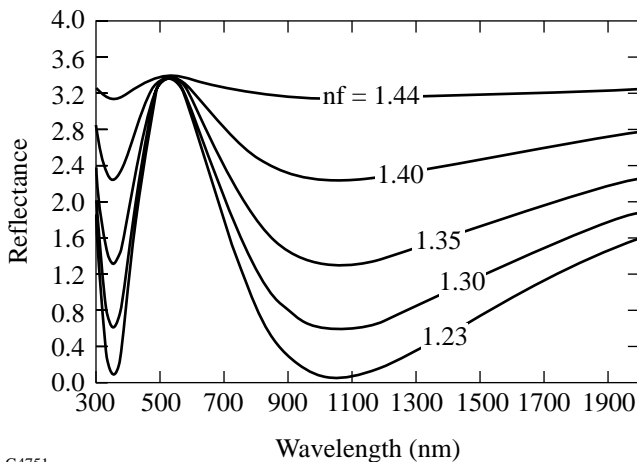
Figure 78.66
A model of reflectance change as the film index is varied for a constant film thickness. Film indices used are 1.44, 1.40, 1.35, 1.30, 1.23.

G4751

ment will evaluate the effect of subsurface defects on the laser-induced damage threshold (LIDT) and also the effect of ion etching in modifying subsurface topography. These tests may also provide a correlation between damage and type of coating.

Progress on this test has been hampered by the paucity of spare optics to complete the matrix. In August 1998, type-(a) optics were installed; as of March 1999, no damage has been observed on these surfaces, and only one of the five sol-gel coatings has enhanced vacuum-side (S2) reflectivity. Transmittance loss was incurred within six weeks of installation. Three of five type-(b) optics were installed—one in October 1998 and two in November 1998; to date no damage or coating degradation has been observed. The remaining tests will be completed in June 1999 and results reported in the future.

2. Spatial-Filter Witness Tests

To investigate the cleanliness conditions of spatial-filter tubes, ten 2-in.-diam, sol-gel-coated, fused-silica samples were installed in OMEGA's stage-E spatial-filter tubes for approximately two months. All samples were damage tested at 1053 nm with a 1-ns pulse before and after exposure to the spatial-filter tube environment. Three beamlines had one sample installed at the input lens location and one sample at the output lens location, and a fourth beamline had two samples installed at each location. The sample orientation within the spatial-filter tube is illustrated in Fig. 78.67. By mounting the samples in this manner, the top surface collects pinhole condensate, while the bottom surface remains shielded.

The results revealed that the spatial-filter tube's cleanliness condition inflicts a stiff penalty, regardless of pinhole debris. As seen in Table 78.IX, all samples showed a significant drop in damage threshold after a two-months' exposure to the

spatial-filter tube environment, and the top and bottom surface threshold data are virtually indistinguishable. The reported thresholds are 1-on-1 damage tests with a 1-mm^2 beam size; approximately 12 sites per sample were tested. Further SEM analysis revealed no high-Z element presence on the post-exposure surfaces, indicative of an absence of spatial-filter pinhole emanations on the top witness surface. It is difficult to predict the trajectory of ablated material, and further tests with samples located at various orientations are required to identify the path of ablated pinhole material that may contribute to lens damage. There is evidence on some pinholes that the edges are melted and craters have formed. While further experiments are needed to confirm pinhole ablation as an initiator for vacuum surface damage sites, the data confirm that oil contamination does decrease the sol-gel-coating damage threshold.
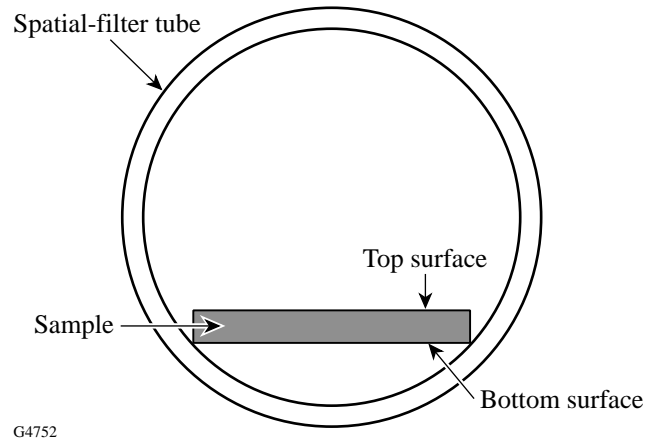
G4752

Figure 78.67
Witness sample orientation within a spatial-filter tube.

Table 78.IX: Witness sample damage threshold results before and after exposure to a spatial-filter tube environment.

Sample Orientation		Before-Exposure Damage Threshold* (J/cm^2)	After-Exposure Damage Threshold* (J/cm^2)
Top surface	average	20.7	11.9
	standard deviation	4.9	2.5
Bottom surface	average	22.1	11.3
	standard deviation	3.9	3.1
*1-on-1 damage tests at 1054 nm with a 1-ns pulse and 1-mm^2 beam size.			

Conclusion

Approximately 50% of OMEGA's stage-C-input, C-output, D-input, E-input, and F-input fused-silica, spatial-filter lenses are damaged. LLE has implemented a plan to maintain the quality of OMEGA optics that includes frequent inspections and *in-situ* cleaning of optics by a skilled support group. Since damaged optics are closely monitored and the one-half critical flaw size is of the order of 10 mm in diameter, OMEGA lenses are not likely to catastrophically fail before replacement occurs. This allows for safe operation of the laser while the damage problem is being brought under control. Owing to the effectiveness of spatial filters in removing critical intensity modulations, propagating bulk or surface damage to components downstream of these damaged lenses has not been observed. Damage always occurs on the lens's vacuum surface regardless of the beam propagation direction, and an unusual clam-shell damage morphology has been observed. It is also known that the sol-gel coating on the vacuum surface fails due to organic contaminants, and this degradation is linked to a drop in the tested laser-damage threshold. A link between sol-gel contamination and lens damage is suspected but yet unproven. Experiments will continue to explore the role of subsurface fractures in the generation of the clam-shell morphology and to identify other absorbing defects on the vacuum surface, possibly originating from pinhole closures, which may be causing the damage.

REFERENCES

1. *OMEGA System Operations Manual Volume I – System Description (S-AA-M-12),* Laboratory for Laser Energetics, University of Rochester (1995), p. 43.

2. J. C. Lambropoulos, "Critical Flaw Size for Catastrophic Failure of Fused-Silica Spatial Filter Lens," 1995 (unpublished).

3. J. H. Campbell *et al.*, in *Laser-Induced Damage in Optical Materials: 1996,* edited by H. E. Bennett et al. (SPIE, Bellingham, WA, 1997), Vol. 2966, pp. 106–125.

4. "Incident Analysis Report: Failure of a Spatial Filter Lens on the Beamlet Laser at Lawrence Livermore National Laboratory on April 3, 1995," Investigation Report May 11, 1995; U.S. Department of Energy, Oakland Operations Office.

5. J. Murray, *ICF Quarterly Report* **7**, 95, Lawrence Livermore National Laboratory, Livermore, CA, UCRL-LR-105821-97-3 (1997).

6. J. Yoshiyama *et al.*, in *Laser-Induced Damage in Optical Materials: 1997*, edited by G. J. Exarhos et al. (SPIE, Bellingham, WA, 1998), Vol. 3244, pp. 331–340.

7. Laboratory for Laser Energetics LLE Review **74**, 71, NTIS document No. DOE/SF/19460-241 (1998). Copies may be obtained from the National Technical Information Service, Springfield, VA 22161.

8. D. J. Smith, J. F. Anzellotti, S. Papernov, and Z. R. Chrzan, in *Laser-Induced Damage in Optical Materials: 1996*, edited by H. E. Bennett *et al*. (SPIE, Bellingham, WA, 1997), Vol. 2966, p. 250.

Direct-Drive Target Designs for the National Ignition Facility

The National Ignition Facility (NIF) is currently under construction at Lawrence Livermore National Laboratory (LLNL). One of the primary missions of the NIF is to achieve fusion ignition by means of inertial confinement fusion (ICF). Two main approaches have been considered for achieving thermonuclear yield in ICF. The first approach, known as indirect-drive ICF,[1] encloses a DT-fuel target inside a hohlraum. The laser beams are incident on the hohlraum's wall where the laser light is converted to x rays. These x rays then implode the target, leading to the ion temperature and ρR product necessary to achieve ignition. The second approach, known as direct-drive ICF, dispenses with the hohlraum and directly illuminates the laser light onto the target.

Direct drive offers a number of advantages[2] over indirect drive: (1) direct-drive designs have potentially higher gains than indirect drive; (2) direct-drive plasma coronas are not as susceptible to laser–plasma instabilities (LPI's) as indirect drive; (3) direct-drive targets are inherently less complex than indirect-drive hohlraum targets. Direct drive also has some potential disadvantages, especially the severe requirements on laser-beam uniformity.

Most of the U.S. research effort has centered on the indirect-drive approach, which is reflected in the decision to commence operations on the NIF in the indirect-drive configuration. NIF, however, is not to preclude direct drive, and it is currently expected that the NIF will be reconfigured for direct-drive operations commencing in 2009. Before the conversion to direct-drive operations, a number of modifications must be made to the NIF. First, to provide a uniform illumination of the direct-drive target, half the final optics assemblies (FOA's) must be relocated from the poles to the waist of the target chamber; second, direct-drive uniformity enhancements (2-D SSD[3] and polarization smoothing) must be added to all beamlines; and third, the cryogenic-handling system must be capable of "cradle-to-grave" operations.

This article describes the direct-drive ignition target designs developed at the University of Rochester's Laboratory for Laser Energetics (LLE). The following three sections will (1) outline the current direct-drive designs under investigation at LLE and NRL; (2) present a sensitivity study of the "all-DT" design; and (3) review the current laser and target specifications required to achieve a successful direct-drive ignition campaign on the NIF.

Direct-Drive Target Design Overview

Many common areas of physics exist between direct- and indirect-drive capsule designs. Both target designs require high compression of the DT fuel with a central high-temperature (>5-keV) ignition region. A typical implosion involves the deposition of energy (laser light in direct drive, x rays in indirect drive) on the target surface, which rapidly heats up and expands. As this *ablator* expands outward, the remainder of the shell is driven inward by the rocket effect compressing the fuel to the necessary density. The implosion can be tailored to give a number of assembled fuel configurations, such as isobaric with a uniform temperature and density in the fuel or isochoric with a high-temperature hot spot surrounding a low-temperature main fuel layer. The most energy efficient[1] configuration is isobaric with a central high-temperature *hot spot* surrounding a low-temperature *main fuel layer*. The central hot spot initiates the fusion reaction, which leads to a burn wave propagating into the main fuel layer; thus, for robust high-gain designs, it is vitally important to assemble the high-temperature hot spot and cold, dense main fuel layer accurately. For direct-drive target designs two main effects can prevent the correct assembly of the fuel: (1) preheat of the fuel and (2) hydrodynamic instabilities of the imploding shell.

Preheat of the DT fuel will increase the pressure of the fuel and thus make the target harder to compress. Preheat can arise from fast electrons, radiation, and the passage of shocks. The amount of preheat can be quantified in terms of the *adiabat* α of the implosion. The adiabat is defined as the ratio of the fuel's specific energy to the Fermi-degenerate specific energy. It can be shown that the gain G of the target scales as $\alpha^{-3/5}$. Fast electrons generated by laser–plasma processes (such as SBS, SRS, and two-plasmon decay) in the plasma corona can couple

into the fuel. These plasma processes occur when the intensity of the laser exceeds certain thresholds; thus, the control of fast-electron production constrains the maximum intensity of the design pulse. Radiative preheat and the passage of shocks are controlled by the target material and the shape of the laser pulse, respectively.

Hydrodynamic instabilities, such as the Rayleigh–Taylor instability (RTI), can seriously degrade the implosion by breaking the spherical symmetry of the implosion. The RTI occurs twice during the implosion: at the outer ablation surface as the shell accelerates inward and at the hot spot–main fuel layer interface as the capsule decelerates at the end of the implosion. Considerable theoretical,[4] numerical,[5] and experimental[6] work has demonstrated that the RT growth rate at the ablation surface is reduced from the classical value by ablative stabilization. From design simulations the ablation velocity v_a has been shown to scale as $\alpha^{-3/5}$. Another important parameter for stability considerations is the in-flight aspect ratio (IFAR). This is the ratio of the shell radius R to its thickness ΔR as the shell implodes. Higher IFAR implosions are more susceptible to hydrodynamic instabilities. Simulations have shown that the IFAR depends primarily on the square of the implosion velocity v^2_{imp} and the adiabat ($\alpha^{-3/5}$).

Control of the isentrope of the implosion is thus important for overall target gain ($G \sim \alpha^{-3/5}$) and target stability. Indirect-drive designs are believed to be sufficiently stable to hydrodynamic instabilities that they can operate very near the Fermi-degenerate limit ($\alpha = 1$). Direct-drive designs require the implosion to operate at a higher isentrope. LLE and NRL are currently investigating three designs (see Fig. 79.1) that use various combinations of shock and radiative heating to control the isentrope.

The first design [Fig. 79.1(a)] employs a solid (cryogenic) DT-shell target with a thin polymer ablator (required to fabricate the cryogenic shell) surrounding the DT-ice shell.[7] For this design the DT acts as both the fuel and the ablator. This design uses shock preheat to control the isentrope of the ablation surface and the fuel.

The second design [Fig. 79.1(b)] employs a low-density foam surrounding a clean cryogenic DT layer (a thin barrier layer separates the foam layer from the DT). The foam layer acts as the ablator. This design uses shock preheat to control the isentrope, but it offers the flexibility of placing the ablation surface and main fuel layer on different isentropes.

The third design [Fig. 79.1(c)] places a high-Z coating over a DT wicked foam ablator, which encases a pure-DT ice layer.[2] This design uses mainly radiative preheat. By carefully selecting the radiative properties of the high-Z ablator, it is possible to preferentially heat the carbon in the foam, boosting the isentrope of the ablation surface, while leaving the fuel on a lower isentrope.

Although the "all-DT" design has the disadvantage that the fuel and ablator are on the same adiabat, it has a number of significant advantages. First, the target is very simple, with no classically unstable RTI interfaces. Second, DT has a very high ablation velocity, which reduces the RTI at the ablation surface. Third, a DT ablator potentially gives higher hydrodynamic efficiencies, thus maximizing the achievable gain. Because of these considerations, a scaled version of this target design has been selected for experimental investigation on the OMEGA laser and is used as the base-line design for establishing the detailed specifications for the NIF. The next section presents a more-detailed review of the all-DT design.
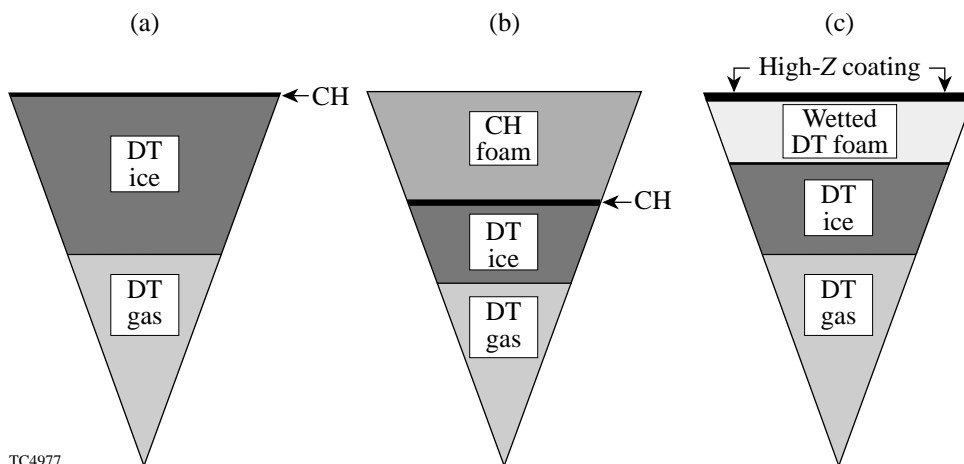

Figure 79.1
Schematic of the direct-drive target designs. (a) The all-DT target design, which relies on shock heating to select the adiabat. (b) The foam ablator design, which relies on shock heating to select the adiabat separately for the ablator and the fuel. (c) The radiative design, which relies on radiative absorption to select the adiabat for the ablator.

TC4977

The Baseline All-DT Target Design

Figure 79.2 shows the gain curves constructed by LLE during the design phase of the NIF[7] for laser energies from 1 to 2 MJ and for implosions on isentropes from $\alpha = 1$ to 4. Variation in the isentrope was achieved by varying the incident laser pulse shape. Based on the results of current OMEGA experiments and theoretical calculations of these NIF designs, we have selected the 1.5-MJ, $\alpha = 3$ continuous-pulse design to be the baseline design for further study. Figure 79.3(a) shows the target specification; Fig. 79.3(b) shows the pulse shape for this design. This pulse shape consists of two distinct temporal

regions: the foot and the main drive. The DT-ice thickness and adiabat of the implosion determine the length and duration of the foot. In this design, the foot is 4.25 ns long at a power of 10 TW. This region launches a 10-Mbar shock through the DT ice. At the time of shock breakout at the rear surface of the DT ice, the pulse ramps up to the drive region, which lasts for 2.5 ns at a power of 450 TW. This rapid rise in intensity generates pressures of approximately 80 Mbar and thus accelerates the DT ice inward. Different adiabats can be achieved by varying the length and intensity of the foot and carefully shaping the rise to the drive pulse. For example, an $\alpha = 2$ design has a longer, lower-intensity foot and a gentler-rising transition region.

The $\alpha = 3$ design is predicted, by 1-D calculations, to have a gain of 45, a neutron-averaged ion temperature of 30 keV, and a neutron-averaged $\rho R = 900$ mg/cm^2. The peak IFAR of this design is 60, and the hot-spot convergence ratio is 29. The conditions near peak compression ($t = 10.4$ ns) are shown in Fig. 79.4.

These direct-drive designs have two distinct shocks: the first is launched at the start of the pulse; the second is generated during the rise to the main drive intensity. Figure 79.5 is a contour map of the radial logarithmic derivative of the pressure [d(lnP)/dr] as a function of Lagrangian coordinate and time. The darker, more-intense regions represent a larger gradient in pressure and thus capture the position of the shocks. The timing between these two shocks determines the gain of the target design. When the first shock breaks out of the DT-ice layer (at 5.8 ns), a rarefaction wave expands outward from the rear surface of the DT ice. If the second shock arrives too late, the shock travels through a decreasing density gradient, which
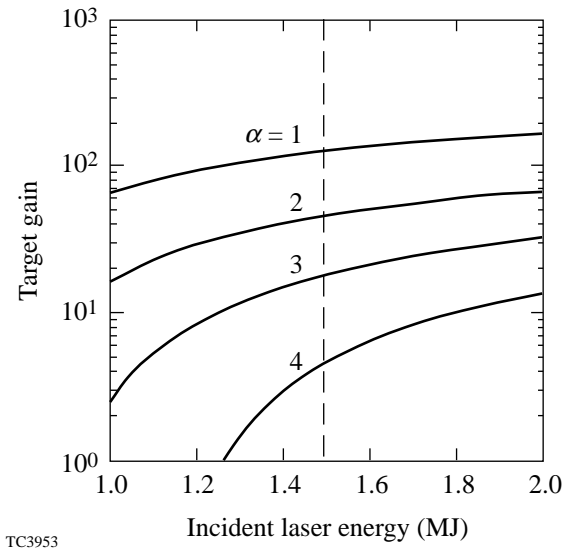
TC3953

Figure 79.2

The gain curves constructed at LLE for various isentropes and incident laser energies. The dashed line corresponds to the NIF baseline 1.5-MJ energy.
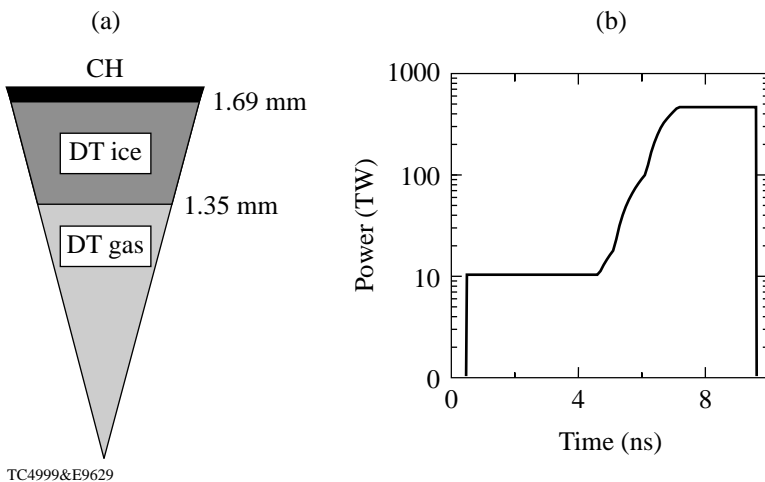
TC4999&E9629

Figure 79.3

The baseline, $\alpha = 3$, "all-DT," 1.5-MJ target design. (a) The target specification and (b) the pulse shape.
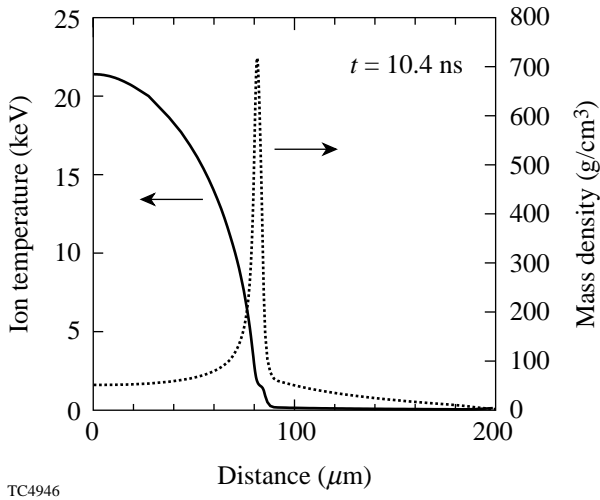
TC4946

Figure 79.4
The ion temperature (solid line) and the mass density (dotted line) near peak compression for the $\alpha = 3$ baseline design.
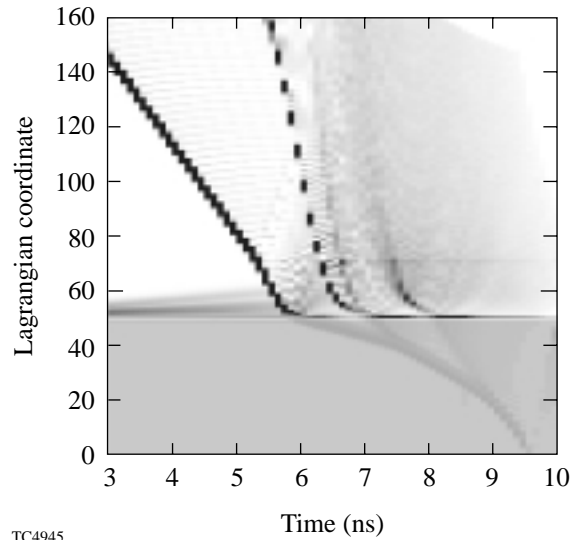

TC4945

Figure 79.5
Shock propagation as shown by a contour map of the logarithmic derivative of the pressure as a function of time and Lagrangian coordinate. The interface between the DT ice and gas is at Lagrangian marker 50.

increases the shock strength. This puts the main fuel layer onto a higher adiabat and thus reduces the gain. Conversely if the second shock arrives too early, the hot spot produces the burn wave before the main fuel layer has reached peak density and thus reduces the overall target gain. An error in shock timing can arise from the following:

1. Inadequate Control of the Laser Pulse Shape

The $\alpha = 3$ laser pulse shape is essentially defined by eight temporal points as shown in Fig. 79.6. To establish the sensitivity of the target design to variations in pulse shape we performed a series of 1-D calculations. These calculations involved varying the power and temporal position of each point (while holding the other points fixed). By adjusting the last point of the laser pulse we ensured that the overall energy in the pulse remained constant at 1.5 MJ. If a temporal point was adjusted to be in front of another point, that point was removed from the pulse. Figure 79.6 shows the contours of gain generated by moving five of the points. Note that as the first point moves earlier in time (thus lengthening the foot region), the power must drop to preserve target gain; however, reduced foot intensity leads to a weaker shock formation, thus reducing the adiabat of the target and leading to a more unstable implosion. We can see that target performance is sensitive to the foot and transition regions of the laser pulse, but is relatively insensitive to the details of the high-power region. Figure 79.7(a) shows the target gain as a function of a change in the foot power. Figure 79.7(b) shows the target gain as a
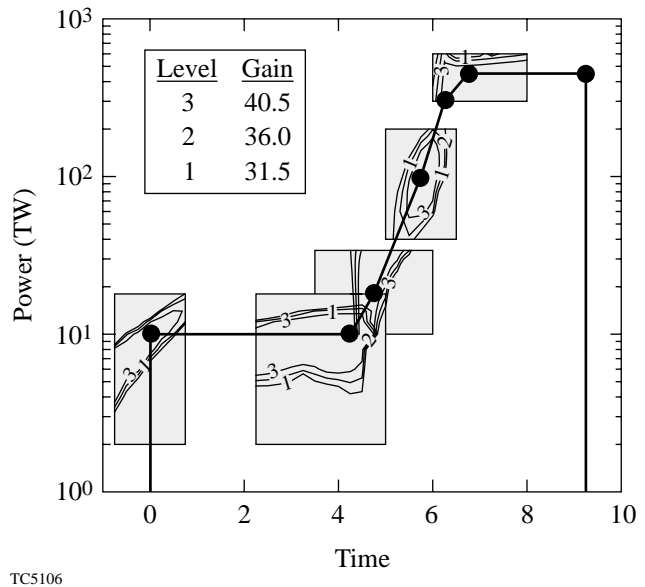

TC5106

Figure 79.6
The $\alpha = 3$ pulse shape with overlaid contours of gain. The circles correspond to the temporal points used to define the pulse shape. The contours correspond to the gain that would be achieved if the temporal point was moved to that time and power location (holding all other points fixed).

function of the length of the foot region. From these curves it has been established that the pulse power in the foot region must be controlled and measured to ±3%, and that the pulse duration is controlled and measured to ±50 ps. These curves suggest a possible "tuning" strategy for the NIF. By varying the length of the foot (and holding the other portion of the pulse constant) we can scan through the optimal gain region and adjust for uncertainties in the shock transit through the DT ice.

2. Uncertainties in the Target's Equation of State (EOS)

1-D simulations with *SESAME* tables, analytic Thomas-Fermi, and Livermore DT-ice tables have been performed to address the uncertainties in EOS. Using the tuning strategy of foot-length and intensity variations, we can optimize the gain for different EOS models. For example, the optimal gain for targets modeled using the analytic Thomas-Fermi EOS required a 600-ps reduction in foot length from the *SESAME*

case. Although we have established that the designs can be retuned to these EOS models, experimental measurements of the EOS of D_2 ice, D_2 wicked foam, and high-Z-doped plastics are required to accurately model the target.

3. Uncertainties in Target Thickness

A series of 1-D simulations have been performed to establish the required control of the DT-ice thickness (which is controlled by the DT-gas-fill pressure). Specifying the control of the ice thickness determines the control and measurement of the fill pressure during ice layering. Figure 79.8 shows the gain as a function of ice-layer thickness (holding the outer radius of the shell fixed). A variation of ±5 μm in a total ice thickness of 340 μm leads to a 2% reduction in gain. This corresponds to a control of the DT-fill pressure of ~20 atm out of a total fill pressure of 1020 atm (at room temperature).
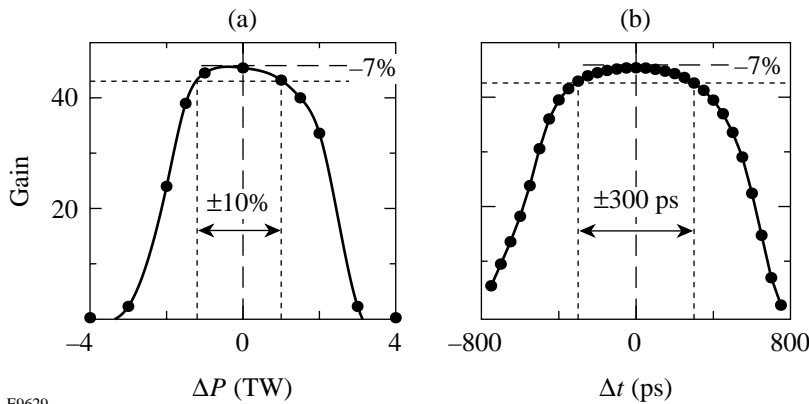

Figure 79.7
The target gain as a function of the change in (a) the foot power and (b) the foot duration from the nominal 10-TW, 4.25-ns parameters.
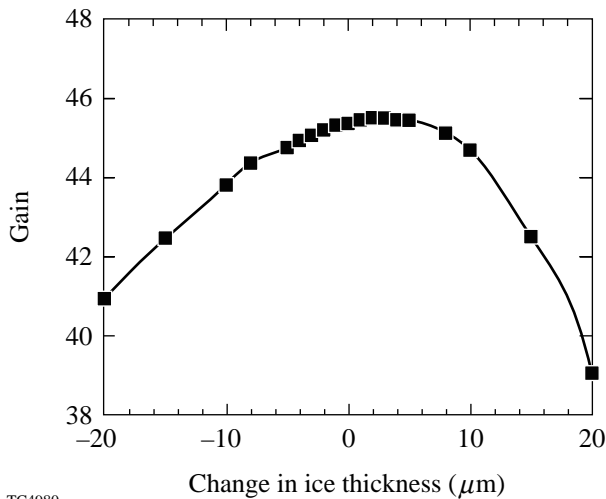

Figure 79.8
The target gain as a function of the change in the ice-layer thickness.

The need to control the hot-electron fraction is similar to the indirect-drive requirements, namely that less than 0.1% of the laser energy is deposited in the DT fuel via hot electrons. Since the laser is more closely coupled to the target in direct drive, however, the transport of hot electrons to the target is more efficient, and the targets are therefore more sensitive to hot electrons than in indirect drive. 1-D simulations were performed with various percentages of laser energy dumped at the critical surface into an 80-keV hot-electron tail. These hot electrons were transported through the target where approximately 4% of the energy absorbed into fast electrons was deposited in the DT-ice fuel layer. Figure 79.9 shows the effect of between 1% and 3% laser energy absorbed into fast electrons on the gain. A 30% reduction in gain occurred when 1% of the incident laser energy was absorbed into fast electrons. The hot electrons are produced by laser–plasma instabilities (LPI's), such as SRS, SBS, and two-plasmon decay.
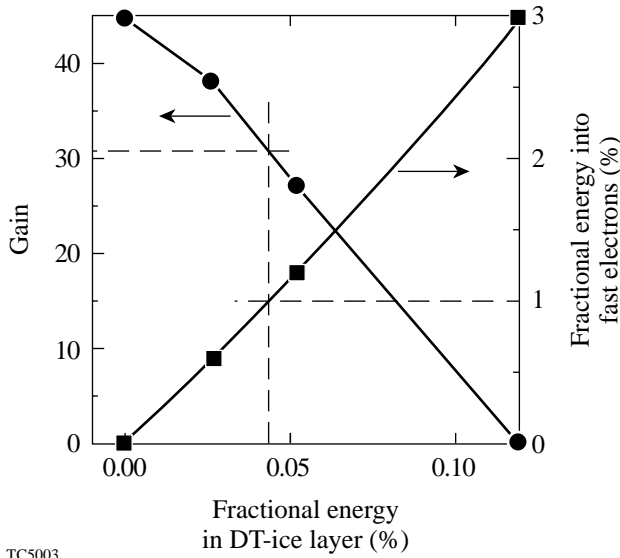

TC5003

Figure 79.9
The effect of varying the fraction of energy dumped into an 80-keV hot-electron tail on the target gain.

Figure 79.10(a) shows the threshold intensities for SRS and SBS; Fig. 79.10(b) shows the total NIF intensity at the quarter- and tenth-critical surfaces. At each time the minimum threshold in the corona is calculated based on simulations of the $\alpha = 3$ density and velocity profiles. For SRS the threshold is seen to be well above the total NIF intensity at tenth-critical; this is the most relevant density since the minimum thresholds tend to occur far out in the corona where scale lengths are long and densities are low. The single-cluster NIF intensity would be lower by a factor of about 12. For SBS the total intensity is

well above threshold after about 6 ns, while the single-cluster intensity is comparable to the threshold. Further study is required to determine how many clusters are likely to participate in driving SBS. SBS has a low threshold at this time because the NIF pulse is rapidly increasing in intensity, producing a local velocity minimum in the density profile and a correspondingly long velocity scale length. These thresholds are calculated on the basis of inhomogeneity scale lengths; the density scale length is the determining factor for SRS and the velocity scale length for SBS. Damping has little effect on the minimum thresholds; the damping contribution depends on the product of the electromagnetic wave damping (mostly collisional, small at low densities) and the electrostatic wave damping (mostly Landau). The Landau damping becomes large for electron-plasma waves (SRS) at low densities and for ion-acoustic waves (SBS) when T_i approaches T_e. The minimum threshold for both instabilities tends to occur at low densities where the small damping of the electromagnetic wave makes the contribution to the threshold negligible. Large Landau damping of the electrostatic waves may, however, substantially reduce growth rates even if the instability is above threshold.

A high level of illumination uniformity is required to achieve ignition. Both direct- and indirect-drive designs require that the targets be driven by pressure nonuniformity levels of less than 1% rms. The angular variation in the intensity distribution on the target is routinely described in terms of spherical-harmonic modes. An ℓ-mode is related to the target radius R and the nonuniformity wavelength λ through $\ell = 2\pi R / \lambda$. The mode spectrum is normally divided into two regions: a low ℓ-mode region ($\ell < 20$) and a high ℓ-mode region ($20 < \ell < 500$). Indirect drive benefits from the conversion of the laser light to x rays. Essentially all modes above $\ell = 10$ are eliminated by x-ray conversion. In direct drive the laser beam alone must achieve the desired level of uniformity; thus, direct drive places much tighter tolerances on the single-beam uniformity and beam-to-beam balance than indirect drive.

Low ℓ-mode (long-wavelength) perturbations are seeded by beam-to-beam variations arising from (1) the mispointing or misfocusing of the laser beams, (2) a lack of energy and power balance, or (3) mispositioning of the target. Such modes grow secularly during the implosion. A simple argument is used to calculate the maximum tolerable variation in the low ℓ-mode spectrum. Since these modes grow secularly, the final distortion δr_f of the compressed fuel at average radius r_f is given by $\delta r_f = \Delta a t^2$, where Δa is the acceleration nonuniformity and t is the implosion time. For a shell initially at radius r_0 the

distortion of the shell is given by $\delta r_f / r_f = \Delta a / a \left(r_0 / r_f - 1 \right)$. Numerical calculations using the 2-D hydrocode *ORCHID* suggest that final core distortions of 50% can be tolerated; thus, for a convergence ratio of 25 (which is typical for direct-drive targets), a peak-to-valley acceleration nonuniformity of 2% can be tolerated. The laser nonuniformity in the low ℓ-mode region must be maintained below 1% rms.

The high ℓ-mode (short-wavelength) region is seeded by the structure within the individual laser beam. These modes excite the Rayleigh–Taylor instability, which causes the modes to grow much more rapidly than in the low ℓ-mode region. Note that extremely high mode numbers are not important since they are ablatively stabilized, rapidly saturate, and do not feed through to the hot-spot region.

The effect of the growth of the hydrodynamic instabilities has been examined by two techniques: The first technique uses detailed 2-D *ORCHID* simulations to directly determine the effects of perturbation on target performance. This technique is computationally intensive and does not give the correct 3-D multimode saturation of the RT instability. The second technique uses a postprocessor to the 1-D simulations. This postprocessor uses a self-consistent model[8] to study the evolution of perturbations at the ablation front and the back surface of an accelerated spherical shell. The model includes the ablative Richtmyer–Meshkov (RM),[9] RT, and Bell–Plesset (BP) instabilities; 3-D Haan saturation[10] is included. The model consists of two differential equations (describing the ablation- and inner-surface perturbations) obtained by solving the linearized conservation equations in the DT gas, the shell, and the blowoff plasma regions. The overdense–ablated plasma interface is approximated as a surface of discontinuity.[11]

Direct-drive target designs must tolerate four sources of nonuniformity to ignite and burn: (1) inner-DT-ice roughness, (2) outside CH capsule finish, (3) drive asymmetry, and (4) laser imprinting. Multidimensional simulations of the deceleration phase have shown that our design will ignite when the inner-surface nonuniformity is less than 1.5 μm at the start of the deceleration phase. By performing an extensive series of calculations with various levels of nonuniformity, it is possible to establish the requirements for the four seed terms.

The hardest seed term to establish is that for laser imprint. A series of planar 2-D simulations have been performed using *ORCHID*. These simulations determined the imprint efficiency for single modes of irradiation nonuniformity. The effect of 2-D SSD was included using the approximation

$$\sigma_{\text{rms}} \sim \sqrt{t_c / t},$$

where

$$t_c = \left[\Delta \nu \sin \left(k \Delta / 2 \right) \right]^{-1}$$

is the coherence time, $\Delta \nu$ is the bandwidth, k is the wave number of the spatial-intensity nonuniformity, and Δ is the speckle size. For example, using a phase-plate nonuniformity spectrum with 1 THz of bandwidth, the laser will imprint a surface nonuniformity equal to $\sigma_{\text{rms}} = 360$ Å (in modes $\ell < 1000$) at the start of the acceleration phase. The additional sources of nonuniformity are then added to that from the laser. For example, Fig. 79.11 shows the mode spectrum of the ablation surface at the start of the acceleration phase for the case of a 1-THz-bandwidth, perfectly uniform outer shell and
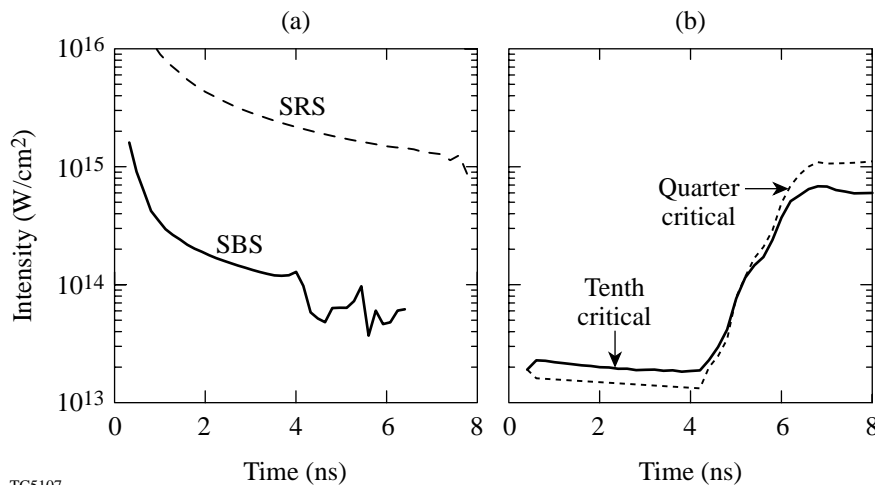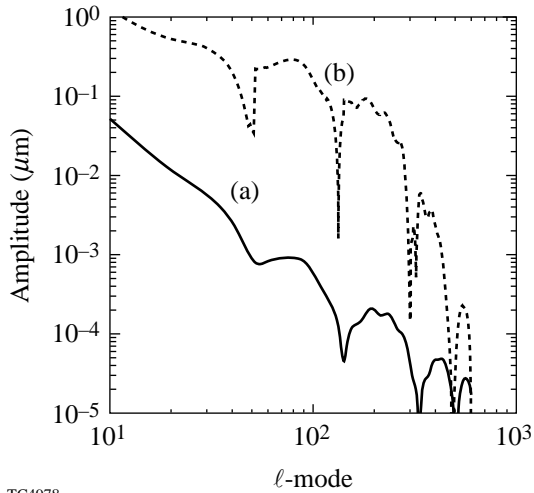

Figure 79.10

(a) The SBS (solid line) and SRS (dashed line) thresholds calculated from the density and velocity profiles as a function of time for the baseline target design. (b) The combined, overlapped beam intensity at the quarter- (dashed line) and tenth-critical (solid line) surfaces as a function of time.

TC5107

an additional $\sigma_{rms} = 1300$-Å perturbation, which has accumulated from the feed-out of 0.5-μm rms from the inner DT-ice layer. Figure 79.11 also shows the mode spectrum of the ablation surface at peak shell velocity, which defines the end of the acceleration phase. The sum of the amplitude of the individual modes gives the total mix width of the ablation-surface instability. Figure 79.12 shows the mix width and the shell thickness as a function of time. In this example we can

clearly see that the shell is larger than this mix width, so we conclude that the $\alpha = 3$ design will survive the acceleration phase when we have 1 THz of bandwidth and 0.5-μm rms of inner DT-ice roughness. At the end of the deceleration phase the total nonuniformity on the inner surface is 1.3 μm, so we would expect this design to ignite.

Figure 79.13 shows the combined effect of different laser-uniformity levels and inner-ice-surface roughness for two different outer-surface finishes on the perturbation amplitude

TC4978

Figure 79.11
The mode spectrum of the outer ablation surface at (a) the start of the acceleration phase and (b) the start of the deceleration phase.
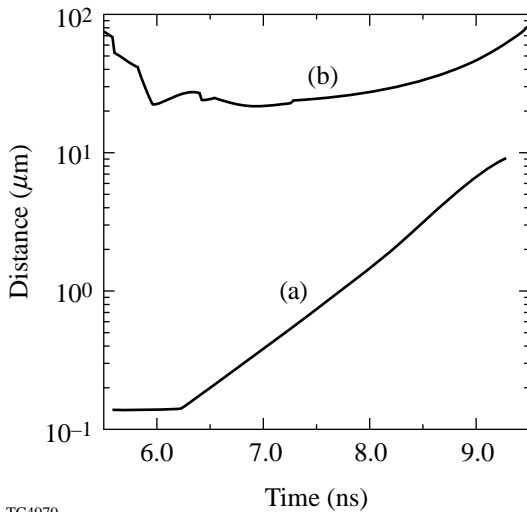
TC4979

Figure 79.12
The (a) ablation-surface amplitude and (b) the shell thickness as a function of time up to the end of the acceleration phase for the baseline, $\alpha = 3$, all-DT target design with 1-THz, 2-D SSD and 0.5-μm initial inner surface, DT-ice finish.

TC5007

Figure 79.13
The combined effect of laser uniformity and inner DT-ice surface roughness (for modes greater than 10) on the rms inner-surface amplitude at the end of the acceleration phase for (a) 0-Å outer-surface finish and (b) 840-Å outer-surface roughness.

of the inner surface at the time of deceleration. For example, 0.5 THz of bandwidth is equivalent (from *ORCHID* simulations) to 520 Å of initial outer-surface perturbation. This is combined with 0.5 μm of inner-surface roughness and with a perfect outer-surface finish [Fig. 13(a)]. The resultant amplitude at deceleration is 1.35 μm. When there is 840 Å [Fig. 13(b)] of outer-surface roughness, the amplitude of the inner surface at deceleration rises to 1.45 μm. These final amplitudes are very close to the maximum tolerable, so we conclude for safety that for a successful ignition campaign using direct drive we will need 1 THz of bandwidth, $< 0.25\ \mu$m of DT-ice nonuniformity in mode $\ell > 10$, and < 800 Å of outer-surface perturbation.

Conclusions

Based on the calculations described in the previous section we have established specifications required on the NIF to ensure a successful direct-drive ignition campaign. Table 79.I summarizes these requirements. It should be noted that independent calculations by Weber,[12] using the 2-D *LASNEX* code, confirm our calculations that the $\alpha = 3$ continuous-pulse design will survive the acceleration phase and should achieve ignition.

Table 79.I: Summary of the specifications for our current modeling of the baseline "all-DT" target design.

Parameter	Requirements
Laser energy	1.5 MJ
Pulse shape	50:1 contrast, 10-ns duration [see Fig. 79.3(b)]
Beam-to-beam power balance	8% in 500 ps
Quad-to-quad power balance (assuming independent quads)	4% in 500 ps
Laser bandwidth	1 THz
Individual beam nonuniformity	3% in 500 ps (all modes)
Outer CH	$<2\ \mu$m
Outer-surface target finish	<800 Å
Inner DT-ice thickness	340 μm$\pm 5\ \mu$m
Inner DT-ice-layer uniformity	$<0.25\ \mu$m ($\ell > 10$) (for $\ell < 10$ exact value to be determined)
Shock-timing accuracy	<50 ps
Preheat	$<0.1\%$ of incident laser energy

REFERENCES

1. J. D. Lindl, Phys. Plasmas **2**, 3933 (1995).

2. S. E. Bodner, D. G. Colombant, J. H. Gardner, R. H. Lehmberg, S. P. Obenschain, L. Phillips, A. J. Schmitt, J. D. Sethian, R. L. McCrory, W. Seka, C. P. Verdon, J. P. Knauer, B. B. Afeyan, and H. T. Powell, Phys. Plasmas **5**, 1901 (1998).

3. S. Skupsky, R. W. Short, T. Kessler, R. S. Craxton, S. Letzring, and J. M. Soures, J. Appl. Phys. **66**, 3456 (1989).

4. H. Takabe *et al.*, Phys. Fluids **28**, 3676 (1985); R. Betti, V. N. Goncharov, R. L. McCrory, and C. P. Verdon, Phys. Plasmas **2**, 3844 (1995).

5. M. Tabak, D. H. Munro, and J. D. Lindl, Phys. Fluids B **2**, 1007 (1990); C. P. Verdon, R. L. McCrory, R. L. Morse, G. R. Baker, D. I. Meiron, and S. A. Orszag, Phys. Fluids **25**, 1653 (1982); J. H. Gardner, S. E. Bodner, and J. P. Dahlburg, Phys. Fluids B **3**, 1070 (1991).

6. J. P. Knauer, C. P. Verdon, D. D. Meyerhofer, T. R. Boehly, D. K. Bradley, V. A. Smalyuk, D. Ofer, P. W. McKenty, S. G. Glendinning, D. H. Kalantar, R. G. Watt, P. L. Gobby, O. Willi, and R. J. Taylor, in *Laser Interaction and Related Plasma Phenomena*, edited by G. H. Miley and E. M. Campbell (American Institute of Physics, New York, 1997), Vol. 406, pp. 284–293; J. Knauer, R. Betti, D. K. Bradley, T. R. Boehly, T. J. B. Collins, V. N. Goncharov, P. W. McKenty, D. D. Meyerhofer, V. A. Smalyuk, C. P. Verdon, S. G. Glendinning, D. H. Kalantar, and R. G. Watt, "Single-Mode Rayleigh-Taylor Growth-Rate Measurements with the OMEGA Laser System," to be published in Physics of Plasmas; J. Grun *et al.*, Phys. Rev. Lett. **58**, 2672 (1987); S. G. Glendinning, S. N. Dixit, B. A. Hammel, D. H. Kalantar, M. H. Key, J. D. Kilkenny, J. P. Knauer, D. M. Pennington, B. A. Remington, R. J. Wallace, and S. V. Weber, Phys. Rev. Lett. **78**, 3318 (1997).

7. C. P. Verdon, Bull. Am. Phys. Soc. **38**, 2010 (1993).

8. V. N. Goncharov, "Self-Consistent Stability Analysis of Ablation Fronts in Inertial Confinement Fusion," Ph.D. thesis, University of Rochester, 1998.

9. V. N. Goncharov, Phys. Rev. Lett. **82**, 2091 (1999).

10. S. W. Haan, Phys. Rev. A **39**, 5812 (1989).

11. A. R. Piriz, J. Sanz, and L. F. Ibanez, Phys. Plasmas **4**, 1117 (1997).

12. S. V. Weber *et al.*, *ICF Quarterly Report* **7**, 43, Lawrence Livermore National Laboratory, Livermore, CA, UCRL-LR-105821-97-2 (1997).

Numerical Investigation of Characterization of Thick Cryogenic-Fuel Layers Using Convergent Beam Interferometry

The effect of hydrodynamic instabilities on the performance of inertial confinement fusion (ICF) experiments is well known. Hydrodynamic instabilities affect ICF capsules during the initial acceleration and final deceleration phases of the implosion. Nonuniformities in the applied drive coupled with imperfections at the target surface seed Rayleigh–Taylor (RT) unstable growth at the ablation front. In addition, the shock wave reflecting off a perturbed inner ice surface returns to the ablation region and also seeds the instability (feed-out). These perturbations grow since low-density, ablated material accelerates the unablated, dense shell. Further growth of these perturbations eventually feeds through the shell and couples with existing perturbations on the inner ice surface. Together these seed RT growth at the ice–gas interface when the ice layer begins to decelerate around the spark plug region near the target's center. As the RT instabilities grow, the cold, dense fuel is mixed into the hot core leading to cooling of the core and reduced target performance.

The success of the ICF program depends on targets designed to limit the amount of RT growth to an acceptable value or whose performance is insensitive to the presence of such perturbations. A good understanding of all nonuniformity sources in the implosion is required to design such targets. Nonuniformity sources include the laser or holraum drive, the coupling of this energy to the target (imprint), and the initial surface finish of both the outer ablator surface and the inner DT ice. To date, significant progress has been made in understanding the role of the first three nonuniformity sources. Characterization of the inner ice surface, however, remains a serious challenge. The ability to accurately characterize this surface is especially critical in light of recent work by Betti[1] in which the feed-out contribution to the ablation region has been shown to be a major factor in overall RT growth during an implosion.

Overview

Cryogenic targets imploded with OMEGA will consist of polymer capsules several micrometers thick with diameters ranging from 900 to 1100 μm. These capsules will be filled with condensed D_2 or DT fuel up to 100 μm thick. Historically,

the fuel content and fuel-layer uniformity of cryogenic targets at LLE have been interferometrically characterized using plane-wave illumination.[2–7] A capsule with a thick cryogenic layer condensed on its interior behaves as a strong negative lens, which has several adverse effects on an interferogram created with plane-wave illumination. Computer simulations of typical interferograms are shown in Fig. 79.14. The highly divergent and spherically aberrated wavefront created by the target cannot be effectively collected and imaged by optics with convenient numerical apertures (<0.2), resulting in loss of information near the perimeter of the target's image. Additionally, interfering this highly curved wavefront with a planar reference wavefront results in an interferogram with a fringe spatial frequency that increases radially to very high values near the perimeter of the target's image. The phase sensitivity

(a)
Concentric

(b)
5% nonconcentricity

T1083
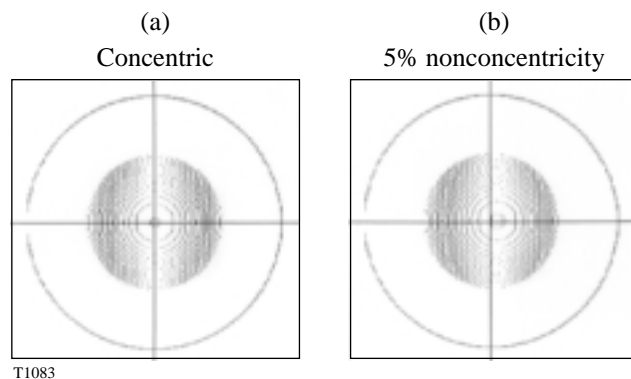
Figure 79.14
Computer-generated interferograms of a 1120-μm-diam, 10-μm-thick capsule that contains 100 μm of condensed fuel. These interferograms were created assuming that both the object and reference beams consisted of planar wavefronts with a 514-nm wavelength, and that $f/6$ optics were used to image the target. All of the surfaces in (a) were perfectly concentric with one another, whereas (b) displays a 5% fuel nonconcentricity, i.e., the center of the spherical inner surface of the condensed fuel layer has been displaced to the right in the figure by 5% of its total thickness. Obviously, a 5% nonconcentricity can be easily detected, but higher-order nonuniformities are much more difficult to detect due to the very high fringe frequency. In addition, information regarding the state of the fuel near the perimeter of the target's image has been lost due to refraction of the object beam outside of the imaging optics' finite collection aperture.

is reduced dramatically when the fringe frequency approaches the Nyquist limit of the detector. As the fringe frequency nears the frequency of pixels in the CCD array, aliasing occurs and the fringes become unresolved.

These limitations can be compensated for by focusing the object beam of a Mach–Zehnder interferometer near the rear focal point of the filled target, causing a nearly collimated beam to emerge. A complete description of this interferometer has been published elsewhere.[8] The optical system used to create an interferogram of a cryogenic target with convergent-beam illumination is shown in Fig. 79.15.
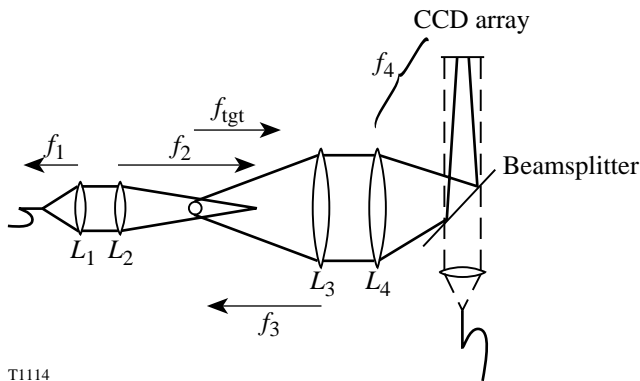
T1114

Figure 79.15
Schematic of the optical system used to create an interferogram of a cryogenic target with convergent-beam illumination. The optics that control the point of focus of the convergent beam and those that image the target are shown. The dashed line denotes the collimated reference beam.

Phase sensitivities of the order of a few hundredths of a wave can be achieved by phase-shifting techniques.[9–11] This involves sequentially acquiring multiple interferograms, each with a unique phase offset caused by introducing a slight path-length change in one of the interferometer's arms. The phase of each point in the interferogram is then obtained, modulo 2π, by performing simple mathematical operations on the set of interferograms. One advantage of phase-shifting methods is that the phase resolution depends primarily on the dynamic range of the CCD array and the contrast of the interferogram, not the number of pixels per fringe.

Methodology

Characterizing a nonuniform cryogenic-fuel layer by interpreting the phase of a wavefront perturbed by passing through it is, unfortunately, not straightforward. Evident in Fig. 79.16, the majority of rays traveling through the target have probed two independent ice surfaces on opposite sides of the target.

Unique measurement of a perturbation on either surface is impossible without collecting an enormous number of interferograms.

The method we propose is very similar to the technique implemented by Wallace[12] to characterize surface perturbations on the outside of ICF capsules. Data is first collected using atomic force microscopy (AFM) along great circles on the target surface. This information is Fourier-analyzed to produce an average one-dimensional (1-D) power spectrum. The 1-D Fourier power spectrum is then mapped into the two-dimensional (2-D) spherical-harmonic spectrum by using an Abel transformation derived by Pollaine.[13] Pollaine showed that a 1-D Fourier power spectrum, representative of the entire surface, could be transformed into the corresponding 2-D power spectrum using

$$P_{2\text{-D}}(l) = \frac{\mathrm{d}}{\mathrm{d}l} \int P_{1\text{-D}}\left(\sqrt{l^2 + n^2}\right) \mathrm{d}n.$$

MacEachern[14] showed that a representative 1-D power spectrum could be obtained by averaging nine independent, experimental 1-D power spectra together. These nine traces are
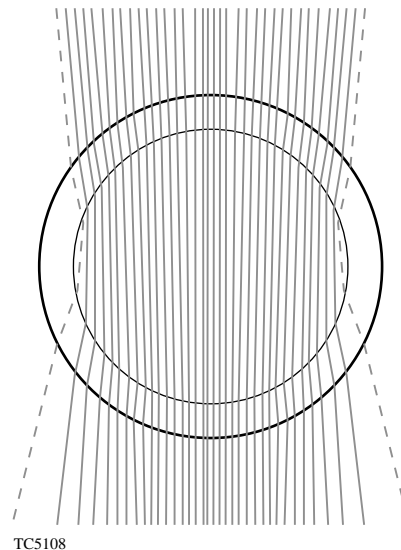
TC5108

Figure 79.16
Ray trace of an $f/5$ laser through an OMEGA cryogenic capsule. The method uses rays very near the perimeter of the target similar to the dashed rays in the figure. Such rays probe two points on the inner surface, which, when averaged, represent two of the scans used in the outer-surface-measurement technique described in the text.

arranged in groups of three and are taken along great circles that lie on the three orthogonal planes that intersect the target's center. Each set of three traces samples an approximately 40-μm-wide swath on the target's surface. The geometry used in this data-acquisition method is shown in Fig. 79.17 with the three traces within a set labeled A, B, and C.
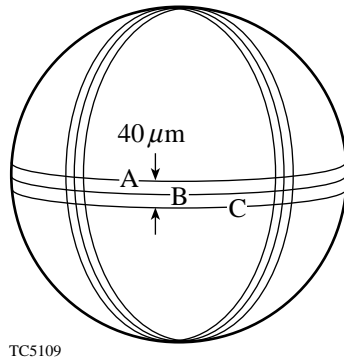

40 μm

A
B
C

TC5109

Figure 79.17
Geometry of data-acquisition traces used in the surface-characterization method. Each of the three sets of traces lies along an orthogonal direction on the sphere. The width between outer traces is approximately 40 μm.

Reexamining Fig. 79.16, it can be seen that there is a subset of rays, traveling very near the equator of the target, where a small cord (~40 μm long) probes two points of the inner ice surface. Such a ray is shown dashed in Fig. 79.16. The perturbed optical-path difference (OPD) along this path represents an average at the two positions. Collecting all of these rays from the overall phase map yields a great circle of data, coming out of the paper, sampling the inner ice surface near the equator at this orientation. This is essentially the same as averaging traces A and C in the method described above and shown in Fig. 79.17. The target is rotated and data is collected along several great circles. This data is analyzed using the process described above for characterizing an outer-surface perturbation spectrum.

Implementation

To implement the characterization method described above, the phase of the wavefront passing through the cryogenic target must be acquired by interferometrically measuring the OPD between it and a planar reference wavefront. Eventually, when the cryogenic filling station at LLE is in operation, this information will be provided by measuring real ICF capsules. Initial analysis, however, has been done using synthetic OPD maps produced using the ray-trace simulation code *Ring*s. *Ring*s,

which was written by Craxton[15] to simulate three-dimensional (3-D) planar interferometric probes, was modified to provide for a convergent *f*/5 probe at 670 nm. The capsule used in our analysis is equivalent to that of a cryogenic target designed to be used in initial experiments on OMEGA. The capsule consists of a thick shell of DT ice (100 μm) surrounded by a single, thin layer of plastic (1 to 5 μm). Fully independent perturbations can be applied to any or all interfaces within the target. Originally, these perturbations were limited to simple geometric terms of the order of less than 4. Routines have since been added that allow perturbations to be imposed based on their complete spherical-harmonic spectrum. Normalization routines control the total applied ice-surface roughness (rms) and spectral dependency of the modal pattern. Multiple, independent great circles can be simulated by aligning the probe axis with respect to selected points on the target.

Rings determines the intersection of a ray at every physical interface within the target to within 1 Å. Once the intersections are determined, the total optical path is calculated for the transit through the preceding layer. Snell's Law is then applied to produce the proper change in direction cosines for transit into the next layer. *Rings* traces many rays through the target and into a collection optic. The resulting phase map is then projected back to an image plane located at the center of the target, which is conjugate to the detector plane in the actual interferometer.

The OPD map must first be analyzed to identify a radius that corresponds to the inner ice surface. As can be seen in Fig. 79.16, this information is near the very edge of the map. Rays that intersect the target at steeper angles are refracted outside of the collection aperture of the interferometer's *f*/5 imaging system. Once identified, this information is not necessarily uniformly spaced along a circle; it must then be interpolated to a great circle of 2^n evenly spaced points to be analyzed by standard FFT routines. Many interpolation schemes were tested. A solution was found that imports the data into the commercially available graphics package Tecplot.[16] Tecplot runs on Pentium PC's and has extensive capabilities to interpolate data to a variety of physical grids, including evenly spaced circles. The interpolated data is then Fourier-analyzed to recover a 1-D power spectrum. The overall procedure to analyze a given OPD takes only a few minutes per view. It is anticipated that an averaged 1-D power spectrum, evaluating six views (as shown in Fig. 79.18), could be obtained in less than one-half hour. The final step—transforming the averaged 1-D power spectrum into the 2-D spectrum— is accomplished using a Fortran program and requires only a few minutes of computer time.

amples were constructed using a variety of total roughness and spectral dependency. The applied perturbations took the form

$$R_1 = R_0 + \sum_{\ell=2}^{n}\left(\frac{a_0\ell^{-\beta}}{\sqrt{2\ell+1}}\sum_{m=-\ell}^{\ell}Y_{\ell,m}\right),$$

where n is the number of applied modes, β is the modal dependence of the applied spectrum, and a_0 has been normal-
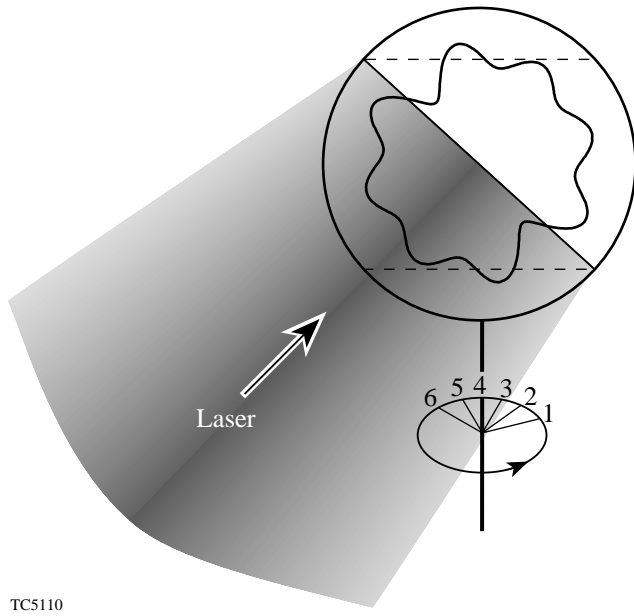

Figure 79.18
Schematic indicating the data-acquisition procedure. The probe laser is incident on the target at an angle of 17.72° below the equator. After collecting data for the position, the target is rotated on-axis 30° and scanned again. The procedure is repeated until six scans are completed.

Numerical Results

The first test of the method described above was to perturb the inner ice layer with pure sinusoidal modes to determine whether the FFT of the great circle of the synthetic OPD would return the applied value. Such a test does not require the Abel transformation. Initially, only single sinusoidal modes ($m = 20$, 40, and 80) were modeled. The results, shown in Fig. 79.19, demonstrate that the method is able to reproduce the applied perturbation quite well. The next step was to perturb the target with a whole spectrum of sinusoidal modes given by

$$R_1 = R_0 + \sum a_0 m^{-1.1}\cos\left\{m\left[\varphi+2\pi b(m)\right]\right\},$$

where $a_0 = 0.739$ μm and $b(m)$ is a random number used to distribute random phase among the modes. The result of these tests, shown in Fig. 79.20, indicate that the method is able to recover the applied sinusoidal spectrum very well.

Building on these results, tests were constructed that would more closely match what one would expect in nature. The pertinent values that are required for numerical simulation of ICF capsules are the total rms and the modal dependency of the overall spherical-harmonic spectrum. As such, several ex-

Figure 79.19
Mode amplitudes of OPD determined through ray trace of targets with inner-ice surface perturbed with an individual sinusoidal mode. The amplitudes of the applied perturbations were chosen to scale as 2000/m nm.
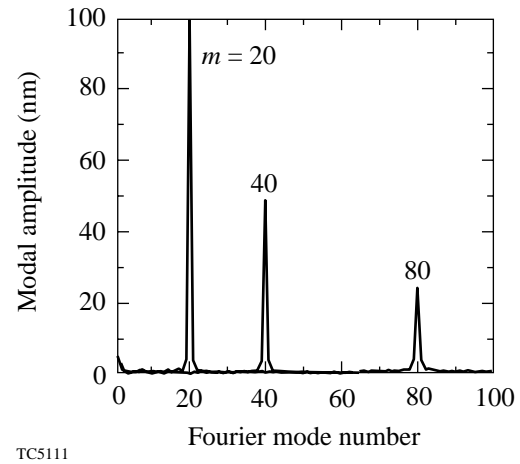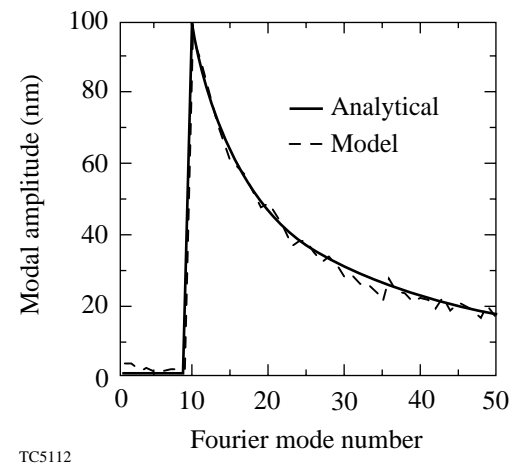

Figure 79.20
Mode amplitudes of OPD determined through ray trace of targets with inner-ice surface perturbed with a spectrum of sinusoidal modes between mode $m = 10$ and $m = 50$. The solid curve represents the exact modal spectrum that was applied to the surface.

ized to return the desired surface rms. The spectral amplitudes were modified in the high-frequency range by applying a Blackman filter[17] to avoid Gibb's phenomenon behavior in the numerical reconstruction of the applied spectrum.

An important point to these calculations is the determination of a cutoff frequency above which any additional modes make little contribution to the overall perturbation at stagnation and, as such, need not be resolved. This cutoff is generally taken to be near mode 50. This cutoff comes from stability arguments of target designs that assume monotonically decreasing perturbation spectra of the order of $\ell^{-\beta}$ at the beginning of the deceleration phase of the implosion. For $\beta = 1.5$, the relative mode amplitudes at about mode 40 and beyond are one to several orders of magnitude lower than the amplitudes of mode numbers below 10. When Haan saturation effects[18] are considered, however, it can be shown that such a cutoff is applicable for perturbation spectra that are even flat ($\beta = 0$) at the onset of deceleration (see Appendix A). Therefore, our analysis, while examining targets with perturbations using modes 2 to 192, resolves only the modal region of the ice roughness between modes 2 and 50.

Similar to the above sinusoidal perturbation tests, our first test with spherical harmonics was to perform an analytical check of the method. Knowing the analytic form of the perturbation spectrum placed on the inner ice layer, we could immediately take the Fourier transform of the resulting perturbed radius representing the inner target equator. This 1-D power spectrum was then transformed to give back the applied 2-D spectrum. The results of this case are shown in Fig. 79.21, where it can be seen that the method gives very good reconstruction of the applied spectrum except in the very high frequency range. Here the method experiences slight trouble in reconstructing the spectrum. The numerical results here are being strongly influenced by the unphysical termination of the spectrum. The results of this test confirmed that a good approximation of the 2-D spectrum of the inner ice surface could be obtained from ray-trace data that correctly maps a great circle of the inner ice surface.

We then examined ray-trace tests that spanned both the rms of the surface and the modal dependency of the spectrum. The results of one of these tests are reported here. When the spherical harmonics are applied, the amplitude of all m-components of a particular ℓ-mode is assumed constant. Additionally, a base-line total rms value used here is defined to include only the power in modes 10 to 50. Several examples, comparing the numerically obtained modal amplitude spectrum with the exact applied perturbation, are shown in Fig. 79.22. The
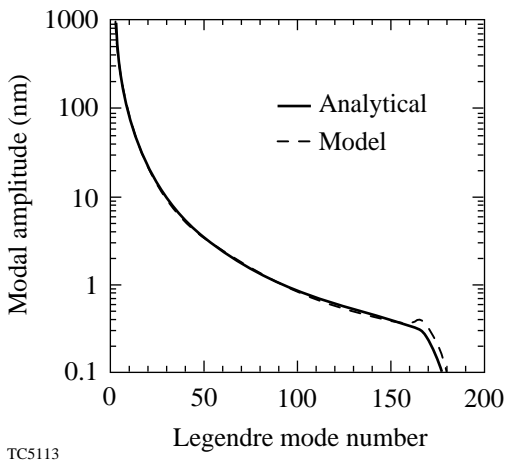
Figure 79.21
Evaluation of an analytical representation of a spherically perturbed inner ice surface. The solid curve represents the exact modal spectrum applied to the surface. The dashed curve is obtained by taking the FFT of the perturbed radius and transforming the 1-D power spectrum into the 2-D power spectrum. Except for the high-frequency regime, the method can be very accurate in resolving the 2-D applied perturbation using 1-D data.
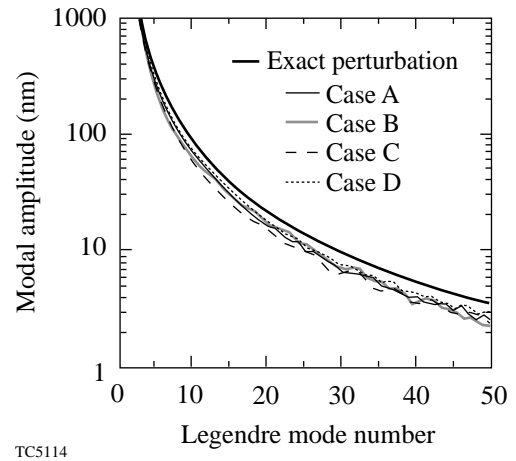
Figure 79.22
Comparison of several ray-trace evaluations of an OMEGA cryogenic capsule with a spherically perturbed inner ice surface. The thick solid curve represents the exact modal spectrum applied to the inner surface. The other curves are obtained by averaging a set (six numerical ray traces) of 1-D power spectra of perturbed OPD and then transforming that average into the 2-D power spectrum. Each curve represents the resulting modal amplitudes obtained at a separate orientation on the target. These orientations are given in Table 79.II.

capsule was perturbed with a full spectrum of modes from $\ell = 2$ to $\ell = 192$. The baseline total rms was set to be 0.25 μm with a spectral parameter $\beta = -1.5$. Four tests (Cases A–D) were performed, representing the acquisition of data at different spherical orientations on the capsule. Each case used six acquired ray traces taken about the capsule to produce the average 1-D power spectrum for the analysis. The spherical orientations are given in Table 79.II. Examining Fig. 79.22, it can be seen that each of the tests provides a very good representation of the modal dependency of the applied perturbation. Case B recovered 89% of the total rms defined from modes 2 to 50, while Case C recovered only 73%. From these results, it can be seen that the method provides good resolution of the perturbations on the inner ice surface.

Future Work

The method we have described will provide a detailed analysis of the inner-ice-surface roughness; however, more work must be performed to determine the sensitivity of the method under a variety of physical constraints. Aberrations in the wavefront caused by the optical system have not been included in the model so far. These can potentially be subtracted from the target's phase map by taking a phase map of the wavefront passing though the interferometer without a target present. The shot noise and finite resolution of the CCD array detector (i.e., their role in limiting the phase sensitivity of the interpolation routine) should also be examined. Finally, the limitation that perturbations on the surfaces of the capsule impose on the sensitivity of ice-surface measurements should be examined.

Appendix A

To determine the critical modes that make up the perturbed interface between the cold, dense fuel and the hot spark-plug region, the RT growth that all modes experience during the deceleration phase in an ICF implosion must be examined. We start by assuming a modal dependency between the modes that is of the form

$$\sigma_\ell = \frac{C_1}{\ell^\beta}.$$

Given the total surface perturbation σ_{rms}, one can integrate over the modes (from 2 to 500) to arrive at the constant C_1 as

$$C_1 = \frac{\sigma_{rms}}{\sqrt{\sum \frac{1}{\ell^{2\beta}}}}.$$

Lindl[19] has shown that during deceleration any unsaturated modes will grow roughly as

$$a_\ell^{lin} = (a_\ell)_0 e^\eta,$$

where

$$\eta = \sqrt{\frac{2\ell}{1 + 0.2\,\ell}}.$$

One can see that η asymptotes quickly to the value $\eta \cong \sqrt{10}\,(\sim 3)$ at about mode 20. As such, in the absence of saturation, all modes above 20 will grow roughly the same. If one assumes the initial perturbation spectrum to be comparable to the initial ice surface, the spectral parameter β can be set to be ~1.5. While most of the modes will grow the same, the final amplitudes of modes greater than 40, as shown in Fig. 79.A1, are relatively

Table 79.II: Orientation angles used in numerical ray-trace tests. Cases A and B represent scans at two orthogonal positions on the sphere. Case C was chosen as a neutral position between A and B. Finally, Case D is for scans along the optical axis proposed for the experimental characterization station at LLE.

Case	Orientation Angles (θ, Φ)					
	Scan 1	Scan 2	Scan 3	Scan 4	Scan 5	Scan 6
A	90, 0	90, 30	90, 60	90, 90	90, 120	90, 150
B	90, 90	60, 90	30, 90	0, 90	30, 180	90, 150
C	90, 0	75, 30	60, 60	45, 90	60, 120	75, 150
D	72.28, 0	72.28, 30	72.28, 60	72.28, 90	72.28, 120	72.28, 150

very small. As such, these modes lend no significant contribution to the overall perturbation at stagnation; however, the initial spectrum involved must also include contributions from perturbations feeding through from the ablation surface. These perturbations will add in quadrature with the ice layer, and the resulting perturbation rms will probably no longer obey $\beta = 1.5$. As shown in Fig. 79.A1, the final amplitude spectrum of these perturbations increases monotonically with decreasing β. While it is hard to conceive of β ever being negative, having β approach zero must be considered.

Of course, as the spectral parameter does approach zero, more power is shifted out of the low-order modes and into the higher-frequency modes. These modes will then become candidates for saturation. Haan has shown[18] that, for a specific mode, as the amplitude approaches its saturation amplitude

$$\left(a_\ell^{\text{sat}} = \frac{2R}{\ell^2} \right),$$

its RT growth undergoes a transition and stops growing exponentially. The amplitude of this perturbation then grows linearly in time and is given by

$$a_\ell = a_\ell^{\text{sat}} \left[1 + \ln\left(\frac{a_\ell^{\text{lin}}}{a_\ell^{\text{sat}}} \right) \right].$$

Therefore, such modes will grow much slower than unsaturated ones and will not contribute significantly to the overall perturbation at stagnation.

A threshold for saturation can be calculated by comparing the Haan saturation amplitude at a given radius to the given perturbation rms at that point:

$$\frac{2R}{\ell_c^2} = \sqrt{\frac{4\pi}{(2\ell_c + 1)}} \, \sigma_\ell = C_1 \sqrt{\frac{4\pi}{(2\ell_c + 1)}} \, \ell_c^{-\beta},$$

where ℓ_c is defined as the modal saturation threshold. Performing some algebra, assuming $2\ell_c \gg 1$, and defining

$$C_2 = \frac{2}{\sqrt{2\pi C_1}},$$

we have

$$\ell_c = (RC_2)^{1/(1.5-\beta)}.$$

Figure 79.A1

(a) Final linear-growth-amplitude spectrum of perturbations with initial amplitudes of the form $\sigma_\ell = C_1/\ell^\beta$. Here C_1 has been normalized to give $1 \, \mu m$ at $\ell = 2$ for all cases of β. (b) Saturation threshold (mode number) for various cases of total σ_{rms} as a function of the spectral parameter β. Note that for $\beta > 1$, only modes $\ell > 100$ are candidates for saturation. As the initial spectrum flattens and more power is shifted from lower mode numbers into higher ones, modes above $\ell = 20$ can become candidates for saturation. As β falls below 1.0, saturation can be expected to play an increasing role in determining the final perturbation spectrum at stagnation.

Assuming $R \sim 200 \, \mu m$, we can graph the saturation threshold for a variety of initial perturbation rms and spectral parameter β. Such results are plotted over the spectral behavior in Fig. 79.A1. From this graph it can be seen that for β below 1.0, saturation can be expected to play a role in determining the perturbation spectrum at stagnation. For values of β above 1.0, saturation no longer aids in limiting the growth of modes below 100; however, as was pointed out above, in this regime the modal amplitudes fall off quickly with increasing mode number and, as such, will not contribute at stagnation.

A fully integrated measure of the importance of the modal spectrum can be attained by examining the mode number at stagnation at which the integral of power up to that mode represents 95% of the total perturbed power. A full stability analysis was performed for a variety of spectral parameters β and initial perturbation rms to obtain such a cutoff. The results, shown in Fig. 79.A2, clearly show 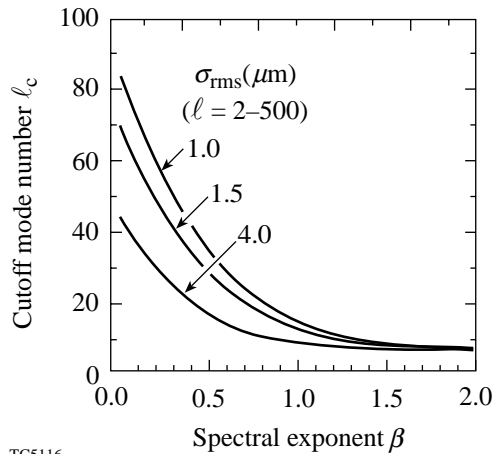that, for expected values of β (0.5 to 1.5), 95% of the total power resides in modes less than 50. For values of β below 0.5, the cutoff mode number does climb above 50, but it is well contained below mode 100 for expected rms values.

TC5116

Figure 79.A2
Cutoff mode number at stagnation at which the integral of perturbed power up to that mode represents 95% of the total perturbed power. For expected values of total σ_{rms} (0–4 μm) and β (0.5–1.5), 95% of the total power resides in modes less than 50. For values of β below 0.5 the cutoff mode number does climb above 50, but it is well contained below mode 100 for expected rms values.

REFERENCES

1. R. Betti, V. Lobatchev, and R. L. McCrory, Phys. Rev. Lett. **81**, 5560 (1998).

2. J. A. Tarvin *et al.*, in *Interferometry*, edited by G. W. Hopkins (SPIE, Bellingham, WA, 1979), Vol. 192, pp. 239–243.

3. T. P. Bernat, D. H. Darling, and J. J. Sanchez, J. Vac. Sci. Technol. **20**, 1362 (1982).

4. K. Kim *et al.*, J. Vac. Sci. Technol. A **3**, 1196 (1985).

5. K. Kim and D. L. Krahn, J. Appl. Phys. **61**, 2729 (1987).

6. T. R. Pattinson and W. J. Felmlee, J. Vac. Sci. Technol. A **6**, 1882 (1988).

7. H. J. Kong, M. D. Wittman, and H. Kim, Appl. Phys. Lett. **55**, 2274 (1989).

8. Laboratory for Laser Energetics LLE Review **58**, 83, NTIS document No. DOE/SF/19460-17 (1994). Copies may be obtained from the National Technical Information Service, Springfield, VA 22161.

9. K. Creath, in *Surface Characterization and Testing*, edited by K. Creath (SPIE, Bellingham, WA, 1986), Vol. 680, pp. 19–28.

10. K. Kinnstaetter *et al.*, Appl. Opt. **27**, 5082 (1988).

11. K. Creath, in *Progress in Optics XXVI*, edited by E. Wolf (North-Holland, Amsterdam, 1988), pp. 351–393.

12. S. M. Pollaine, S. P. Hatchett, and S. H. Langer, *ICF Annual Report 1994*, 87, Lawrence Livermore National Laboratory, Livermore, CA, UCRL-LR-105820-94 (1994).

13. R. J. Wallace, R. L. McEachern, and W. W. Wilcox, *ICF Annual Report 1994*, 79, Lawrence Livermore National Laboratory, Livermore, CA, UCRL-LR-105820-94 (1994).

14. R. L. McEachern, C. E. Moore, and R. J. Wallace, J. Vac. Sci. Technol. A **13**, 983 (1995).

15. R. S. Craxton, LLE, unpublished.

16. Tecplot Data Visualization Software, ©1996 by Amtec Engineering, Inc., P.O. Box 3633, Bellevue, WA 98009-3633.

17. A. V. Oppenheim and R. W. Schafer, *Discrete-Time Signal Processing* (Prentice-Hall, Englewood Cliffs, NJ, 1989).

18. S. W. Haan, Phys. Rev. A **39**, 5812 (1989).

19. J. D. Lindl, *Inertial Confinement Fusion: The Quest for Ignition and Energy Gain Using Indirect Drive* (Springer-Verlag, New York, 1998), pp. 66–67.

Studies of Target Implosion Using *K*-Shell Absorption Spectroscopy of an Embedded Titanium Layer

In laser-imploded target studies, the measurement of shell compression and uniformity is essential to understand target performance. Previously we have used targets in which a titanium-doped layer was incorporated into the target shell. The doped layer provided a variety of diagnostic signatures (absorption lines, *K*-edge absorption, Kα imaging) for determining the areal density and density profile of the shell around peak compression.[1–5] In this article we apply some of these methods to demonstrate the improvement in target performance when implementing SSD[6] (smoothing by spectral dispersion). In particular, we study slow-rising laser pulses (for low-adiabat implosions), where the effect of SSD smoothing is more pronounced. In addition, we introduce a new method for studying the uniformity of imploded shells: using a recently developed[5] pinhole-array x-ray spectrometer we obtain core images at energies below and above the *K*-edge energy of titanium. The nonuniformity of such images depends on the nonuniformity of both the emitting core and the absorbing shell; however, the ratio between the images above and below the *K* edge essentially depends on the nonuniformity of the shell alone. Finally, we compare the results with those of 1-D *LILAC* simulations, as well as 2-D *ORCHID* simulations, which allow for the imprinting of laser nonuniformity on the target. The experimental results are replicated much better by *ORCHID* than by *LILAC*.

Areal-Density Measurement Using *K*-Shell Absorption

To demonstrate the effect of SSD on target performance we chose two pairs of laser shots from two different series; for each pair all conditions were nearly identical except for the presence of SSD. The target and laser conditions for these shots are listed on the first four lines of Table 79.III. The two target shots with SSD are almost identical as are the two shots without SSD and they can be used interchangeably. The pulse shape in these four shots was the 2.5-ns, slow-rising pulse shape ALPHA306: starting with a flat, 0.5-ns foot at 2.5% of the peak, followed by a 1.1 ns of a slowly rising ramp, then a 0.2 ns of a faster-rising ramp, it finally reaches a 0.7-ns flat top. This pulse has been shown to place the colder part of the shell during the laser irradiation of typical CH shells on an adiabat of $\alpha \sim 3$. It is particularly suitable for studying the effect of SSD smoothing on reducing imprinting because faster-rising pulses cause early decoupling of laser and shell, which reduces the imprint even without SSD. All four targets were voided, to

Table 79.III: Experimental parameters for the laser shots discussed in this article. The first four shots demonstrate improvement in performance due to SSD; the fifth shot is discussed in the last section of this article. All shots had a Ti-doped layer embedded in the shell (atom concentration of Ti is given in brackets). ALFA306 is a slow-rising, 2.5-ns pulse shape.

Shot No.	Inner radius (μm)	Inner CD layer (μm)	CH(Ti) layer (μm)	Outer CH layer (μm)	Total shell thickness (μm)	Fill gas (atm)	2-D SSD bandwidth (Å)	Pulse shape	Laser energy (kJ)
13151	444.5	5.8	4.8 (4%)	14.3	24.9	void	1.25 × 1.65	ALFA306	21.0
13152	445.0	5.7	5.1 (4%)	14.3	25.1	void	–	ALFA306	21.7
13936	448.5	5.0	5.7 (4.3%)	15.7	26.4	void	1.28 × 1.7	ALFA306	19.5
13939	442.5	5.0	5.7 (4.3%)	15.7	26.4	void	–	ALFA306	22.6
15156	438.5	0.8	2.6 (6.2%)	16.6	20.0	DD (3)	1.26 × 1.76	1-ns square	26.2

resemble the implosion of future cryogenic targets. The structure of the targets was chosen so that the doped layer would become nearly identical with the cold layer at peak compression. The thickness of the overcoat CH layer was chosen so as to be ablated away during the laser pulse; indeed, the laser burned through it toward the end of the pulse. The inner layer was thick enough to constitute the hot, compressed core. This conclusion is based on the observation of Ti plasma lines emitted at the center of the target. In the last section we describe measurements of shell nonuniformity obtained with a different pulse shape: a 1-ns square pulse.

The x-ray spectra were recorded by a space-resolving, time-integrating spectrograph and a streak spectrograph. The first spectrograph used a Ge(111) crystal and a 25-μm-wide spatially resolving slit. The continuum core emission was clearly visible above the much-weaker radiation of larger extent from the interaction region (see Fig. 4 in Ref. 3; also, Fig. 79.28 below); thus, for measuring the absorption of core radiation within the shell, the radiation from the interaction region can be easily subtracted. The crystal calibration curve (see Fig. 4 in Ref. 1) is relatively flat in the 3- to 6-keV region. The streak spectrograph used a RbAP crystal with the image recorded on film. The sensitivity of the film is determined with a density wedge developed simultaneously with the data; however, because the photocathode is not uniformly sensitive across its surface, we used the streak data to monitor the temporal changes but the areal-density determinations relied on the time-integrated spectra. This point is further discussed below.
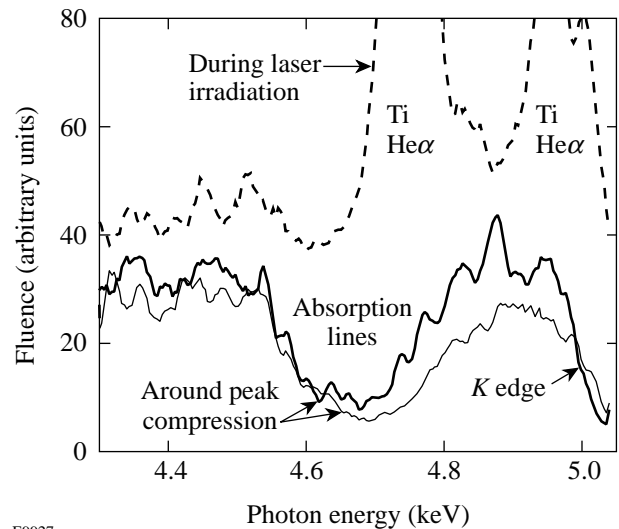
Figure 79.23 shows a comparison of the calibrated, time-integrated spectra from shots 13151 and 13152. Figure 79.24 shows lineouts through the streak spectrum for shot 13152 at three different times; the streak spectra for shot 13151 are qualitatively similar. The upper spectrum is emitted during the laser irradiation, and the lower two spectra are emitted at two instances during the compression; the complete record shows that when the laser irradiation terminates, the x-ray emission falls and then rises again during compression. For clarity, the upper curve in Fig. 79.24 was raised by 30. Figure 79.24 clearly shows that the lines of highly ionized Ti ions are emitted during the laser irradiation; their large width (in both Figs. 79.23 and 79.24) is due to source broadening, corresponding to emission from the laser-interaction region. This is also evident from the spatially resolved spectra (e.g., see Fig. 79.28 below). Figure 79.23 shows a higher intensity of these Ti lines when SSD was not implemented. This is consistent with the results of burnthrough experiments[7] that show a faster burnthrough when SSD is absent, due to a higher level of laser imprint.

Turning to the core emission, we see that continuum radiation from the imploded core (formed by the inner layer of the shell) is absorbed when traversing the cold titanium-doped layer. Two types of absorption are evident: $1s$–$2l$ absorption lines in Ti ions with successive L-shell vacancies (around

Figure 79.23
Comparison of spectra from two shots (conditions listed in Table 79.III). The main difference is the larger drop above the K edge of Ti (around ~ 5 keV) due to SSD smoothing, indicating a higher cold-shell areal density.

Figure 79.24
Lineouts through the streak spectrum at three different times. The upper spectrum is emitted during the laser irradiation, the lower two spectra at different instances during the compression. Ti lines are seen to be emitted during the laser irradiation. The absorption lines and K-edge absorption are seen to occur simultaneously. For clarity the upper curve was raised by 30.

4.6 keV) and Ti *K*-edge absorption (at ~5 keV). We show in the next section that the lines are absorbed in a layer of temperature in the range of ~200 to ~400 eV surrounding the core (the "cool" shell layer), whereas the radiation above the Ti *K* edge is absorbed in a colder layer of temperature in the range of ~150 to ~220 eV surrounding the former layer (the "cold" shell layer).

The drop in intensity across the Ti *K* edge yields the areal density of the titanium alone, using standard tables of absorption in titanium foils; calculations[8] show that at higher temperatures, when *M*- and *L*-shell electrons are successively removed, the *K* edge shifts to higher energies but at a given energy above the edge the absorption hardly changes with ionization. The intensity ratio $R_K = I(< E_K)/I(> E_K)$, where $< E_K$ means an energy just below and $> E_K$ just above the Ti *K* edge, is related to the difference in opacity $\Delta\tau = \tau(> E_K) - \tau(< E_K)$: $R_K = \exp(\Delta\tau)$. More precisely, this value is used as an initial guess in calculating the spectrum above the *K* edge before its absorption and adjusting it to join smoothly the measured spectrum below the *K* edge (see Fig. 6 in Ref. 1). For shot 13151 (with SSD) the Ti areal density is found to be 1.7 mg/cm^2, and for shot 13152 (without SSD) it is 0.78 mg/cm^2. Knowing the Ti concentration, the areal density of the cold doped layer is found to be 7.3 mg/cm^2 and 3.4 mg/cm^2, respectively. These values of $\rho\Delta R$ were obtained from the time-integrated spectra because of their higher spectral resolution as compared with the streak-spectra data; however, the streak data provide additional support for these results. During the time when the core emission is intense, the absorption seen in the streak data does not change appreciably so that the peak $\rho\Delta R$ does not exceed the average $\rho\Delta R$ by more than a factor of ~1.3. It should be noted that the background continuum emitted by the laser-interaction region is distinct from the core continuum in both time and space. Thus, in determining the continuum absorption the background can be removed through either time resolution or space resolution (see Fig. 4 in Ref. 3).

In addition to the *K*-edge absorption, the absorption lines around 4.6 keV yield the areal density of the cool region. Using the method explained in Ref. 9 and used in Ref. 1, we derive ~3.5 mg/cm^2 for the $\rho\Delta R$ of that region. The total areal density of the doped layer is the sum of the $\rho\Delta R$ derived from the *K*-edge absorption and the $\rho\Delta R$ derived from the absorption lines since, as Fig. 79.24 shows, *the two absorptions for the most part occur simultaneously*. Thus, the total areal density of the doped layer with and without SSD becomes 10.8 mg/cm^2 and 6.9 mg/cm^2, respectively. Applying a correction derived

from the streak spectra, the *peak $\rho\Delta R$ values* are ~14 mg/cm^2 and 9 mg/cm^2, respectively. The uncertainty in these values is ±25%.

Figure 79.23 shows that, whereas the *K*-edge jump differs appreciably for the two spectra, the line absorption as well as the core continuum emission is very similar. The two are related because the lines are absorbed on the fringes of the hot core; thus, the energy dumped into the core depends more on the absorbed laser energy and less on the irradiation uniformity.

The total areal density of the compressed shell can be obtained approximately by multiplying the measured $\rho\Delta R$ of the doped layer by a factor $Q = (\rho\Delta R)_{0,\text{unablated}}/(\rho\Delta R)_{0,\text{doped}}$, where $(\rho\Delta R)_{0,\text{ unablated}}$ is the areal density of the part of the shell that is not ablated (i.e., is imploded) and $(\rho\Delta R)_{0,\text{doped}}$ is the areal density of the doped layer, both in the initial target. The former is known from burnthrough experiments.[7] To demonstrate the validity of this procedure we show in Fig. 79.25(a) the *LILAC*-calculated ratio $R = \rho\Delta R(\text{shell})/\rho\Delta R(\text{doped layer})$ as a function of time for various separations *S* of the doped layer from the inner shell surface (in the original target). For each curve the target is that of shot 13151, except that *S* was assigned a different value in each case. The calculated shell $\rho\Delta R$ is also shown (the peak $\rho\Delta R$ is ~0.5 g/cm^2). During the first 3 ns of the pulse the ratio *R* decreases because of ablation but during the following compression, especially for $S \sim 1 \mu$m, it changes only slightly. Since an outer layer of about 13 μm is ablated in shot 13151, the value of *Q* is ~2.5; as Fig. 79.25(a) shows, when $S \sim 1 \mu$m, this value, when multiplied by the measured doped-layer $\rho\Delta R$, would yield the correct total shell $\rho\Delta R$ at peak compression. Thus, for targets with $S < 1 \mu$m the procedure would overestimate the total shell $\rho\Delta R$, whereas for $S > 1 \mu$m it would underestimate it. We further calculate *R* by a model that assumes a constant-density shell that converges radially without compression. Figure 79.25(b) shows the results as a function of the compression ratio; the various curves correspond to the curves of Fig. 79.25(a). The initial target in Fig. 79.25(b) is a 12-μm-thick shell, which corresponds to the unablated target in shot 13151. As seen, the corresponding curves in the two figures are very similar, even though the $\rho\Delta R$ values in the incompressible model are much smaller than in the *LILAC* calculations. This indicates that the procedure is insensitive to the details of the implosion.

The separation of the doped layer in the targets listed in Table 79.III is larger than the optimal; thus, this method will underestimate the total shell $\rho\Delta R$ by about a factor of 2. Since
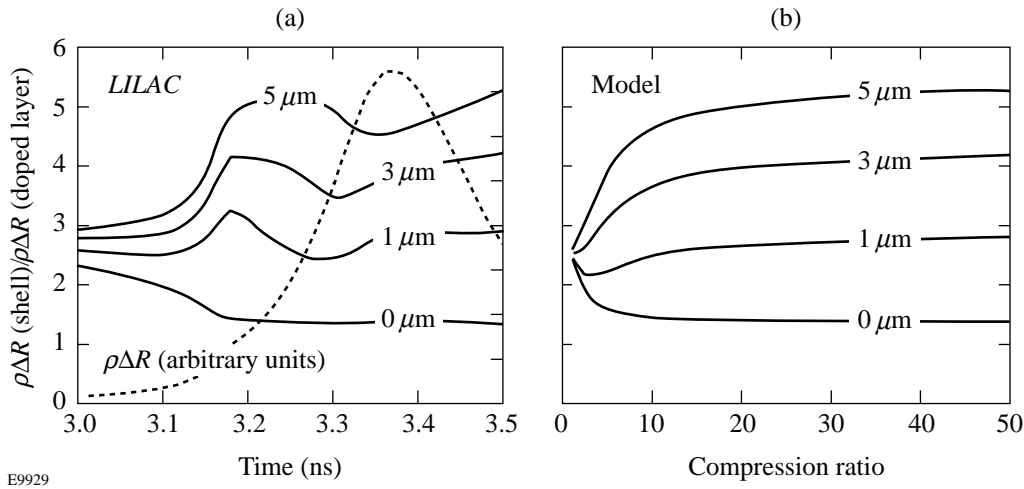
Figure 79.25

The calculated ratio $R = \rho\Delta R(\text{shell})/\rho\Delta R(\text{doped layer})$ for various separations S of the doped layer from the inner shell surface (in the original target). (a) *LILAC*-calculated R as a function of time; the curves correspond to shot 13151 except that S is different for each curve. The calculated shell $\rho\Delta R$ is also shown. (b) Model-calculated R as function of compression ratio; the initial target is assumed to correspond to shot 13151 after the ablation (of 13 μm CH) has been completed.

the value of Q is ~2.5 for the shots of Fig. 79.23 and accounting for this factor-of-2 underestimate, the total shell $\rho\Delta R$ is found to be 70 mg/cm^2 for shot 13151 and 45 mg/cm^2 for shot 13152. The peak shell $\rho\Delta R$ simulated by the 1-D code *LILAC* is ~500 mg/cm^2. This value is higher by a factor of ~7 than what was measured on shot 13151 (with SSD) and by a factor of ~11 on shot 13152 (without SSD). On the other hand, *ORCHID* simulations yield a peak total $\rho\Delta R$ of ~100 mg/cm^2, which is much closer to the experimental value. Further comparisons between the experimental results and code simulations are given below.

The areal-density values obtained above assume a uniform $\rho\Delta R$ over the shell surface. For a shell with modulations in $\rho\Delta R$, *the value* $\rho\Delta R_M$ *measured by opacity will always underestimate the average* $<\rho\Delta R>$ because low-opacity regions have more weight in an integral opacity measurement. For example, if we assume that a fraction α of the shell area consists of radial holes (i.e., opacity $\tau = 0$) and the rest has a constant opacity τ, we find

$$\rho\Delta R_M \big/ \langle\rho\Delta R\rangle = -\ln\big[\alpha + (1-\alpha)\exp(-\tau)\big]\big/(1-\alpha)\tau, \quad (1)$$

which is always less than 1. Also, it can be shown that for a given measured opacity τ_M, the relation $\alpha < \exp(-\tau_M)$ holds. In Fig. 79.23 the opacity of the absorption lines reaches the value 1.6 from which it follows that $\alpha < 0.2$. In the last section we describe a method for actually measuring the modulations in the areal density of the shell.

The Temperature of the Compressed Shell

The temperature of the shell at peak compression is an additional important parameter characterizing the implosion. We first use the absorption lines in Fig. 79.23 to deduce the temperature of the cool layer. These absorption lines each correspond to a Ti ion with an increasing number of L-shell vacancies; thus, the intensity distribution within the absorption-lines manifold corresponds to a distribution of ionization states from Ti^{+13} to Ti^{+20}. This distribution depends mostly on the temperature but also on the density. We use the collisional-radiative code *POPION*[10] to calculate the distribution of Ti ionization states as a function of temperature and density (for the experimental case of a 6% atom concentration of Ti in CH). Figure 79.26 shows as an example the average charge Z of Ti ions as a function of temperature for two density values: 1 g/cm^3 and 10 g/cm^3. As shown later, the shell density at peak compression is found to be within this range. *POPION* calculations show that for densities within this range, the measured absorption-line intensity distribution indicates a temperature in the range ~250 to ~350 eV. Additionally, the absorption-line intensity distribution is actually wider than that calculated for any single temperature, indicating absorption over a temperature gradient. Including this effect, the total range of possible temperatures indicated by the absorption lines is ~200 to ~400 eV.

We next turn to the determination of the cold-shell temperature. Unlike the cool layer where absorption lines are formed, no absorption lines are available for measuring the temperature

of the cold shell (where there are no *L*-shell vacancies into which absorption can take place). Instead, we can use the fluorescent Kα lines that are emitted following photoionization of *K*-shell electrons. To observe these lines more readily we use an off-center view that misses the core emission. We show in Fig. 79.27 the spectrum for shot 13151 in two views: through the center of the target and off the center. Indeed, the off-center view reveals a fluorescent Kα line emitted by *F*-like ions, coinciding in energy with the lowest-energy, *F*-like absorption feature. In the axial view this fluorescence cannot be seen because of the overlapping absorption at the same energy. For a colder shell the Kα line would appear at a slightly lower-energy position, indicating ionization of *M*-shell but not of *L*-shell electrons (the lowest-energy, or cold, Kα line is at 4.508 keV). In that case the Kα line would appear even in the axial view, not being subject to absorption, as has been the case in thicker-shell implosions.[3] The *F*-like Kα line is emitted following the *K*-shell photoionization of the Ne-like ions; thus, the bulk of the cold layer is in the closed-shell, Ne-like state; however, the width of the Kα line indicates that a smaller fraction of the Ti ions may be in lower ionizations. Using this result and *POPION* calculations we estimate the temperature of the cold shell as $T \sim 150$ to ~250 eV. For shot 13152 (without SSD) the cold-shell temperature is essentially the same.

It should be noted that in addition to the Kα line emitted in the cold shell, fluorescent Kα lines corresponding to each of the absorption lines of Fig. 7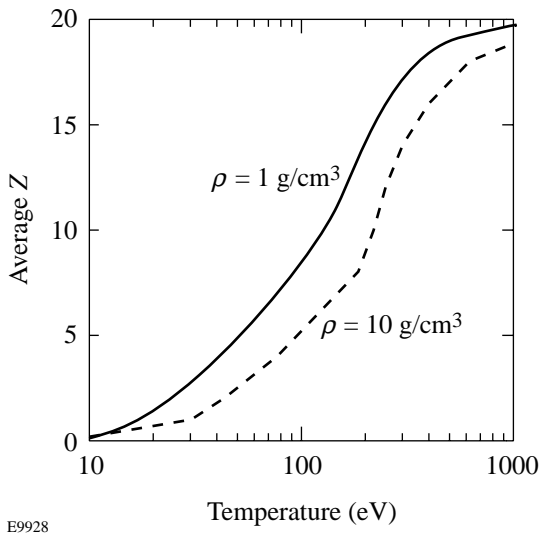9.27 should also be emitted within the cool layer. They cannot be seen in the spectrum because the $\rho\Delta R$ associated with each species having *L*-shell vacancies is only a fraction of the total cool-shell $\rho\Delta R$, which in turn is smaller than the cold-shell $\rho\Delta R$.

The position of the *K* edge can in principle provide an additional signature of the cold-shell temperature because for successive ionizations the *K* edge shifts to higher energies (see Fig. 72.8 in Ref. 2). For Ne-like Ti ions the *K*-edge shift is ~300 eV. This shift, however, is calculated for an isolated ion; at high densities *the K edge shifts to lower energies* due to interaction with neighboring ions. Using the model of Stewart and Pyatt,[11] assuming $T \sim 200$ eV and a density that changes over the range of 1 to 10 times solid density, the *K* edge of Ne-like Ti should shift toward lower energies by ~120 to ~300 eV; thus, the two effects partly cancel each other. Indeed, no significant *K*-edge shift is seen in Fig. 79.23. Accordingly, the *K*-edge shift is not a very useful diagnostic of shell temperature.

Kα Imaging of the Cold Shell

Previously we have shown that Kα emission constitutes an image of the cold shell around the time of peak compression.[3,5] Using this method we show here that shell compression improves with the implementation of SSD. In Ref. 5 a pinhole-array spectrometer was used to obtain two-dimensional images, whereas here a slit spectrograph is used to obtain essentially one-dimensional images; for shaped-pulse implosions the core

Figure 79.26
The average charge *Z* of Ti ions as calculated by the collisional-radiative code *POPION*. It is assumed that the titanium forms a 4% mixture (by atom) in CH.
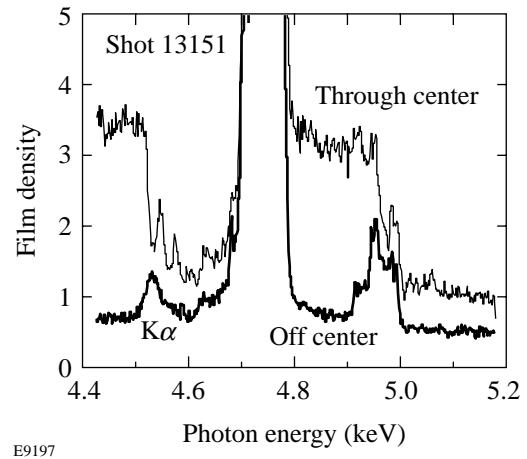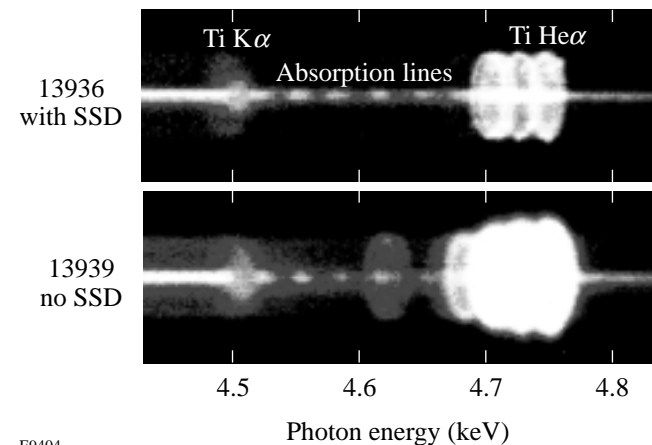

Figure 79.27
Determination of the cold-shell temperature through the fluorescing Kα lines. Only a view off the target center clearly shows the fluorescing line; its state of ionization (*F*-like Ti) indicates a cold-shell temperature of ~200 eV.

images are typically too weak to obtain high-quality images with the former instrument. In Fig. 79.28 we show part of the image obtained with the spatially resolving spectrograph, on two comparable shots, with and without SSD. The slit provides one-dimensional resolution in the vertical direction. In addition, the crystal provides low spatial resolution in the direction of dispersion (due to the Bragg's law); thus, the emission of Ti lines caused by burnthrough, because of their large extent, appears as two-dimensional images. This is important for separating Kα emission pumped by coronal radiation traveling inward during laser irradiation from Kα emission pumped by core radiation traveling outward during peak compression (Kα lines can only be emitted following pumping by a source located in a hotter region). The images of the Ti Heα line and its nearby satellites are elliptically shaped because there is no magnification in the direction of dispersion, whereas magnification in the perpendicular direction is provided by the slit. As in the spectra of Fig. 79.23, we see a much higher intensity of burnthrough radiation (e.g., the Ti Heα lines) in the no-SSD case, indicating a faster (and thus deeper) burnthrough due to instability growth. In fact, the Ti Heα line and its satellites appear as three limb-effect rings in the upper spectrum but are totally saturated in the lower spectrum. The lower spectrum also shows ring images of shifted Kα lines in the range of 4.6 to 4.7 keV. Their size is slightly smaller than that of the Ti Heα rings, indicating that they are pumped by radiation from the burnthrough region during the laser irradiation (see Fig. 75.30

Figure 79.28

Effect of SSD as evidenced by x-ray spectra. A slit provides one-dimensional spatial resolution in the vertical direction; the crystal provides a low spatial resolution in the dispersion direction. Low-temperature Kα line (at ~4.52 keV) is pumped by core radiation; higher-temperature Kα lines (4.6 to 4.7 keV) are pumped by burnthrough to the Ti-doped layer.

in Ref. 12 and discussion thereof). The species emitting these lines are of relatively high ionization (e.g., B-like and Be-like Ti), indicating that radiation emitted during the burnthrough preheats the outer layer of the cold shell, ahead of the heat front, to ~300 to ~600 eV. These ring images show that *the accelerating shell does maintain its integrity with no large-scale breakup seen*. Such images can be used to study the uniformity of the accelerating shell. As in these target shots, the doping level can be made low enough so as not to greatly modify the behavior of the target and the doped layer can be placed deep enough that a burnthrough occurs at the end of the laser pulse. In this way the radiation from the doped layer does not interfere with the laser interaction and acceleration that occur earlier. *The radiation from the burnthrough thus provides a "flash" photography of the shell at the end of the acceleration phase.*

In addition to these emission rings of Kα lines, a much stronger Kα line seen at ~4.52 keV (similar to that in Fig. 79.27) is emitted around the core and is clearly pumped by core radiation. The Kα lines are difficult to see in the streak spectra (which would further prove this point) because the integration over the target volume precludes an off-center view; on the other hand, the emission of the cold Kα line at peak compression was previously observed in streak data[5] because, as explained above, it is not absorbed in the shell. Also, related simulations described in Ref. 12 (Fig. 75.30) strongly support this conclusion. The temperature indicated by this feature has been estimated above to be ~150 to ~250 eV. Thus, the outer part of the doped layer is heated by the laser burnthrough to a temperature >1 keV (sufficient to excite Ti^{+20} and Ti^{+21} lines); radiation from this heated region flows inward and causes heating of additional material to ~300 to ~600 eV, all of which is ablated. The bulk of the doped layer, however, remains colder and implodes, reaching temperatures of ~150 to ~250 eV at peak compression. It should be noted that most of the radiative preheating is caused by sub-keV radiation whose range is smaller than the areal density of the initially ~5-μm-thick doped layer. Vertical lineouts through the Kα feature at ~4.52 keV have been Abel inverted,[13] separately for the two branches above and below the core image. The results (Fig. 79.29) clearly show that SSD smoothing results in both *a higher convergence and a higher shell compression*. This is consistent with the conclusion from Fig. 79.23 that SSD smoothing leads to a higher shell $\rho\Delta R$.

The Kα profiles in Fig. 79.29 can be converted to density profiles by requiring that the integral of the normalized profiles yields the measured $\rho\Delta R$ of the doped layer. Using this procedure we obtain peak density of ~1.2 g/cm^3 for shot 13936 and

~0.5 g/cm^3 for shot 13939. These values underestimate the density because time integration broadens the Kα spatial profiles. On the other hand, if the opacity above the K edge is much larger than 1, the Kα profile will be narrower than the density profile because of depletion of the pumping radiation; this is not the case in the present results.

1-D *LILAC* and 2-D *ORCHID* Simulations

The shots listed in Table 79.III were simulated with both the 1-D code *LILAC* and the 2-D code *ORCHID*. Present low-adiabat, shaped-pulse implosions perform below 1-D predictions (even with SSD),[14] and their replication is a stringent test for 2-D simulations. A particularly sensitive parameter characterizing target performance is the density profile of the cold shell around peak compression. As explained above, this density profile is determined by normalizing the Ti Kα fluorescence profiles (Fig. 79.29) to the shell $\rho\Delta R$ as measured by the K-edge absorption and the $1s$–$2l$ absorption lines. These profiles correspond to the part of the shell that is both doped and cold. As noted above, the target parameters were chosen so that all of the cold shell at peak compression would be doped so the Kα profile would correspond to the entire cold shell. Since we observe burnthrough of the laser into the doped layer (see Figs. 79.23 and 79.28), we can safely assume that none of the CH overcoat is cold during the compression. In Fig. 79.28, in addition to the ring-shaped images of the Ti Heα line at

4.75 keV (and its nearby satellites), a strong emission of these lines is also seen at the center of the target. To see this more clearly, we show in Fig. 79.30 the spatial profile of the calibrated intensity at the energy of the Ti Heα line, and at a nearby energy of the continuum; comparing the two lineouts clearly indicates a strong central emission of the Ti Heα line. Thus, the inner part of the doped layer must be part of the hot core, and the cold part of the shell contains only doped material. If the shell becomes highly distorted during either the acceleration or the deceleration, some of the Ti Heα emission may be due to mixing; in this case, some of the cold material will be undoped and the measured $\rho\Delta R$ through Ti absorption will underestimate the true cold-shell $\rho\Delta R$.

ORCHID simulations include the imprint of laser nonuniformity. For each beam, the known mode spectrum due to the phase plates was used, and modes up to $\ell = 300$ were added with random relative phases. The effect of multiple-beam overlap was calculated separately and accounted for. The effect of SSD was simulated by randomly reversing the phase of the laser modes at intervals equal to the coherence time (which is inversely proportional to the bandwidth and decreases with increasing mode number). Figure 79.31(a) shows typical profiles, azimuthally averaged, at peak compression; the averaged temperature was weighted by the density. A hot core is seen to be surrounded by a dense, colder layer. Before
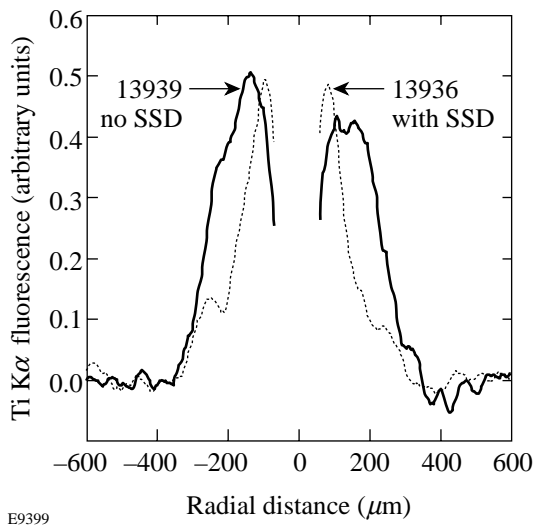
Figure 79.29
Abel inversion of image lineouts (from Fig. 79.28) at the F-like Kα line. The curves delineate the position and thickness of the cold shell around the time of peak compression. Higher convergence and compression due to SSD smoothing are evident.
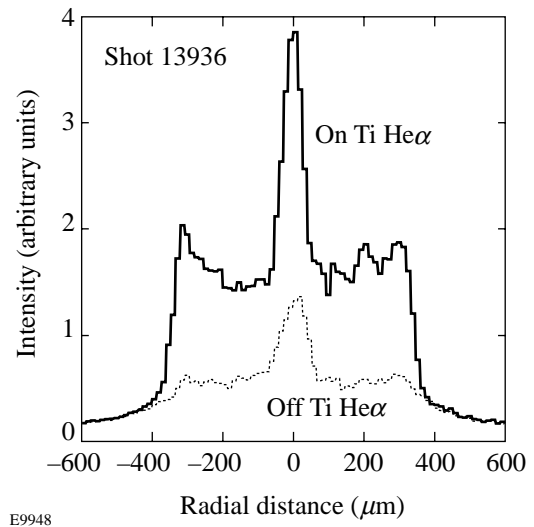
Figure 79.30
Spatial profile of the intensity at the energy of the Ti Heα line and at a nearby energy of the continuum (shot 13936) showing central emission of the line. This demonstrates that the cold shell around peak compression, detected by absorption, is mostly titanium doped.

comparing the *ORCHID* results to the experiment we note that the Ti Kα emission measures only the cold part of the shell. More specifically, the Kα line was shown in Fig. 79.27 to be emitted by neon-like and possibly lower ionizations. Thus, the density profile measured by the Kα line fluorescence refers only to that part of the total density that is cold enough to have a charge state $Z \le 12$. To compare the *ORCHID* density profiles to the experiment we multiply the former by the fraction of Ti ions in charge states $Z \le 12$, calculated by the collisional-radiative *POPION* code.[10] For the most part, the Ti in these calculations is in the neon-like state with only a small contri-

bution from lower ionizations. In Fig. 79.31(b) we show typical cold-shell density profiles obtained in this way at three times around peak compression. Finally, to allow for comparison with the time-integrated Kα profiles, we calculate the time-averaged *ORCHID* density profile. We note that the Kα line intensity is proportional to the intensity of pumping core radiation (in addition to being proportional to the cold-shell $\rho\Delta R$ or, after Abel inverting, to ρ). Therefore, the average density profile was obtained by weighting the instantaneous density profiles by the core intensity just below the Ti K edge, obtained from the streak spectrograph data. Good agreement is seen in *both the shape and absolute magnitude* of the two density profiles: the time-averaged *ORCHID* profile and the profile measured through the Ti Kα fluorescence. On the other hand, the 1-D code *LILAC* shows a much narrower profile of vastly higher density (most of the sharp density peak in that profile is cold and should have been measured by the Kα profile in a 1-D implosion).

In spite of the inherent inaccuracies in both the experiment and simulations, Fig. 79.31 shows that the cold-shell imaging diagnostics employed here provides a sensitive signature for testing the performance of 2-D codes in simulating unstable implosions. Further comparisons of measured and *ORCHID*-calculated <u>modulations</u> in compressed-shell $\rho\Delta R$ are underway.

Measurement of Shell $\rho\Delta R$ Modulation Through *K*-Edge Imaging

In addition to the integral measurements of shell $\rho\Delta R$ described above, we introduce a new method for *imaging the shell* $\rho\Delta R$ at peak compression, effectively using the core radiation as a backlighter for the shell. Such images are the final product of shell deformation due to the Rayleigh–Taylor instability and the Bell–Plesset effect and are thus of great interest in laser-fusion studies. Spatial modulations in a core image viewed through an absorbing shell depend on both the modulations in core emission as well as the modulations in shell $\rho\Delta R$. To isolate the latter, we use targets with a Ti-doped layer embedded within the shell and take the ratio of an image $I_{<K}$ just below the Ti K edge (at 4.96 keV) and an image $I_{>K}$ just above it. Since the absorption $\mu_{>K}$ above the K edge is much higher (by a factor of ~9.5) than the absorption $\mu_{>K}$ below it, the $\rho\Delta R$ image can be obtained through

$$\rho\Delta R = \ln\left(I_{<K}\big/I_{>K}\right)\big/\left(\mu_{>K} - \mu_{<K}\right). \qquad (2)$$

The method relies on the fact that the emitted continuum intensity (before absorption) changes very little between the two images. The thickness and doping level of the doped layer
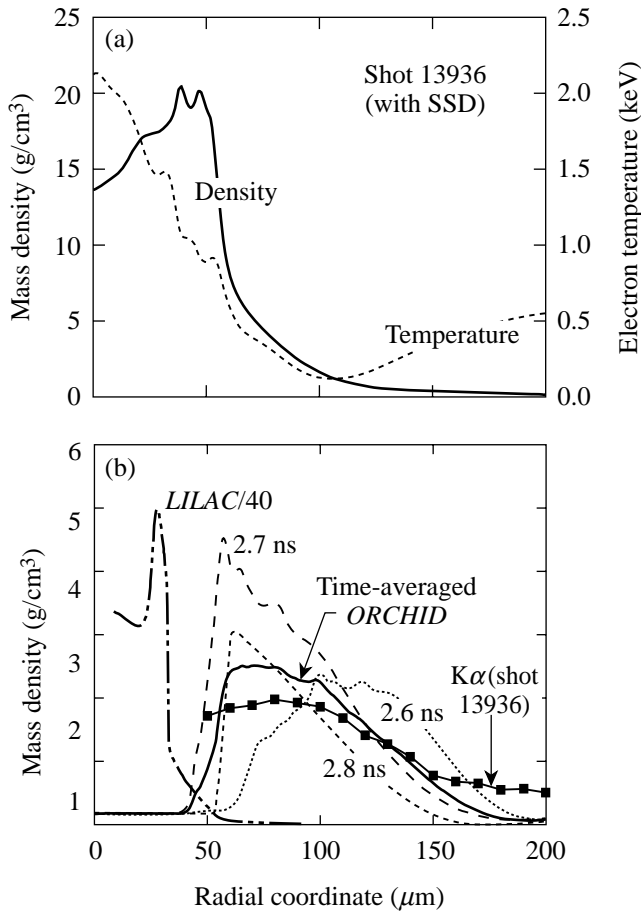
E9937

Figure 79.31
(a) Azimuthally averaged density and electron temperature profiles at peak compression calculated by *ORCHID* for shot 13936 (with SSD). (b) Density profiles of the cold shell for shot 13936. The 1-D *LILAC* profile shown is at peak compression. Three typical 2-D *ORCHID* profiles during different times of the compression are also shown. Using such profiles, the time-averaged density profile was obtained, weighted by the core intensity. The experimental time-integrated cold-shell density profile was obtained from the Ti Kα image.

can be conveniently adjusted to result in an opacity $\rho \Delta R \, \mu_{>K}$ ~1 to 2.

A particularly convenient way of obtaining such images is by employing the recently developed pinhole-array spectrometer.[5] Several hundred narrow-bandwidth images in the range of ~4 to ~7 keV are obtained at ~10-eV energy shifts between adjacent images. This device is particularly useful for K-edge imaging because monochromatic images provide high sensitivity to $\rho \Delta R$ modulations; also, the large number of images obtained close to either side of the K edge enables an improved noise analysis and consistency checks.

As a first test of the proposed method we applied it to an implosion (shot 15156) using a 1-ns square laser pulse. This choice was made because fast-rising pulses produce more-intense core radiation. The target and laser conditions are listed on the last line in Table 79.III. We use a pinhole-array spectrometer with 10-μm holes, giving a spatial resolution of ~16 μm. Figure 79.32 shows part of the image around the Ti K edge (4.964 keV); the crystal dispersion is in the horizontal direction. Each image is a monochromatic image of the core (of ~100-μm diameter), at a slightly different energy. In the vertical direction successive images are at energies separated by ~10 eV; in the horizontal (dispersion) direction the separation is ~100 eV. The energy bandwidth for each image is ~5 eV.[5] The six images on the left [Fig. 79.32(a)] are at ener-

gies just below the Ti K edge; the six images on the right [Fig. 79.32(b)] are just above the edge. The emission from the laser-interaction region is not seen in these images because, unlike the shots shown in Figs. 79.23 and 79.27, there has been no burnthrough to the Ti-doped layer in shot 15156. This is because of the thicker CH overlayer and the shorter laser pulse in this shot. The images below the K edge show structure on a scale length of about 20 to 30 μm. The images above the K edge show a similar structure. As explained, the structure in images below the edge is caused by nonuniformities in the core emission; the structure in the images above the edge reflects those same nonuniformities, plus any nonuniformities in the $\rho \Delta R$ of the absorbing shell. The purpose of the analysis described here is to separate the two sources of nonuniformity. To that end we perform 2-D Fourier analysis of the images in optical-density units and azimuthally average the results. In most other shots under similar conditions the core emission is more uniform; however, this shot was chosen to test the method's capability. The images in Fig. 79.32 are in optical-depth units [i.e., OD ~ ln(I), where the intensity I was deduced from the DEF-film density]. First, we must obtain the spatial spectrum of the noise (both in the images and in the film); to that end we subtract the Fourier spectra of two core images at energies below the K edge. Since the gross structure in all the images just below the K edge is the same, the difference between such images is caused only by the noise. Figure 79.33 shows the noise spectrum (thin solid line) thus obtained as an

(a) Below the Ti K edge   (b) Above the Ti K edge
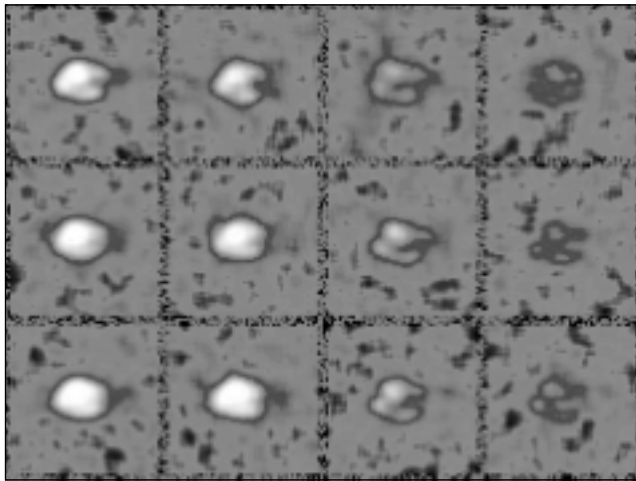
E9930

Figure 79.32
Sample of time-integrated monochromatic images of the core radiation obtained with a pinhole-array spectrometer, at energies (a) below the titanium K edge and (b) above the titanium K edge.
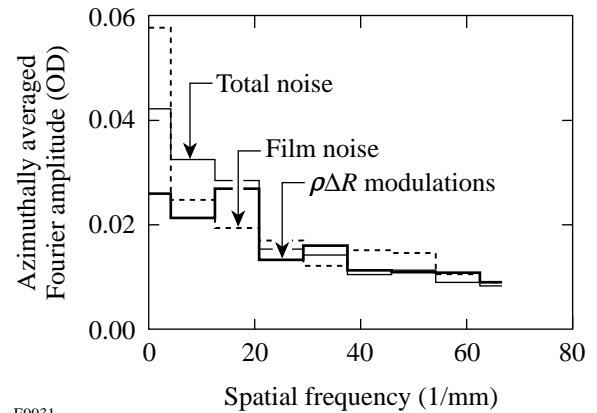
E9931

Figure 79.33
The azimuthally averaged Fourier amplitude of the measured optical depth versus spatial frequency for (a) the noise in the images below the K edge (thin solid line), (b) the film noise taken in an area between the images (dashed line), and (c) the modulations in $\rho \Delta R$ of the titanium-doped layer (thick solid line).

azimuthally averaged Fourier amplitude of optical-depth modulations versus spatial frequencies, using two of the images shown in Fig. 79.32(a); the results of using different image pairs from the same figure are very similar. The maximum spatial frequency corresponds to the spatial resolution of ~16 μm. Next we deduce the spectrum of film noise by analyzing in the same way a region on the film between the images, of equal area to that of the images; the dashed line in Fig. 79.33 shows the results. Finally, we derive the modulations in shell $\rho\Delta R$ by analyzing the difference in optical depth between two images at energies below and above the K edge. The spectrum of this difference, shown by the thick solid line in Fig. 79.33, contains noise plus modulations in the opacity of the titanium-doped layer. As seen in Eq. (2), the modulations in optical depth are proportional to the areal-density modulations of the doped layer. The three curves in Fig. 79.33 are very close for spatial frequencies above ~10 mm^{-1} or wavelengths shorter than 100 μm (the latter being about equal to the core size), indicating that *the film noise accounts for all the modulations in the images*; thus, there are no measured modulations in the shell areal density above the noise level for wavelengths between ~16 and ~100 μm. The sensitivity of this measurement was estimated using the noise spectrum obtained above. Assuming that modulations of the shell $\rho\Delta R$ are contained in the region of wavelengths from 10 to 80 μm, the σ_{rms} amplitude of the layer modulations must be more than a third of its thickness to become distinguishable from the noise. Thus, this analysis does not show modulations exceeding ~30% in the $\rho\Delta R$ of the doped layer, of wavelengths longer than ~16 μm and smaller than ~100 μm. We attribute this to the fast-rising square laser pulse, which reduces laser imprint and thus target distortions. Slower-rising pulse shapes (such as the ALPHA306 pulse used to obtain Fig. 79.23 data) are known to produce less-stable implosions, but the core intensity in such target shots was insufficient to perform meaningful analysis with this method. In future experiments we plan to increase the sensitivity of the measurement by replacing the diffracting crystal in the pinhole-array spectrometer with filters for sampling the spectrum below and above the Ti K edge. The loss in spectral definition can be partly offset by accounting for the spectrum, independently measured from a target without a doped layer.

REFERENCES

1. B. Yaakobi, F. J. Marshall, D. K. Bradley, J. A. Delettrez, R. S. Craxton, and R. Epstein, Phys. Plasmas **4**, 3021 (1997).

2. Laboratory for Laser Energetics LLE Review **72**, 168, NTIS document No. DOE/SF/19460-199 (1997). Copies may be obtained from the National Technical Information Service, Springfield, VA 22161.

3. B. Yaakobi and F. J. Marshall, J. Quant. Spectrosc. Radiat. Transfer **61**, 465 (1999).

4. D. K. Bradley, J. A. Delettrez, R. Epstein, R. P. J. Town, C. P. Verdon, B. Yaakobi, S. Regan, F. J. Marshall, T. R. Boehly, J. P. Knauer, D. D. Meyerhofer, V. A. Smalyuk, W. Seka, D. A. Haynes, Jr., M. Gunderson, G. Junkel, C. F. Hooper, Jr., P. M. Bell, T. J. Ognibene, and R. A. Lerche, Phys. Plasmas **5**, 1870 (1998).

5. B. Yaakobi, F. J. Marshall, and D. K. Bradley, Appl. Opt. **37**, 8074 (1998).

6. Laboratory for Laser Energetics LLE Review **37**, 29, NTIS document No. DOE/DP40200-83 (1998). Copies may be obtained from the National Technical Information Service, Springfield, VA 22161.

7. D. K. Bradley, J. A. Delettrez, and C. P. Verdon, Phys. Rev. Lett. **68**, 2774 (1992); J. Delettrez, D. K. Bradley, and C. P. Verdon, Phys. Plasmas **1**, 2342 (1994).

8. D. J. Botto, J. McEnnan, and R. H. Pratt, Phys. Rev. A **18**, 580 (1978).

9. B. Yaakobi, R. S. Craxton, R. Epstein, and Q. Su, J. Quant. Spectrosc. Radiat. Transfer **58**, 75 (1997).

10. R. Epstein, S. Skupsky, and J. Delettrez, J. Quant. Spectrosc. Radiat. Transfer **35**, 131 (1986).

11. J. C. Stewart and K. D. Pyatt, Jr., Astrophys. J. **144**, 1203 (1966).

12. Laboratory for Laser Energetics LLE Review **75**, 182, NTIS document No. DOE/SF/19460-246 (1998). Copies may be obtained from the National Technical Information Service, Springfield, VA 22161.

13. C. M. Vest and D. G. Steel, Opt. Lett. **3**, 54 (1978).

14. Laboratory for Laser Energetics LLE Review **78**, 82, NTIS document No. DOE/SF/19460-295 (1999). Copies may be obtained from the National Technical Information Service, Springfield, VA 22161.

Experimental Investigation of Smoothing by Spectral Dispersion

In the direct-drive approach to inertial confinement fusion (ICF), capsules are irradiated directly by a large number of symmetrically arranged laser beams.[1,2] Nonuniformities in the laser irradiation may seed the Rayleigh–Taylor hydrodynamic instability, which degrades target performance;[3] therefore, a combination of beam-smoothing techniques is employed to achieve the high irradiation uniformity required for direct-drive laser-fusion experiments. These techniques, which include two-dimensional smoothing by spectral dispersion (2-D SSD),[4–6] distributed phase plates (DPP's),[7,8] polarization smoothing (DPR's),[9–11] and multiple-beam overlap, will also be implemented on the 1.8-MJ, 351-nm, 192-beam National Ignition Facility (NIF),[12] which is currently under construction at the Lawrence Livermore National Laboratory. Direct-drive laser fusion requires a high degree of laser-irradiation uniformity on target: the rms irradiation nonuniformity must be below 1% when the laser intensity has been averaged over a few hundred picoseconds.[2,5]

Characterization of the laser-irradiation nonuniformity is essential for ICF research since the efficiency with which the nonuniformities in the laser-irradiation imprint target mass perturbations (i.e., laser imprint) depends on the early-time intensity history and the spatial wavelength of the nonuniformity.[13] The strategy of 2-D SSD with phase plates, which is the preferred mechanism for reducing laser-beam irradiation nonuniformity in glass lasers, is to vary the interference (speckle) pattern of the phase plate on a time scale that is short compared to the characteristic hydrodynamic response time of the target (i.e., imprinting time). (An alternate technique, ISI, has been developed for KrF lasers.[14]) Predictions show that 2-D SSD smoothing with $\Delta\nu_{UV} \approx 1$ THz will smooth the spherical-harmonic modes of $\ell = 20$ through 150 to acceptable levels for ICF.[5] The bandwidth on OMEGA[15] will be increased from 0.2 to 1 THz during this year, which will decrease the smoothing time by a factor of 5.

In this research the temporal rate of beam smoothing produced by 2-D SSD with the current bandwidth of $\Delta\nu_{UV} \approx 0.2$ THz is quantified by analyzing measured ultraviolet

equivalent-target-plane (UVETP) images of a single OMEGA laser beam. The next three sections describe (1) laser-beam smoothing with 2-D SSD and phase plates, (2) 2-D SSD model calculations, and (3) the diagnostic used to record UVETP images of laser pulses having constant peak power and varying duration (100 ps to 3.5 ns). Power spectra calculated from the measured UVETP images along with the measured smoothing rate of 2-D SSD are presented and compared with theoretical predictions in the **Experimental Results and Analysis** section. This work shows that the theoretical predictions of 2-D SSD laser-beam smoothing are in excellent agreement with the measured temporal smoothing rates.

Background

Smoothing of laser beams using SSD has been described in Ref. 4. On OMEGA the phase plates are placed before the focusing lens and produce far-field spots with highly reproducible spatial intensity envelopes and speckle distributions. Smoothing by spectral dispersion is achieved by frequency modulating the phase of a laser beam, wavelength dispersing the beam, and passing it through a phase plate so that the spectral components are separated in the target plane by at least one-half the beam's diffraction-limited width. The reduction in laser-irradiation nonuniformity is wavelength dependent. The longest wavelength of nonuniformity that can be smoothed by SSD is twice the maximum spatial shift $S_{max} = F\Delta\theta$ of the speckle pattern that can be produced by the laser, where $\Delta\theta$ is the angular spread of the wavelength-dispersed light propagating through the laser and F is the focal length of the OMEGA lens. (The ultimate limit of S is given by the maximum allowable angular spread in the spatial filter in the laser system.) Thus, spherical-harmonic modes of nonuniformity down to $l_{cut} = 2\pi R/(2S_{max})$, where R is the target radius, can be smoothed with 2-D SSD.[5] Spherical targets on OMEGA have $R \simeq 500~\mu$m, and the present 2-D SSD system has $S_{max} = 100~\mu$m; hence $l_{cut} = 16$.

Model Calculations

The time-integrated far field is calculated by temporal integration of the modulus squared of a two-dimensional

spatial Fourier transform of the UV near field. The complex-valued electric field that describes the UV near field can be written as

$$E(x,y,t) \equiv E_0(x,y,t)e^{i\phi_{2\text{-D SSD}}(x,y,t)}e^{i\phi_B(x,y,t)}e^{i\phi_{\text{DPP}}(x,y)}, \quad (1)$$

where $E_0(x,y,t)$ defines the temporal and spatial beam shapes, $\phi_{2\text{-D SSD}}(x,y,t)$ is the 2-D SSD phase contribution, $\phi_B(x,y,t)$ is the intensity-dependent phase contribution of the B-integral,[16] and $\phi_{\text{DPP}}(x,y)$ is the static phase-plate contribution, which depends on the particular phase-plate design.

The spatially and temporally varying phase due to 2-D SSD is[17]

$$\phi_{2\text{-D SSD}}(x,y,t) \equiv 3\delta_{Mx}\sin\left[\omega_{Mx}\left(t+\xi_x x\right)\right]$$

$$+3\delta_{My}\sin\left[\omega_{My}\left(t+\xi_y y\right)\right], \quad (2)$$

where the x and y subscripts denote the two smoothing dimensions, $\delta_{Mx,y}$ is the modulation depth, $v_{Mx,y} = \omega_{Mx,y}/2\pi$ is the RF modulation frequency, and $\xi_{x,y}$ is the angular grating dispersion. The factor of 3 in Eq. (2) indicates that the electric field has undergone frequency tripling from the IR to UV. The 2-D SSD system parameters on OMEGA for the UVETP

measurements are $\delta_{Mx} = 5.12$, $v_{Mx} \equiv 3.3$ GHz, $\xi_x = 1.11$ ns/m, $\Delta\lambda_{Mx} = 1.25$ Å, $\delta_{My} = 7.89$, $v_{My} \equiv 3.0$ GHz, $\xi_y = 1.11$ ns/m, and $\Delta\lambda_{My} = 1.75$ Å, assuming a nominal beam diameter of 27.5 cm. The modulation depths and the bandwidths are given for the IR. The maximum angular spread $\Delta\theta$ is given by $\Delta\theta = \xi(c/\lambda)\Delta\lambda$, where c is the speed of light and $\lambda = 1053$ nm. Cases without frequency modulation are modeled by setting modulation depths equal to zero, i.e., $\delta_{Mx} = 0$ and $\delta_{My} = 0$.

Our simulations indicate that B-integral effects are negligible for all cases except when the frequency modulation is turned off.

UVETP Diagnostic

The layout of the diagnostic used to acquire the UVETP images of a single OMEGA beam is shown in Fig. 79.34. Time-integrated UVETP images were recorded with a CCD camera. All of the measurements presented in this article exploit the low noise level and the large dynamic range of the CCD to extract power spectra from the UVETP images with negligible noise levels. The UV-sensitive CCD camera is a back-thinned SITe 003B chip in a Photometrics Series 300 camera.[18] The sensor has an array of 1024×1024 photosensitive elements with a pixel size of 24 μm $\times$ 24 μm. The spatial sampling rate is ~2 pixels/μm, which is approximately five times the f-number-limited spatial frequency $f_0 \equiv \Delta/\lambda F$, where D is the beam diameter of the OMEGA lens and $\lambda = 351$ nm.
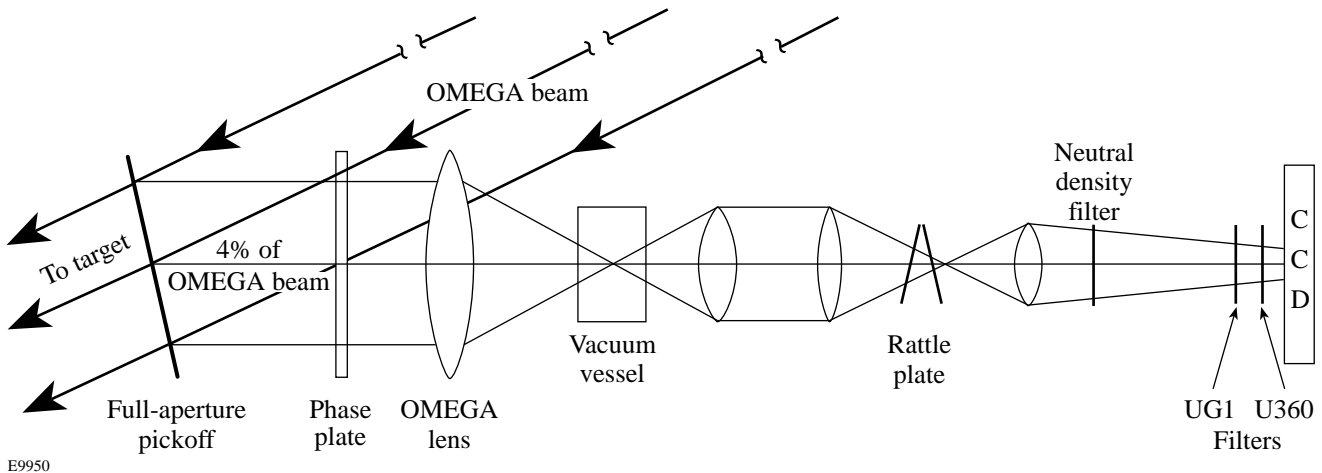

E9950

Figure 79.34
Schematic of the UVETP diagnostic. The on-target spot size is magnified by $M = 46$ on the CCD camera.

A full-aperture optical wedge in one of the 60 laser beams (BL-19) directs 4% of the laser light to an OMEGA focusing lens (see Fig. 79.34). The phase plate is placed directly in front of the lens, mimicking the target/beam configuration. The beam is brought through focus in a vacuum tube, down collimated with a doublet lens, brought to focus with a 2-m lens, and relayed to the CCD camera with the final lens. The beam intensity is reduced with three 4% reflections (not shown in Fig. 79.34) and the fifth-order reflection of a rattle plate (consisting of two surfaces with $R = 70\%$ per surface). The optical background is reduced to negligible levels with a light shield surrounding the CCD optics and the CCD camera. The light levels incident on the CCD are optimized by attenuating the beam with a neutral density filter that is placed after the final lens. Background-visible and IR signals are blocked with broadband UG1[19] and U360[20] UV bandpass filters mounted in front of the CCD camera. Compared with the laser spot size on target the UVETP image on the CCD camera is magnified by a factor of ~46.

Small-scale and whole-beam B-integral effects were found to provide smoothing of beams without frequency modulation. (The detailed analysis of beams without frequency modulation will be presented in a later publication.) A UVETP image of a laser pulse with zero accumulated B-integral (B-integral <1.0 rad in the UV) and no frequency modulation was measured to quantify the amount of beam smoothing due to the B-integral at higher laser powers. The power spectrum is the azimuthal sum at each spatial frequency of the square of the Fourier amplitudes. The power spectrum is normalized to the

dc component, and the single-beam irradiation nonuniformity σ_{rms} is defined as the square root of the ratio of the power in the high frequencies (i.e., $k \geq 0.04$ μm^{-1} in the OMEGA target plane) to the power in the low frequencies (i.e., $k < 0.04$ μm^{-1}). The highest (cutoff) wave number $k = 2.68$ μm^{-1} corresponds to the f-number-limited spatial frequency. A spectrum for a zero-B-integral laser pulse without frequency modulation is presented in Fig. 79.35 and its irradiation nonuniformity, $\sigma_{rms} = 93.4\%$, is the highest measured under any condition and is near the 100% value expected from theory. The theoretical power spectrum simulated with the time-dependent code (described in the previous section) is also shown in Fig. 79.35 and includes the spatiotemporal near-field irradiance and small-scale and whole-beam B-integral effects. The higher value of σ_{rms} predicted by the model is caused by the discrepancy between the model and the measurement in the low wave numbers (see Fig. 79.35). Nevertheless, the predicted speckle structure shows excellent agreement with the measurement; hence, the zero accumulated B-integral shot serves as a calibration that demonstrates the capability of the UVETP diagnostic to measure highly modulated spatial intensity profiles of pulses with no frequency modulation.

Experimental Results and Analysis

Measured UVETP images of 3.5-ns square laser pulses without frequency modulation and with 2-D SSD are presented in Figs. 79.36(a) and Fig 79.36(b), respectively. These images qualitatively illustrate the effect of laser-beam smoothing with 2-D SSD. The images with 2-D SSD show a smooth spatial intensity envelope [see single pixel lineout overplotted on
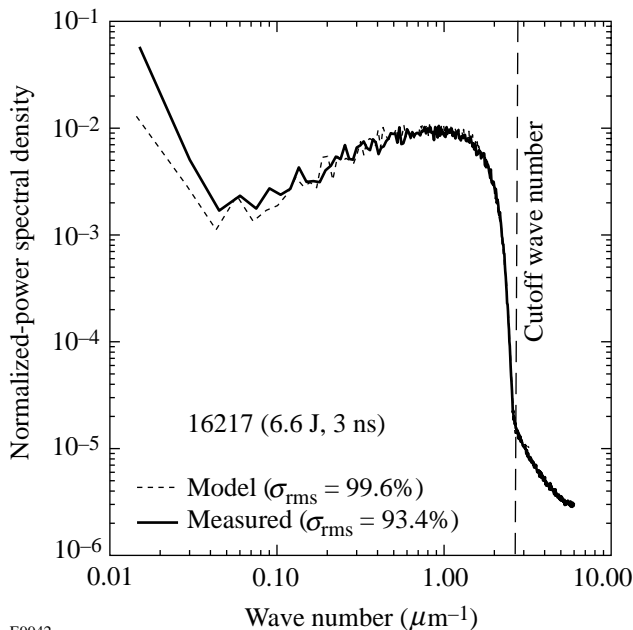
E9942

Figure 79.35
Power spectra obtained from a UVETP image of a laser pulse with zero accumulated B-integral (B-integral < 1.0 radian in the UV) without frequency modulation. The power spectrum is the azimuthal sum at each frequency of the square of the Fourier amplitudes, and the cutoff wave number corresponds to the f-number-limited spatial frequency. The power spectra are normalized to the dc component, and the σ_{rms} is defined as the square root of the ratio of the power in the high frequencies (i.e., $k \geq 0.04$ μm^{-1} in the OMEGA target plane) to the power in the low frequencies (i.e., $k < 0.04$ μm^{-1}). Solid/dashed lines represent measured/modeled power spectra. The predicted speckle structure shows excellent agreement with the measurement; hence, the zero accumulated B-integral shot serves as a calibration that demonstrates the capability of the UVETP diagnostic to fully resolve individual speckles.

image in Fig. 79.36(b)], while the pulses without frequency modulation have a highly modulated spatial intensity profile [see single pixel lineout overplotted on image in Fig. 79.36(a)]. The spatial resolution and overall detector size of the CCD restrict the UVETP measurement to slightly more than one-half of the laser-beam profile. As seen in Fig. 79.36, the laser beam is centered nominally on the photodetector, and 550 μm of the 950-μm (defined as the 95% enclosed energy contour) laser spot is sampled.

The temporal rate of 2-D SSD smoothing is deduced from the power spectra of the measured UVETP images of laser

pulses having constant peak power and pulse lengths ranging from 100 ps to 3.5 ns. Power spectra calculated from measured UVETP images of (a) 100-ps and (b) 3-ns laser pulses smoothed with 2-D SSD are presented in Fig. 79.37. The time-dependent nature of 2-D SSD smoothing is evident in the measured results with lower measured values of σ_{rms} for the longer pulse lengths. The low-wave-number power spectrum is determined by the spatial intensity envelope of the far field. The UVETP diagnostic was configured with a phase plate that produced a far-field spot with a super-Gaussian spatial intensity envelope $\left[I \sim \exp(r/r_0)^{2.5} \right]$ for these pulses.

(a)   (b)

E9939

E9951
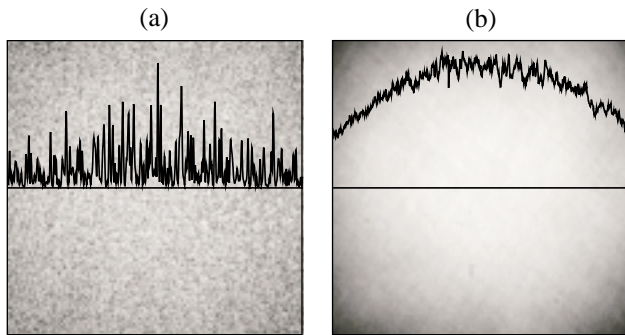
Figure 79.36

Measured UVETP images of 3.5-ns square laser pulses (a) without frequency modulation and (b) with 2-D SSD at $\Delta\nu_{UV} \approx 0.2$ THz. As demonstrated with the single pixel lineout through the center of the beam, the laser pulse with 2-D SSD has a smooth spatial intensity envelope, while the pulse without frequency modulation has a highly modulated spatial intensity profile. The spatial resolution and overall detector size of the CCD restrict the UVETP measurement to slightly more than one-half of the laser-beam profile. The laser beam is centered nominally on the photodetector, and 550 μm of the 950-μm laser spot (defined as the 95% enclosed energy contour) is sampled.
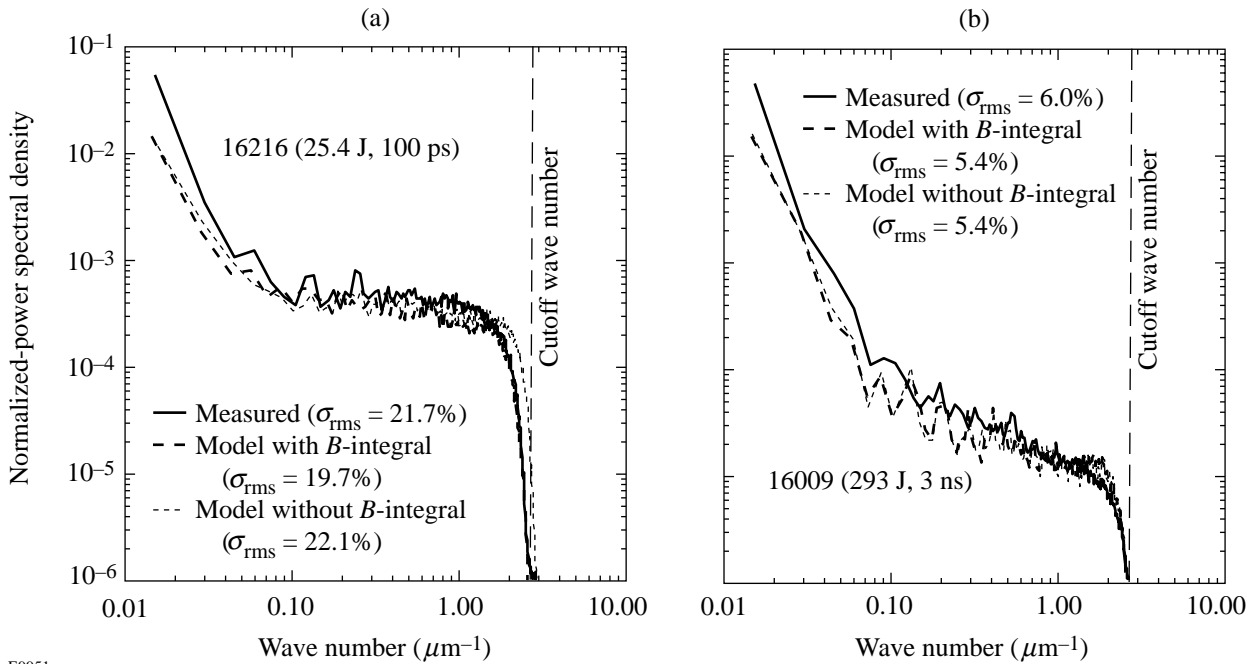
Figure 79.37

Power spectra calculated from UVETP images of (a) 100-ps and (b) 3-ns laser pulses with 2-D SSD. The thick, solid line represents the measured power spectrum. The thick, dashed line represents the time-dependent simulation that includes both the spatiotemporal behavior of the near-field irradiance and small-scale and whole-beam B-integral effects. The thin, dashed line represents a time-dependent model neglecting B-integral effects. Both models are in agreement with the measured results, and B-integral effects are negligible for all cases except for pulses without frequency modulation.

The 2-D SSD power spectra simulated with the time-dependent code (described in a previous section) with and without *B*-integral effects are plotted in Fig. 79.37. The *B*-integral effects are completely negligible as shown in this figure. The excellent agreement between the simulated power spectra and the measured spectra is clearly apparent in Fig. 79.37.

The measured temporal rate of 2-D SSD smoothing is shown in Fig. 79.38, which is a compilation of data from over 150 laser shots that clearly demonstrates the decrease in the measured σ_{rms} with increasing pulse length. Statistical error bars are smaller than the symbols. The 3.5-ns pulse has the lowest measured $\sigma_{rms} = 6.0\%$. The measurement of the laser-irradiation nonuniformity for the 3.5-ns pulses without frequency modulation is also presented for comparison. The thin line is the time-integrated simulation of the single-beam irradiation nonuniformity σ_{rms} that neglects the *B*-integral effects and assumes a static near field with a uniform irradiance. It is in agreement with the measured results (black circles), and it predicts that an asymptotic level of smoothing is reached just after 3 ns. The thick, solid line in Fig. 79.38 represents model predictions for the σ_{rms}:

$$\sigma_{rms} = \sqrt{\sigma_0^2\left(\frac{t_c}{t+t_c}\right)+\sigma_{asymp}^2} \,, \qquad (3)$$

where $t_c = 1/\Delta\nu_{UV} = 5$ ps is the coherence time, $\Delta\nu_{UV} = 0.2$ THz is the UV bandwidth, t is the averaging time (i.e.,

pulse length), σ_0 is the initial laser nonuniformity, and σ_{asymp} is the asymptotic level of 2-D SSD smoothing calculated from the time-integrated far-field simulation. This prediction adds the asymptotic levels of smoothing in quadrature to the model given in Ref. 14. The dashed line in Fig. 79.38 is a plot of Eq. (3) with the σ_{asymp} set to zero. The deviation of the thick, solid line from the dashed line around 1 ns signifies that the beam smoothing is approaching its asymptotic limit. The asymptotic behavior can be observed in the measured values of σ_{rms}.

The dependence of the rate of smoothing on the wave number k is examined in Fig. 79.39, where σ_{rms} is plotted as a function of pulse length for the spectral wavelength ranges of $\lambda = 20$-μm, $\lambda = 30$-μm, $\lambda = 60$-μm, and $\lambda = 150$-μm wavelengths, corresponding to $k = 0.31$ μm^{-1}, $k = 0.21$ μm^{-1}, $k = 0.10$ μm^{-1}, and $k = 0.04$ μm^{-1}. Statistical error bars are again smaller than the symbols for the majority of the data. For OMEGA, this corresponds to spherical-harmonic modes of $\ell = 20$ through 150, which are considered the most dangerous for ICF implosions.[5] Again the time-integrated 2-D SSD predictions are in good agreement with the experimental observations (*B*-integral effects are negligible here, too). The data have also been fitted using Eq. (3) with the approximation[5,21]

$$t_c = \left[\Delta\nu_{UV} \times \sin\left(k\delta/2\right)\right]^{-1}, \qquad (4)$$

where δ is the separation between spectral modes. (For one color cycle δ corresponds to one-half of a speckle width,
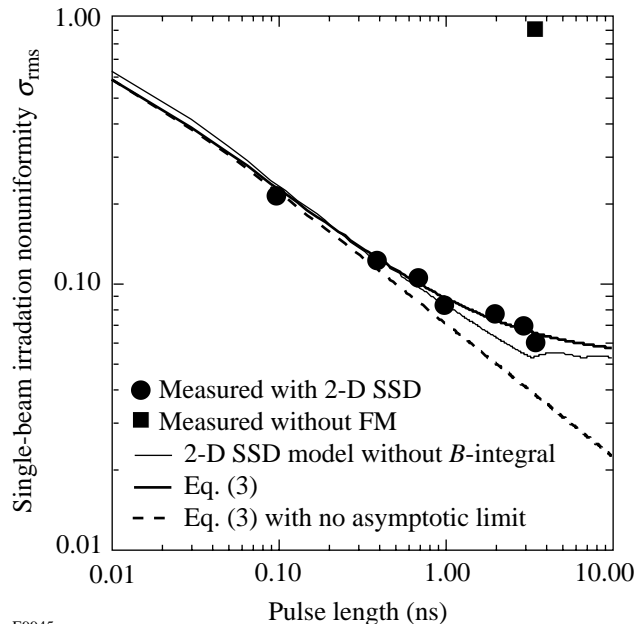
Figure 79.38
A compilation of data from over 150 laser shots demonstrates the temporal smoothing rates of 2-D SSD. Statistical error bars are smaller than the symbols. The 3.5-ns pulse has the lowest measured $\sigma_{rms} = 6.0\%$. The 3.5-ns pulse without frequency modulation is shown for comparison. The thin, solid line is the time-integrated simulation of the single-beam irradiation nonuniformity σ_{rms} that neglects the *B*-integral effects and assumes a static near field with a uniform irradiance. The thick, solid line represents the model predictions for σ_{rms} using Eq. (3). The dashed line is the model prediction for σ_{rms} with $\sigma_{asymp} = 0$.

E9945

i.e., $\delta = F\lambda/D = 2.35\ \mu\text{m}$.) In a manner similar to Fig. 79.38, the case neglecting the asymptotic behavior of Eq. (3) is also plotted in Fig. 79.39. The initial value of the laser nonuniformity σ_0 for each spectral range was determined by taking the average value of the measured σ_{rms} for shots without frequency modulation. The data in Fig. 79.39 demonstrate that the

shorter wavelengths ($\lambda = 20\ \mu\text{m}$) are smoothed more effectively than the longer wavelengths. It can also be observed that the longer-wavelength modes approach their asymptotic limits sooner than the shorter ones. Only a small amount of smoothing is observed for $\lambda = 150\text{-}\mu\text{m}$ wavelength (corresponding to $l \approx 20$), which is in agreement with the prediction.
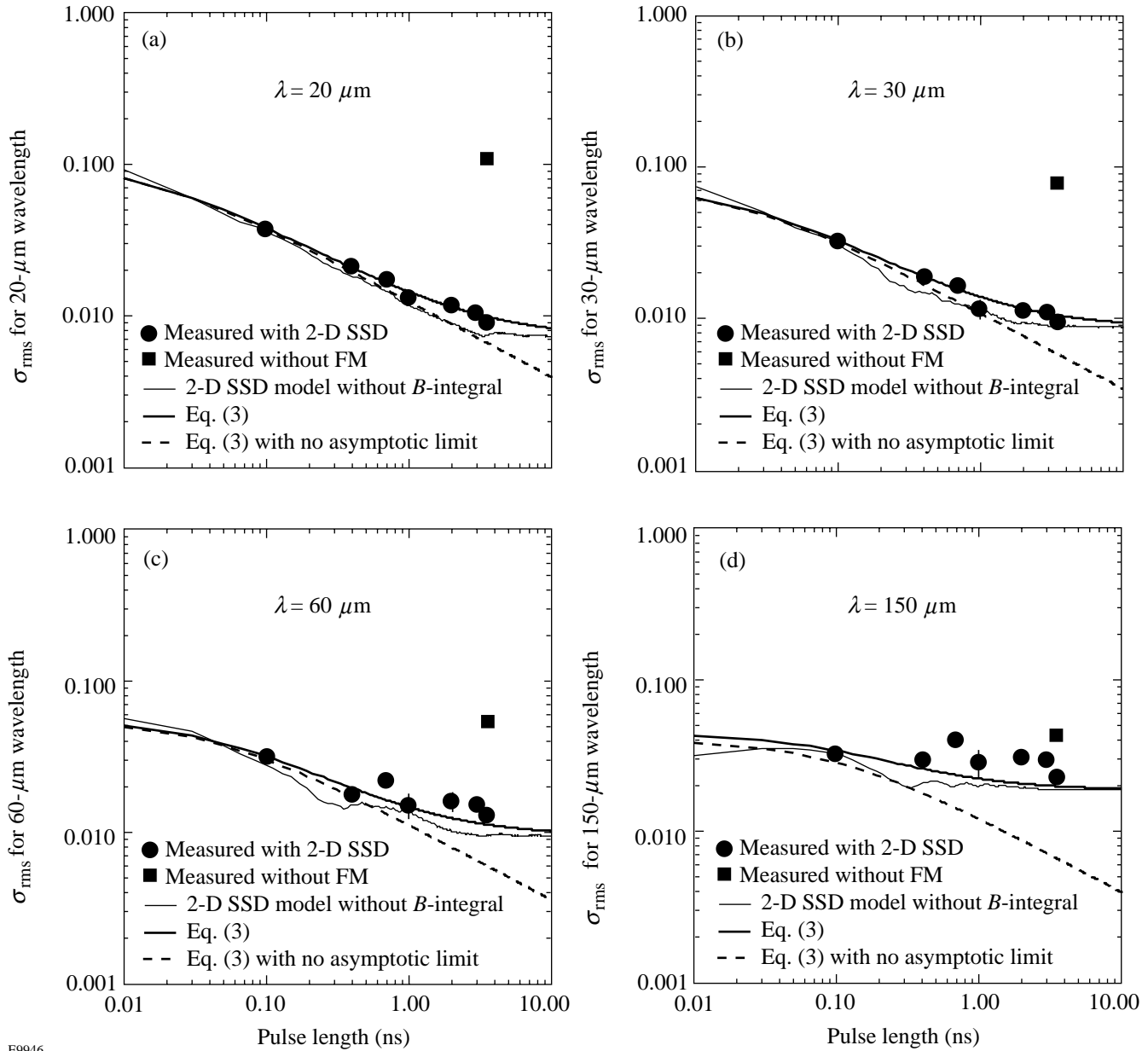
Figure 79.39

Temporal smoothing rates for specific spatial wavelengths (a) $\lambda = 20\ \mu\text{m}$ ($k = 0.31\ \mu\text{m}^{-1}$), (b) $\lambda = 30\ \mu\text{m}$ ($k = 0.21\ \mu\text{m}^{-1}$), (c) $\lambda = 60\ \mu\text{m}$ ($k = 0.10\ \mu\text{m}^{-1}$), and (d) $\lambda = 150\ \mu\text{m}$ ($k = 0.04\ \mu\text{m}^{-1}$). Statistical error bars are smaller than the symbols for the majority of the data. The 2-D SSD predictions are in good agreement with the experimental observations. The thick, solid line represents the model predictions for σ_{rms} using Eqs. (3) and (4). The dashed line is a model prediction for $\sigma_{\text{asymp}} = 0$. The thin, solid line is the predicted σ_{rms} from a 2-D SSD simulation using a static near field with a uniform irradiance and neglecting B-integral effects.

Conclusion

Direct-drive ICF experiments require a laser system with excellent irradiation uniformity. Two-dimensional smoothing by spectral dispersion is currently the best mechanism for reducing laser-beam nonuniformities for high-power/energy glass lasers. UVETP images of a single OMEGA laser beam were recorded to quantify the single-beam irradiation nonuniformity. The smoothing rate of 2-D SSD (with the current UV bandwidth of $\Delta \nu_{UV} \approx 0.2$ THz) was determined by analyzing the power spectra of measured UVETP images of laser pulses having constant peak power and pulse lengths ranging from 100 ps to 3.5 ns. Simulated 2-D SSD power spectra and temporal smoothing rates are in excellent agreement with the experimental data and permit confident extrapolation to larger laser systems and higher UV bandwidths.

REFERENCES

1. C. P. Verdon, Bull. Am. Phys. Soc. **38**, 2010 (1993).

2. S. E. Bodner, D. G. Colombant, J. H. Gardner, R. H. Lehmberg, S. P. Obenschain, L. Phillips, A. J. Schmitt, J. D. Sethian, R. L. McCrory, W. Seka, C. P. Verdon, J. P. Knauer, B. B. Afeyan, and H. T. Powell, Phys. Plasmas **5**, 1901 (1998).

3. D. K. Bradley, J. A. Delettrez, and C. P. Verdon, Phys. Rev. Lett. **68**, 2774 (1992); J. Delettrez, D. K. Bradley, and C. P. Verdon, Phys. Plasmas **1**, 2342 (1994); J. D. Kilkenny, S. G. Glendinning, S. W. Haan, B. A. Hammel, J. D. Lindl, D. Munro, B. A. Remington, S. V. Weber, J. P. Knauer, and C. P. Verdon, Phys. Plasmas **1**, 1379 (1994); R. Epstein, J. Appl. Phys. **82**, 2123 (1997); V. A. Smalyuk, T. R. Boehly, D. K. Bradley, V. N. Goncharov, J. A. Delettrez, J. P. Knauer, D. D. Meyerhofer, D. Oron, and D. Shvarts, Phys. Rev. Lett. **81**, 5342 (1998).

4. S. Skupsky, R. W. Short, T. Kessler, R. S. Craxton, S. Letzring, and J. M. Soures, J. Appl. Phys. **66**, 3456 (1989).

5. Laboratory for Laser Energetics LLE Review **69**, 1, NTIS document No. DOE/SF/19460-152 (1996); S. Skupsky and R. S. Craxton, Phys. Plasmas **6**, 2157 (1999).

6. J. E. Rothenberg, J. Opt. Soc. Am. B **14**, 1664 (1997).

7. T. J. Kessler, Y. Lin, J. J. Armstrong, and B. Velazquez, in *Laser Coherence Control: Technology and Applications*, edited by H. T. Powell and T. J. Kessler (SPIE, Bellingham, WA, 1993), Vol. 1870, pp. 95–104.

8. Y. Lin, T. J. Kessler, and G. N. Lawrence, Opt. Lett. **21**, 1703 (1996).

9. Y. Kato, unpublished notes (1984); K. Tsubakimoto *et al.*, Opt. Commun. **91**, 9 (1992); K. Tsubakimoto *et al.*, Opt. Commun. **103**, 185 (1993).

10. Laboratory for Laser Energetics LLE Review **45**, 1, NTIS document No. DOE/DP40200-149 (1990); T. E. Gunderman, J.-C. Lee, T. J. Kessler, S. D. Jacobs, D. J. Smith, and S. Skupsky, in *Conference on Lasers and Electro-Optics*, Vol. 7, 1990 OSA Technical Digest Series (Optical Society of America, Washington, DC, 1990), p. 354.

11. T. R. Boehly, V. A. Smalyuk, D. D. Meyerhofer, J. P. Knauer, D. K. Bradley, R. S. Craxton, M. J. Guardalben, S. Skupsky, and T. J. Kessler, J. Appl. Phys. **85**, 3444 (1999).

12. J. Paisner *et al.*, Laser Focus World **30**, 75 (1994).

13. M. Desselberger *et al.*, Phys. Rev. Lett. **68**, 1539 (1992); S. G. Glendinning, S. V. Weber, P. Bell, L. B. DaSilva, S. N. Dixit, M. A. Henesian, D. R. Kania, J. D. Kilkenny, H. T. Powell, R. J. Wallace, P. J. Wegner, J. P. Knauer, and C. P. Verdon, *ibid*. **69**, 1201 (1992); D. H. Kalantar, M. H. Key, L. B. DaSilva, S. G. Glendinning, J. P. Knauer, B. A. Remington, F. Weber, and S. V. Weber, *ibid*. **76**, 3574 (1996); S. G. Glendinning, S. N. Dixit, B. A. Hammel, D. H. Kalantar, M. H. Key, J. D. Kilkenny, J. P. Knauer, D. M. Pennington, B. A. Remington, R. J. Wallace, and S. V. Weber, Phys. Rev. E **54**, 4473 (1996); R. J. Taylor *et al.*, Phys. Rev. Lett. **79**, 1861 (1997); D. H. Kalantar, M. H. Key, L. B. Da Silva, S. G. Glendinning, B. A. Remington, J. E. Rothenberg, F. Weber, S. V. Weber, E. Wolfrum, N. S. Kim, D. Neely, J. Zhang, J. S. Wark, A. Demir, J. Lin, R. Smith, G. J. Tallents, C. L. S. Lewis, A. MacPhee, J. Warwick, and J. P. Knauer, Phys. Plasmas **4**, 1985 (1997); S. G. Glendinning, S. N. Dixit, B. A. Hammel, D. H. Kalantar, M. H. Key, J. D. Kilkenny, J. P. Knauer, D. M. Pennington, B. A. Remington, J. Rothenberg, R. J. Wallace, and S. V. Weber, Phys. Rev. Lett. **80**, 1904 (1998); T. R. Boehly, V. A. Smalyuk, O. Gotchev, J. P. Knauer, D. D. Meyerhofer, D. K. Bradley, J. A. Delettrez, S. Skupsky, and R. P. J. Town, Bull. Am. Phys. Soc. **43**, 1664 (1998).

14. R. H. Lehmberg and S. P. Obenschain, Opt. Commun. **46**, 27 (1983); R. H. Lehmberg, A. J. Schmitt, and S. E. Bodner, J. Appl. Phys. **62**, 2680 (1987).

15. T. R. Boehly, D. L. Brown, R. S. Craxton, R. L. Keck, J. P. Knauer, J. H. Kelly, T. J. Kessler, S. A. Kumpan, S. J. Loucks, S. A. Letzring, F. J. Marshall, R. L. McCrory, S. F. B. Morse, W. Seka, J. M. Soures, and C. P. Verdon, Opt. Commun. **133**, 495 (1997).

16. D. C. Brown, in *High-Peak-Power Nd:Glass Laser Systems*, edited by D. L. MacAdam, Springer Series in Optical Sciences (Springer-Verlag, Berlin, 1981), Vol. 25, p. 45.

17. Laboratory for Laser Energetics LLE Review **78**, 62, NTIS document No. DOE/SF/19460-295 (1999). Copies may be obtained from the National Technical Information Service, Springfield, VA 22161.

18. Photometrics Ltd., Tucson, AZ 85706.

19. Color filter glass, Schott Glass Technologies, Inc., Duryea, PA 18642.

20. Color filter glass, Hoya Corporation, Tokyo 161-8525, Japan.

21. S. Skupsky, LLE, private communication (1999).

Nonlinear Evolution of Broad-Bandwidth, Laser-Imprinted Nonuniformities in Planar Targets Accelerated by 351-nm Laser Light

In an inertial confinement fusion (ICF) implosion, the target is hydrodynamically unstable, and, as a result, mass modulations in the target (either existing or created by the drive) can grow sufficiently large to disrupt the implosion, reducing its thermonuclear yield.[1] In direct-drive ICF, the nonuniformities in the drive laser can create mass modulations in the target by a process called laser imprinting. It is, therefore, important to understand the evolution of three-dimensional (3-D) broadband initial spectra produced by laser imprinting. Target designs[2,3] rely on the saturation of unstable growth of these broadband spectra by nonlinear effects (predicted by Haan's model[4]), so it is critical to the success of ICF that this saturation be measured and understood.

The linear growth of the Rayleigh–Taylor (RT) instability has been extensively studied in planar targets accelerated by direct drive (laser irradiation).[5–8] These experiments, generally performed with preimposed two-dimensional (2-D) sinusoidal perturbations, were well simulated by hydrocodes, providing confidence that both the energy coupling and the amount of unstable growth are well modeled. The experiments discussed in this article are closely related to those that measure the growth of preimposed mass perturbations.[5,8] The latter provide a baseline calibration for various hydrodynamic effects that occur in the broadband imprinting experiments.

Nonlinear effects are inherent and very important to the evolution of broadband spectra. Several works[9–13] that used laser imprint as the initial perturbation for RT growth have shown the nonlinear evolution of broadband imprinted features. Because of the complexity of nonlinear physics, however, only a qualitative analysis of broadband saturation was shown.[9–13] In recent years several models have been developed to explain nonlinear RT evolution in Fourier[4,14–18] and real space.[17] Multimode nonlinear behavior has been measured in indirect-drive RT experiments with preimposed 3-D, multimode initial perturbations in planar targets.[19,20]

Recent work has shown experimentally[21] that three-dimensional broadband imprinted features exhibit growth that satu-

rates at amplitudes consistent with Haan's model.[4] Here we extended that work to provide a more-detailed analysis of the RT nonlinear evolution of the broadband spectra seeded by laser nonuniformities. In our experiments we used predominantly 20-μm-thick CH targets, which closely resemble the target shells typically used on OMEGA spherical implosions. On OMEGA,[22] the planar targets were accelerated by 351-nm laser beams. Various experiments were performed by different beam-smoothing techniques including distributed phase plates (DPP's),[23] smoothing by spectral dispersion (SSD),[24] and distributed polarization rotators (DPR's).[9,10] Through-foil x-ray radiography was used to measure mass modulations created in planar targets as a result of imprinting and subsequent growth.[25,26] Experimental data are compared with predictions of the Haan model for the evolution of broadband perturbation spectra. The limitations of RT growth by finite target thickness and target "bowing" due to decreased drive toward target edges are also discussed in this article.

It should be noted that the RT instability studied here exists primarily at the ablation surface, the point where the steep temperature front meets the cold overdense material of the shocked target. Perturbations in the target result from both mass modulations (ripples at the ablation surface) and density modulations produced in the bulk of the target. The latter are created primarily by the propagation of nonuniform shocks[5,27,28] produced by intensity nonuniformities in the laser drive that modulate the drive pressure. Through-foil radiographic systems are sensitive to the density–thickness product (optical depth) of the target and, as such, cannot distinguish between mass and density modulations.[5,8] After about 1 ns of acceleration in these experiments, the variations in optical depth produced by the nonuniform shocks become negligible compared to those produced by the ablation-front amplitude. At this point, it is reasonable to ascribe most of the modulation in measured optical depth to the amplitude of the perturbations at the ablation surface.[5]

The next four sections of this article describe experimental configuration, Haan's model for nonlinear saturation of broad-

band nonuniformities, data analysis techniques, and measurements of saturation levels for broadband spectra. The last four sections discuss late-time evolution of broadband spectra, target bowing, limitations of RT growth by finite target-thickness effects, and, finally, results.
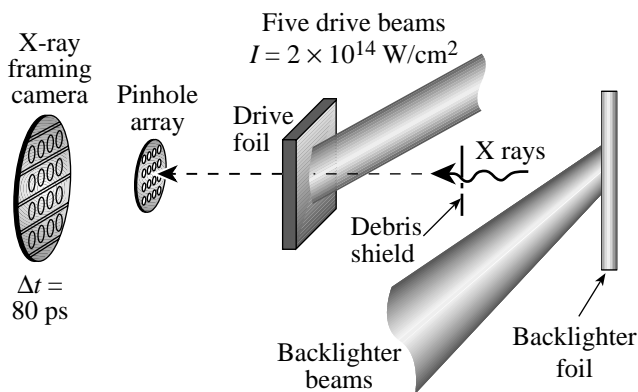
Experimental Configuration

Initially smooth, 20- and 40-μm-thick CH targets (ρ = 1.05 g/cm^2) were irradiated at 2×10^{14} W/cm^2 in 3-ns square pulses by five overlapping UV beams (see Fig. 79.40). All five beams had distributed phase plates (DPP's)[23] to enhance the on-target uniformity. Each of the drive beams was focused to a ~900-μm-diam spot size (at the 5% intensity contour) with an on-target intensity distribution measured to be $I \sim \exp\left[-(r/r_0)^4\right]$.[8] The energy per beam delivered on a target was ~400 J. For some shots SSD[24] and DPR's[9,10] were used. The 2-D SSD had IR bandwidths of 1.25 Å × 1.75 Å producing a 0.25-THz bandwidth at 351 nm. The resultant, five-beam overlapped spot (time integrated) had a constant-intensity region of ~600-μm diameter. The experiments were conducted with three different configurations of beam-smoothing techniques: (1) with DPP's, (2) with DPP's and SSD, and (3) with DPP's, SSD, and DPR's. The on-target uniformity for these cases can be estimated by dividing the time-integrated, single-beam nonuniformities (98%, 8.5%, and 6%) by the square root of 5 (for five beams), yielding 44%, 3.8%, and 2.7%, respectively, for the three configurations.[9,10] The targets were backlit with x rays produced by a uranium backlighter located 9 mm from the driven target and irradiated at

X-ray framing camera

Pinhole array

Five drive beams
$I = 2 \times 10^{14}$ W/cm^2

Drive foil

X rays

$\Delta t = $ 80 ps

Debris shield

Backlighter beams

Backlighter foil

E8418

Figure 79.40
Experimental configuration. Five overlapped beams drive a 20-μm-thick CH foil. An additional 12 beams produce x rays from a uranium backlighter foil. X rays traverse the target and are imaged by a pinhole array on a framing camera.

~1×10^{14} W/cm^2 (using 12 additional beams). X rays transmitted through the target and a 3-μm-thick aluminum blast shield (located between the backlighter and drive foils) were imaged by 8-μm pinholes on an x-ray framing camera filtered with 6 μm of aluminum. This yielded the highest sensitivity for an average photon energy of ~1.3 keV. The distance between the target and the pinhole array was 2.9 cm, and the distance between the pinhole array and the framing camera was 35 cm, resulting in a magnification of ~12. The framing camera produced eight temporally displaced images, each of ~80-ps duration. The use of optical fiducial pulses coupled with an electronic monitor of the framing camera output produced a frame-timing precision of ~70 ps. The framing camera images were captured on Kodak T-Max 3200 film, which was digitized with a Perkin-Elmer PDS microdensitometer with a 20-μm-square scanning aperture. The measured target optical depth is the natural logarithm of the intensity-converted images of a target.

The experiment involved multiple shots where radiographs were obtained at different times. For each shot, up to six images of the same area (400 μm square) of the target (found by the cross-correlation method described later in this article) were analyzed. These images were acquired in time intervals 1.0 to 2.8 ns after the beginning of the drive. The backlighter shape was removed by subtracting a fourth-order, two-dimensional envelope fit to data. The resulting images were the measured modulations of optical depth $D_m(\mathbf{f})$. Using the measured system resolution, noise, and sensitivity, we applied a Wiener filter to reduce noise and deconvolved the system's modulation transfer function (MTF) to recover the target's areal-density modulations $D_t(\mathbf{f})$.[26] The noise in these measurements was dominated by photon statistics of the backlighter x rays, and the system resolution was limited by an 8-μm pinhole.[26]

The primary objective of this experiment is to recover the amplitude of the perturbation at the ablation surface using the measured optical-depth modulations. To do this rigorously requires significant effort. One approach is to use computer simulations of the experiment and detection system to quantify the relationship between modulations in the radiographs and perturbations in the target.[29] Since three-dimensional simulations of laser-imprinted perturbations are difficult, it is advantageous to obtain this relationship experimentally. We simplify the latter process by establishing several reasonable assumptions about the detection system. First, as a result of Al filters, a relatively narrow band ($\Delta E \simeq 200$ eV) of x rays around 1.3 keV is used for radiography. Around 3.5 keV (uranium M-band emission) the spectral component's effect on system

sensitivity and resolution was measured and calculated to be negligible.[26] Second, the backlighter spectrum and filter transmission remain constant during the measurement. Third, the backlighter is produced by 12 beams with phase plates, resulting in a very uniform and predictable backlighter shape. Fourth, there is little heating of the solid part of the target; therefore, the mass absorption coefficient μ is constant in time. Fifth, the amplitudes of the growing imprinted features are large enough that the propagation of a nonuniform shock has little effect on the total optical depth of the target.[5] Given these assumptions, the measured optical depth and the optical depth of the target (areal density) are linearly related as

$$D_m(\mathbf{r},t) = \int d\mathbf{r}' R_{\text{sys}}(\mathbf{r}-\mathbf{r}') D_t(\mathbf{r}',t), \qquad (1)$$

where R_{sys} is the point spread function (PSF) of the entire system. The latter is the convolution of the PSF's of the pinhole, the framing camera, the film, and the digitizing aperture of the densitometer. In frequency space, the total system modulation transfer function (MTF) is the product of the MTF's of each of these components. Equation (1) has been derived assuming that the amplitude of the target's optical-depth modulations is small compared to unity. Since Eq. (1) is a linear approximation, it does not treat the generation of harmonics and coupling of modes produced by nonlinearities in the detection system. We have simulated these nonlinearities for modulation amplitudes greater than those measured routinely in our experiments and found that nonlinear effects were negligible compared to the noise in the system. This knowledge was used to create a Weiner filter that uses a linear approximation to the detection system in order to recover the target areal-density modulations.[26]

As an example, Fig. 79.41 shows a fully processed image of the target optical depth at 2.4 ns for a shot with all of the laser-smoothing techniques (DPP's, SSD, and DPR's) employed. The range of 3.6 OD corresponds to a target areal-density (ρR) modulation of about 3.6×10^{-3} g/cm^2. For comparison, the areal density (ρR) of the undriven target is about 2×10^{-3} g/cm^2.

At early times, the contribution to areal-density modulations in the bulk of a target, produced by the propagation of nonuniform shocks, is comparable to those from amplitude modulation at the ablation surface.[5] After ~1 ns of drive, however, the ablation-front modulations with spatial frequencies in the region 10 to 100 mm^{-1} (where measurements are performed) experience sufficient RT growth to dominate any

density modulation produced by nonuniform shocks. Thus, at times >1 ns, the amplitude at the ablation surface is well represented by measured modulations.

Once the modulation in target optical depth $D_t(\mathbf{r},t)$ is obtained, the perturbation amplitude in the target $\xi(\mathbf{r},t)$ can be found using spectrally weighted attenuation length λ_{CH},[26] which is inversely proportional to the mass absorption coefficient and the target density:

$$\xi(\mathbf{r},t) = D_t(\mathbf{r},t)\lambda_{\text{CH}}. \qquad (2)$$

λ_{CH} can be constructed using the target compression C_p calculated by 1-D hydrocode *LILAC*[30] and the measured attenuation length λ_x of the undriven target:

$$\lambda_{\text{CH}} = \frac{\lambda_x}{C_p}. \qquad (3)$$

This relation can be used as long as the driven target maintains the cold value of its mass absorption coefficient. Typically, during our experiments the calculated target temperature $(T < 10 \text{ eV})$ is far below the values that could change the mass absorption coefficient to ~1-keV x rays. λ_x was measured by radiographing undriven, 20-μm-thick CH targets that had

1.8 OD
1.4 OD
1.0 OD
0.6 OD
0.2 OD
–0.2 OD
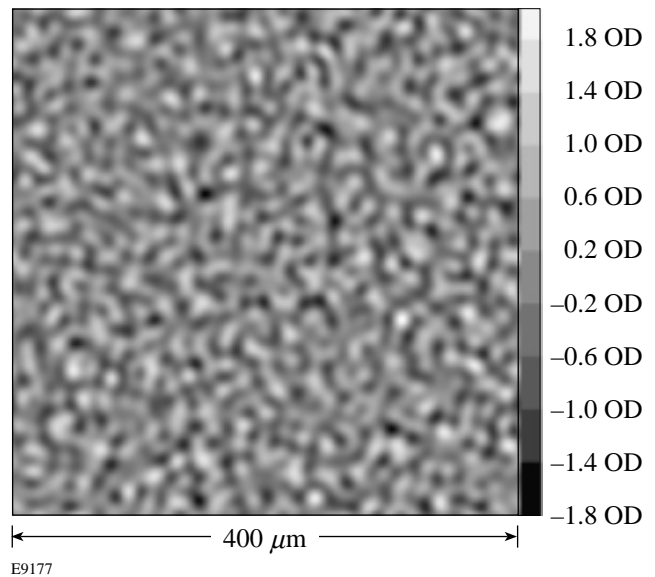–0.6 OD
–1.0 OD
–1.4 OD
–1.8 OD

|← 400 μm →|

E9177

Figure 79.41
Fully processed image of the target optical depth (OD) perturbations captured at 2.4 ns for one of the six shots with all smoothing techniques including DPP's, SSD, and DPR's.

preimposed, low-amplitude (0.5-μm) sinusoidal modulations with wavelengths of 60 and 30 μm. Using these modulations as control references, λ_x was determined to be 10±2 μm. These experiments also showed that both backlighter spectrum and filter transmission remained constant during the measurements.

Haan's Model for Broadband Spectra

In the linear regime of the RT instability, individual modes do not interact and therefore grow exponentially at rates determined by the dispersion relation[31–33]

$$\gamma = \alpha \sqrt{\frac{kg}{1 + L_m k}} - \beta k V_a, \qquad (4)$$

where γ is the instability growth rate, k is the wave number of the perturbed mode, g is the target acceleration, L_m is the minimum density-gradient scale length, and V_a is the ablation velocity. For CH targets $L_m \sim 1$ μm and the constants have values of $\alpha \sim 1$ and $\beta \sim 1.7$. Equation (4) determines how the actual growth rate differs from the classical rate $\gamma \sim \sqrt{kg}$ as a result of density scale length and ablation. For a single-mode initial perturbation, nonlinear effects cause the exponential growth of the mode to saturate at an amplitude $\xi_k \simeq 0.1 \lambda$ and to subsequently grow linearly in time.[4] Harmonics of the fundamental mode are generated by mode coupling[14] during the exponential growth (in linear phase), leading to the formation of bubbles (penetration of lighter fluid into heavier) and spikes (penetration of heavier fluid into lighter).

The evolution of 3-D broadband perturbations is more complicated. The fastest-growing modes rapidly drive harmonics and coupled modes. The contribution of the mode coupling becomes comparable to the exponential growth for some of the modes, even at small (in the linear regime) amplitudes. As a result, some modes grow faster than others, while some shrink and change their phase;[18] however, the average amplitude of all of the modes at a given spatial frequency grows exponentially at a rate given by Eq. (4).[4,14] Saturation occurs due to the collective behavior of modes because adjacent modes can constructively interfere to create local structures with amplitudes much larger than those of individual modes. As these features experience saturation, the individual modes saturate at amplitudes much less than 0.1 λ. After reaching this saturation level, the modes grow, on average, linearly in time. The transition from the linear (exponential growth) to the nonlinear stage (linear growth) is continuous. Haan formulated a model[4] for the saturation of a 3-D broadband spectrum and found a saturation level of the azimuthally

averaged amplitude given by[15,16]

$$S(k) = 2/Lk^2, \qquad (5)$$

where L is the size of the analysis box. The L dependence occurs because the individual Fourier amplitudes of the broadband features depend on the size of analysis region; whereas the rms amplitude σ_{rms}, a measure of the deviation of the function $\xi(\mathbf{x})$ from its average value $\bar{\xi}$, does not. Using the Fourier transform $\xi(\mathbf{k})$ of the function $\xi(\mathbf{x})$, the rms amplitude σ_{rms} is defined as

$$\sigma_{rms} = \sqrt{\sum_k |\xi(\mathbf{k})|^2 - |\xi(\mathbf{k}=0)|^2}. \qquad (6)$$

The rms amplitude is the physically measurable quantity and therefore must have the same value independent of how it is derived. The number of Fourier modes decreases as the box size is reduced. The nonuniformity's σ_{rms} is the square root of the sum of all modes' absolute values squared, as shown by Eq. (6), so the amplitudes of the modes must, concomitantly, increase to keep the nonuniformity's σ_{rms} constant.

After it reaches the saturation level $S(k)$, the evolution of the average amplitude $\xi_k(t)$ is given by[4]

$$\xi_k(t) = S(k)\left[1 + \ln\left(\frac{\xi_k^{\exp}(t)}{S(k)}\right)\right], \qquad (7)$$

where $\xi_k^{\exp}(t) = \xi_k(t=0)\exp(\gamma t)$ is the exponential growth in the linear stage of instability. This is equivalent to growth at a constant velocity $V(k)$ in the saturation regime

$$V(k) = S(k)\gamma(k). \qquad (8)$$

The behavior predicted by this model is shown in Fig. 79.42 for an initial perturbation spectrum that had constant power per mode as a function of spatial frequency. This is representative of the broadband features imprinted by irradiation non-uniformities that arise primarily from the speckle pattern produced by DPP's and SSD.[34] The evolution of this spectrum (plotted as the average amplitudes versus spatial frequency for seven different times between $t = 1.3$ to 2.2 ns) is modeled simply by applying the growth-rate dispersion relation [Eq. (4)], the saturation level [Eq. (5)], and the evolution in the saturation regime [Eq. (7)], where the target acceleration $g = 50$ μm/ns^2, ablation velocity $V_a = 2.5$ μm/ns, and the

nonuniformity's initial $\sigma_{rms} = 0.09$ μm. The amplitudes are converted to target optical depth by dividing by the measured, spectrally weighed, attenuation length $\lambda_x = 10\pm2$ μm and multiplying by the simulated compression of the target (about 2 for 1.5 ns). The simulated target density at the ablation surface is shown in Fig. 79.43. The high-frequency modes grow most rapidly and saturate at the level given by Eq. (5), while the low-frequency modes grow more slowly. As a result, the mid-frequency modes experience the largest growth factors, producing a peak in the spectrum. As the evolution progresses, the mid-frequency modes begin to saturate, and the peak moves to longer wavelengths. This behavior is relatively insensitive to the initial spectrum or drive conditions; therefore, most broad-bandwidth initial spectra will evolve similarly given sufficient time. Variations in growth rates of up to 50%, or in the σ_{rms} of the initial spectrum of up to two orders of magnitude, have little effect on the predicted spectral evolution; the only requirement is that the spectrum be broadband. For example, according to Haan's model the initial perturbation spectrum that has constant Fourier amplitude and $\sigma_{rms} = 0.5$ μm undergoes similar evolution to that shown in

Fig. 79.42 but it occurs at earlier times (between $t = 0.8$ to 1.6 ns) if the drive conditions are the same. This behavior has been tested experimentally by varying amplitudes of initial perturbation using a variety of laser-smoothing techniques.

Image Cross-Correlations

The experiment involves multiple shots with CH targets and with different smoothing techniques applied. For each shot, up to six unfiltered images of the same area of the target, found with a cross-correlation technique, were processed with a 400-μm analysis box. Figure 79.44 shows two images of the target acquired at 2.4 ns and 2.5 ns for a shot with all smoothing techniques employed. The same 400-μm-sq area of the target was found in each of these images when the cross-correlation between the two analysis regions was maximized. The cross-

E9825
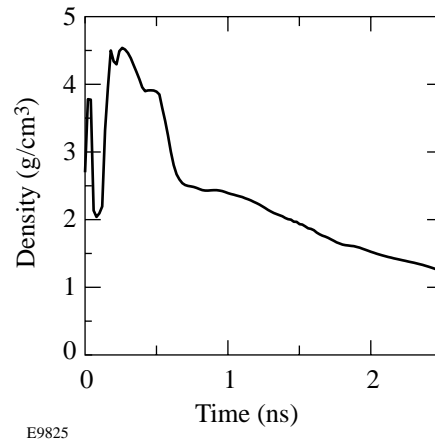
Figure 79.43
Calculated target density at the ablation surface as a function of time.

E9193b

Figure 79.42
Predicted Fourier amplitudes of optical depth using Haan's model for an assumed spectrum of perturbations with initial flat power per mode ($\sigma_{rms} = 0.09$ μm) spectrum, target acceleration of $g = 50$ μm /ns^2, ablation velocity of $V_a = 2.5$ μm /ns, and $L = 400$ μm at times 1.3, 1.4, 1.6, 1.8, 1.9, 2.0, and 2.2 ns. Haan's saturation amplitude S is shown by the dashed line.

E9538
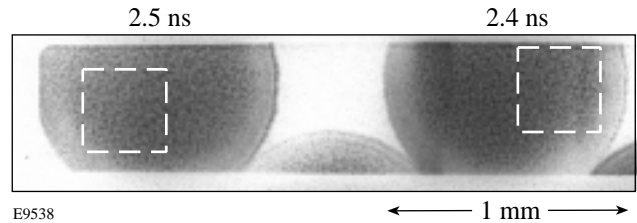
Figure 79.44
Two images of the target acquired at 2.4 ns and 2.5 ns for a shot with all smoothing techniques employed. Two 400-μm-square regions indicated by the square boxes were taken for cross-correlation analysis.

correlation function for two images with target optical depths $D_{t1}(\mathbf{r})$ and $D_{t2}(\mathbf{r})$ is given by

$$C(\mathbf{r}) = \frac{\int d\mathbf{r}' D_{t1}(\mathbf{r}' + \mathbf{r}) D_{t2}(\mathbf{r}')}{\sqrt{\int d\mathbf{r} D_{t1}(\mathbf{r})^2 \int d\mathbf{r} D_{t2}(\mathbf{r})^2}}. \qquad (9)$$

If two images of the target are shifted by some distance a, then the maximum of the cross-correlation function $C(\mathbf{r})$ will be shifted by the same distance from the center of coordinates ($\mathbf{r} = 0$), as can be seen from Eq. (9). For example, if two images at 2.4 ns and 2.5 ns are misaligned by $a_x = 133$ μm in horizontal and $a_y = 67$ μm in vertical directions, the peak of the cross-correlation function between these two images is shifted from the center of coordinates by the same distances a_x and a_y as

shown in Fig. 79.45(a). When one of the images is moved by the distances a_x and a_y, aligning these two images, the peak of the cross-correlation function moves toward the center of coordinates as shown in Fig. 79.45(b). At the same time, the cross-correlation coefficient between these two images, which is defined as the maximum of $C(\mathbf{r})$, increases from 17% for misaligned images to 34% for aligned images because larger areas of the target overlap for two aligned images.

The details of target nonuniformity structure are unique and specific only to images taken at the same shot. It is therefore expected that the cross-correlation technique should find little correlation between two images taken from different shots. The typical cross-correlation function of two images taken on different shots is shown in Fig. 79.45(c). This function has no

E9539
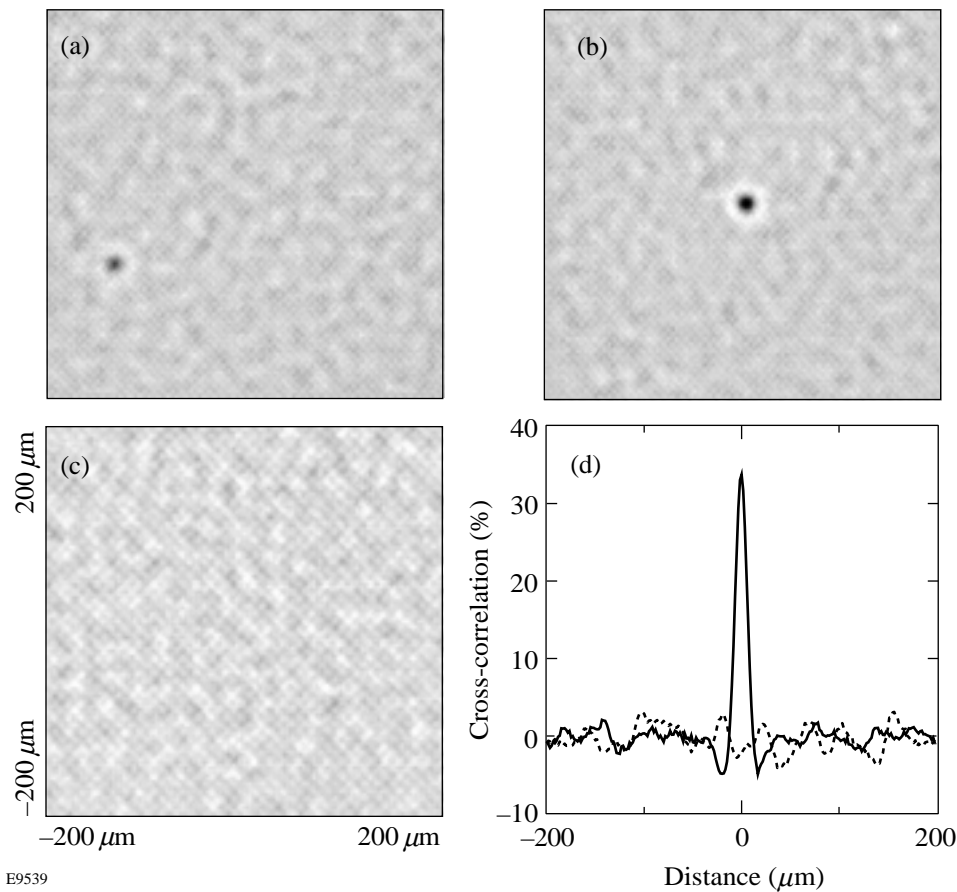
Figure 79.45
The cross-correlation function between two images. (a) Two images are shifted by 133 μm in the horizontal direction and 67 μm in the vertical direction, respectively. The cross-correlation coefficient between the two images is 17%. (b) When two images are aligned, the maximum of the cross-correlation function is then located at the center of coordinates at $\mathbf{r} = 0$. The cross-correlation coefficient between the two images increases to 34%. (c) The cross-correlation function between the two images taken on different shots showing little correlation. (d) The lineout through the center of coordinates of the cross-correlation function shown in (c) for two images taken at different shots (dashed line). The lineout through the center of coordinates of the cross-correlation function shown in (b) for 2.4-ns and 2.5-ns images taken during the same shot (solid line).

pronounced peaks; it fluctuates around zero, as shown by the dashed line in Fig. 79.45(d), which is the lineout of this function through the center of coordinates. This indicates that there is no correlation between features in images from different shots. In contrast, images taken on the same shot (such as those acquired at 2.4 and 2.5 ns and shown in Fig. 79.44) are well correlated. This is shown by the lineout through the center of their cross-correlation function as shown in Fig. 79.45(d) by the solid line. The cross-correlation between images greatly increased after they were Wiener filtered: for example, the cross-correlation coefficient between these images increased from 34% to 70%. This indicates that the image processing efficiently reduced the noise in these images. The upper limit of the cross-correlation is determined by the amount of evolution the target perturbations experienced between the times the images were captured.

The accuracy of the image alignment using the cross-correlation technique has been defined in the following way: For a particular shot, five images (A, B, C, D, and E) were aligned with a sixth image (F) by moving the peaks of all five cross-correlation functions toward their centers of coordinates. Then each of the five images was cross-correlated to each other. It was found that the peaks of all these cross-correlation functions were located no farther than 1 pixel (1.67 μm) from the centers determined by the first step. This indicates that the accuracy of the alignment is not worse than 2 μm.

Figure 79.46 shows six fully processed (Wiener-filtered) sub-images ($L = 100$ μm) of the target optical depth for one of the shots with full smoothing (DPP's, SSD, and DPR's applied) captured at 1.6, 1.9, 2.0, 2.2, 2.4, and 2.5 ns and aligned by the cross-correlation technique. The temporal evolution to longer-scale structures is evident. All images are well correlated indicating that the evolution is of the same features. Figure 79.47 shows the cross-correlation coefficients $C(\mathbf{r}=0)$ between these different images. The solid line shows that the cross-correlation $C(\mathbf{r}=0)$ of the image at 2.5 ns with itself equals 1 (at 2.5 ns) and its cross-correlation with other images (at other times) decreases as a time separation between images increases. The dashed line in Fig. 79.47 shows the same behavior for the cross-correlation of the image at 2.2 ns with the other images. In fact, the same behavior has been observed for each time frame in all six shots, i.e., the cross-correlation between neighboring images is always higher than with more-distant images, which confirms that the image processing allows an observation of the evolution of the same features of target perturbations.

Nonlinear Saturation of RT Growth

As was pointed out earlier, predictions by the Haan's model for the shape of the late-time spectrum are relatively insensitive to the initial perturbation spectrum; therefore, most broadbandwidth initial spectra evolve similarly. Variations of up to two orders of magnitude in the initial amplitudes of the spectrum have little effect on the predicted spectral evolution. This prediction has been tested experimentally by varying the amplitudes of initial perturbation using different laser-smoothing techniques. The primary experiment involves multiple shots with planar, 20-μm-thick CH targets taken with different smoothing techniques employed: with DPP's, SSD, and DPR's (six shots), with DPP's and SSD (three shots), and with DPP's only (two shots).
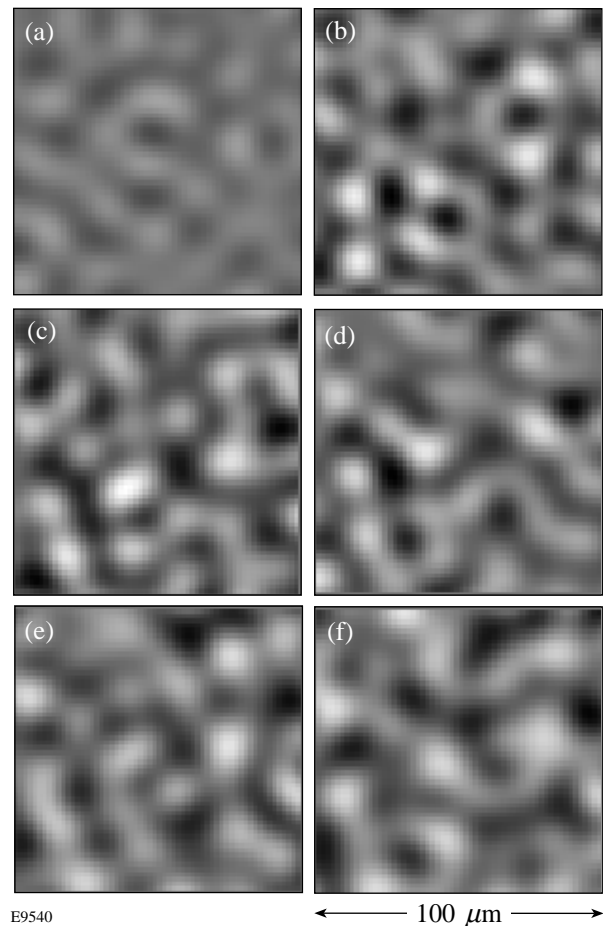

E9540   ←——— 100 μm ———→

Figure 79.46
Fully processed sub-images (with a box size of 100 μm) of the target optical depth captured at (a) 1.6, (b) 1.9, (c) 2.0, (d) 2.2, (e) 2.4, and (f) 2.5 ns for one of the six shots taken with laser conditions that include DPP's, SSD, and DPR's. The evolution in time to longer-scale structures is evident.
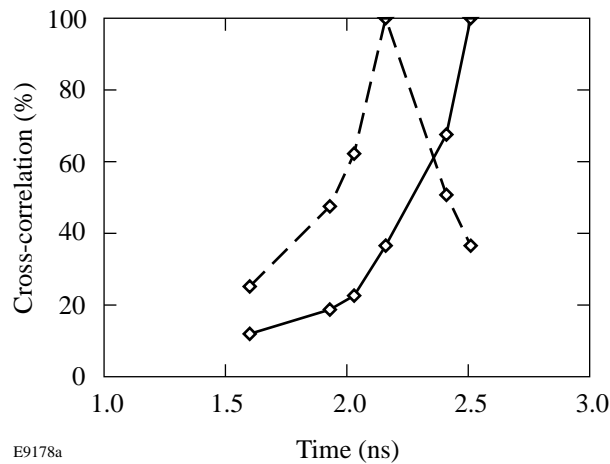
E9178a

Figure 79.47

Cross-correlation of different time images for one of the six shots taken with laser conditions that include DPP's, SSD, and DPR's. The cross-correlation coefficients of images captured at 2.5 ns and 2.2 ns with all other images are shown by the solid line and the dashed line, respectively.

The evolution of the averaged amplitudes (obtained by azimuthally averaging the Fourier amplitudes at each spatial frequency) of the measured target's optical-depth modulation as a function of spatial frequency with planar, 20-μm-thick CH targets is shown in Fig. 79.48(a) for one shot at times of 1.4 to 2.2 ns and in Fig. 79.48(b) for another shot at somewhat later times of 1.6 to 2.4 ns. In these shots laser beams had full smoothing techniques employed (i.e., DPP's, SSD, and DPR's). Figures 79.48(c) and 79.48(d) show the evolution of nonuniformity spectra for shots with DPP's and SSD for times of 1.6 to 1.9 ns for one shot and of 1.6 to 2.0 ns for the other, and Figs. 79.48(e) and 79.48(f) for shots with DPP's only for times of 1.3 to 1.5 ns for one shot and of 1.6 to 1.8 ns for the other. The initial amplitudes of imprinted perturbations are expected to be higher in shots with less laser uniformity.

One can readily see that the measured spectra are peaked and that the peak shifts toward longer wavelengths as time progresses, similar to the predicted behavior shown in Fig. 79.42. Moreover, the dashed line, which shows the Haan saturation level, is in good agreement with the position of the spectral peak. The saturation level was converted to optical depth using the spectrally weighed attenuation length λ_x and the predicted compression (about 2 at times ~1 to 2 ns). Similar behavior was observed for all shots taken under all drive conditions with different smoothing techniques employed. For the data with less laser uniformity [Figs. 79.48(e) and 79.48(f), DPP's only], the initial imprinted amplitudes are higher, and as a result, the RT evolution is observed earlier in time than in the

case with more-uniform drive, which includes SSD and DPR's [Figs. 79.48(a) and 79.48(b)].

Figure 79.48 shows that the measured growth of the amplitudes at 20-μm wavelength is much less pronounced than that of 30 μm for all shots. This is because the amplitudes at 20 μm are predicted to be already above Haan's saturation level at about 0.01 OD, while amplitudes at 30 μm experience a transition from exponential growth to the saturated growth with constant velocity at about 0.022 OD. The amplitude at 60 μm is predicted to be below the saturation level and therefore should grow exponentially during this time interval. To support these assertions, we measured the growth of low-amplitude, preimposed, 2-D, 60-μm-wavelength and 30-μm-wavelength, single-mode, sinusoidal perturbations on 20-μm-thick CH foils driven with the irradiation conditions that included DPP's, SSD, and DPR's. Targets with initial perturbation amplitudes of 0.05 and 0.125 μm at 60-μm wavelength and 0.025 μm at 30-μm wavelength were used. These initial amplitudes are sufficiently low that they are expected to be in the linear regime for at least 2.5 ns, yet have high enough amplitudes that mode coupling from the broadband spectrum has no effect on their evolution. Figure 79.49(a) shows that the broadband features at 60 μm (the combined data from six shots) grow at a similar rate as the preimposed 60-μm modulations (upper data points for two shots). Exponential fits to these data (three solid lines) indicate growth rates of 0.96 ±0.02 ns^{-1} and 1.02±0.02 ns^{-1} for the preimposed modulations and 0.91±0.05 ns^{-1} for the broadband modulations. Figure 79.49(b) shows that the broadband features at 30 μm (the combined data from six shots) experience a transition from linear to nonlinear phases at an amplitude of about 0.02 OD, which is 30 times lower than the single-mode saturation value of 0.6 OD (0.1 λ). At the same time, the two preimposed 30-μm modulations (upper data points) grow exponentially with growth rates of 1.45±0.02 ns^{-1} and 1.54±0.02 ns^{-1}, respectively. These data clearly show the wavelength-dependent saturation level.

The preimposed 30-μm and 60-μm modulations were fitted with an exponential in order to compare growth rates with those measured for early times[5,8] (see later in the **Finite Target Thickness Effect** section). For broadband modulations, both exponential and polynomial fits have been used to quantify the transition from the exponential to saturated growth. Figure 79.49(b) shows that for broadband modulations at 60 μm, the exponential fit (solid line) closely matches the third-order polynomial fit (dashed line). The standard deviations are 0.0021 OD and 0.0022 OD, respectively. For 30-μm broadband modulations shown in Fig. 79.49(b), however, the expo-

nential (dashed line) does not fit data well (the standard deviation is 0.0039 OD) compared to the polynomial fit (solid line; the standard deviation is 0.0022 OD), which closely follows the saturated evolution of these broadband data.

Figure 79.50 summarizes data from 11 shots performed with (1) DPP's, SSD, and DPR's [six shots, Figs. 79.50(a), 79.50(d), and 79.50(g) for the average broadband amplitudes at wavelengths of 60 μm, 30 μm, and 20 μm, respectively],
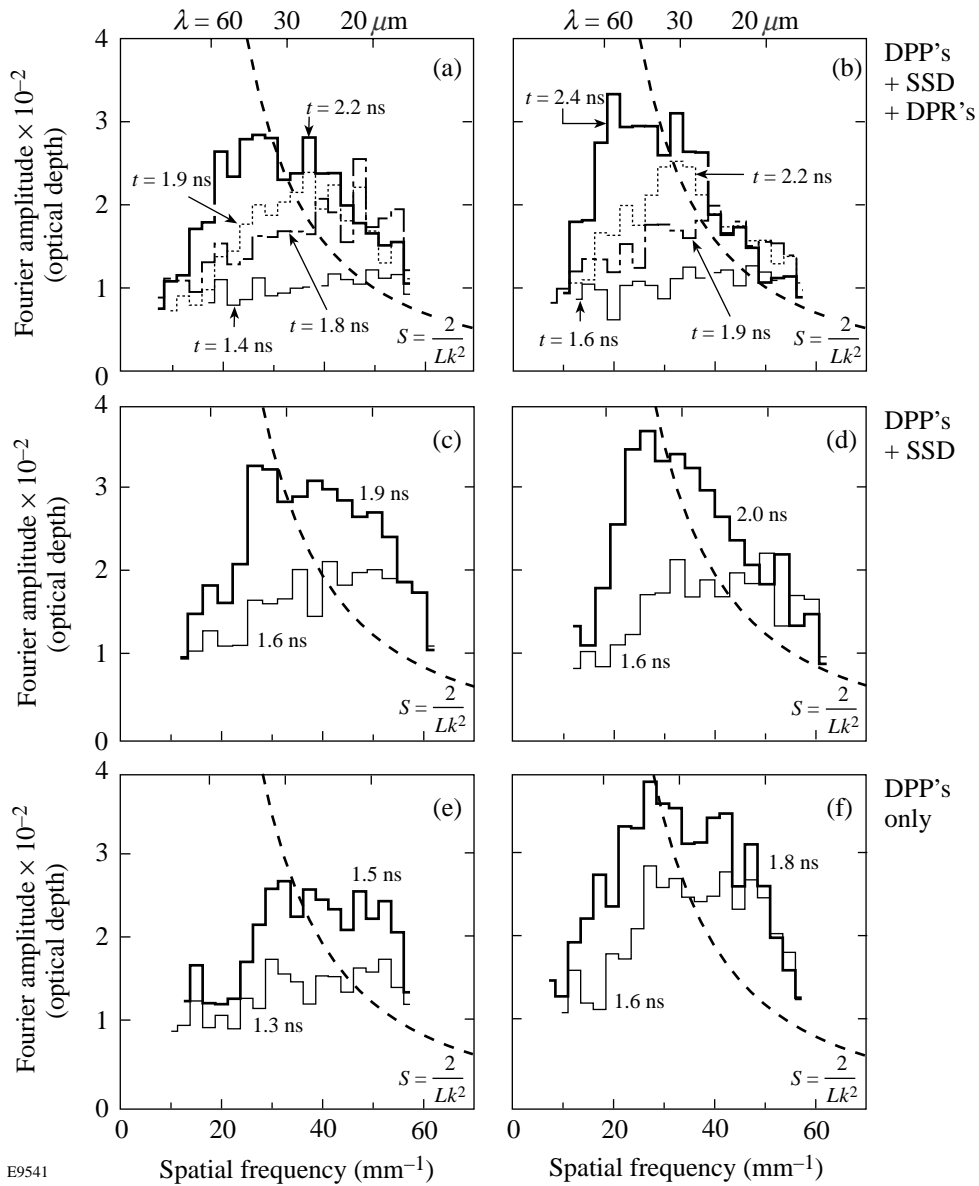
Figure 79.48

The measured azimuthally averaged Fourier amplitudes of the optical-depth modulations as a function of spatial frequency for six shots: (a) a 20-μm-thick foil at times 1.4, 1.8, 1.9, and 2.2 ns with laser conditions that include DPP's, SSD, and DPR's; (b) at 1.6, 1.9, 2.2, and 2.4 ns with DPP's, SSD, and DPR's; (c) at 1.6 and 1.9 ns with DPP's and SSD; (d) at 1.6 and 2.0 ns with DPP's and SSD; (e) at 1.3 and 1.5 ns with DPP's; and (f) at 1.6 and 1.8 ns with DPP's. Haan's saturation amplitude S is shown by the dashed line.

(2) DPP's and SSD [three shots, Figs. 79.50(b), 79.50(e), and 79.50(h)]; and (3) DPP's only [two shots, Figs. 79.50(c), 79.50(f), and 79.50(i)]. It is expected that SSD smoothes out perturbations at high spatial frequencies much more efficiently than at low spatial frequencies;[34] therefore, the expected initial

imprinted spectra with and without SSD have not only different nonuniformities σ_{rms}, but also different shapes. According to Haan's model, however, later in time, and after considerable RT growth, the perturbation spectra are expected to be similar but shifted in time with the evolution occurring later in the case of DPP's plus SSD compared to DPP's only.

The measured temporal evolution for all three cases is similar, as evident from the evolution of the amplitudes of broadband perturbations at 60-μm, 30-μm, and 20-μm wavelengths. The 30-μm- and 20-μm-wavelength perturbations saturate at different times for different smoothing conditions but always at the same levels. The 60-μm perturbations grow in the linear regime (exponential growth) with similar growth rates (0.70±0.05 ns^{-1}, 0.93±0.05 ns^{-1}, and 0.91±0.05 ns^{-1} with DPP's only; DPP's and SSD; and DPP's, SSD, and DPR's, respectively, for all smoothing conditions). As shown earlier, these growth rates are in very good agreement with the measured growth rates of preimposed 2-D sinusoidal perturbations at a 60-μm wavelength [Fig. 79.49(a), upper data points].

For cases with less laser uniformity [case (3): DPP's only], the initial imprinted amplitudes are higher, and as a result, the RT evolution is advanced in time [~250 ps earlier than in case (2), and ~500 ps earlier than in case (1)]. This observation is evident for the 60-μm, 30-μm, and 20-μm wavelengths of broadband perturbations. Note also that the 30-μm-wavelength perturbations saturate at higher amplitude than the 20-μm perturbations, as expected.

Even though the experimental data (see Fig. 79.48) cannot show the saturation level $S(k) = 2/Lk^2$ explicitly, it was tested by comparing peaks of measured Fourier spectra with those predicted by using Haan's model. Such comparison becomes possible because the shape of Fourier spectra and the position of their peaks depend primarily on the saturation level rather than on the initial or drive conditions (shown experimentally in Fig. 79.48). For example, from Fig. 79.48(a) one can see that measured spectral peaks at spatial frequencies of 30 mm^{-1} and 50 mm^{-1} are positioned at the values of Fourier amplitudes of approximately 2.7×10^{-2} and 1.2×10^{-2} OD, at times 2.2 ns and 1.4 ns, respectively. The predicted spectral peaks at these spatial frequencies are at the values of approximately 3.7×10^{-2} and 1.2×10^{-2} OD, respectively, as shown in Fig. 79.42.

The main experimental errors in measurements of target optical depth shown in Fig. 79.48 include noise in the experimental system (dominated by photon statistics of the backlighter x rays), uncertainty of the system resolution, and nonlinearities

Figure 79.49

(a) Average Fourier amplitudes of optical depth of imprinted features versus time at 60-μm wavelength for six shots (distinguished by different symbols) and the amplitude of preimposed 60-μm perturbations of corrugated targets with initial amplitudes of 0.05 and 0.125 μm (upper data). (b) The same for the 30-μm wavelength with the amplitudes of initial, preimposed, 30-μm perturbations of 0.025 μm (upper data). Exponential fits (solid lines) were used for the preimposed corrugation data, 60-μm imprinted data (solid lines), and 30-μm imprinted data (dashed line), and a third-order polynomial fit was used to the imprinted data at 60 μm (dashed line) and 30 μm (solid line).

in the detection system, which was considered to be linear during Wiener filtering and MTF deconvolution.[26] The total uncertainty of optical-depth measurements at the spatial frequency range of 30 to 50 mm^{-1} was determined to be about 10^{-3} OD. It included the relative error of system resolution measurement, which was about 4%, and the uncertainty due to nonlinearity in the detection system, which was about 2% of the noise in the experimental system.[26]

The Haan's model predictions shown in Fig. 79.42 were converted to the optical depth using spectrally weighted attenuation length λ_{CH},[26] which depends on the calculated target compression C_p and the measured attenuation length λ_x of the undriven target [see Eq. (3)]. λ_x was determined to be 10 ± 2 μm,[26] and the target compression was calculated to be about $C_p = 1.7\pm0.3$ during the time interval of 1.4 to 2.2 ns.

E9542

Figure 79.50

(a) Average Fourier amplitudes of optical depth of imprinted features versus time at 60-μm wavelength for six shots (distinguished by different symbols) with DPP's, SSD, and DPR's. Exponential fit (solid line) indicates the growth rate of 0.91±0.05 ns^{-1}. (b) The same for the three shots with DPP's and SSD. Exponential fit (solid line) indicates the growth rate of 0.93±0.05 ns^{-1}. (c) The same for the two shots with DPP's only. Exponential fit (solid line) indicates the growth rate of 0.70±0.05 ns^{-1}. (d) Average Fourier amplitudes of optical depth of imprinted features versus time at 30-μm wavelength for six shots with DPP's, SSD, and DPR's. The solid line is a third-order polynomial fit. (e) The same for the three shots with DPP's and SSD. (f) The same for the two shots with DPP's only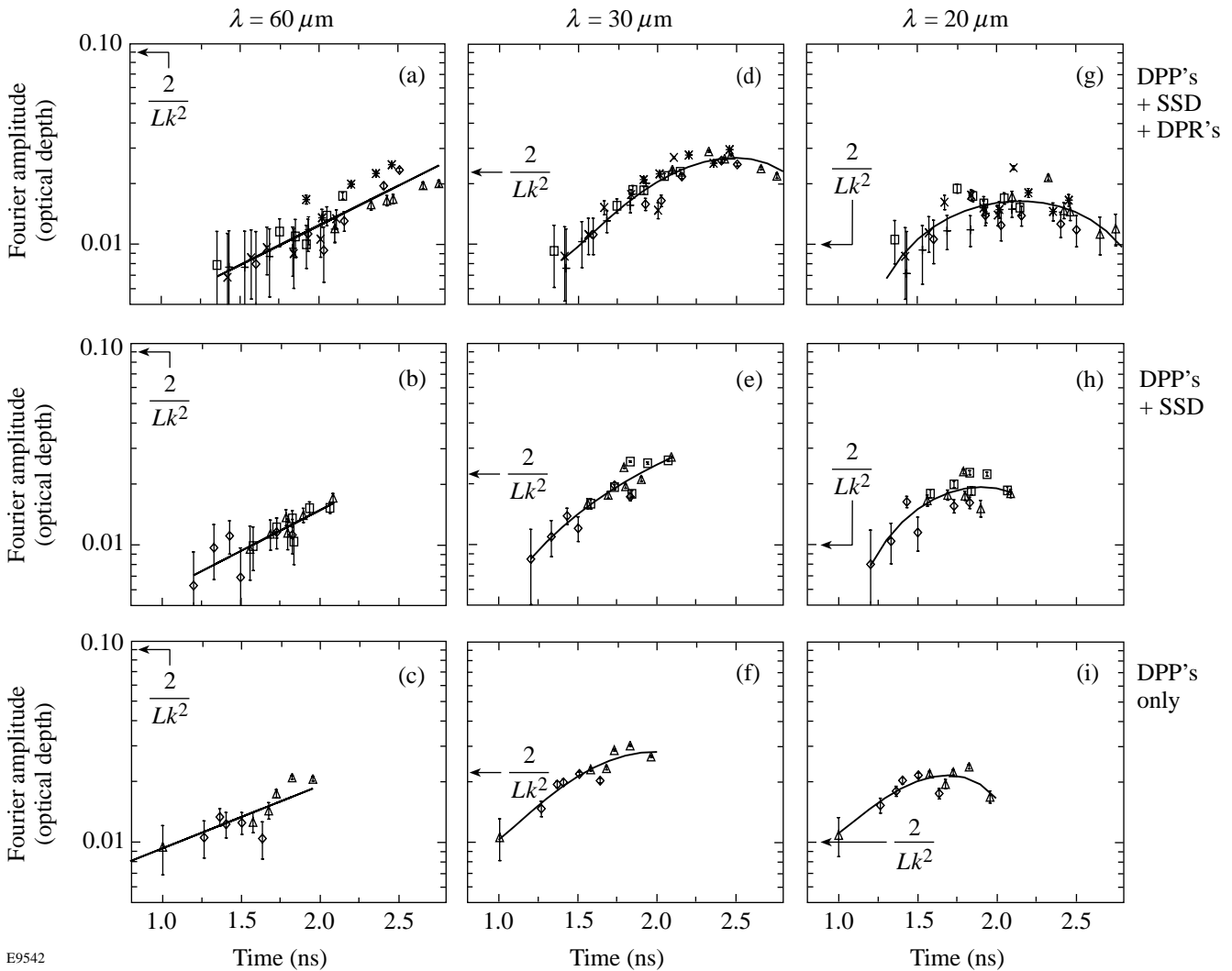. (g) Average Fourier amplitudes of optical depth of imprinted features versus time at 20-μm wavelength for six shots with DPP's, SSD, and DPR's. The solid line is a third-order polynomial fit. (h) The same for the three shots with DPP's and SSD. (i) The same for the two shots with DPP's only.

Using all of these uncertainties, the measured amplitudes of optical-depth modulations that have been converted to perturbation amplitudes in the target [using Eq. (2)] are $15.9 \times 10^{-2} \pm 4.5 \times 10^{-2}\ \mu m$ and $7.1 \times 10^{-2} \pm 1.6 \times 10^{-2}\ \mu m$ at spatial frequencies of 30 mm^{-1} and 50 mm^{-1}, respectively. Those predicted by Haan's model are $18 \times 10^{-2}\ \mu m$ and $6.0 \times 10^{-2}\ \mu m$ at spatial frequencies of 30 mm^{-1} and 50 mm^{-1}, respectively.

To demonstrate the agreement of these data with the Haan's model, we have compared the measurements and the predictions for the peak of the nonuniformity spectrum in accelerated targets. As has been discussed, the location of the peak follows the predicted trend to longer wavelengths, but it is important to compare the actual amplitude of that peak. Since that amplitude is independent of the initial conditions, we are able to plot together all data shown in Fig. 79.48, irrespective of the different laser-uniformity conditions. Again, the amplitude is obtained using the measured attenuation length of the undriven target and the calculated target compression (Fig. 79.43 shows the density as a function of time). In Fig. 79.51, the amplitudes at which the peaks in the measured spectra occur are plotted versus those for the predicted spectra. These data show that the Haan's model well represents the spectral peaks of broadband nonuniformities.

E9826
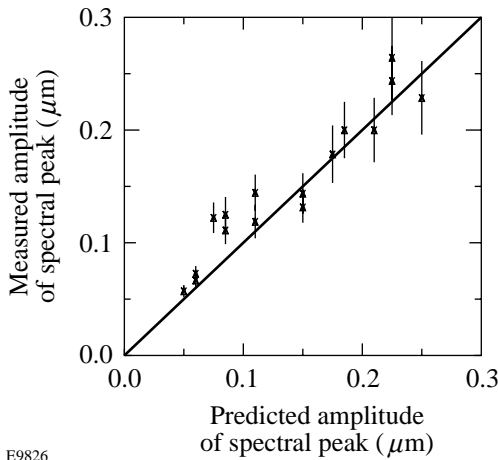
Figure 79.51
The amplitude of measured spectral peak as a function of predicted spectral peak.

In summary, broad-bandwidth perturbations were observed to saturate at levels predicted by Haan's model,[4] which were much lower than the single-mode saturation levels ($0.1\ \lambda$). This has been shown by the combined data from shots having different drive uniformities. This behavior was noted in both the shape of the spatial Fourier spectra and the temporal

behavior of modes at various wavelengths. In addition, it was found that the growth of 3-D perturbations from the broadband spectrum in the linear regime is the same as that for the linear growth of preimposed 2-D perturbations, also in agreement with Haan's model. The measured spectral evolution including the saturation level is insensitive to the details of the initial perturbation spectrum; this is also in agreement with Haan's model.

The relationship between the evolution of the preimposed modes and their coupling to the broadband spectrum must be clarified. The results inferred from Fig. 79.49 require that the growth of the preimposed modes remain in the linear regime (exponential growth) and unaffected by mode coupling. It was experimentally observed that the absolute values of Fourier amplitudes of the broadband spectra are randomly distributed from zero to about twice the average level $2\bar{\xi}_k(t)$ for any azimuthal lineout with wave vector k and at any time t. Therefore, the evolution of any mode $\xi_k(t)$ from the azimuthal lineout at a wave vector k of the broadband spectrum is confined between zero and $2\bar{\xi}_k(t)$. This means that the effects of nonlinear mode coupling on any particular mode $\xi_k(t)$ from all other modes is of the order of $\bar{\xi}_k(t)$ or less. This observation is in agreement with the theoretical work performed by Haan[14] for ablatively accelerated targets. If the amplitude of some particular mode $\xi_k(t)$, growing in the linear regime, is much higher than the average level of broadband spectrum $\xi_k(t) \gg \bar{\xi}_k(t)$ as for the preimposed modes from Fig. 79.49, then nonlinear effects will be only a small fraction of its amplitude $\xi_k(t)$. For example, the evolution of the mode $\xi_k(t)$ can be approximated to second-order accuracy and neglecting high-order terms by[14]

$$
\xi_k(t) = \xi_k^{\exp}(t)
$$
$$
+ 1/2\, k\left[\sum_{k'} \xi_{k'}^{\exp}(t)\xi_{k+k'}^{\exp}(t) - 1/2 \sum_{k'<k} \xi_{k'}^{\exp}(t)\xi_{k-k'}^{\exp}(t) \right], \quad (10)
$$

where $\xi_k^{\exp}(t) = \xi(t=0)\exp[\gamma(k)t]$ is the exponential (or first-order) amplitude of mode k. If the amplitude of some particular mode $\xi_k(t)$, growing in the linear regime, is much higher than the average level of broadband spectrum $\xi_k(t) \gg \bar{\xi}_k(t)$ as for preimposed modes from Fig. 79.49, then nonlinear effects will be only a small fraction of its amplitude $\xi_k(t)$ [i.e., the first linear term in Eq. (10) is much larger than the second nonlinear term]. This means that the effect of mode coupling on the amplitudes of 60-μm and 30-μm preimposed modes [which are 10 to 20 times above the average level of broadband

amplitudes (see Fig. 79.49)] is small (of the order of 5% to 10% of their amplitudes) and can be neglected compared with their exponential growth in the linear regime.

The same concept can be expected in a simple physical picture. Figure 79.52 schematically shows an image of the driven target that has a single-mode perturbation (dashed lines) and broadband features with individual 3-D bubbles (solid lines). In some small regions (containing only one or two bubbles), the material flow in the horizontal direction can be dominated by the flow from individual 3-D bubbles. In 3-D, the material from bubbles flows in all directions, but it flows only in one horizontal direction from 2-D bubbles. In the whole region of box size L, however, the material flow in the horizontal direction is dominated by the flow from the tips of the 2-D bubble (dashed lines) because the overall contribution to the flow in this direction from the 3-D bubbles becomes much smaller in the whole region with box size L. Therefore, the overall effect of the broadband features on the evolution of a single mode is insignificant providing that the amplitude of the single mode is high enough. This consideration in real space is complimentary to that in Fourier space described in the previous paragraph.

Late-Time Perturbation Evolution

In Fig. 79.50, the amplitudes of both the 20-μm- and 30-μm-wavelength broadband perturbations decrease late in time (at 2.5 to 2.8 ns for the case with all smoothing techniques employed). In the nonlinear regime, Haan's model predicts the growth of these perturbations to be linear in time (constant velocity growth) after they reach their saturation levels. This is in contradiction with experimental data. Figure 79.53 shows nonuniformity spectra at 2.5 ns (dashed line) and 2.8 ns (solid line) for one of the shots with all laser-smoothing techniques employed including DPP's, SSD, and DPR's. It clearly shows a decrease in amplitude of all spatial frequencies higher than 30 mm^{-1}. Figure 79.54 shows images of the target at 2.5 ns (a)
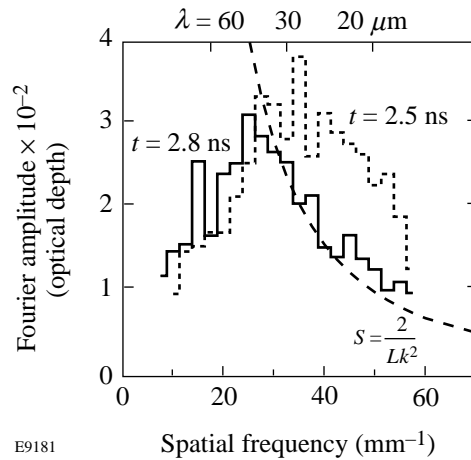
Figure 79.53
Experimentally measured late-time perturbation spectra. Azimuthally averaged Fourier amplitude of the optical-depth modulation as a function of spatial frequency for a 20-μm-thick foil at 2.5 and 2.8 ns and with laser-smoothing techniques including DPP's, SSD, and DPR's. The saturation amplitude S is shown by the dashed line.

Figure 79.52
Schematic image of the driven target, which has a single-mode perturbation (dashed lines) and broadband features with individual 3-D bubbles (solid lines). In the small regions (containing only one or two bubbles), the material flow in the horizontal direction can be dominated by the flow from individual 3-D bubbles (solid lines). In the whole region with box size L, however, the material flow in the horizontal direction is dominated by the flow from the tips of the 2-D bubble (dashed lines).

Figure 79.54
Late-time images of the target optical-depth perturbations captured at (a) 2.5 ns and (b) 2.8 ns with a 20-μm-thick target and with laser-smoothing techniques including DPP's, SSD, and DPR's.

and 2.8 ns (b). Compared to the image at 2.5 ns, features in the 2.8-ns image become much more round as neighboring bubbles coalesce, and the typical scale length of all the features becomes larger in the latter image. A 2-D model for bubble competition[17] predicts that such bubble coalescence occurs at higher bubble amplitudes and consequently much farther into the nonlinear regime than shown here. At the end of the drive (~3 ns) 1-D *LILAC* simulations predict an increase in ablation velocity (by a factor of 2) with the target decompressing quickly. In this case, target perturbations in optical depth could decrease because of the stabilizing effect of ablation.

Another possible explanation for the observed spectral behavior is that even earlier in the nonlinear regime (before the bubble coalescence), some short-scale-length bubbles move underneath larger, long-scale-length bubbles because larger bubbles grow faster than smaller bubbles.[17] The areal-density (or optical-depth) measurement becomes insensitive to short-scale-length bubbles because, in the direction of the x-ray propagation, the short-scale-length bubble becomes a part of the long-scale-length bubble, even though physically the two bubbles are still separate.

"Bowing" of the Target

Bowing of the target is another effect that has been observed and quantified in these experiments. Figure 79.55 schematically explains this effect. Before the shot, the CH target is attached to the massive Mylar washer. Without this washer a part of the laser energy from the laser beams, which irradiate the target at non-normal incidence, would miss the target and propagate toward opposing ports of the OMEGA target chamber, threatening to damage the laser system. During the drive,
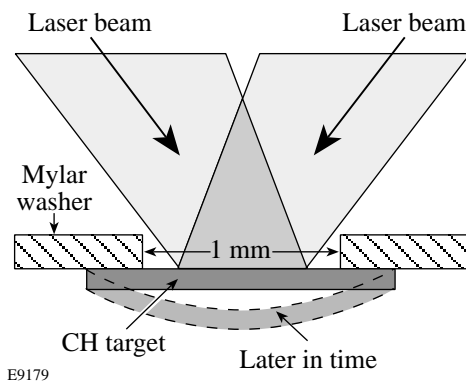
the central ~1-mm portion of a target accelerates, while the portion attached to the washer stays undriven. Toward the end of the drive the target becomes "stretched" (see Fig. 79.55). Experiments performed by Knauer[5] with the same drive condition on similar targets with preimposed 2-D corrugation showed that the wavelength of the corrugations increased 7% to 10% toward the end of the drive. This effect was explained by the target bowing and, as a result, stretching all features on the target, as though they were magnified.

Figure 79.56 describes this effect quantitatively for one of the shots, using six target images of different time frames at 1.6, 1.9, 2.0, 2.2, 2.4, and 2.5 ns. It was assumed (for simplicity) that the main effect of the bowing was a magnification of late-time images with respect to early-time images. If so, the correlation of the magnified early-time image with late-time image should be higher than the correlation of the unmagnified images. (The bowing analysis was performed using raw, unfiltered target images because Wiener-filtered images were all processed with a fixed box size, not allowing this box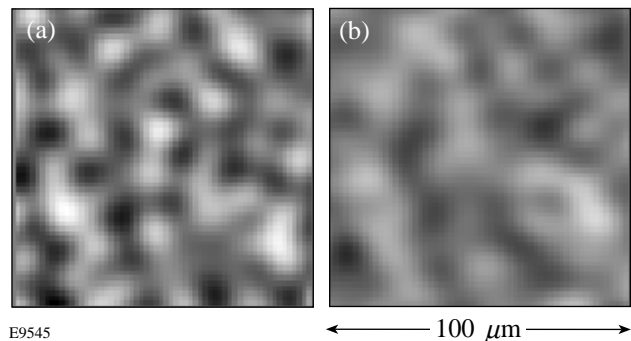 size to vary, which is necessary to perform bowing analysis.) The dotted line in Fig. 79.56 shows the cross-correlation coefficient of the image at 2.2 ns with the image at 2.5 ns as the function of the magnification of the 2.2-ns image. The cross-correlation coefficient is maximized when the 2.2 ns image is magnified 1.04 times. To maximize the correlation of the same 2.2-ns image with the early-time image at 1.6 ns, it must be demagnified 0.97 times as shown by a dashed line in Fig. 79.56. The thick solid line shows the cross-correlation

Figure 79.55
Schematic of the foil setup. The CH foil is attached to the massive Mylar washer. After the drive begins, it bows (dashed contour) because the drive pressure is applied only to its central part.

Figure 79.56
"Bowing" of the target. The cross-correlation of the image at 2.2 ns with the images at 2.5 ns, at 2.4 ns, itself, at 2.0 ns, at 1.9 ns, and 1.6 ns as a function of the magnification of the 2.2-ns image. The smoothing techniques for this shot included DPP's, SSD, and DPR's.

coefficient of the image at 2.2 ns with itself. The shorter the time interval between images, the less magnification (or demagnification) is required for one of the images to be maximally correlated to the features in the other images. This analysis shows that as time progresses, the target images become magnified by about 7% to 10% between the 1.6-ns and 2.5-ns images. This effect is small enough to have minimal effect on the perturbation evolution. For example, Fig. 79.56 shows that all features of the 2.4-ns image are magnified by ~2.5% with respect to the earlier image at 2.2 ns. Figure 79.48(b) shows the spectral evolution for the same shot. The spectrum is peaked at ~34 mm^{-1} for the image at 2.2 ns, and the peak is shifted to ~20 mm^{-1} for the image at 2.4 ns. This ~40% change in the wavelength of the spectral peak has only a ~2.5% contribution from the bowing effect.

Finite Target Thickness Effect

The growth rates for 60-μm and 30-μm preimposed modulations, measured from 1.6 to 2.5 ns, are smaller by a factor of 2 to 2.5 than those measured for earlier times (from 0 to 1.2 ns) by Knauer[5] in similar experiments. These experiments used a larger initial amplitude of preimposed modulations (a_0 = 0.5 μm) and were driven with full smoothing techniques employed. This effect can be attributed to the perforation of the target by short-wavelength perturbations.

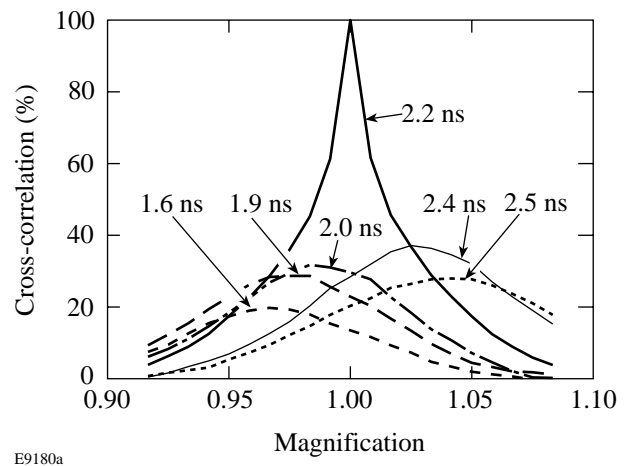The short-wavelength perturbations imprinted by the laser beams are too small to be resolved in the experiments described in this article. Yet, they are estimated to evolve at late times to a σ_{rms} amplitude that equals about three to four (compressed and ablated) thicknesses of the target. If some bubbles penetrate the target, the mass available to feed the growth of the longer-wavelength preimposed modulations by lateral flow is limited; therefore, the growth of these modes is reduced.[15]

This effect has been studied numerically using calculations on the hydrocode *LEEOR2D*.[18] These simulations were conducted for conditions corresponding to the experiment with 20-μm-thick targets irradiated with five overlapped laser beams having various smoothing techniques and with various pulse shapes. One of the pulse shapes used was, as in the experiments, a 3-ns square with an exponential rise of 100 ps per decade and a peak intensity of 2×10^{14} W/cm^2.

Two levels of laser nonuniformity were simulated. The first, using DPP smoothed beams, had the same 1-D nonuniformity's power per mode as experimentally measured using 2-D time-integrated photographs of laser beams.[9] The second was of

beams smoothed by DPP's, SSD and DPR's. The smoothing time of the SSD was 25 ps, approximately the effective smoothing time for the pulse used here.[34] Simulations using smooth laser beams were also performed.

2-D calculations of the perturbation evolution with an initial broadband spectrum of laser nonuniformities with and without preimposed 60- and 30-μm-wavelength, single-mode perturbations with initial amplitudes of 0.05 μm have been performed. For each case, the 2-D calculation with the preimposed modulation represents the direction of the preimposed modulation in the 3-D experiment, and the calculation without the preimposed modulation represents the perpendicular direction. The calculated amplitude of the preimposed mode was defined as the Fourier component of that mode in the latter calculation subtracted from that in the former calculation.

Even though the drive and smoothing conditions used in the simulations were similar to those used in the experiments described above, the comparison between the results of the 2-D simulations and the 3-D experiments must be considered only qualitatively because both the initial perturbations and the RT evolution are similar but not identical in 2-D and 3-D. Figure 79.57 shows the calculated evolution of the amplitude of the target areal density (normalized to the initial target density) of the preimposed 60- [Fig. 79.57(a)] and 30-μm-wavelength [Fig. 79.57(b)] modes for the three levels of laser nonuniformity described above. The amplitude of the preimposed modulations grows similarly for all cases until ~1.5 ns. After 1.5 ns, the amplitude of the preimposed mode continues to grow in the case of the smooth drive but is reduced
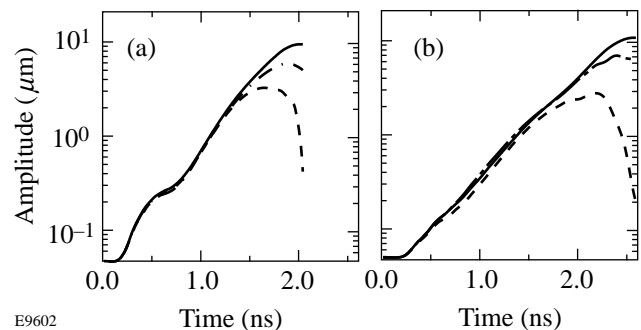

Figure 79.57
The evolution of the amplitude of the target areal density (normalized to the initial density) of preimposed (a) 30-μm- and (b) 60-μm-wavelength modes with smooth laser beams (solid), with DPP's, DPR's, and SSD (dash-dot), and with DPP's only (dashed) calculated using 2-D hydrodynamic simulations.

in the cases of the perturbed drives. This reduction is greater and starts earlier for the case of DPP only, without SSD and DPR's. This behavior is attributed to the perforation of the foil by the short-wavelength modes introduced by the laser nonuniformities.

This evolution can also be seen in Fig. 79.58, where the logarithmic growth rate of the areal-density perturbations of the preimposed modes $\left[\gamma = (da/dt)/a\right]$ is plotted versus time. The growth rate decreases for both 60- [Fig. 79.58(a)] and 30-μm [(Fig. 79.58(b)] wavelengths of the preimposed mode due to the presence of the broadband spectrum of perturbations introduced by the laser nonuniformities.

E9603
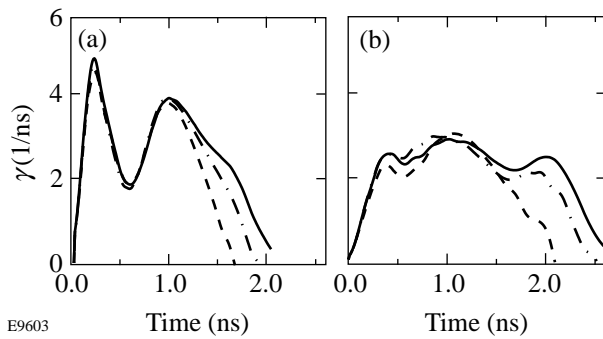
Figure 79.58
The evolution of the logarithmic growth rate $\left[\gamma = (da/dt)/a\right]$ of the areal-density perturbations of (a) 30-μm and (b) 60-μm preimposed modes with smooth laser beams (solid), with DPP's, DPR's, and SSD (dash-dot), and with DPP's only (dashed).

The perforation of the target is most clearly seen in the density maps of the target, shown in Fig. 79.59 for the various 30-μm-wavelength calculations. It can be seen that the short-wavelength perturbations in the target perforate it at $t = 1.4$ ns for the case of DPP [Fig. 79.59(b)] and at $t = 1.6$ ns for the case of DPP's, SSD, and DPR's [Fig. 79.59(f)]. In the case of the uniform drive, the target is not yet perforated at these times, as can be seen in Fig. 79.60. When looking at later times, however, the perforation can clearly be seen to occur between $t = 1.8$ ns and $t = 2$ ns (Fig. 79.60).

One can clearly see the correlation between the times of perforation of the target in these density maps and the saturation in the growth of the preimposed modes, seen in Figs. 79.57 and 79.58. This correlation strengthens the explanation suggested above, that the growth of the preimposed modes is reduced when the broadband perturbations introduced by the laser nonuniformities perforate the target. The reason this

reduction has not been measured in other experiments[5] is that the initial amplitude of the imposed perturbation in these experiments was larger; therefore, all measurements were performed at earlier times, when the imprinted perturbations had not yet evolved to large enough amplitudes and therefore the target was still not perforated.

To confirm that the saturation level and the late-time spectra do not depend on the target thickness, Fig. 79.61 shows the results of an additional experiment using a laser drive with DPP's only for 40-μm foil thickness. The measured spectra are shown for a 40-μm CH foil at 2.7 for one shot, and at 2.7 and 2.8 ns for the other shot. The saturation level was again calculated using the spectrally weighed attenuation length λ_x (which does not change significantly going from 20- to 40-μm foils) and the predicted compression (about 2 at ~2 to 3 ns). It can be seen that the finite target thickness does not affect the saturation level since the shapes of measured spectra are similar for both 20- and 40-μm target thicknesses, which is also in agreement with Haan's model. Note that the resulting

E9626
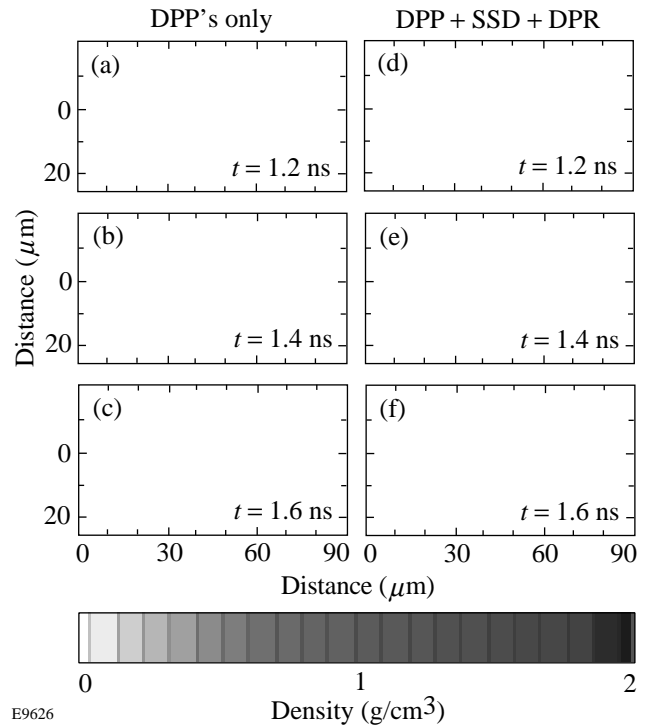
Figure 79.59
Density color maps of the target from the calculation with preimposed 30-μm mode driven by laser beams having DPP's only at (a) $t = 1.2$ ns, (b) $t = 1.4$ ns, (c) $t = 1.6$ ns, and by laser beams having DPP's, SSD, and DPR's at (d) $t = 1.2$ ns, (e) $t = 1.4$ ns, and (f) $t = 1.6$ ns.

acceleration of the 40-μm-thick foils was about a factor of 2 lower and the shock breakout time a factor of 2 later compared to 20-μm foils. The measured noise level is also about twice as high since approximately four-times-fewer photons are transmitted through the 40-μm foil. As a result, the imprint was detected only near the end of the drive and with DPP-only drive. When additional smoothing by SSD and DPR's were added, the initial imprinted amplitudes of target nonuniformity were small enough that, even at the end of the drive, no signal was measured above the noise.

Summary

This article has presented the measured evolution of 3-D broadband perturbations produced by laser imprinting in CH foils, accelerated by UV light. Using through-foil radiography these features were observed to saturate at levels in agreement with those predicted by Haan's model.[4] This behavior was noted in both the shape of the spatial Fourier spectra and in the temporal behavior of modes at various wavelengths. In addition, we noted that the growth of perturbations from broadband spectrum in the linear regime was the same as that for the linear growth of preimposed 2-D perturbations, also in agreement with the Haan model. These experiments were designed to test predicted saturation levels that are used in target designs for ICF experiments. We believe this is a clear experimental demonstration that the Haan model correctly predicts the saturation levels, spectral shape, and temporal evolution of broadband perturbations that are RT unstable. The contributions of measurement error and the effects of finite target thickness and target bowing have been shown to have little effect on our conclusions.
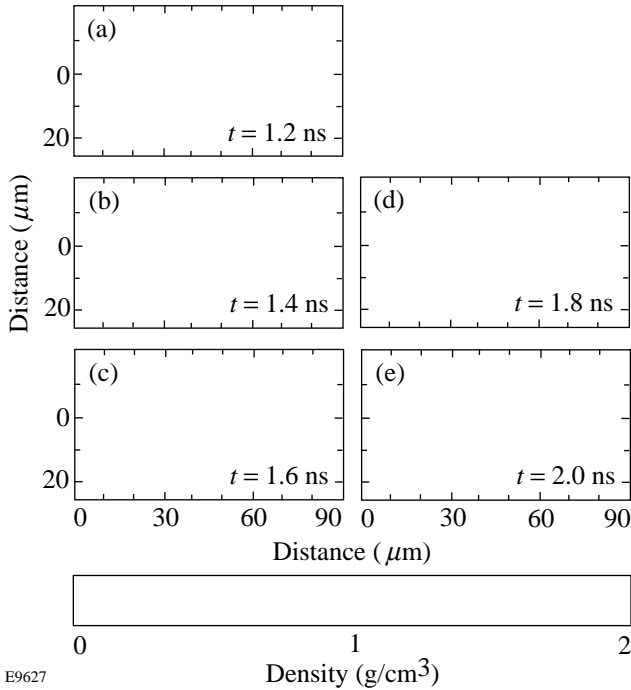
Figure 79.60
Density color maps of the target from the calculation with preimposed 30-μm mode driven by uniform laser beams at (a) $t = 1.2$ ns, (b) $t = 1.4$ ns, (c) $t = 1.6$ ns, (d) $t = 1.8$ ns, and (e) $t = 2.0$ ns.

E9627

ACKNOWLEDGMENT
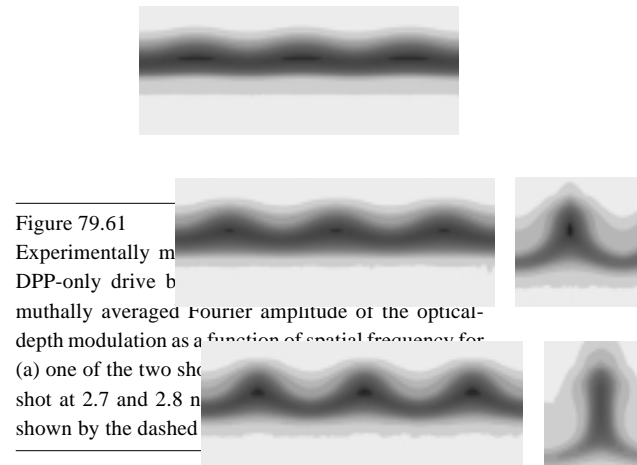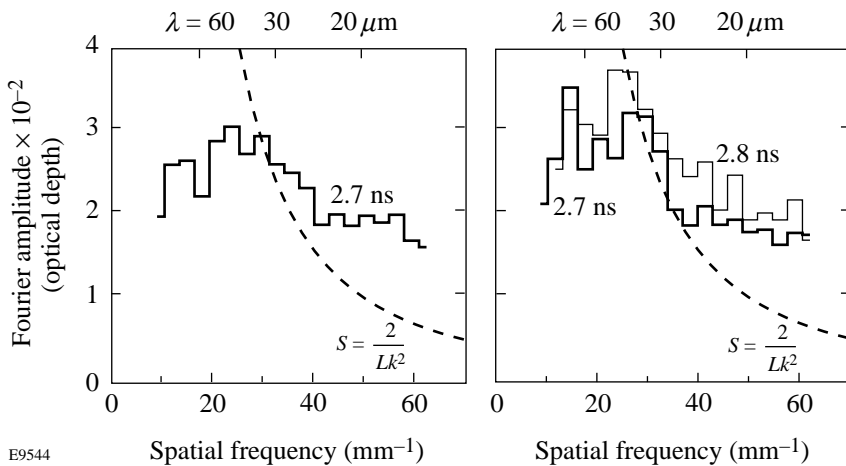
Figure 79.61
Experimentally m...
DPP-only drive b...
muthally averaged Fourier amplitude of the optical-depth modulation as a function of spatial frequency for (a) one of the two sho...
shot at 2.7 and 2.8 n...
shown by the dashed...

E9544

REFERENCES

1. D. K. Bradley, J. A. Delettrez, R. Epstein, R. P. J. Town, C. P. Verdon, B. Yaakobi, S. Regan, F. J. Marshall, T. R. Boehly, J. P. Knauer, D. D. Meyerhofer, V. A. Smalyuk, W. Seka, D. A. Haynes, Jr., M. Gunderson, G. Junkel, C. F. Hooper, Jr., P. M. Bell, T. J. Ognibene, and R. A. Lerche, Phys. Plasmas **5**, 1870 (1998).

2. S. E. Bodner, D. G. Colombant, J. H. Gardner, R. H. Lehmberg, S. P. Obenschain, L. Phillips, A. J. Schmitt, J. D. Sethian, R. L. McCrory, W. Seka, C. P. Verdon, J. P. Knauer, B. B. Afeyan, and H. T. Powell, Phys. Plasmas **5**, 1901 (1998).

3. S. V. Weber, S. G. Glendinning, D. H. Kalantar, M. H. Key, B. A. Remington, J. E. Rothenberg, E. Wolfrum, C. P. Verdon, and J. P. Knauer, Phys. Plasmas **4**, 1978 (1997).

4. S. W. Haan, Phys. Rev. A **39**, 5812 (1989).

5. J. P. Knauer, C. P. Verdon, D. D. Meyerhofer, T. R. Boehly, D. K. Bradley, V. A. Smalyuk, D. Ofer, P. W. McKenty, S. G. Glendinning, D. H. Kalantar, R. G. Watt, P. L. Gobby, O. Willi, and R. J. Taylor, in *Laser Interaction and Related Plasma Phenomena*, edited by G. H. Miley and E. M. Campbell (American Institute of Physics, New York, 1997), Vol. 406, pp. 284–293.

6. S. G. Glendinning, S. N. Dixit, B. A. Hammel, D. H. Kalantar, M. H. Key, J. D. Kilkenny, J. P. Knauer, D. M. Pennington, B. A. Remington, R. J. Wallace, and S. V. Weber, Phys. Rev. Lett. **78**, 3318 (1997).

7. K. Shigemori *et al.*, Phys. Rev. Lett. **78**, 250 (1997).

8. J. P. Knauer, R. Betti, D. K. Bradley, T. R. Boehly, T. J. B. Collins, V. N. Goncharov, P. W. McKenty, D. D. Meyerhofer, V. A. Smalyuk, C. P. Verdon, S. G. Glendinning, D. H. Kalantar, and R. G. Watt, "Single-Mode Rayleigh-Taylor Growth-Rate Measurements with the OMEGA Laser System," to be published in Physics of Plasmas.

9. T. R. Boehly, V. A. Smalyuk, D. D. Meyerhofer, J. P. Knauer, D. K. Bradley, C. P. Verdon, and D. Kalantar, in *Laser Interaction and Related Plasma Phenomena*, edited by G. H. Miley and E. M. Campbell (American Institute of Physics, New York, 1997), Vol. 406, pp. 122–129.

10. T. R. Boehly, V. A. Smalyuk, D. D. Meyerhofer, J. P. Knauer, D. K. Bradley, R. S. Craxton, M. J. Guardalben, S. Skupsky, and T. J. Kessler, J. Appl. Phys. **85**, 3444 (1999).

11. B. A. Remington *et al.*, Phys. Fluids B **5**, 2589 (1993).

12. R. J. Taylor *et al.*, Phys. Rev. Lett. **76**, 1643 (1996).

13. C. J. Pawley *et al.*, Phys. Plasmas **4**, 1969 (1997).

14. S. W. Haan, Phys. Fluids B **3**, 2349 (1991).

15. M. J. Dunning and S. W. Haan, Phys. Plasmas **2**, 1669 (1995).

16. J. P. Dahlburg *et al.*, Phys. Plasmas **2**, 2453 (1995).

17. D. Shvarts, U. Alon, D. Ofer, R. L. McCrory, and C. P. Verdon, Phys. Plasmas **2**, 2465 (1995).

18. D. Ofer, U. Alon, D. Shvarts, R. L. McCrory, and C. P. Verdon, Phys. Plasmas **3**, 3073 (1996).

19. M. M. Marinak *et al.*, Phys. Rev. Lett. **75**, 3677 (1995).

20. M. M. Marinak *et al.*, Phys. Rev. Lett. **80**, 4426 (1998).

21. V. A. Smalyuk, T. R. Boehly, D. K. Bradley, V. N. Goncharov, J. A. Delettrez, J. P. Knauer, D. D. Meyerhofer, D. Oron, and D. Shvarts, Phys. Rev. Lett. **81**, 5342 (1998).

22. T. R. Boehly, D. L. Brown, R. S. Craxton, R. L. Keck, J. P. Knauer, J. H. Kelly, T. J. Kessler, S. A. Kumpan, S. J. Loucks, S. A. Letzring, F. J. Marshall, R. L. McCrory, S. F. B. Morse, W. Seka, J. M. Soures, and C. P. Verdon, Opt. Commun. **133**, 495 (1997).

23. Y. Lin, T. J. Kessler, and G. N. Lawrence, Opt. Lett. **20**, 764 (1995).

24. S. Skupsky, R. W. Short, T. Kessler, R. S. Craxton, S. Letzring, and J. M. Soures, J. Appl. Phys. **66**, 3456 (1989).

25. S. G. Glendinning *et al.*, in *Applications of Laser Plasma Radiation II*, edited by M. C. Richardson and G. A. Kyrala (SPIE, Bellingham, WA, 1995), Vol. 2523, pp. 29–39.

26. V. A. Smalyuk, T. R. Boehly, D. K. Bradley, J. P. Knauer, and D. D. Meyerhofer, Rev. Sci. Instrum. **70**, 647 (1999).

27. T. Endo *et al.*, Phys. Rev. Lett. **74**, 3608 (1995).

28. R. Ishizaki and K. Nishihara, Phys. Rev. Lett. **78**, 1920 (1997).

29. B. A. Remington *et al.*, Phys. Fluids B **4**, 967 (1992).

30. M. C. Richardson, P. W. McKenty, F. J. Marshall, C. P. Verdon, J. M. Soures, R. L. McCrory, O. Barnouin, R. S. Craxton, J. Delettrez, R. J. Hutchison, P. A. Jaanimagi, R. Keck, T. Kessler, H. Kim, S. A. Letzring, D. M. Roback, W. Seka, S. Skupsky, B. Yaakobi, S. M. Lane, and S. Prussin, in *Laser Interaction and Related Plasma Phenomena*, edited by H. Hora and G. H. Miley (Plenum Press, New York, 1986), Vol. 7, pp. 421–448.

31. R. Betti, V. N. Goncharov, R. L. McCrory, and C. P. Verdon, Phys. Plasmas **5**, 1446 (1998).

32. H. Takabe, L. Montierth, and R. L. Morse, Phys. Fluids **26**, 2299 (1983).

33. H. Takabe *et al.*, Phys. Fluids **28**, 3676 (1985).

34. S. Skupsky, LLE, private communication (1998).

Uniaxial/Biaxial Stress Paradox in Optical-Materials Hardening

Owing to its excellent homogeneity and low-intrinsic absorption properties, fused silica remains the preferred material for high-power laser applications over a wide wavelength range, but especially in the UV. In particular, large-aperture glass and excimer lasers, such as Nova, Beamlet, OMEGA, NIKE, and, in the foreseeable future, the National Ignition Facility (NIF), the Megajoule laser (LMJ, France), and others, owe their existence to readily available, large-diameter fused silica finding use in the form of beam-transport lenses and windows. Often these lenses and windows separate atmospheric pressure from vacuum areas, such as on spatial filters and target tanks, experiencing not only high-fluence irradiation conditions but also pressure-differential–induced stresses. The combination of the two presents an interesting challenge in terms of laser damage, as the formation of pits and cracks during conventional damage may get aggravated by the presence of stress and lead to dramatic device failure by fragmentation and acceleration of the lens or window shards into the evacuated space.

Even in the absence of a vacuum issue with its concomitant stress, laser damage to fused silica under periodic illumination by UV light, such as found in UV-lithography or medical-instrument applications, limits system performance and increases maintenance costs. This motivates the search for simple methods to alleviate the onset of or, at least, the detrimental consequences of laser damage. In earlier work,[1–4] dynamic aspects of laser-induced crack formation in fused silica and its correlation with stress, both self-induced[2] and externally applied,[3,4] have been studied by us with an eye toward preparing the foundation for such remedies. In the current work, we try to answer several important questions raised by this prior work.

In brief, a laser-initiated crack has been shown to grow upon repeated irradiation by either IR[5] or UV[1,5] laser pulses, causing a *hoop stress*[2] to form in its immediate surroundings, the existence of which is essential for further growth. This causal relation was tested by breaking the *hoop-stress symmetry* with the help of an external stress field and thereby arresting further crack propagation, even at pump fluences much larger than those necessary for starting the crack initially. This was demonstrated for fused silica initiated at either the substrate exit or entrance surface. Surfaces, with few exceptions, suffer from lower laser-damage thresholds than bulk—a fact attributable to the consequences of the requisite, but extremely intrusive, acts of cutting, grinding, polishing, and cleaning the surfaces. Cleaved surfaces that are spared these procedures offer comparably higher damage thresholds.[6] The surfaces of fused silica are of special interest in that a *near-surface layer* of material *densification*[7] is surmised to be formed during polishing, which, by itself, may prompt *near-surface residual-stress fields* to develop. One key question arising from the prior work[3,4] thus became whether or not, in the absence of a densification layer and its residual-stress field, the effects observed in fused silica will remain. Or, put another way, will externally applied stresses also delay laser-damage initiation in cleaved silica bulk and/or in materials for which no such densification layer exists? To find the answer, this work addresses, in addition to polished fused silica, alternate model systems: cleaved silica bulk and BK-7, borosilicate glass.

A second question arises from the earlier *observed increase in surface-damage initiation threshold* and *crack growth arrest* with external stresses applied in the laser-beam direction. The question is whether or not the direction of the applied load has an effect on the surface-damage initiation threshold and crack growth. To answer this question, different applied load configurations are considered in this work; among them are the uniaxial compressions in the *x* or *z* direction, the biaxial compression in the *x* and *z* directions for rectangular samples (fused silica and BK-7), as well as radially applied pressure for round fused-silica samples.

Sample irradiation was carried out by the fundamental and frequency-tripled outputs of a Nd:glass oscillator/single-pass amplifier system. This system produced a beam of nearly Gaussian profile after passage through a vacuum spatial filter, prior to any frequency conversion. The beam was then focused by a 2-m-focal-length fused-silica lens to a ~600-μm spot size

at the sample entrance surface. Laser pulses, produced at a repetition rate of one pulse every 10 s, had nominal pulse duration of 1 ns at 1053 nm and 500 ps at 351 nm.

A PDP-II computer and CAMAC [computer-aided measurement and control (J. White Co. 800)] crate system were used for data acquisition and experiment control. The system included a charge-injection-device (CID) camera located in a sample-equivalent plane for recording the fluence distribution in the beam spot.

The beam-incident direction was chosen to be ≤10° off-normal to the sample entrance face to prevent any back-reflection of residual, unconverted IR from seeding the amplifier in the backward direction, and setting up a 351-nm Fresnel interference pattern between the sample entrance and exit surfaces that would invalidate the calculated fluence distribution.

In this work, *damage* is defined to be any visible permanent modification to the surface of the glass material, observable with a 110×-magnification, dark-field microscope. The smallest damage spots observed as faint scatter sites were approximately 0.5 to 1 μm in diameter. Due to the thickness of the samples, spatial and temporal distortions of the beam were avoided; therefore, both front- and exit-surface damages were considered. Damage thresholds were determined by averaging between the highest laser fluence incident on the sample that produced no damage and the lowest laser fluence that did produce damage.

The samples studied in this work were rectangular, 64 × 13.6×4.3-mm and circular, 50-mm-diam, fused-silica samples of Corning 7940 UV, grade A. They were conventionally pitch polished to *laser quality* (rms ≤ 10 Å) on the entrance and exit surfaces and to *cosmetic quality* around the edges to monitor *in situ* the crack propagation, as were the BK-7 samples, which were also commercial blocks (52 × 11.5 × 5 mm).

Samples were mechanically loaded by clamping each between aluminum plates separately attached to a load cell (Eaton, Model 3397-25, max. load capacity: 25 lbs). A predetermined, constant uniaxial, compressive load was applied in each geometrical configuration. Details of the experimental setup of the applied load used in the laser-beam direction can be found in Ref. 8.

Laser-damage thresholds (for pulse lengths greater than picoseconds) are always reported as *average values* derived

from a statistical number of sample sites *per tested specimen*. In all *nondeterministic*, i.e., extrinsic-impurity-driven laser-damage processes, the damage occurrence hinges on the statistical presence or absence of one or more absorbing impurities within a given irradiated area. This statistical distribution in defect volume density is now convoluted by a site-to-site–varying stress distribution. In an ideal experiment, a large enough number of tests on samples and sites with precisely known local stress will deconvolve the two distributions. In practice, however, this is unrealistic. Rather, simulation of local stress conditions by finite-element methods permits one to find with acceptable accuracy, for various loading-geometry-boundary conditions, the stresses within the aperture, based on which one may choose many irradiation sites on a single sample. A three-dimensional, finite-element analysis code ANSYS 5.4A®, developed by ANSYS Inc., was used to determine the stress distribution within loaded samples.

Figure 79.62 shows the 500-ps/351-nm damage-onset fluence threshold for fused-silica exit and entrance surfaces versus the stress σ_{zz} resulting from a compressive load in the laser-beam direction. The question to address is whether or not a link exists between the silica surface–densification layer (and its residual-stress distribution) and the damage-threshold
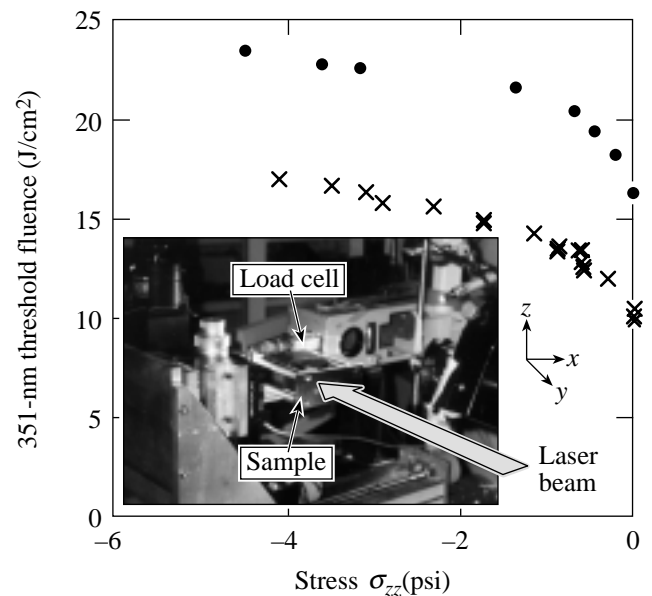
G4786

Figure 79.62
Entrance (•)- and exit (×)-surface, 351-nm damage-initiation thresholds as functions of applied stress in fused silica for the laser beam direction–loading configuration.

trend. Applying external stresses will bias these effects. In light of Fig. 79.62, it appears plausible that increasing stresses within the sample are decreasing the effect of the densified layer and, at the same time, are increasing the damage-onset threshold. To confirm or rule out this premise, further tests were needed on cleaved silica bulk and on a material that does not densify when polished. Figure 79.63 displays the exit-surface-damage-threshold results versus applied stress obtained for BK-7 with 1-ns, 1053-nm pulses. A data point from Ref. 9, obtained at 1 ns, 1064 nm (also represented in Fig. 79.63), shows good agreement with our *stress-free* measurements. Furthermore, Fig. 79.64 illustrates the front-surface-damage thresholds against the externally applied stresses obtained for cleaved bulk silica. From Figs. 79.63 and 79.64, it becomes clear that a damage-initiation-threshold enhancement in response to externally applied stress is also obtained for borosilicate glass as well as for cleaved bulk silica, ruling out causal relations between densification, applied stress, and damage-initiation-threshold enhancement in all systems considered here.

Next, we address correlations between (1) the external stress and the laser-beam polarization and/or (2) the external stress and thermal stress. In other words, (1) What is the effect of external stress on the damage threshold and crack growth for a certain beam polarization? and (2) What is the magnitude of transient, thermal stresses induced by laser heating of the material compared to the magnitude of the externally applied stresses?

The answer to the second question was obtained by using ANSYS in a thermal, transient analysis. A metallic defect (Hf) of size $200 \times 200 \times 100$ Å embedded in the fused-silica matrix was considered and assumed to have reached a temperature of 20,000 K by the end of the laser pulse (1 ns). Details of the transient thermal finite-element analysis can be found in Ref. 10. The thermal stresses deduced from ANSYS $\{\sim \alpha E \Delta T$, where α is the thermal expansion coefficient, E the Young's modulus, and ΔT the temperature [relative to the strain-free temperature (room temperature)] of a given point in the matrix$\}$ were found to be two orders of magnitude larger than the applied mechanical stresses, rendering them all but irrelevant.

The issue of mechanical stress versus beam polarization was addressed by using the original loading setup in two different geometrical loading configurations; the load was first applied in the x direction (Fig. 79.65), and second in the z direction (Fig. 79.66). For these two configurations, the result-
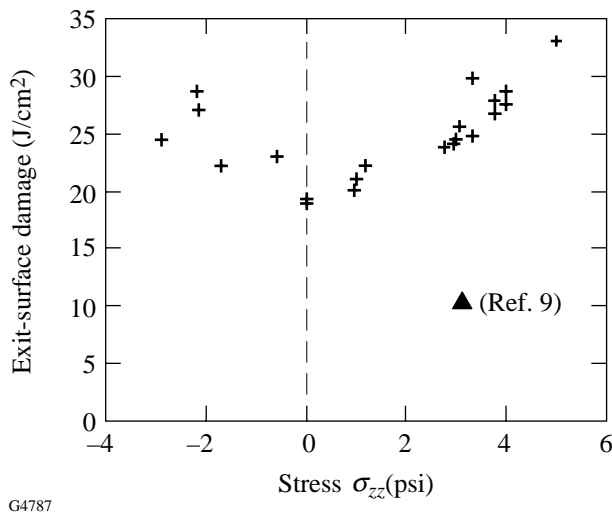
Figure 79.63

Exit-surface, 1053-nm damage-initiation threshold as a function of externally applied stresses obtained with borosilicate glass (BK-7) for the same loading configuration as Fig. 79.62. For comparison a data point (triangle) obtained at 1064 nm, 1 ns from Ref. 9 is reported.
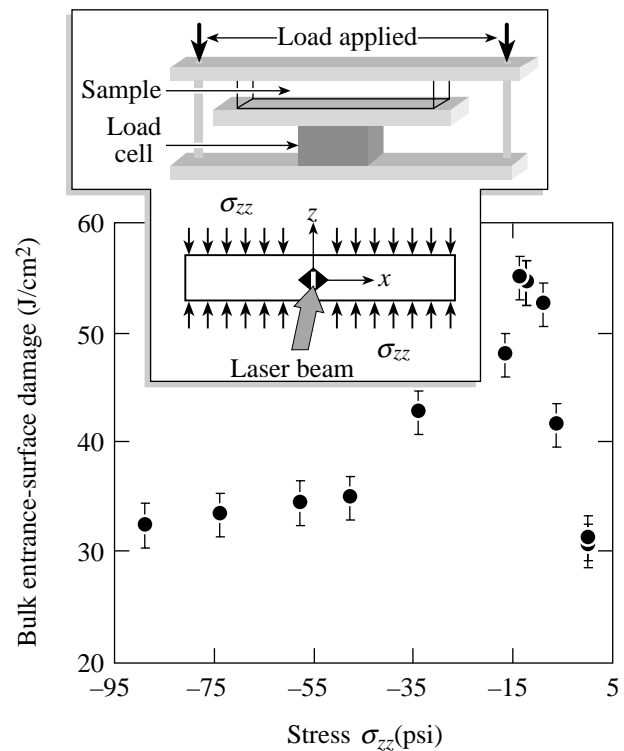
Figure 79.64

Entrance-surface, 351-nm, 500-ps, damage-initiation threshold as functions of applied pressure in the z direction (perpendicular to the laser beam) in cleaved silica bulk.

ing stress estimated from ANSYS is uniaxial along the x axis or the z axis, respectively. For uniaxial stress, Figs. 79.65 and 79.66 show the damage threshold to reach a maximum around −5 psi and to drop to its initial, stress-free value for loads larger than −15 psi. The same behavior was obtained with BK-7 loaded in the z direction (Fig. 79.66), ruling out any relationship between the stress-onset damage threshold and the laser-beam polarization.

To investigate the effect of the loading geometry on the damage threshold, a setup was designed that provided simultaneous stresses in both the x and z directions. Figure 79.67 shows the results obtained with this configuration for both entrance and exit surfaces of fused silica. The damage threshold reaches a maximum around $\sigma_{zz} = \sigma_{xx} = -5$ psi and stays constant thereafter, a behavior similar to that found for the configuration in Fig. 79.62, where the ANSYS-derived stress distribution shows stresses in both the x and z directions, although $\sigma_{zz} > \sigma_{xx}$. On the other hand, experiments carried out on circular fused-silica samples are illustrated in Fig. 79.68. Although the current setup did not permit pressures larger than 4.2 psi to be applied, Fig. 79.68 hints that the maximum threshold would be reached also around 4 to 5 psi.

Key results from Fig. 79.62 and Figs. 79.65–79.68 are: (1) Independently of the loading geometry used, the maximum threshold for fused silica is obtained around an applied stress of −5 psi. (2) A geometrical loading approximating practical situations is that of Fig. 79.62, where a plateau is reached (the configuration used in Fig. 79.67 is very difficult to implement in practice).
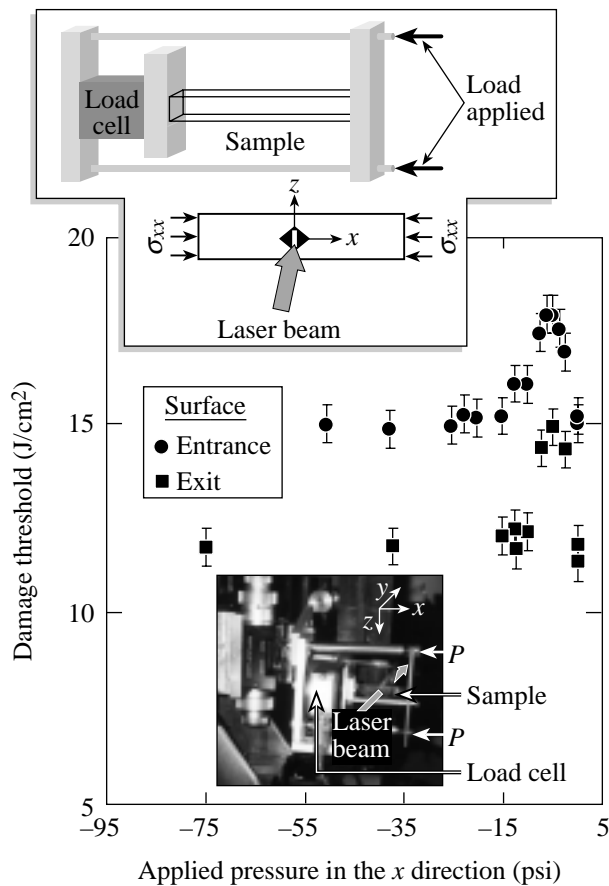
G4789

Figure 79.65
Entrance- and exit-surface, 351-nm, 500-ps damage-initiation thresholds as functions of applied pressure in the x direction (perpendicular to the laser beam) in polished fused silica. The load P is applied via two screws.
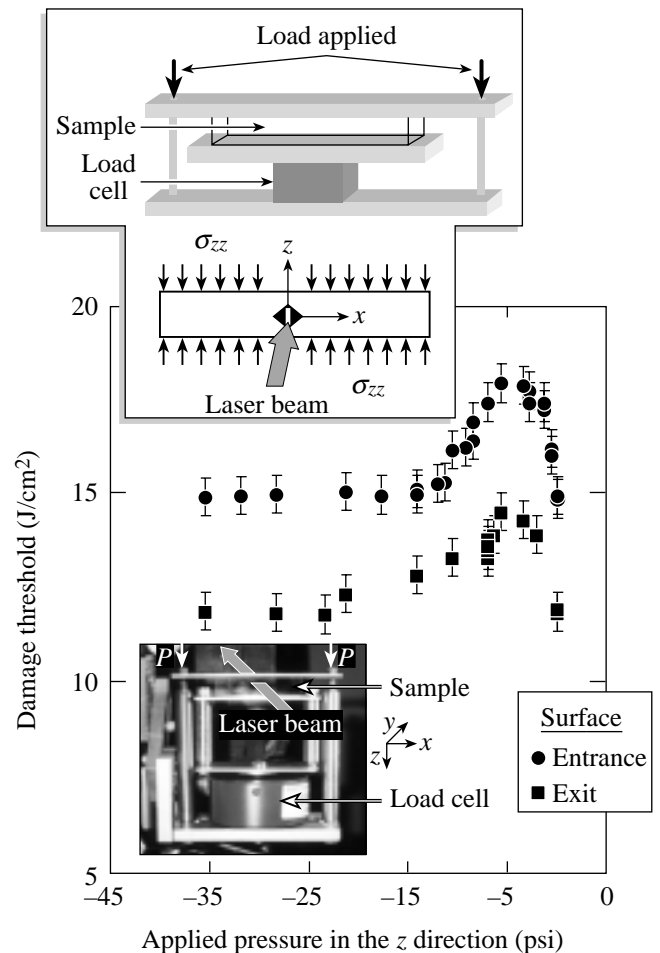
G4790

Figure 79.66
Entrance- and exit-surface, 351-nm, 500-ps damage-initiation thresholds as functions of applied pressure in the z direction (perpendicular to the laser beam) in polished fused silica. The load P is applied via two screws.

Experiments on crack growth using *uniaxial* stress configurations were also carried out, but *no crack arrest* was observed for any of these configurations, leading one to conclude again that the optimum result for both damage-threshold enhancement and crack-growth arrest in fused silica can be obtained only in a biaxial stress configuration.

In conclusion, this work presents experimental results on stress-inhibited, laser-driven crack growth and stress-delayed, laser-damage-initiation thresholds in fused silica and borosilicate glass (BK-7). The use of different loading geometries providing uniaxial and biaxial stresses shows that the *biaxial* stress configuration offers superior efficiency in raising the

laser-damage-initiation threshold by up to 78% and arresting crack growth down to 30% relative to stress-free conditions. The results also raise the intriguing paradox of biaxial symmetry breaking proving superior to uniaxial effects—a paradox that calls for further tests.

ACKNOWLEDGMENT
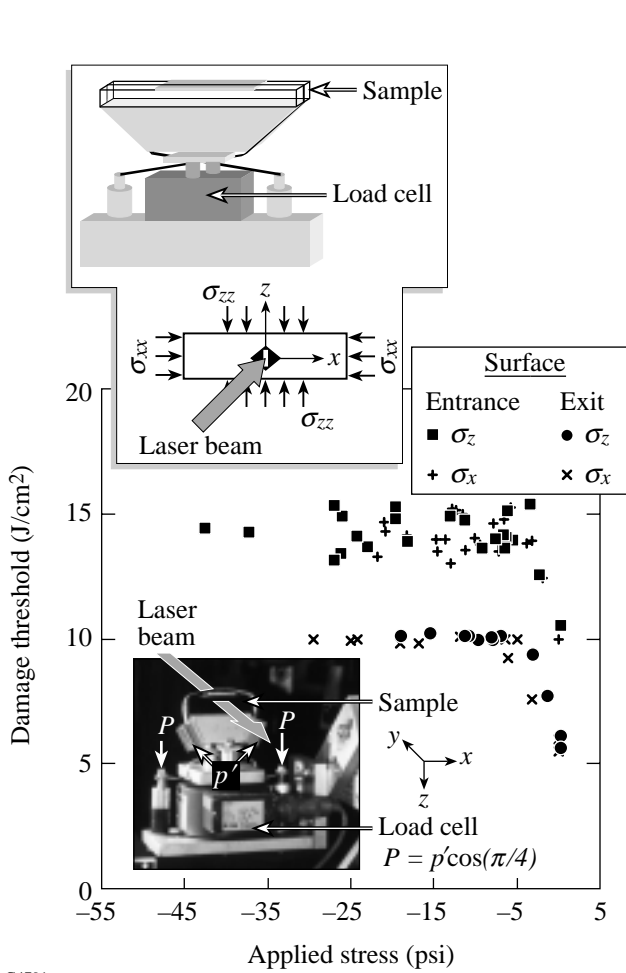
Figure 79.67
Entrance- and exit-surface, 351-nm, 500-ps damage-initiation thresholds as functions of applied stresses in polished fused silica for the case of a compression load in the *x*-*z* plane.
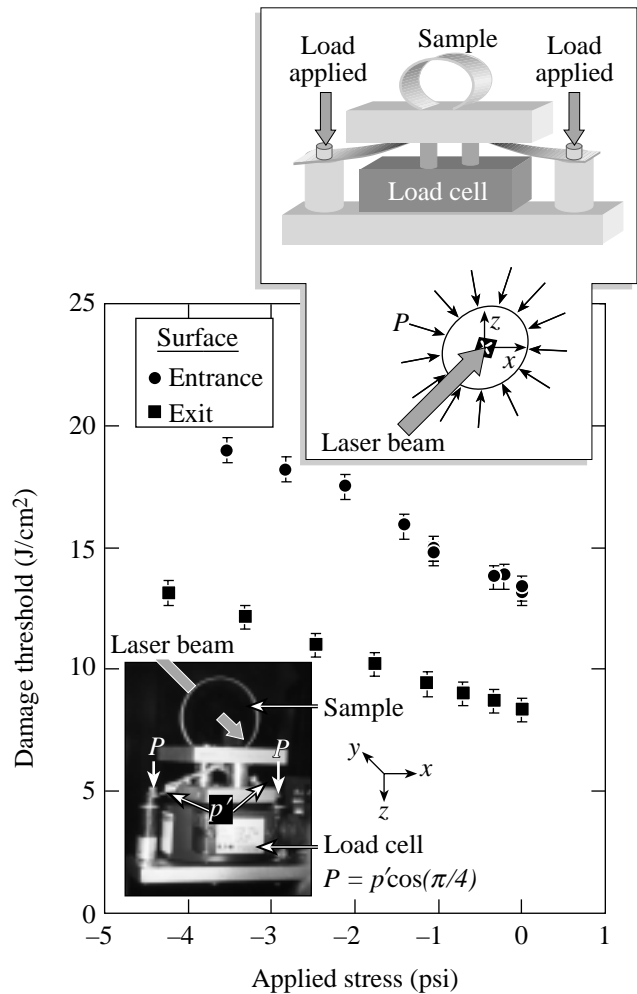
Figure 79.68
Entrance- and exit-surface, 351-nm, 500-ps damage-initiation thresholds as functions of applied pressure in round, polished-fused-silica samples.

REFERENCES

1. F. Dahmani, J. C. Lambropoulos, A. W. Schmid, S. Papernov, and S. J. Burns, J. Mater. Res. **14**, 597 (1999).

2. F. Dahmani, A. W. Schmid, J. C. Lambropoulos, and S. Burns, Appl. Opt. **37**, 7772 (1998).

3. F. Dahmani, S. J. Burns, J. C. Lambropoulos, S. Papernov, and A. W. Schmid, Opt. Lett. **24**, 516 (1999).

4. F. Dahmani, J. C. Lambropoulos, A. W. Schmid, S. Papernov, and S. J. Burns, "Crack Arrest and Stress Dependence of Laser-Induced Surface Damage in Fused Silica and Borosilicate Glass," submitted to Applied Optics.

5. A. Salleo, R. Chinsio, and F. Y. Génin, in *Laser-Induced Damage in Optical Materials: 1998*, edited by G. J. Exarhos *et al.* (SPIE, Bellingham, WA, 1998), Vol. 3578, pp. 456–471.

6. S. Papernov, D. Zaksas, J. F. Anzellotti, D. J. Smith, A. W. Schmid, D. R. Collier, and F. A. Carbone, in *Laser-Induced Damage in Optical Materials: 1997*, edited by G. J. Exarhos *et al.* (SPIE, Bellingham, WA, 1998), Vol. 3244, pp. 434–445.

7. H. Yokota *et al.*, Surf. Sci. **16**, 265 (1969).

8. Laboratory for Laser Energetics LLE Review **77**, 26, NTIS document No. DOE/SF/19460-284 (1998). Copies may be obtained from the National Technical Information Service, Springfield, VA 22161.

9. F. Rainer, R. P. Gonzales, and A. J. Morgan, in *Laser-Induced Damage in Optical Materials: 1989*, Natl. Inst. Stand. Technol. (U.S.), Spec. Publ. 801 (U.S. Government Printing Office, Washington, DC, 1990), Vol. 1438, pp. 58–73.

10. S. Papernov and A. W. Schmid, J. Appl. Phys. **82**, 5422 (1997).

Observation of Electron Trapping in an Intense Laser Beam

Since the discovery of the ponderomotive force over 40 years ago, it has been known that charged particles interacting with an oscillating electromagnetic field will seek regions of low intensity.[1] It was immediately proposed that with the appropriate field distribution, particles could be trapped with this force.[2] The case of electron confinement with a specially shaped laser focus has been discussed since then.[3–5] Recently we reported on the optical generation of a three-dimensional, ponderomotive-optical trap with a high-peak-power laser.[6] In this article we present the first evidence of electron trapping in a high-intensity laser field, with confinement of electrons with energies up to 10 keV. To our knowledge, this work represents the first controlled manipulation of electrons in a high-intensity laser field by the modulation of the spatial intensity distribution of the beam. This opens up a new direction of study in high-intensity laser–electron interactions. Here, we present the effects of trapping on linear Thomson scattering. A trapping beam could also be used to enhance the recently observed nonlinear Thomson scattering.[7] While some further experiments may use the particular geometry described in this work, more generally we have shown that near-field phase control of a high-power laser beam can lead to tailored focal regions that may be optimized for a myriad of experiments.

Electrons interact with a laser field via the Lorentz force. For field distributions with a slowly varying temporal and spatial envelope, the motion of the electrons can be decomposed into a high-frequency quiver and a slower, "dark-seeking" drift.[8] The quiver motion is a direct result of the rapidly oscillating electromagnetic field, while the drift is a consequence of the ponderomotive force (the cycle-averaged Lorentz force). The ponderomotive force takes the form $\mathbf{F}_{\text{pond}} = -\boldsymbol{\nabla}\, U_{\text{pond}}$, where $U_{\text{pond}} = \left(e^2 I \lambda^2\right)/\left(2\pi m c^3\right)$ (I is the intensity, λ is the wavelength, c is the speed of light, and e and m are the electron charge and rest mass, respectively). At low intensities, the quiver velocity is nonrelativistic and the magnetic field term in the Lorentz force can be ignored. The electron motion is a result of the electric field alone and is purely harmonic. Under these conditions, the electron undergoes linear Thomson scattering.[9] For high intensities

($I \sim 10^{18}$ W/cm^2 for $\lambda = 1$-μm light), the fully relativistic Lorentz force must be used and the electron quivers anharmonically. In this case, the electron emits harmonics of the incident field (nonlinear Thomson scattering).[7,10,11] To reach such intensities, a short-pulse, high-energy laser beam must be focused to a small spot size. Tight focusing yields high peak intensities but also results in large-intensity gradients and, therefore, large ponderomotive forces. In an ordinary centrally peaked focus, the strongest gradients point radially inward, so the ponderomotive force pushes electrons outward, directly away from the regions of high intensity.

To control the drift of electrons from the focal region, we have developed a scheme to create a focus with a local minimum at its center.[6] A uniphase laser beam, regardless of its amplitude distribution, will focus to a centrally peaked spot due to the constructive interference at the center of the focal region. By inducing a π-phase shift in the central portion of an incident beam, the light from the unshifted outer region will destructively interfere with the shifted light. If half of the incident field is shifted, there will be complete destructive interference at the center of the focus, creating a field null surrounded on all sides by regions of nonzero intensity. This occurs for a π-region diameter of $1.65w$ for a Gaussian beam, where w is the incident beam's $1/e^2$ (in intensity) radius.[6]

Computer simulations of electron trajectories in a Gaussian focus and a trapping focus have been performed. With the trap, the electrons spend a significantly longer time interacting with the intense field. In one simulation, the electrons were released into the field by barrier-suppression ionization[12] from He^{1+} at an intensity of 1.5×10^{15} W/cm^2 by a laser pulse with the same characteristics as in our laboratory:[13] $I_{\text{peak}} = 10^{18}$ W/cm^2, $w_0 = 5\ \mu$m, $\tau = 2$ ps, $\lambda = 1.05\ \mu$m, where I_{peak} is the peak intensity of the ordinary beam, w_0 is the $1/e^2$ (in intensity) radius of the focal spot, τ is the FWHM pulse width, and λ is the central wavelength. The fully relativistic Lorentz force was used in this and all subsequent simulations. A typical electron released into the trapping region experiences an average intensity approximately three times as high for a time approximately six

times as long as an electron released into a comparable Gaussian focus (generated with the same near-field power distribution). These values depend on the electron's initial location in the focal region. Similar results are obtained with different gas species and charge states. By tuning the trap minimum away from zero (by changing the size of the π region),[6] the peak intensity that the electron experiences can be increased by a factor of 10, while maintaining trapping.

The most direct signature of electron trapping is the enhanced linear Thomson scattering that results from the increased laser–electron interaction. Figure 79.69 shows the results of a computer code used to generate images of Thomson-scattered radiation from three different focal regions. The code uses the same laser pulse as described above and propagates electrons ionized from up to the first eight charge states in argon by barrier-suppression ionization. Since the total, time-integrated Thomson scattering is a linear function of intensity, interaction time, and number of electrons, the total signal at a given point in the focal region was approximated as the sum over all times of the product of electron number, instantaneous laser intensity, and time step. Figure 79.69(a) shows the $w_0 = 5$-μm Gaussian focal-plane image, Fig. 79.69(b) the focal-plane image generated by a flat-top incident beam (which mimics the extra structure present in the experimental, unaltered focal spot), and Fig. 79.69(c) the focal-plane image generated by passing a flat-top incident

beam through an appropriately sized π-phase plate. The value of the intensity walls surrounding the central minimum of the trapping beam is approximately 12% of the nontrapping beam's peak intensity. For the peak intensity achievable with this laser system, this corresponds to a wall intensity of 1.2 $\times 10^{17}$ W/cm^2, which is equal to a ponderomotive barrier of 12 keV. Figure 79.69(d) shows the two-dimensional x,z projection of the Thomson-scattered light from the Gaussian focus (the laser is polarized along the x direction and propagates along the z direction), Fig. 79.69(e) shows the predicted signal from the flat-top beam, and Fig. 79.69(f) shows the predicted signal from the trapping flat-top beam. Figure 79.69(g) shows the total predicted Thomson-scattered signal for each beam type as a function of z. This corresponds to a transverse integral along x for each z position. The thin dashed line is the signal from the Gaussian focus, the dot–dashed line is the signal from the nontrapping flat-top focus, and the solid line is the signal from the trapping flat-top focus. The signal from the regular flat-top focus is substantially higher than the signal from the Gaussian focus at $z = 0$. This is due to the weak trapping that occurs in the low-intensity rings that surround the central spot. Even though the rings can capture only low-energy electrons, they represent a large volume and therefore add considerably to the total signal. At $z = 0$, the peak intensity value of the rings is 2% of the peak intensity of the central spot. A central peak intensity of 10^{18} W/cm^2 corresponds to 2-keV electrons being trapped by the rings. In contrast, the trapping
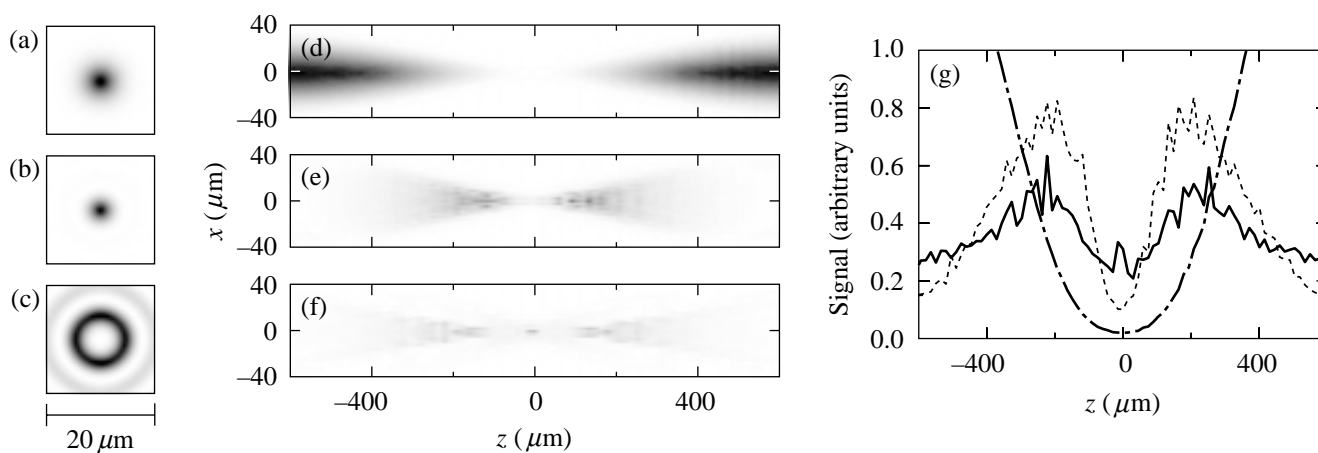
Figure 79.69
Computer simulations of Thomson scattering. (a) Focal-plane image of a Gaussian beam, (b) focal-plane image generated with a flat-top incident beam, (c) focal-plane image of a trapping beam generated with a flat-top incident beam, (d) image of the Thomson-scattered light from a Gaussian focus as viewed orthogonally to the plane of polarization, (e) Thomson-scattered image from the flat-top beam, (f) Thomson-scattered image from the trapping flat-top beam, (g) total Thomson-scattered signal as a function of z (laser propagation direction) for the Gaussian beam (thin dashed line), the nontrapping flat-top beam (dot–dashed line), and the trapping flat-top beam (solid line). The increase in signal from the center of the trapping focus is due to the confinement of electrons, while the decrease away from $z = 0$ is due to more-rapid ponderomotive expulsion along the steeper gradients in those portions of the trapping focal region.

focus generated with the phase plate can confine 12-keV electrons at $z = 0$. As expected, the trapping focus has the largest signal in the central focal region. Away from $z = 0$, the signal is lower than in the nontrapping case because of the more strongly peaked beam profiles of the trapping beam in those regions, resulting in more-rapid ponderomotive expulsion.

To generate the trapping focus in the laboratory, a segmented wave-plate arrangement was used to induce the π-phase shift on the laser pulse.[6] A disk and annulus were cut from a half-wave plate, and the disk was rotated by 90° with respect to the annulus. In this position, the o axis of the disk coincided with the e axis of the annulus and vice versa. Since the operation of a half-wave plate relies on the retardation of a half-wave between the o and e waves, this simple arrangement adds a π-phase shift to the inner portion of the beam with respect to the outer region. The size of the disk (4-cm diameter) was chosen such that approximately half of the incident field was shifted. The laser beam had an essentially flat-top profile of 6.5-cm diameter, with extra energy at the center and edges of the beam.

The experimental setup for imaging Thomson-scattered radiation from the laser focus is shown in Fig. 79.70. The horizontally polarized (perpendicular to the plane of the figure) laser pulse enters a high-vacuum chamber from the right and is focused by an internally mounted aspherical focusing

E9684

Figure 79.70
Experimental arrangement for imaging Thomson-scattered light from a high-intensity laser focus. The tube and cone serve to reduce the substantial laser light background, and recombination light is eliminated by an infrared bandpass filter. The chamber is typically backfilled with a low density (1 to 5 Torr) of argon or nitrogen.

lens ($f = 20$ cm, $\phi = 12$ cm, with an 8-mm-diam block in the center). The chamber is typically backfilled with 1 to 5 Torr of nitrogen or argon. To generate the trapping beam, the wave-plate pieces are placed directly before the entrance window. The focused beam passes into and out of an aluminum tube (outer diameter of 4.4 cm) through a pair of 1.9-cm holes. The end of the tube is blocked by a solid aluminum cone that serves as a dark background for the height-adjustable 4× microscope objective. Both the tube and the cone were bead blasted and black anodized for maximum absorption of background light. The focal region is transversely imaged onto a CCD camera (CCD1) by the objective and a camera lens (back focal length of 15 mm, open aperture of 10 mm) after passing through an infrared bandpass filter ($T_{max} = 38\%$ at $\lambda = 1055.5$ nm, $\lambda_{FWHM} = 2.5$ nm). The tip of the objective was approximately 8 mm from the laser axis. The total magnification of the imaging system (from the laser focus to the 4.8-mm × 3.6-mm CCD1 array) was 1.0. After passing through the tube, the diverging laser beam is refocused by a second lens (identical to the focusing lens) onto a second CCD camera (CCD2) approximately 6 m away (the convergence angle of the beam is exaggerated in the schematic). CCD2 was used to take typical focal-plane images.

The experimental results for Thomson-scattered radiation from 2.5 Torr of argon are shown in Fig. 79.71. Figure 79.71(a) shows the nontrapping focal-plane image at CCD2 (which was coupled to a 10× microscope objective for a total magnification of 150 from inside the vacuum chamber to the CCD2 array). Figure 79.71(b) shows the trapping focal-plane image generated with the wave-plate pieces in place. The value of the intensity walls surrounding the central minimum of the trapping beam at $z = 0$ is approximately 15% of the nontrapping beam's peak intensity, and the central minimum is less than 3% of the nontrapping beam's peak intensity. For a nontrapping beam's peak intensity of 10^{18} W/cm^2, this corresponds to a trap depth of 12 keV at $z = 0$. Away from $z = 0$, the trap wall's height falls to approximately 10% of the nontrapping beam's peak intensity, giving a three-dimensional trap depth of approximately 7 keV. The focal-plane images were not noticeably affected for backfill pressures of less than 10 Torr. Figure 79.71(c) shows the image of the Thomson-scattered radiation from the regular beam, and Fig. 79.71(d) the scattered image from the trapping beam. Each image is an average of 30 laser shots. The average laser energy was 500 mJ, which corresponds to a peak intensity of 7×10^{17} W/cm^2 for the nontrapping beam. The shape of the images was independent of gas species (argon or nitrogen) or pressure (1 Torr or 2.5 Torr), and the total signal strength varied linearly with
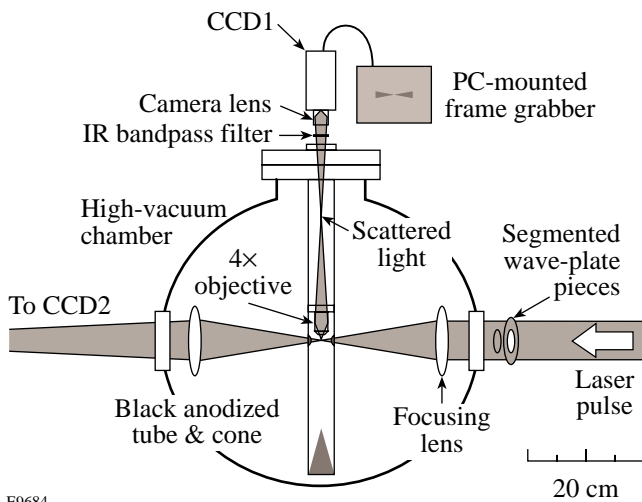
pressure. Rotating the polarization of the incident beam so it was aligned with the observation direction completely extinguished the signal, as expected for linear Thomson scattering. The total signal as a function of z [as in Fig. 79.69(g)] is shown in Fig. 79.71(e). The signal from the trapping focus is higher at $z = 0$ because of electron confinement and lower away from $z = 0$ because of steeper intensity gradients, in agreement with predictions [see Fig. 79.69(g)]. The asymmetry in the signal about $z = 0$ is due to the asymmetry in the intensity distribution of the laser along the propagation direction.

In addition to increased signal strength, the signal shows the expected enhanced dependence on laser intensity. In a smooth, Gaussian focus, electrons exit the focal region well before the peak of the pulse. For an electron from a given charge state released into the field at a given position, the initial intensity and spatial intensity gradient that it experiences will be the same regardless of peak intensity. As the electron leaves the laser focus, the intensity that it experiences as a function of time will be only slightly modified by the change in its temporal position in the laser pulse envelope. The total signal will, however, increase because of the increasing focal volume with intensity.[14] The effect of the increase in focal volume can be minimized by considering only the signal from the center of the focal region ($-z_0 < z < z_0$, where $z_0 = 75\ \mu$m is the Rayleigh range of a Gaussian beam with $w_0 = 5\ \mu$m). With the trapping focus, electrons interact with the laser pulse for a much longer period of time; therefore, the Thomson-scattered signal will be more sensitive to the peak intensity of the laser.

Figure 79.72(a) shows the experimentally measured, Thomson-scattered signal from the center of the focal region as a function of laser intensity. The horizontal axis represents the peak intensity of the unaltered, nontrapping beam (laser energy could have been used equally well, where 700 mJ is equal to $10^{18}\ \text{W/cm}^2$). The solid line is a straight-line fit to the trapping-beam signal (open squares), and the dashed line is a fit to the unaltered-beam signal (open circles). The gas species was either argon or nitrogen at a pressure of 1.0 or 2.5 Torr for any given run. The signal value is the total signal from the center of the focal region ($-75\ \mu$m $< z < 75\ \mu$m); the data from each run was normalized to the average signal strength (at $E = 700$ mJ) for each beam type, and each shot was background subtracted. The normalization of the trapping-beam data was performed independently of the normalization of the nontrapping-beam data. As expected, the signal strength and slope are enhanced for the trapping beam. The scatter in the data is likely due to fluctuations in the beam quality.

Figure 79.72(b) shows the predicted intensity scaling from the computer simulation for an ordinary focus (open circles, dashed line) and a trapping focus (open squares, solid line) generated from an incident flat-top beam focused into argon gas. The choice of gas species is arbitrary since the overall trends are universal. As in Fig. 79.72(a), the signal is taken from the center of the focal region. Because of the minimal amount of trapping with the ordinary beam, the scattered signal is low and varies weakly with laser intensity. As in the experiment, the signal from the trapping beam is larger and depends
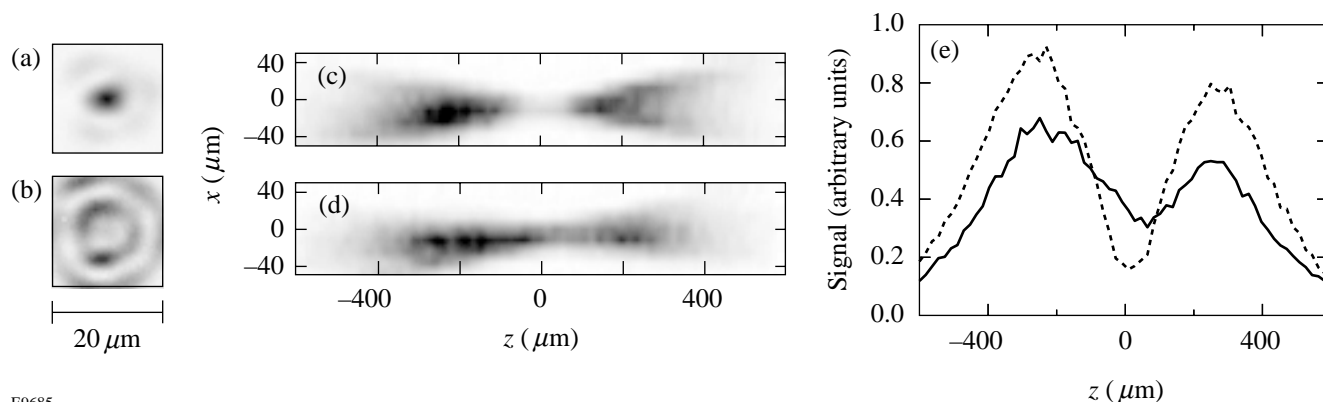
E9685

Figure 79.71
Observed focal-plane images and Thomson-scattered images. (a) Ordinary-beam focal-plane image taken at high power ($E = 500$ mJ) with CCD2, (b) trapping-beam focal-plane image, (c) image of Thomson-scattered radiation taken with CCD1 (30-laser-shot average) generated with the ordinary beam with 2.5 Torr of argon, viewed normal to the polarization direction, (d) image generated with the trapping beam, (e) total Thomson-scattered signal as a function of the laser-propagation direction (z). The signal from the trapping beam is greater at the center of the focal region and smaller on either side, as predicted.

more strongly on laser energy. The calculated contrast in signal strength and slope between ordinary and trapping beams is even greater when using a perfect Gaussian incident beam. A greater calculated signal enhancement is observed when using a "bright" trap, whose trapping region has a nonzero intensity minimum.[6] In such a trap, the effect on the nonlinear Thomson-scattered signal is especially pronounced since electrons are confined in a region of high field. Simulations also show that for an unaltered beam's peak intensity of $I_0 = 10^{19}$ W/cm^2, the nonlinear Thomson-scattering signal[10,11] from the center of a bright trap ($I_{center} = 0.20\ I_0$) is 2.2×10^4 times larger than the signal from the center of a Gaussian focus.

In conclusion, we have made the first observation of electron trapping in an intense laser beam. A novel, segmented-wave-plate scheme was used to generate the trapping focus. Electron trapping in the altered focus resulted in enhanced linear Thomson scattering from the center of the focal region as predicted by computer simulations. The observed increase in energy dependence was also expected. Computer simulations show that the trapping focus would also increase the signal generated by nonlinear Thomson scattering.

ACKNOWLEDGMENT

REFERENCES

1. H. A. H. Boot and R. B. R.-S.-Harvie, Nature **180**, 1187 (1957).

2. A. V. Gapanov and M. A. Miller, J. Exptl. Theoret. Phys. (USSR) **34**, 242 (1958).

3. N. J. Phillips and J. J. Sanderson, Phys. Lett. **21**, 533 (1966).

4. U. Mohideen *et al.*, J. Opt. Soc. Am. B **9**, 2190 (1992).

5. C. I. Moore, J. Mod. Opt. **39**, 2171 (1992).

6. J. L. Chaloupka, Y. Fisher, T. J. Kessler, and D. D. Meyerhofer, Opt. Lett. **22**, 1021 (1997).

7. S. Chen, A. Maksimchuk, and D. Umstadter, Nature **396**, 653 (1998).

8. J. H. Eberly, in *Progress in Optics*, edited by E. Wolf (North-Holland, Amsterdam, 1969), Vol. 7.

9. J. D. Jackson, *Classical Electrodynamics,* 2nd ed. (Wiley, New York, 1975).

10. Vachaspati, Phys. Rev. **128**, 664 (1962).

11. E. S. Sarachik and G. T. Schappert, Phys. Rev. D **1**, 2738 (1970).

12. S. Augst, D. D. Meyerhofer, D. Strickland, and S. L. Chin, J. Opt. Soc. Am. B **8**, 858 (1991).

13. Y.-H. Chuang, D. D. Meyerhofer, S. Augst, H. Chen, J. Peatross, and S. Uchida, J. Opt. Soc. Am. B **8**, 1226 (1991).

14. M. D. Perry *et al.*, Phys. Rev. A **37**, 747 (1988).

Figure 79.72

Energy dependence of Thomson-scattered light from the center of the focal region. (a) Experimental results of linear Thomson scattering from several data-taking runs with the ordinary beam (open circles, dashed line) and the trapping beam (open squares, solid line). (b) Results from a computer simulation with an ordinary focus (open circles, dashed line) and a trapping focus (open squares, solid line) generated by an incident flat-top beam. Both experiment and simulation show an increase in signal strength and energy dependence for the trapping beams due to the increased electron–laser interaction.

Modeling Laser Imprint for Inertial Confinement Fusion Targets

In inertial confinement fusion (ICF), a spherical shell filled with a DT-gas mixture is compressed to high densities and temperatures to achieve ignition condition.[1] Degradation from spherical symmetry during the implosion, however, limits the achievable compression ratios and could quench the ignition. The main source of such asymmetry is hydrodynamic instabilities (such as the Rayleigh–Taylor and Bell–Plesset instabilities) seeded by both irradiation nonuniformities and impurities in the target materials. In this article we describe a process that generates mass perturbations on an initially uniform target driven by a modulated laser illumination. Such a process is referred to as a "laser imprint." The control of laser imprint is of crucial importance for the successful implosion of direct-drive ICF targets. To evaluate the imprint growth, the following two physical problems must be considered: (1) generation of nonuniformities in ablation pressure due to spatial modulations in a laser intensity, and (2) mass perturbation growth on a target driven by nonuniform ablation pressure. A detailed analysis of the first problem can be found in Refs. 2. The second problem, however, has not been adequately treated in the past. In Ref. 3, for example, perturbation growth was derived by using the Chapman–Jouguet deflagration model. As discussed in Refs. 4, such a model neglects thermal smoothing of perturbations in the conduction zone (a region between the critical surface and ablation front), and in addition, it does not reproduce the main restoring force, which is due to a difference in the dynamic pressure at the peaks and valleys of the front distortion.[5,6] An improved model has been proposed in Ref. 4, where thermal smoothing of the pressure perturbations has been included. At the ablation front, however, the authors used the "Landau–Darrieus" boundary condition that, similar to the result of Ref. 3, neglects the main stabilizing force due to the dynamic overpressure.

The main goal of this article is to give a theoretical description of the hydrodynamic coupling between the pressure perturbation and the ablation-front modulation. The developed theory is relevant to the stability of high-isentrope ($\alpha \geq 2$, where α is the ratio of the pressure at a given density to the Fermi pressure) ICF targets directly driven by a laser pulse that consists of a low-intensity (a few 10^{13} W/cm^2) foot followed by the main drive pulse. During the foot pulse, the ablation pressure created by the mass ablation generates a shock wave that propagates through the shell. Since the laser intensity is constant during the shock transit time, the pressure behind the shock is uniform and the ablation front travels at a constant velocity. Later, as intensity increases during the main pulse (in direct-drive cryogenic target designs the beginning of the main pulse is timed to the first shock breakout of the shell[7]), the shell starts to accelerate and front perturbations η begin to grow because of Rayleigh–Taylor (RT) instability $\eta \sim \eta_0 e^{\gamma_{\mathrm{RT}} t}$, where γ_{RT} is the RT instability growth rate. If the perturbation amplitude becomes too large during the implosion, the shell breaks up, and the ignition condition cannot be reached. To quantify the shell integrity, we introduce an "integrity factor" $\Upsilon = A_{\mathrm{mix}}/\Delta R$, which is defined as a ratio of the mix amplitude (bubble amplitude) A_{mix} to the shell thickness ΔR. The bubble amplitude is taken to be[1] $A_{\mathrm{mix}} = \sqrt{2}\sigma$, where

$$\sigma^2 = \Sigma_{l,m} \left|\eta_{l,m}(t)\right|^2 \Big/ (4\pi)$$

is the rms sum of the modes, $\eta_{l,m} = \int d\Omega Y_{l,m}^*(\Omega) R(\Omega,t)$, $R(\Omega,t)$ is the radius at solid angle Ω and time t, and $Y_{l,m}^*$ is the complex conjugate of the l,m spherical harmonic. The shell remains intact during the implosion if the integrity factor is less than unity ($\Upsilon < 1$ for all time). Simulations performed for direct-drive cryogenic OMEGA and NIF target designs show that to satisfy the condition $\Upsilon < 1$ during the implosion, the integrity factor Υ_0 at the shock breakout time t_{br} must be less than $\Upsilon_0^{\mathrm{max}} = 0.01$. In this article we present a model to estimate $\Upsilon_0^{\mathrm{imp}}$ due to the laser imprint. Such a model sheds some light on physical mechanisms driving the laser-imprint growth. To proceed with our analysis, first we note that during the prepulse, the shell's outer radius R is much larger than the target thickness ΔR, and convergence effects can be neglected. All perturbations are then decomposed in the Fourier space $\eta = \Sigma_k \eta_k e^{ikx}$, where

$$\eta_k \simeq \eta_{l,m}\sqrt{\frac{(2l+1)}{8\pi}},$$

$k \simeq l/R$ is the wave number, and l is mode number. Since the perturbation amplitude in the linear regime is proportional to the laser nonuniformity, we introduce a normalized amplitude $\eta_{k,\delta I} \equiv \eta_k/(\delta I_k/I_0)$, where δI_k is the Fourier component of the intensity modulation and I_0 is the average intensity. Then, the integrity factor takes the following form:

$$\Upsilon^2 \equiv \Sigma_k \, \Upsilon_k^2 = \Sigma_k \left| \eta_{k,\delta I} (\delta I_k/I_0)/\Delta R \right|^2.$$

Nonuniformity in the laser illumination $\delta I_k/I_0$ can be obtained from the spectrum of the laser speckle on target produced by the distributed phase plates (DPP's). Thus, to estimate the integrity factor, we must calculate an imprint amplitude $\eta_{\text{imp}} \equiv \eta_{k,\delta I}/\Delta R$ at the shock breakout time (beginning of the main pulse) $t = t_{\text{br}} = \Delta R_0/U_s$, where ΔR_0 is the uncompressed shell thickness and U_s is the shock speed. For strong shocks [when the ratio of the ablation pressure p_a and the initial pressure of the undriven shell p_0 is large $(\Pi \equiv p_a/p_0 \gg 1)$] and the ratio of specific heat $\gamma = 5/3$, the shock breakout time is $t_{\text{br}} \simeq 2\Delta R/c_s$, where c_s is sound speed of compressed material and $\Delta R \simeq \Delta R_0/4$.

The laser imprint growth is determined by several physical effects. First, as the laser energy is absorbed by the outmost layer of the shell at the beginning of implosion, the shell material heats up, launching a heat wave toward the pellet center. Material behind the heat front expands outward, creating an ablation pressure p_a that induces a shock wave propagating through the shell. Nonuniformities in the intensity across the laser beam cause different parts of the beam to ablate shell material at different rates, generating an ablation-pressure modulation $\tilde{p}_a$ along the ablation front. Since the shock speed U_s scales as a square root of the shock strength Π ($U_s \sim \sqrt{\Pi}$ for $\Pi \gg 1$), stronger shocks launched at the peaks of ablation pressure propagate faster than the shocks launched at the pressure valleys. A difference in the shock speed distorts the shock front and creates a perturbed velocity field inside the compressed region. A velocity perturbation at the ablation front, in turn, leads to a linear-in-time front distortion growth $\eta \sim \tilde{v}_x t$, where $\tilde{v}_x \sim \tilde{p}_a U_s/(2p_a)$, and the x axis points in the direction of laser propagation. Note that such a growth is wavelength independent. Then, in order to conserve the tangential component of the fluid velocity, a rippled shock front generates a lateral mass flow from the convex part of the shock front (which protrudes the most into the cold region) into the

concave part (Fig. 80.1). A change in density, according to the adiabatic condition $\partial_t \tilde{p} = c_s^2 \partial_t \tilde{\rho}$, leads to a pressure deficiency in the convex part and a pressure excess in the concave part. Since the pressure perturbation at the ablation front is fixed by the laser-beam nonuniformities, the lateral flow creates a negative pressure gradient toward the convex part of the shock front and a positive one toward the concave part. The pressure gradient accelerates fluid elements $\rho d_t^2 \eta = \rho \tilde{a} \sim \partial_x \tilde{p}_a$, leading to an additional perturbation growth $\eta \sim \partial_x \tilde{p}_a/(2\rho)t^2$, where ρ is the compressed density and η is the ablation front amplitude. After the shock front has moved a distance of the order of perturbation wavelength from the ablation front, the latter reaches a steady state (assuming that the ablation pressure modulation is constant in time), and the pressure perturbation in the vicinity of the ablation front obeys Laplace's equation $\partial_x^2 \tilde{p} - k^2 \tilde{p} = 0$. Keeping only a decaying solution of that equation, $\tilde{p} \sim \tilde{p}_a e^{-kx}$, leads to a finite pressure gradient, a perturbed acceleration of the ablation front, $\tilde{a} \sim \partial_x \tilde{p}_a/\rho \simeq k\tilde{p}_a/\rho$, and a quadratic-in-time asymptotic perturbation growth $\eta(kc_s t \gg 1) \sim (\tilde{p}_a/\rho)kt^2/2$.
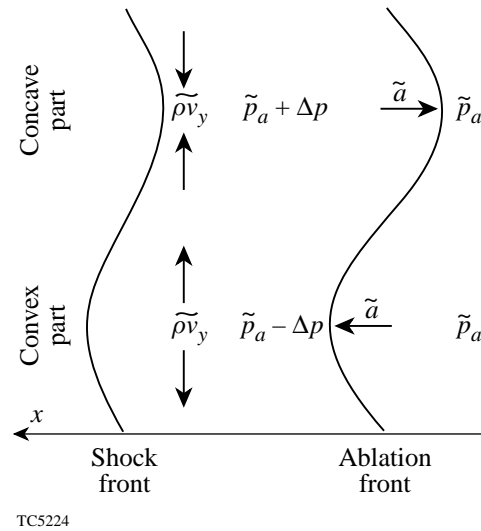
Figure 80.1
Lateral mass flow generated by the rippled shock creates a pressure excess behind the concave part of the shock front and a pressure deficiency behind the convex part.

A rigorous derivation of the perturbation evolution in the "classical" case (constant-in-time ablation-pressure modulation and no mass ablation) is performed by solving the mass, momentum, and energy conservation equations. Such a derivation (to be discussed in detail in a forthcoming paper[8]) yields a result similar to the one obtained above by using a simple physical argument. For strong shocks $\Pi \gg 1$ and $\gamma = 5/3$, the

solution is

$$\eta(t) \simeq \frac{\tilde{p}_a}{p_a}\left(0.7\, c_s t + 0.3\, k c_s^2 t^2\right). \qquad (1)$$

Note that Eq. (1) can be reproduced by solving a simple second-order differential equation

$$d_t^2 \eta = \tilde{a} = k\frac{\tilde{p}_a}{\gamma p_a}c_s^2 \qquad (2)$$

with the initial conditions $\eta(0) = 0$ and $\eta'(0) = 0.7\left(\tilde{p}_a/p_a\right)c_s$. To calculate the imprint amplitude η_{imp}, we assume[2] $p_a \sim I^{2/3}$ and $\delta I_k / I_0 = (3/2)\tilde{p}_a / p_a$, hence

$$\eta_{\mathrm{imp}}^{\mathrm{cl}} \simeq 0.8\, k\Delta R + 0.9 \simeq 0.8\frac{l}{A} + 0.9, \qquad (3)$$

where $A = R/\Delta R$ is the shell's in-flight aspect ratio (IFAR). Equation (3) shows that the imprint amplitude of long-wavelength modes ($k\Delta R \ll 1$ or $l < 15$ for directly driven NIF targets) is wavelength independent; at short wavelengths, however, the imprint amplitude is proportional to the mode number l and inversely proportional to the IFAR. In addition, the imprint amplitude in the classical case does not depend on the laser intensity. Next, we calculate the integrity factor for a direct-drive $\alpha = 3$ NIF target design[7] using η_{imp} in the form of Eq. (3). The amplitudes $\delta I_k / I_0$ can be estimated by using the results of Ref. 9. The calculation yields $Y_0^{\mathrm{imp}} \simeq 0.2$, which is a factor of 20 larger than the stability threshold Y_0^{max}. The RT instability seeded by such a perturbation would disrupt the shell during the acceleration phase of implosion and quench the ignition. In direct-drive ICF, however, several physical processes significantly reduce the imprint growth. Next, we consider the main stabilizing mechanisms inherent to laser-driven targets: thermal conduction smoothing and mass ablation.

Thermal Conduction Smoothing

As the heat front (ablation front) propagates into the cold portion of the target, material heats up and expands outward creating a hot plasma corona. The laser light is absorbed in a region (absorption region) where the density of blown-off material is much lower than the compressed shell density. Thus, a finite zone (conduction zone) of hot plasma exists between where the laser energy is deposited and the ablation front. Because of the high temperatures, any pressure perturbations inside such a region are smoothed out by the thermal conduction. The simplest theory[10] predicts that pressure perturbations decay exponentially away from the critical surface

("cloudy-day effect") $\tilde{p} \sim e^{-kx}$; thus, nonuniformities in the ablation pressure are reduced by a factor e^{-kD_c}, where D_c is a distance between the absorption region and the ablation front. More-sophisticated models of thermal smoothing[2] yield similar behavior of the reduction coefficient. To simplify the analysis, the distance D_c is taken to be $D_c \simeq V_c t$; this leads to an exponential decay in the ablation pressure perturbation $\tilde{p}_a \simeq \tilde{p}_a(0)e^{-kV_c t}$. After $t = (kV_c)^{-1}$, laser nonuniformities with the wave number k decouple from the ablation front, nullifying the k-Fourier component of the perturbed acceleration $\tilde{a}$. The ripple of the ablation front, however, continues to grow due to a finite velocity perturbation

$$\eta\left[t > (kV_c)^{-1}\right] \sim \tilde{v}_x t.$$

Scaling laws of the perturbation growth can be derived by solving Eq. (2) and substituting $\tilde{p}_a = \tilde{p}_a(0)e^{-kV_c t}$ into its right-hand side:

$$d_t^2 \eta_a = k\frac{\tilde{p}_a(0)}{\gamma p_a}c_s^2 e^{-kV_c t}. \qquad (4)$$

The imprint amplitude in this case takes the following form:

$$\eta_{\mathrm{imp}}^{\mathrm{th}} \simeq \frac{0.4\, A}{l}\left(\frac{c_s}{V_c}\right)^2 \left(e^{-\Delta_c} - 1\right) + 0.9 + 0.8\frac{c_s}{V_c}, \qquad (5)$$

where $\Delta_c = 2(l/A)V_c/c_s$. Equation (5) shows that for modes with $\Delta_c > 1$ ($l > 10$ for direct-drive NIF targets) thermal smoothing reduces the imprint amplitude by a factor $\eta_{\mathrm{imp}}^{\mathrm{th}}/\eta_{\mathrm{imp}}^{\mathrm{cl}} \sim A/l$.

Mass Ablation

An additional reduction in the imprint growth is due to the mass ablation. The main stabilizing mechanism produced by ablation is the dynamic overpressure or "rocket effect"[5,6] that can be described as follows: Laser-beam nonuniformities create ablation-pressure modulations along the target surface. Such modulations (see discussion earlier in the text) distort the ablation front: front peaks protrude into the hot plasma corona, and the valleys move toward the cold target material. Analysis of Ref. 5 shows that because of high thermal conductivity in the blowoff region, temperature is uniform along the heat (ablation) front. Thus the ablation front's distortion growth slightly increases the temperature gradient at the front peaks and decreases it at the front valleys. An increase in the temperature gradient leads to an additional heat flow that speeds up the

heat front and increases the velocity of the blown-off material V_{bl}. Higher blowoff ("exhaust") velocity creates an excess in the dynamic pressure ("rocket effect" increases). At the perturbation valleys, the picture is reversed: a reduction in the temperature gradient decreases the ablation and blowoff velocities, thus the dynamic pressure and the rocket effect are also reduced. We can conclude that the modulation in the dynamic pressure created by the thermal conduction reduces the perturbation growth and ultimately stabilizes the growth completely. Calculations[5] show that the amplitude of the dynamic pressure is proportional to the front distortion $\tilde{p}_d = \dot{m} V_{\mathrm{bl}} k \eta$. Hence, perturbations reach a saturation value η_{sat} when the dynamic-pressure modulation balances the ablation-pressure modulation $\tilde{p}_a \sim \dot{m} V_{\mathrm{bl}} k \eta_{\mathrm{sat}}$, where $\dot{m} = \rho V$ is the mass ablation rate. Next, to perform a quantitative stability analysis, we solve the system of conservation equations assuming a sharp interface at the ablation front and a constant-in-time ablation-pressure modulation $\tilde{p}_a$.[8] Skipping lengthy calculations, we report a final formula for the asymptotic behavior ($kc_s t \gg 1$) of the front-surface perturbations in the case of strong shocks $\Pi \gg 1$ and $\gamma = 5/3$:

$$\frac{\eta(t)}{\tilde{p}_a/(\gamma p_a)} \simeq \frac{kc_s^2}{\omega^2}(1 - D\cos\omega t)$$

$$+ \frac{c_s}{\omega}\left(1.2 - \frac{2c_s}{V_{\mathrm{bl}}}\right)D\sin\omega t + \eta_v(t), \qquad (6)$$

where $D = e^{-2kV_a t}$, V_a and V_{bl} are the ablation and blowoff velocities, respectively, and $\omega = k\sqrt{V_a V_{\mathrm{bl}}}$. The last term η_v is due to the vorticity convection from the shock toward the ablation front:

$$\eta_v = \frac{2c_s}{kV_{\mathrm{bl}}}\left[e^{kV_a t}\int_{kV_a t}^{\infty} e^{-\tau}\Omega(2\tau)d\tau - 1.2\ D\cos\omega t\right],$$

where

$$\Omega = i(\nabla \times \mathbf{v})_z \big/ (kc_s \tilde{p}_a / \gamma p_a) \simeq 3J_0(\tau) - 2J_4(\tau)$$

is the normalized vorticity and $J_n(\tau)$ is the Bessel function. Equation (6) shows that the front perturbation grows according to Eq. (1) until the distortion amplitude becomes big enough and the dynamic overpressure balances the ablation-pressure perturbation. After that time, the ablation front oscillates around an average amplitude $\langle\eta\rangle = \eta_{\mathrm{sat}}$. In addition, the difference in the ablation velocity at the distortion peaks and valleys and also the vorticity convection from the ablation

front damp the perturbation amplitude [factor $e^{-2kV_a t}$ in Eq. (6)].

The next step is to combine effects of the mass ablation and thermal smoothing. An analytical solution of conservation equations in this case has a very lengthy form.[8] We omit a rigorous derivation of such a solution in this article, however, noting that the essential physics of the imprint growth reduction can be described by an approximate solution derived from Eq. (2) with the following modifications: To take into account the mass ablation effects, first, we add to the left-hand side of Eq. (2) the stabilizing term due to the dynamic overpressure (rocket effect) $\omega^2 \eta$, and then, the damping term $4kV_a d_t \eta$, which is due to the difference in the mass ablation rate at the front peaks and valleys and also to the vorticity convection downstream from the ablation front. Thermal smoothing of the pressure perturbations inside the conduction zone is included, the same way as in Eq. (4), by introducing a reduction factor $e^{-kV_c t}$ into the right-hand side of Eq. (2). As a result, the equation describing the evolution of the ablation-front distortion takes the following form:

$$d_t^2 \eta + 4kV_a d_t \eta + \omega^2 \eta = k\frac{\tilde{p}_a(0)}{\gamma p_a}c_s^2 e^{-kV_c t}. \qquad (7)$$

Observe that neglecting the reduction factor $e^{-kV_c t}$ yields solution (6) (except for the vorticity term η_v). Substituting the solution of Eq. (7) into the definition of the imprint amplitude gives

$$\eta_{\mathrm{imp}}^{\mathrm{abl}} \simeq 0.4\frac{A}{l}\hat{\eta}\left(e^{-\Delta_c} - e^{-2\Delta_a}\cos\Delta_{\mathrm{bl}}\right)$$

$$+ \frac{e^{-2\Delta_a}}{\Delta_{\mathrm{bl}}}\left(0.9 + 0.8\frac{V_c}{c_s}\hat{\eta}\right)\sin\Delta_{\mathrm{bl}} + \eta_v^{\mathrm{imp}}, \qquad (8)$$

where

$$\hat{\eta} = c_s^2 \big/ \left(V_a V_{\mathrm{bl}} + V_c^2\right),$$

$$\Delta_a = 2(l/A)V_a/c_s,$$

$$\Delta_{\mathrm{bl}} = 2(l/A)\sqrt{V_a V_{\mathrm{bl}}}\big/c_s,$$

and

$$\eta_\nu^{\mathrm{imp}} = 0.8(A/l)(c_s/V_{\mathrm{bl}})e^{\Delta_a}$$

$$\times \int_{\Delta_a}^{\infty} e^{-\tau} \Omega(2\tau) d\tau - 1.2 e^{-2\Delta_a} \cos \Delta_{\mathrm{bl}}.$$

Equation (8) shows that in the presence of the mass ablation, the imprint amplitude has an oscillatory dependence on the mode number. For modes with $\Delta_a < 1$, the oscillation period and amplitude are determined by the velocity and acceleration perturbation growth reduced by the dynamic overpressure and the mass ablation [the first two terms in Eq. (8)]. For modes with $\Delta_a > 1$, the acceleration and velocity perturbations deposited at the ablation front are damped by the mass ablation [factor e^{-2kV_at} in Eq. (6)], and the behavior of such modes are determined by the vorticity convection from the shock front [the last term in Eq. (8)]. Figure 80.2 shows a comparison of the imprint amplitude calculated for conditions specified in Ref. 7 with and without stabilizing effects. Observe a significant reduction in the imprint growth due to the thermal smoothing and the mass ablation. To apply Eq. (8) to the ICF target designs, the blowoff velocity is taken to be[6,11]

$$V_{\mathrm{bl}} = V_a \Big/ \Big[\mu(\nu)(kL_0)^{1/\nu}\Big],$$

where ν is the power index for thermal conduction, L_0 is the characteristic thickness of the ablation front,
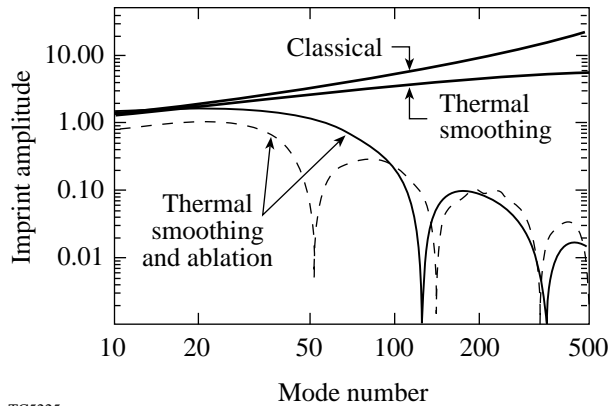
Figure 80.2
Plot of imprint amplitude versus mode number calculated using Eqs. (3), (5), and (8) (solid lines) and 2-D *ORCHID* simulation (dashed line) for a direct-drive, "all-DT," $\alpha = 3$, NIF target design.

$$\mu = (2/\nu)^{1/\nu} \Big/ \Gamma(1+1/\nu) + 0.12/\nu^2,$$

and $\Gamma(x)$ is the gamma function. The parameters L_0 and ν are obtained by using the fitting procedure described in Ref. 11. For a direct-drive, "all-DT," $\alpha = 3$, NIF cryogenic target design,[7] the 1-D numerical simulations and the fitting procedure give $V_a = 2.5$ μm/ns, $V_c \simeq 30$ μm/ns, $c_s \simeq 37$ μm/ns, $L_0 \simeq 0.03$ μm, and $\nu \simeq 2$. The imprint efficiency calculated by using Eqs. (3), (5), and (8) is plotted in Fig. 80.2 (solid line). For comparison, the results of the 2-D *ORCHID*[12] simulations of single-wavelength imprint amplitudes (dashed line) are shown on the same plot with the model prediction. Observe that the developed model accurately reproduces the oscillatory behavior of the imprint growth. Next, using Eq. (8), the integrity factor is calculated to be $\Upsilon_0^{\mathrm{imp}} = 1.2 \times 10^{-2}$. Since the outer-surface roughness and also the perturbation "feedout" from the inner surface[13] make an additional contribution to the rms nonuniformity, the total integrity factor is expected to exceed the stability threshold $\Upsilon_0^{\mathrm{max}}$, thus an additional reduction in the imprint amplitude is required for a successful implosion. A significant improvement in beam uniformity has been made in recent years by introducing SSD[14] (smoothing by spectral dispersion) and ISI[15] (induced spatial incoherence) smoothing techniques. To include the effect of SSD in our simulations, the intensity nonuniformities have been reduced by factor

$$\sqrt{t_c/(t_c + 4t)}$$

that gives on average a reduction in rms nonuniformity

$$\sigma = \sqrt{t_c/t_{\mathrm{avg}}}\, \sigma_0,$$

where the coherence time is taken to be[14]

$$t_c = \Big[\Delta\nu \sin(k\delta/2)\Big]^{-1},$$

$\Delta\nu$ is the bandwidth, t_{avg} is the averaging time, and δ is the speckle size. Simulations show that using the 2-D SSD smoothing technique with 1-THz laser bandwidth reduces the integrity factor to $\Upsilon_0^{\mathrm{imp}} = 10^{-3}$, which is a factor of 10 lower than the threshold Υ_0.

In summary, a model describing the evolution of the laser imprint was developed. The model shows that the imprint growth is determined by the velocity and acceleration pertur-

bations generated by the laser-beam nonuniformities. Thermal smoothing inside a hot plasma corona suppresses only the acceleration perturbation, while the mass ablation suppresses both velocity and acceleration perturbations. The model predicts that a direct-drive cryogenic NIF target will remain intact during the implosion when the laser is smoothed with 1-THz SSD used in current direct-drive target designs.

ACKNOWLEDGMENT

REFERENCES

1. J. D. Lindl, *Inertial Confinement Fusion: The Quest for Ignition and Energy Gain Using Indirect Drive* (Springer-Verlag, New York, 1998).

2. J. Sanz *et al.*, Phys. Fluids **31**, 2320 (1988); W. M. Manheimer, D. G. Colombant, and J. H. Gardner, Phys. Fluids **25**, 1644 (1982).

3. R. Ishizaki and K. Nishihara, Phys. Rev. Lett. **78**, 1920 (1997).

4. R. J. Taylor *et al.*, Phys. Rev. Lett. **79**, 1861 (1997); A. L. Velikovich *et al.*, Phys. Plasmas **5**, 1491 (1998).

5. J. Sanz, Phys. Rev. E **53**, 4026 (1996); V. N. Goncharov, R. Betti, R. L. McCrory, P. Sorotokin, and C. P. Verdon, Phys. Plasmas **3**, 1402 (1996); A. R. Piriz, J. Sanz, and L. F. Ibanez, Phys. Plasmas **4**, 1117 (1997).

6. V. N. Goncharov, Phys. Rev. Lett. **82**, 2091 (1999).

7. S. V. Weber, S. G. Glendinning, D. H. Kalantar, M. H. Key, B. A. Remington, J. E. Rothenberg, E. Wolfrum, C. P. Verdon, and J. P. Knauer, Phys. Plasmas **4**, 1978 (1997); R. P. J. Town, F. J. Marshall, J. A. Delettrez, R. Epstein, P. W. McKenty, D. D. Meyerhofer, P. B. Radha, S. Skupsky, and C. Stoeckl, Bull. Am. Phys. Soc. **43**, 1666 (1998).

8. V. N. Goncharov, R. Betti, J. A. Delettrez, P. W. McKenty, S. Skupsky, and R. P. J. Town, "Stability Analysis of Directly Driven OMEGA and NIF Targets," to be submitted to Physics of Plasmas.

9. R. Epstein, J. Appl. Phys. **82**, 2123 (1997).

10. K. A. Brueckner and S. Jorna, Rev. Mod. Phys. **46**, 325 (1974); S. E. Bodner, J. Fusion Energy **1**, 221 (1981).

11. R. Betti, V. N. Goncharov, R. L. McCrory, and C. P. Verdon, Phys. Plasmas **5**, 1446 (1998).

12. R. L. McCrory and C. P. Verdon, in *Computer Applications in Plasma Science and Engineering*, edited by A. T. Drobot (Springer-Verlag, New York, 1991).

13. R. Betti, V. Lobatchev, and R. L. McCrory, Phys. Rev. Lett. **81**, 5560 (1998).

14. S. Skupsky, R. W. Short, T. Kessler, R. S. Craxton, S. Letzring, and J. M. Soures, J. Appl. Phys. **66**, 3456 (1989); S. Skupsky and R. S. Craxton, Phys. Plasmas **6**, 2157 (1999).

15. R. H. Lehmberg, A. J. Schmitt, and S. E. Bodner, J. Appl. Phys. **62**, 2680 (1987).

Stability of Self-Focused Filaments in Laser-Produced Plasmas

The filamentation instability causes local intensity maxima in a laser beam propagating through a plasma to self-focus to high intensities. This process can affect many aspects of the beam propagation and absorption, so it has long been a subject of interest in laser–plasma interaction research. The theoretical thresholds and growth rates for the linear phase of the filamentation instability are readily determined analytically.[1] As the instability develops beyond the linear phase and the filament becomes smaller and more intense, the self-focusing effect is counterbalanced by diffraction. This leads to the possibility of a nonlinear inhomogeneous equilibrium—a steady-state, high-intensity, low-density filament in which the plasma pressure outside is balanced by the ponderomotive force of the light inside. This nonlinear phase of the instability, which produces the highest intensities and is therefore of the greatest practical interest, is difficult to treat analytically because of the strong density and intensity inhomogeneities associated with such a filament. The nonlinear stage of filamentation is usually studied using simulation codes that directly integrate the equations of motion for the fields and particles or fluids.[2] One important problem that is difficult to study in this way, however, concerns the long-term stability of the nonlinearly saturated filament, once formed. A stable filament would have a greater influence on absorption nonuniformity and on beam bending[3]—important considerations for direct- and indirect-drive laser-fusion schemes, respectively. It would also be expected to make a greater contribution to parametric instabilities.[4–6] An investigation of the stability of a filament through simulation would require the simulation to cover a large spatial extent of plasma over a long period of time. At present, due to computational limitations,[7] such extensive simulations necessitate some approximations in the equations used to describe the filament, in particular the paraxial approximation to the wave equation for the light propagation. This approximation requires that the propagating light not develop wave-vector components that deviate far from the initial direction of the beam. Recent studies[8] indicate, however, that the filaments most likely to be stable are very intense and have very small radii, of the order of the light wavelength, so that the paraxial approximation is question-able. Moreover, a simulation can treat only one specific set of irradiation and plasma parameters at a time, and extrapolating from simulations based on a limited sampling of parameter space to general results on stability is problematic.

A purely analytic approach to filament stability requires many approximations and idealizations to render the problem at all tractable; for this reason applying the few results that have been obtained analytically to realistic filaments is difficult. These results do suggest, however, that filaments may be unstable to kinking or bending perturbations[9] and to necking or "sausage" perturbations,[10] with the latter having a faster growth rate.

In this article the stability problem of a realistic filament will be addressed for the first time using a semi-analytic approach. A dispersion relation is obtained that describes the linear growth of a sausage-type perturbation of a self-consistent, self-focused cylindrical filament in equilibrium. This dispersion relation is analogous to the simple polynomial dispersion relations obtained for the instabilities of a plane electromagnetic wave in a homogeneous plasma.[11] Rather than being a polynomial in the perturbation wave number and frequency as in the homogeneous case, however, the filament dispersion relation depends on these quantities through ordinary differential equations that must be solved numerically for each value of the frequency and wave number. This is still much easier than the simultaneous solution of several coupled partial differential equations as required by a simulation, yet it allows the consideration of a physically realistic filament equilibrium, arbitrarily long space and time intervals, and the use of the full wave equation to describe the light propagation.

We will show that filament stability depends crucially on filament size. First, consider the case where the filament is small enough that only one waveguide mode will propagate. The pump (laser) light propagates through the filament in this fundamental mode at frequency ω_0 and axial wave number k_0. Amplitude modulation (sausaging) results from adding a per-turbing light wave in the same mode at a differing frequency

$\omega_0 + \Delta\omega$ and wave number $k_0 + \Delta k$, $\Delta\omega$ and Δk being related by the dispersion relation for the waveguide mode. This intensity modulation itself has frequency $\Delta\omega$ and wave number Δk and tends to move along the filament at the waveguide group velocity $\Delta\omega/\Delta k$, which in general is comparable to the speed of light. Because the speed of the perturbation greatly exceeds the ion-sound speed, the perturbation interacts weakly with the surrounding plasma, limiting potential growth rates. A much stronger interaction can be expected if the filament is large enough to allow two or more waveguide modes to propagate. In this case the perturbing light can be in a second mode with a different dispersion relation. Thus, it can have a frequency $\omega_1 \cong \omega_0$ but a significantly smaller axial wave number $k_1 < k_0$, so that $\Delta\omega/\Delta k = (\omega_0 - \omega_1)/(k_0 - k_1)$ is much smaller than the speed of light and can be comparable to the ion-sound speed, leading to an enhanced interaction.

To explore these ideas quantitatively, we consider an equilibrium filament consisting of a low-density cylindrical channel in a higher-density homogeneous background plasma. The channel is formed by the ponderomotive pressure of light propagating within the channel in the fundamental waveguide mode. Assume that in equilibrium the axis of the filament lies in the z direction and the filament intensity and density vary only as a function of r. Write the electric field E_0 of the pump wave as

$$\frac{e}{v_T m \omega_0} E_0(r,z,t) = \psi_0(r) e^{i(k_0 z - \omega_0 t)} + \text{c.c.}, \qquad (1)$$

so that ψ_0 represents the oscillatory velocity $v_0 = e E_{\max}/m\omega_0$ normalized to v_T, the electron thermal velocity. The pump satisfies the wave equation in cylindrical geometry

$$\left[c^2 \left(\frac{d^2}{dr^2} + \frac{1}{r}\frac{d}{dr} \right) + \omega_0^2 - \omega_{p0}^2(r) - c^2 k_0^2 \right] \psi_0(r) = 0, \quad (2)$$

with boundary conditions $\psi_0(r) \to 0$ as $r \to \infty$, $(d\psi_0/dr)_{r=0} = 0$ for a bound-state waveguide mode propagating in a cylindrical filament. The square of the plasma frequency $\omega_{p0}^2(r)$ is proportional to the density, which is determined by pressure balance with the ponderomotive force of the pump:

$$\frac{\omega_{p0}^2(r)}{\omega_0^2} = \frac{n_0(r)}{n_c} = \frac{N_0}{n_c} e^{-\frac{1}{4}\psi_0^2(r)}, \qquad (3)$$

where N_0 is the background density outside the filament and n_c is the critical density. Equations (2) and (3) give a nonlinear differential equation for ψ_0, which together with the boundary conditions results in an eigenvalue problem determining k_0, ψ_0, and the filament density profile $n_0(r)$. The pump propagates in the fundamental mode; however, if the filament is deep and wide enough, higher-order waveguide modes will also propagate in it. These eigenmodes satisfy the equation

$$\left[\frac{d^2}{ds^2} + \frac{1}{s}\frac{d}{ds} - \frac{n_0(s)}{n_c} \right] \phi_j(s) = \Gamma_j \phi_j(s), \qquad (4)$$

where $j = 0$ represents the fundamental mode, $s \equiv \omega_0 r/c$, and the eigenvalue Γ_j determines the relation between the axial wave number k_j of the eigenmode and its frequency ω_j: $c^2 k_j^2/\omega_0^2 - \omega_j^2/\omega_0^2 = \Gamma_j$. In general, the spectrum of eigenvalues Γ_j will contain discrete values for bound modes with $\Gamma_j - N_0/n_c$ and a continuum of unbound modes with $\Gamma_j - N_0/n_c$. Since we are interested in instability, we will be primarily concerned with the bound modes; the unbound modes propagate away from the filament before they have an opportunity to grow significantly. The eigenfunctions are orthogonal and assumed normalized to unity. The pump is assumed proportional to the fundamental eigenmode: $\psi_0(s) = \alpha_0 \phi_0(s)$, where α_0 may be taken real and represents the pump amplitude.

We employ fluid equations for the plasma density; linearizing n around the equilibrium density profile $n_0(r)$ results in an inhomogeneous driven wave equation for the density perturbation $n_1(r,z,t)$:

$$\frac{\partial^2 n_1}{\partial t^2} - c_s^2 \left\{ \nabla^2 n_1 - \frac{\nabla n_0}{n_0}\cdot\nabla n_1 + \left[\frac{(\nabla n_0)^2}{n_0^2} - \frac{\nabla^2 n_0}{n_0} \right] n_1 \right\}$$

$$= -\frac{Z}{M}\left[n_0 \nabla\cdot\mathbf{F}_p + (\nabla n_0)\cdot\mathbf{F}_p \right], \qquad (5)$$

where c_s is the ion acoustic speed, Z and M are the ion charge and mass, respectively, and $\mathbf{F}_p$ is the ponderomotive force resulting from the electromagnetic waves.

The density perturbation n_1 is assumed to have real wave number k in the z direction (along the filament) and frequency ω, which may be complex: $n_1(r,z,t) = n(r) e^{i(kz - \omega t)} + \text{c.c.}$ The interaction of the density perturbation with the pump generates a perturbed electromagnetic wave:

$$\psi_1(r,z,t) = \left\{ \psi_+(r)e^{i\left[(k+k_0)z-(\omega+\omega_0)t\right]} \right.$$

$$\left. + \psi_-(r)e^{i\left[(k-k_0)z-(\omega-\omega_0)t\right]} \right\} + \text{c.c.},$$

where, since the frequency ω may be much smaller than ω_0, both upshifted and downshifted terms are kept. The linearized wave equation then becomes

$$\left[\frac{d^2}{ds^2} + \frac{1}{s}\frac{d}{ds} + \left(1 \pm \frac{c_s}{c}\Omega\right)^2 - (\kappa_0 \pm \kappa)^2 - \frac{n_0(s)}{n_c} \right] \psi_\pm(s)$$

$$= \frac{n(s)}{n_c}\psi_0(s). \tag{6}$$

The first-order ponderomotive force resulting from the beating of the pump and perturbed electromagnetic waves is

$$\mathbf{F}_p = -mv_T^2 \nabla \left(\psi^2\right)_1$$

$$= -mv_T^2 \nabla \left\{ \left[\psi_0^*(s)\psi_+(s) + \psi_0(s)\psi_-(s) \right] \right.$$

$$\left. \times e^{i(\kappa\zeta - \Omega\tau)} + \text{c.c.} \right\}. \tag{7}$$

In Eqs. (6) and (7) we have introduced the dimensionless quantities $\Omega = \omega c/\omega_0 c_s$, $\kappa = \omega_0 k/c$, $\varsigma = \omega_0 z/c$, and $\tau = c_s\omega_0 t/c$. Substituting Eq. (7) into Eq. (5), we obtain an equation for the perturbed density in terms of the perturbed electromagnetic fields:

$$\left[\frac{d^2}{ds^2} + \left(\frac{1}{s} - \frac{1}{n_0}\frac{dn_0}{ds}\right) + \Omega^2 - \kappa^2 + \frac{1}{n_0^2}\left(\frac{dn_0}{ds}\right)^2 \right.$$

$$\left. - \frac{1}{n_0}\frac{d^2n_0}{ds^2} - \frac{1}{n_0}\frac{1}{s}\frac{dn_0}{ds} \right] \frac{n(s)}{n_c}$$

$$= -\frac{n_0(s)}{n_c}\left[\frac{d^2}{ds^2} + \left(\frac{1}{s} + \frac{1}{n_0}\frac{dn_0}{ds}\frac{d}{ds}\right) - \kappa^2 \right]$$

$$\times \left(\psi_0\psi_+ + \psi_0\psi_-\right). \tag{8}$$

It is useful to expand the electromagnetic fields in terms of the orthonormal eigenfunctions $\phi_j(s)$ of Eq. (4):

$$\psi_\pm(s) = \sum_{j=1}^{\infty} \beta_j^\pm \phi_j(s).$$

Defining $\eta_j(s)$ as the solution of

$$\left[\frac{d^2}{ds^2} + \left(\frac{1}{s} - \frac{1}{n_0}\frac{dn_0}{ds}\right)\frac{d}{ds} + \Omega^2 - \kappa^2 + \frac{1}{n_0^2}\left(\frac{dn_0}{ds}\right)^2 \right.$$

$$\left. - \frac{1}{n_0}\frac{d^2n_0}{ds^2} - \frac{1}{n_0}\frac{1}{s}\frac{dn_0}{ds} \right] \eta_j(s)$$

$$= -\frac{n_0(s)}{n_c}\left[\frac{d^2}{ds^2} + \left(\frac{1}{s} + \frac{1}{n_0}\frac{dn_0}{ds}\right)\frac{d}{ds} - \kappa^2 \right]\phi_0(s)\phi_j(s), \tag{9}$$

satisfying the boundary conditions $\eta_j'(0) = 0$ and outgoing waves as $s \to \infty$, we see from Eq. (8) that the density perturbation can be written as

$$\frac{n(s)}{n_c} = \alpha_0 \sum_j \left(\beta_j^+ + \beta_j^-\right)\eta_j(s). \tag{10}$$

Combining Eqs. (6) and (10) then gives a linear relation among the coefficients $\beta_j^\pm$:

$$\left[\left(1 \pm \frac{c_s}{c}\Omega\right)^2 - 1 - (\kappa_0 \pm \kappa)^2 + \Gamma_j \right]\beta_j^\pm$$

$$= \alpha_0^2 \sum_{j'} \left(\beta_{j'}^\pm + \beta_{j'}^\mp\right)L_{jj'}, \tag{11}$$

where the $L_{jj'}$ denote the integrals over the wave functions: $L_{jj'} = \int_0^\infty \phi_j(s)\eta_{j'}(s)\phi_0(s)s\,ds$.

While the sums in Eq. (11) extend over an infinite range of j, only the finite number of discrete bound states are of interest in studying instabilities, and in small filaments only a few of these may exist. Truncating the sums in Eq. (11) to the bound states leads to a finite set of linear homogeneous equations in the $\beta_j^\pm$, and setting the determinant of the coefficients to zero

gives a dispersion relation relating Ω and κ. Unlike the homogeneous case, however, this dispersion relation is not a polynomial but a more complicated function of Ω and κ, since the coefficients $L_{jj'}$ depend on Ω and κ through the solutions of the differential equation (9). These solutions are readily obtained numerically, however, allowing the evaluation of the dispersion relation and the determination of the unstable modes of the filament and their growth rates.

As an example, consider a background plasma with a uniform density of half-critical, $N_0/n_c = 0.5$, and an ion sound speed of $c_s = 10^{-3} c$, corresponding to an electron temperature of approximately 1 keV. For a given central field amplitude $\psi_0(0)$, the filament density and intensity profiles are found by integrating Eqs. (2) and (3), adjusting the axial wave number k_0 so that the boundary conditions are satisfied. The waveguide modes are then found from Eq. (4). At this density and temperature a central intensity of $\psi_0(0) \equiv v_0/v_T = 7$ is found to be sufficient to produce a filament wide enough to allow two electromagnetic modes to propagate. The resulting pump field amplitude and filament density profile are shown in Fig. 80.3(a), and the two normalized waveguide modes are shown in Fig. 80.3(b).
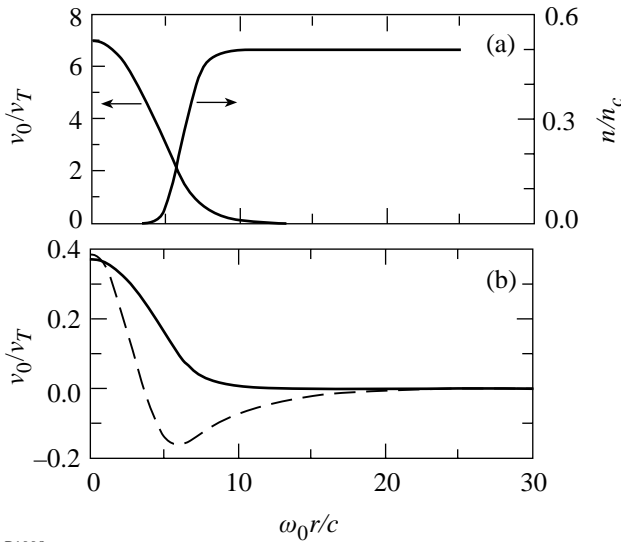
Figure 80.3
(a) Self-consistent equilibrium field and density profiles for a filament with background plasma density $n_0/n_c = 0.5$ and central intensity $v_0/v_T = 7$; (b) the two normalized bound eigenmodes for this filament.

The temporal growth rates and real frequencies for perturbations having the form of the fundamental eigenmode are shown in Figs. 80.4(a) and 80.4(b), plotted against the normal-

ized axial wave number κ. The group velocity of the perturbation normalized to the sound speed can be obtained from the slope of the real frequency curve in Fig. 80.4(b) and, as expected, is near the speed of light: $v_g/c_s \cong 900$ (recall $c/c_s = 1000$ in this example). Thus, a perturbation will propagate along the filament at nearly the speed of light as it grows, leading to a spatial growth rate that can be estimated by dividing the temporal growth rates in Fig. 80.3(a) by $v_g/c_s \cong 900$. This spatial growth rate is quite small, of order $10^{-4} \omega_0/c$. For a typical laser-fusion experiment wavelength of $0.351\,\mu$m, for example, a small perturbation to a filament could propagate for several thousand microns before becoming large enough to disrupt the filament. Laser-produced plasmas of interest are generally much smaller than this, so that small filaments (radius < one wavelength) are effectively stable to perturbations of this form.
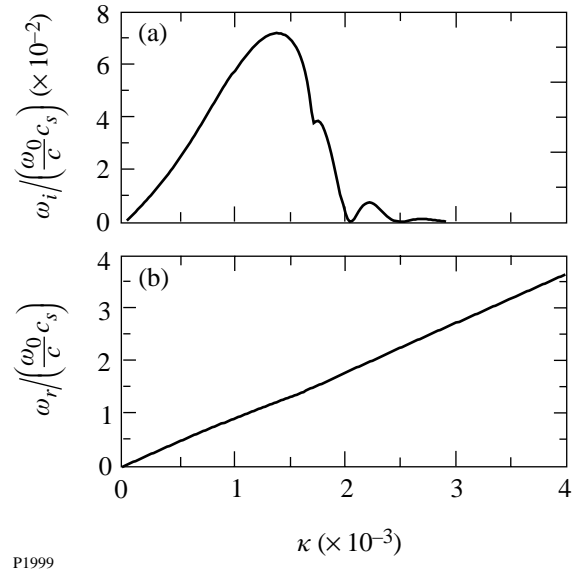
Figure 80.4
Growth rates (a) and real frequencies (b) for perturbations in the form of the fundamental eigenmode (solid line) in Fig. 80.3(b).

The situation is more interesting for filaments large enough that two or more waveguide modes will propagate. Figures 80.5(a) and 80.5(b) show the temporal growth rate and real frequency for the perturbation corresponding to the second waveguide mode for the same filament parameters as in Fig. 80.4. Note that the growth rate is now considerably larger, but more significant is the fact that the axial wave number of the perturbation (given by the difference in the two waveguide-mode wave numbers) is much larger than in the single-mode case. This makes the group velocity [Fig. 80.5(c)] at which the perturbation propagates much smaller, and the resulting

spatial growth rate much larger. This effect is due to the fact that having two different dispersion relations for the interacting modes allows larger values of Δk for a given $\Delta \omega$. More importantly, however, the fact that the group velocity in Fig. 80.5(c) passes through zero suggests the possibility of an absolute instability, which grows without propagation. If we define κ_{max} to be the value of κ for which the temporal growth rate in Fig. 80.5(a) is a maximum, and Ω_{max}, Ω'_{max}, Ω''_{max} to be the corresponding frequency and its first and second derivatives with respect to κ, the condition for absolute instability is[12]

$$\text{Im}(\Omega_{max}) > \frac{1}{2}(\Omega'_{max})^2 \text{Im}\left(\frac{1}{\Omega''_{max}}\right).$$

Evaluation of these quantities shows that this condition is well satisfied (the left side in this example is 0.164, and the right is 0.047), so that the instability is indeed absolute. This means
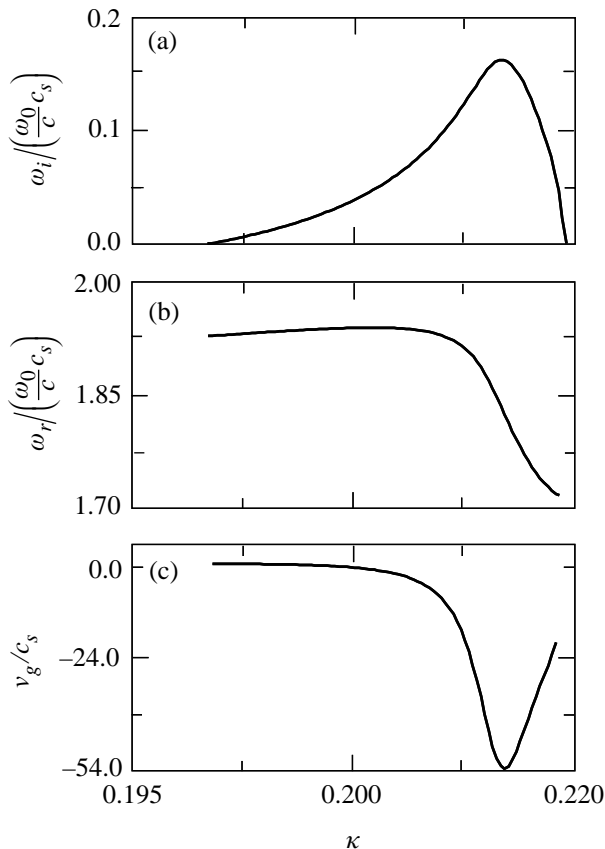
Figure 80.5
Growth rates (a), real frequencies (b), and group velocities (c) for perturbations in the form of the second eigenmode (dashed line) in Fig. 80.3(b).

P2000

that the perturbation will remain in place as it grows, rather than propagating along the filament. Unless saturated by some nonlinear mechanism, such an instability would be expected to quickly disrupt the filament.

When the filament is large enough that many modes will propagate, one approaches a "classical" regime where the propagating light may be treated by the paraxial approximation or ray tracing. From the above analysis it is expected that such filaments would be unstable, which seems to be the case in simulations.[7,8]

The above stability analysis has been concerned with a sausage-type perturbation, i.e., one with no azimuthal variation in the cylindrical coordinates centered on the equilibrium filament. "Kink-type" modes, with nonvanishing azimuthal wave numbers, could be treated using a straightforward extension of the above analysis. Such modes would, of course, require a filament large enough to carry these higher-order modes, so small single-mode filaments would be unaffected. Larger filaments could be unstable to both kink and sausage perturbations; which one dominates in practice is a subject for further research. Another topic requiring further study is the effect of plasma inhomogeneity, though by analogy with other wave–plasma interactions, inhomogeneity might be expected to reduce instability growth rates.

In conclusion, the first analysis of filament stability using a realistic self-consistent filament equilibrium and a wave-equation treatment of light propagation has been carried out using a semi-analytic approach. It is found that small filaments that carry light in only one waveguide mode have only a weak convective instability and, in most cases of interest in laser–plasma interactions, may be regarded as essentially stable. Filaments large enough to carry two or more waveguide modes are unstable to sausage-type perturbations, which can be absolutely unstable and may lead in typical cases to distortion or breakup of the filament within a few tens of microns.

ACKNOWLEDGMENT

REFERENCES

1. P. Kaw, G. Schmidt, and T. Wilcox, Phys. Fluids **16**, 1522 (1973).

2. D. E. Hinkel *et al.*, Phys. Plasmas **5**, 1887 (1998).

3. D. E. Hinkel, E. A. Williams, and C. H. Still, Phys. Rev. Lett. **77**, 1298 (1996).

4. T. Afshar-rad *et al.*, Phys. Fluids B **4**, 1301 (1992).

5. R. W. Short, W. Seka, and R. Bahr, Phys. Fluids **30**, 3245 (1987).

6. R. W. Short and A. Simon, Phys. Plasmas **5**, 4134 (1998).

7. A. J. Schmitt and B. B. Afeyan, Phys. Plasmas **5**, 503 (1998).

8. F. Vidal and T. W. Johnston, Phys. Rev. Lett. **77**, 1282 (1996).

9. E. Valeo, Phys. Fluids **17**, 1391 (1974).

10. E. J. Valeo and K. G. Estabrook, Phys. Rev. Lett. **34**, 1008 (1975).

11. W. L. Kruer, *The Physics of Laser–Plasma Interactions*, Frontiers in Physics, Vol. 73, edited by D. Pines (Addison-Wesley, Redwood City, CA, 1988).

12. L. S. Hall and W. Heckrotte, Phys. Rev. **166**, 120 (1968).

Broadband Beam Smoothing on OMEGA with Two-Dimensional Smoothing by Spectral Dispersion

High laser-irradiation uniformity is an important requirement for successful implosions of inertial confinement fusion (ICF) targets,[1] particularly for the direct-drive OMEGA laser system that directly illuminates ICF targets. Direct-drive laser irradiation that is not perfectly uniform imprints on the target surface and perturbs the spherical symmetry. This seeds the Rayleigh–Taylor hydrodynamic instability during the target acceleration phase and can severely degrade target performance. Target imprinting is determined when the critical surface decouples from the ablation surface. The critical surface corresponds to the highest density reached by the plasma, where the laser frequency equals the plasma frequency. The ablation surface corresponds roughly to the surface separating the inward-flowing (imploding) plasma and the outward-flowing "exhaust." Direct-drive smoothing techniques must minimize the level of irradiation nonuniformity on a time scale comparable to or shorter than this imprinting phase. Initial target experiments indicate that this imprinting phase lasts for several hundred picoseconds on OMEGA and depends on the spatial wavelength of the most important perturbations.

Direct-drive laser irradiation uniformity for different ranges of spatial frequencies is achieved on OMEGA by a number of techniques.[1] The number of beams, as well as power and energy balance among beams, predominantly affects irradiation nonuniformity at low spatial frequencies, while higher spatial frequencies are determined by the individual beam uniformity achievable with smoothing by spectral dispersion (SSD).

The technique of SSD significantly reduces irradiation nonuniformity by rapidly shifting the laser speckle pattern generated on the target by distributed phase plates (DPP's).[2] A high-frequency electro-optic phase modulator produces a time-varying wavelength modulation that is angularly dispersed by a diffraction grating. Significant smoothing is achieved on a time scale approximately equal to the inverse bandwidth impressed by the phase modulator. Two-dimensional SSD (2-D SSD) extends the smoothing benefits of SSD by combining the deflections of the laser speckle pattern on target in two orthogonal directions. Two separate stages of bulk electro-optic phase modulators and gratings are employed that generate and disperse bandwidth in two orthogonal directions.

Broadband Two-Dimensional SSD Generation

The principal relationships governing irradiation uniformity with SSD are illustrated in Fig. 80.6(a), which plots the rms irradiation nonuniformity for all spatial frequencies (for modes with $\ell \leq 500$) on target for several different SSD configurations versus integrating time. The initial smoothing rate is directly proportional to the SSD bandwidth since the coherence time for the speckle pattern produced by the DPP is inversely related to the effective bandwidth in any time slice of the pulse. The asymptotic nonuniformity is inversely related to the square root of the number of independent speckle patterns on the target. For an SSD system employing critical dispersion, this corresponds to the number of FM sidebands imposed on the beam by the phase modulator.

Incorporating a higher-frequency phase modulator in the 2-D SSD system offers two different approaches to improving irradiation uniformity on OMEGA: increasing the total SSD bandwidth or producing multiple SSD color cycles.

1. Large SSD bandwidths can be generated for a given number of critically dispersed FM sidebands and propagated through the laser system since less grating dispersion is required to achieve a single color cycle. Increased SSD bandwidths smooth laser irradiation faster. An asymmetric 2-D SSD configuration on OMEGA using phase modulators operating at 3.3 and 10.4 GHz can produce infrared bandwidths of 1.5×11 Å at nominally 1×1 color cycles, respectively. This infrared bandwidth corresponds to a UV bandwidth of approximately 1 THz.

2. Multiple SSD color cycles can be produced with a higher modulation frequency using the current grating design without exceeding the beam divergence limit imposed by the laser system pinholes. Increasing the number of color cycles accelerates the smoothing at the mid-range spatial frequencies ($\ell = 50$–200) that pose the greatest threat of
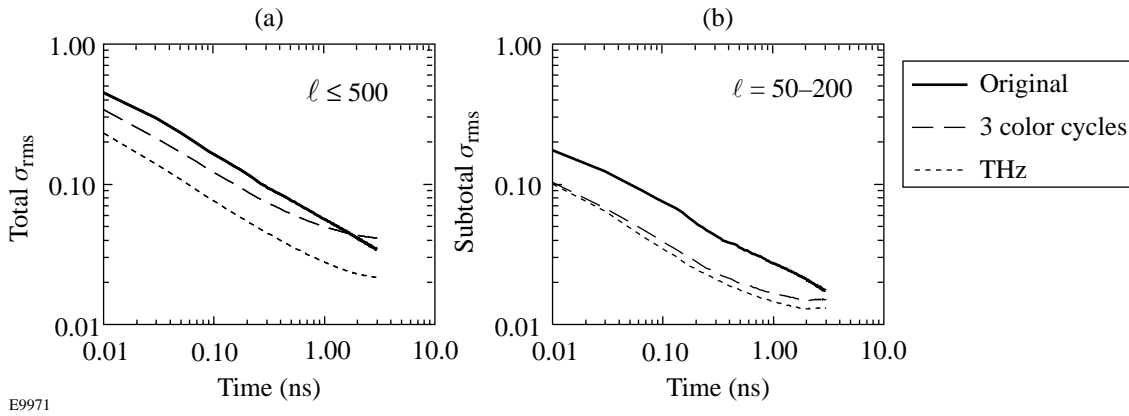
Figure 80.6
The intial rate of SSD smoothing is governed by the total bandwidth, while the asymptotic nonuniformity is related to the total number of independent speckle patterns on target. If at least one SSD color cycle is present, this corresponds to the number of FM sidebands produced by the phase modulators. (a) Plotting total nonuniformity ($\ell \leq 500$) versus averaging time shows that comparable smoothing levels should be achieved approximately four times sooner with the 1-THz SSD (1.5×11 Å, 1×1 color cycles) system than the original 2-D SSD (1.25×1.75 Å, 1×1 color cycles) system implemented on OMEGA, while the three-color-cycle 2-D SSD (1.5×3 Å, 1×3 color cycles) system actually achieves worse asymptotic levels since fewer independent speckles modes are produced. (b) Smoothing performance for the spatial frequencies associated with ℓ-modes in the range between 50 and 200 shows different behavior. The three-color-cycle SSD system performance during the first stage of smoothing is comparable to the 1-THz SSD system since the multiple color cycles preferentially smooth these spatial frequencies.

seeding hydrodynamic instabilities in direct-drive implosions. The current OMEGA FCC configuration can efficiently convert infrared bandwidths of 1.5×3.0 Å from modulators operating at 3.3 and 10.4 GHz to generate 1×3 color cycles, respectively.

The single-beam smoothing performance for several 2-D SSD implementations on OMEGA is compared in Fig. 80.6. Total rms nonuniformity is plotted versus integration time in Fig. 80.6(a). The original 2-D SSD implementation on OMEGA delivered approximately 0.2 THz of total SSD bandwidth in the ultraviolet (1.25×1.75 Å IR, 1×1 color cycles). Asymptotic nonuniformity levels of better than 2% are achieved after approximately 250 ps when multiple-beam overlap is included. In comparison, the 1-THz system (1.5×11 Å, 1×1 color cycles) planned for installation in November 1999 achieves improved asymptotic uniformity since it produces a larger number of independent speckle patterns and larger beam deflections. Furthermore, the integration time required to achieve 2% nonuniformity is reduced to about 70 ps.

The total smoothing performance of the three-color-cycle 2-D SSD system recently installed on OMEGA (1.5×3.0 Å, 1×3 color cycles) is also shown in Fig. 80.6(a). Poorer asymptotic performance is expected than for either of the other two systems since fewer independent speckle patterns are produced. Figure 80.6(b) presents the rms nonuniformity for

the mid-range spatial frequencies versus integration time for the same 2-D SSD systems shown in Fig. 80.6(a). For these spatial frequencies, it can be seen that the smoothing performance of the three-color-cycle system is comparable to the 1-THz system. Direct comparisons of the target performance with both of these improved 2-D SSD systems will be performed once the 1-THz system is implemented.

For OMEGA, it is advantageous to implement the larger bandwidth and beam divergence in the second direction of the 2-D SSD setup since the bandwidth from the second modulator is not dispersed until after the most-limiting spatial-filter pinhole located in the large-aperture ring amplifier (LARA)[3] in the driver line. This constraint results from spatial-filtering requirements associated with the serrated aperture apodizer used to set the OMEGA beam profile. A slotted LARA spatial-filter pinhole with its long axis aligned along the direction of dispersed bandwidth is employed to maximize spatial filtering of the beam.

Larger spatial-filter pinholes are another important requirement for propagating broadband 2-D SSD on OMEGA. Pinhole sizes for the spatial filters in each of the six stages of OMEGA were originally chosen such that computed instantaneous intensities on the edge of any pinhole did not exceed 100 GW/cm²[4] for a non-SSD, 1-ns FWHM Gaussian pulse. To perform this computation, a complete diffraction and non-

linear propagation model of the system was constructed. Amplitude noise, using the data of Stowers and Patton,[5,6] was applied to optical surfaces and the resulting pinhole irradiance calculated. For pinholes early in the system where spatial noise and its nonlinear growth were not an issue, the pinhole sizes were set no lower than approximately 13 times diffraction-limited in order to facilitate fabrication and alignment. Later optical time-domain reflectometry (OTDR) measurements on OMEGA indicated that in the beamline stages, the pinhole sizes were close to optimum for non-SSD high-energy shots. These same pinholes were operated with 1.25×1.75-Å bandwidth SSD with no deleterious effect or resultant amplitude modulation. Spatial noise measurements were also performed on OMEGA using a high-dynamic-range, far-field diagnostic, as shown in Fig. 80.7. The nonlinear growth of this noise was analyzed to establish the largest acceptable pinholes.
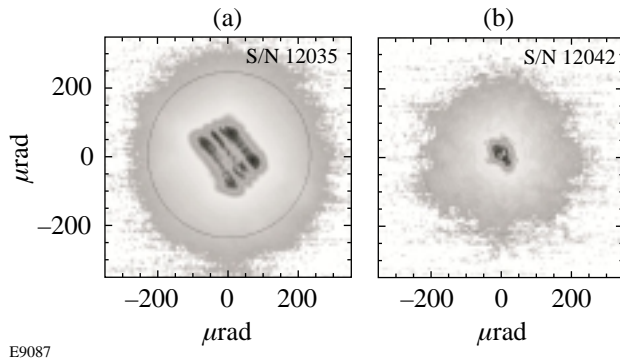
Figure 80.7
OMEGA spatial noise measurements and growth analysis set how much pinholes could be enlarged to accommodate broadband 2-D SSD.

For the current 1.5×3.0-Å SSD bandwidths, the pinholes were increased in diameter by the increase in the major dimension of the far-field spot (~50%). Since increased pinhole size increased the risk of system damage due to ripple growth[7] and Narcissus[8] (pencil beam) spots, a single beamline (40) of OMEGA was operated with these larger pinholes for a full year prior to their installation in the remainder of the system. No damage was observed in any of the optics in that beamline, which was exercised over the full range of OMEGA output energy and pulse shapes.

The 2-D SSD architecture implementing double-pass phase modulators and gratings shown in Fig. 80.8 was chosen for several reasons. Double-pass operation of a phase modulator increases its effective modulation efficiency, provided proper phase matching of the second pass is maintained. As a result, significantly lower microwave powers are required to achieve a given bandwidth while reducing the risk of air breakdown from the microwave fields in the microwave modulator resonators. Multiple-pass modulator operation can further increase the modulation efficiency but at the expense of increased system complexity.

Including a double-pass grating in the first SSD dimension also significantly reduces the space envelope required. Combining the first dimension predelay (G1) and dispersion (G2) functions into a single grating requires a far-field retroreflection to accomplish an image inversion; otherwise, the second pass through the grating would produce additional pulse distortion.
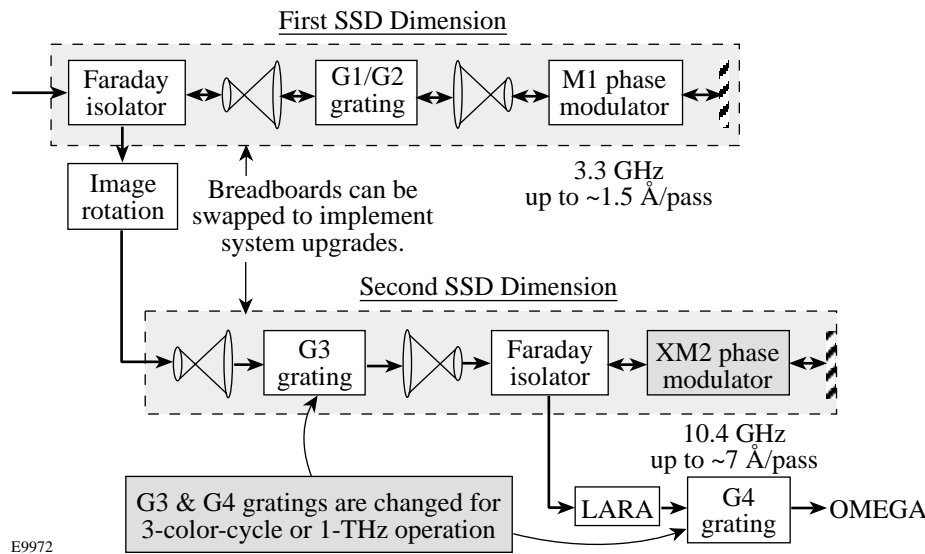
Figure 80.8
A double-pass, 2-D SSD architecture increases phase-modulator efficiency and reduces the space envelope required for a 2-D SSD system.

The two most important aspects of system performance for the improved 2-D SSD systems developed for OMEGA are bandwidth and FM-to-AM conversion. The 2-D SSD system is utilized as a "two-dimensional spectrometer" to measure the SSD bandwidths generated by each modulator, while an infrared streak camera system was developed to identify, measure, and minimize FM-to-AM conversion in the 2-D SSD system, as detailed below.

Accurate SSD bandwidth measurements for both phase modulators can be obtained simultaneously by capturing a far-field image of an SSD beam, as shown in Fig. 80.9, since the bandwidth generated by each phase modulator is dispersed in essentially orthogonal directions. Corrections for inexact dispersion matching between gratings G3 and G4, as well as imprecise image rotation between SSD directions, are accounted for using image-unwarping algorithms. The phase-modulation depth produced by each modulator is then

determined by identifying the value for which a simulated spectrum best reproduces the measured spectral lineouts in each SSD direction, including the instrument's point spread function. For the three-color-cycle 2-D SSD system, FM spectra produced by the 10.4-GHz modulator are self-calibrating since the individual FM sidebands are completely resolved and the modulation frequency is accurately known.

Measuring the FM-to-AM conversion performance of the 2-D SSD systems is difficult, particularly for the 10.4-GHz modulation, since an instrument with sufficient bandwidth to measure the microwave modulation frequency and its harmonics is required. Additionally, the ability to verify performance across the beam profile is also important since some FM-to-AM conversion mechanisms manifest themselves in local variations. These requirements, plus the low repetition rate of our SSD pulses (5 Hz), eliminate sampling techniques and make an infrared streak camera the best instrument. The
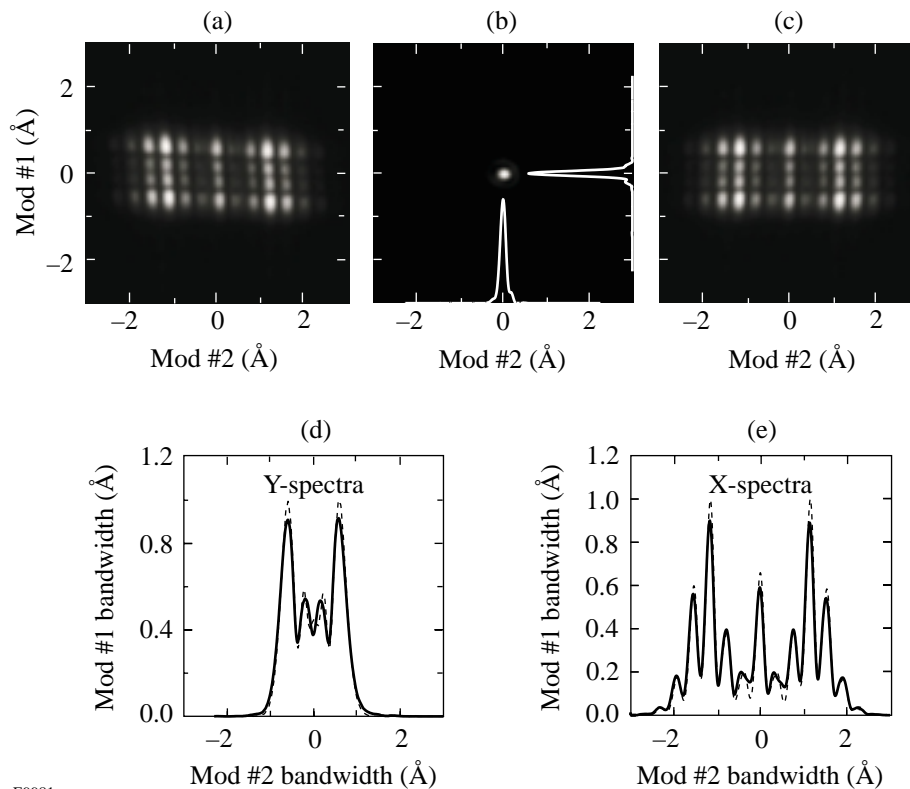
Figure 80.9

Far-field images of the 2-D SSD can be evaluated to measure FM bandwidth produced by each SSD modulator. (a) A raw image is captured on a scientific CCD. (b) The image for an unmodulated pulse is also captured to establish the instrumental response. (c) The image is corrected to account for image rotation errors introduced by the 2-D SSD system. In the corrected image, the bandwidth produced by each modulator is dispersed in orthogonal directions. (d) and (e) The bandwidth produced by each modulator is estimated by finding the simulated spectra (dashed), including the instrumental response, that best fit the measured spectra (solid).

uncoated photocathode of the streak camera is index matched to a wedged, AR-coated window to eliminate spurious etalon effects that would otherwise introduce amplitude modulation artifacts. Streak camera flat-field and time-base corrections are applied to account for instrumental nonlinearities.

FM-to-AM conversion in the 2-D SSD system is discriminated from modulation in the shaped-pulse input by transmitting a reference signal sampled before the 2-D SSD system to the streak camera using an optical fiber, as shown in Fig. 80.10(a). Lineouts at different spatial locations of the streak image [Fig. 80.10(b)] are normalized to this reference signal and the amplitude modulation estimated by finding the peak-to-valley variations of the ratio of these signals [Fig. 80.10(c)]. The signal-to-noise ratio of this measurement depends on the number of pixel rows averaged to produce the lineouts and appears to be limited by photon statistics. The harmonic content of the AM is easily obtained by fast Fourier transforming the difference of the signal and reference lineouts, as shown in Fig. 80.10(d). Statistically analyzing multiple streak images provides estimates of the uncertainty of these measurements.

FM-to-AM conversion in the 2-D SSD system was minimized by adjusting various system parameters and parametrically plotting the measured amplitude modulation to identify the optimal settings. For example, it is well known that propagation from an image plane of an SSD grating results in amplitude modulation. Amplitude modulation is minimized at an image plane of a grating that disperses SSD bandwidth. If an SSD grating is not properly located at the image plane of earlier gratings, the phase relationships between FM sidebands are disturbed and irreversibly convert FM to AM. SSD grating imaging was accomplished by plotting the measured AM as a function of image relay position, as shown in Fig. 80.11(a).

(a)

(b)   (c)   (d)

E9979
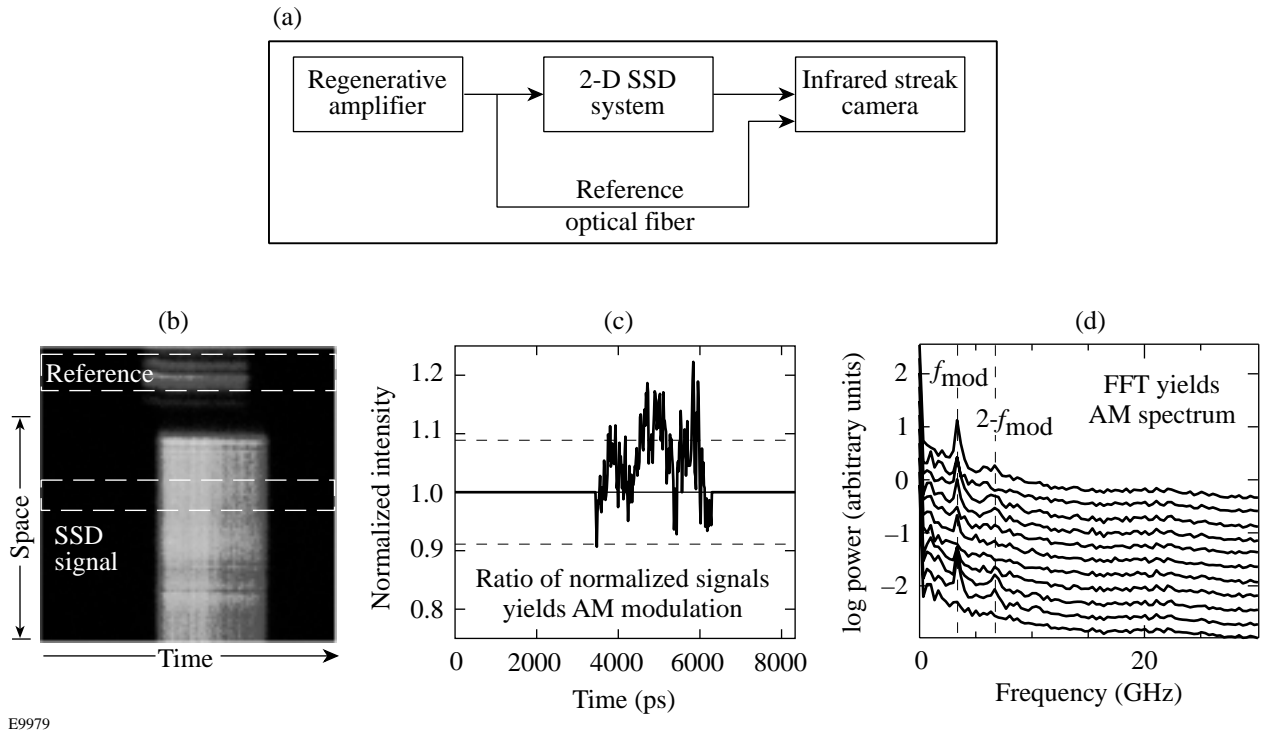
Figure 80.10

An infrared streak camera was employed to identify and measure sources of FM-to-AM conversion. (a) Streak camera measurements of FM-to-AM conversion were performed by comparing the pulse shape at the image plane of the SSD gratings after the SSD system to the pulse shape injected into the 2-D SSD system that is sampled by an optical fiber. (b) The SSD region is divided into regions, and average row lineouts are calculated. A reference pulse shape from the optical fiber delayed input is also acquired. The SSD and reference signals are energy normalized and aligned in time. (c) The ratio of each SSD signal to the reference is used to measure the FM-to-AM conversion. The peak-to-valley in a 333-ps sliding window is calculated for each lineout, and the average value is used as an estimate for the AM. (d) The spectra of the amplitude modulation for a number of different image conditions shown in Fig. 80.11(a) show peaks at the modulation frequency (3.3 GHz) as well as the second harmonic (6.6 GHz) when grating imaging is not optimized. An underlying $1/f$-like noise spectrum is evident that limits the minimum measurable AM even when no SSD is applied to the beam.
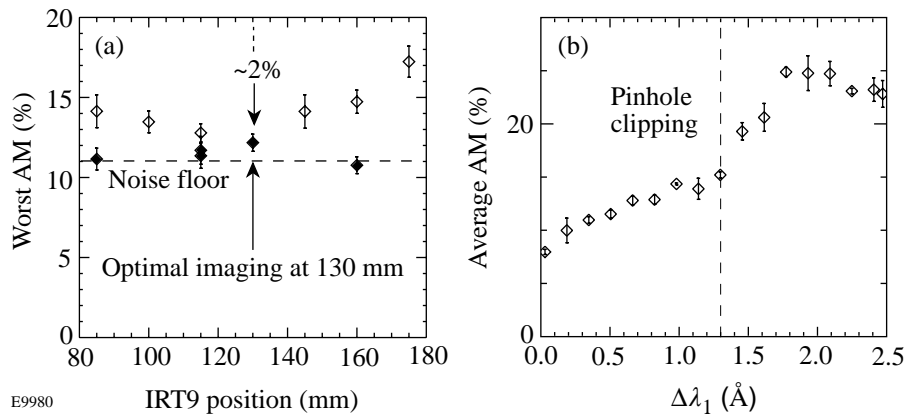
Figure 80.11

AM measurements described in Fig. 80.10 are used to optimize the 2-D SSD system performance. (a) SSD grating imaging is set by minimizing amplitude modulation. Measured AM grows linearly as a function of image plane separation, except near the noise floor where it adds in quadrature with the noise. (b) The onset of pinhole clipping in the slotted LARA spatial filter (1.0×1.8 mm) is characterized by scanning bandwidth produced by the first modulator. The final slotted pinhole dimensions (1.0×2.4 mm) were set to accommodate the specified 1.5 Å, plus extra margin for operational tolerances.

The length of the major axis of the slotted LARA spatial-filter pinhole was also established using this method, as shown in Fig. 80.11(b). The bandwidth generated by the first SSD modulator is dispersed before the LARA. As bandwidth is increased for a given pinhole size, pinhole clipping causes the measured AM values to increase rapidly. For a 1.0×1.8-mm pinhole, clipping is first observed at a bandwidth of approximately 1.3 Å. The final slotted pinhole (1.0×2.4 mm) should maximize spatial-filtering effects while maintaining reasonable operational tolerances.

Summary

Direct-drive ICF experiments require a laser system with excellent irradiation uniformity. Major elements of LLE's beam-uniformity program have been completed, including demonstration of a 10.4-Ghz bulk-phase modulator capable of producing either large SSD bandwidths or multiple color cycles, implementation of a flexible double-pass 2-D SSD architecture, and diagnostics for quantifying the performance of these improved smoothing techniques. The remaining elements of this program will be completed when broadband (1-THz) 2-D SSD is implemented on OMEGA later this year.

REFERENCES

1. S. Skupsky and R. S. Craxton, Phys. Plasmas **6**, 2157 (1999).

2. S. Skupsky, R. W. Short, T. Kessler, R. S. Craxton, S. Letzring, and J. M. Soures, J. Appl. Phys. **66**, 3456 (1989).

3. A. Babushkin, J. H. Kelly, C. T. Cotton, M. A. Labuzeta, M. O. Miller, T. A. Safford, R. G. Roides, W. Seka, I. Will, M. D. Tracy, and D. L. Brown, in *Third International Conference on Solid State Lasers for Application to Inertial Confinement Fusion*, edited by W. H. Lowdermilk (SPIE, Bellingham, WA, 1999), Vol. 3492, pp. 939–943.

4. J. M. Auerbach *et al.*, Appl. Opt. **18**, 2495 (1979).

5. I. F. Stowers and H. G. Patton, in *Laser-Induced Damage in Optical Materials: 1977*, edited by A. J. Glass and A. H. Guenther, Natl. Bur. Stand. (U.S.), Spec. Publ. 509 (U.S. Government Printing Office, Washington, DC, 1977), pp. 440–454.

6. W. W. Simmons and W. E. Warren, *Laser Program Annual Report 1978*, Lawrence Livermore National Laboratory, Livermore, CA, UCRL-50021-78, **2**, 7-111 (1978).

7. D. C. Brown, in *High-Peak-Power Nd:Glass Laser Systems*, edited by D. L. MacAdam, Springer Series in Optical Sciences (Springer-Verlag, Berlin, 1981), Chap. 7.

8. J. E. Murray *et al.*, in *Solid-State Lasers for Application to Inertial Confinement Fusion (ICF)*, edited by W. F. Krupke (SPIE, Bellingham, WA, 1995), Vol. 2633, pp. 608–614.

The Effect of Pulse Shape on Laser Imprinting and Beam Smoothing

Inertial confinement fusion (ICF) targets are inherently hydro-dynamically unstable;[1–3] as a result, perturbations in the target shell can grow exponentially because of Rayleigh–Taylor (RT) instability.[4] For high-convergence implosions it is important to minimize target perturbations and their growth. In direct-drive ICF, nonuniformities in the drive laser produce pressure perturbations that cause mass and velocity perturbations in the target. These "imprinted" perturbations seed the RT instability and ultimately disrupt the implosion. To minimize imprinting, the drive laser must be as uniform as possible. This requires complex laser beam–smoothing techniques.[5] In many ICF target designs the temporal shape of the drive is determined by compression hydrodynamics and thermodynamics (stability and isentrope) and not necessarily to minimize imprint. It is therefore important that the effect of temporal pulse shape on imprinting and beam smoothing be measured and understood. Various experiments have measured imprinting[6–12] and have used control perturbations to normalize the results.[10,12] The experiments reported here are the first to demonstrate the pulse shape's effect on imprinting.

A series of experiments on the OMEGA laser system[13] measured imprinting efficiency using preimposed modulations on planar targets to calibrate the imprint level. The imprinting produced by different temporal pulse shapes and beam-smoothing techniques is compared. Rapidly rising (~100 ps/decade) pulses produce less imprint than pulses with ~1-ns rise time when no temporal beam smoothing is employed. Furthermore, the effect of smoothing by spectral dispersion (SSD)[5] is less pronounced for these rapid-rise pulses. These observations are consistent with plasma smoothing[14] by thermal conduction and differences in the rate at which each pulse produces plasma early in the laser–target interaction.

Imprinting occurs when drive nonuniformities produce pressure perturbations at the target surface that, in turn, produce velocity and mass perturbations at the ablation surface where the RT instability occurs. Laser energy is absorbed in the region outside the critical surface and conducted axially to the ablation surface. If sufficient depth of plasma is present, lateral thermal conduction can provide smoothing of the deposition nonuniformities, thus ending imprinting.[14] Previous simulations[15,16] have investigated imprinting and have indicated that, for a given laser wavelength, imprint efficiency depends linearly on $\delta I/I$ for the intensities relevant to ICF (i.e., $\delta m \propto \delta I/I$), but the duration of imprinting varies depending on the plasma smoothing. Numerical simulations described below show that the condition for smoothing a perturbation of wavelength k is that $k d_c \sim 2$, where d_c is the distance between the ablation surface and a central location in the energy deposition profile.[10] As that thermal conduction region grows, longer wavelengths can be smoothed; thus, for each wavelength the duration of laser imprinting and its total magnitude depends on the time to develop a sufficiently sized conduction zone. Since a slowly rising pulse produces a plasma at a slower rate, imprinting occurs over a longer time, resulting in a higher imprint level in the absence of beam smoothing. The plasma formation rate therefore affects the wavelength dispersion of smoothing. For a given wavelength of interest, imprinting ultimately ceases when the conduction region grows to a sizable fraction of that wavelength. When $k d_c$ is about 2, d_c is about one-third the wavelength of the perturbation. To check the wavelength dependence, the imprint levels of both 30- and 60-μm wavelengths were measured. These correspond to ℓ-modes of 50 and 100 on mm-sized targets, which are pertinent to direct-drive ICF and are in the linear RT growth regime during these measurements.

In these experiments, 20-μm-thick CH ($\rho = 1.05$ g/cm^3) targets with preimposed modulations were irradiated at 2×10^{14} W/cm^2 by six overlapping UV beams from the OMEGA laser. Target nonuniformities were measured using through-foil x-ray radiography.[17] Experiments were performed with two laser pulse shapes: a 3-ns square (in time) pulse and a 3-ns ramp pulse. The square pulse had a rise time of 100 ps per decade of intensity and an intensity of 2×10^{14} W/cm^2. The ramp pulse rose linearly from ~10^{13} to 2.5×10^{14} W/cm^2 in 3 ns. The latter pulse had a 100 ps/decade

rise to $\sim 10^{13}$ W/cm^2 before the ramp commenced. For each pulse shape, experiments were performed with and without 2-D SSD beam smoothing.

The driven targets were backlit with x rays produced by a uranium backlighter irradiated at 2×10^{14} W/cm^2 (with 11 additional beams). X rays transmitted through the target and a 3-μm-thick Al blast shield were imaged by a framing camera with 8-μm pinholes filtered with 20 μm of Be and 6 μm of Al. This yielded the highest sensitivity for average photon energy of $\sim$1.3 keV.[17] The framing camera produced eight temporally distinct images of $\sim$100-ps duration and a magnification of 12. The use of optical fiducial pulses, coupled with an electronic monitor of the framing-camera output, provided a frame-timing precision of about 70 ps.

Unfortunately laser imprint cannot easily be measured directly, so measurements often rely on some level of RT growth to produce detectable signals. Targets with low-amplitude, single-mode initial perturbations are used here to provide a calibration from which the initial amplitude of laser imprinting was determined. The basis of this calibration is that in the linear regime the imprinted perturbations ultimately experience similar unstable RT growth to those of preimposed modulations.[8] Although imprinting also produces velocity perturbations, it is useful to assign an equivalent surface roughness to imprinting. This "mass equivalence" is used as a measure of the imprint. The mass equivalence is found by extrapolating the temporal evolution of the imprinted amplitudes back to $t = 0$ by measuring the ratio of the amplitudes of the imprinted and preimposed modes after RT growth has occurred. This requires that the RT instability for those modes remain in the linear regime and do not experience saturation or nonlinear effects.[18] Saturation of RT growth is discussed at length in Ref. 19, where it was shown that at $\lambda = 60$ μm, both the single-mode and the imprinted perturbations behaved linearly for our experimental conditions and observation times. The 30-μm-wavelength imprinting data was measured before the onset of saturation.[19]

The mass equivalence[15] for a specific wave number can be defined as

$$A_{\text{eq}}(k,0) = \left[A_{\text{imprint}}(k,t) / A_{\text{pre}}(k,t) \right] A_{\text{pre}}(k,0), \qquad (1)$$

where $A_{\text{imprint}}(k,t)$ is the measured amplitude of the imprinted features, $A_{\text{pre}}(k,t)$ is the measured amplitude of the preimposed modulation, and $A_{\text{pre}}(0)$ is the known initial amplitude of the

preimposed modulation. Using the measurements of the laser nonuniformity, a measure of imprint efficiency[15] is defined as

$$\eta_i(k) = \frac{A_{\text{eq}}(k,0)}{(\delta I/I)},$$

where $\delta I/I$ is the fractional irradiation nonuniformity at the same wavelength.

The amplitudes of these perturbations are obtained using a Fourier analysis of the radiographed images. The Fourier amplitude of the imprint at a given wavelength is defined as the rms of all mode amplitudes at that wavelength, i.e., those modes at a given radius (centered at zero frequency) in frequency space. (The contribution of the preimposed modulation is not included.) The values are summed in quadrature because they are expected to be uncorrelated since they result from the random speckle in the laser. The analysis box is 300 μm in the target plane; thus, in Fourier space, the pixel size is 3.3 mm^{-1}. The pixels at radius 5±0.5 provide the amplitudes of modes with wavelengths between 55 μm and 67 μm, and those at 10±0.5 pixels provide amplitudes for wavelengths between 29 μm and 32 μm.

The preimposed single-mode modulations are two dimensional and possess localized features along a single axis in the Fourier plane at the spatial frequency of this modulation. Figure 80.12(a) depicts a typical radiographic image from these experiments; note that the vertical preimposed modulations are just visible in the mottled pattern produced by the laser imprint. The 2-D Fourier transform of this image after Weiner filtering[17] is shown as a surface plot in Fig. 80.12(b), where the signals from the preimposed modulations stand out from the broadband imprinted features that populate most of the 2-D Fourier space. Figure 80.12(c) depicts a one-pixel-wide annulus that illustrates how the amplitudes for the imprinting are measured. The ratio of the rms value of these amplitudes to that of the preimposed mode times the initial amplitude is used to determine the mass equivalence of imprinting of the control mode. (The box size is optimized for the preimposed mode, thereby ensuring that all the power in that mode is contained in the single pixel.)

For these experiments a variety of beam-smoothing techniques were used. A single-beam laser with only a distributed phase plate (DPP)[20] and no SSD provides a static speckle pattern with $\sim$80% to 100% nonuniformity in wavelengths from 2 μm to 250 μm.[21] The overlap of six beams reduces this

nonuniformity by $\sim \sqrt{6}$. SSD provides a time-varying reduction of the nonuniformity by continually shifting the DPP pattern on the target. The smoothing rate and the asymptotic smoothing level depend on the 2-D SSD bandwidth, which in this experiment is $\Delta \nu = 0.2$ THz$_{UV}$. In some cases, distributed polarization rotators (DPR's)[22] were added. These provide an instantaneous $\sqrt{2}$ reduction of nonuniformity[23] by separating each beam into two orthogonally polarized beams that are separated by 80 μm in the target plane.

Figure 80.13 shows the measured mass equivalence (in μm) of imprinting at 60-μm wavelength for all three smoothing conditions for the 3-ns square pulse in a series of shots with similar drive intensities. The temporal axis shows the time at which each frame was taken. The mass-equivalence data separate into distinct sets associated with each uniformity condition and are constant in time. Both observations are expected and confirm the utility of this technique. When the growth of the imprinted features are in the linear regime, they should remain a constant ratio of the amplitude of the preimposed mode, leading to a constant mass equivalence. This quantity's dependence on the initial uniformity produced by the various beam-smoothing techniques indicates the sensitivity of this method. For example, the addition of DPR's to the SSD experiments (open squares) reduces the mass equivalence by the expected factor of $\sqrt{2}$ (shaded squares).

The pulse shape's effect on imprinting was then studied by repeating these measurements with a slowly rising pulse, i.e., with an ~2.5-ns rise to the maximum intensity. Figure 80.14 shows the deduced mass equivalence as a function of time for the two pulse shapes, each with and without SSD. Again the data group according to laser conditions (pulse shape or SSD) and exhibit an approximately constant value over considerable times.

These data show that without SSD the ramp pulse produces about 50% more imprinting (higher mass equivalence) than the square pulse. They also indicate that although SSD produces a greater reduction of imprinting on the ramp pulse, the net imprint level after SSD is about the same for both pulses.

Similar experiments were performed using preimposed modulations with $\lambda = 30$ μm. Table 80.I lists the mass-equivalence results for all the experiments. In addition, the imprint efficiency was calculated for the experiments without SSD using the irradiation nonuniformities reported in Ref. 19. The uniformity results were scaled by the differences in analysis boxes between the radiography ($L = 300$ μm; $\Delta k = 0.021$) and the optical experiments ($L = 440$ μm; $\Delta k = 0.0143$). In addition, the values obtained in Ref. 19 were reduced by $\sqrt{6}$ since these experiments utilized six beams. Thus, $\delta I/I$ was 0.00684 for 30 μm and 0.00493 for 60 μm. Lastly, a factor of 2 was included to relate the complex amplitude for ΔI to the mass equivalence, which was normalized to a real cosine function. Since the SSD produces time-varying uniformity, it is difficult to assign a single number to the uniformity and hence the imprint efficiency is not calculated.

(a)   (b)   (c)

E9398

Image   FFT and Wiener filter   FFT ($\lambda = 60$ μm)
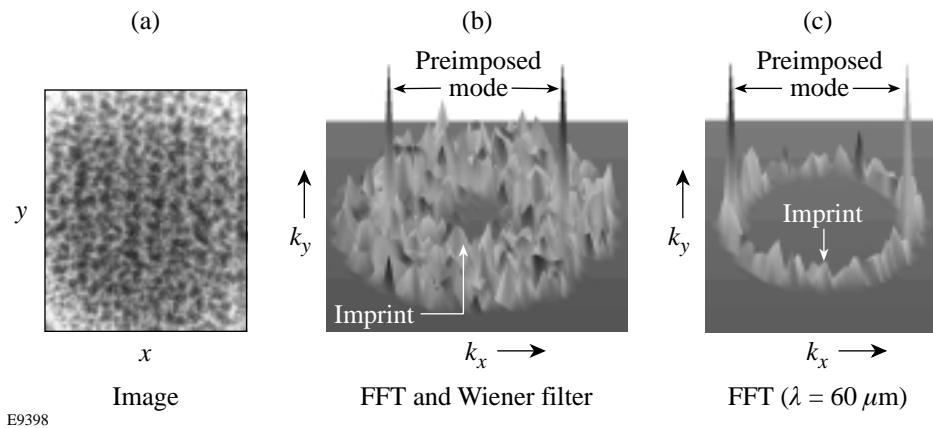
Figure 80.12
(a) Sample of an x-ray radiograph of a target with preimposed 60-μm-wavelength perturbations (vertical striations). The mottled pattern throughout the image is caused by the imprinted features. (b) Representation of the Fourier spectrum of the image in (a), showing the broadband imprinted features as well as two peaks from the preimposed single-mode modulations. (c) The annulus at 55 μm to 68 μm containing two components: the preimposed modulations and the imprinted features. The latter is used as a control feature to gauge the initial amplitude of the imprinted features.

As discussed above, thermal smoothing in the plasma ultimately terminates laser imprint. The duration of imprinting, then, depends on the time required to produce sufficient plasma atmosphere to enable smoothing. One would expect that, compared to the square pulse, the ramp pulse should imprint for a longer duration because the ramp pulse delivers energy at a slower rate and the smoothing plasma is produced more slowly, leading to larger mass equivalence. The imprint efficiencies measured here are lower than those observed by Glendinning et al.[12] for a slower rise and lower-intensity ramp pulse, as expected.

Simulations of the experiments were performed with the 2-D hydrodynamics code ORCHID[24] to determine the predicted imprint efficiency and the time that pressure perturbations at the ablation surface become negligible as the result of plasma smoothing. The imprint efficiencies were calculated by imposing a single-mode nonuniformity in the laser irradiation. The evolution of the resulting perturbations was compared to that of preimposed mass perturbations of the same wavelength. The experimental temporal pulse shapes were used in the simulations. The simulation results shown in Table 80.I are in reasonable agreement with the measured
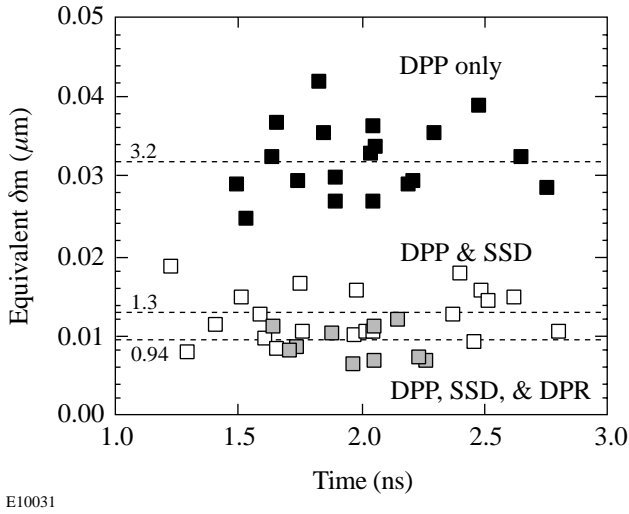
Figure 80.13
The mass equivalence (at 60 μm) derived from planar targets driven by laser beams having a 3-ns square pulse and three types of beam smoothing applied: DPP only (solid), DPP + SSD (open), and DPP + SSD + DPR (shaded). Note that the data segregate according to the laser nonuniformity. The mass equivalence is a measure of the total amount of imprinting, which is seen to decrease as greater beam smoothing is applied.
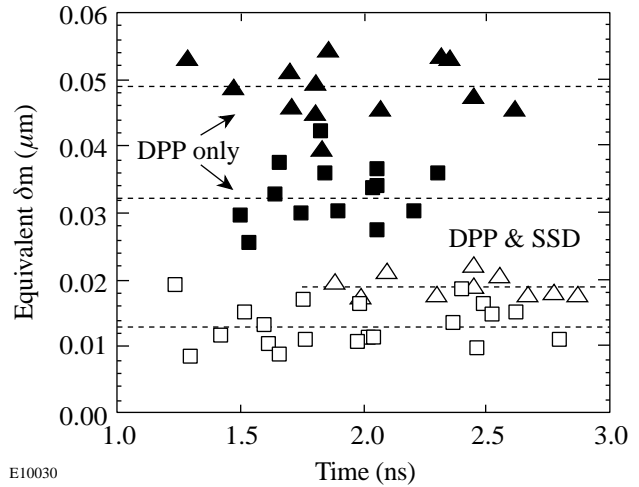
Figure 80.14
The deduced mass equivalence of the imprinted features (at 60 μm) for two pulse shapes: 3-ns square (squares) and ramp (triangles). These data show that for the same laser nonuniformity, a ramp pulse produces more imprinting. The solid and open symbols correspond, respectively, to each of the pulses without and with 2-D SSD. They indicate that the effect of SSD is greater for the ramp pulse, but the net imprint level is similar for the two pulses.

Table 80.I: Mass equivalence and imprint efficiency for various conditions.

Pulse-Shape Uniformity	Mass Equivalence (μm)		Imprint Efficiency: $\delta m/(\delta I/I)$ (μm)			
			Experiment		Simulation	
	60 μm	30 μm	60 μm	30 μm	60 μm	30 μm
Square (no SSD)	0.032±0.005	0.022±0.004	3.3±0.04	1.6±0.03	1.7	1.1
Ramp (no SSD)	0.049±0.008	0.023±0.005	5.0±0.06	1.7±0.04	3.1	2.3
Square (SSD)	0.013±0.003	0.010±0.003				
Ramp (SSD)	0.017±0.005	0.011±0.004				

values. Similar imprint efficiencies were calculated with the 2-D hydrodynamics code *LEOR*.[25] The 2-D simulations underestimate the efficiency at 60 μm, similar to the observations of Glendinning *et al.*[12]

The inherent surface roughness of these foils (transverse to the imposed modulations) was measured to be less than 1% of the imposed mode and, therefore, does not contribute significantly to the error in these measurements. One must consider, however, that the measured signal for the preimposed mode also has a contribution from the imprinted signal at that distinct mode. Since the relative phase of these two signals is arbitrary, the resultant signal can vary significantly when the imprint is a sizable fraction of the preimposed mode, as it is in the no-SSD cases.

Figure 80.15 shows the amplitude of the pressure perturbations (solid curves) at the ablation surface as a function of time for two cases: a ramp pulse and a square pulse, both without SSD. In these simulations a static 60-μm spatial-intensity perturbation of 5% was imposed on the irradiation intensity. Note that the smoothing rate is slower for the ramp pulse and the perturbations persist for a longer period. The temporal evolution (dashed curves) of the conduction zone (d_c) for the two pulse shapes is also shown. This is defined as the distance between the ablation surface and the mean of the energy deposition profile as weighted by a diffusion length: e^{-kz}.
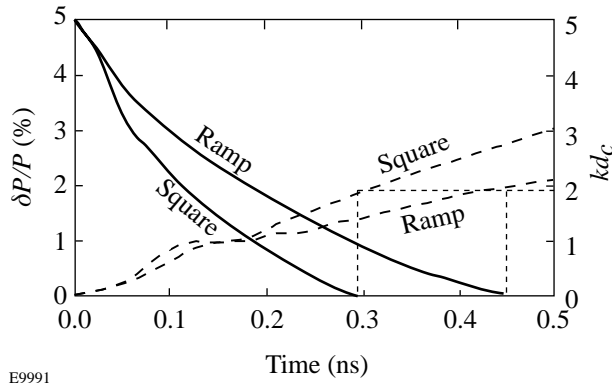
Figure 80.15
The amplitude of perturbations (solid lines) in the ablation pressure (at the ablation surface) as a function of time. The size of the conduction zone (dashed lines) as a function of time in CH targets driven by the square and ramp pulses. These graphs show that imprinting should stop at 300 ps for the square pulse and 450 ps for the ramp pulse. Note that for the square pulse the pressure perturbations are smoothed in 300 ps while for the ramp pulse this occurs at 450 ps.

Imprinting is expected to cease when pressure perturbations at the ablation surface are reduced to negligible levels. Figure 80.15 shows that this occurs for both pulse shapes when d_c ~2. Simple considerations of the distance between critical and ablation surfaces are insufficient to explain the behavior of the two pulses; rather the energy deposition profiles must also be accounted for because considerable smoothing can take place in the plasma region outside the critical surface.

When 2-D SSD is employed, the uniformity at $t = 0$ is the same as without SSD and reduces rapidly in time as $1/\nu$, where ν is the laser bandwidth. For these experiments the UV bandwidth is ~0.2 THz. While at this bandwidth the asymptotic smoothing level for 60 μm is reached in ~1.2 ns,[21] considerable smoothing occurs in less than 400 ps. The experimental results are consistent with this since SSD reduces the imprint for both pulse shapes, although there is greater reduction for the ramp pulse. Since imprinting in the ramp pulse lasts longer, SSD is able to provide greater benefit. The resulting imprint is similar for both pulses with SSD because the effective smoothing time for SSD is shorter than the duration of imprinting for both pulse shapes. Thus, significant SSD smoothing occurs before a large-enough conduction zone is produced. The calculated reduction of the mass equivalence with SSD present is somewhat larger (~60%) than the experimental observations.

This work has shown that for identical nonuniformities, the imprint level depends on the pulse shape, as expected. The total imprinting depends on the irradiation nonuniformity, the imprint efficiency, and the duration of imprint. Since the latter varies with pulse shape and other laser conditions, imprint efficiency cannot be considered invariant. These quantities are also laser wavelength dependent.[10,11] In addition, other processes such as shinethrough and laser–plasma instabilities (filamentation) could alter the intensity distribution within the plasma.

Preimposed modulations have been used as a reference to determine the mass equivalence of features imprinted by a drive laser. This technique behaves linearly under the experimental conditions described here. Slowly rising pulses produce more imprint and experience more smoothing because of SSD than steeply rising pulses. This is a result of the different rates at which smoothing plasma is initially formed, which ultimately determines the duration of imprinting. Numerical simulations confirm this physical picture and yield imprint efficiencies in reasonable agreement with the measured values.

REFERENCES

1. J. Nuckolls *et al.*, Nature **239**, 139 (1972).

2. J. D. Lindl, Phys. Plasmas **2**, 3933 (1995).

3. S. E. Bodner *et al.*, Phys. Plasmas **5**, 1901 (1998).

4. G. Taylor, Proc. R. Soc. London, Ser. A **201**, 192 (1950); Lord Rayleigh, Proc. London Math. Soc. **XIV**, 170 (1883).

5. S. Skupsky and R. S. Craxton, Phys. Plasmas **6**, 2157 (1999).

6. M. Desselberger *et al.*, Phys. Rev. Lett. **68**, 1539 (1992).

7. D. H. Kalantar, M. H. Key, L. B. DaSilva, S. G. Glendinning, J. P. Knauer, B. A. Remington, F. Weber, and S. V. Weber, Phys. Rev. Lett. **76**, 3574 (1996).

8. S. G. Glendinning, S. N. Dixit, B. A. Hammel, D. H. Kalantar, M. H. Key, J. D. Kilkenny, J. P. Knauer, D. M. Pennington, B. A. Remington, R. J. Wallace, and S. V. Weber, Phys. Rev. E **54**, 4473 (1996).

9. R. J. Taylor *et al.*, Phys. Rev. Lett. **76**, 1643 (1996).

10. H. Azechi *et al.*, Phys. Plasmas **4**, 4079 (1997).

11. C. J. Pawley *et al.*, Phys. Plasmas **4**, 1969 (1997).

12. S. G. Glendinning, S. N. Dixit, B. A. Hammel, D. H. Kalantar, M. H. Key, J. D. Kilkenny, J. P. Knauer, D. M. Pennington, B. A. Remington, J. Rothenberg, R. J. Wallace, and S. V. Weber, Phys. Rev. Lett. **80**, 1904 (1998).

13. T. R. Boehly, D. L. Brown, R. S. Craxton, R. L. Keck, J. P. Knauer, J. H. Kelly, T. J. Kessler, S. A. Kumpan, S. J. Loucks, S. A. Letzring, F. J. Marshall, R. L. McCrory, S. F. B. Morse, W. Seka, J. M. Soures, and C. P. Verdon, Opt. Commun. **133**, 495 (1997).

14. K. A. Brueckner and S. Jorna, Rev. Mod. Phys. **46**, 325 (1974).

15. S. V. Weber, S. G. Glendinning, D. H. Kalantar, M. H. Key, B. A. Remington, J. E. Rothenberg, E. Wolfrum, C. P. Verdon, and J. P. Knauer, Phys. Plasmas **4**, 1978 (1997).

16. R. J. Taylor *et al.*, Phys. Rev. Lett. **79**, 1861 (1997).

17. V. A. Smalyuk, T. R. Boehly, D. K. Bradley, J. P. Knauer, and D. D. Meyerhofer, Rev. Sci. Instrum. **70**, 647 (1999).

18. S. W. Haan, Phys. Rev. A **39**, 5812 (1989).

19. V. A. Smalyuk, T. R. Boehly, D. K. Bradley, V. N. Goncharov, J. A. Delettrez, J. P. Knauer, D. D. Meyerhofer, D. Oron, and D. Shvarts, Phys. Rev. Lett. **81**, 5342 (1998); V. A. Smalyuk, T. R. Boehly, D. K. Bradley, V. N. Goncharov, J. A. Delettrez, J. P. Knauer, D. D. Meyerhofer, D. Oron, D. Shvarts, Y. Srebro, and R. P. J. Town, Phys. Plasmas **6**, 4022 (1999).

20. Y. Lin, T. J. Kessler, and G. N. Lawrence, Opt. Lett. **20**, 764 (1995).

21. S. P. Regan, J. Marozas, J. H. Kelly, T. R. Boehly, W. R. Donaldson, P. A. Jaanimagi, R. L. Keck, T. J. Kessler, D. D. Meyerhofer, W. Seka, S. Skupsky, and V. A. Smalyuk, "Experimental Investigation of Smoothing by Spectral Dispersion," submitted to the Journal of the Optical Society of America B. This article also appears in Laboratory for Laser Energetics Review **79**, 149, NTIS document No. DOE/SF/19460-317 (1999). Copies may be obtained from the National Technical Information Service, Springfield, VA 22161.

22. Y. Kato, unpublished notes from work at LLE (1984); Laboratory for Laser Energetics LLE Review **45**, 1, NTIS document No. DOE/DP40200-149 (1990). Copies may be obtained from the National Technical Information Service, Springfield, VA 22161.

23. T. R. Boehly, V. A. Smalyuk, D. D. Meyerhofer, J. P. Knauer, D. K. Bradley, R. S. Craxton, M. J. Guardalben, S. Skupsky, and T. J. Kessler, J. Appl. Phys. **85**, 3444 (1999).

24. R. L. McCrory and C. P. Verdon, in *Inertial Confinement Fusion*, edited by A. Caruso and E. Sindoni (Editrice Compositori, Bologna, Italy, 1989), p. 83.

25. D. Shvarts, U. Alon, D. Ofer, R. L. McCrory, and C. P. Verdon, Phys. Plasmas **2**, 2465 (1995).

The Output Signal-to-Noise Ratio of a
Nd:YLF Regenerative Amplifier

A regenerative amplifier (regen) is a common element in a variety of laser systems because of its compactness and ability to significantly boost the energy of an optical pulse with minimal temporal distortion and added noise.[1,2] Net gains of the order of 10^8 are easily obtainable. Noise is the unwanted portion of the optical signal that can originate from stochastic or deterministic processes within the system. For some applications, even small amounts of noise are an important concern. One such application is laser fusion, where an optical pulse with less that 1 nJ of energy is amplified with an overall net gain of approximately 10^{14} to the 60-kJ level, frequency tripled to a 351-nm wavelength, and focused onto fusion targets. In such a system, even a relatively small amount of prepulse signal can be detrimental to target performance; therefore, to minimize the prepulse noise signal it is very important to control and maximize the signal-to-noise ratio (SNR) at every step of the amplification process.

In this article we present measurements of the output SNR (defined as the ratio of the peak power of the amplified signal to the average power of the prepulse noise) of a regen used as the first amplification stage in the OMEGA laser system. We compare our measurements to a simple theoretical model that we developed. We find that the prepulse noise signal in the output of our regen has two main contributions: one is due to the intrinsic noise generated within the regen during the amplification process, as studied previously,[2] and the other is due to the prepulse signal on the optical pulse injected into the regen. Our model of the regen output SNR includes both contributions. We experimentally demonstrate that the regen output SNR can be very high for an injected pulse with low noise. We also demonstrate that, in general, the regen output SNR equals the SNR of the pulse injected into the regen in the limit of strong signal injection. Our measurements are in excellent agreement with our theoretical model.

Theory

The total optical power circulating in the regen evolves according to the equation[3]

$$\frac{dP}{dt} = \gamma\, P(t) + \gamma\, N_{\text{se}}, \tag{1}$$

where γ is the exponential net gain coefficient, P is the optical power circulating in the regen, and N_{se} is phenomenologically included as the noise power in the regen due to spontaneous emission. Equation (1) can be integrated to give

$$P(t) = G\, P_0 + G\, N_{\text{inj}} + N_{\text{se}}(G-1), \tag{2}$$

where $G = \exp(\gamma t)$ is the net gain of the regen, P_0 is the signal power injected into the regen, and

$$N_{\text{inj}} = \frac{P_0}{\text{SNR}_{\text{in}}} \tag{3}$$

is the noise on the signal injected into the regen with SNR_{in} the signal-to-noise ratio of the signal injected into the regen.

It is instructive to describe each term on the right-hand side of Eq. (2). The first term simply represents amplification of the injected signal into the regen and is the regen output signal in the absence of noise. The second and third terms are noise terms. The second term is the amplified injected noise power that describes the amplification of the noise injected into the regen with the optical pulse. The third term is due to the amplification of the spontaneous emission noise generated by the regen itself. The output SNR of the regen is then given by

$$\text{SNR}_{\text{out}} = \frac{P_0}{N_{\text{se}}(1-1/G) + N_{\text{inj}}}. \tag{4}$$

For most cases of practical interest the total net gain is much greater than unity ($G \gg 1$). If the injected noise power is much less than the spontaneous emission noise power ($N_{\text{inj}} \ll N_{\text{se}}$), the second term in the denominator can be neglected and the output SNR of the regen is proportional to the power injected into the regen. For the case where the injected noise power is

much greater than the spontaneous emission noise power ($N_{\text{inj}} \gg N_{\text{se}}$), the first term in the denominator can be dropped. In this case the output SNR_{out} of the regen equals the injected SNR_{in} and is independent of the amount of injected signal power. This model of the regen output SNR is verified by the experiments described below.

Experimental Results

Experiments have been performed to verify the above theory. The details of the regen operation are given elsewhere.[4,5] A pulse is injected into the regen and allowed to evolve until the circulating pulse energy reaches a threshold value. Losses are then introduced in the cavity to maintain the round-trip gain at unity. Later, the cavity losses are removed, and a Q-switched train of amplified pulses separated by the regen cavity round-trip time of 26 ns evolves. In our experiment we define the regen output SNR as the ratio of the peak power of a pulse in the pulse train to the power measured between this pulse and an adjacent pulse (i.e., the interpulse noise). This definition is illustrated schematically in Fig. 80.16.

To measure the output SNR of our regen, a high-contrast (>1000:1) Pockels cell with a 10-ns square transmission func-

Signal-to-noise ratio: $\text{SNR} = \dfrac{P}{N_{\text{inj}} + N_{\text{se}}}$

E10034
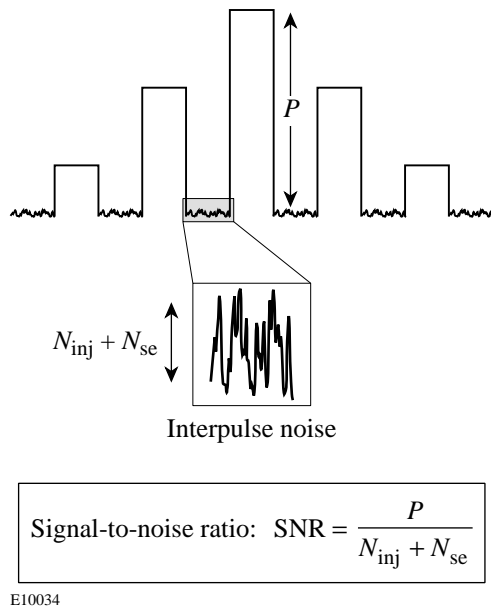
Figure 80.16
Signal-to-noise ratio (SNR) measurement setup. The regen output SNR is defined as the ratio of the power of the injected pulse averaged over a cavity round-trip time to the noise power measured between two regen output pulses.

tion is used to select the output power of the regen at various times in the output-pulse train. The timing of the Pockels cell transmission window is first adjusted to pass a single optical pulse from the regen output. The pulse is attenuated and sent to a photodetector, and the peak voltage of the detector is measured and recorded as the regen signal. The Pockels cell transmission window is then moved in time by 13 ns, which is half the regen round-trip time, in order to measure the interpulse noise power between this pulse and the previous pulse in the regen output-pulse train. The calibrated attenuation is removed from the detector, and the average voltage of the photodetector over a portion (~2 ns) of the 10-ns Pockels cell transmission window is measured and recorded as the regen noise power. The overall bandwidth of our measurement system is approximately 1 GHz. These measurements are made as the power of the injected signal is varied. In this way the regen output SNR is recorded versus the power of the injected signal.

The pulse injected into the regen is generated with two integrated electro-optic modulators.[6] We apply a square electrical pulse to each modulator synchronous with the transmission through the modulator of an optical pulse from a single-longitudinal-mode (SLM) laser. The transmission function of a dual-channel modulator in this case is given by

$$I_{\text{out}}(t) = I_{\text{in}}(t) \, \sin^4\left\{ \frac{\pi}{2}\left[\frac{V(t) + V_{\text{dc}}}{V_\pi} \right] + \phi \right\}, \qquad (5)$$

where $I_{\text{in}}(t)$ is the intensity profile at the modulator input, $V(t)$ is the modulation voltage applied to each channel of the modulator, V_π is the half-wave voltage of the modulator (~10 V), ϕ is a constant phase shift, and V_{dc} is a dc voltage that can be applied to cancel the constant phase shift. Square electrical pulses of 3-ns duration with amplitude V_π are synchronously applied to both channels of the modulator. The short-duration voltage waveforms are applied to the modulator during the peak of the 200-ns Gaussian pulse sent into the modulator from the SLM laser. For this reason, the input-intensity profile to the modulator, $I_{\text{in}}(t)$, is assumed to be a constant independent of time. The resulting 3-ns square optical pulse from the modulator is injected into the regen.

A dc bias voltage (V_{dc}) is applied to the modulators to compensate the constant phase term in Eq. (5). When optimally compensated in this way, the modulators provide "zero" transmission for zero applied modulation voltage. This results in a high-contrast pulse (that is, very low prepulse signal) from the modulator. For our experiments, we alter SNR_{in} of the pulse

injected into the regen by changing the dc bias voltage (V_{dc}). As the dc bias voltage is varied away from the high-contrast value, light from the SLM laser leaks through the modulator prior to and after the 3-ns optical pulse. The ratio of the peak power in the 3-ns optical pulse from the modulator to the prepulse (postpulse) power from the modulator is our definition of the SNR_{in} of the pulse injected into the regen. With this definition, the SNR_{in} depends only on the dc-applied voltage to the modulators and is calculated from Eq. (5). This prepulse and postpulse power injected into the regen is the nature of the regen interpulse noise given by the second term in the denominator in Eq. (4). Varying the dc-applied voltage to the modulators varies the SNR of the injected pulse into the regen. The injected power into the regen is varied by attenuating the optical pulse at the input to the modulator.

Measurements of the output SNR of a regen versus the injected power into the regen are shown in Fig. 80.17. For the three curves, the injected SNR was varied as indicated. Using Eq. (4), plots of the regen output SNR are overplotted with the data. To obtain best fits to the data we used 375 nW for N_{se} in all plots, and to determine SNR_{in} we used our measured dc voltages applied to the modulators in Eq. (4). As seen in Fig. 80.17, our measurements are in excellent agreement with theory.
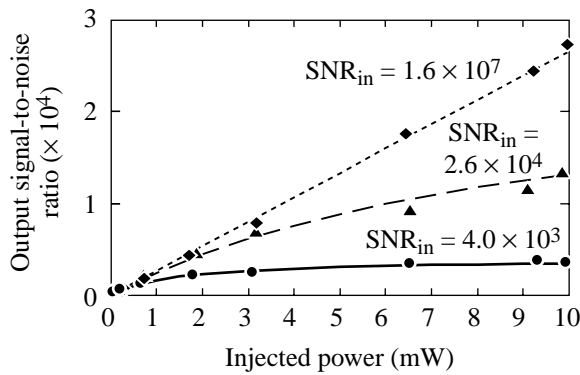
Figure 80.17
Signal-to-noise ratio measurements at the output of a regen versus the injected power into the regen for three values of the SNR of the injected power into the regen.

Separate measurements were made to estimate the amount of equivalent spontaneous-emission noise power, N_{se}, in the regen. A pulse was injected into the regen and the buildup time for the pulse to reach a power level of ~100 W in the regen was measured for different power levels of the injected signal. In Fig. 80.18 the average power of the injected pulse is plotted on a semi-log scale versus the buildup time in the regen. From Eq. (2) and $G \gg 1$ the time t_1 for the regen output power to reach a fixed predetermend power level P_1 is given by

$$t_1 = \frac{\ln P_1 - \ln\left(P_0 + N_{inj} + N_{se}\right)}{\gamma}. \tag{6}$$

When the injected signal power into the regen is much greater that the spontaneous-emission noise power ($P_0 \gg N_{se}$), the buildup time t_1 exhibits an exponential dependence on the injected power P_0. The logarithmic fit to the experimental data points in Fig. 80.18 reveals good agreement with this theory. From this logarithmic fit we can estimate N_{se} by using the measured buildup time of 789 ns for the case with no signal injected into the regen. From this we estimate N_{se} to be approximately 80 nW, which is within a factor of 5 of the 375-nW value that was used to obtain the best fit to our data in Fig. 80.17.
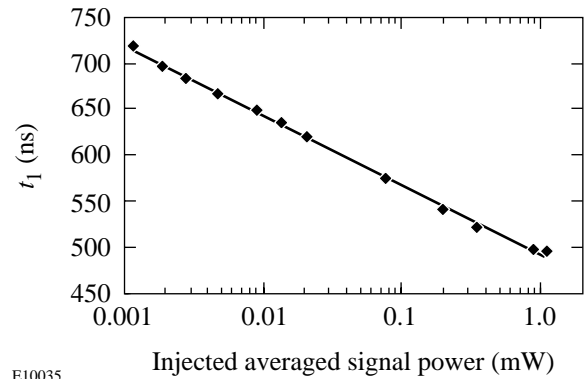
Figure 80.18
Measured time t_1 required for the regen output to reach a preset power level versus averaged power of the pulse injected into the regen. The power of the injected pulse was averaged over one regen round-trip.

Conclusions

We measured the output SNR of a regen and compare our measurements to a simple model that we developed. We show that the noise in the output of a regen has two contributions: one is due to amplified spontaneous emission; the other is due to noise (in our case in the form of a prepulse) injected into the regen. We simulate noise on the input pulse to the regen and conclude from our measurements that the regen output SNR saturates to the SNR of the pulse injected into the regen. We measured an output SNR from the regen as high as 2.7×10^4.

REFERENCES

1. W. H. Lowdermilk and J. E. Murray, J. Appl. Phys. **51**, 2436 (1980); **51**, 3548 (1980).

2. W. Koechner, *Solid-State Laser Engineering*, 3rd rev. ed., Optical Sciences Series, Vol. 1 (Springer-Verlag, New York, 1992).

3. A. Yariv, *Optical Electronics*, 4th ed. (Saunders College Publishing, Philadelphia, 1995).

4. A. Babushkin, W. Bittle, S. A. Letzring, M. D. Skeldon, and W. Seka, in *Third International Conference on Solid State Lasers for Application to Inertial Confinement Fusion*, edited by W. H. Lowdermilk (SPIE, Bellingham, WA, 1999), Vol. 3492, pp. 124–130.

5. M. D. Skeldon, A. Babushkin, W. Bittle, A. V. Okishev, and W. Seka, IEEE J. Quantum Electron. **34**, 286 (1998).

6. Modulator technical data at http://www.crisel-instruments.it/alemia/html/index01.htm.

Development of New Magnetorheological Fluids
for Polishing CaF$_2$ and KDP

Magnetorheological finishing (MRF) is a novel and recently commercialized[1] process for figuring and polishing plano, convex, and concave optics—both spherical and aspherical—from a wide variety of optical materials. A recently written review article provides an overview of the history, theory, and implementation of this technology.[2] The utility and productivity of MRF have been proven for a wide spectrum of optical glasses and demonstrated for a variety of non-glass optical materials.[3,4] A 1.0-nm smoothness with removal rates of 1 to 10 μm/min is routinely achieved. Seven years of research and development culminated in 1998 with QED Technologies' introduction of a commercial MRF machine, designated the Q22. A focus of continuing research is the development of MR fluid compositions and operating parameters to finish optical materials with an ever-widening range of physical properties. Efforts are simultaneously made to extend our understanding of the fundamental mechanisms of material removal in the MRF process. Extremely hard, extremely soft, single-crystal, polycrystalline, or water-soluble optical materials—each presents unique challenges to the MRF process.

A magnetorheological (MR) fluid is a suspension of magnetically soft ferromagnetic particles in a carrier liquid. Typically, the particles are of the order of a few microns in diameter, and their volume concentration is 30% to 40%. When exposed to a magnetic field, the viscosity and yield stress of the suspension increase several orders of magnitude. The transition is rapid and reversible. The magnetically soft media used to manufacture MR fluids, which are subsequently used in MRF, are carbonyl iron (CI) powders. They are prepared by decomposing iron pentacarbonyl,[5] resulting in spherical particles of almost pure iron, typically 2 to 6 μm in diameter. Incorporating nonmagnetic polishing abrasives results in an MR polishing fluid that can be manipulated to form a renewable and compliant sub-aperture lap for optical finishing.

MRF Research Platforms and Polishing Spots

The Center for Optics Manufacturing (COM) has two research platforms to facilitate the continuing research of MRF: The first, commonly known as the horizontal trough machine, was the basis of the first prototype MRF machine (described and shown in Fig. 1 of Ref. 2), which is still routinely used but without the fluid circulation system. The MR fluid resides in a rotating horizontal trough. The test optic must be spherical convex. While technically overshadowed by newer machines, it continues to be very productive. Experiments can be conducted with only about 100 ml of MR fluid. In addition, the machine can be quickly cleaned to prepare for another experiment. This is particularly useful for screening experiments of new nonaqueous compositions.

A new research platform, designated the spot-taking machine (STM), was designed and constructed by QED Technologies and installed at COM in August 1998 (a photograph of this machine is shown in Fig. 80.19). The MR fluid circulation and conditioning system and rotating wheel are identical to that of the commercial MRF machine. The electromagnet and pole pieces are the same as those on the Q22 with one exception: the pole pieces on the Q22 are tapered downward when moving away from the center to create more clearance when polishing concave optics. The conditioner mixes the MR fluid, maintains its temperature, and monitors and controls its viscosity.

The fluid, typically at an apparent viscosity between 0.04 and 0.1 Pa•s (40 to 100 cps, at a shear rate of ~800 s^{-1}), is delivered through a nozzle by a peristaltic pump onto the surface of the vertical rotating wheel moving at approximately 1 m/s. The wheel is a section of a 150-mm-diam sphere. As the MR fluid ribbon is carried into the magnetic field, the fluid viscosity increases approximately three orders of magnitude in a few milliseconds and becomes a Bingham plastic fluid.[1,2] The high gradient of the magnetic field has the effect of segregating a portion of the nonmagnetic polishing abrasive to the upper layer of the polishing ribbon.[1,6] The surface of the optic is inserted typically 0.5 mm into the ribbon at this point on the wheel, forming a continuously renewed compliant sub-aperture lap. After flowing under the optic, the wheel carries the fluid out of the magnetic field, where it returns to its original low-viscosity state. A collection device removes the
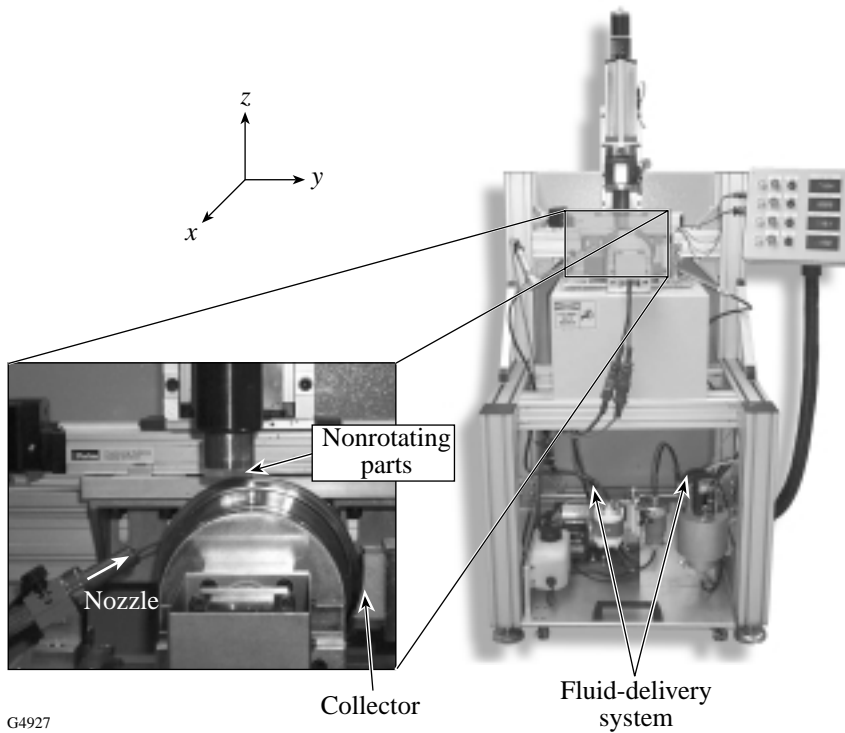
Figure 80.19
A new MRF research platform, the spot-taking machine, incorporates the same fluid-delivery system and vertical wheel as the commercial MRF machine.

fluid from the wheel and returns it to the conditioning system. A typical charge for the system is 1 liter of fluid, which lasts for two weeks of operation.

The STM has a single z-axis controller (see Fig. 80.19) to position a test flat into the ribbon for a programmed length of time, typically just a few seconds, and then remove it. The y-axis position (parallel to the ribbon) and spindle rotation can be manually adjusted to put multiple spots on a given test flat. The small volume removed, measured interferometrically, is called a "spot" or removal function. Figure 80.20 shows examples of interferograms of spots on two test flats.

By analyzing spots made with these two research platforms we can make critical evaluations on candidate MR fluid compositions. The dimensions of the spots can be measured interferometrically[7] to calculate material-removal rates and measure spot profiles. The surface texture within the spot can be optically profiled[8] to quantify microroughness and reveal surface defects. This information is then used to make informed decisions regarding changes to the fluid composition and/or machine parameters. In addition, the fluid is observed to see that it can be successfully pumped through the delivery system and that it forms a stable ribbon.
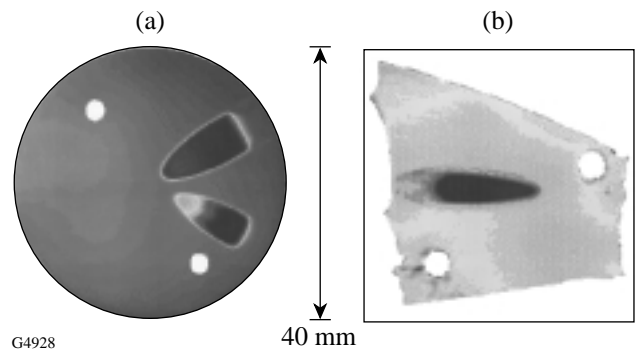
Figure 80.20
(a) An example of an interferogram of two spots made on a CaF$_2$ test flat. (b) An interferogram of a spot made on a shard broken from a larger plate of KDP. Fiducial marks are used to align interferograms of the original and spotted test flat. Subtraction of the original from the spot interferogram gives the removal function.

One advantage of MRF is the range of operating parameters that can be manipulated to influence the characteristics of the removal function. These include

- MR fluid composition: Carbonyl iron type and concentration, nonmagnetic abrasive type and concentration, carrier fluid and stabilizers can all be adjusted. For aqueous compositions, the MR fluid viscosity can be changed in real-time by adding or removing water.

- Magnetic field: Increasing the magnetic field increases both the stiffness of the ribbon and the removal rates. The practical upper limit is near the saturation magnetization of the magnetic particles. The practical lower limit is where the ribbon is not held tightly against the wheel, resulting in uneven flow under the optic.

- Wheel speed: The removal rate is proportional to the wheel speed. A typical value is 150 rpm but it can be varied from 100 to 400 rpm (0.79 to 3.15 m/s, 150-mm-diam wheel).

- Nozzle: Nozzles with different diameter and shaped orifices can be installed. The standard nozzle is circular and 3 mm in diameter.

- Ribbon height: Increasing the flow rate, typically between 0.5 and 1.0 liter/min, increases the height, or thickness, of the ribbon for a given wheel speed. A typical height is 1.0 to 2.0 mm.

- Depth (inversely, gap): Decreasing the gap between the optic and the wheel increases the depth of penetration into the ribbon and increases the area, or footprint, of the spot.

This range of operating conditions permits many options when conducting experiments on a wide variety of optical materials.

MRF of CaF$_2$ and KDP

In this article we present details of recent work to adapt MRF to two soft, single-crystal optical materials: calcium fluoride, CaF$_2$, and potassium dihydrogen phosphate, KH$_2$PO$_4$ or KDP. It was necessary to formulate two new magnetorheological fluid compositions in order to successfully apply MRF to these two materials. The standard MR fluid, suitable for a wide variety of optical materials, consists of (in vol %) 36% CI, 55% water, 6% cerium oxide, and 3% stabilizers. CaF$_2$ is incompatible with the standard MR fluid typically used for optical glasses, resulting in "sleeks" and unacceptable roughness. KDP is extremely water soluble and therefore also cannot be finished with the standard aqueous MR fluid. Some mechanical properties for these two materials are compared to typical optical glasses in Table 80.II.

Results with CaF$_2$

Single-crystal calcium fluoride is the optical material that is expected to meet the projection and illumination requirements for photolithography optics as the semiconductor industry begins the transition from 365 and 248 nm to 193 and 157 nm.[15] CaF$_2$ crystals are fairly soft, so the polishing technique used must carefully reduce surface roughness without creating surface sleeks or fine scratches. These defects can lead to scattering, subsurface damage, and microscopic flaws in a coated surface.[16] In addition, CaF$_2$ is thermally sensitive, anisotropic, and easily chipped. Manufacturing large optics, such as 100-mm catadioptic cubes or 400-mm refractive lenses, by conventional means is nontrivial.[17,18] A $\lambda/10$ flatness specification at 193 nm is more than three times tighter than a $\lambda/10$ specification at 633 nm.[18] Fortunately, as discussed elsewhere,[2] one of the greatest strengths of MRF is its ability to deterministically finish optics to very high precision.

Table 80.II: Physical properties of CaF$_2$ and KDP compared to typical optical glasses.

Material	Source	Structure	Water solubility (g/100 g)	Near-surface hardness (GPa)	Young's modulus (GPA)	Fracture toughness (MPa-m$^{0.5}$)
KDP	Cleveland Crystals, Inc.	single-crystal tetragonal, type-II cut	33 (Ref. 10)	2.16 (Ref. 14)	49.2 (Ref. 14)	0.1-0.2 (Ref. 13)
CaF$_2$	Optovac, Inc.	single-crystal cubic c-cut	0.0017 (Ref. 9)	2.47 (Ref. 14)	110 (Ref. 12)	0.33 (Ref. 12)
BK-7	Schott, Ohara	glass	insoluble	7.70 (Ref.14)	79.6 (Ref. 14)	0.85 (Ref. 11)
Fused silica	Corning	glass	insoluble	9.79 (Ref. 14)	74.7 (Ref. 14)	0.75 (Ref. 11)

The initial strategy for developing an MR fluid for polishing CaF$_2$ called for the replacement of cerium oxide as the nonmagnetic abrasive and making the fluid more gentle due to the softness of this material. Toward this end, many fluid compositions were screened with spot experiments using the horizontal trough machine. For all of the experiments with CaF$_2$, the test optics were initially pitch polished to an average rms roughness of 0.85±0.05 nm. Compositions containing (in vol %) 36% CI, 25% PEG 200, 38% water, <1% stabilizers, and then a fraction of a percent of nanodiamond powder[19] were tested to determine material-removal rates and microroughness. PEG 200[20] was included because of its lubricious behavior, which was intended to protect the surface from scratching and eliminate embedded particles. Figure 80.21 is a plot of the peak removal rate for a range of nanodiamond concentrations. The removal rate rises quickly with nanodiamond concentration but rolls over above ~0.1 vol %. The roughness values within the generated spots varied from 1.0 to 1.65 nm and showed no clear trend as a function of nanodiamond concentration.
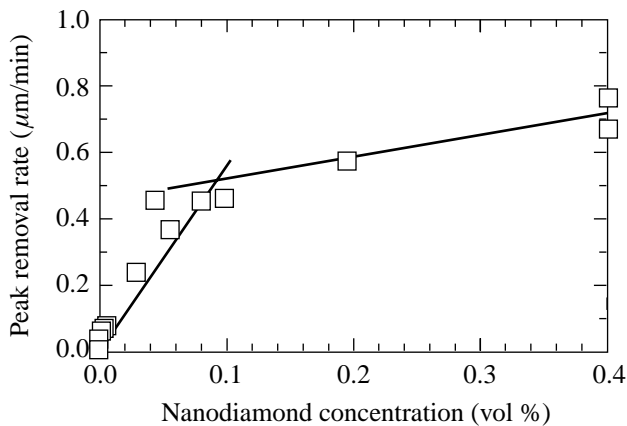
G4929

Figure 80.21
Plot of peak removal rate for CaF$_2$ versus nanodiamond concentration on the trough machine for MR fluid containing 36% CI, 25% PEG 200, 38% water, and <1% stabilizers.

Although it is possible to magnetorheologically finish CaF$_2$ to low roughness values with compositions containing PEG 200 and nanodiamonds, the very low peak removal rates observed encouraged us to revisit water-based compositions. For this reason, we tested a MR fluid containing (in vol %) 48% CI, 49% water, 3% stabilizers, and ~0.2% nanodiamond powder. This slurry composition had been developed and previously tested for MRF of very hard materials, such as SiC and sapphire, and was found to be rheologically stable. Spots made on the horizontal trough machine at a 3.0-kG magnetic field strength resulted in a very stiff ribbon and very high

peak removal rates > 8 μm/min; however, the rms roughness values were consistently ~2.0 nm. Decreasing the magnetic field strength to 0.85 kG decreased the peak removal rate to 1.3 μm/min but also decreased the rms roughness to ~1.25 nm. This indicated that decreasing the magnetic field strength and decreasing the stiffness of the fluid ribbon would produce lower values of surface roughness.

The same composition was next tested in the STM. Spots were made at three levels of magnetic field strength. At a value of 0.34 kG, it was discovered that the ribbon was very soft and formed a large, ill-defined spot. The peak removal rate was an acceptable 1.6 μm/min, but the spot shape was not usable. Increasing the magnetic field strength to 0.98 kG produced a stiffer ribbon and well-defined spot. The resulting peak removal rate was very high, 7.8 μm/min, and the average rms roughness was very good at 1.00±0.06 nm. At 1.85 kG the peak removal rate increased even further to 11.8 μm/min, and the rms roughness was slightly higher at 1.15±0.06 nm. (These results are summarized in Table 80.III.) Extended life testing in the STM and the Q22 confirmed the composition to be sufficiently stable over time for polishing trials.

Table 80.III: Peak removal rate and roughness for MRF spots on CaF$_2$ at various magnetic field strengths.

Magnetic field (kG)	Peak removal rate (μm/min)	Microroughness
0.34	1.6	poor spot shape
0.98	7.8	1.00±0.06
1.85	11.8	1.15±0.06

Results with KDP

KH$_2$PO$_4$, or KDP, is an important electro-optic material. It is currently used for frequency conversion of LLE's OMEGA laser. It will be part of the National Ignition Facility's laser under construction at Lawrence Livermore National Laboratory. It is also commonly used in electro-optic devices such as Pockels cells.[10]

Polishing KDP poses several difficult challenges: KDP is expensive in large sizes. It is difficult to polish high-aspect-ratio KDP flats with conventional pitch-lapping techniques. KDP is extremely soluble in water. To magnetorheologically finish KDP, the MR fluid carrier liquid must be nonaqueous, and it must be possible to clean the MR fluid off of the optic with a KDP-compatible solvent. Finally, KDP is very soft with

a near-surface hardness of 2.16 GPa (Berkovich microindentor, 5-nN load).

Currently, single-point diamond turning (SPDT) is considered state of the art for finishing KDP, yielding surfaces with 1.0- to 3.0-nm rms roughness.[21] This process is capable of producing 30-cm-diam flat plates for use in large laser systems. SPDT is done by showering mineral oil over the workpiece. This provides lubricity for cutting and helps to control temperature. The oil is removed from the KDP surface with toluene or xylene.

Many oil-based MR fluid compositions have been developed for use in mechanical engineering applications.[6] For practical reasons, it is highly desirable to use a carrier fluid that is nonflammable and capable of being cleaned out of a MRF machine with aqueous-based detergents. During the search for an MR fluid for KDP, chemical compatibility issues became a serious concern. A number of tested water-miscible fluids were found to leave a "fog" on the surface of KDP. (Results of compatibility tests are summarized in Table 80.IV.) Even just a few minutes of contact with 200-proof ethanol transfers enough moisture from the air to leave visible defects on the surface of a KDP flat. Several otherwise-promising MR fluid compositions had to be discarded for this reason. After numerous trials, the base composition found to produce the best results with KDP consisted of (in vol %) 40% CI and 60% dicarboxylic acid ester. This carrier liquid has a very low vapor pressure, does not evaporate, and is easily cleaned out of the STM. This nonaqueous MR fluid is shear-thinning with a viscosity of 0.09 Pa•s (90 cps) at a shear rate of 800 s^{-1} (approximately the shear rate for the fluid in the delivery nozzle of the STM).

The results reported in this article were obtained on surfaces of KDP that were initially prepared by single-point diamond turning.[22] The average rms roughness of this initial surface (five measurements over five sites[8]) was 1.5±0.2 nm. A representative optical roughness map of the initial diamond-turned surface is shown in Fig. 80.22. The turning marks are clearly visible.

Spots were first made with the MR fluid without any nonmagnetic abrasive under a fixed set of conditions.[23] An example of profile scans of a spot[7] are shown in Fig. 80.23. The peak removal rate, calculated from a depth of deepest penetration of the spot, 0.53 μm, was 1.59 μm/min. The rms microroughness was increased to 6.4±0.8 nm. Figure 80.24 gives an optical roughness map of the surface within this spot. The grooves from the flow of the MR fluid are clearly visible.

G4930
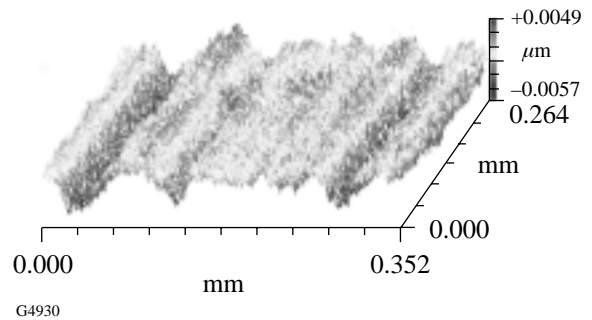
Figure 80.22
Representative optical roughness map[8] of the initial single-point-diamond-turned surface of KDP used for these experiments. The diamond-turning marks are clearly visible. Microroughness: pv = 15.6±3.9 nm; rms = 1.5±0.1 nm.

Table 80.IV: KDP compatibility test results for candidate carrier fluids.

Fluid	Results/Comments
Glycerol	No fogging; viscosity too high for pumping in STM
Ethylene glycol	Serious fogging in just a few seconds of contact
Polyethylene glycol, M.W. 200	Light fogging after several minutes; halo around MRF spots
Liquid paraffin	No fogging in 60 min; oil-based carrier fluid undersirable
Decahydronaphthalene	No fogging; too volatile
Ethanol, 200 proof	Fogging when exposed in air; not in dry N$_2$; too volatile
Dicarboxylic acid ester	No fogging after extended contact; no halo around spots

The original diamond-turning marks, which would be running approximately perpendicular to the MRF grooves, have been eliminated. The removal rate was in a convenient range, but the goal was not to increase the surface roughness.

Nanodiamond powder[19] was then added to the MR fluid, corresponding to a nominal concentration of 0.05 vol %. The addition of this amount of abrasive had no effect on the MR fluid viscosity. Spots taken with this fluid under the same conditions[23] showed that the peak removal rate increased moderately to 2.10 μm/min. But more importantly, the rms microroughness of 1.6±0.2 was essentially unchanged from that of the initial diamond-turned surface. Figure 80.25 gives a representative optical roughness map of the surface within this spot. The addition of nanodiamonds also decreased the amplitude of the grooves formed by MRF. We expect that these grooves would be eliminated entirely with part rotation during full-scale polishing runs.

The KDP surfaces produced by MRF have been evaluated for laser-damage resistance at LLE. Results are summarized in Table 80.V. MRF maintains the high laser-damage threshold of a diamond-turned KDP part at both $\lambda = 351$ nm and $\lambda = 1054$ nm.

In light of these encouraging results on KDP with this new slurry composition, the next scheduled task is to scale up to full polish runs on a production MRF machine like the Q22. This will allow a quantitative evaluation of removal efficiency, figure correction capability, and smoothing.

Figure 80.24

Optical roughness map[8] of spot made on SPDT KDP part using MR fluid without nonmagnetic abrasive. Microroughness: pv = 64.8±15.8 nm; rms = 6.4±0.8 nm.
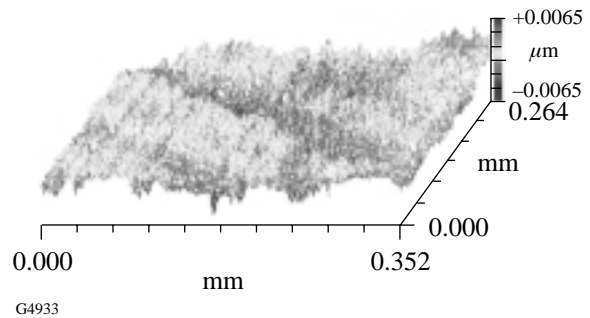
Figure 80.25

Optical roughness map[8] of surface within spot made on SPDT KDP part with MR fluid with 0.05-vol % nanodiamond abrasive. Microroughness: pv = 20.1±7.1 nm; rms = 1.6±0.3 nm.

Figure 80.23

Longitudinal and transverse profile scan[7] of a spot made on SPDT KDP with MR fluid without nonmagnetic abrasive. Peak removal rate was 1.59 μm/min; depth of deepest penetration was 0.53 μm.

Summary

This article shows how sub-aperture removal functions, i.e., polishing "spots," are generated on test flats using two magnetorheological finishing (MRF) research platforms. Evaluation of polishing spots is used to further our understanding of MRF and to extend its capabilities to new classes of optical materials. Examples are presented that demonstrate how new MR fluid compositions and operating parameters may be developed for processing CaF$_2$ and KDP using the evaluation of polishing spots.

ACKNOWLEDGMENT

Table 80.V: Laser-damage test results for KDP parts processed with MRF and SPDT.

J/cm^2	@ 3ω, 1 ns		@1ω, 1 ns	
	1-on-1	N-on-1	1-on-1	N-on-1
MRF	11.23±0.61	14.08±1.06	12.17±1.80	14.76±1.67
Diamond turned	10.63±0.68	14.56±1.08		

REFERENCES

1. D. Golini, Laser Focus World **34**, 187 (1998).

2. D. Golini *et al.*, "Magnetorheological Finishing (MRF) in Commercial Precision Optics Manufacturing," to be published in *Optical Manufacturing and Testing III*, edited by H. P. Stahl (SPIE, Bellingham, WA, 1999), Vol. 3782.

3. D. Golini, S. Jacobs, W. Kordonski, and P. Dumas, in *Advanced Materials for Optics and Precision Structures*, edited by M. A. Ealey, R. A. Paquin, and T. B. Parsonage, Critical Reviews of Optical Science and Technology (SPIE, Bellingham, WA, 1997), Vol. CR67, pp. 251–274.

4. S. D. Jacobs, F. Yang, E. M. Fess, J. B. Feingold, B. E. Gillman, W. I. Kordonski, H. Edwards, and D. Golini, in *Optical Manufacturing and Testing II*, edited by H. P. Stahl (SPIE, Bellingham, WA, 1997), Vol. 3134, pp. 258–269.

5. F. L. Ebenhoech, Prog. Powder Metall. **42**, 133 (1986).

6. B. Berkovski, ed. *Magnetic Fluids and Applications Handbook*, UNESCO Series of Learning Materials (Begell House, New York, 1996), Chap. 6.

7. Zygo Mark IVxp™ or Zygo GPIxpHR™ phase-shifting interferometer systems were used for all data acquisition and analysis related to polishing spots, workpiece surface figure, and transmitted wavefront quality reported in this paper; Zygo Corporation, Middlefield, CT 06455.

8. Zygo NewView™ 100 White Light Optical Profiler, areal over 0.25 mm × 0.35 mm with a 20× Mirau objective, no filter; Zygo Corporation, Middlefield, CT 06455.

9. R. C. Weast, ed. *CRC Handbook of Chemistry and Physics*, 68th ed. (CRC Press, Boca Raton, FL, 1987).

10. J. T. Milek and M. Neuberger, *Linear Electrooptic Modular Materials*, Handbook of Electronic Materials, Vol. 8 (IFI/Plenum, New York, 1972).

11. J. C. Lambropoulos, S. Xu, and T. Fang, Appl. Opt. **36**, 1501 (1997).

12. W. F. Krupke *et al.*, J. Opt. Soc. Am. B **3**, 102 (1986).

13. Value varies with orientation. T. Fang, "Near-Surface Mechanical Properties of Optical Materials in Deterministic Microgrinding," Ph.D. thesis, University of Rochester, 1997.

14. Nano IIs nanoindentor, 5-mN load, Nano Instruments, Oak Ridge, TN 37830; Berkovich indentor.

15. R. DeJule, Semicond. Int. **22** (1), 36 (1999).

16. R. DeJule, Semicond. Int. **22** (2), 38 (1999).

17. R. DeJule, Semicond. Int. **22** (3), 36 (1999).

18. D. Collier and W. Pantley, Laser Focus World **34**, 63 (1998).

19. Dianan® Nano Diamond powder, Straus Chemical Corporation, Elk Grove Village, IL 60007.

20. Carbowax® Polyethylene Glycol 200, Union Carbide Corporation, Danbury, CT 06817-0001.

21. R. C. Montesanti and S. L. Thompson, Lawrence Livermore National Laboratory, Livermore, CA, UCRL-ID-121651 (1995).

22. Cleveland Crystals Inc., Cleveland, OH 44110.

23. Experimental parameters: wheel speed, 150 rpm; magnet current, 15.0 amps (2.22 kG); ribbon height, 2.0 mm; depth into ribbon, 0.5 mm.

LLE's Summer High School Research Program

During the summer of 1999, 12 students from Rochester-area high schools participated in the Laboratory for Laser Energetics' Summer High School Research Program. The goal of this program is to excite a group of high school students about careers in the areas of science and technology by exposing them to research in a state-of-the-art environment. Too often, students are exposed to "research" only through classroom laboratories, which have prescribed procedures and predictable results. In LLE's summer program, the students experience all of the trials, tribulations, and rewards of scientific research. By participating in research in a real environment, the students often become more excited about careers in science and technology. In addition, LLE gains from the contributions of the many highly talented students who are attracted to the program.

The students spent most of their time working on their individual research projects with members of LLE's technical staff. The projects were related to current research activities at LLE and covered a broad range of areas of interest including laser modeling, diagnostic development, chemistry, liquid crystal devices, and opacity data visualization (see Table 80.VI).

The students attended weekly seminars on technical topics associated with LLE's research. Topics this year included lasers, fusion, holography, optical materials, global warming, measurement errors, and scientific ethics. The students also received safety training, learned how to give scientific presentations, and were introduced to LLE's resources, especially the computational facilities.

The program culminated with the High School Student Summer Research Symposium on 25 August at which the students presented the results of their research to an audience including parents, teachers, and LLE staff. The students' written reports will be bound into a permanent record of their work that can be cited in scientific publications. These reports are available by contacting LLE.

One hundred and five high school students have now participated in the program since it began in 1989. The students this year were selected from approximately 80 applicants.

In 1997, LLE added a new component to its high school outreach activities: an annual award to an Inspirational Science Teacher. This award honors teachers who have inspired High School Program participants in the areas of science, mathematics, and technology and includes a $1000 cash prize. Teachers are nominated by alumni of the High School Program. The 1999 William D. Ryan Inspirational Teacher Award was presented at the symposium to Mr. John Harvey of Honeoye Falls–Lima Senior High School. Mr. Harvey, a mathematics teacher, was nominated by Jeremy Yelle and David Rea, participants in the 1997 program. Mr. Yelle wrote, "I have never met another teacher that was so passionate for what he teaches and communicates himself well enough to get even the most complicated of ideas into the simplest of minds." He added, "Mr. Harvey has expanded my interest in science and mathematics not only by opening doors and giving his insight, but also showing me that mathematics can be learned not only in a classroom, but in an open forum, or even in the applications of daily life." Mr. Rea wrote, "I can think of no teacher that has given me a greater gift of learning than Mr. John Harvey." He added, "Mr. Harvey must also be recognized for his dedication to students after the books have closed and the homework has been passed in." Mr. Peter Cardamone, principal of Honeoye Falls–Lima Senior High School, added, "John's excellence in teaching is balanced well with his concern and interest in students under his tutelage."

Table 80.VI: High School Students and Projects—Summer 1999.

Student	High School	Supervisor	Project
Kendra Bussey	Pittsford Sutherland	K. Marshall	Synthesis of Highly Soluble Near-IR Dyes for the Liquid Crystal Point-Diffraction Interferometer
Michael Harvey	R. J. Davis, Livonia	M. Skeldon	Characterization of the Signal-to-Noise Ratio in a Regenerative Amplifier
Peter Hopkins	The Harley School	S. Craxton	Comparing Opacity Data Groups with a Java-Based Graphical User Interface
Jyoti Kandlikar	Brighton	R. Epstein	Statistical Properties of Continuous and Discrete Distributed Phase Plates
Brian Kubera	Webster	R. Boni	Bandwidth Measurement of Fiber Optic Bundles
Aman Narang	The Harley School	W. Donaldson	Spectroscopic Analysis of an OMEGA Beamline
Lutao Ning	Brighton	M. Guardalben	Characterization of the Liquid Crystal Point-Diffraction Interferometer
Rohit Rao	Brighton	S. Craxton	Computer-Aided Modeling of the Liquid Crystal Point-Diffraction Interferometer
Alice Tran	Spencerport	C. Stoeckl	Integrating Hard X-Ray Diagnostics into OMEGA Operations
Jordan VanLare	Victor	K. Marshall	Calculating the Optical and Dielectric Anisotropy of Liquid Crystalline Systems
Jeffrey Vaughan	Fairport	P. Jaanimagi	Correcting Distortion in an X-Ray Streak Camera
Emily Walton	Fairport	J. Knauer	Measurement of Scattered 351-nm Light from OMEGA Targets

FY99 Laser Facility Report

FY99 was a productive year on OMEGA; 1207 shots on target were shared by LLE, LLNL, LANL, and NLUF users (see Table 80.VII). Shot operations were conducted on a 12 h/day, 3 day/week schedule; for many campaigns the standard 1-h cycle time for OMEGA was achieved. Uninterrupted 12-h shot sequences resulted in improved efficiency and effectiveness in completing experimental goals.

The following major system modifications were implemented during FY99:

- Upgrade of 2-D SSD to 0.3-THz bandwidth at three color cycles

- Installation of the majority of the hardware necessary to conduct cryogenic target shots

- Installation of the LLNL Active Shock Breakout (ASBO) diagnostic

- Migration to Oracle™ database systems

- Implementation of second tripler frequency-conversion crystals on beams used for planar experiments

- Installation of two full-aperture backscatter stations

- Replacement of the target chamber roughing systems with dry pumps to support incorporation of a tritium-removal system

Improved individual-beam uniformity resulting from an upgrade of the 2-D SSD system is discussed in the article beginning on p. 197. The modification included removing the first-generation 2-D SSD system from OMEGA and replacing it with a pre-assembled modular unit that included high-frequency, multipass electro-optic modulators. Activation of the new 2-D SSD system went smoothly, and its reliability has been exceptional. Notable features include the flexibility to easily migrate to a full 1.0-THz bandwidth (planned for early FY00), an integrated diagnostic suite, and improved LLE-fabricated holographic optics.

Coincident with the installation of the THz-capable SSD system, second tripler frequency-conversion crystal assemblies were added to 13 of 60 beams. These additional frequency-tripling crystals will provide efficient frequency conversion for laser bandwidths up to the 1-THz level and represent the first stage of a project to modify all 60 beams. With this subset of crystals the planar-foil imprint and Rayleigh–Taylor growth investigations will be extended to higher-uniformity regimes.

The upper and lower pylons of the cryogenic target-handling system (CTHS) were installed on OMEGA. The lower pylon installed on the bottom of the target chamber supports the insertion of targets using the moving cryostat. The upper pylon installed on the target chamber's north pole supports the cryogenic shroud retraction system. The CTHS will be fully activated in FY00.

Table 80.VII: The OMEGA shot summary for FY99.

LLE-RTI	337
LLE-ISE	243
LLE-LSP	62
LLE diagnostic development	85
NLUF	144
LLNL	173
LANL	163
Total	1207

National Laser Users' Facility News

FY99 Experiments

During FY99 significant progress was made on several National Laser Users' Facility (NLUF) projects.

David Cohen and colleagues from the University of Wisconsin at Madison in collaboration with investigators from Prism Computational Sciences, the University of Rochester (UR/LLE), Los Alamos National Laboratory (LANL), Lawrence Livermore National Laboratory (LLNL), and Sandia National Laboratory (SNL) carried out a series of x-ray spectroscopic measurements to explore the physics of radiation-driven, NIF-type ablators.

Hans Griem and colleagues from the University of Maryland conducted experiments using soft x-ray spectroscopy to investigate the plasma conditions at early times in ICF direct-drive capsules.

Bruce Remington, Harry Robey, and colleagues from LLNL in collaboration with investigators from the University of California (UC) at Davis, the University of Arizona, UR/LLE, the University of Chicago, Drexel University, CEA Saclay, Osaka University, State University of New York (SUNY) at Stony Brook, and LANL performed studies of supernova hydrodynamics on OMEGA. These experiments were a continuation of experiments initiated on the Nova laser at LLNL and now being performed on LLE's OMEGA under the NLUF program.

Dan Kalantar and colleagues from LLNL in collaboration with investigators from UC San Diego, the University of Oxford, California Institute of Technology, and LANL carried out studies of the dynamic properties of shock-compressed solids via *in-situ* transient x-ray diffraction.

Richard Petrasso and colleagues from the Massachusetts Institute of Technology (MIT) in collaboration with Stephen Padalino and colleagues from SUNY Geneseo as well as investigators from UR/LLE and LLNL conducted experiments to characterize high-density plasma conditions in imploded ICF capsules using charged-particle spectroscopy on OMEGA. These experiments explored several techniques for measuring fuel and ablator areal densities. The SUNY Geneseo group also carried out a collaborative series of tests to investigate the feasibility of carbon activation as a means of measuring tertiary neutron yield in high-performance OMEGA and NIF ICF capsules.

Charles Hooper and colleagues from the University of Florida along with investigators from the University of Nevada and UR/LLE performed a series of experiments to investigate via x-ray absorption spectroscopy the x-ray emission characteristics of ultrahigh-density plasma.

Bedros Afeyan from Polymath Research in collaboration with colleagues from LLNL, LANL, and UR/LLE carried out experiments to investigate optical-mixing-controlled stimulated scattering instabilities in NIF-like, long-scale-length plasmas.

Figure 80.26 shows an example of work carried out under the FY99 NLUF program; it illustrates the work of a team headed by H. Robey and B. Remington of LLNL to study two aspects of the physics of supernovae. These experiments studied the growth rate of the Richtmyer–Meshkov (RM) and Rayleigh–Taylor (RT) instabilities of a perturbation seeded by the arrival of a rippled shock wave on an initially unperturbed interface. Figure 80.26 shows images demonstrating the time evolution of the shock structure of a laser-driven, planar, copper ablator and a CH payload. In these experiments, the Cu/CH interface had an imposed perturbation wavelength of 200 μm, and the Cu ablator was driven with ~3 kJ in a square-top, 1-ns pulse. A separate x-ray backlighter and an x-ray framing camera were used to obtain the x-ray radiographs of Fig. 80.26. The backlighter pulses were also 1 ns long but delayed by up to 78 ns relative to the drive pulses.

In FY99 a total of 144 OMEGA target shots were dedicated to the NLUF program. In addition to NLUF-supported programs, several direct- and indirect-drive experiments, also

coordinated through the NLUF Manager, were carried out on OMEGA by groups from LLNL and LANL. These experiments included campaigns on direct-drive cylinders, hohlraum symmetry, equation of state, RM and RT instabilities, tetrahedral-hohlraum implosions, double-shell targets, diagnostics development, radiation flow, opacity, and other topics. The variety of FY99 experiments is best illustrated by Fig. 80.27, which shows examples of targets shot on OMEGA during the fiscal year.

FY00 Proposals

Thirteen proposals were submitted to NLUF for FY2000. A DOE technical evaluation panel chaired by the NLUF Manager and including Dr. David Bradley (LLNL), Dr. David Montgomery (LANL), Dr. Ramon Leeper (SNL), and Dr. Ned Sautoff (PPPL) reviewed the proposals at a meeting held on 26 May 1999 and recommended approval of seven proposals for funding (see Table 80.VIII).

(a)   (b)

#17539   #17548

Grid

Cu

Polyimide

CH (4.3% Br)   Shock

$T = 39$ ns $T = 65$ ns
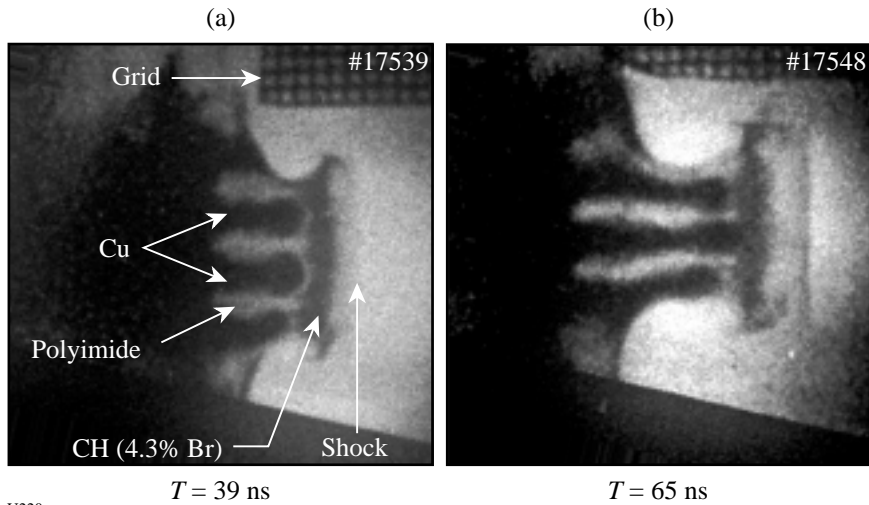
U220

Figure 80.26
Two x-ray-backlighted images from two SNRT #1 experiments showing the time evolution of the shock and instability structure at late times.

(a)   (b)   (c)

(d)

(e)

(f)

E10032
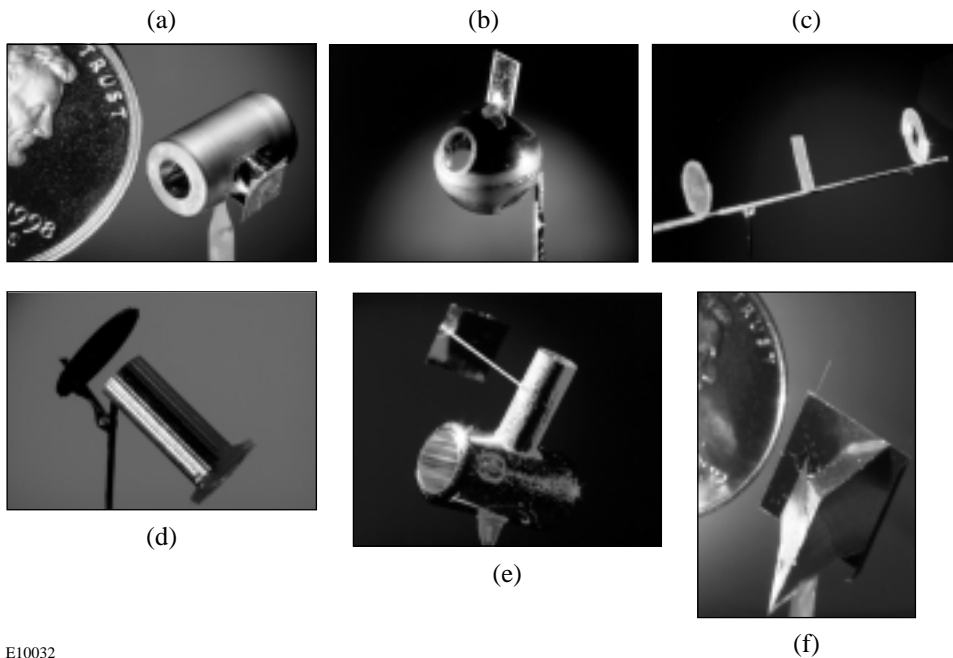
Figure 80.27
OMEGA routinely irradiates a variety of targets. (a) Cylindrical hohlraum target used for radiation ablation studies; (b) tetrahedral hohlraum target; (c) planar target; (d) direct-drive cylinder target; (e) radiation-driven shock target; and (f) x-ray diffraction target.

Table 80.VIII: Approved FY00 NLUF Proposals.

Principal Investigator	Affiliation	Proposal Title
R. Fisher	General Atomics	High-Spatial-Resolution Neutron Imaging of Inertial Fusion Target Plasmas Using Bubble Neutron Detectors
M. Myers	University of California at San Diego	Continuing Studies of Dynamic Properties of Shock-Compressed Solids by *In-Situ* Transient X-Ray Diffraction
R. P. Drake	University of Michigan	Supernova Hydrodynamics on the OMEGA Laser
R. Petrasso	Massachusetts Institute of Technology	Charged-Particle Spectroscopy on OMEGA: Recent Results, Next Steps
D. Cohen	Prism Computational Sciences	Development of X-Ray Tracer Diagnostics for Radiatively Driven NIF Ignition Capsule Ablators
K. Fletcher	SUNY Geneseo	Investigation of Solid-State Detection for Charged-Particle Spectroscopy
B. Afeyan	Polymath Research	Optical-Mixing-Controlled Stimulated Scattering Instability Experiments on OMEGA II: The Effects of Temporal Beam Smoothing and Crossing Angle Variation in CH and Al Plasmas.

Publications and Conference Presentations

--- Publications ---

E. L. Alfonso, F.-Y Tsai, S.-H. Chen, R. Q. Gram, and D. R. Harding, "Fabrication of Polyimide Shells by Vapor Phase Deposition for Use as ICF Targets," Fusion Technol. **35**, 131 (1999).

S. R. Arrasmith, S. D. Jacobs, I. A. Kozhinova, L. L. Gregg, A. B. Shorey, H. J. Romanofsky, D. Golini, W. I. Kordonski, S. Hogan, and P. Dumas, "Studies of Material Removal in Magnetorheological Finishing (MRF) from Polishing Spots," in *Finishing of Advanced Ceramics and Glasses*, edited by R. Sabia, V. A. Greenhut, and C. G. Pantano, Ceramic Transactions, Vol. 102 (The American Ceramic Society, Westerville, OH, 1999), pp. 201–210.

A. Babushkin, W. A. Bittle, S. A. Letzring, M. D. Skeldon, and W. Seka, "Regenerative Amplifier for the OMEGA Laser System," in *Solid State Lasers for Application to Inertial Confinement Fusion*, edited by W. H. Lowdermilk (SPIE, Bellingham, WA, 1999), Vol. 3492, pp. 124–130.

A. Babushkin, W. A. Bittle, M. D. Skeldon, and W. Seka, "Diode-Pumped Regenerative Amplifier for the OMEGA Laser System," in *Conference on Lasers and Electro-Optics*, OSA Technical Digest (Optical Society of America, Washington, DC, 1999), pp. 407–408.

A. Babushkin, R. S. Craxton, S. Oskoui, M. J. Guardalben, R. L. Keck, and W. Seka, "Demonstration of Dual-Tripler Broadband Third-Harmonic Generation and Implications for OMEGA and the NIF," in *Solid State Lasers for Application to Inertial Confinement Fusion*, edited by W. H. Lowdermilk (SPIE, Bellingham, WA, 1999), Vol. 3492, pp. 406–413.

A. Babushkin, J. H. Kelly, C. T. Cotton, M. A. Labuzeta, M. O. Miller, T. A. Safford, R. G. Roides, and W. Seka, "Compact Nd^{3+}-Based Laser System with Gain $G \leq 10^{13}$ and Output Energy of 20 J," in *Solid State Lasers for Application to Inertial Confinement Fusion*, edited by W. H. Lowdermilk (SPIE, Bellingham, WA, 1999), Vol. 3492, pp. 939–943.

R. Betti, V. Lobatchev, and R. L. McCrory, "Feedout, Secular Distortion, and R-T Seeding Induced by Long-Wavelength Perturbations in Accelerated Planar Foils," Phys. Rev. Lett. **81**, 5560 (1998).

T. R. Boehly, R. L. McCrory, C. P. Verdon, W. Seka, S. J. Loucks, A. Babushkin, R. E. Bahr, R. Boni, D. K. Bradley, R. S. Craxton, J. A. Delettrez, W. R. Donaldson, R. Epstein, D. Harding, P. A. Jaanimagi, S. D. Jacobs, K. Kearney, R. L. Keck, J. H. Kelly, T. J. Kessler, R. L. Kremens, J. P. Knauer, D. J. Lonobile, L. D. Lund, F. J. Marshall, P. W. McKenty, D. D. Meyerhofer, S. F. B. Morse, A. Okishev, S. Papernov, G. Pien, T. Safford, J. D. Schnittman, R. Short, M. J. Shoup III, M. Skeldon, S. Skupsky, A. W. Schmid, V. A. Smalyuk, D. J. Smith, J. M. Soures, M. D. Wittman, and B. Yaakobi, "Inertial Confinement Fusion Experiments with OMEGA—A 30-kJ, 60-Beam UV Laser," Fusion Eng. Des. **44**, 35 (1999).

T. R. Boehly, V. A. Smalyuk, D. D. Meyerhofer, J. P. Knauer, D. K. Bradley, R. S. Craxton, M. J. Guardalben, S. Skupsky, and T. J. Kessler, "Reduction of Laser Imprinting Using Polarization Smoothing on a Solid-State Fusion Laser," J. Appl. Phys. **85**, 3444 (1999).

S.-H. Chen, B. M. Conger, J. C. Mastrangelo, and A. S. Kende, "Synthesis and Optical Properties of Thermotropic Polythiophene and Poly(*p*-phenylene) Derivatives," Macromolecules **31**, 8051 (1998).

S.-H. Chen, D. Katsis, P. H. Chen, J. C. Mastrangelo, and T. Tsutsui, "Circularly Polarized Light Produced with Glassy Liquid Crystal Films," Polymer Reprints **40**, 1171 (1999).

S.-H. Chen, D. Katsis, A. W. Schmid, J. C. Mastrangelo, T. Tsutsui, and T. N. Blanton, "Circularly Polarized Light Generated by Photoexcitation of Luminophores in Glassy Liquid-Crystal Films," Nature **397**, 506 (1999).

S.-H. Chen, J. C. Mastrangelo, and R. J. Jin, "Glassy Liquid Crystal Films as Broadband Polarizers and Reflectors via Spatially Modulated Photoracemization," Adv. Mater. **11**, 1183 (1999).

T. J. B. Collins, A. Frank, J. E. Bjorkman, and M. Livio, "Supernova 1987A: Rotation and a Binary Companion," Astrophys. J. **512**, 322 (1999).

T. J. B. Collins, H. L. Helfer, and H. M. Van Horn, "A Model for Quasi-Periodic Oscillations in Cataclysmic Variables Based on Boundary-Layer Oscillations," Astrophys. J. **508**, L159 (1998).

B. M. Conger, J. C. Mastrangelo, D. Katsis, and S.-H. Chen, "Fluorescence of Pyrenyl and Carbazolyl Derivatives in Liquid Solution and Solid Film," J. Phys. Chem. A **102**, 9213 (1998).

S. Cremer, C. P. Verdon, and R. D. Petrasso, "Tertiary Proton Diagnostics in Future ICF Experiments," Phys. Plasmas **5**, 4009 (1998).

M. Currie, R. Sobolewski, and T. Y. Hsiang, "Subterahertz Signal Crosstalk in Transmission Line Interconnects," Appl. Phys. Lett. **73**, 1910 (1998).

F. Dahmani, S. Burns, and J. C. Lambropoulous, "Arresting Ultraviolet-Laser Damage in Fused Silica," Opt. Lett. **24**, 516 (1999).

F. Dahmani, J. C. Lambropoulos, S. Burns, S. Papernov, and A. W. Schmid, "How Small Stresses Affect 351-nm Damage Onset in Fused Silica," in *Laser-Induced Damage in Optical Materials: 1998*, edited by G. J. Exarhos, A. H. Guenther, M. R. Kozlowski, K. L. Lewis, and M. J. Soileau (SPIE, Bellingham, WA, 1999), Vol. 3578, pp. 431–435.

F. Dahmani, J. C. Lambropoulos, A. W. Schmid, S. J. Burns, and C. Pratt, "Nanoindentation Technique for Measuring Residual Stress Field Around a Laser-Induced Crack in Fused Silica," J. Mater. Sci. **33**, 4677 (1998).

F. Dahmani, J. C. Lambropoulos, A. W. Schmid, S. Papernov, and S. J. Burns, "Fracture of Fused Silica with 351-nm-Laser-Generated Surface Cracks," J. Mater. Res. **14**, 597 (1999).

F. Dahmani, A. W. Schmid, J. C. Lambropoulos, and S. J. Burns, "Dependence of Birefringence and Residual Stress Near Laser-Induced Cracks in Fused Silica on Laser Fluence and on Laser-Pulse Number," Appl. Opt. **37**, 7772 (1998).

O. M. Efimov, L. B. Glebov, S. Papernov, and A. W. Schmid, "Laser-Induced Damage of Photo-Thermo-Refractive Glasses for Optical-Holographic-Element Writing," in *Laser-Induced Damage in Optical Materials: 1998*, edited by G. J. Exarhos, A. H. Guenther, M. R. Kozlowski, K. L. Lewis, and M. J. Soileau (SPIE, Bellingham, WA, 1999), Vol. 3578, pp. 564–574.

R. E. Giacone, C. J. McKinstrie, and T. Kolber, "Angular Dependence of Stimulated Brillouin Scattering in a Homogeneous Two-Dimensional Plasma," Phys. Plasmas **6**, 3587 (1999).

V. N. Goncharov, "Theory of the Ablative Richtmyer–Meshkov Instability," Phys. Rev. Lett. **82**, 2091 (1999).

K. Green, W. R. Donaldson, R. L. Keck, A. V. Okishev, M. D. Skeldon, W. Seka, and R. Sobolewski, "Transient Bandwidth Analysis of Photoconductive Microwave Switches Implemented in the OMEGA Pulse-Shaping System," in *Solid State Lasers for Application to Inertial Confinement Fusion*, edited by W. H. Lowdermilk (SPIE, Bellingham, WA, 1999), Vol. 3492, pp. 165–172.

K. S. Il'in, G. N. Gol'tsman, B. M. Voronov, and R. Sobolewski, "Characterization of the Electron Energy Relaxation Process in NbN Hot-Electron Devices," in the *Proceedings of the 10th International Symposium on Space Terahertz Technology*, edited by T. W. Crowe and R. M. Weikle (University of Virginia, Charlottesville, VA, 1999), pp. 390–397.

K. S. Il'in, I. I. Milostnaya, A. A. Verevkin, G. N. Gol'tsman, E. M. Gershenzon, and R. Sobolewski, "Ultimate Quantum Efficiency of a Superconducting Hot-Electron Photodetector," Appl. Phys. Lett. **73**, 3938 (1998).

S. D. Jacobs, S. A. Arrasmith, I. A. Kozhinova, L. L. Gregg, A. B. Shorey, H. J. Romanofsky, D. Golini, W. I. Kordonski, P. Dumas, and S. Hogan, "An Overview of Magnetorheological Finishing (MRF) for Precision Optics," in *Finishing of Advanced Ceramics and Glasses*, edited by R. Sabia, V. A. Greenhut, and C. G. Pantano, Ceramic Transactions, Vol. 102 (The American Ceramic Society, Westerville, OH, 1999), pp. 185–199.

S. D. Jacobs, W. I. Kordonski, and H. M. Pollicove, "Precision Control of Aqueous Magnetorheological Fluids for Finishing of Optics," in the *Proceedings of the Sixth International Conference on Electro-Rheological Fluids, Magneto-Rheological Suspensions and Their Applications*, edited by M. Nakano and K. Koyama (World Scientific, Singapore, 1998), pp. 861–869.

A. V. Kanaev and C. J. McKinstrie, "Exact Green's Function for a Class of Parametric Instabilities," Phys. Plasmas **5**, 4511 (1998).

D. Katsis, P. H. M. Chen, J. C. Mastrangelo, S.-H. Chen, and T. N. Blanton, "Vitrified Chiral-Nematic Liquid Crystalline Films for Selective Reflection and Circular Polarization," Chem. Mater. **11**, 1590 (1999).

D. Katsis, A. W. Schmid, and S.-H. Chen, "Mechanistic Insight into Circularly Polarized Photoluminescence from a Chiral-Nematic Film," Liq. Cryst. **26**, 181 (1999).

E. M. Korenic, S. D. Jacobs, S. M. Faris, and L. Li, "Cholesteric Liquid Crystal Flakes—A New Form of Domain," Mol. Cryst. Liq. Cryst. **317**, 197 (1998).

E. M. Korenic, S. D. Jacobs, S. M. Faris, and L. Li, "Cholesteric Liquid Crystal Transmission Profile Asymmetry," Mol. Cryst. Liq. Cryst. **317**, 221 (1998).

J. M. Larkin, W. R. Donaldson, T. H. Foster, and R. S. Knox, "Reverse Intersystem Crossing from a Triplet State of Rose Bengal Populated by Sequential 532- + 1064-nm Laser Excitation," Chem. Phys. **244**, 319 (1999).

M. Lindgren, M. Currie, W.-S. Zeng, R. Sobolewski, S. Cherednichenko, B. Voronov, and G. N. Gol'tsman, "Picosecond Response of a Superconducting Hot-Electron NbN Photodetector," Appl. Supercond. **6**, 423 (1998).

M. Lindgren, M. Currie, C. Williams, T. Y. Hsiang, P. M. Fauchet, R. Sobolewski, S. H. Moffat, R. A. Hughes, J. S. Preston, and F. A. Hegmann, "Intrinsic Picosecond Response Times of Y-Ba-Cu-O Superconducting Photodetectors," Appl. Phys. Lett. **74**, 853 (1999).

J. A. Marozas, "The Cross-Phase Modulation Between Two Intense Orthogonally Polarized Laser Beams Co-Propagating Through a Kerr-like Medium," in *Solid State Lasers for Application to Inertial Confinement Fusion*, edited by W. H. Lowdermilk (SPIE, Bellingham, WA, 1999), Vol. 3492, pp. 454–465.

F. J. Marshall and G. R. Bennett, "A High-Energy X-Ray Microscope for Inertial Confinement Fusion," Rev. Sci. Instrum. **70**, 617 (1999).

K. L. Marshall, J. Haddock, N. Bickel, D. Singel, and S. D. Jacobs, "Angular-Scattering Characteristics of Ferroelectric Liquid-Crystal Electro-Optical Devices Operating in the Transient-Scattering and the Extended-Scattering Modes," Appl. Opt. **38**, 1287 (1999).

R. L. McCrory and J. M. Soures, "Status of Direct-Drive Inertial Confinement Fusion Research at the Laboratory for Laser Energetics," in *Current Trends in International Fusion Research*, edited by E. Panarella (NRC Research Press, Ottawa, Canada, 1999), pp. 251–259 (invited).

C. J. McKinstrie, R. E. Giacone, and E. A. Startsev, "Accurate Formulas for the Landau Damping Rates of Electrostatic Waves," Phys. Plasmas **6**, 463 (1999).

A. V. Okishev, "High-Repetition-Rate, Diode-Pumped, Multipass Preamplifier for the OMEGA Master Oscillator," in *Conference on Lasers and Electro-Optics*, OSA Technical Digest (Optical Society of America, Washington, DC, 1999), p. 407.

A. V. Okishev, D. Jacobs-Perkins, S. F. B. Morse, D. Scott, and W. Seka, "Prepulse Contrast Monitor for the OMEGA Driver Line," in *Conference on Lasers and Electro-Optics*, OSA Technical Digest (Optical Society of America, Washington, DC, 1999), pp. 406–407.

A. V. Okishev, M. D. Skeldon, R. L. Keck, R. Roides, K. Green, and W. Seka, "A High-Bandwidth Optical-Pulse-Shaping/ Fiber-Optic Distribution System for the High-Energy OMEGA Laser-Fusion Facility," in the *Optical Fiber Communication Conference and the International Conference on Integrated Optics and Optical Fiber Communication 1999 Technical Digest* (Optical Society of America, Washington, DC, 1999), pp. 286–288.

A. V. Okishev, M. D. Skeldon, and W. Seka, "A Highly Stable, Diode-Pumped Master Oscillator for the OMEGA Laser Facility," in *Advanced Solid-State Lasers 1999 Technical Digest* (Optical Society of America, Washington, DC, 1999), pp. 124–126.

A. V. Okishev, M. D. Skeldon, and W. Seka, "Multipurpose, Diode-Pumped Nd:YLF Laser for OMEGA Pulse Shaping and Diagnostic Applications," in *Solid State Lasers for Application to Inertial Confinement Fusion*, edited by W. H. Lowdermilk (SPIE, Bellingham, WA, 1999), Vol. 3492, pp. 118–123.

S. P. Regan, D. K. Bradley, A. V. Chirokikh, R. S. Craxton, D. D. Meyerhofer, W. Seka, R. W. Short, A. Simon, R. P. J. Town, B. Yaakobi, J. J. Carroll III, and R. P. Drake, "Laser–Plasma Interactions in Long-Scale-Length Plasmas Under Direct-Drive National Ignition Facility Conditions," Phys. Plasmas **6**, 2072 (1999).

A. L. Rigatti, D. J. Smith, A. W. Schmid, S. Papernov, and J. H. Kelly, "Damage in Fused-Silica Spatial-Filter Lenses on the OMEGA Laser System," in *Laser-Induced Damage in Optical Materials: 1998*, edited by G. J. Exarhos, A. H. Guenther, M. R. Kozlowski, K. L. Lewis, and M. J. Soileau (SPIE, Bellingham, WA, 1999), Vol. 3578, pp. 472–479.

R. W. Short and A. Simon, "Collisionless Damping of Localized Plasma Waves in Laser-Produced Plasmas and Application to Stimulated Raman Scattering in Filaments," Phys. Plasmas **5**, 4134 (1998).

R. W. Short and A. Simon, "Landau Damping and Transit-Time Damping of Localized Plasma Waves in General Geometries," Phys. Plasmas **5**, 4124 (1998).

M. D. Skeldon, A. V. Okishev, R. L. Keck, and W. Seka, "An Optical Pulse-Shaping System Based on Aperture-Coupled Striplines for OMEGA Pulse-Shaping Applications," in *Con-*

ference on Lasers and Electro-Optics, OSA Technical Digest (Optical Society of America, Washington, DC, 1999), p. 408.

M. D. Skeldon, A. V. Okishev, R. L. Keck, W. Seka, and S. Letzring, "An Optical Pulse Shaping System Based on Aperture-Coupled Striplines for OMEGA Pulse Shaping Applications," in *Solid State Lasers for Application to Inertial Confinement Fusion*, edited by W. H. Lowdermilk (SPIE, Bellingham, WA, 1999), Vol. 3492, pp. 131–135.

M. D. Skeldon, R. B. Saager, and W. Seka, "Quantitative Pump-Induced Wavefront Distortions in Laser-Diode- and Flashlamp-Pumped Nd:YLF Laser Rods," IEEE J. Quantum Electron. **35**, 381 (1999).

S. Skupsky and R. S. Craxton, "Irradiation Uniformity for High-Compression Laser-Fusion Experiments," Phys. Plasmas **6**, 2157 (1999).

V. A. Smalyuk, T. R. Boehly, D. K. Bradley, V. N. Goncharov, J. A. Delettrez, J. P. Knauer, D. D. Meyerhofer, D. Oron, and D. Shvarts, "Saturation of the Rayleigh–Taylor Growth of Broad-Bandwidth, Laser-Imposed Nonuniformities in Planar Targets," Phys. Rev. Lett. **81**, 5342 (1998).

V. A. Smalyuk, T. R. Boehly, D. K. Bradley, V. N. Goncharov, J. A. Delettrez, J. P. Knauer, D. D. Meyerhofer, D. Oron, D. Shvarts, Y. Srebro, and R. P. J. Town, "Nonlinear Evolution of Broad-Bandwidth, Laser-Imprinted Nonuniformities in Planar Targets Accelerated by 351-nm Laser Light," Phys. Plasmas **6**, 4022 (1999).

V. A. Smalyuk, T. R. Boehly, D. K. Bradley, J. P. Knauer, and D. D. Meyerhofer, "Characterization of an X-ray Radiographic System Used for Laser-Driven Planar Target Experiments," Rev. Sci. Instrum. **70**, 647 (1999).

D. J. Smith, J. A. Warner, N. E. LeBarron, and S. LaDelia, "Production of Distributed Phase Plates Using an Energetic Ion Process," in *Laser-Induced Damage in Optical Materials: 1998*, edited by G. J. Exarhos, A. H. Guenther, M. R. Kozlowski, K. L. Lewis, and M. J. Soileau (SPIE, Bellingham, WA, 1999), Vol. 3578, pp. 702–717.

R. Sobolewski, "Ultrafast Dynamics of Nonequilibrium Quasi-particles in High-Temperature Superconductors," in *Superconducting and Related Oxides: Physics and Nano-*

engineering III, edited by D. Pavuna and I. Bozovic (SPIE, Bellingham, WA, 1999), Vol. 3481, pp. 480–491.

J. M. Wallace, T. J. Murphy, N. D. Delamater, K. A. Klare, J. A. Oertel, G. R. Magelssen, E. L. Lindman, A. A. Hauer, P. Gobby, J. D. Schnittman, R. S. Craxton, W. Seka, R. Kremens, D. K. Bradley, S. M. Pollaine, R. E. Turner, O. L. Landen, D. Drake, and J. J. MacFarlane, "Inertial Confinement Fusion with Tetrahedral Hohlraums at OMEGA," Phys. Rev. Lett. **82**, 3807 (1999).

M. D. Wittman and R. S. Craxton, "Self-Interference Patterns and Their Application to Inertial-Fusion Target Characterization," Appl. Opt. **38**, 5365 (1999).

B. Yaakobi and F. J. Marshall, "Imaging the Cold, Compressed Shell in Laser Implosions Using the Ka Fluorescence of a Titanium Dopant," J. Quant. Spectrosc. Radiat. Transfer **61**, 465 (1999).

B. Yaakobi, F. J. Marshall, and D. K. Bradley, "Pinhole-Array X-Ray Spectrometer for Laser-Fusion Experiments," Appl. Opt. **37**, 8074 (1998).

J. D. Zuegel and W. Seka, "Upconversion and Reduced $^4F_{3/2}$ Upper-State Lifetime in Intensely Pumped Nd:YLF," Appl. Opt. **38**, 2714 (1999).

M. D. Zuerlein, D. Fried, J. D. B. Featherstone, and W. Seka, "Optical Properties of Dental Enamel in the Mid-IR Determined by Pulsed Photothermal Radiometry," IEEE J. Sel. Top. Quantum Electron. **5**, 1083 (1999).

Conference Presentations

J. L. Chaloupka and D. D. Meyerhofer, "A Single-Beam, High-Field Trap for Energetic Electrons," 1998 OSA Annual Meeting/ILS–XIV, Baltimore, MD, 4–9 October 1998.

———————

J. M. Soures, R. L. McCrory, P. B. Radha, R. Betti, W. Bittle, T. R. Boehly, R. Boni, D. K. Bradley, T. J. B. Collins, R. S. Craxton, J. A. Delettrez, W. R. Donaldson, R. Epstein, V. Yu. Glebov, V. N. Goncharov, D. R. Harding, P. A. Jaanimagi, R. L. Keck, J. H. Kelly, T. J. Kessler, J. P. Knauer, C. K. Li, S. J. Loucks, F. J. Marshall, P. W. McKenty, D. D. Meyerhofer, S. F. B. Morse, S. Padalino, R. Petrasso, S. Regan, W. Seka, R. W. Short, A. Simon, S. Skupsky, D. J. Smith, R. P. J. Town, B. Yaakobi, and J. D. Zuegel, "Recent Advances in Direct-Drive ICF Target Physics at the Laboratory for Laser Energetics," 1998 IAEA Conference, Yokohama, Japan, 19–24 October 1998.

———————

The following presentations were made at the 40th Annual Meeting APS Division of Plasma Physics, New Orleans, LA, 16–20 November 1998:

P. Amendt, R. E. Turner, O. Landen, S. G. Glendinning, D. Kalantar, M. Cable, J. Colvin, C. Decker, L. Suter, R. Wallace, D. K. Bradley, S. F. B. Morse, G. Pien, W. Seka, and J. M. Soures, "High-Convergence, Indirect-Drive Implosions on OMEGA: Design and Simulations."

C. A. Back, J. D. Bauer, R. E. Turner, B. F. Lasinski, L. J. Suter, O. L. Landen, W. W. Hsing, and J. M. Soures, "Temporally and Radially Resolved Breakout of Heat Wave in Radiatively Heated Foam Targets."

C. W. Barnes, D. L. Tubbs, J. B. Beck, J. A. Oertel, N. Shambo, S. A. Voss, R. G. Watt, T. R. Boehly, D. K. Bradley, and J. P. Knauer, "Direct-Drive Cylindrical Implosions on the OMEGA Laser."

G. R. Bennett, J. M. Wallace, T. J. Murphy, A. A. Hauer, J. A. Oertel, D. C. Wilson, P. L. Gobby, N. D. Delamater, R. E. Chrien, R. S. Craxton, and J. D. Schnittman, "High-Convergence Implosions Within Tetrahedral Hohlraums."

R. Betti and E. Fedutenko, "Stable Regimes for External Modes in High-β Tokamak Plasmas."

T. R. Boehly, V. A. Smalyuk, O. Gotchev, J. P. Knauer, D. D. Meyerhofer, D. K. Bradley, J. A. Delettrez, S. Skupsky, and R. P. J. Town, "The Effect of Pulse Shape and Beam Smoothing on Laser Imprinting."

D. K. Bradley, J. A. Delettrez, S. P. Regan, S. Skupsky, and D. D. Meyerhofer, "Spherical Rayleigh–Taylor Experiments on the 60-Beam OMEGA Laser System Using the Burn-through Technique."

T. J. B. Collins, J. P. Knauer, S. Skupsky, and C. P. Verdon, "Control of Ablation Velocity Through Prepulses in Direct-Drive ICF."

R. S. Craxton, S. Skupsky, A. Babushkin, J. H. Kelly, T. J. Kessler, J. M. Soures, and J. D. Zuegel, "Enhanced Beam Smoothing on OMEGA and the NIF."

J. A. Delettrez, V. N. Goncharov, S. Skupsky, T. R. Boehly, D. K. Bradley, J. P. Knauer, D. D. Meyerhofer, S. P. Regan, and V. A. Smalyuk, "The Effect of Pulse Shape on Laser Imprint and SSD Smoothing."

J. Dirrenberger, V. Lobatchev, and R. L. McCrory, "Seeds and Early Development of the Rayleigh–Taylor Instability in Laser-Accelerated Targets."

R. Elton, E. Iglesias, H. Griem, G. Pien, D. K. Bradley, J. A. Delettrez, and R. Epstein, "Early-Time Extreme-UV Emission from OMEGA Plasmas."

R. Epstein, T. J. B. Collins, J. A. Delettrez, S. Skupsky, and R. P. J. Town, "Simulation of the Radiative Preheat of Target Foils and Shells in Laser-Driven Ablation and Implosion Experiments."

Y. Fisher, T. R. Boehly, D. K. Bradley, D. R. Harding, D. D. Meyerhofer, and M. D. Wittman, "Shinethrough Properties of Various Barrier-Layer Materials."

C. G. R. Geddes, J. Sanchez, G. Collins, and P. W. McKenty, "Interferometric Characterization of Hydrogen Ice Layers in NIF-Scale Targets."

R. E. Giacone, C. J. McKinstrie, and E. A. Startsev, "Accurate Formulas for the Landau Damping Rates of Electro-static Waves."

V. Yu. Glebov, J. P. Knauer, F. J. Marshall, P. W. McKenty, D. D. Meyerhofer, N. S. Rogers, C. Stoeckl, M. D. Cable, and R. E. Turner, "Recent ρR Measurements on OMEGA Using the MEDUSA Scintillator Array."

V. N. Goncharov, R. Betti, R. L. McCrory, and C. Cherfils, "Linear Stability Analysis of Ablation Fronts During the Shock Transit Time."

D. Haynes, C. Hooper, N. Delamater, C. Barnes, J. Oertel, G. Pollak, D. Tubbs, R. Watt, T. R. Boehly, D. K. Bradley, P. A. Jaanimagi, and J. P. Knauer, "X-Ray Spectroscopy of Directly Driven Cylindrical Implosions."

D. G. Hicks, C. K. Li, F. H. Séguin, R. D. Petrasso, J. M. Soures, D. R. Harding, D. D. Meyerhofer, W. Seka, A. Simon, R. W. Short, T. W. Phillips, T. C. Sangster, M. D. Cable, T. P. Bernat, and J. D. Schnittman, "Measurement of Accelerated Ions from OMEGA Targets."

G. C. Junkel, M. A. Gunderson, D. A. Haynes, Jr., C. F. Hooper, Jr., D. K. Bradley, J. A. Delettrez, P. A. Jaanimagi, and S. P. Regan, "Multi-electron Line Broadening in Hot, Dense Plasmas Including Detailed Line Shift Calculations."

A. V. Kanaev and C. J. McKinstrie, "Exact Green Function for a Class of Parametric Instabilities."

R. L. Keck, W. R. Donaldson, W. Seka, and R. Boni, "Beam Power Matching on the OMEGA Laser."

J. P. Knauer, R. Betti, T. R. Boehly, D. K. Bradley, T. J. B. Collins, J. A. Delettrez, P. W. McKenty, D. D. Meyerhofer, V. A. Smalyuk, and R. P. J. Town, "Growth of Rayleigh–Taylor Unstable, CH Ablation Interfaces Doped with Silicon."

C. K. Li, D. G. Hicks, F. H. Séguin, R. D. Petrasso, J. M. Soures, D. R. Harding, J. P. Knauer, J. Law, P. B. Radha, S. Skupsky, S. Padalino, T. W. Phillips, T. C. Sangster, and M. D. Cable, "Measurements of Temperature and Areal Density Using Charged-Particle Spectroscopy on OMEGA."

V. Lobatchev and R. Betti, "Linear Feed-out of Rear Surface Nonuniformities in Planar Geometry."

F. J. Marshall, B. Yaakobi, D. D. Meyerhofer, R. P. J. Town, J. A. Delettrez, V. Yu. Glebov, D. K. Bradley, J. P. Knauer, M. D. Cable, and T. J. Ognibene, "Surrogate Cryogenic Target Experiments on OMEGA."

P. W. McKenty, V. Yu. Glebov, D. D. Meyerhofer, N. S. Rogers, C. Stoeckl, J. D. Zuegel, M. D. Cable, T. J. Ognibene, R. A. Lerche, and R. L. Griffith, "Neutron Burn Truncation Experiments on OMEGA."

C. J. McKinstrie and E. A. Startsev, "Analysis of the Forward and Backward Stimulated Brillouin Scattering of Crossed Laser Beams."

D. D. Meyerhofer, D. K. Bradley, J. A. Delettrez, V. Yu. Glebov, J. P. Knauer, F. J. Marshall, P. W. McKenty, S. P. Regan, S. Skupsky, C. Stoeckl, and R. P. J. Town, "Hydrodynamic Performance of Spherical CH Targets on OMEGA Using Shaped Laser Pulses."

T. J. Murphy, J. M. Wallace, K. A. Klare, N. D. Delamater, G. R. Bennett, A. A. Hauer, J. A. Oertel, S. M. Pollaine, R. S. Craxton, and J. D. Schnittman, "Analysis of Imploded Capsule Images from Spherical Hohlraums with Tetrahedral Illumination."

R. D. Petrasso, C. K. Li, D. G. Hicks, F. H. Séguin, J. M. Soures, V. Yu. Glebov, D. R. Harding, J. P. Knauer, J. Law, D. D. Meyerhofer, P. B. Radha, J. D. Schnittman, W. Seka, R. W. Short, A. Simon, S. Skupsky, C. Stoeckl, T. W. Phillips, T. C. Sangster, T. Ognibene, M. D. Cable, and S. Padalino, "Charged-Particle Spectroscopy on OMEGA: Initial Results" (invited).

P. B. Radha, S. Skupsky, J. M. Soures, and R. D. Petrasso, "A Novel Diagnostic for ρR in ICF Targets."

S. P. Regan, T. R. Boehly, D. K. Bradley, T. J. B. Collins, J. A. Delettrez, J. P. Knauer, D. D. Meyerhofer, P. W. McKenty, and V. A. Smalyuk, "A Comparison of Planar Burnthrough Experiments with Single-Mode Rayleigh–Taylor Instability Growth Rate on OMEGA."

S. P. Regan, D. K. Bradley, J. J. Carroll III, A. V. Chirokikh, R. S. Craxton, R. P. Drake, D. D. Meyerhofer, W. Seka, R. W. Short, A. Simon, R. P. J. Town, and B. Yaakobi, "Laser–Plasma Interactions in NIF Direct-Drive-Scale Plasmas" (invited).

J. D. Schnittman, R. S. Craxton, S. M. Pollaine, R. E. Turner, J. M. Wallace, T. J. Murphy, N. D. Delamater, J. A. Oertel, A. A. Hauer, and K. A. Klare, "Capsule Implosion Symmetry in OMEGA Tetrehedral Hohlraums."

W. Seka, A. V. Chirokikh, D. D. Meyerhofer, S. P. Regan, D. K. Bradley, B. Yaakobi, R. S. Craxton, R. W. Short, and A. Simon, "Stimulated Brillouin Scattering in Direct-Drive NIF Conditions."

N. A. Shambo, W. Barnes, J. A. Oertel, R. G. Watt, T. R. Boehly, D. K. Bradley, and J. P. Knauer, "Neutron Emission from Direct-Drive Cylindrical Implosions."

R. W. Short, C. K. Li, D. G. Hicks, R. D. Petrasso, J. M. Soures, and W. Seka, "Interpretation of Ion-Acceleration Effects Observed in Charged-Particle Spectroscopy on OMEGA."

A. Simon, "Return Current Electron Beams and Their Generation of Raman Scattering."

S. Skupsky, "The Effect of Laser Nonuniformity in Direct-Drive Laser-Fusion Experiments" (invited).

V. A. Smalyuk, T. R. Boehly, D. K. Bradley, J. P. Knauer, D. D. Meyerhofer, D. Oron, Y. Srebro, and D. Shvarts, "Late-Time Evolution of Broad-Bandwidth, Laser-Imposed Nonuniformities in Accelerated Foils."

J. M. Soures, D. R. Harding, P. B. Radha, S. Skupsky, C. K. Li, D. G. Hicks, R. D. Petrasso, and F. H. Séguin, "Simultaneous Measurement of Areal Density and Temperature in D^3He-Filled Imploding Capsules."

E. A. Startsev and C. J. McKinstrie, "Simulation of the Forward and Backward Stimulated Brillouin Scattering of Crossed Laser Beams."

C. Stoeckl, P. W. McKenty, V. Yu. Glebov, D. D. Meyerhofer, N. S. Rogers, J. D. Zuegel, M. D. Cable, T. J. Ognibene, and R. A. Lerche, "Neutron Burn History Measurements on OMEGA."

R. P. J. Town, F. J. Marshall, J. A. Delettrez, R. Epstein, P. W. McKenty, D. D. Meyerhofer, P. B. Radha, S. Skupsky, and C. Stoeckl, "OMEGA Surrogate Capsule Designs and Experiments."

R. E. Turner, P. A. Amendt, S. G. Glendinning, D. H. Kalantar, O. L. Landen, R. J. Wallace, M. D. Cable, B. A. Hammel, D. Bradley, V. Yu. Glebov, S. Morse, G. Pien, N. Rogers, W. Seka, and J. M. Soures, "X-ray Drive Symmetry and Implosion Performance in OMEGA Cylindrical Hohlraums Driven by NIF-like Multiple Cone Geometry."

J. M. Wallace, G. R. Bennett, T. J. Murphy, J. A. Oertel, P. Gobby, A. A. Hauer, W. S. Varnum, D. C. Wilson, R. S. Craxton, J. D. Schnittman, and S. M. Pollaine, "Design and Analysis of High-Convergence Capsule Implosions in OMEGA Tetrahedral Hohlraums."

B. Yaakobi, F. J. Marshall, and D. K. Bradley, "Kα Cold Target Imaging and Preheat Measurement Using a Pinhole-Array X-Ray Spectrometer."

———————

V. N. Goncharov, "Theory of the Ablative Richtmyer–Meshkov Instability," Conference on Hydrodynamic and Magnetohydrodynamic Interface Instabilities: Unsteady or Discontinuous Flows, Paris, France, 11–12 January 1999.

———————

W. R. Donaldson, R. Boni, R. L. Keck, and P. A. Jaanimagi, "UV-Power Balance on the OMEGA Laser," LASE '99, San Jose, CA, 22–29 January 1999.

———————

A. V. Okishev, M. D. Skeldon, and W. Seka, "A Highly Stable, Diode-Pumped Master Oscillator for the OMEGA Laser Facility," 1999 Advanced Solid-State Lasers Fourteenth Topical Meeting, Boston, MA, 31 January–3 February 1999.

———————

The following presentations were made at the Banff Workshop on Laser Plasma Interaction Physics, Banff, Canada, 17–20 February 1999:

W. Seka, S. P. Regan, D. D. Meyerhofer, B. Yaakobi, R. S. Craxton, A. Simon, and R. W. Short, "Recent SBS and SRS Results Under Direct-Drive NIF Conditions."

R. W. Short, "Effects of SSD on Forward SBS and Filamentation."

———————

A. V. Okishev, M. D. Skeldon, R. L. Keck, R. G. Roides, K. Green, and W. Seka, "A High-Bandwidth Optical Pulse-Shaping/Fiber-Optic Distribution System for the High-Energy OMEGA Laser Fusion Facility," OFC/IOOC '99, San Diego, CA, 21–26 February 1999.

———————

S. Il'in, G. N. Gol'tsman, B. M. Voronov, and R. Sobolewski, "Characterization of the Electron Energy Relaxation Process

in NbN Hot-Electron Devices," 10th International Symposium on Space Terahertz Technology, Charlottesville, VA, 16–18 March 1999.

———————

J. M. Larkin, W. R. Donaldson, T. H. Foster, and R. S. Knox, "Reverse Intersystem Crossing From a Triplet State of Rose Bengal Populated by Sequential 532- and 1064-nm Laser Excitation," APS 1999 Centennial Meeting, Atlanta, GA, 20–26 March 1999.

———————

The following presentations were made at the Spring Meeting of the Materials Research Society, San Francisco, CA, 5–9 April 1999:

I. A. Kozhinova, S. R. Arrasmith, L. L. Gregg, and S. D. Jacobs, "Origin of Corrosion in Magnetorheological Fluids Used for Optical Finishing."

A. B. Shorey, S. D. Jacobs, W. I. Kordonski, S. R. Gorodkin, and K. M. Kwong, "Design and Testing of a New Magnetorheometer."

———————

S. A. Arrasmith, S. D. Jacobs, A. B. Shorey, D. Golini, W. I. Kordonski, S. Hogan, and P. Dumas, "Studies of Material Removal in Magnetorheological Finishing (MRF) from Polishing Spots," 101st Annual Meeting of the American Ceramics Society, Indianapolis, IN, 25–28 April 1999.

———————

The following presentations were made at CLEO/QELS 1999, Baltimore, MD, 23–28 May 1999:

A. Babushkin, W. A. Bittle, M. D. Skeldon, and W. Seka, "Diode-Pumped Regenerative Amplifier for the OMEGA Laser System."

A. Maksimchuk, J. Queneuille, G. Chériaux, G. Mourou, and R. S. Craxton, "Efficient Second-Harmonic Generation of Sub-100-fs Pulses from High-Power Nd:Glass Laser."

A. V. Okishev, "High-Repetition-Rate, Diode-Pumped, Multipass Preamplifier for the OMEGA Master Oscillator."

A. V. Okishev, D. Jacobs-Perkins, S. F. B. Morse, D. Scott, and W. Seka, "Prepulse Contrast Monitor for the OMEGA Drive Line."

M. D. Skeldon, A. V. Okishev, R. L. Keck, and W. Seka, "An Optical Pulse-Shaping System Based on Aperture-Coupled Striplines for OMEGA Pulse-Shaping Applications."

The following presentations were made at the 29th Annual Anomalous Absorption Conference, Pacific Grove, CA, 13–18 June 1999:

R. S. Craxton, D. D. Meyerhofer, S. P. Regan, W. Seka, R. P. J. Town, and B. Yaakobi, "Simulations of OMEGA Long-Scale-Length Plasmas Representative of the Transition Portion of NIF Direct-Drive Pulses."

J. A. Delettrez, S. P. Regan, T. R. Boehly, C. Stoeckl, D. D. Meyerhofer, P. B. Radha, J. Gardner, Y. Aglitskiy, T. Lehecka, S. Obenschain, C. Pawley, and S. Serlin, "Analysis of Planar Burnthrough Experiments on OMEGA and NIKE."

R. Epstein, T. J. B. Collins, J. A. Delettrez, V. N. Goncharov, S. Skupsky, R. P. J. Town, and B. Yaakobi, "Simulation of the Radiative Preheat of Target Foils and Shells in Laser-Driven Ablation and Implosion Experiments."

V. Yu. Glebov, D. D. Meyerhofer, P. B. Radha, W. Seka, S. Skupsky, J. M. Soures, C. Stoeckl, T. C. Sangster, S. Padalino, J. Nyquist, and R. D. Petrasso, "Tertiary Neutron Diagnostic by Carbon Activation."

V. N. Goncharov, "Modeling of Laser Imprint for OMEGA and NIF Capsules."

A. V. Kanaev and C. J. McKinstrie, "Numerical Two-Dimensional Studies of Near-Forward Stimulated Brillouin Scattering of a Laser Beam in Plasmas."

M. V. Kozlov and C. J. McKinstrie, "Analysis and Simulation of Sound Waves Governed by the Ion Fluid and Poisson Equations."

V. Lobatchev and R. Betti, "Numerical Study of Linear Feed-out of Short-Wavelength, Rear-Surface Perturbations in Planar Geometry."

C. J. McKinstrie and M. V. Kozlov, "Analysis and Simulation of Sound Waves Governed by the Korteweg–de Vries Equation."

D. D. Meyerhofer, R. Bahr, R. S. Craxton, S. P. Regan, W. Seka, R. P. J. Town, and B. Yaakobi, "Laser–Plasma Interactions in Plasmas Characteristic of the Direct-Drive NIF Foot-to-Main Drive Region."

S. P. Regan, J. A. Delettrez, T. R. Boehly, D. K. Bradley, J. P. Knauer, D. D. Meyerhofer, and C. Stoeckl, "Planar Burn-through Experiments on OMEGA and NIKE."

R. W. Short, "Forward SBS, Filamentation, and SSD."

V. A. Smalyuk, F. J. Marshall, D. D. Meyerhofer, and B. Yaakobi, "Imaging of Compressed Shells with Embedded Thin, Cold, Titanium-Doped Layers on OMEGA."

Y. Srebro, D. Oron, D. Shvarts, T. R. Boehly, V. N. Goncharov, O. Gotchev, V. N. Smalyuk, S. Skupsky, and D. D. Meyerhofer, "Hydrodynamic Simulations of Static and Dynamic Laser Imprint."

E. A. Startsev and C. J. McKinstrie, "Particle-in-Cell Simulation of Ponderomotive Particle Acceleration in a Plasma."

C. Stoeckl, V. Yu. Glebov, D. D. Meyerhofer, W. Seka, V. A. Smalyuk, and J. D. Zuegel, "Hard X-Ray Signatures for Laser–Plasma Instabilities on OMEGA."

The following presentations were made at ISEC '99, Berkeley, CA, 21–25 June 1999:

R. Adam, C. Williams, R. Sobolewski, O. Harnack, and M. Darula, "Experiments and Simulations of Picosecond Pulse Switching and Turn-on Delay Time in Y-Ba-Cu-O Josephson Junctions."

K. S. Il'in, A. A. Verevkin, G. N. Gol'tsman, and R. Sobolewski, "Infrared Hot-Electron NbN Superconducting Photodetectors for Imaging Applications."

J. L. Chaloupka and D. D. Meyerhofer, "Observation of Electron Trapping in an Intense Laser Beam," Applications of High-Field and Short-Wavelength Sources VIII Topical Meeting, Potsdam, Germany, 27–30 June 1999.

The following presentations were made by R. P. J. Town at the 1999 Fusion Summer Study Workshop, Snowmass, CO, 11–23 July 1999: "The OMEGA Laser System," "Rayleigh–Taylor Experiments on the OMEGA Laser," and "Direct-Drive Issues on the NIF."

The following presentations were made at SPIE's International Symposium on Optical Science, Engineering, and Instrumentation, Denver, CO, 18–23 July 1999:

S. R. Arrasmith, I. A. Kozhinova, L. L. Gregg, H. J. Romanofsky, A. B. Shorey, S. D. Jacobs, D. Golini, W. I. Kordonski, P. Dumas, and S. Hogan, "Details of the Polishing Spot in Magnetorheological Finishing."

D. D. Meyerhofer, T. Ditmire, N. Hay, M. H. R. Hutchinson, M. B. Mason, and J. W. G. Tisch, "Measurements of the Spatiotemporal Properties of High-Order Harmonics."

A. B. Shorey, L. L. Gregg, H. J. Romanofsky, S. R. Arrasmith, I. A. Kozhinova, and S. D. Jacobs, "A Study of Material Removal During Magnetorheological Finishing."

The following presentations were made at Inertial Fusion Sciences and Applications (IFSA) 1999, Bordeaux, France, 12–17 September 1999:

V. N. Goncharov, S. Skupsky, P. W. McKenty, J. A. Delettrez, R. P. J. Town, and C. Cherfiles-Clérouin, "Stability Analysis of Directly Driven OMEGA and NIF Capsules."

D. R. Harding, R. Q. Gram, M. D. Wittman, L. D. Lund, D. Lonobile, M. J. Shoup III, S. J. Loucks, G. Besenbruch, K. Schultz, A. Nobile, and S. Letzring, "Direct-Drive Cryogenic Targets and the OMEGA Cryogenic Target Handling System."

R. L. McCrory, R. E. Bahr, T. R. Boehly, T. J. B. Collins, R. S. Craxton, J. A. Delettrez, W. R. Donaldson, R. Epstein, V. N. Goncharov, R. Q. Gram, D. R. Harding, P. A. Jaanimagi, R. L. Keck, J. P. Knauer, S. J. Loucks, F. J. Marshall, P. W. McKenty, D. D. Meyerhofer, S. F. B. Morse, P. B. Radha, S. P. Regan, W. Seka, S. Skupsky, V. A. Smalyuk, J. M. Soures, C. Stoeckl, R. P. J. Town, M. D. Wittman, B. Yaakobi, J. D. Zuegel, R. D. Petrasso, D. G. Hicks, C. K. Li, and O. V. Gotchev, "OMEGA Experiments and Preparation for Direct-Drive Ignition on the National Ignition Facility."

D. D. Meyerhofer, T. R. Boehly, D. K. Bradley, T. J. B. Collins, J. A. Delettrez, Y. Fisher, V. N. Goncharov, O. Gotchev, J. P. Knauer, P. W. McKenty, S. P. Regan, W. Seka, S. Skupsky, V. A. Smalyuk, R. P. J. Town, and B. Yaakobi, "Direct-Drive Imprinting and Rayleigh–Taylor Experiments on OMEGA."

W. Seka, D. D. Meyerhofer, S. P. Regan, R. S. Craxton, B. Yaakobi, C. Stoeckl, A. Simon, R. W. Short, and R. E. Bahr, "NIF-Scale Direct-Drive Interaction on OMEGA."

S. Skupsky, T. J. B. Collins, R. S. Craxton, J. A. Delettrez, R. Epstein, V. N. Goncharov, P. W. McKenty, P. B. Radha, R. P. J. Town, D. D. Meyerhofer, W. Seka, and R. L. McCrory, "Simulation of OMEGA Experiments as a Prelude to Direct-Drive NIF Ignition Experiments."

B. Yaakobi, F. J. Marshall, V. Yu. Glebov, R. D. Petrasso, J. M. Soures, V. A. Smalyuk, D. D. Meyerhofer, W. Seka, J. A. Delettrez, and R. P. J. Town, "Spherical Implosion Experiments on OMEGA: Measurements of the Cold, Compressed Shell."

J. D. Zuegel, D. Jacobs-Perkins, J. Marozas, R. G. Roides, R. S. Craxton, J. H. Kelly, S. Skupsky, W. Seka, and S. Letzring, "Broadband Beam Smoothing on OMEGA with Two-Dimensional Smoothing by Spectral Dispersion."

S. R. Arrasmith, S. D. Jacobs, I. A. Kozhinova, A. B. Shorey, D. Golini, W. I. Kordonski, S. Hogan, and P. Dumas, "Development and Characterization of Magnetorheological Fluids for Optical Finishing," Fine Powder Processing '99, University Park, PA, 20–22 September 1999.

The following presentations were made at the Optical Society of America's Annual Meeting, Santa Clara, CA, 26 September–1 October 1999:

D. Golini and S. D. Jacobs, "Magnetorheological Finishing of Aspheres."

S. D. Jacobs, S. A. Arrasmith, I. A. Kozhinova, L. L. Gregg, H. J. Romanofsky, A. B. Shorey, D. Golini, W. I. Kordonski, P. Dumas, and S. Hogan, "Magnetorheological Finishing of KDP."